

Interactive Interfaces of Smart Composites

Dissertation

zur Erlangung des akademischen Grades

Doktor der Ingenieurwissenschaften

(Dr.-Ing.)

der Technischen Fakultät

der Christian-Albrechts-Universität zu Kiel

Sindu Shree

May 2019

Referent: Prof. Dr. Rainer Adlung

1. Koreferent: Prof. Dr. Anne Staubitz

2. Koreferent: Prof. Dr. Thorsten M. Gesing

Datum der mündlichen Prüfung: 22.08.2019

Zum Druck genehmigt: 22.08.2019

Dedicated to the strongest and
the kindest woman in my life,
Yashoda.

Abstract

A composite is a mixture of two or more materials with a clear phase difference, where, the fundamental components retain their significant properties hence the resultant mixture exhibits several unique behaviors. Fabrication of composites w.r.t., various applications and its analyses is the objective of the enclosed study. Carbon and tetrapodal ZnO based composite interfaces are utilized to improve gas sensing, optical, catalytic, thermal and electrical properties. Effects of shape and concentration of ZnO are optimized as an antibacterial filler in the electrospun poly(caprolactone) fibers.

In wind turbine blades, airplane wings, marine transportation and biomedical instrumentation a crucial issue lies in damage detection, a damage caused by any reason if not caught on time leads to acute material failure. This is life-threatening and also a growing reason for increased waste generation. Current work aims to provide an in-situ damage detection procedure to resolve this issue in a sophisticated at the same time a simplistic method. Inspired by human skin, self-reporting materials have been tested as damage detectors. Utilization of a molecular switch, spiropyran, as a self-reporter was proposed in the framework of SFB 677 (Function by Switching), project C-14. Spiropyran, a molecular switch, is studied for its multifunctionality as it can undergo reversible and visual transformation in response to various stimuli, mainly, light, heat and force. For the very first time, mechanochromism of spiropyran as a particle filler in a polymer composite is presented here. Furthermore, dependence of the type of matrix and reinforcement on the switchability of spiropyran is verified. A protocol to correlate the gradual color change of spiropyran in a polymer composite to the accumulated impact force is established. In addition, spiropyran functionalized polymeric fibers are investigated for strain induced color change.

Zusammenfassung

Ein Komposit stellt eine Mischung aus zwei oder mehr Materialien mit einer eindeutigen Phasenunterscheidbarkeit da. Dabei bleiben die kennzeichnenden Eigenschaften der Fundamentalkomponenten erhalten, infolgedessen das resultierende Material ein eigenes teils einzigartiges Verhalten aufweist. Die eingereichte Arbeit fokussiert sich auf die Herstellung von Kompositen mit Bezug auf unterschiedlichen Applikationen und deren Analysen. Kompositgrenzflächen werden zur Optimierung von Gassensoren, optischen, katalytischen, thermischen und elektrischen Eigenschaften verwendet. Im Fall von kohlenstoff- und Zinkoxide-(ZnO)Tetrapoden-basierten Kompositen wurde eine erhebliche Steigerung der vorhergenannten Eigenschaften beobachtet. Form und Konzentration von ZnO wurden zur Verwendung als antibakterieller Füller und deren Effektsteigerung in elektrogewebenen PCL Fasern optimiert. Weiterhin finden Komposite sich in einer Vielzahl Anwendungen wieder, zu welchen unter anderem Windturbinenblätter, Flugzeugflügel, Seetransportmittel und biomedizinische Instrumente zählen.

Allen diesen technischen Anwendungsfeldern ist die eminente Wichtigkeit einer eindeutigen und frühzeitigen Schadenserkennung gemein. Zu spät bemerkte Beschädigungen führen zu irreparablen Materialfehlern; somit zu Funktionsstörungen oder zu vorzeitigen Lebensdauerausfällen des Gesamtsystems und vermeidbarer Abfallerzeugung. Diese Arbeit liefert eine entsprechende *in-situ* Schadensdetektion, welche auf einer anspruchsvollen gleichzeitig vereinfachten Methodik basiert. Inspiriert durch menschliche Haut wurden selbstanzeigende Materialien als Schadensdetektor geprüft. Im Sonderforschungsbereich (SFB) 677 der Deutschen Forschungsgemeinschaft (DFG) „Funktion durch Schalten“ wird ein solches Selbstanzeigen durch die Nutzung von molekularen Schaltern generiert. Spiropyran untergeht eine reversible und visuell sichtbare Transformation als Reaktion auf physikalische Stimuli wie Licht, Wärme und mechanische Krafteinwirkung. Erstmals kann der Mechanochromismus von Spiropyran, welches als Partikelfüller in einem Polymerkomposit eingearbeitet wurde, beobachtet werden. In Abhängigkeit der verwendeten Matrix wurde eine Verstärkung der transformativen Schaltbarkeit von Spiropyran verifiziert. Eine direkte Beziehung und ein Protokoll zur Korrelierung des graduellen Farbwechsels von Spiropyran innerhalb einer gegebenen

Polymermatrix und einer akkumulierten Krafteinwirkung sind bestimmt worden. Zusätzlich wurden Polymerfasern, funktionalisiert durch Spiropryan, gemäß ihrem dehnungsinduzierten Farbwechsel untersucht

Contents

1. Introduction.....	6
2. Knowledge Integration.....	13
2.1. Composites	13
2.1.1. Synthesis of Micro- and Nano particles	14
2.1.2. Production and Application of Micro- and Nanocomposites.....	16
2.2. Analytical Methods to Characterize Nanocomposites	19
2.2.1. Raman Spectroscopy.....	19
2.2.2. Atomic Force Microscopy.....	26
2.3. Polymer Composites	30
2.3.1. Matrices and Reinforcement	30
2.3.2. Methods of Fabrication of Glassfiber Reinforced Polymer Composite	34
2.3.3. Sources of Damages and its Analyses	36
2.4. Self-Reporting Polymer and Polymer Composites	40
3. Interactions at the Interface of Tetrapodal ZnO and Fullerenes.....	45
4. Influence of Activated Carbon on the catalysis of Tetrapodal ZnO	71
5. Tetrapodal ZnO Decorated by Entangled MWCNTs	88
6. Antibacterial Scaffolds made of Fibrous Polymer Composite.....	123
7. Multi-functional Spiropyran based Polymer Composites	144
Light, Force, and Heat: A Multi-Stimuli Composite that Reveals its Violent Past	145
Mechanochromic Matrix Predicts Impact Induced Damage in a Reinforced Polymer Composite	165
Spiropyran based smart composites: Memorizing Polymer with Enhanced Molecular Switches.....	193
8. Spiropyran Functionalized Microfibers.....	196

9. Photoexpansion of Poly(silazobenzyl-siloxane) Thin Film.....	254
10. Inference and Outlook.....	301
List of abbreviations	304
List of Publications	305
Acknowledgements	307
Declaration	309

1. Introduction

Currently, materials and construction engineering on a global scale are based on composites. A single material struggles to meet all the requirements of a challenging and demanding advanced function. In contrast, a composite system built on well-tailored materials offer a single solution to a multitude of issues.^[1] Composites are categorized based on the fundamental substances used, e.g. ceramics, polymers and metals.^[2] Thereby, any two or more chemically inert materials can be combined to produce a composite. Successful usages of composites can be found in the automobile industry^[3,4], aerospace engineering^[5], biotechnology^[6] and medical science^[7,8]. A special group of self-reporting composite system assist in multiple stress exposed technologies, i.e., wind turbine blades, airplane wings, marine transportation and biomedical instrumentation. Preventive and early damage identification support the precise root-cause analysis and hinders the occurrence of material failures that lead to severe impairment.

A relatively new category, which saw a significant incline in development and application since the early 2000s is **hybrid nanointerfaces (HNI)**^[9-13], i.e., composite interfaces created by mixing different micro/nanomaterial for instance boron nitride coated copper nanowire^[13], ZnO particles in combination with metal nanoparticles^[14] etc. Due to their high surface to volume ratio, nano composites offer significantly improved electronic, optical and catalytic properties compared to their respective bulk forms. Advantages of nano interfaces can be found in numerous devices; to name a few, gas^[15] and thermal barriers^[16], thin film capacitors^[17], solid polymer electrolytes^[18], catalysts^[19]. Moreover, production of these hybrid material is less complicated than doping or alloying, as in the conventional semiconductor industrial process or challenging synthesis steps with high energy feed-ins are obsolete for hybrid composites, enabling cost efficient manufacturing.^[11,12,14-19] Several techniques of HNI fabrication have been proposed, this includes spray drying^[20], hydrothermal synthesis^[21], aerosol spray pyrolysis^[22], infiltration^[23] and sintering^[14]. In particular, production and applications of ZnO centered HNIs have been thoroughly explored.^[24-26] The thermal and chemical stability and the biocompatibility, elevates ZnO to be a valuable foundational material.^[27,28] The optical^[29], catalytic^[30] and electronic^[31]

properties of ZnO are shown to be adjustable by hybridization. The complex structures of ZnO offer variety of possibilities, specially tetrapods, they can be sintered into differently shaped and sized interconnected three-dimensional templates.^[28,32] The direct and wide band gapped ZnO (3.37 eV) can be stimulated with low powered ultraviolet (UV) light and the blue-green photoluminescence produced as a result of such stimulation can be altered by functionalization or hybridization.^[33,34] Furthermore, hybrid materials based on metal or metal oxide micro-, nano-structures can be processed as additives in **polymer composites** (PC).^[1] In a polymer matrix composite, carbon/glass fibers, CNTs, TiO₂, SiO₂, ZnO and Al₂O₃ nanoparticles, s.o., are utilized as nano fillers.^[35-38] Interconnected nano sized reinforcements have been observed to considerably enhance properties, e.g., modulus, strength, thermal and chemical stability of the matrix.^[37] Tetrapodal-ZnO (T-ZnO) as an additive has proven to enrich the antifouling property of polythiourethane (PTU)^[35], antibacterial activity of the electrospun poly(caprolactone) (PCL) fibers^[39] and has been observed to induce self-reporting property in polydimethylsiloxane (PDMS)^[40]. For many applications such as impellers, wind turbine blades, dental implants and self-reporting material PCs have been useful.^[1,37,40]

Continuous UV exposure can cause material decomposition, it is necessary to locate such affected areas of an instrument. While the force induced damages and initial stages of wear are especially hard to locate and minor errors arising during production can cause material failure on application of force. Under such circumstances self-reporting coatings play a very important role. The existing non-destructive postpartum analyses^[41] i.e., visual inspection^[42], acoustic waves-based technique^[43], pulsed ultrasonic and sonic spectroscopy^[41] and shearography^[44] of the reinforced polymer composites can perceive these types of damage. However, all these techniques exhibit the disadvantage of an inefficient source determination and the prediction of the material failure. Impairments caused by accumulated impact or compression are among the common cause of material failure in wind turbine blades, airplane wings and several other appliances.^[45,46] These inherently occurring damages are inevitable nevertheless, a complete material failure can be avoided by introducing a self-reporter i.e., an indicator which provides a signal in response to changes in its surrounding, may it be a sudden increase in UV irradiation or temperature or most importantly mechanical stress.

Self-reporting polymers are a common subject of research and in most studies a molecular switch is used as a reporter.^[47,48] Molecular switches are a class of organic molecules which transforms reversibly in response to various stimuli.^[49,50] Prominent examples are azobenzene^[51], diarylethenes^[52], spiropyrans,^[49] spirooxazines^[53] and diazocines^[50]. The presented collective research focuses on azobenzene and spiropyran, both of the switches can reversibly isomerize between *trans* and *cis* form. Spiropyran (colorless/yellow) answers to several triggers including force^[54], UV (365 nm)^[55] and temperature^[56] with a noticeable color change by undergoing a reversible C–O bond cleavage to form merocyanine (purple).^[57] This transformation can be reversed by visible light (530 nm) irradiation or by thermal relaxation.^[49,57] *trans*-Azobenzene folds at a N=N bridge to form *cis*-azobenzene under UV (365 nm) irradiation which can be reversed by blue light irradiation (450 nm) or by thermal relaxation at room temperature.^[51,58] Both the molecules can easily be functionalized to be incorporated into polymers. Azobenzene in a polymer can exhibit photomechanical behavior i.e., light initiated transformation of azobenzene imparts macroscopic movements.^[59,60] For such photomechanical effects azobenzene polymers have to be pre-aligned to behave like a liquid crystal.^[59,61–63] Likewise, spiropyran integrated into the backbone or sidechains of polymethacrylate (PMA)^[54], PMMA^[64], polyurethane (PU)^[65,66], polynorbornenes^[67], exhibits excellent reversible responses to the above mentioned stimuli. In various studies spiropyran has displayed high potential to operate as a self-reporter to light without its covalent integration into the polymers.^[68–70] Main objective of the current research is to utilize spiropyran as a composite to produce a stress, UV and temperature sensitive reinforced PC cost effectively. A quantitative method to recognize the accumulated impact force through the intensity of the color change is proposed.

In the given work, T-ZnO based HNIs with fullerenes were monitored for their modified optical and gas sensing properties in *chapter 3*, with activated carbon were studied for an efficient reduction of a highly hazardous waste water contaminant (hexavalent Cr) in *chapter 4*, and with MWCNTs were optimized to obtain a competent electrically and thermally conducting composite in *chapter 5*. Antibacterial and cell growth activities of the PCL/T-ZnO composite scaffold were investigated in *chapter 6*. The self-reporting ability of spiropyran as an additive in different matrices was investigated in *chapter 7* and the effects of different

reinforcements such as glassfibers and T-ZnO were examined as well. The mechanosensitivity of spiropyran functionalized PMA microfibers were explored in *chapter 8*. Lastly, photomechanical effect of the azobenzene-based polysiloxane film was analyzed in Chapter 9. The analytical methods that were utilized for in-depth investigations of the physical and chemical properties of the composites were periodic impact testing, Raman spectroscopy, AFM, UV-Visible spectroscopy and SEM. The given work is a developmental step towards producing inexpensive and eco-friendly construction material with *in-situ* sensors, to obtain a direct indication of damage before it leads to instrument malfunction.

References

- [1] R. M. Wang, S. R. Zheng, Y. P. Zheng, *Polymer Matrix Composites and Technology*, Woodhead Publishing Limited, Cambridge, UK, **2011**.
- [2] H. Altenbach, J. Altenbach, W. Kissing, in *Mech. Compos. Struct. Elem.*, Springer-Verlag, Berlin, **2004**, 1–14.
- [3] J. M. Garcés, D. J. Moll, J. Bicerano, R. Fibiger, D. G. McLeod, *Adv. Mater.*, **2000**, *12*, 1835.
- [4] J. Holbery, D. Houston, *J. Mater.* **2006**, *58*, 80.
- [5] P. E. Irving, C. Soutis, *Polymer Composites in the Aerospace Industry*, Woodhead Publishing, **2014**.
- [6] R. P. Wool, X. S. Sun, *Bio-Based Polymers and Composites*, Academic Press, Burlington, **2005**.
- [7] E. Salernitano, C. Migliaresi, *J. Appl. Biomater. Biomech.*, **2014**, *1*, 3.
- [8] S. Ramakrishna, J. Mayer, E. Wintermantel, K. W. Leong, *Compos. Sci. Technol.*, **2001**, *61*, 1189.
- [9] P. H. C. Camargo, Satyanarayana Kestur Gundappa, W. Fernando, *Mater. Res.*, 2009, *12*, 1.
- [10] E. Holder, N. Tessler, A. L. Rogach, *J. Mater. Chem.*, **2008**, *18*, 1064.
- [11] C. Ray, T. Pal, *J. Mater. Chem. A*, **2017**, *5*, 9465.
- [12] J. Li, S. Tang, L. Lu, H. C. Zeng, *J. Am. Chem. Soc.*, **2007**, *129*, 9401.
- [13] Y. Zhou, F. Liu, C.-Y. Chen, *Adv. Compos. Hybrid Mater.*, **2019**, *2*, 46.
- [14] O. Lupan, V. Postica, J. Gröttrup, A. K. Mishra, N. H. De Leeuw, J. F. C. Carreira, J. Rodrigues, N. Ben Sedrine, M. R. Correia, T. Monteiro, V. Cretu, I. Tiginyanu, D. Smazna, Y. K. Mishra, R. Adelung, *ACS Appl. Mater. Interfaces*, **2017**, *9*, 4084.
- [15] A. Das, A. Leuteritz, P. Kavimani Nagar, B. Adhikari, K. W. Stöckelhuber, R. Jurk, G. Heinrich, *Int. Polym. Sci. Technol.*, **2016**, *43*, 170.
- [16] X. Q. Cao, R. Vassen, F. Tietz, D. Stoeber, *J. Eur. Ceram. Soc.*, **2006**, *26*, 247.

- [17] R. N. Das, M. D. Poliks, J. M. Lauffer, V. R. Markovich, in *56th Electron. Components Technol. Conf.*, **2006**.
- [18] S. Song, Y. Wu, W. Tang, F. Deng, J. Yao, Z. Liu, R. Hu, Alamusi, Z. Wen, L. Lu, N. Hu, *ACS Sustain. Chem. Eng.*, **2019**, *7*, 7163.
- [19] Z. Xie, Z. Liu, Y. Wang, Q. Yang, L. Xu, W. Ding, *Int. J. Mol. Sci.*, **2010**, *11*, 2152.
- [20] A. Stunda-Zujeva, Z. Irbe, L. Berzina-Cimdina, *Ceram. Int.* **2017**, *43*, 11543.
- [21] S. Perera, R. G. Mariano, K. Vu, N. Nijem, O. Seitz, Y. Chabal, K. Balkus, *ACS Catal.*, **2012**, *2*, 949.
- [22] F. Iskandar, H. Chang, K. Okuyama, *Adv. Powder Technol.*, **2003**, *14*, 349.
- [23] F. Schütt, S. Signetti, H. Krüger, S. Röder, D. Smazna, S. Kaps, S. N. Gorb, Y. K. Mishra, N. M. Pugno, R. Adelung, *Nat. Commun.*, **2017**, *8*, 1.
- [24] R. N. Mariammal, C. Stella, S. S. Kanmani, S. Umopathy, K. Ramachandran, *AIP Conf. Proc.*, **2012**, *1447*, 391.
- [25] Y.-L. Chen, Z.-A. Hu, Y.-Q. Chang, H.-W. Wang, Z.-Y. Zhang, Y.-Y. Yang, H.-Y. Wu, *J. Phys. Chem. C*, **2011**, *115*, 2563.
- [26] F. Schütt, V. Postica, R. Adelung, O. Lupan, *ACS Appl. Mater. Interfaces*, **2017**, *9*, 23107.
- [27] A. Kolodziejczak-Radzimska, T. Jesionowski, *Materials*, **2014**, *7*, 2833.
- [28] Y. K. Mishra, R. Adelung, *Mater. Today*, **2018**, *21*, 631.
- [29] D. S. Kim, S. M. Lee, R. Scholz, M. Knez, U. Gösele, J. Fallert, H. Kalt, M. Zacharias, *Appl. Phys. Lett.*, **2008**, *93*, 17.
- [30] Y. Huang, R. Li, D. Chen, X. Hu, P. Chen, Z. Chen, D. Li, *Catalysts*, **2018**, *8*, 151.
- [31] L. Xu, B. Wei, W. Liu, H. Zhang, C. Su, *Nanoscale Res. Lett.*, **2013**, *8*, 1.
- [32] Y. K. Mishra, S. Kaps, A. Schuchardt, I. Paulowicz, X. Jin, D. Gedamu, S. Wille, O. Lupan, R. Adelung, *KONA Powder Part. J.*, **2014**, *31*, 92.
- [33] X. D. Zhou, X. H. Xiao, J. X. Xu, G. X. Cai, F. Ren, C. Z. Jiang, *Europhysics Lett.*, **2011**, *93*, 57009.
- [34] J. Rodrigues, D. Smazna, N. Ben Sedrine, E. Nogales, R. Adelung, Y. K. Mishra, B. Mendez, M. R. Correia, T. Monteiro, *Nanoscale Adv.*, **2019**, 1516.
- [35] I. Hölken, M. Hoppe, Y. K. Mishra, S. N. Gorb, R. Adelung, M. J. Baum, *Phys. Chem. Chem. Phys.*, **2016**, *18*, 7114.
- [36] N. Hamedi, S. Hassanajili, M. T. Sajedi, *Silicon*, **2018**, *10*, 1243.
- [37] T. P. Sathishkumar, S. Satheeshkumar, J. Naveen, *J. Reinf. Plast. Compos.*, **2014**, *33*, 1258.
- [38] V. Choudhary, A. Gupta, in *Carbon Nanotub. Polym. Nanocomposites*, InTech, **2011**, 64-90.
- [39] A. Nasajpour, S. Ansari, C. Rinoldi, A. S. Rad, T. Aghaloo, S. R. Shin, Y. K. Mishra, R. Adelung, W. Swieszkowski, N. Annabi, A. Khademhosseini, A. Moshaverinia, A. Tamayol, *Adv. Funct. Mater.*, **2017**, *28*, 1703437.
- [40] X. Jin, M. Götz, S. Wille, Y. K. Mishra, R. Adelung, C. Zollfrank, *Adv. Mater.*, **2013**, *25*, 1342.
- [41] R. Yang, Y. He, H. Zhang, *Renew. Sustain. Energy Rev.*, **2016**, *60*, 1225.
- [42] S. Ataya, M. M. Z. Ahmed, *Eng. Fail. Anal.*, **2013**, *35*, 480.

- [43] A. Jüngert, in *7th Fib PhD Symp. Stuttgart, Ger.*, **2008**, 1.
- [44] Y. Y. Hung, Y. S. Chen, S. P. Ng, L. Liu, Y. H. Huang, B. L. Luk, R. W. L. Ip, C. M. L. Wu, P. S. Chung, *Mater. Sci. Eng. R Reports*, **2009**, 64, 73.
- [45] V. Giurgiutiu, *Structural Health Monitoring of Aerospace Composites*, Academic Press, Oxford, **2016**.
- [46] C. C. Ciang, J. R. Lee, H. J. Bang, *Meas. Sci. Technol.*, **2008**, 19.
- [47] K. Makyła, C. Müller, S. Lörcher, T. Winkler, M. G. Nussbaumer, M. Eder, N. Bruns, *Adv. Mater.*, **2013**, 25, 2701.
- [48] O. Rifaie-Graham, E. A. Apebende, L. K. Bast, N. Bruns, *Adv. Mater.* **2018**, 30, 1.
- [49] R. Klajn, *Chem. Soc. Rev.*, **2014**, 43, 148.
- [50] B. L. Feringa, W. R. Browne, *Molecular Switches*, Wiley-VCH Verlag GmbH & Co. KGaA, Weinheim, Germany, **2011**.
- [51] H. M. D. Bandara, S. C. Burdette, *Chem. Soc. Rev.*, **2012**, 41, 1809.
- [52] T. Fukaminato, S. Ishida, R. Métivier, *NPG Asia Mater.*, **2018**, 10, 859.
- [53] V. A. Lokshin, A. Samat, A. V. Metelitsa, *Russ. Chem. Rev.*, **2002**, 71, 893.
- [54] D. A. Davis, A. Hamilton, J. Yang, L. D. Cremer, D. Van Gough, S. L. Potisek, M. T. Ong, P. V. Braun, T. J. Martínez, S. R. White, J. S. Moore, N. R. Sottos, *Nature*, **2009**, 459, 68.
- [55] B. Seefeldt, R. Kasper, M. Beining, J. Mattay, J. Arden-jacob, N. Kemnitzer, K. Heinz, M. Heilemann, M. Sauer, *Photochem. Photobiol. Sci.*, **2016**, 9, 213.
- [56] C. F. Koelsch, *J. Org. Chem.*, **1962**, 419, 1362.
- [57] M. Schulz-Senft, P. J. Gates, F. D. Sönnichsen, A. Staubitz, *Dye. Pigment.* **2017**, 136, 292.
- [58] T. Schultz, M. Z. Zgierski, J. Quenneville, T. J. Martinez, S. Ullrich, A. Stolow, *Femtochemistry and Femtobiology*, Elsevier Science, Paris, France, **2007**, 45-48.
- [59] E. Kizilkan, J. Strueben, X. Jin, C. F. Schaber, R. Adelung, A. Staubitz, S. N. Gorb, *R. Soc. Open Sci.*, **2016**, 3.
- [60] H.-K. Kim, X.-S. Wang, Y. Fujita, A. Sudo, H. Nishida, M. Fujii, T. Endo, *Macromol. Rapid Commun.*, **2005**, 26, 1032.
- [61] S. L. Oscurato, M. Salvatore, P. Maddalena, A. Ambrosio, *Nanophotonics*, **2018**, 7, 1387.
- [62] Z. Mahimwalla, K. G. Yager, J. Mamiya, A. Shishido, A. Priimagi, C. J. Barrett, *Polym. Bull.* **2012**, 69, 967.
- [63] K. M. Lee, N. V. Tabiryan, T. J. Bunning, T. J. White, *J. Mater. Chem.*, **2012**, 22, 691.
- [64] J. R. Hemmer, P. D. Smith, M. Van Horn, S. Alnemrat, B. P. Mason, J. R. De Alaniz, S. Osswald, J. P. Hooper, *J. Polym. Sci. Part B Polym. Phys.*, **2014**, 52, 1347.
- [65] C. K. Lee, B. A. Beiermann, M. N. Silberstein, J. Wang, J. S. Moore, N. R. Sottos, P. V Braun, *Macromolecules*, **2013**, 46, 3746.
- [66] L. Oggioni, C. Toccafondi, G. Pariani, L. Colella, M. Canepa, C. Bertarelli, A. Bianco, *Polymers*, 2017, 9, 462.
- [67] L. Hauser, A. C. Knall, M. Roth, G. Trimmel, M. Edler, T. Griesser, W. Kern, *Monatshefte für Chemie*, **2012**, 143, 1551.
- [68] E. Samoylova, L. Ceseracciu, M. Allione, A. Diaspro, A. C. Barone, A. Athanassiou, *Appl.*

- Phys. Lett.*, **2011**, 99, 1.
- [69] M. Bremer, R. Reinke, B. Hesseler, M. Taale, D. Ingwersen, S. Schwarzer, C. Selhuber-Unkel, M. Gerken, *J. Nanomater.*, **2017**, 2017, 1.
- [70] J. Bonafino, M.-L. V. Tse, C.-F. J. Pun, X. Cheng, W. K. E. Chan, A. Boersma, H.-Y. Tam, *Opt. Photonics J.*, **2013**, 03, 11.

2. Knowledge Integration

This section provides a theoretical background on the materials and the analytical methods employed within the given work. Also elaborates the motivation of the current study. Further extensive information to the following topics: types of composites, their synthesis, applications and analyses.

2.1. Composites

By definition, a composite is a combination of physically and chemically different substances which are not altered when grouped together, however, is collectively used to enhance particular properties.^[1,2] Application of artificial composites range from automobile and aerospace components, orthopedic and dental surgeries, Li-ion batteries and catalysis.^[1,3] Composite systems can be exercised with various materials such as metals, wood, ceramics, polymers as a matrix and glass and carbon fibers, micro and nano semiconductor particles, as reinforcing additives (**Figure 1**).^[4] Without matrix composites are well-known as hybrid materials and are used to enhance optical, thermal and electrical conductivity in conducting and semiconducting particles.^[4]

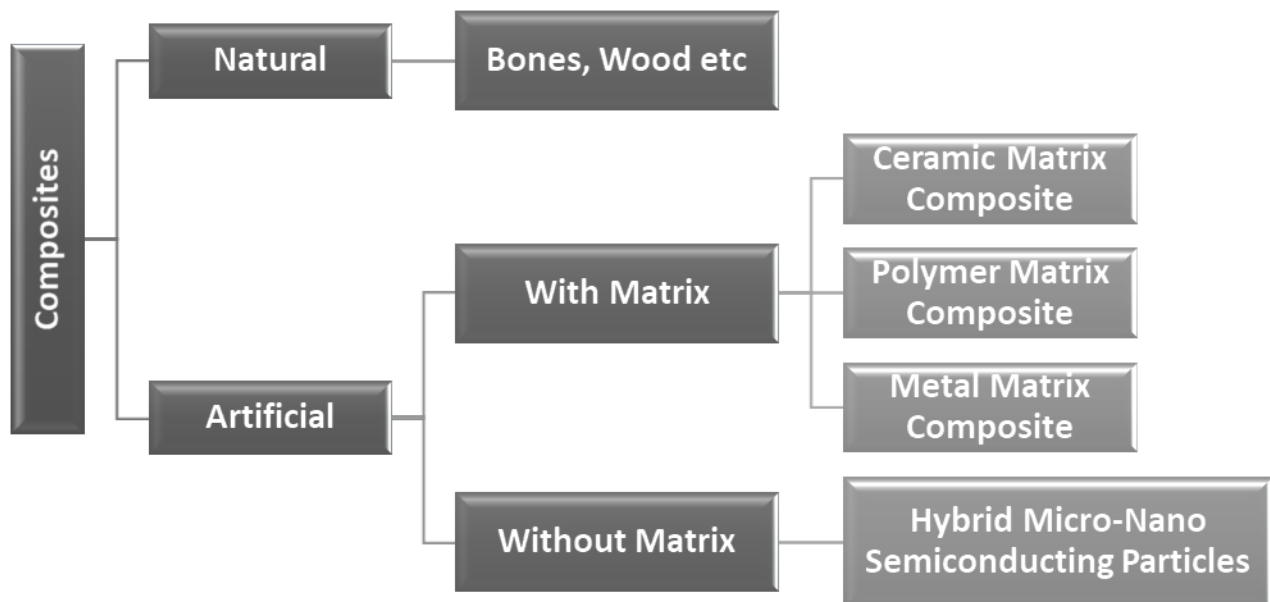


Figure 1. Categorization of composites based of their occurrence and the fundamental materials utilized.

2.1.1. Synthesis of Micro- and Nano particles

Industrially applicable nanomaterials, e.g. CNTs, TiO₂, ZnO, Al₂O₃, Si and SiO_x particles of different shapes are conventionally produced by sol-gel process, nano structuring, chemical vapor condensation and flame-based synthesis. [5-7] This subchapter provides brief descriptions on the syntheses of the micro- and nanomaterials that were mainly utilized in the given work.

- Flame transport synthesis (FTS) is only one of many well-known methods to produce particles for composites and was mainly employed as it is a rapid and comparably simple method to produce various structures of numerous metal oxides. Among the metal oxide semiconductors due to its versatility, T-ZnO is a highly utilized base material for composites, three-dimensional templates, and reinforcing PMCs. A strong luminescence, wide band gap (3.37 eV) and the tetrapodal shape makes T-ZnO the most suitable composite material to enhance electrical, mechanical and optical properties of a system. Hence, micro-, nano-tetrapodal ZnO particles were produced by FTS. This method of T-ZnO production involves zinc powder and polyvinyl butyral (PVB). The Zn powder and PVB are mixed at 1:2 weight ratio and taken in a ceramic crucible. The crucible is then placed in a muffle furnace pre-heated to 500 °C. A source of pressured air is provided from the rear end of the furnace. Constant flow of pressured air helps to keep the furnace temperature constant. After 30 min of process time the crucible is removed from the furnace and cooled before collecting the low-density particles.[8] These particles can be processed depending on the application.[9] Also, FTS can be modified to produce other metal oxide particles such as SnO₂.

- Carbon based material such as CNTs, fullerenes, graphite and graphene oxide are among the most used substances to produce composites.[1] They are cost efficient to produce, combination of carbon-based material and metal oxides provide high versatility.[10,11] CNTs are fabricated by electric arc discharge, laser ablation and chemical vapor deposition (CVD), s.o., the obtained CNTs are later purified to remove catalysts and carbon precursors.[12] Mass production of fullerenes, graphite and graphene have also been established and more information can be found in the work published by Kelly et al.[13]

- An alternative to graphite anodes in Li-ion batteries is an array of Si microwires, fabricated by lithographic nano structuring of p-Si followed by macropore etching. Stepping away from the conventional methods of fabrication Hansen et al.,^[14] present a non-aqueous, macro-pore etching process in organic electrolyte combined with 10 wt% hydrofluoric acid (HF) and polyethylene glycol (PEG). Wires of 70 μm length and 1.2 μm diameter showed highest stability during cycling and Li uptake. Following the method described by Föll et.al.,^[15] production of desired shapes and sizes of Si wires is feasible.

In the current work, these micro-nano structures were further used as the base material for creating hybrid composites.

2.1.2. Production and Application of Micro- and Nanocomposites

An approach of effectively enhancing a particular functionality of a material is to create nanocomposites, as they further improve multiple properties. Selected hybrid materials and known methods of producing them are discussed here.

- The T-ZnO particles produced by the FTS can be pressed into desired shapes and sizes (see **Figure 2**) and sintering these forms at 1150 °C for 5 h increases the interconnections for stability. A composite made from infiltrating a cylindrical template of T-ZnO with CNTs as published in Schütt et.al.,^[16] showed improved temperature selectivity in ammonia sensors.^[11]

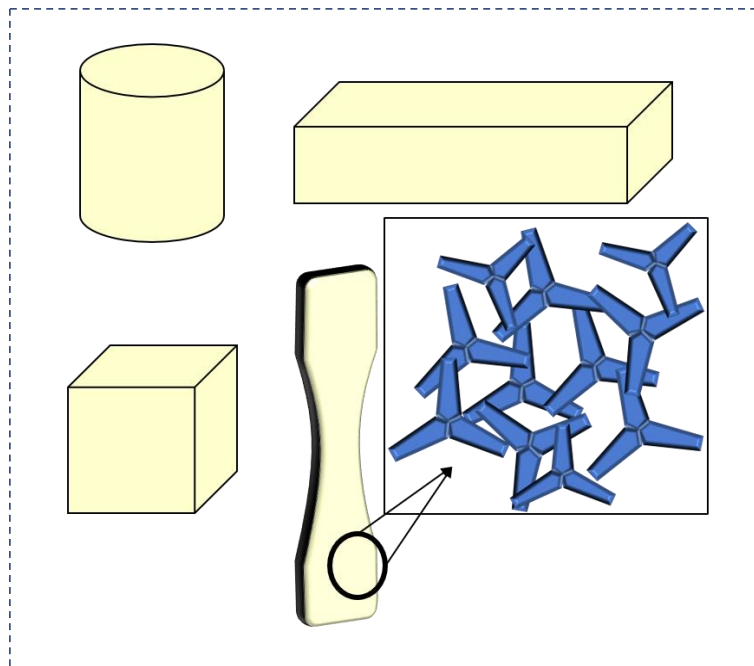


Figure 2. Three-dimensional interconnected network of T-ZnO particles produced by the FTS pressed into different forms and these shapes are stabilized by sintering at 1150 °C for 5 h.

Following the same principle, a composite of hollow tetrapodal networks of CNTs and bioactive quartz are fabricated by reducing the ZnO in an H₂ atmosphere after infiltrating the sacrificial T-ZnO template. This hollow network CNTs hybridized with bioactive quartz is used as a scaffold for osteoblast growth.^[17]

- A well-known light weight material, aerographite^[18], produced following the CVD process using a sacrificial T-ZnO template was decorated with Si/SiO_x nanoparticles in the

study by Smazna et.al.^[19] Aerographite was glazed with Si/SiO_x nanoparticles in an atmospheric plasma chamber by introducing hexamethyldisiloxane (HMDSO) into the effluent plasma jet.

- Another possibility of hybridization is by chemical deposition, Smazna et.al.,^[20] present a method of ZnO-Ga₂O₃ composite fabrication. The ZnO microwires were immersed under UV irradiation for 12 h in a solution made by dissolving gallium acetylacetonate in chloroform. Post chemical treatment the coated microwires were annealed at 600 °C for 1 h in O₂ or Ar atmosphere.^[20]

- Ultra-thin films of TiO₂ (thickness: 15-45 nm) fabricated by atomic layer deposition (ALD) when sputtered with gold nanodots created a composite that is highly UV sensitive. The photoconductivity in Au functionalized TiO₂ film increases due to the Schottky barrier created at the nanoscale interface between the anatase TiO₂ film and Au nanoclusters. These nano-interfaces enhance the electron depletion region and suppress electron-hole recombination in turn improving the UV sensing of the film by an order of magnitude.^[21]

- Similar studies as above were performed on the UV, gas and gas/vapor sensing properties of TiO₂ thin films functionalized with Au and Ag nanodots and Ag-Pt and Ag-Au bimetal nanoclusters. The TiO₂ thin films were produced by the aerosol spray pyrolysis technique.^[22] A mixture of titanium diisopropoxide (TTIP), acetylacetone and isopropanol in appropriate was fed into the spraying chamber with oxygen gas flux. After spraying, the thin films were annealed at 450 °C for 1 h. The heat treated TiO₂ films were sputtered with solo metal and bimetal nanodots to enhance its sensitivity.^[22]

- Spray drying is a technique adopted when large quantities of multicomponent hybrid materials with narrow size distribution are required. This is a slurry-based method to produce single- or multicomponent granules or spherical particles.^[23-25] The slurry is prepared by dispersing the desired primary powders in a solvent and for composites, the particles are mechanically pre-mixed before dispersion and this mixture is fed into a rotary atomizer for droplet formation. These droplets are sprayed and dried, the generated particles are then collected. Some of the examples of hybrid composites produced with spray drying are ZrO₂-Al₂O₃, MWCNTs coated Na₂FePO₄F and TiO₂ in combination with mica and h-BN are.

Size and shape distribution of the particles depends mainly on the type of solvent, viscosity of the mixture, concentration, humidity and temperature.^[23,24]

Presented study in the *chapters 3* and *5*, three-dimensional templates made of interconnected T-ZnO network were uniformly infiltrated with dispersions of fullerenes and MWCNTs respectively. Post infiltration the templates were dried appropriately before testing their properties. In the chapter 4, T-ZnO/activated carbon composite was synthesized hydrothermally, more details on this can be found in the referenced chapter.

2.2. Analytical Methods to Characterize Nanocomposites

Crucial point of any study is its post experimental analysis, which helps narrow down the material combinations that works best for the required function. Post analyses assist in understanding the reasons for a material failure as well. Some of the known techniques to analyze physical structural stability and morphology of a nanocomposite are scanning electron microscopy (SEM), X-ray diffractogram (XRD) and atomic force microscopy (AFM). Methods to study chemical structural stability and crystallography of a composite before and after the experiments are transmission electron microscopy (TEM), Raman spectroscopy, so forth. This chapter provides a brief summary of the working principle of Raman spectroscopy and AFM, methods that were mainly employed in the given work and a few dedicated examples to introduce the upcoming study. Detailed descriptions of the fundamental working principles can be found elsewhere.

2.2.1. Raman spectroscopy

Raman spectrometer measures signature molecular motions induced by monochromatic light. This enables unambiguous identification of materials and bonding nature. Inelastic scattering of an incident photon produced as a result of its interaction with matter is called Raman scattering.^[26] Incident photons scatter with lower or higher energy after causing nuclear motion (elaborated in **Figure 3**).

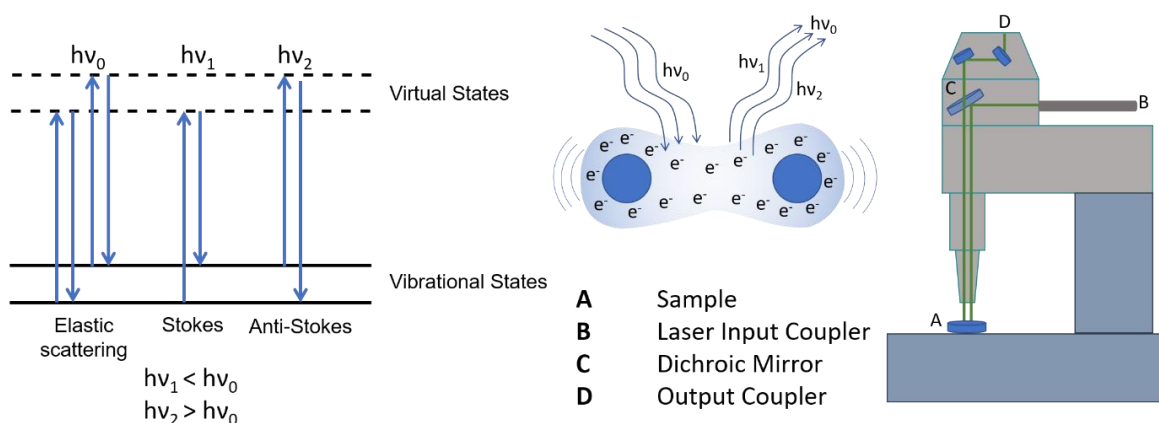


Figure 3. On the left is a schematic of the scattering processes. In the middle is a sketch of the interaction between the incident photons and a molecule, showing elastic and inelastic scattering. On the right is a representative image of the WITec RA 300 spectrometer.

The electron-phonon mediated photon scattering makes Raman spectroscopy especially useful in studying carbon-based materials and semiconductors. Essential information such as degree crystallinity or oxidation and defects can be obtained from a Raman spectrum. The following sections provide direct examples of Raman spectroscopy as an analytical procedure for the resulting data.

- **Crystallinity of Silicon**

Due to the disorderness and dangling bonds present in an amorphous Si, crystallinity has a direct co-relation to the conductivity of Si.^[27] The dangling bonds or other defects create efficient recombination centers for electrons and holes decreasing conductivity.^[27] Degree of crystallinity of Si microstructures can simply be tracked by Raman spectrometer. The characteristic first-order peak of Si shows up at $\sim 520\text{ cm}^{-1}$ (see **Figure 4(a)**) due to degenerated transverse optical (TO) phonon modes and a second-order transverse optical phonons cause a peak at $\sim 960\text{ cm}^{-1}$. A second-order transversal acoustic phonon contribute to the peak at $\sim 300\text{ cm}^{-1}$ (**Figure 4(a)**).^[26] Shape and position of the first-order peak depends on the symmetry of the Si crystal. This peak shows a red shift when oxidized or amorphized.^[14,28] As conductivity decreases with decreasing degree of crystallinity in Si, this is a vital information to have for a battery with a Si anode. In study by Hansen et.al,^[14] on Li-ion battery, Raman spectroscopy was employed to investigate the solid electrolyte interface (SEI) and the effects of various combinations of electrolytes on the structural stability of Si microwires (**Figure 4**).

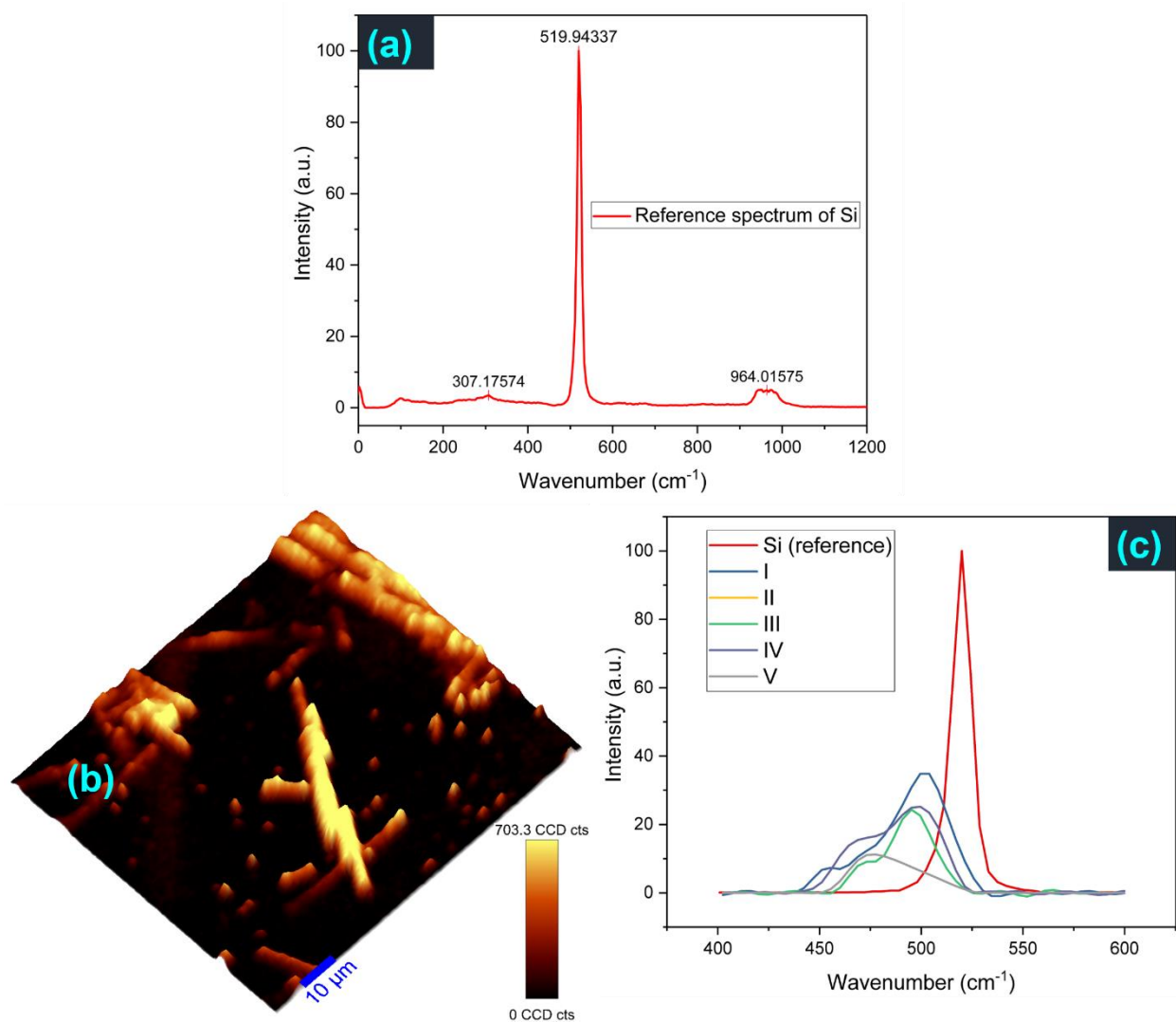


Figure 4. Investigation of crystallinity of Si under scanning Raman spectroscopy. (a) Reference Raman spectrum of Si showing characteristic peaks. (b) Raman map of Si microwires acquired before lithiation at the distinctive first-order peak of Si at ~ 520 cm^{-1} with its corresponding scalebar. (c) Raman spectra of reference Si and Si microwires acquired after lithiation at different spots.

During the electrolyte-electrode interaction oxygen diffuses through the SEI, oxidizing the Si microwires. Uniform crystallinity of Si wires before lithiation is shown in the Raman map (**Figure 4(b)**) acquired at ~ 520 cm^{-1} . The same Si wires cycled in diethylene carbonate (DEC) showed a drastic effect on its crystallinity. Except the reference spectrum in **Figure 4(c)**, the spectra (I-V) were extracted from various spots on different wires. The large shift in the TO mode from ~ 499 to 473 cm^{-1} and the change in symmetry of the peak indicate a systematic amorphization. Such study helps in determining the most suitable electrolyte and other parameters for the lithiation and delithiation of Si microwires.^[14]

- **A study of defects in ZnO**

Defects play an important role in the photocatalytic behavior as in the electrical and thermal conductivity in ZnO. An exemplary study of the semiconductor, ZnO, was conducted under Raman spectrometer to track its surface defects, oxygen and Zn vacancies. ZnO is a group II-VI semiconductor with a wide band gap (3.37 eV), making it photocatalytic under UV irradiation. ZnO possess a hexagonal wurtzite-type unit cell (space group, P6₃mc) and can be grown in complex shapes such as tetrapods, needles, wires etc.^[9] The tetrahedron ZnO (i.e., each Zn²⁺ ion is surrounded by four O²⁻ ions and vice versa) has 12 lattice phonons (9 optical and 3 acoustic), this can be expressed as following: $\Gamma = 2A_1 + 2B_1 + 2E_1 + 2E_2$ (where, A and B represent modes with one-fold degeneracy and E represents modes with two-fold degeneracy).^[29] Going by the studies of Schumm et al.,^[30] and Russo et.al.,^[31] and Wong et.al.,^[32] the two B₁ modes are inactive, the two E₂ modes are only Raman active (E₂ modes are divided depending on its frequencies E₂^{low} and E₂^{high}), a pair of E₁ mode and an A₁ mode are both Raman and IR active (these polar phonon modes are further divided into LO, longitudinal optical and TO, transverse optical components).^[30-32] These are the nine optical phonons. As for the rest, an A₁ mode and a pair E₁ modes are the acoustic phonons.^[33] In the signature Raman spectrum of ZnO, there are six primary peaks. Values with its corresponding labels and description listed below (**Table 1** and **Figure 5**) were the acquired from the T-ZnO network post sintering. These sintered templates were employed further in composite preparation.

Table 1. Represents labelled Raman shift and the direction of lattice vibration w.r.t c-axis observed in sintered interconnected network of T-ZnO produced by FTS.

Labels	Raman shift (cm ⁻¹)	Displacement to c-axis
E ₂ ^{low} (heavy Zn sub-lattice)	104.79	Perpendicular
E ₂ ^{high} (O rich sub-lattice)	442.31	Perpendicular
A ₁ (TO)	335.68	Parallel
A ₁ (LO)	547.67	Parallel
E ₁ (TO)	384.71	Perpendicular
E ₁ (LO)	582.51	Perpendicular

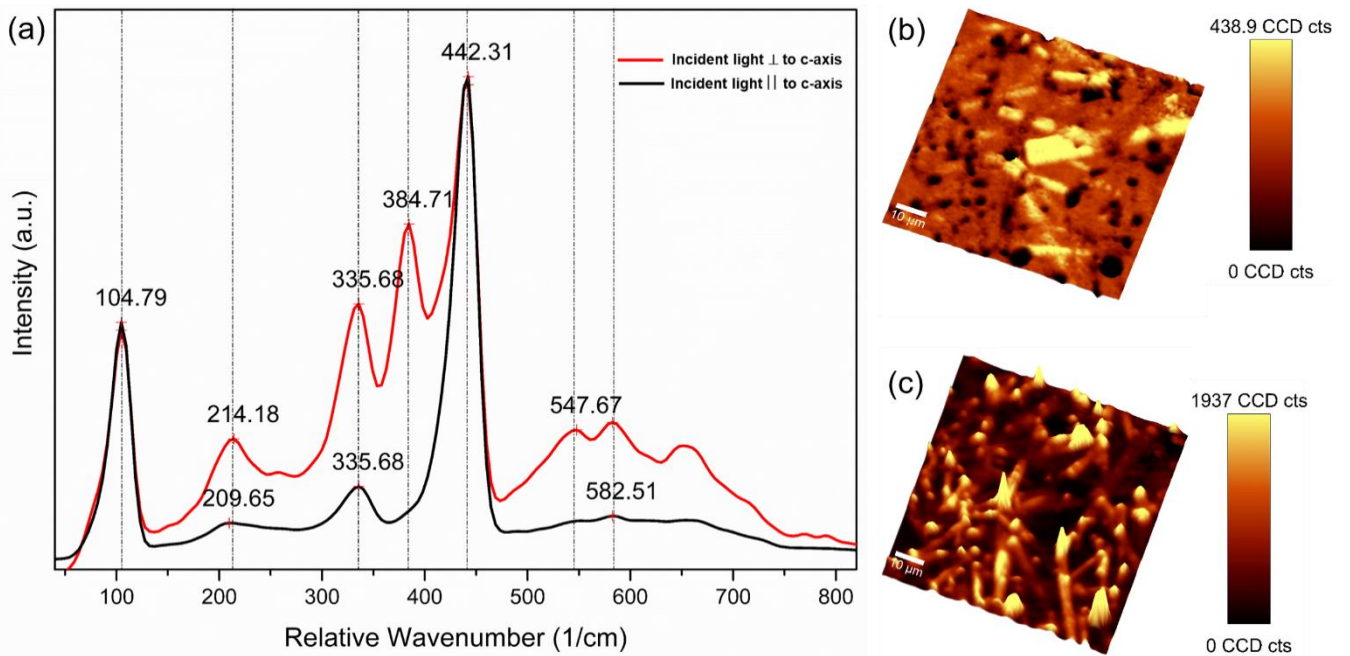


Figure 5. Raman spectra and $80 \times 80 \mu\text{m}^2$ scans ($\lambda_{\text{ex}}, 532 \text{ nm}$ and integration time 43 ms) of a sintered interconnected network of T-ZnO produced by FTS. (a) Raman spectra extracted from two different areas in a scan, the red spectrum extracted from the scan (b) and the black spectrum extracted from the scan (c). (b) and (c) Subsequent Raman maps a sintered T-ZnO network measured at the peak, 384.71 cm^{-1} and 442.31 cm^{-1} respectively.

Key difference between the Raman spectra extracted from different parts of tetrapods is the peak at 384.71 cm^{-1} . This peak is associated with rigid sub-lattice vibrations perpendicular to c-axis and is not accessible from every direction of incidence.^[31,34] Crystals with its c-axis perpendicular to the incident light expose the polar $E_1(\text{TO})$ oscillations enhancing its intensity. Although not every crystal that is perpendicular to the incident light shows this peak, this is a sign of point defects such as oxygen vacancies and Zn interstitials. At these sites, intensity of the characteristic peak of ZnO (442.31 cm^{-1}) reduces similarly observed by Das et.al., indicating disorderness.^[34,35] Commonly observed phenomenon is the rise of peaks between $570\text{-}590 \text{ cm}^{-1}$ due to structural defects.^[30,34,36]

- **Quantitative studies of carbon-based material via Raman spectroscopy**

Sensitivity of Raman spectroscopy towards symmetric covalent bands with no natural dipole moment is extraordinary. Effects of ambient conditions on the carbon-based material in a nanocomposite can also be studied using Raman spectroscopy. Characteristic Raman

peaks of MWCNT networks, fullerenes and graphene-oxide (see **Figure 6**) with its labels are listed in the **Table 2**.^[37,39]

Table 2. Characteristic Raman peaks and its labels of different carbon-material

Type of Carbon material	Labels	Raman shift (cm ⁻¹)
Graphene-Oxide	D-band	1348.95
	G-band	1591.74
	G'-band	2668.86
Fullerene, C ₆₀	D-band	1331.81
	Pentagonal pinch mode	1462.21
	G-band	1575.12
MWCNTs	D-band	1336.86
	G-band	1572.27

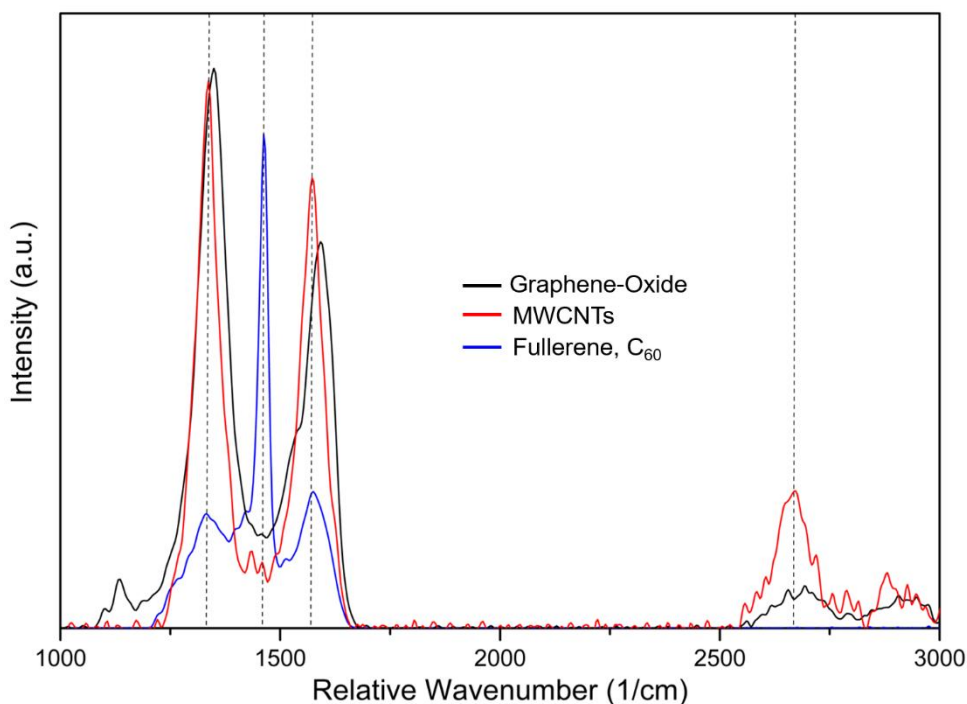


Figure 6. Different carbon-materials such as graphene-oxide, MWCNTs and C₆₀ were investigated under Raman spectrometer (single spectrum, integration time: 0.5 s, accumulation: 10). Dotted lines show the shift in the characteristic peaks due to varying structures.

Even though it the same C-C bonding in all the tested carbon-material, that gives rise to these peaks (see **Figure 6**), the structure of the material causes shows red or blue shift.^[37,38] Slightest Changes in these peaks is a clear evidence of any structural (e.g. defects, disorderness and s.o.) or electronic modification. Hence is a significant tool in analyzing carbon-material based nanocomposites.^[37,39]

The investigations represented here were performed under WITec Alpha RA 300 spectrometer (**Figure 3**) installed with two lasers 532 and 633 nm (with corresponding laser powers 60 mW and 35 mW) was employed to analyze the chemical composition of the nanocomposites in the presented study. As this is a scanning Raman microscope with a laser spot of 1.5 μm , area up to 200 μm^2 can be measured. The scattered photons are collected and integrated by a 100 μm glassfiber. In the framework of the given work, Raman spectra of carbon-ZnO nanointerfaces were compared to these experimental and literature values for in-depth assessment.

2.2.2. Atomic force microscopy

Atomic force microscopy helps quantify relative height, topography and roughness of a surface. These parameters are especially important when working with thin films. After growing or depositing the thin films it is necessary to know their surface morphology, as the electrical, mechanical and optical properties depend on the uniformity of the film. Surface roughness is a controlling parameter in catalytic experiments. In an AFM, a laser spot focused on an oscillating cantilever is reflected onto a photodiode to track its deflection that occurs due to the interaction between the tip and surface (see **Figure 7(a)**).

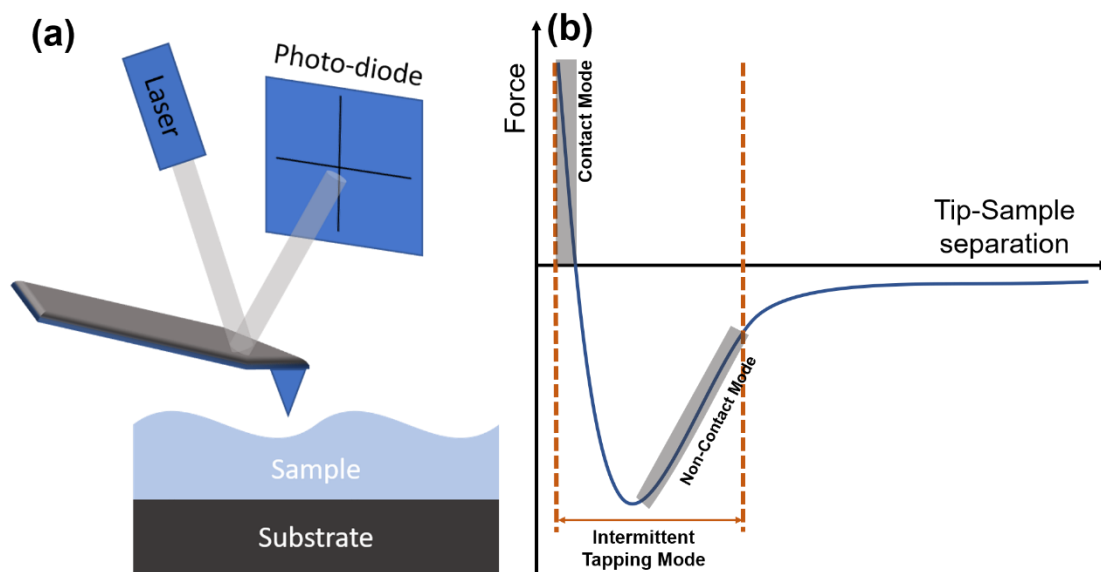


Figure 7. (a) Sketch of an AFM set-up showing its basic working principle, a laser spot is focused on the cantilever and the tip interacts with the surface of the sample. (b) Representation of Lennard-Jones potential approximation applied to determine the suitable mode to work in.

From the Lennard-Jones potential approximation,^[40] the distance between the sample and tip governs the type of force between them (**Figure 7(b)**). The contact mode and non-contact mode operate merely in repulsive and attractive regime respectively.^[40] In the intermittent tapping mode, a cantilever (with spring constant, 2-200 Nm^{-1}) oscillates between attractive and repulsive regime at a frequency of 50-300 kHz.^[40] The surfaces examined in the given work were measured in tapping mode. Depending on the material being tested resonance frequency is chosen. It is a non-destructive method to map a surface.

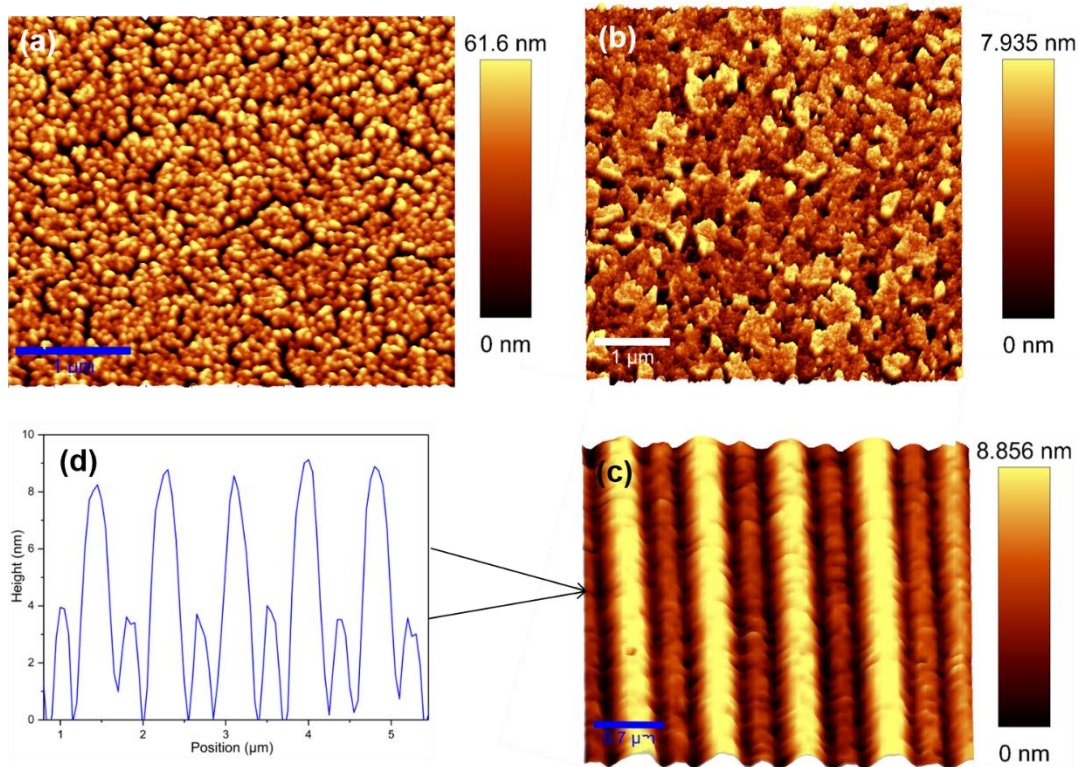


Figure 8. (a) A topographical scan of a sputtered TiO_2 thin film alongside its corresponding scale bar (b) A topographical 3D image of a quartz substrate coated with clusters of ZnO nanoparticles, beside it is its scale bar. (c) Is a 3D topographical images of fringes on a Si surface created by a pulsed laser irradiation, analogous scale bar is presented next to it. (d) Is a height vs position plot extracted from the scan (c) to calculate the average height of the fringes.

Exemplary measurements are presented in the **Figure 8**. A topographical scan of a TiO_2 thin film (see **Figure 8(a)**) fabricated in a custom-made unipolar reactive pulsed DC magnetron sputtering chamber. As the surface roughness determines the photocatalytic activity of the TiO_2 , AFM is a crucial tool for studying the deposited nano films. Average roughness of the presented scan was calculated to be ~ 13 nm.^[41] A surface roughness study on clusters of ZnO nanoparticles coated on a quartz substrate is shown in **Figure 8(b)**, average roughness of the surface was measured to be 1.72 nm. Another example topographical study presented is a Si surface structured with a pulsed laser (**Figure 8(c)**) and the aim was to distinguish the interference pattern created on the surface, heights of the large and small fringes are $8.58 \text{ nm} \pm 0.53$ and $3.9 \text{ nm} \pm 0.57$ respectively. These measurements were obtained from the WITec RA 300 spectrometer, which is installed with a possibility to perform AFM scans as well. The cantilevers used to measure the here

presented samples were from Oxford instruments (Asylum research). For tapping mode, a silicon pyramidal tip (tip radius, 5-10 nm) on a silicon cantilever with 75 kHz, 2.8 Nm⁻¹ with an Al reflex coating.

References

- [1] H. Altenbach, J. Altenbach, W. Kissing, in *Mech. Compos. Struct. Elem.*, Springer-Verlag, Berlin, **2004**, 1–14.
- [2] D. D. L. Chung, *Composite Materials*, Springer, London, **2010**.
- [3] R. P. . Nijssen, *Composite Materials An Introduction*, **2015**.
- [4] B. L. Ellis, K. Town, L. F. Nazar, *Electrochim. Acta*, **2012**, *84*, 145.
- [5] M. C. Newton, P. A. Warburton, *Mater. Today*, **2007**, *10*, 50.
- [6] L. J. An, J. Wang, T. F. Zhang, H. L. Yang, Z. H. Sun, *Adv. Mater. Res.*, **2011**, *380*, 335.
- [7] C. Te Wu, W. P. Liao, J. J. Wu, *J. Mater. Chem.*, **2011**, *21*, 2871.
- [8] Y. K. Mishra, S. Kaps, A. Schuchardt, I. Paulowicz, X. Jin, D. Gedamu, S. Freitag, M. Claus, S. Wille, A. Kovalev, S. N. Gorb, R. Adelung, *Part. Part. Syst. Charact.*, **2013**, *30*, 775.
- [9] Y. K. Mishra, R. Adelung, *Mater. Today*, **2018**, *21*, 631.
- [10] O. Lupan, V. Postica, J. Gröttrup, A. K. Mishra, N. H. De Leeuw, J. F. C. Carreira, J. Rodrigues, N. Ben Sedrine, M. R. Correia, T. Monteiro, V. Cretu, I. Tiginyanu, D. Smazna, Y. K. Mishra, R. Adelung, *ACS Appl. Mater. Interfaces*, **2017**, *9*, 4084.
- [11] F. Schütt, V. Postica, R. Adelung, O. Lupan, *ACS Appl. Mater. Interfaces*, **2017**, *9*, 23107.
- [12] A. Eatemadi, H. Daraee, H. Karimkhanloo, M. Kouhi, N. Zarghami, A. Akbarzadeh, M. Abasi, Y. Hanifehpour, S. W. Joo, *Nanoscale Res. Lett.*, **2014**, *9*, 1.
- [13] K. F. Kelly, W. E. Billups, *Acc. Chem. Res.*, **2013**, *46*, 4.
- [14] S. Hansen, S. Shree, G. Neubüser, J. Carstensen, L. Kienle, R. Adelung, *J. Power Sources*, **2018**, *381*, 8.
- [15] H. Föll, H. Hartz, J. Carstensen, O. Riemenschneider, *Phys Status Solidi Rapid Res Lett.*, **2010**, *4*, 4.
- [16] F. Schütt, S. Signetti, H. Krüger, S. Röder, D. Smazna, S. Kaps, S. N. Gorb, Y. K. Mishra, N. M. Pugno, R. Adelung, *Nat. Commun.*, **2017**, *8*, 1.
- [17] M. Taale, F. Schütt, K. Zheng, Y. K. Mishra, A. R. Boccaccini, R. Adelung, C. Selhuber-Unkel, *ACS Appl. Mater. Interfaces*, **2018**, *10*, 43874
- [18] M. Mecklenburg, A. Schuchardt, Y. K. Mishra, S. Kaps, R. Adelung, A. Lotnyk, L. Kienle, K. Schulte, *Adv. Mater.*, **2012**, *24*, 3486.
- [19] D. Smazna, S. Shree, M. Hoppe, L. Hansen, J. Marx, J. Dittman, Z. Kareh, B. Fiedler, H. Kersten, R. Adelung, *Contrib. to Plasma Phys.*, **2018**, *58*, 384.
- [20] D. Smazna, N. Wolff, S. Shree, F. Schütt, Y. K. Mishra, L. Kienle, R. Adelung, *IEEE 7th Int. Conf. Nanomater. Appl. Prop. N.*, **2017**.
- [21] O. Lupan, V. Postica, N. Ababii, T. Reimer, S. Shree, M. Hoppe, O. Polonskyi, V. Sontea, S. Chemnitz, F. Faupel, R. Adelung, *Mater. Sci. Semicond. Process.*, **2018**, *87*, 44.

- [22] N. Ababii, M. Hoppe, S. Shree, A. Vahl, M. Ulfa, T. Pauporté, B. Viana, V. Cretu, N. Magariu, V. Postica, V. Sontea, M.-I. Terasa, O. Polonskyi, F. Faupel, R. Adelung, O. Lupan, *Sensors Actuators A Phys.*, **2019**.
- [23] A. B. D. Nandiyanto, K. Okuyama, *Adv. Powder Technol.*, **2011**, 22, 1.
- [24] A. Stunda-Zujeva, Z. Irbe, L. Berzina-Cimdina, *Ceram. Int.*, **2017**, 43, 11543.
- [25] F. Iskandar, H. Chang, K. Okuyama, *Adv. Powder Technol.*, **2003**, 14, 349.
- [26] E. Smith, G. Dent, *Modern Raman Spectroscopy*, John Wiley & Sons Ltd, England, **2005**.
- [27] M. Moreno, R. Ambrosio, T. Arturo, A. Torres, P. Rosales, A. Itzmoyotl, M. Domínguez, in *Cryst. Non-Crystalline Solids*, InTech, Croatia, 2018, 147
- [28] S. Khachadorian, *Vibrational Properties of Silicon*, Dr. Diss., **2011**.
- [29] T. C. Damen, S. P. S. Porto, B. Tell, *Phys. Rev.*, **1966**, 142, 570.
- [30] M. Schumm, *ZnO-based semiconductors studied by Raman spectroscopy: semimagnetic alloying, doping, and nanostructures*, Dr. Diss., **2008**.
- [31] V. Russo, M. Ghidelli, P. Gondoni, C. S. Casari, A. Li Bassi, *J. Appl. Phys.*, **2014**, 115.
- [32] K. Mun Wong, S. M. Alay-E-Abbas, Y. Fang, A. Shaukat, Y. Lei, *J. Appl. Phys.*, **2013**, 114.
- [33] A. Calzolari, M. B. Nardelli, *Sci. Rep.*, **2013**, 3, 1.
- [34] J. Das, S. K. Pradhan, D. R. Sahu, D. K. Mishra, S. N. Sarangi, B. B. Nayak, S. Verma, B. K. Roul, *Phys. B.*, **2010**, 405, 2492.
- [35] R. Kumari, A. Sahai, N. Goswami, *Prog. Nat. Sci. Mater. Int.*, **2015**, 25, 300.
- [36] R. Cuscó, E. Alarcón-Lladó, J. Ibáñez, L. Artús, J. Jiménez, B. Wang, M. J. Callahan, *Phys. Rev. B - Condens. Matter Mater. Phys.*, **2007**, 75.
- [37] J. R. Dennison, M. Holtz, G. Swain, *Spectroscopy*, **1996**, 11, 38.
- [38] L. Bokobza, J. L. Bruneel, M. Couzi, *Vib. Spectrosc.*, **2014**, 74, 57.
- [39] Y. Wang, D. C. Alsmeyer, R. L. McCreery, *Chem. Mater.* **1990**, 2, 557.
- [40] G. Leggett, *Atomic Force Microscopy*, John Wiley & Sons, Inc., New Jersey, **2005**.
- [41] A. Vahl, J. Dittmann, J. Jetter, S. Veziroglu, S. Shree, N. Ababii, O. Lupan, O. C. Aktas, T. Strunskus, E. Quandt, R. Adelung, S. K. Sharma, F. Faupel, *Nanotechnology*, **2019**, 30, 235603.

2.3. Polymer Composites

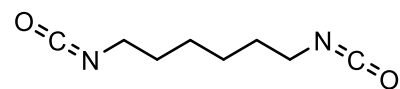
This section provides an insight into the polymer composite system. The two important components that makes up a polymer composite are the fillers or the reinforcement and the polymer matrix surrounding it. In a multi-phase composite with a distinct interface the fillers and the matrix remain chemically inert. The chemically and physically independent matrix and the filler combine to give extraordinary properties such as higher ultimate tensile strength, thermal and electrical properties, impact strength and corrosion resistivity.^[1] Additives delay the polymer aging process, also enhance the surface properties.

2.3.1. Matrices and Reinforcement

Polymer composite (PC) can be classified based on the chosen matrix, thermoplastic and thermoset. Examples of polymers in a thermoplastic PC are polymethylmethacrylate, polyethylene, polycarbonates, polyamide-imides, polyether ether ketone, poly-sulfone. The thermoset polymer includes epoxies, polyesters, urea, silicone. In addition, these two there is elastomer matrix, polymer with low Young's modulus, viscoelastic and high yield strength. Elastomers are amorphous polymer with glass transition temperature lower than room temperature. Some examples of such matrix are thermoplastic elastomers, polysulfide rubber, polybutadiene, silicone rubber and natural rubber.^[1-3] Brief description of the polymers employed in the context of this thesis are the following,

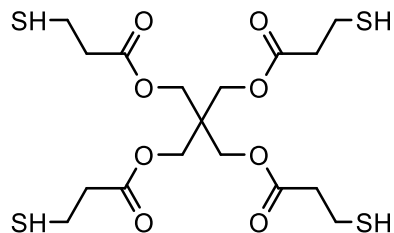
- **Polythiourethane (PTU)**

Polythiourethane is highly cross-linked thermoset made from two components which are pentaerythritol tetrakis(3-mercaptopropionate) (PETMP) and hexamethylene diisocyanate (HDI). Respective chemical structures and molecular weights are provided below (see **Scheme 1.**). When the monomers, PETMP and HDI are mixed at appropriate ratios i.e., 2 mmol, 1 g and 8 mmol, 1.4 g respectively, components undergo polyaddition reaction to form the polymer. PTU is a solvent free polymerization, hence, no harmful gases are produced during the synthesis. Among the components, PETMP is the less reactive than HDI due to the added stabilizers. Due to this fact, fillers such as dyes and nanoparticles are first thoroughly dispersed in PETMP, later HDI is added. This mixture is degassed and poured into a mold with desired shape and dimensions.



HDI

Chemical Formula: $C_8H_{12}N_2O_2$
Molecular Weight: 168.20 g/mol



PETMP

Chemical Formula: $C_{17}H_{28}O_8S_4$
Molecular Weight: 488.64 g/mol

Scheme 1. Chemical structures, formulas and molecular weights of the two components (HDI and PETMP) of PTU.

- **Epoxy**

Epoxy is a colloquial name given to the cross-linked polymer resulting from curing the pre-polymer epoxy resin. For the PC studies in the current work epoxy resin was cured by an amine-based hardener. Common constituents of an epoxy resin are pre-polymer epoxy resin, bisphenol-A-(epichlorhydrin), bisphenol-F-epoxy resin, 1,6-bis(2,3-epoxypropoxy)hexane and common constituents of a hardener are phenol (styrenated), 2,2,4-trimethylhexane-1,6-diamine, m-phenylenebis(methylamine), phenol (methylstyrenated). By altering the quantity of each of these constituents the reaction time and the degree of cross-linking can be changed.^[1] The mixing ratios of the epoxy and the hardener is varied to vary the curing time and the mechanical properties of the end product. For reinforcement, fillers can be mixed into the resin or the hardener before curing.^[1] Other methods of reinforcement are elaborated in the sub chapter 2.3.2 *Methods of Fabrication of Glassfiber Reinforced Polymer Composite*

Polymer composites can also be categorized based on the reinforcement used e.g., particles, fibers and flakes. Flexibility and the optical property of the composite depends on the shape and orientation of the fillers. Depending on the function of the PC the additives are chosen. Different and appropriate fillers are utilized for different functions such as an electromagnetic absorbing, conductive or magnetic or optically translucent PC. Multiple additives are used for a multi-functional PC.

- PCs for an electromagnetic-wave absorbing application, additives such as carbon powder and fiber, carborundum powder and fiber, graphite, aluminum fiber, barium titanate

and so forth. These composites absorb electromagnetic energy and convert it to other forms of energy such as heat and electricity. The absorbing properties of the additives can be enhanced by varying the shape of the fibers used to triangular, squared or polygonal.

- Applications where electromagnetic-wave transparency is required organic fibers, made of aramid or high molecular weight polyethylene and quartz fibers are used. Transparency of a PC to electromagnetic-wave depends on the dielectric property of the matrix and the additive. Usually organic polymers have good dielectric properties, hence, bismaleimide resins, cyanate ester resins s.o., are utilized.

- Reinforced PCs are most widely used in the painting and coating industries. By simply mixing pigments (iron oxide, titania, alumina particles and so forth) as fillers into paints, industries achieve UV reflective, anti-corrosion s.o., properties. Such material properties showed remarkable increase the age and the stability of a building. The extremely high interfacial area that glass and carbon nanofibers offer increases toughness of the material without drastically altering stiffness. Glass and carbon fiber reinforced PC (GFRPC and CFRPC) are applied in various fields such as automotive, aerospace, windmills and marine technology.^[4]

Contemporary studies are focused on enhancing all the above-mentioned properties with as less additives as possible to increase cost efficiency time. Many investigations have shown nano, micro particles with its extremely high surface to volume ratio enhance optical, electrical and thermal properties at just 0.5–10 wt% filling factor.^[5,6]

- Titanium dioxide nanoparticles are electro-spun with polyvinyl alcohol, polyacrylamide, polyglycolic acid, poly(butylene terephthalate), to produce biocompatible scaffold material for wound dressing.^[7]

- Multi-walled CNTs (MWCNTs) are covalently or non-covalently functionalized to establish uniform dispersion in solvents and to prevent re-agglomeration. Functionalization enhances the interaction between the nanotubes and polymers. MWCNTs (1 wt%) improved tensile strength of polystyrene up to 25 % as reported by Qian et al^[8]. Indentation resistance of epoxy resin can be increase by addition of 2 wt% of aligned CNTs exhibit superior electrical and thermal conductivities.^[9] With just 0.021 wt% of aligned single walled CNTs improved

electrical conductivity of epoxy resin by several orders.^[10] MWCNTs used as fillers in polymeric thin films.^[6]

- About 0.5 – 1.0 wt% of T-ZnO microparticles were can be electro-spun as additives with PCL. These fiber mats have excellent osteoconductive property and are used as periodontal membrane. T-ZnO makes this biodegradable membrane antibacterial.^[11]

- Anti-fouling studies by Hölken et al., observed that the addition of 5 wt% of T-ZnO microparticles to polythiourethane showed highest mechanical strength and lowest biofouling.^[12]

The enclosed published work involves extensive study using T-ZnO and woven glassfiber as additives to enhance optical and mechanical strength.

2.3.2. Methods of Fabrication of Glassfiber Reinforced Polymer Composite

Glassfiber reinforced polymer composites (GFRPC) can be fabricated by several methods and some of the vastly employed procedures are explained in this section.

- **Hand lay-up technique**

Laminates using woven glassfiber mat were produced with this technique introduced by Aramide et al^[13]. A silicone mold of desired shape and dimensions is cleaned and coated with a releasing agent, hard wax is commonly used, unsaturated resin/hardener is layered evenly in the mold (see **Figure 9**). Once the resin hardens, alternate layers of the glassfiber mat and the resin are applied, a final top coating of the resin as shown in the **Figure 9**. Tensile strength can be varied by varying the glassfiber content.^[14]

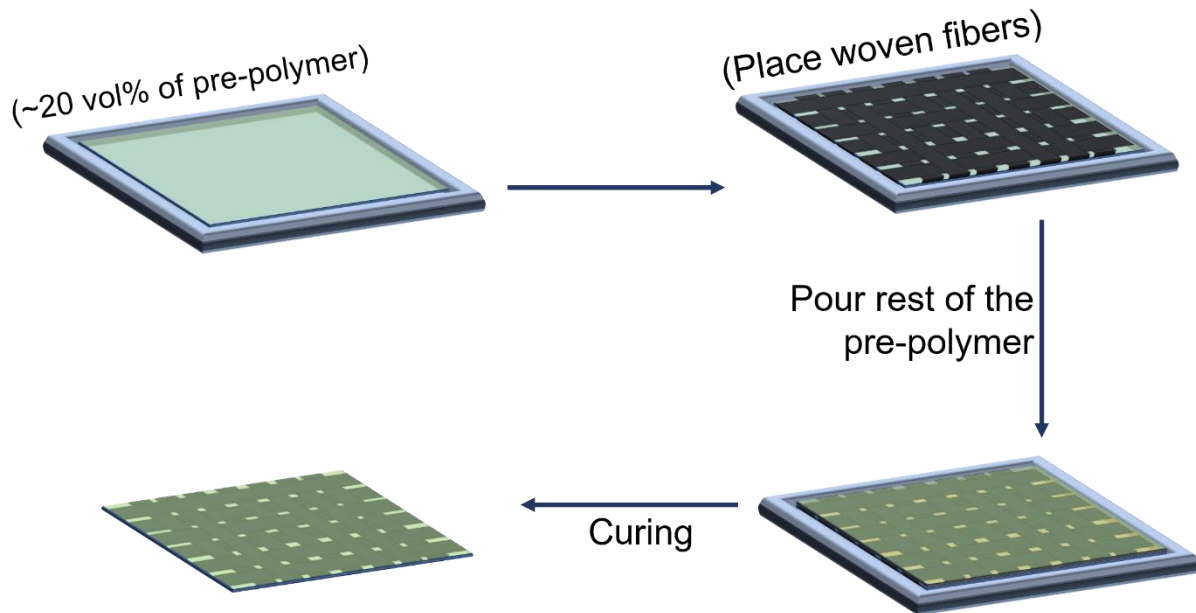


Figure 9. Schematic representation of the Hand lay-up method of producing GFRPC laminates. As a first step, about 20 vol% of the pre-polymer i.e., epoxy resin and hardener mixture was poured into a desired mold.

- **Compression molding**

Erden et al^[14] and Hameed et al.,^[15] also follow the *hand lay-up* method followed by compression molding to produce laminates. The glassfiber mats were infiltrated by oligomeric siloxane modified polyester matrix in Erden et al., and compressed for 120 min at room temperature at 120 bars.^[15] In the study by Hameed et al., poly(styrene-co-acrylonitrile) modified epoxy resin was used as the matrix around the glassfiber mats. These laminates were compressed into a mold before curing.

- **Bag-molding technique**

This method of laminate production can be implemented to optimize the fiber to resin ratio in a composite. A mechanical pressure is applied on to a fiber mat coated with unsaturated resin, laid out in a desired mold inside/under a flexible diaphragm or a bag. This facilitates in reduction of resin content whilst curing meanwhile decreasing the weight of the entire composite. By this method of lamination air trapped between layers can be removed effortlessly. This technique lowers humidity, controlling the cross-linking process and prevents the fibers from shifting while curing.^[16,17]

- **Resin injection molding**

Resin injection molding techniques is employed to produce various form of reinforced composites. Resin is mixed with a curing agent/hardener and is injected into a mold under high pressure using an impinging mixer. Reinforcement involves mixing broken glassfibers, mica in the resin/hardener mixture before being injected into a mold. For a lamina, woven glassfiber mat is laid out in a mold and the pre-polymer mixture is injected onto the glassfiber mesh.

Several other techniques such as pultrusion, spray-up, resin transfer molding can be opted to produce reinforced polymer composites. For the study shown in the third of *section 7*, a lamina with a single layer of glassfiber mat was produced following the *hand lay-up* method.

2.3.3. Sources of Damages and its Analyses

Quintessential aspect for improving the cost efficiency and life time of a composite is the quantifiable and reproduceable analysis of the damage level. To understand the necessity of such damage analyses it is imperative to list the sources of damages and existing methods of analyzing them. Exposure to UV irradiation, high temperature and humidity changes, applied stress/strain and impact force s.o., are some of the external phenomena that can damage a lamina (see **Figure 10**). Source of a damage can be anything from faulty fabrication to external impact. Even in an automated production, fibers can be misaligned and other defects such as delamination and adhesion failure between additives and matrix (**Figure 10**) can be created. Automotive, aerospace and power generation e.g., windmill industries have several approaches for post damage analyses.

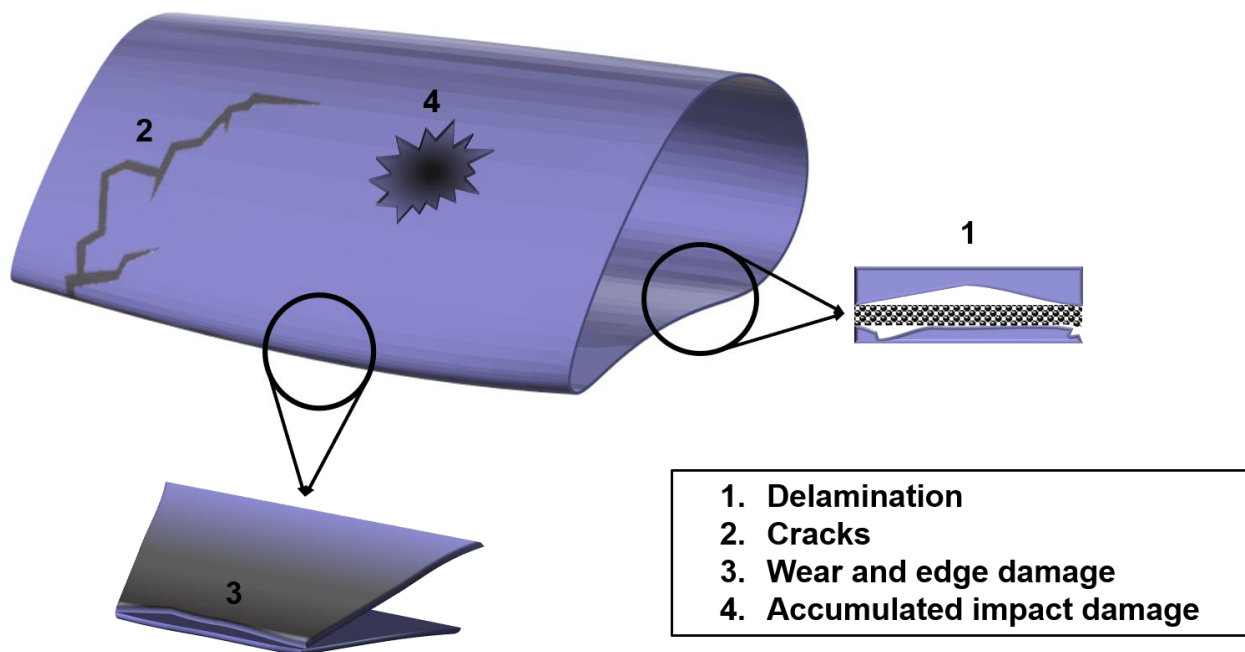


Figure 10. Graphical display of commonly occurring damages in a WBT. The part shown is the mid segment of a WBT. Different types of damages at different areas which leads to material failure are labeled.

Non-destructive testing (NDT) commonly followed to monitor wind turbine blades (WTBs) are^[18]:

- Study by Ataya et al., ^[19] summarized, form, location and causes of damages on the trailing edge of a WTB. The investigation showed trailing edge being the binding region of

two shells with a long line of adhesive joint is prone to damages caused by operational and environmental conditions. In this study the authors monitored the turbines with the most commonly used NDT called *visual inspection*. After the labeling the WBTs, location of discontinuities and damages are tracked with a high-resolution camera. Longitudinal cracks through the adhesive material along the trailing edge, transversal cracks and edge cuts were observed.^[19] This method can only be used in post failure analysis, as the part that has to be inspected needs to be dismantled. Hence this method fails to report a damage before complete material failure.

- Jüngert et al.,^[20] employed acoustic wave-based technique to detect the damage in WBTs. Acoustic wave-based technique belongs to a class of local resonance spectroscopy, which is an NDT performed regularly by the inspectors. WBT is tapped with a small impulse hammer to produce sound waves which are recorded by a microphone. Resonance of the waves produced are dependent on the structural integrity of the WBT. Delaminations and trapped air bubbles can be recognized buy this measure.^[20] Acoustic emission is combined with digital image correlation by Zhou et al.,^[21] to study GFPRC delamination under compression. This method helps recognize cracking of the matrix, fiber/matrix debonding also known as delamination and fiber rupturing. For this method to be accurate, background noise created by the wind has to be subtracted. Even with the subtraction, similar to the precious technique, it is only useful after the delamination or other kind of damage has occurred.

- Echo-based method i.e., pulsed ultrasonic and sonic waves are directed towards an interested WBT surface and echo response received from the surface provides information about the structural integrity of the WBT. For easy identification of the damage areas, 2D or 3D scans can be generated using this method.^[20,21] Key disadvantage of this technique is depth of penetration, barely the surface can be analyzed.

- NDTs based on electromagnetic waves are among the most accurate methods in currently in use as it offers subsurface access, with which deeper defects, polymer degradations and thermal impacts can be determined. Electromagnetic NDT can be further divided based on its source such as microwave,^[22] terahertz,^[23] eddy current,^[24] radio frequency eddy current^[24] and pulsed eddy current.^[25] Requirement of using eddy current is

to have a conductive composite, defects in CFRPCs and metal matrix composite lamina be more accurately tested compared to other NDTs. Microwave and terahertz can penetrate dielectric material, hence can be used to scan GFRPCs.^[22-23]

All the aforementioned techniques however non-destructive have several disadvantages, these methods are mostly post failure analysis. They help in replacing the faulty parts nevertheless does not help find the source of a material failure. For safety measures, a damage must be found well before it leads to material failure. A plausible method to possess damage control is to utilize self-reporting material, a material that indicates impairments before severe failures occur in the system. Next chapter on self-reporting *2.4. Self-Reporting Polymer and Polymer Composites* provides several materials that can be employed as damage indicators.

References

- [1] R. M. Wang, S. R. Zheng, Y. P. Zheng, *Polymer Matrix Composites and Technology*, **2011**.
- [2] J. P. Jose, S. Thomas, K. Joseph, S. K. Malhotra, K. Goda, M. S. Sreekala, in *Polym. Compos.*, Wiley-VCH Verlag GmbH & Co. KGaA, **2012**, 1-16.
- [3] K. A. Allen, in *Polym. Compos. Process.*, Springer, Boston, Massachusetts, **2012**, 1–10.
- [4] T. P. Sathishkumar, S. Satheeshkumar, J. Naveen, *J. Reinf. Plast. Compos.*, **2014**, *33*, 1258.
- [5] V. Choudhary, A. Gupta, in *Carbon Nanotub. Polym. Nanocomposites*, InTech, **2011**, 64.
- [6] B. Safadi, R. Andrews, E. A. Grulke, *J. Appl. Polym. Sci.*, **2002**, *84*, 2660.
- [7] K. Ghosal, C. Agatemor, Z. Špitálský, S. Thomas, E. Kny, *Chem. Eng. J.*, **2019**, *358*, 1262.
- [8] D. Qian, E. C. Dickey, R. Andrews, T. Rantell, *Appl. Phys. Lett.*, **2000**, *76*, 2868.
- [9] M. Cadek, J. N. Coleman, V. Barron, K. Hedicke, W. J. Blau, *Appl. Phys. Lett.*, **2002**, *81*, 5123.
- [10] C. A. Martin, J. K. W. Sandler, M. S. P. Shaffer, M. K. Schwarz, W. Bauhofer, K. Schulte, A. H. Windle, *Compos. Sci. Technol.*, **2004**, *64*, 2309.
- [11] A. Nasajpour, S. Ansari, C. Rinoldi, A. S. Rad, T. Aghaloo, S. R. Shin, Y. K. Mishra, R. Adelung, W. Swieszkowski, N. Annabi, A. Khademhosseini, A. Moshaverinia, A. Tamayol, *Adv. Funct. Mater.*, **2017**, *28*, 1703437.
- [12] I. Hölken, M. Hoppe, Y. K. Mishra, S. N. Gorb, R. Adelung, M. J. Baum, *Phys. Chem. Chem. Phys.*, **2016**, *18*, 7114.
- [13] F. O. Aramide, P. O. Atanda, O. O. Olorunniwo, *Int. J. Compos. Mater.*, **2013**, *2*, 147.
- [14] S. Erden, K. Sever, Y. Seki, M. Sarikanat, *Fibers Polym.*, **2010**, *11*, 732.
- [15] N. Hameed, P. A. Sreekumar, B. Francis, W. Yang, S. Thomas, *Compos. Part A Appl. Sci. Manuf.*, **2007**, *38*, 2422.
- [16] A. George, *Optimization of Resin Infusion Processing for Composite Materials: Simulation and Characterization Strategies*, Dr. Diss, **2011**.
- [17] K. Abdurohman, T. Satrio, N. L. Muzayadah, Teten, *J. Phys. Conf. Ser.*, **2018**, *1130*, 012018.
- [18] R. Yang, Y. He, H. Zhang, *Renew. Sustain. Energy Rev.*, **2016**, *60*, 1225.
- [19] S. Ataya, M. M. Z. Ahmed, *Eng. Fail. Anal.*, **2013**, *35*, 480.
- [20] A. Jüngert, in *7th Fib PhD Symp. Stuttgart, Ger.*, **2008**, 10.
- [21] W. Zhou, W. zheng Zhao, Y. nan Zhang, Z. jun Ding, *Compos. Struct.*, **2018**, *195*, 349.
- [22] M. Pieraccini, F. Parrini, M. Fratini, C. Atzeni, P. Spinelli, *Renew. Energy*, **2008**, *33*, 13.
- [23] T. Chady, P. Lopato, B. Szymanik, *J. Sensors*, **2012**, *2012*, 1.
- [24] G. Mook, R. Lange, O. Koeser, *Compos. Sci. Technol.*, **2001**, *61*, 865.
- [25] Y. He, G. Tian, H. Zhang, M. Alamin, A. Simm, P. Jackson, *IEEE Sens. J.*, **2012**, *12*, 2113.

2.4. Self-Reporting Polymer and Polymer Composites

Self-reporting is an umbrella term used for materials which senses and reports changes in its surrounding environment. This chapter offers reliable solutions for the inadequacies encountered in the methods of damage detection listed in the sub *chapter 2.3.3 Sources of Damages and its Analyses*. A material providing visual indication of changes in ambient condition such as temperature, humidity, pH, polarity, UV intensity, and mechanical stress without any assistance from an external device is known as self-reporting material. Human skin is a complex natural self-reporter, gives a visual indication of everything it experiences by a change of texture, hydration or color. Commonly used stimuli responsive products are lenses that darkens under sunlight and strips that changes color depending on the pH of the medium. Use of self-reporters can be practical in biotechnological, aeronautical and automobile industries where a slightest modification in parameters can cause severe complications. Photochromes, mechanochromes and thermochromes are the prominent self-reporting material that changes color in response to light, force and heat respectively.^[1]

Stimuli responsive material can be made of anything from a molecular switch^[1] to ceramics^[2] to polymers^[3] to nanocomposites^[4]. A class of stimuli responsive material used in the presented published work is a molecular switch such as azobenzene, spiropyrans, diarylethenes and crown ethers, which can shift between two or more stable states in response to temperature, light, pH and electric current.^[5-7] Such shifts between states are reversible and is known as isomerization.^[8] Isomers, in particular stereoisomers, possess identical functional groups and number of atoms but differ in its spatial arrangement. These isomers have substantially different optical, thermal and electronic properties,^[9] such a change in an organic molecular switch can be triggered by light, pH, polarity, temperature and mechanical force. Depending on the trigger, the switching mechanisms are further divided as photoisomerization, thermoisomerization, mechanoisomerization and so forth. Due to these triggers a molecular switch undergoes stereoisomerism, where, a molecule shifts between *cis to trans* or *E to Z* isomers reversibly (see **Figure 11**).^[10,11] In particular, azobenzene and spiropyran were studied in different environments in the given research work.

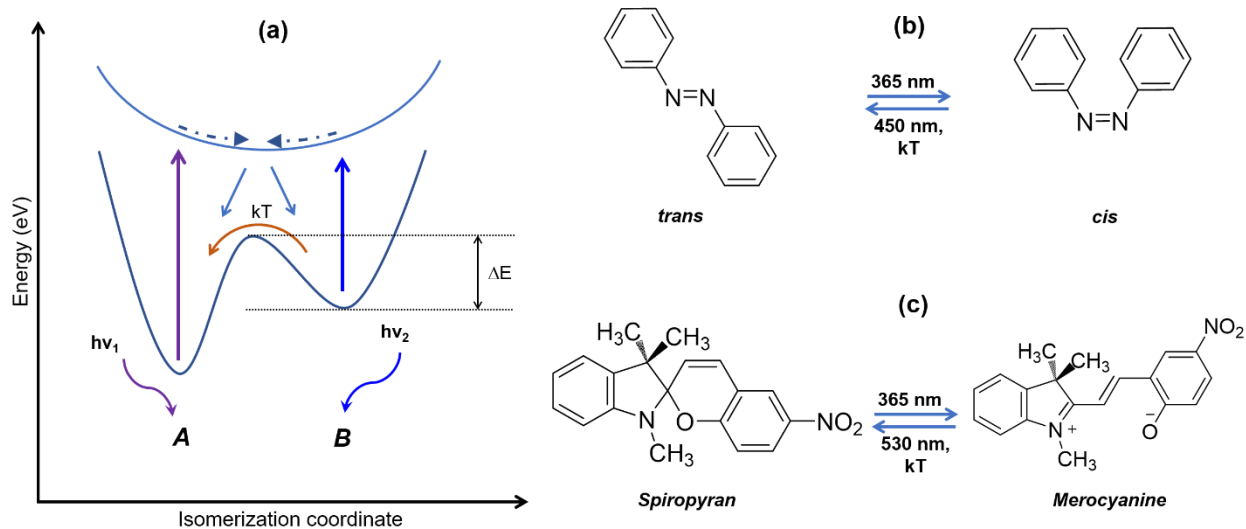


Figure 11. Basic mechanism behind photoisomerization of the molecular switches, azobenzene and spiropyran. (a) Sketch of the energy vs isomerization reaction of an isolated molecule, shows reversible excitation mechanism under irradiation. Isolated molecule in its isomeric state **A/B** irradiated by $h\nu_1/h\nu_2$ light gets excited to higher energy state and relaxes to either **A/B** state depending on the irradiation. Transition from **A** to **B** is only possible with UV irradiation, however, due to the lower energy barrier (ΔE) between the metastable state and the **B**-ground state, **B** to **A** transition is possible under visible light irradiation or direct thermal relaxation as shown by the orange curve. (b) Isomerization of azobenzene causing torsion of N=N. (c) Isomerization of spiropyran to merocyanine by undergoing C-O cleavage under the influence of light, temperature and force.

➤ Azobenzene

Two benzene rings connected by a double bonded nitrogen bridge, azobenzene, is at its most stable state in *trans* form. *trans*-Azobenzene (9.9 Å) can be transformed to the much shorter *cis* form (5.5 Å) under UV light (365 nm) irradiation (**Figure 11(b)**) and back by blue light (450 nm) irradiation or by thermal relaxation (see **Figure 11(a)**).^[11] Because of the significant difference in structure, azobenzene is an attractive molecular switch for disciplines such as catalysis, photomechanics, adhesives etc. Léonard et al., used azobenzene and its derivatives as a photocontrolled promoter in several catalysis.^[12] Smart surfaces i.e., azobenzene grafted surfaces were studied by Zhang et.al.^[13] Self-assembled azobenzene on SiO₂ surface was employed to create selective protein adsorption.^[13] Investigations made by Kizilkan et.al.,^[14] on liquid crystalline elastomeric films containing azobenzene externally coated by silicone showed photocontrollable adhesion. Polymers bearing azobenzene moieties was synthesized by Matějka et.al.,^[15] Li et.al.,^[16] and Kim et.al.,^[17] to produce photocontrolled mechanical macroscopic movements. Shinkai et.al.,^[18] developed two crown ether rings combined with an azobenzene bridge to photocontrol the ion captivity.

Azobenzene in siloxanes have gained high interest in the recent years due to the flexibility and stability of siloxanes. In the chapter 9, photomechanical studies were performed by AFM of the first example of a cross-linkable polysiloxane with azobenzene incorporated in its main chain is presented.

➤ Spiropyran

Spiropyran is class of molecular switch that has numerous triggers to cause isomerization from its closed form to the open form also known as merocyanine.^[19] Mechanical force, heat and UV are the main triggers studied in the published work presented here. Spiropyran (dipole moment, ~4-6 D) isomerizes in a similar manner as shown in **Figure 11(a)** to merocyanine (dipole moment, ~14-16 D) by breaking the C_{spiro}-O bond in response to a stimulus, creating a zwitter ion (see **Figure 11(c)**).^[19] However, depending on the environment, merocyanine can further isomerize^[20] or stack as H or J aggregate^[21]. Polarity of the medium determines the path of isomerization and the color of this molecule strongly.^[18,22,23] The transition is commonly accompanied with an evident color change, making this molecular shift easily detectable.^[19] Spiropyran is commonly colorless to yellow and merocyanine is purple to blue. Due to the large change in dipole moment, spiropyran grafted on to surfaces has been recorded to show switching wettability.^[24] Spiropyran is a versatile molecule as it can be functionalized and polymerized into main or side chains of different polymers for example PMA,^[25] PMMA^[25] and PU^[19]. It has been studied for its mechanosensitivity, where a polymer with spiropyran in its main chain shows color change under mechanical stress. One such example is PMA with a backbone containing spiropyran, synthesized by Davis et.al.^[25] Spiropyran is first functionalized with α -bromoester and polymerized via single-electron-transfer living radical polymerization. With 500 MA units on either side of spiropyran, the polymer shows excellent self-reporting property.^[25] In the presented work, this polymer was blended with PMMA and centrifugally spun to obtain durable self-reporting fibers, study on this is presented in *chapter 8*.

Self-reporting polymer composites are among the well-researched materials. As a stimulus responding filler, ZnO is used in PDMS based polymer composites. Changes in the photoluminescence of T-ZnO with applied tensile force was tracked by Jin et al.^[26] Green emission occurs due to the surface defects of T-ZnO under UV irradiation, this emission

decreases in response to increasing strain. These composites are produced by dispersing T-ZnO microparticles into the elastomeric PDMS matrix.^[26]

Other recently researched materials in this field are glass and carbon fiber reinforced polymer composites (GFRPC and CFRPC respectively). GFRPCs functionalized with fluorescent proteins indicates delamination at the fiber-matrix interface. Using the high conductivity of carbon fibers to its advantage, damage in CFRPC can be determined by measuring the resistance of the polymer composite. Resistance increases due to deformation in composites. Yet another example of a self-reporting polymer composite is fluorescent dye filled hollow fibers embedded in an epoxy based matrix. Unpredictable cracks activate the dye and these cracks can be discovered with the help of its fluorescence.^[27] However effective these methods are in finding the initial location of the material failure, the biggest challenge is to find the damage before it gets severe and before any material malfunction occurs. This was accomplished in the course of the presented study by using the mechochrome spiropyran as an additive in polythiourethane based polymer composite. More details can be found in the articles included in *section 7*.

References

- [1] B. L. Feringa, W. R. Browne, *Molecular Switches*, Wiley-VCH Verlag GmbH & Co. KGaA, Weinheim, Germany, **2011**.
- [2] W. Wu, Z. L. Wang, *Nat. Rev. Mater.* **2016**, *1*, 16031.
- [3] B. Tandon, P. Kamble, R. T. Olsson, J. J. Blaker, S. H. Cartmell, *Molecules* **2019**, *24*, 1903.
- [4] W. Lee, D. Kim, S. Lee, J. Park, S. Oh, G. Kim, J. Lim, J. Kim, *Nano Today* **2018**, *23*, 97.
- [5] J. Q. Zhong, K. Wu, G. Q. Xu, J. D. Lin, W. P. Hu, A. T. S. Wee, W. Chen, J. L. Zhang, *Chem. Soc. Rev.*, **2015**, *44*, 2998.
- [6] B. K. Pathem, S. A. Claridge, Y. B. Zheng, P. S. Weiss, *Annu. Rev. Phys. Chem.*, **2013**, *64*, 605.
- [7] A. M. Osman, M. Z. A. Badr, A. E. Abdel-Rahman, *J. Chem. Soc. C*, **1971**, *0*, 2264.
- [8] J. N. Bull, M. S. Scholz, E. Carrascosa, E. J. Bieske, *Phys. Chem. Chem. Phys.*, **2017**, *20*, 509.
- [9] H. M. D. Bandara, S. C. Burdette, *Chem. Soc. Rev.*, **2012**, *41*, 1809.
- [10] H. Tian, J. Zhang, *Photochromic Materials*, Wiley-VCH Verlag GmbH & Co. KGaA, Weinheim, Germany, **2016**.
- [11] S. L. Oscurato, M. Salvatore, P. Maddalena, A. Ambrosio, *Nanophotonics*, **2018**, *7*, 1387.
- [12] E. Léonard, F. Mangin, C. Villette, M. Billamboz, C. Len, *Catal. Sci. Technol.*, **2016**, *6*, 379.
- [13] J. L. Zhang, J. Q. Zhong, J. D. Lin, W. P. Hu, K. Wu, G. Q. Xu, A. T. S. Wee, W. Chen, *Chem. Soc. Rev.*, **2015**, *44*, 2998.
- [14] E. Kizilkan, S. N. Gorb, *ACS Appl. Mater. Interfaces*, **2018**, *10*, 26752.
- [15] L. Matějka, M. Ilavský, K. Dušek, O. Wichterle, *Polymer*, **1981**, *22*, 1511.
- [16] Y. Li, Y. He, X. Tong, X. Wang, *J. Am. Chem. Soc.*, **2005**, *127*, 2402.
- [17] H.-K. Kim, X.-S. Wang, Y. Fujita, A. Sudo, H. Nishida, M. Fujii, T. Endo, *Macromol. Rapid Commun.*, **2005**, *26*, 1032.
- [18] S. Shinkai, M. Ishihara, O. Manabe, *Polym. J.*, **1985**, *17*, 1141.
- [19] R. Klajn, *Chem. Soc. Rev.*, **2014**, *43*, 148.
- [20] C. P. McCoy, L. Donnelly, D. S. Jones, S. P. Gorman, *Tetrahedron Lett.* **2007**, *48*, 657.
- [21] E. Uchida, R. Azumi, Y. Norikane, *Chem. Lett.* **2014**, *43*, 1619.
- [22] B. Seefeldt, R. Kasper, M. Beining, J. Mattay, J. Arden-jacob, N. Kemnitzer, K. Heinz, M. Heilemann, M. Sauer, *Photochem. Photobiol. Sci.*, **2016**, *9*, 213.
- [23] M. Schulz-Senft, P. J. Gates, F. D. Sönnichsen, A. Staubitz, *Dye. Pigment.*, **2017**, *136*, 292.
- [24] M. Bremer, R. Reinke, B. Hesseler, M. Taale, D. Ingwersen, S. Schwarzer, C. Selhuber-Unkel, M. Gerken, *J. Nanomater.*, **2017**, *1*.
- [25] D. A. Davis, A. Hamilton, J. Yang, L. D. Cremar, D. Van Gough, S. L. Potisek, M. T. Ong, P. V. Braun, T. J. Martínez, S. R. White, J. S. Moore, N. R. Sottos, *Nature*, **2009**, *459*, 68.
- [26] X. Jin, M. Götz, S. Wille, Y. K. Mishra, R. Adelung, C. Zollfrank, *Adv. Mater.*, **2013**, *25*, 1342.
- [27] O. Rifaie-Graham, E. A. Apebende, L. K. Bast, N. Bruns, *Adv. Mater.*, **2018**, *30*, 1.

3. Interactions at the Interface of Tetrapodal ZnO and Fullerenes

A study on the influence of fullerene (C_{60}) hybridization on the photoluminescent and electrical properties of T-ZnO is presented in this chapter. The C_{60} and T-ZnO composite creates nanoscale interfaces which were observed to be beneficial for gas sensing. Optical and structural examination of the the two constituents were performed to acquire an insight into the interactions occurring at the HNI.

Personal contributions in the following article:





- Assisting in sample fabrication
- Raman spectroscopic investigations and its data analyses
- Partial manuscript preparation

The following content is adapted from “D. Smazna, J. Rodrigues, S. Shree, V. Postica, G. Neubüser, A. F. Martins, N. Ben Sedrine, N. K. Jena, L. Siebert, F. Schütt, O. Lupan, R. Ahuja, M. R. Correia, T. Monteiro, L. Kienle, Y. Yang, R. Adelung and Y. K. Mishra, *Nanoscale*, **2018**, *10*, 10050” with formal permission from *The Royal Society of Chemistry*.



Cite this: *Nanoscale*, 2018, 10, 10050

Buckminsterfullerene hybridized zinc oxide tetrapods: defects and charge transfer induced optical and electrical response†

Daria Smazna,^a Joana Rodrigues,^b  Sindu Shree,^a Vasile Postica,^c  Gero Neubüser,^a A. F. Martins,^b N. Ben Sedrine,^b Naresh K. Jena,^d Leonard Siebert,^a Fabian Schütt,^a Oleg Lupan,^{a,c} Rajeev Ahuja,^d M. R. Correia,^b Teresa Monteiro,^{*b} Lorenz Kienle,^{*a} Ya Yang,^e  Rainer Adelung^{*a} and Yogendra Kumar Mishra  ^{*a}

Buckminster fullerene (C₆₀) based hybrid metal oxide materials are receiving considerable attention because of their excellent fundamental and applied aspects, like semiconducting, electron transfer, luminescent behaviors, etc. and this work briefly discusses the successful fabrication of C₆₀ decorated ZnO tetrapod materials and their detailed structure–property relationships including device sensing applications. The electron microscopy investigations indicate that a quite dense surface coverage of ZnO tetrapods with C₆₀ clusters is achieved. The spectroscopy studies confirmed the identification of the C₆₀ vibrational modes and the C₆₀ induced changes in the absorption and luminescence properties of the ZnO tetrapods. An increased C₆₀ concentration on ZnO results in steeper ZnO bandgap absorption followed by well-defined free exciton and 3.31 eV line emissions. As expected, higher amounts of C₆₀ increase the intensity of C₆₀-related visible absorption bands. Pumping the samples with photons with an energy corresponding to these absorption band maxima leads to additional emission from ZnO showing an effective charge transfer phenomenon from C₆₀ to the ZnO host. The density of states model obtained from DFT studies for pure and C₆₀ coated ZnO surfaces confirms the experimental observations. The fabricated C₆₀–ZnO hybrid tetrapod based micro- and nanodevices showed interesting ethanol gas sensing characteristics.

Received 21st February 2018,
Accepted 24th April 2018

DOI: 10.1039/c8nr01504j

rsc.li/nanoscale

Introduction

Since its discovery, buckminsterfullerene (C₆₀), among all the low dimensional carbon allotropes, has always introduced new fundamental and applied research paradigms in various disciplines due to its unique physical and chemical properties.¹ Together with other fullerenes (such as C₇₀, C₈₄ etc.), buckyballs belong to the semiconductor family with a bandgap energy from 1.5 to 1.98 eV, which makes them attractive for optical and electrical applications.² Taking into account their excellent charge extraction and accommodation capabilities,³ diverse applications in photovoltaics,^{1b} photocatalytic water purification,⁴ as a photocorrosion protective layer,⁵ energy⁶ or even as an

antibacterial barrier,⁷ have been proposed. Generally, in most of the applications, fullerenes were immersed in a hybrid layer in the form of fullerene agglomerates. In this strategy, fullerenes were involved as the bulk phase, allowing only a small fraction of individual fullerene molecules to be accessible for interaction with the other phases/materials. Surface accessibility is the most important criterion towards many applications. To achieve a higher surface accessibility compared to conventional methods, advanced synthesis strategies in adequate hierarchical forms need to be developed. In this context, three-dimensional (3D) architected substrates play an important role as they can support nanocrystals (or several monolayers) of fullerenes on their surface, thereby increasing the overall accessibility. An appropriate highly porous and non-conductive 3D cellular material in which fullerenes can be homogeneously decorated on the surface would provide new fundamental research scopes in the direction of the fundamental structure–property relationship and can also lead to a large number of advanced applications because of high surface accessibility and simplicity of use.

^a Institute for Materials Science, Kiel University, Kaiserstr. 2, D-24143, Kiel, Germany. E-mail: lk@tf.uni-kiel.de, ra@tf.uni-kiel.de, ykm@tf.uni-kiel.de

^b Departamento de Física & I3N, Universidade de Aveiro, 3810-193 Aveiro, Portugal. E-mail: tita@ua.pt

^c Department of Microelectronics and Biomedical Engineering, Technical University of Moldova, 168 Stefan cel Mare Blvd., MD-2004, Chisinau, Republic of Moldova

^d Condensed Matter Theory, Materials Theory Division, Department of Physics and Astronomy, Uppsala University, Box 516, SE-751 20, Uppsala, Sweden

^e CAS Center for Excellence in Nanoscience, Beijing Institute of Nanoenergy and Nanosystems, Chinese Academy of Sciences, Beijing, 100083, China

†Electronic supplementary information (ESI) available. See DOI: 10.1039/c8nr01504j

Nanoarchitected porous materials in the 3D form are the most adequate candidates for such desired applications, boosting their research focus in the last couple of years. Various physical, chemical, and biologically inspired and other innovative strategies have been adopted for their fabrication. However, issues like versatile fabrication, cost effective process, upscalability, etc., have been the main concerns for the advanced materials community. Structural aspects of nanomaterials could play a very important role in this context, since a macroscopic porous network material can be easily built out of complex shaped nanostructures, for example from nanoseaurchins, tetrapods, multipods, etc., in a cost-effective way which could be rather efficient in contrast to complex multistep processes or clean room technologies.⁸ Because of its unique crystalline nature, zinc oxide (ZnO) is a remarkable candidate for complex nanostructuring and the usually flame based process offers the possibility of a large scale growth of nano- and micro-tetrapods.^{8a,b} These tetrapods are formed with four interconnected arms via a central core, facilitating the easy accessibility of 1D nanoscale features in a complex 3D shape and offering large technological opportunities.^{8b,9} Additionally, these zinc oxide tetrapods can be used as building blocks for synthesizing highly porous 3D interconnected networks, which can be used as solid backbones for fabricating hybrid materials or as sacrificial templates¹⁰ for developing a new class of porous 3D materials.^{8a,b,11}

With n-type conductivity, ZnO is one of the most active materials from the II–VI metal oxide semiconductor family because of its hexagonal-wurtzite crystal structure, featuring a high polarity along the c-axis, supported versatile growth nature and unique physical (e.g. optical and electrical) properties.^{1e,12} The complex shapes additionally facilitate ZnO nanomaterials with many structural aspects, thereby making tetrapods from ZnO a very relevant nanomaterial candidate for various technological applications.^{8b} In order to enhance or even tune their properties, the ZnO nanostructures need to be hybridized with other nanostructured materials. For the successful fabrication of any hybrid materials, two necessary requirements should be fulfilled, (i) structural appropriateness of the underneath backbone, and (ii) desired properties of the nanostructures utilized for hybridization. Three dimensional networks consisting of interconnected ZnO tetrapods, which can be synthesized in large amounts by the flame transport synthesis, are a very adequate choice as the template.¹¹ Owing to the three dimensional shape of the tetrapodal microparticles, highly porous networks can be fabricated. Due to the super-hydrophilic properties of such templates and the large free volume, these networks can be homogeneously coated using any kind of nanoparticle dispersion.¹¹ Fullerene C₆₀ exhibits remarkable properties such as strong UV absorption, excellent electron accepting, charge transfer, etc.^{1e} when used in the form of a very thin coating. Therefore, the characteristic features of individual C₆₀ molecules are very useful for the desired functionalities. Both being very unique nanomaterials in terms of physical properties, accordingly we aimed to synthesize a 3D hybrid material in the form of C₆₀ coated ZnO tetrapods and investigate its optical, electronic, and sensing properties in detail.

Actually, ZnO and C₆₀ are very complementary, because they can significantly enhance each other's functionalities, thus making

the hybrid system a very interesting candidate in terms of technological relevance.¹³ For example, ZnO is a very important gas sensing material and its sensitivity as well as selectivity can be further improved by decorating the ZnO surface with carbon nanostructures.^{12c,14} On the other hand, ZnO-fullerene based hybrid structures have shown increased electron mobility leading to an enhanced efficiency of solar cells.^{1b} Several hybrid material systems based on carbon–ZnO have been synthesized towards different applications^{14a,15} but to the best of our knowledge, the effect of fullerene layers on the ZnO surface has been less explored, and mainly with studies of its properties at room temperature (RT).¹⁶ A temperature dependent investigation might reveal more about the mutual effects of ZnO and C₆₀ with respect to each other's properties, for example, electron transfer behaviors,^{1a} optical responses and electrical conductivity changes, etc.

ZnO inherits n-type electrical conductivity due to unavoidable defects which can be easily enhanced by doping with group III elements.¹⁷ For optoelectronics applications, e.g., LEDs, a p–n junction is required which provides the necessity to make ZnO p-type as well. But achieving p-type conductivity in ZnO is really difficult and has been a topic of discussion since ever.¹⁸ Although a successful p-doping of ZnO utilizing N,¹⁹ As or P sources has been reported, its stability and reproducibility are still an open topic. In general, p-type conductivity is achieved by doping with acceptor elements and this requirement is nicely fulfilled by fullerene molecules due to their strong charge ejecting properties.²⁰ Inspired by the unique properties of ZnO material and C₆₀, we have fabricated a C₆₀–ZnO tetrapod based hybrid 3D porous networked material, where fullerene molecules are strongly attached to the surface of nano-microscale arms of ZnO tetrapods by using a simple infiltration technique.¹¹ ZnO itself exhibits exceptional optical properties and the addition of C₆₀ introduces additional states within the bandgap, which promotes further advanced applications. In the present work, we successfully varied the amount of C₆₀ on ZnO tetrapods and investigated the samples' morphological, structural and optical properties in detail, under various conditions. The C₆₀ decorated ZnO samples have also been explored via low temperature photoluminescence (PL) studies, which indicate electron transfer processes from C₆₀ to ZnO. The computational modeling for the density of states of the C₆₀–ZnO hybrid system also supports the experimental results and preliminary gas sensing studies hinted its potential towards technological applications, showing excellent ethanol sensing properties. Since ethanol is one of the main products of alcoholic fermentation in winemaking processes,²¹ various studies have been performed to develop cost-effective ethanol sensors for continuous monitoring of the ethanol concentration during the wine production.²²

Motivated by the abovementioned features, we synthesized hybrid composites using flame based ZnO tetrapods covered with different C₆₀ floodings in a simple strategy.¹¹ The hybrid composites were fully characterized by morphological, structural, optical and electrical techniques. Optical spectroscopy investigations highlighted the effect of the C₆₀ addition on the absorption and luminescence properties of ZnO. Noticeable differences were observed in the near band edge (NBE) region with the amount of the C₆₀ floodings, namely an increase in the relative intensity of the free exciton (FX) and 3.31 eV emission line.

Furthermore, exciting the composite samples at the maximum of the C_{60} absorption band led to the observation of the ZnO green luminescence, evidencing the occurrence of charge transfer processes. Further rationalization of the interaction of C_{60} with ZnO and the related charge transfer process was also supported by density functional theory (DFT) calculations.

Experimental

ZnO network synthesis

For the scaffold material for deposition of fullerenes a newly developed flame transport synthesis^{8a,23} was further modified. For this purpose, a conventional muffle furnace,^{8a} with a metal

crucible, is preheated up to 950 °C, and a nitrogen rich atmosphere is achieved using a N_2 gas flow of 41 lh^{-1} . After that, a simple Zn wire (of a total weight of 10–15 g, with a purity of approx. 99.95%) was inserted and placed into the metal crucible. After the temperature stabilization, pressured air was let into the furnace leading to a rapid Zn oxidation and thus to the formation of a large amount of ZnO 3D structures. In the next step, 3D ZnO pellets were formed out of the produced ZnO powder by compressing and sintering it at 1150 °C for 5 hours (Fig. 1a and S1a†).

Fullerene solution preparation

A water-based solution of fullerene powder (with 99.5% purity purchased at Sigma Aldrich) was prepared based on the

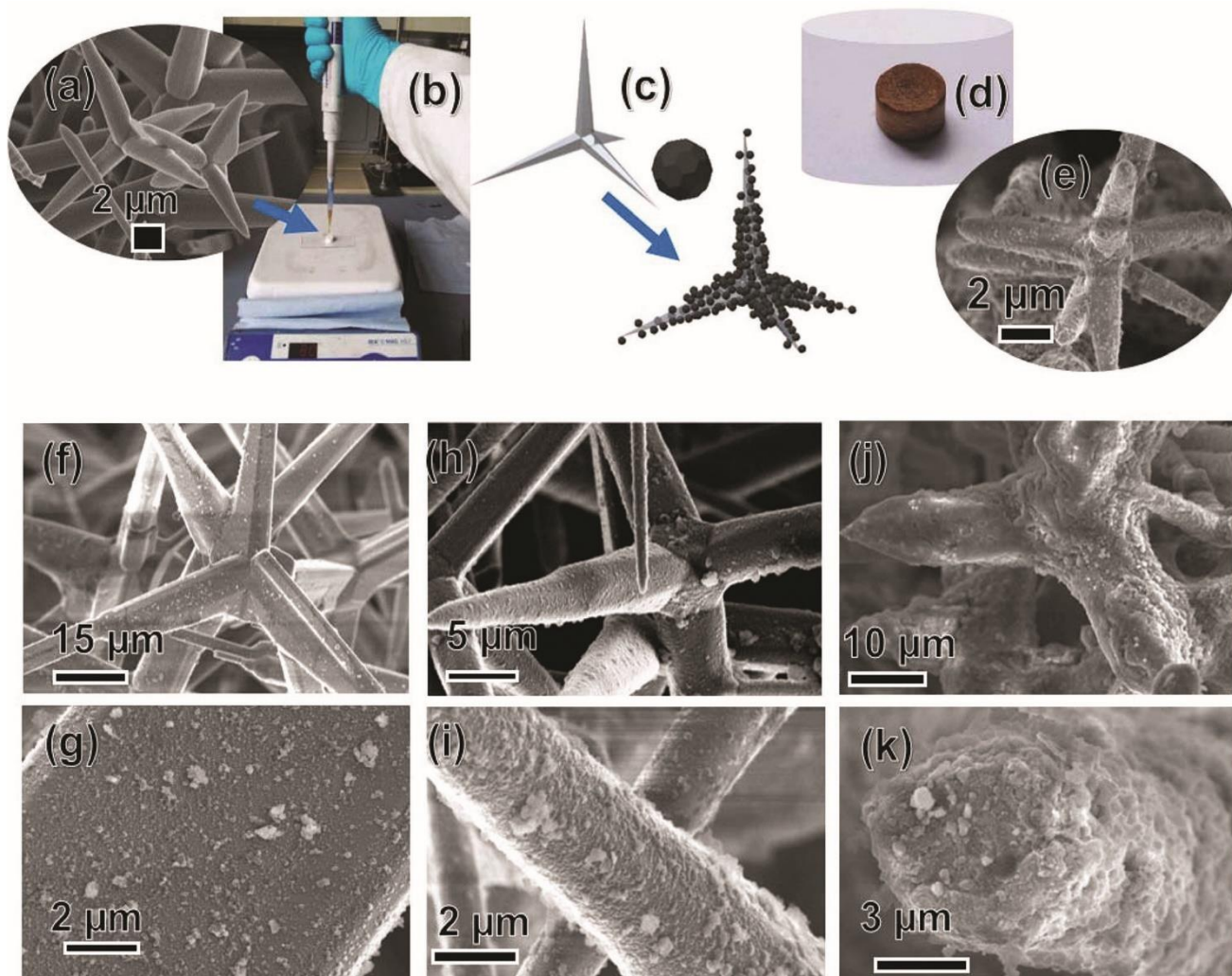


Fig. 1 ZnO microstructures and the process scheme: (a) SEM image of a ZnO-tetrapodal network after sintering. (b) Actual drop-coating process with a C_{60} solution. (c) Schematics of the surface after a flooding process was performed. (d) Camera image of a ZnO pellet after the coating. (e) SEM image of the ZnO network coated with C_{60} . (f)–(k) SEM images of the density variation of C_{60} on ZnO. (f,g) – 10 floodings, (h,i) – 20 floodings, (j,k) – 60 floodings.

method proposed,²⁴ where toluene was taken as a solvent (C_{60} exhibits excellent solubility in toluene).²⁵ First fullerene powder was diluted into toluene and then an identical amount (fullerene + toluene) of water was added into the solution and sonicated for several hours (typically 4 to 5 hours) until all the toluene was evaporated. Mixing

the C_{60} in the toluene, with a slightly lower concentration (2.0 $mg\ ml^{-1}$) than the maximum reported solvable concentration (3.8 $mg\ ml^{-1}$),²⁴ and dispersing it with an ultrasonic tip, resulted in a dark purple solution with no visible precipitation of fullerenes. Additionally, the beaker with C_{60} -toluene solution was placed into the ultrasonic

bath and the same amount of distilled water was rapidly added to the pristine solution. During the preparation of the solution with toluene no visible C₆₀ precipitates were observed, however when the distilled water was added to the mixture and the sonication process started, two clear phases were visible: a dark purple phase (standing for toluene + C₆₀) and a white phase (representing the possible hydrogenation of C₆₀).²⁶ After several hours when the toluene was evaporated, the color of the solution changed to a yellowish-brown^{5,27} and a water based solution of fullerenes was successfully produced.

Drop-coating of the ZnO network

The so prepared C₆₀ solution was subsequently drop-cast onto fresh sintered pellets of ZnO that were kept on a hot plate (~80 °C), as shown in Fig. 1b. The moderate density of the pellets was chosen (0.3 g cm⁻³) to guarantee a high porosity of the template for the optimal accessibility of the tetrapod surface for the C₆₀ molecules. For the small size of the cylindrical pellets (3 mm in thickness and 6 mm in diameter), 50 µL of the solution was taken per round. A hot plate maintaining a temperature of 65 °C was utilized to accelerate the evaporation process. Intervals of 1.5 hours were kept between the rounds to let the water and the remaining solvents present in the solution evaporate (ESI Video, V1†). The total number of coating cycles was varied from 5–60, thus resulting in the total amount of fullerenes on the ZnO surface in the range of 0.5–6 mg, respectively. In the final step the C₆₀ coated ZnO templates were dried in a vacuum furnace (at 65 °C, 100 mbar, for at least 8 hours). Even though some drop-casting procedures took several weeks, the solution remained unchanged and formed no visible precipitates. Fresh sintered ZnO pellets revealed extreme hydrophilic properties, allowing a fast penetration of the droplet of the water solution of C₆₀, while the pellets that were kept for several weeks in the room with the typical humidity and the absence of UV light turned out to be hydrophobic. Performing a heating treatment of these templates at 600 °C in the ambient atmosphere for 30 min solves the problem of hydrophobicity.

Characterization

The produced ZnO/C₆₀ composites were characterized by scanning and transmission electron microscopy (SEM, TEM), Raman spectroscopy, absorption, photoluminescence, PL-excitation (PLE) and electrical measurements. SEM analysis was performed in a Zeiss Supra 55 V with a working voltage of 15 kV and a working current of 10 µA. For TEM characterization a Technai F30 STwin was used (with FEG, accelerating voltage of 300 kV, Cs = 1.2 and an EDAX EDX detector). A small amount of the hybrid network, consisting mostly of single tetrapods or even of only the tetrapod part, was placed on a Cu grid with a carbon mesh sample holder. In order to evaluate the

chemical and structural composition of the ZnO/C₆₀ composites, RT Raman spectra were obtained by using a alpha300 RA, WITec system, with a triple grating spectrometer (600 gr mm⁻¹) and a CCD detector. The measurements were performed in a backscattering geometry using the 532.2 nm line of a cw laser. The spot size of the laser on the sample was ~1.41 µm, the maximum power at the sample was ~52 mW and the entire scattered beam was collected by an optical fiber with a diameter of 50 µm. The spectra were taken with a spectral resolution of 1 cm⁻¹. Additional measurements were performed in a Jobin Yvon HR800 spectrometer, using the 442 nm wavelength radiation from a cw He–Cd laser, a ×100 magnification lens and a 1800 gr mm⁻¹ diffraction grating.

The RT samples absorption was recorded in a UV/Vis JASCO V-560 system equipped with deuterium and halogen lamps and a ISV-469 integrated sphere. Steady state PL spectroscopy was performed as a function of temperature (from 10 K to RT) using a cold finger He cryostat. The 325 nm line of a cw He–Cd laser (power density $I_0 < 0.6 \text{ W cm}^{-2}$) was used as the excitation source, corresponding to an energy of ~3.8 eV. The luminescence radiation was dispersed using a Spex 1704 monochromator (1 m, 1200 gr mm⁻¹), then it was detected with a cooled Hamamatsu R928 photomultiplier. All the measurements were conducted using a neutral density ND1 filter to avoid damaging the samples by overheating with the UV radiation. The RT PLE was assessed in a Fluorolog-3 Horiba Scientific set-up with a double additive grating Gemini 180 monochromator (1200 gr mm⁻¹ and 2 × 180 mm) in the excitation and a triple grating iHR550 spectrometer in the emission (1200 gr mm⁻¹ and 550 mm). As excitation source a 450 W Xe lamp was used. The PLE has been measured by setting the monochromator in the maxima of the optically active defects and the excitation has been scanned to higher energies. Additionally, the same Fluorolog-3 system was used to perform energy dependent RT PL measurements. Namely, the RT PL of the ZnO/C₆₀ was evaluated by exciting the samples with below ZnO bandgap energy, corresponding to the blue absorption maxima reached after the functionalization with C₆₀.

I–V measurements were performed using a self-designed setup consisting of a PC-controlled micromanipulator with Cu/ Au sputtered contacts, Keithley that is controlled through a Labview program allowing to measure the current flowing through the template at the set intervals in the studied voltage ranges. (Due to the still high template resistance 2-wire measurements were performed.) Cylindrical templates of the same ZnO density with and without C₆₀ coating were analyzed. Several types of electrical contacts deposited at both ends of a cylindrical template were tested: adhesive

silver paste with its solvent being evaporated, or sputtered gold contacts, or sputtered Ni–Au contacts.

Device preparation and gas sensing measurements

The devices based on ZnO/C₆₀ were fabricated using the same approach reported in previous studies,²⁸ while devices based on individual hybrid microstructures were fabricated in a FIB/ SEM system using the procedure reported by Lupan et al.²⁸ Hybrid individual microstructures were contacted with a Pt complex to Au/Cr pads (Fig. S8a†). UV measurements were performed at RT in the dark and in air (relative humidity ~ 30%) and upon UV illumination at $\lambda = 365$ nm (~3.4 eV) and an intensity of ~10 mW cm⁻², as was reported earlier.^{8b} In the case of devices based on networks, gas sensing measurements were performed in the range of 20–400 °C, in order to determine the optimal operating temperature (OPT). For the devices based on individual structures, the measurements were only performed at RT. More details on gas sensing measurements were presented in our recent work.²⁸ The gas response (*S*) was defined as,

$$S = \left[\frac{R_{gas} - R_{air}}{R_{air}} \right] \times 100\%$$

where, *R*_{gas} and *R*_{air} are the resistance of the sensor under exposure to gas and ambient air, respectively.

DFT computational modeling

Under the framework of density functional theory (DFT)²⁹ computational modeling is performed using the Vienna ab initio simulation package (VASP).³⁰ The projector-augmented-wave (PAW)³¹ method as implemented in VASP is used with the Perdew–Burke–Ernzerhof³² (PBE) variant of the generalized gradient approximation (GGA) as the exchange correlation functional. A plane-wave cutoff of 520 eV has been kept for the kinetic energy. We have also included van der Waals correction in the form of Grimme's semi-empirical corrections.^{32a} The hexagonal stable phase of ZnO (space group P6₃mc) has been considered in our modeling where each Zn atom occupies the tetrahedral void formed by 4 adjacent O atoms and a similar configuration is maintained for O atoms. We have considered a supercell of ZnO to model the surface adsorption of C₆₀ molecules on the oxide. The fullerene molecule is adsorbed on the (0 0 1) surface of ZnO. A space of 30 Å is kept along the *c*-direction to avoid any spurious interactions of the simulation cell with their periodic images. During structural relaxation, to minimize the computational cost associated with a relatively large supercell, only top one layer of ZnO along with the adsorbed molecules on it is allowed to relax keeping the bottom layers of ZnO fixed. The Brillouin zone was sampled with a *k*-mesh of within the Monkhorst-Pack³³ scheme.

Results and discussion

The fabrication strategy for the C₆₀–ZnO based hybrid composites is presented in Fig. 1(a–d). The micro- and nanoscale tetrapods with pyramidal arms (length in the range of 10 to 50 μm, base and tip diameters ~10 μm and 500 nm, respectively) as shown in the scanning electron microscopy image in Fig. 1(a) are utilized as a backbone for C₆₀ molecules decoration. The tetrapod based 3D interconnected network tablets with a porosity of ~92%, which were achieved by post-sintering (favors interconnections), were infiltrated with commercially available C₆₀ in the solution form via a pipette (Fig. 1b and ESI Video, V1†). The high porosity and hydrophilicity in the network allow a homogeneous flow of C₆₀ based solution in the entire network and drying results in an attachment of C₆₀ molecules on the surface of the ZnO tetrapod arms (Fig. 1c). The amount of C₆₀ molecules decorated on ZnO tetrapods depends on the number of infiltrations and the used concentration of the dispersion. The initial ZnO templates are white in color (Fig. 1b), turning into brownish color (Fig. 1d and S1†) after C₆₀ infiltrations (~50 floodings). The number of floodings is the most important parameter deciding the C₆₀ coverage at ZnO tetrapod arms and, depending on the requirements, from well separated C₆₀ molecules to continuous C₆₀ layers (mono and multiple) on the surface of ZnO tetrapod arms can be easily achieved by the here adopted dropcast strategy. Typical SEM images corresponding to C₆₀ coated ZnO tetrapods from the hybrid network in Fig. 1d are shown in Fig. 1e, S2 and S3.† The detailed SEM analysis of the coated templates revealed a homogeneous coverage of the ZnO tetrapods and, depending on the number of cycles (ESI Video, V1†), more or less dense distribution of C₆₀ was achieved (Fig. 1f–k, S2 and S3†). However, measuring the smallest particle at the ZnO surface, it is visible that C₆₀ is drawn together forming clusters with sizes varying from 100 nm to 1 μm (Fig. 1g, i, k and S3†).

The crystallinity of the ZnO/C₆₀ was evaluated by electron microscopy and Raman spectroscopy. In particular, transmission electron microscopy studies revealed the presence of fullerite, a crystalline solid C₆₀ modification.³⁴ In bright field mode several clusters attached to ZnO tetrapods have been identified as shown in Fig. 2(a and b). High resolution TEM studies confirmed a highly crystalline arrangement, demonstrated in Fig. 2c. The corresponding fast Fourier transform pattern (Fig. 2d) matches well with a simulated electron diffraction pattern from the cubic C₆₀³⁵ in the [1 0 2] orientation (Fig. 2e). Based on the high resolution images, the interplanar spacing corresponds to 3.23 Å for (4 0 2) (literature value: 3.17 Å (ref. 36)) and 7.89 Å for (1 1 1) (literature value:

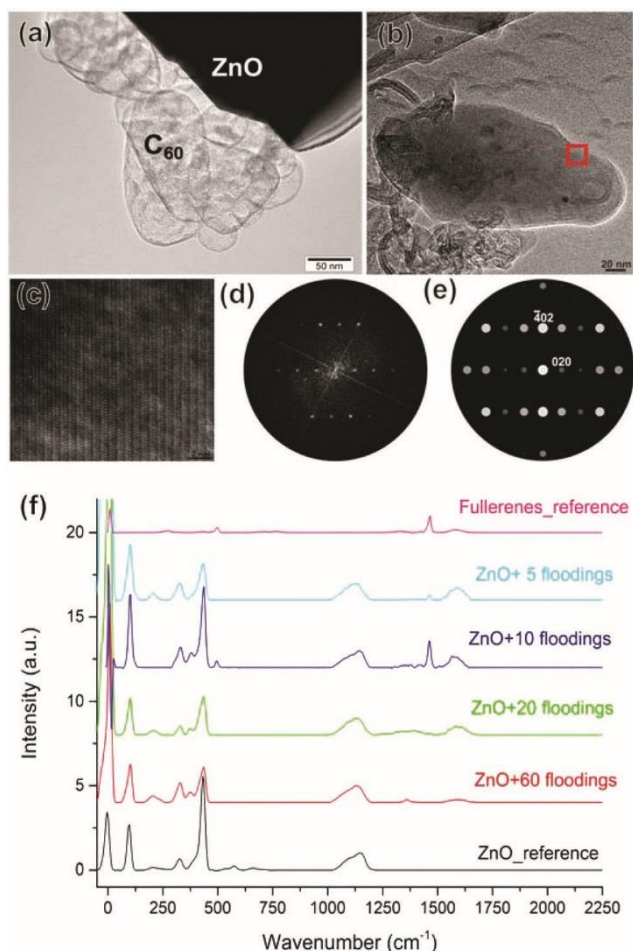


Fig. 2 (a) TEM low magnification bright field micrograph of several C_{60} clusters on top of a ZnO tetrapod surface (appearing black due to the larger thickness compared to the thickness of C_{60} clusters). (b) TEM bright field image of a single cluster of C_{60} . (c) HRTEM micrograph from the position marked in (b) aligned to [102]. (d) FFT pattern from (c). (e) Simulated ED-pattern from [102] orientation. (f) Raman spectra of reference fullerene powder (pink), reference ZnO network (black) and ZnO network coated with fullerenes. Number of floodings for the analyzed samples was: 5 (cyan), 10 (blue), 20 (green) and 60 (red). For the ZnO network with 60 floodings of C_{60} on the surface the D peak at 1350 cm^{-1} becomes sharper and more defined.

8.18 \AA (ref. 36)). The deviation for (020) indicates an increased lattice parameter b . Moreover, a tilt in α and γ was observed. Similar to Fig. 2a many fullerite fractions have been identified next to ZnO tetrapods. Basically, C_{60} molecules were arranged to form spherical clusters with diameters from 50 to 1000 nm (Fig. S3 and S4a†). By a selected area electron diffraction (SAED) pattern taken from the red marked region (Fig. S4b†) it was shown that every cluster is an independent crystalline domain (Fig. S4c†) and every interface between two spheres represents a domain boundary. Thus in the beginning small clusters of C_{60} molecules start to agglomerate. While continuously growing occasionally clusters merge and form a common boundary.

RT Raman spectra of the ZnO/ C_{60} composites are presented in Fig. 2f. Beside the vibrational modes known for the ZnO (black curve), all of the peaks have been identified and correspond to the values reported in the literature for fullerenes.³⁷ For the latter, the strongest peak at 1469 cm^{-1} , the pentagonal pinch mode (PPM) corresponding to a totally symmetric $Ag(2)$ mode,³⁸ is seen in samples having the number of floodings from 5 to 20 (cyan, blue and green curves in Fig. 2f). The samples with 10 floodings (blue curve) show most clearly the presence of the further fullerene peaks $Ag(1)$ at 495 cm^{-1} and a broader peak at $1565\text{--}1581\text{ cm}^{-1}$ that could be assigned to the $Hg(8)$ mode. An interesting phenomenon is observed for the sample with the much higher counting (60 floodings, red curve), namely the distinct D band peak at 1350 cm^{-1} , well known for the carbon materials indicating the presence of defects. Explanation for that might be the fullerene structures building a layer on top of ZnO and producing edge defects that are Raman active.³⁸

PL and PL excitation measurements were carried out in order to investigate the influence on the optical properties of the 3D ZnO networks by the addition of C_{60} . Fig. 3a depicts the normalized PL spectra of the ZnO/ C_{60} samples (from the UV to the near infrared) obtained at RT. All samples exhibit a dominant green/yellow emission band with maxima slightly shifted between the samples. While for the samples with 10 and 20 floodings the maxima are located at $\sim 2.23\text{ eV}$, the samples with the lowest (5) and highest (60) C_{60} content evidence a high energy shift of the band maximum peak position ($\sim 2.27\text{--}2.28\text{ eV}$). As reported in the literature,^{17b} this PL band is frequently composed by the overlap of different emitting centers, which may have different relative intensities in the analyzed samples, resulting in the shift of the maxima of the overall emission. Even so, if the emission is originated from the same optical center, the $\sim 50\text{ meV}$ apart could be related to distinct band bending effects on the ZnO electronic structure and ZnO/ C_{60} interface, assuming that the green/yellow band involves effective mass described electronic states. At 14 K (Fig. 3b), spectra are also dominated by the visible band, evidencing a vibrational assisted structure, similar to the so-called structured green band, widely reported in the literature.^{17b,39} Regarding the NBE recombination that appears in the UV region (inset of Fig. 3b and Fig. S5†), noticeable changes can be observed with increasing C_{60} content, meaning that distinct interactions between the ZnO surface and C_{60} molecules occur for the different hybrid systems. In particular, a strong quenching of the NBE is seen in the sample with the lowest (5) flooding. In this case, the NBE seems to be absent when compared with the visible emission, however an ultraviolet/blue band at 3.0 eV was also detected, probably

related to disorder-induced defects, as was previously observed in thin films.⁴⁰ For the samples with higher floodings (10 to 60), a well-defined NBE emission was observed (Fig. 3c and S6†). While the sample with 10 floodings exhibits NBE PL mainly dominated by the Al-donor bound exciton transition, increasing the C₆₀ floodings (20 and 60) promotes changes in the dominant donor bound exciton recombination, accompanied by the observation of the emission at 3.31 eV and its phonon-replicas. This line has been widely discussed in the literature⁴¹ and associated with distinct recombination mechanisms, such as structural defect-related transitions^{41,42} or surface excitonic contribution.⁴³

with the presence of surface states, as identified by the influence of distinct plasma treatments on the recombination line intensity. In fact, the same authors observed an increase in the relative intensity of this line when ZnO tetrapods grown by LAFD were mixed with carbon nanotubes (CNTs).⁴⁵ This fact constitutes another indication that the 3.31 eV emission is affected by surface states. When incorporated in the CNT composite, the surface of the ZnO tetrapods was in direct contact with the functionalized CNTs, leading to a higher concentration of electron-hole pairs on the surface of the ZnO 3D structures. The enhancement of the PL intensity in ZnO/carbon composites was previously reported in the literature,^{15b,c}

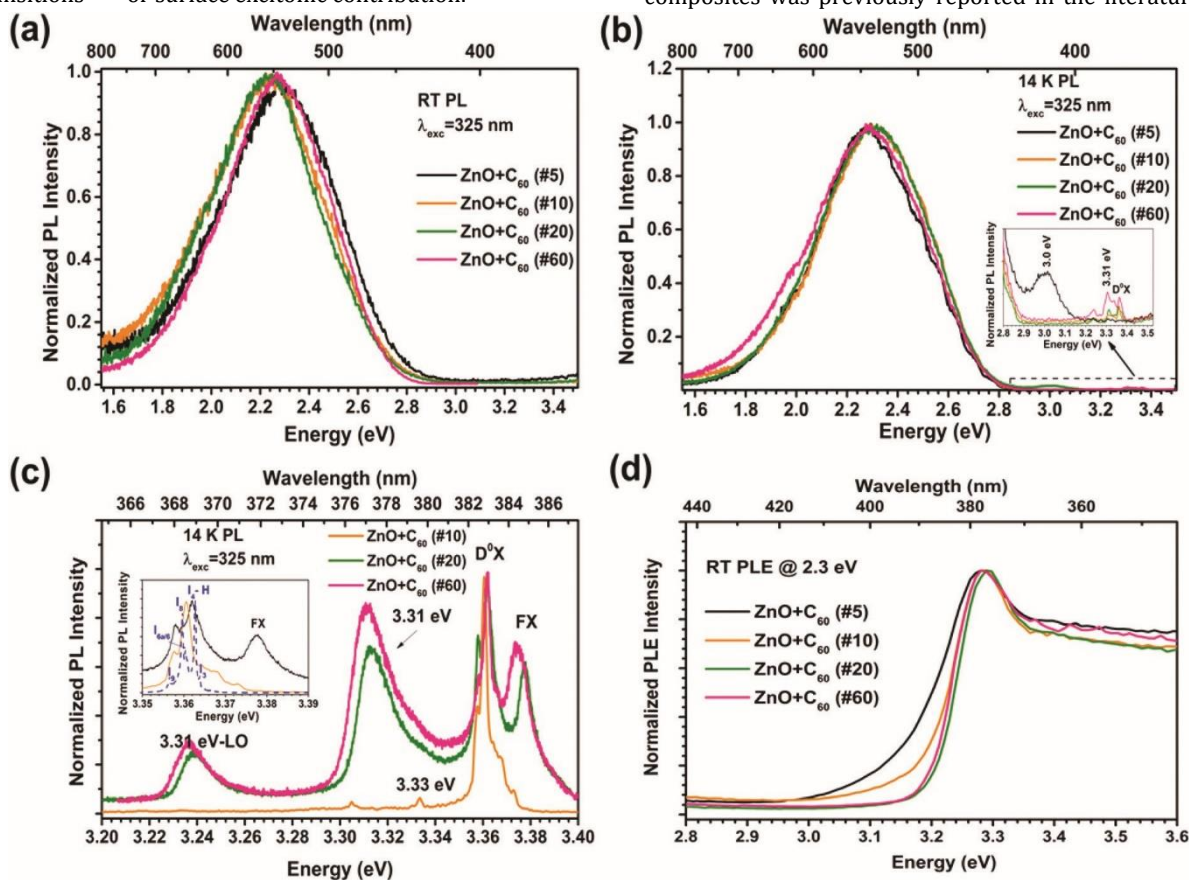


Fig. 3 (a) Normalized RT PL of the studied ZnO-T-C₆₀ samples, excited with 325 nm (3.8 eV photon energy) and using a ND1 filter. (b) Normalized 14 K PL spectra of the same samples under the same excitation conditions. The inset shows an amplification of the UV region. (c) Normalized 14 K PL spectra of the NBE region for the samples with 10, 20 and 60 floodings, evidencing a well-resolved emission. The inset includes high resolution spectra in the FX-D0X region and a comparison with the bulk ZnO emission (dashed line). (d) RT PLE spectra of the ZnO-T-C₆₀ samples with different floodings, monitored at 2.3 eV (visible band maximum).

Recently, this emission was studied in detail by J. Rodrigues et al.⁴⁴ in ZnO microrods grown by laser assisted flow deposition (LAFD). This line was seen to dominate the low temperature PL spectrum in the UV region, evidencing a spectral shape similar to the one obtained for the ZnO/C₆₀ samples with 20 and 60 floodings. The reported work suggests a strong correlation of the 3.31 eV emission line

and attributed to the generation of a higher concentration of optically active centers, namely improving surface and excitonic related recombination. A similar phenomenon is likely to be present in the ZnO samples with a higher amount of C₆₀ on its surface and thus the enhancement of

the relative intensity of the 3.31 eV emission. It is important to note that the intensity of this line increases with the increase of C_{60} , as in Fig. 3c. Moreover, besides the enhancement of the 3.31 eV emission, also the intensity of FX recombination is seen to increase (inset of Fig. 3c and Fig. S6†), accompanied by a decrease in the relative intensity of Al donor-bound exciton, meaning that with the used conditions an enhancement of free carrier concentration is favored rather than the carriers captured through the Al shallow donor. With the increase of C_{60} floodings differences in the electronic states band alignments are expected, inducing changes in the preferential recombination paths. Indeed, the offset between the lowest unoccupied molecular orbital (LUMO) of C_{60} and the conduction band minimum (CBM) of ZnO defines the barrier for charge transfer between the two materials and was seen to depend on the thickness of the C_{60} layer covering the ZnO structures.⁴⁶

These differences are also reflected in the RT PLE spectra (Fig. 3d) when monitored at the visible band

maxima. The spectra show that the emission is mainly populated with photons with energy equal to or higher than the ZnO bandgap. Furthermore, it can be also shown that the ZnO bandgap absorption feature becomes slightly narrower as the C_{60} floodings increase, exhibiting a steeper absorption and a slight shift towards the expected bandgap to pure ZnO. Such behavior indicates a suppression of the effective mass described electronic states in the population pathways of the broad emission, suggesting that a charge transfer from ZnO to C_{60} cannot be discarded. As shown in Fig. 3d, the band tail observed below the ZnO bandgap is more pronounced for samples with lower C_{60} floodings.

Comparing these results with the ones observed for the NBE emission, one notes that the absence of this emission in the sample with the lowest C_{60} floodings is accompanied by a more pronounced effect in the band tail states of the PLE spectra, while steeper absorption results in a wellresolved NBE (Fig. 3c and Fig. S6†). Absorption measurements (Fig. 4a) reveal, besides the ZnO bandgap, additional visible and near infrared absorption bands in the

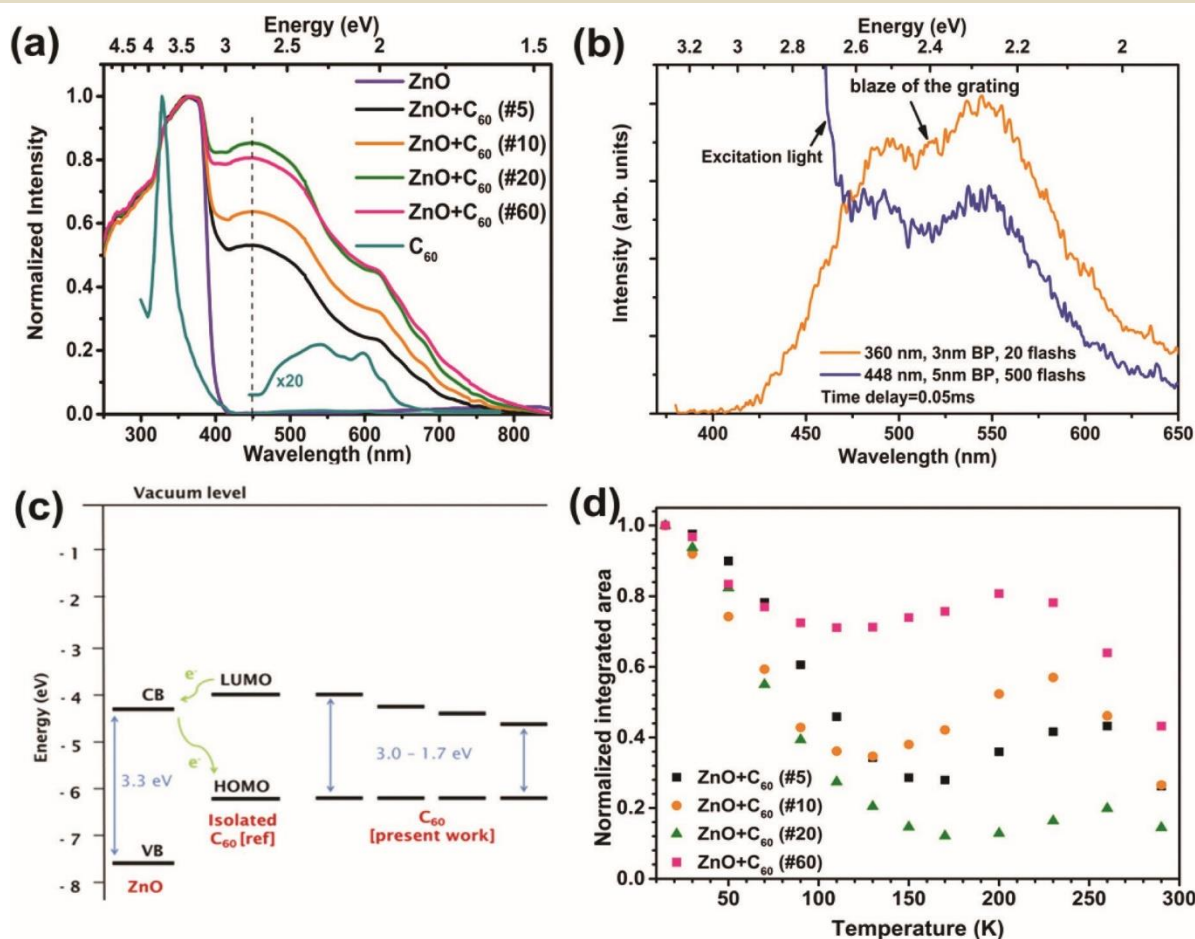


Fig. 4 (a) Absorbance spectra of the ZnO-T- C_{60} (C_{60}) absorption spectrum reproduced from ref. 56 and 57 and (b) RT TRPL of the sample with 20 floodings acquired after 0.05 ms of the pulse of a Xe flash lamp. The valley at ~517 nm (~2.40 eV) corresponds to the blaze of the grating. (c) Schematic representation of the band alignment for ZnO and C_{60} molecules, based on the spectroscopy results and ref. 3. (d) Relative intensity of the visible band as a function of the temperature for the analyzed samples.

samples with C_{60} on the surface, where the band with the highest intensity is peaked at 448 nm (~ 2.77 eV). The wide absorption region appears when C_{60} is added to the ZnO tetrapods, with its intensity increasing as the C_{60} amount increases up to 20 floodings. For comparison, the RT absorption of a C_{60} sample from ref. 47 is included in Fig. 4a. As can be seen, the most intense absorption band in the visible region (dashed line in Fig. 4a) of the composite samples is not present in the C_{60} absorption spectrum, suggesting that its origin is likely related to ZnO- C_{60} interactions. The additional absorption bands are related to the C_{60} molecules.

In order to evaluate the possibility of charge transfer from the C_{60} molecules to ZnO, PL measurements were carried out exciting the samples at 448 nm (maximum of the mentioned absorption band), using a Xe flash lamp with a delay time close to the pulse lamp width in order to approach the steadystate conditions (Fig. 4b). For comparison purposes a band to band excitation was also performed using the same delay. In both cases a ZnO green

band was detected, evidencing that this ZnO emission band can be populated via both excitation processes. The excitation at 448 nm corroborates the hypothesis of charge transfer from the C_{60} to ZnO. These results are also in line with the behavior observed for the ZnO NBE where an increase in the relative intensity of the FX and the 3.31 eV line was seen to occur with the increase of the amount of C_{60} in the ZnO surface, meaning that more electrons are being transferred to the ZnO conduction band and surface states, respectively. Fig. 4c shows a schematic representation of the possible band alignment for these materials, evidencing the two described charge transfer mechanisms suggested by the spectroscopic measurements.

In order to gain a better insight into the mechanisms involved in the luminescence process, temperature dependent PL studies were carried out, as can be seen in the ESI (Fig. S7†). Fig. 4d shows the dependence of the integrated green/yellow PL intensity band on the temperature. All the analyzed samples exhibited a similar

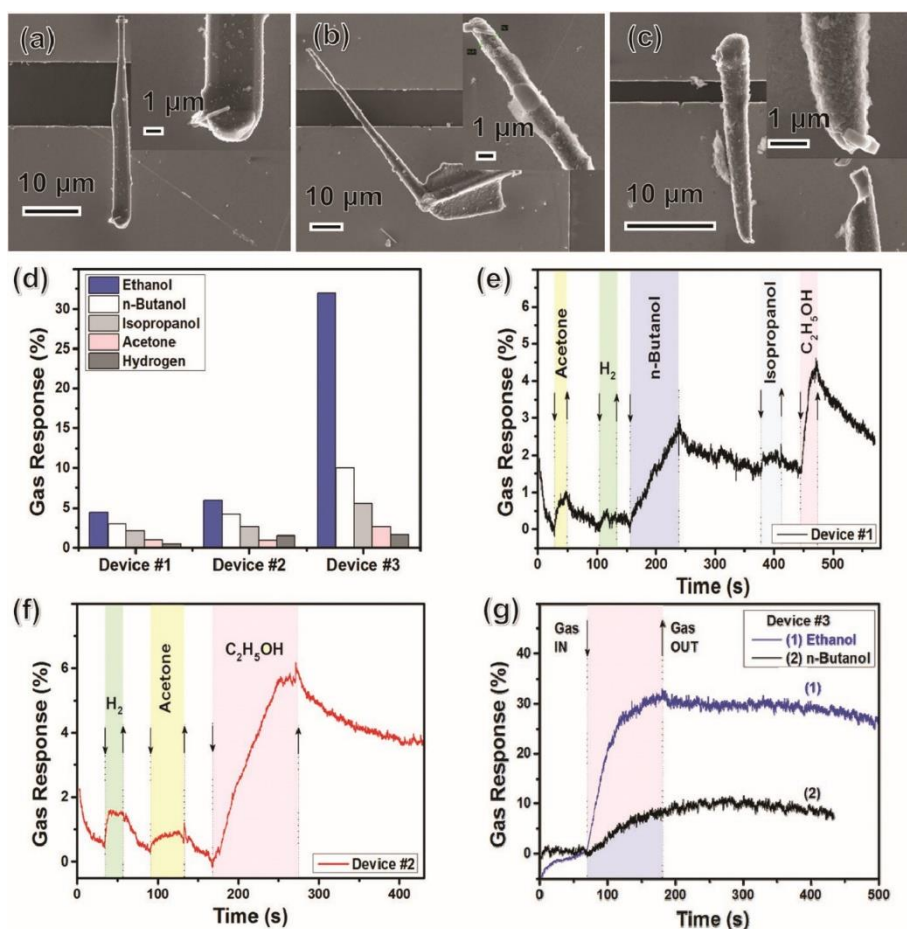


Fig. 5 SEM images of devices based on individual ZnO-T- C_{60} arms at lower and higher magnification to demonstrate the presence of C_{60} on the surface of a ZnO-T arm and electrical connections, respectively: (a) Device #1 - 10 floodings; (b) Device #2 - 20 floodings; (c) Device #3 - 60 floodings. (d) The calculated gas response at RT of fabricated devices using individual hybrid structures ZnO-T- C_{60} . The transient gas response at RT of: (e) Device #1; (f) Device #2; (g) Device #3.

behavior, with the overall intensity of the visible band decreasing up to 130–150 K followed by an increase in the intensity between these temperatures and 230–260 K and with a subsequent decrease up to RT. These results corroborate the hypothesis of having different optical active centers contributing to the broad visible emission. With increasing temperature, competitive nonradiative mechanisms start to take place, leading to a decrease in the intensity of all the emitting centers present. As the temperature rises, one of the defect states involved in green/yellow emission becomes thermally populated at the expense of another, resulting in an increase of the overall intensity. Finally, at higher temperatures, the nonradiative transitions dominate and the band intensity decreases again. A similar behavior was previously observed for ZnO with Zn_2SnO_4 and with Bi_2O_3 hybrid networks synthesized by the same method.^{39c}

Hybrid nanostructures, especially ZnO based, exhibit a very important role towards nanosensing, which also motivated us to investigate their sensing capabilities. Based upon the number of C_{60} floodings, individual micro- and nanoelectronic devices were fabricated and their detailed electrical sensing characteristics with respect to different volatile gases have been studied. Fig. 5 shows the SEM images of devices fabricated using individual zinc oxide tetrapod (ZnO-T) arms coated with C_{60} (ZnO-T- C_{60}). Three sets of devices were fabricated with relatively different contents of C_{60} on the surface of the ZnO-T arm: 10 floodings (Fig. 5a, its inset and Fig. S8a†), 20 floodings (Fig. 5b and inset) and 60 floodings (Fig. 5c and inset). The current–voltage (I–V) characteristics of the devices are presented in Fig. S8b,† showing the formation of asymmetrical double Schottky contacts, due to a higher work function of Pt contacts.⁴⁸ All individual structures have similar diameters in the range of 1–3 μm from one end to another. The calculated gas response of devices to different vapors of volatile organic compounds (VOCs) and hydrogen (H_2) gas is shown in Fig. 5d. The concentration of VOCs was 100 ppm and of H_2 gas was 1000 ppm. Actually, a previous study showed that pristine individual ZnO micro- and nanostructures showed a higher gas response to hydrogen gas (100 ppm),⁴⁹ with the highest gas response of $\sim 34\%$ (for pristine ZnO with a diameter of ~ 100 nm (ref. 49)). However, in the present case, a higher response to ethanol compared to H_2 gas is observed (see Fig. 5d).

Electrical contacts might lead to a varied sensing response and therefore nanodevices with both types (ohmic and Schottky) of contacts were fabricated and investigated, showing identical electrical/sensing characteristics. Hence, silver paste based ZnO/ C_{60} devices were chosen for the matter of simplicity. In line with the generation of more free carriers with increasing C_{60} floodings, a notable increase in the conductivity is observed

(ESI, Fig. S9a†). Based on the linearity of the I–V curves, it can be assumed that an ohmic contact was achieved for the network templates and the corresponding dynamic UV sensing response is presented in Fig. S9b.† The calculated response (I_{UV}/I_{dark}) is ~ 1.6 , which is much lower compared to pristine ZnO-T networks reported earlier (>500). This can be explained based on complete covering of the ZnO tetrapod surface with C_{60} , hampering its accessibility for UV light to photogenerate the electron–hole pairs. The same situation was observed in the case of single ZnO-T- C_{60} structures (not shown here), which suggest that a lower content of fullerene on the surface of ZnO tetrapod arms would be rather preferable for gas sensing applications.

The here fabricated devices based on hybrid networks and individual structures demonstrated interesting gas sensing properties. By increasing the content of C_{60} the gas response to ethanol vapors is enhanced (taking into account that the diameter of structures is practically similar, Fig. 5). Thus, for Devices #1 (10 floodings), #2 (20 floodings) and #3 (60 floodings) the gas response to ethanol vapors is 4.43%, 6% and 32%, respectively (see Fig. 5d). The dynamic response to VOCs (100 ppm) and H_2 (1000 ppm) is shown in Fig. 5e, f and g for Devices #1, #2 and #3, respectively. Due to the operation of devices at RT, the response and recovery time are relatively high. The calculated response and recovery time (defined as the time to reach and recover the 90% of full response) of ethanol vapors are, respectively, 45 s and >350 s for Device #1, 70 s and >350 s for Device #2, 80 s and >15 min for Device #3. Thus, the evident increase in response/recovery times by increasing the content of C_{60} is confirmed, which could be related to the lower accessibility of gaseous species to the ZnO surface or to a higher influence of C_{60} on the gas response mechanism. It has been demonstrated that carbon based materials have a slow recovery at RT to VOCs or different gases >such as NH_3 and NO_2 .⁵⁰ Thus, a higher content of C_{60} can improve the ethanol vapor response, but results in slower recovery.

C_{60} mainly exhibits n-type semiconductor conductivity and the oxygen content can drastically change its electrical resistance.^{14d,51} Also, previous reports showed that C_{60} thin films have good response to VOCs.^{14a,d,e} Thus, the increase in gas response to ethanol vapors can be attributed to an increase in C_{60} content. The main mechanism can be thus explained on the basis of the interaction of VOCs and H_2 molecules with oxygen from the C_{60} layer, creating CO_2 and water, respectively,⁵² as well as charge transfer between C_{60} and gas molecules.^{14a} However, additional studies need to be performed in order to determine the nature of complex adsorption of VOC molecules (physiosorption or chemisorption).^{14e} The incomplete recoveries to the initial baseline in the present devices indicate the adsorption of VOC molecules via chemical adsorption, i.e., a

comparatively strong interaction with C₆₀.^{14e} Additionally, the C₆₀ crystals behave like a sponge (with nanoscale porosity) in which the possibility of intercalation of VOCs cannot be ignored.⁵³ The interactions between few VOCs and C₆₀ might lead to certain weak ionic bonds which then result in localizing them within the C₆₀ crystal even at RT.⁵³ Due to RT, these reactions are relatively slow, which lead to lower response and especially recovery of devices (Fig. 5e–g).

Parameters such as sensitivity and limit of detection were also investigated for Device #3. Fig. S10† shows the dependence of ethanol sensitivity at RT versus concentration of ethanol vapors. The sensitivity was defined as the gas response (S) divided by the concentration of ethanol, i.e. %/ppm.⁵⁴ The theoretical detection limit was estimated to be 5 ppm as was reported in detail by Dua et al., i.e. using (signal/noise) ratio.⁵⁵ In general, such high response of microscale individual structures (diameter ~1 μm–3 μm), as in the case of Device #3 (~32%), can be easily explained on the basis of the C₆₀ coverage on ZnO, because the surface contribution to the electron transport through the ZnO-T arm is quite lower.⁵⁶ Since both the C₆₀ thin films and ZnO show n-type gas sensing behaviors,^{14d,51,57} it is very hard to distinguish which dominates the gas response in the case of the C₆₀–ZnO hybrid. However, the increased gas response to VOCs and increased recovery time hint that the C₆₀ film from the surface of the ZnO-T arm is most likely a dominating factor for the here fabricated devices. In the case of ZnO-T-C₆₀ networks, the degradation in response by increasing the temperature was observed. Fig. S11a† shows the gas response of networks versus operating temperature. The optimal temperature seems to be at 300 °C and the highest gas response was observed for the ethanol vapors. The data were calculated by applying one pulse at each operating temperature. However, by repeating measurements at the same temperature, the evident degradation in response was observed. Fig. S11b† shows the transient gas response of ZnO-T-C₆₀ networks at 300 °C by exposing repeatedly to the same concentration of ethanol vapors 5 times. A large shift in the electrical baseline is observed, which also induces the change in gas response. Such behavior was observed at temperatures higher than 200 °C, which can be attributed to the destruction (conversion to amorphous structures and disintegration into icosahedral) of C₆₀ molecules, as reported by Chen et al.⁵⁸

The adsorption behavior of C₆₀ fullerene on the surface of ZnO was assessed by computing the binding energy of the system ($E(\text{ZnO}+\text{C}_{60}) - E\text{ZnO} - E\text{C}_{60}$). We obtain a binding energy of -5.1 eV, which indicates relatively stronger binding of fullerene on the ZnO surface. For a deeper understanding of the binding process, we have presented the total and partial density of states (DOS) for

ZnO + C₆₀ in Fig. 6a. It is clear from this figure that following the adsorption of fullerene, significant states are induced which is evident from the partial DOS of C atoms from C₆₀. Moreover, states at the Fermi level with visible contribution of C₆₀ are evident from this figure. This can explain the effect of C₆₀ on the observed enhancement of conductivity. We have performed a Bader charge analysis of the binding process and calculated the amount of charge transfer associated with fullerene adsorption on ZnO. We have observed that there is a charge transfer from C₆₀ to the ZnO surface with a net charge of +0.629 (e) on the fullerene molecule.

It is known from the literature that the chemical nature of C₆₀ resembles an n-type semiconductor and it is a highly electronically rich specie. The stronger interaction of C₆₀ with the ZnO surface and the resulting charge transfer are supportive of the above fact. To address the promising

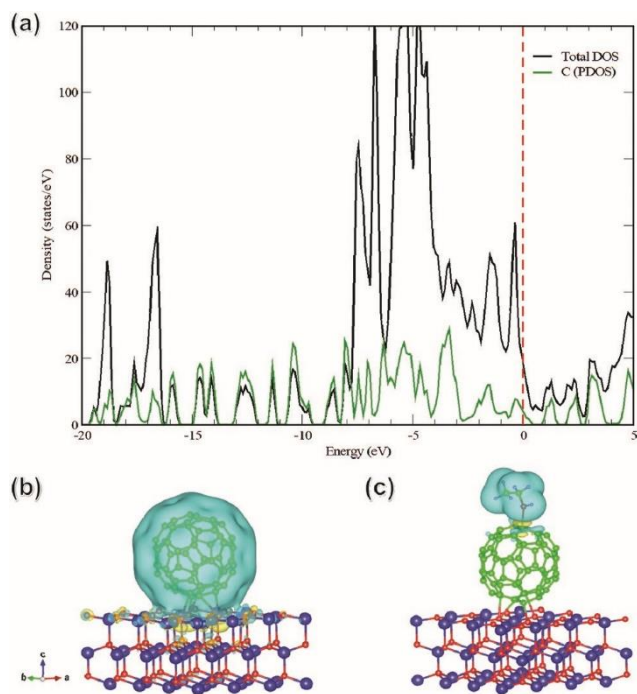


Fig. 6 (a) Total and partial DOS for fullerene (C₆₀) adsorbed on ZnO surface, (b) charge density difference isosurfaces for binding of C₆₀ on ZnO surface, and (c) binding of ethanol on ZnO + C₆₀ system. (The vertical red dashed line in (a) represents the Fermi energy. For isosurface, the yellow color depicts charge depletion and the cyan color charge accumulation. The isovalue used is 0.001 (a.u.). Atom color code: Zn (blue); O (red); C (green).

ethanol sensing properties of C₆₀ covered ZnO as observed in our experiments, we further considered the adsorption of an ethanol molecule on the ZnO + C₆₀ system. The adsorption energy in this case is found to be -0.39 eV, which indicates weak physisorption. The overall adsorption of C₆₀ on the ZnO surface and subsequent adsorption of ethanol are pictorially depicted as isosurface

plots in Fig. 6b and c. The favorable sensing of ethanol gas on C₆₀ can be attributed to the charging effect of the fullerene molecule on the ZnO surface.

Conclusions

In summary, we have demonstrated a simple strategy for cost effective fabrication of C₆₀ decorated ZnO tetrapod-based hybrid nanostructures and the corresponding 3D interconnected networks, which offer easy accessibility of features from individual as well as agglomerated C₆₀ molecules in 3D space. The remarkable features from both C₆₀ and ZnO tetrapods complement each other and cumulatively result in new and interesting properties in the hybrid composite form, suitable for advanced applications. Detailed photoluminescence, photoluminescence excitation and absorption studies revealed interesting optical properties, including hints about the charge transfer process between the adsorbed C₆₀ molecules and underneath ZnO. The charge transfer process was additionally confirmed by density functional theory calculations. The ZnO/C₆₀ nanostructure based individual nanodevices revealed interesting sensing behaviors towards volatile organic compounds where the operating temperature plays a very crucial role. The interesting optical and electrical properties open further avenues for the application of these ZnO/C₆₀ tetrapod based hybrid materials towards advanced technologies. However, understanding further properties would be highly interesting for the fundamental materials science community.

Author contributions

DS, RA, and YKM identified the idea and planned the study. DS, SS, LS, and FS synthesized and analyzed the materials. JR, AFM, NBS, MRC and TM carried out optical studies. DSM, GN and LK performed TEM studies. O. L. fabricated the micro and nanosensors on single C₆₀-ZnO-T and sensors based on individual structures. DS, VP, and OL performed sensing investigations. NKJ and Rajeev A finalized DFT studies. DS, TM, Rajeev A, LK, YY, RA and YKM analyzed the data and wrote the paper with contributions from other authors.

Conflicts of interest

There are no conflicts to declare.

Acknowledgements

The Kiel authors thank the Deutsche Forschungsgemeinschaft for financial support under schemes: SFB 1261 TP [(A05, RA) & (A06, LK)], and SFB 677 (C14). Additionally, a part of the work was funded by

FEDER funds through the COMPETE 2020 Programme and FCT (Portuguese Foundation for Science and Technology) funds through the project UID/CTM/50025/2013. The Uppsala authors would like to thank Swedish Research Council (Grant No. 2016-06014) for financial support and SNIC and UPPMAX, Sweden for providing the computing time. This research was partly supported by the project Institutional 45inst-15.817.02.29A funded by the Government of the Republic of Moldova.

References

- (a) S. Kirner, M. Sekita and D. M. Guldi, *Adv. Mater.*, 2014, 26, 1482–1493; (b) T. Hu, L. Chen, K. Yuan and Y. Chen, *Nanoscale*, 2015, 7, 9194–9203; (c) H. W. Kroto, J. R. Heath, S. C. O'Brien, R. F. Curl and R. E. Smalley, *Nature*, 1985, 318, 162–163; (d) J. Liu, A. G. Rinzler, H. Dai, J. H. Hafner, R. K. Bradley, P. J. Boul, A. Lu, T. Iverson, K. Shelimov and C. B. Huffman, *Science*, 1998, 280, 1253–1256; (e) D. M. Guldi and M. Prato, *Acc. Chem. Res.*, 2000, 33, 695–703.
- (a) T. Liu and A. Troisi, *Adv. Mater.*, 2013, 25, 1038–1041; (b) D. M. Guldi, *Chem. Soc. Rev.*, 2002, 31, 22–36.
- J. H. Shim, K. S. Lee, J. W. Seo and D. I. Son, *J. Nanosci. Nanotechnol.*, 2016, 16, 12017–12020.
- T. Song, J. Huo, T. Liao, J. Zeng, J. Qin and H. Zeng, *Chem. Eng. J.*, 2016, 287, 359–366.
- J. Wu, L. B. Alemany, W. Li, L. Petrie, C. Welker and J. D. Fortner, *Environ. Sci. Technol.*, 2014, 48, 7384–7392.
- M. Pfohl, K. Glaser, A. Graf, A. Mertens, D. D. Tune, T. Puerckhauer, A. Alam, L. Wei, Y. Chen and J. Zaumseil, *Adv. Energy Mater.*, 2016, 6, 1600890.
- D. Virovska, D. Paneva, N. Manolova, I. Rashkov and D. Karashanova, *Mater. Sci. Eng., C*, 2016, 60, 184–194.
- (a) Y. K. Mishra, S. Kaps, A. Schuchardt, I. Paulowicz, X. Jin, D. Gedamu, S. Freitag, M. Claus, S. Wille, A. Kovalev, S. N. Gorb and R. Adelung, *Part. Part. Syst. Charact.*, 2013, 30, 775–783; (b) Y. K. Mishra and R. Adelung, *Mater. Today*, 2018, DOI: 10.1016/j.mattod.2017.11.003; (c) D. Gedamu, I. Paulowicz, S. Kaps, O. Lupan, S. Wille, G. Haidarschin, Y. K. Mishra and R. Adelung, *Adv. Mater.*, 2014, 26, 1541–1550.
- I. Paulowicz, V. Postica, O. Lupan, N. Wolff, S. Shree, A. Cojocaru, M. Deng, Y. K. Mishra, I. Tiginyanu, L. Kienle and R. Adelung, *Sens. Actuators, B*, 2018, 262, 425–435.
- I. Hölken, G. Neubüser, V. Postica, L. Bumke, O. Lupan, M. Baum, Y. K. Mishra, L. Kienle and R. Adelung, *ACS Appl. Mater. Interfaces*, 2016, 8, 20491–20498.
- F. Schütt, S. Signetti, H. Krüger, S. Röder, D. Smazna, S. Kaps, S. N. Gorb, Y. K. Mishra, N. M. Pugno and R. Adelung, *Nat. Commun.*, 2017, 8, 1215.
- (a) Z. L. Wang, *Mater. Today*, 2004, 7, 26–33; (b) A. B. Djurišić, Y. H. Leung, K. H. Tam, Y. F. Hsu, L. Ding, W. K. Ge, Y. C. Zhong, K. S. Wong, W. K. Chan, H. L. Tam, K. W. Cheah,

- W. M. Kwok and D. L. Phillips, *Nanotechnology*, 2007, 18, 95702; (c) Z. Yang and X. Dou, *Adv. Funct. Mater.*, 2016, 26, 2406–2425.
- 13 D. M. Guldi, F. Zerbetto, V. Georgakilas and M. Prato, *Acc. Chem. Res.*, 2005, 38, 38–43.
 - 14 (a) P. Bairi, K. Minami, W. Nakanishi, J. P. Hill, K. Ariga and L. K. Shrestha, *ACS Nano*, 2016, 10, 6631–6637; (b) A. P. Saab, M. Laub, V. I. Srdanov and G. D. Stucky, *Adv. Mater.*, 1998, 10, 462–465; (c) H.-B. Lin and J.-S. Shih, *Sens. Actuators, B*, 2003, 92, 243–254; (d) G. Sberveglieri, G. Faglia, C. Perego, P. Nelli, R. N. Marks, T. Virgili, C. Taliani and R. Zamboni, *Synth. Met.*, 1996, 77, 273–275; (e) Y.-C. Chao and J.-S. Shih, *Anal. Chim. Acta*, 1998, 374, 39–46.
 - 15 (a) W.-D. Zhang, L.-C. Jiang and J.-S. Ye, *J. Phys. Chem. C*, 2009, 113, 16247–16253; (b) J. Rodrigues, D. Mata, A. J. S. Fernandes, M. A. Neto, R. F. Silva, T. Monteiro and F. M. Costa, *Acta Mater.*, 2012, 60, 5143–5150; (c) B. K. Gupta, V. Grover, G. Gupta and V. Shanker, *Nanotechnology*, 2010, 21, 475701.
 - 16 M. Baibarac, I. Baltog, A. Matea and S. Lefrant, *J. Cryst. Growth*, 2015, 419, 158–164.
 - 17 (a) A. Janotti and C. G. Van de Walle, *Rep. Prog. Phys.*, 2009, 72, 126501; (b) Ü. Özgür, Y. I. Alivov, C. Liu, A. Teke, M. A. Reshchikov, S. Doğan, V. Avrutin, S.-J. Cho and H. Morkoç, *J. Appl. Phys.*, 2005, 98, 41301.
 - 18 L. Liu, J. Xu, D. Wang, M. Jiang, S. Wang, B. Li, Z. Zhang, D. Zhao, C.-X. Shan, B. Yao and D. Z. Shen, *Phys. Rev. Lett.*, 2012, 108, 215501.
 - 19 A. Tsukazaki, A. Ohtomo, T. Onuma, M. Ohtani, T. Makino, L. Sumiya, K. Ohtani, S. F. Chichibu, S. Fuke and Y. Segawa, *Nat. Mater.*, 2005, 4, 42–46.
 - 20 H. Li and J. L. Bredas, *Adv. Mater.*, 2016, 28, 3928–3936.
 - 21 T. B. Goriushkina, A. P. Soldatkin and S. V. Dzyadevych, *J. Agric. Food Chem.*, 2009, 57, 6528–6535.
 - 21 (a) J. Lozano, M. Fernández, J. Fontecha, M. Aleixandre, J. Santos, I. Sayago, T. Arroyo, J. Cabellos, F. Gutiérrez and M. Horrillo, *Sens. Actuators, B*, 2006, 120, 166–171; (b) V. Postica, I. Hölken, V. Schneider, V. Kaidas, O. Polonskyi, V. Cretu, I. Tiginyanu, F. Faupel, R. Adelung and O. Lupan, *Mater. Sci. Semicond. Process.*, 2016, 49, 20–33; (c) O. Lupan, V. Postica, J. Gröttrup, A. K. Mishra, N. H. de Leeuw and R. Adelung, *Sens. Actuators, B*, 2017, 245, 448–461.
 - 22 Y. K. Mishra, G. Modi, V. Cretu, V. Postica, O. Lupan, T. Reimer, I. Paulowicz, V. Hrkac, W. Benecke and L. Kienle, *ACS Appl. Mater. Interfaces*, 2015, 7, 14303–14316.
 - 23 Y. I. Prylutskyi, V. I. Petrenko, O. I. Ivankov, O. A. Kyzyma, L. A. Bulavin, O. O. Litsis, M. P. Evstigneev, V. V. Cherepanov, A. G. Naumovets and U. Ritter, *Langmuir*, 2014, 30, 3967–3970.
 - 24 R. Ruoff, D. S. Tse, R. Malhotra and D. C. Lorents, *J. Phys. Chem.*, 1993, 97, 3379–3383.
 - 25 F. Cataldo and S. Iglesias-Groth, *Carbon Materials, Chemistry and Physics*, 2010, vol. 2TS–Th. 27 C. N. Kramer, *Fullerene Research Advances*, Nova Science Publishers, New York, 2007.
 - 26 O. Lupan, V. Postica, M. Mecklenburg, K. Schulte, Y. K. Mishra, B. Fiedler and R. Adelung, *J. Mater. Chem. A*, 2016, 4, 16723–16730.
 - 27 W. Kohn and L. J. Sham, *Phys. Rev.*, 1965, 140, A1133–A1138.
 - 28 (a) G. Kresse and J. Furthmüller, *Comput. Mater. Sci.*, 1996, 6, 15–50; (b) G. Kresse and D. Joubert, *Phys. Rev. B: Condens. Matter Mater. Phys.*, 1999, 59, 1758–1775.
 - 31 P. E. Blochl, *Phys. Rev. B: Condens. Matter Mater. Phys.*, 1994, 50, 17953–17979.
 - 29 (a) S. Grimme, *J. Comput. Chem.*, 2006, 27, 1787–1799; (b) J. P. Perdew, K. Burke and M. Ernzerhof, *Phys. Rev. Lett.*, 1996, 77, 3865–3868.
 - 30 H. J. Monkhorst and J. D. Pack, *Phys. Rev. B: Solid State*, 1976, 13, 5188–5192.
 - 31 W. Krätschmer, L. D. Lamb, K. Fostiropoulos and D. R. Huffman, *Nature*, 1990, 347, 354.
 - 35 H.-B. Bürgi, R. Restori and D. Schwarzenbach, *Acta Crystallogr., Sect. B: Struct. Sci.*, 1993, 49, 832–838.
 - 32 D. L. Dorset and M. P. McCourt, *Acta Crystallogr., Sect. A: Found. Crystallogr.*, 1994, 50, 344–351.
 - 33 (a) R. Cusc, E. Alarcon-Llad, J. Ibanez, L. Artus, J. Jimenez, B. Wang and M. J. Callahan, *Phys. Rev. B: Condens. Matter Mater. Phys.*, 2007, 75, G3; (b) P. K. Giri, S. Bhattacharyya, D. K. Singh, R. Kesavamoorthy, B. K. Panigrahi and K. G. M. Nair, *J. Appl. Phys.*, 2007, 102, 93515; (c) N. Rana, S. Chand and A. K. Gathania, *Ceram. Int.*, 2015, 41, 12032–12037.
 - 34 (a) S. Guha, J. Menendez, J. B. Page, G. B. Adams, G. S. Spencer, J. P. Lehman, P. Giannozzi and A. S. Baroni, *Phys. Rev. Lett.*, 1994, 72, 3359; (b) H. Kuzmany, R. Pfeiffer, M. Hulman and C. Kramberger, *Philos. Trans. R. Soc., A*, 2004, 362, 2375–2406; (c) H. Fu, T. Xu, S. Zhu and Y. Zhu, *Environ. Sci. Technol.*, 2008, 42, 8064–8069.
 - 35 (a) A. F. Kohan, G. Ceder, D. Morgan and C. G. Van de Walle, *Phys. Rev. B: Condens. Matter Mater. Phys.*, 2000, 61, 15019–15027; (b) R. Dingle, *Phys. Rev. Lett.*, 1969, 23, 579–581; (c) O. Lupan, V. Postica, J. Gröttrup, A. K. Mishra, N. H. De Leeuw, J. F. C. Carreira, J. Rodrigues, N. Ben Sedrine, M. R. Correia and T. Monteiro, *ACS Appl. Mater. Interfaces*, 2017, 9, 4084–4099.
 - 36 M. Peres, S. Magalhães, M. R. Soares, M. J. Soares, L. Rino, D. Alves, K. Lorenz, M. R. Correia, A. C. Lourenço and T. Monteiro, *Phys. Status Solidi C*, 2013, 10, 662–666.
 - 37 (a) M. Schirra, R. Schneider, A. Reiser, G. M. Prinz, M. Feneberg, J. Biskupek, U. Kaiser, C. E. Krill, K. Thonke and R. Sauer, *Phys. Rev. B: Condens. Matter Mater. Phys.*, 2008, 77, K08; (b) D. Tainoff, B. Masenelli, P. Melinon, A. Belsky, G. Ledoux, D. Amans, C. Dujardin, N. Fedorov and P. Martin, *J. Lumin.*, 2009, 129, 1798–1801.

- 38 K. Thonke, M. Schirra, R. Schneider, A. Reiser, G. M. Prinz, M. Feneberg, J. Biskupek, U. Kaiser and R. Sauer, *Microelectron. J.*, 2009, 40, 210–214.
- 39 (a) J. Fallert, R. Hauschild, F. Stelzl, A. Urban, M. Wissinger, H. Zhou, C. Klingshirn and H. Kalt, *J. Appl. Phys.*, 2007, 101, 73506; (b) S. S. Kurbanov and T. W. Kang, *J. Lumin.*, 2010, 130, 767–770.
- 40 J. Rodrigues, T. Holz, R. F. Allah, D. Gonzalez, T. Ben, M. R. Correia, T. Monteiro and F. M. Costa, *Sci. Rep.*, 2015, 5, 10783.
- 41 J. Rodrigues, D. Mata, A. Pimentel, D. Nunes, R. Martins, E. Fortunato, A. J. Neves, T. Monteiro and F. M. Costa, *Mater. Sci. Eng., B*, 2015, 195, 38–44.
- 42 P. Schulz, L. L. Kelly, P. Winget, H. Li, H. Kim, P. F. Ndione, A. K. Sigdel, J. J. Berry, S. Graham, J.-L. Brédas, A. Kahn and O. L. A. Monti, *Adv. Funct. Mater.*, 2014, 24, 7381–7389.
- 43 (a) D. M. Guldi and M. Prato, *Acc. Chem. Res.*, 2000, 33, 695–703; (b) G. H. Sarova and M. N. Berberan-Santos, *Chem. Phys. Lett.*, 2004, 397, 402–407. 48 S. N. Das, J. P. Kar, J.-H. Choi, T. I. Lee, K.-J. Moon and J.-M. Myoung, *J. Phys. Chem. C*, 2010, 114, 1689–1693.
- 44 O. Lupan, V. V. Ursaki, G. Chai, L. Chow, G. A. Emelchenko, I. M. Tiginyanu, A. N. Gruzintsev and A. N. Redkin, *Sens. Actuators, B*, 2010, 144, 56–66.
- 45 Z. Ting, M. Syed, V. M. Nosang and A. D. Marc, *Nanotechnology*, 2008, 19, 332001.
- 46 A. Hamed, Y. Y. Sun, Y. K. Tao, R. L. Meng and P. H. Hor, *Phys. Rev. B: Condens. Matter Mater. Phys.*, 1993, 47, 10873–10880.
- 48 O. Lupan, V. Cretu, V. Postica, N. Ababii, O. Polonskyi, V. Kaidas, F. Schutt, Y. K. Mishra, E. Monaico, I. Tiginyanu, V. Sontea, T. Strunskus, F. Faupel and R. Adelung, *Sens. Actuators, B*, 2016, 224, 434–448.
- 49 B. Morosin, R. Assink, R. Dunn, T. Massis, J. Schirber and G. Kwei, *Phys. Rev. B: Condens. Matter Mater. Phys.*, 1997, 56, 13611.
- 50 S. T. Shishiyanu, T. S. Shishiyanu and O. I. Lupan, *Sens. Actuators, B*, 2005, 107, 379–386.
- 51 (a) V. Dua, S. P. Surwade, S. Ammu, S. R. Agnihotra, S. Jain, K. E. Roberts, S. Park, R. S. Ruoff and S. K. Manohar, *Angew. Chem., Int. Ed.*, 2010, 49, 2154–2157; (b) J. Li, Y. Lu, Q. Ye, M. Cinke, J. Han and M. Meyyappan, *Nano Lett.*, 2003, 3, 929–933.
- 52 V. V. Sysoev, B. K. Button, K. Wepsiec, S. Dmitriev and A. Kolmakov, *Nano Lett.*, 2006, 6, 1584–1588.
- 53 T. Arai, Y. Murakami, H. Suematsu, K. Kikuchi, Y. Achiba and I. Ikemoto, *Solid State Commun.*, 1992, 84, 827–829.
- 54 H. S. Chen, A. R. Kortan, R. C. Haddon, M. L. Kaplan, C. H. Chen, A. M. Muijsce, H. Chou and D. A. Fleming, *Appl. Phys. Lett.*, 1991, 59, 2956–2958.

Electronic Supporting Information

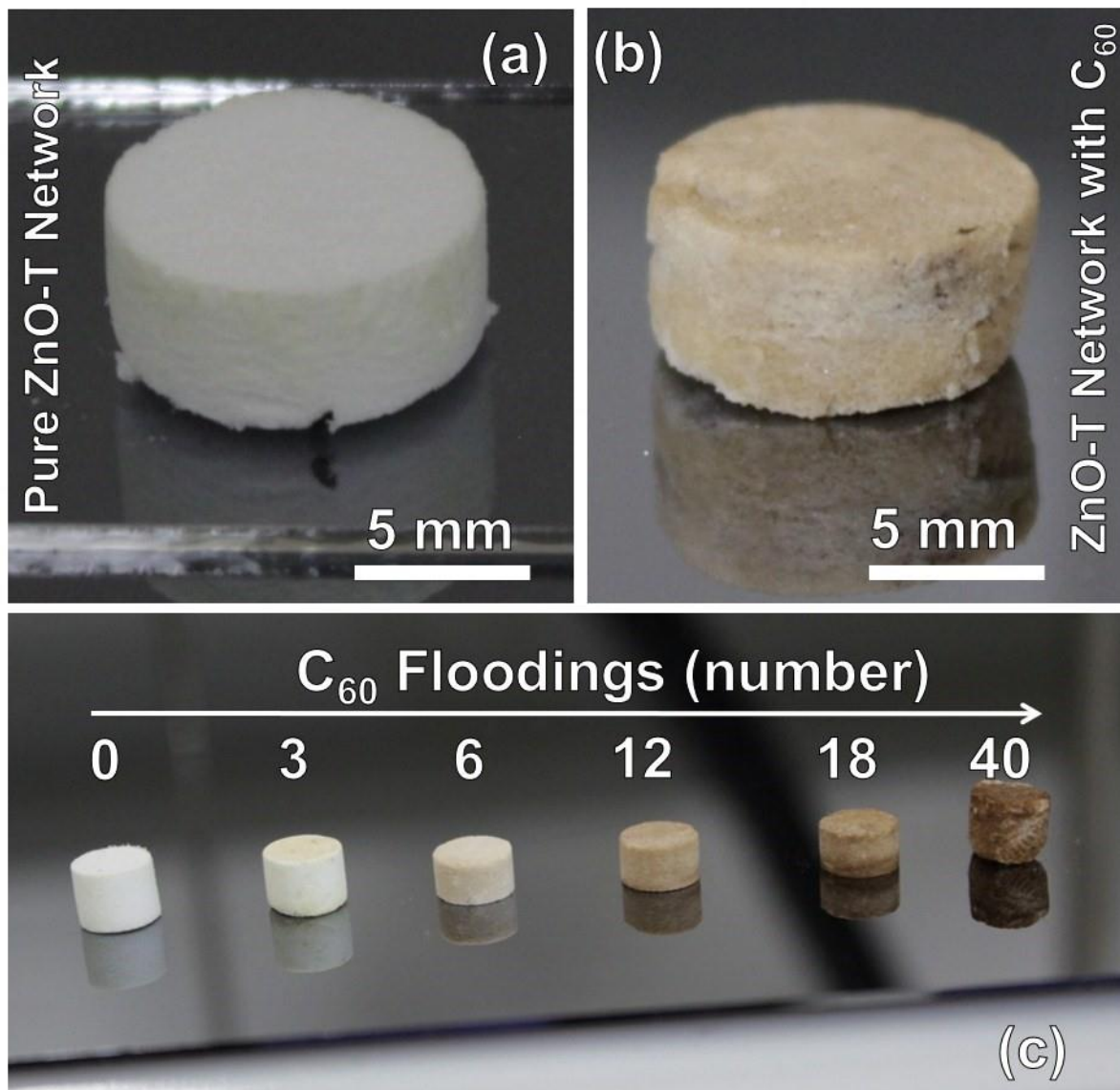


Figure S1: Camera images of the ZnO pellet before drop casting (a), and after 5 C₆₀ floodings (b). (c) Camera images of ZnO samples demonstrating their color change with increasing the amount of C₆₀ flooding times: 0-40 floodings (left to right).

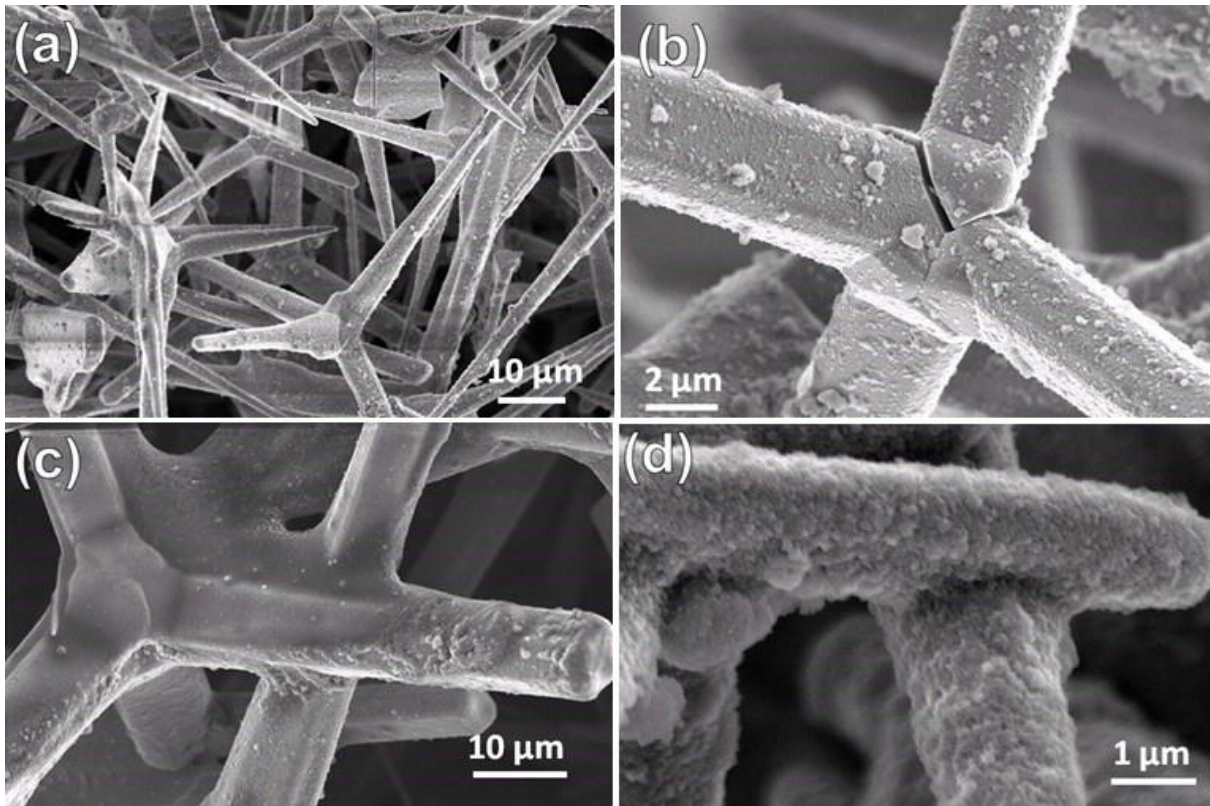


Figure S2: SEM images of ZnO networks after 10 floodings (a,b) and 40 floodings (c,d). After 40 drop-casting cycles agglomerations of C60 are observed at the interconnection points between single tetrapods.

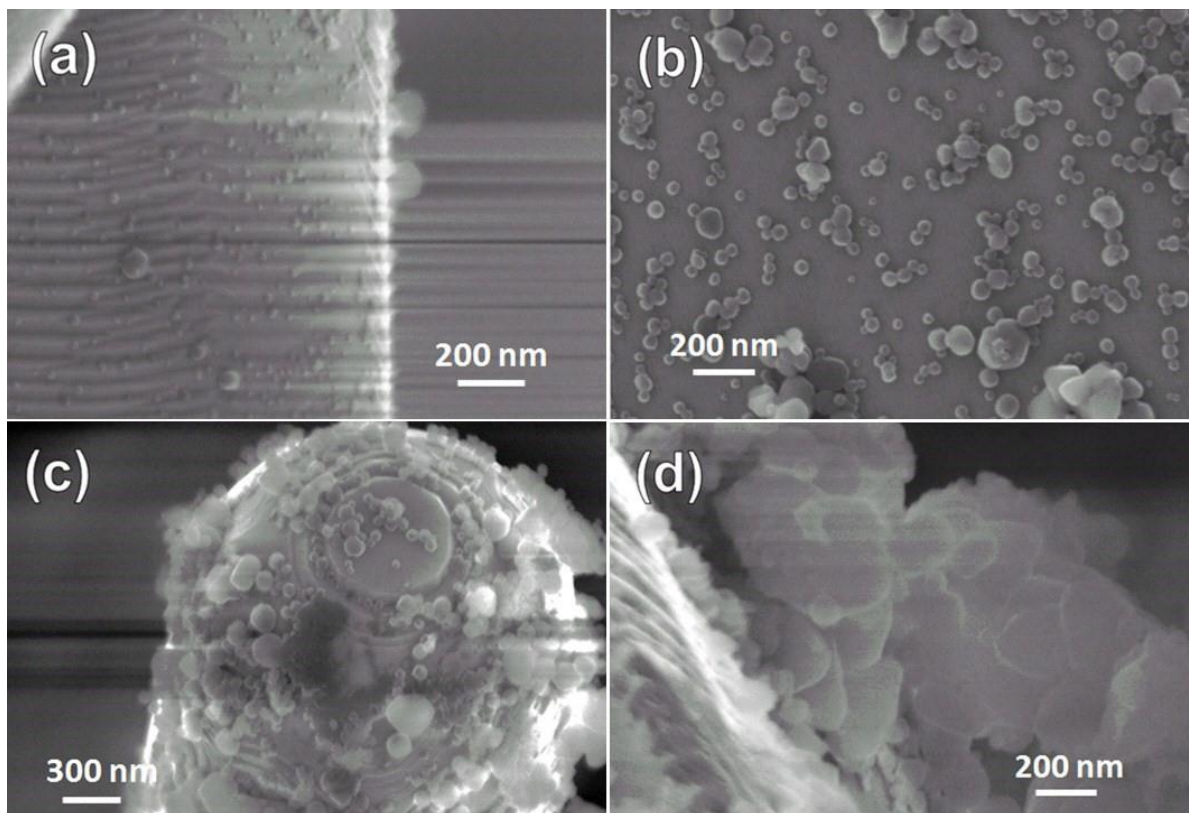
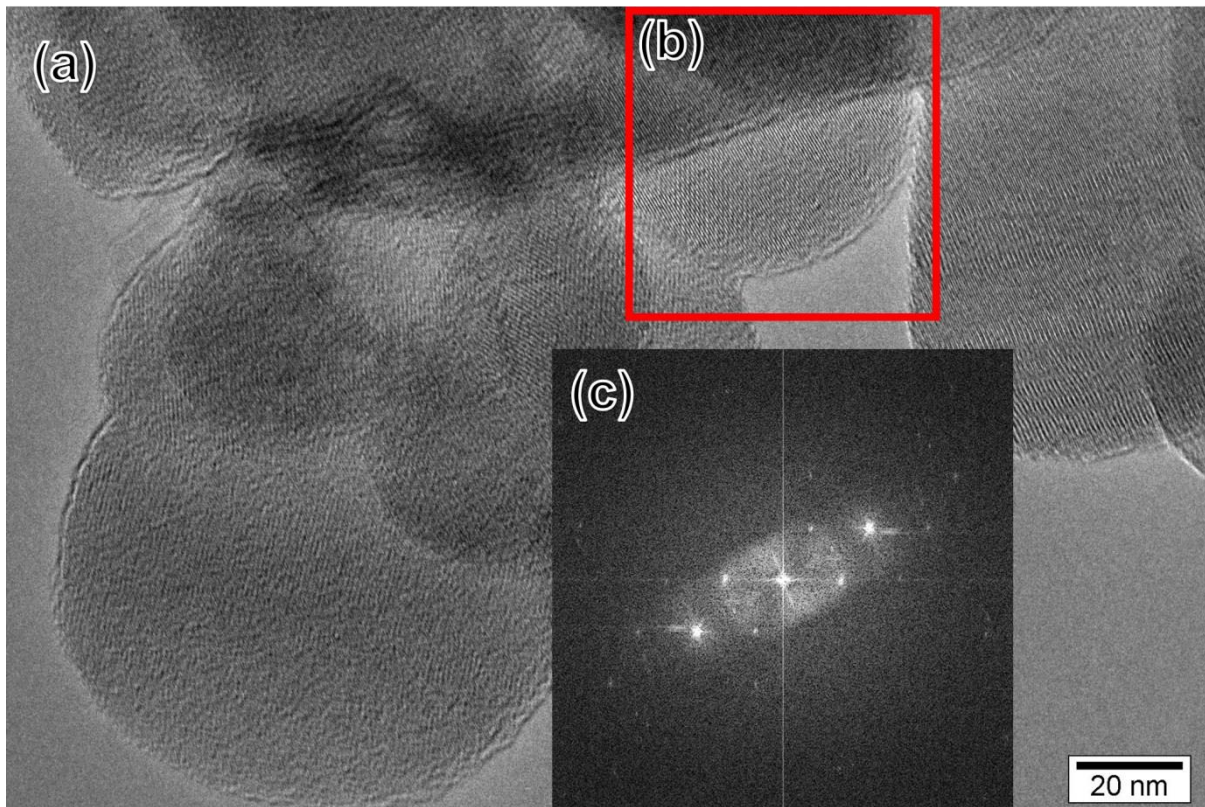


Figure S3: SEM images (higher magnification) of ZnO-T surface with C60 after 3 floodings (a), 10 floodings (b), 40 floodings (c) and 60 floodings (d). For the low number of coatings with C60 (3 and 10, a and b, respectively) isolated C60 clusters are observed. By higher number of floodings the clusters tend to join forming a layer at the ZnO surface.



HV	HFW	Mag	Spot	Pos X	Pos Y	Pos Z	Tilt X	Tilt Y	
200 kV	226,6 nm	250000 x	4	-159,77 μm	492,08 μm	79,03 μm	-0,05 $^\circ$	-0,04 $^\circ$	-
									50 nm

Figure S4: (a) TEM higher magnification image with an overview on fullerene clusters. From the red marked region (b) a FFT pattern was simulated (c), which indicates the crystallinity of the clusters. Also distinctive are the lines indicating the rows of the fullerene aligned into crystals.

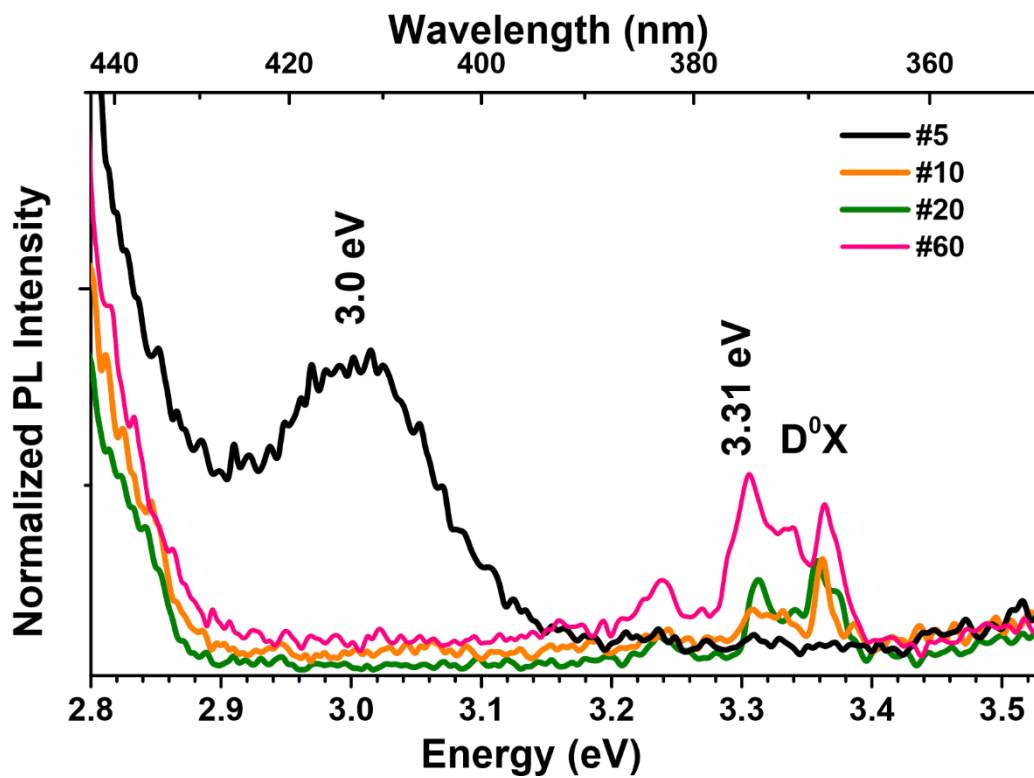


Figure S5: 14 K near band edge recombination (NBE) of the ZnO-T-C60 composites. The spectra were obtained with above ZnO bandgap excitation.

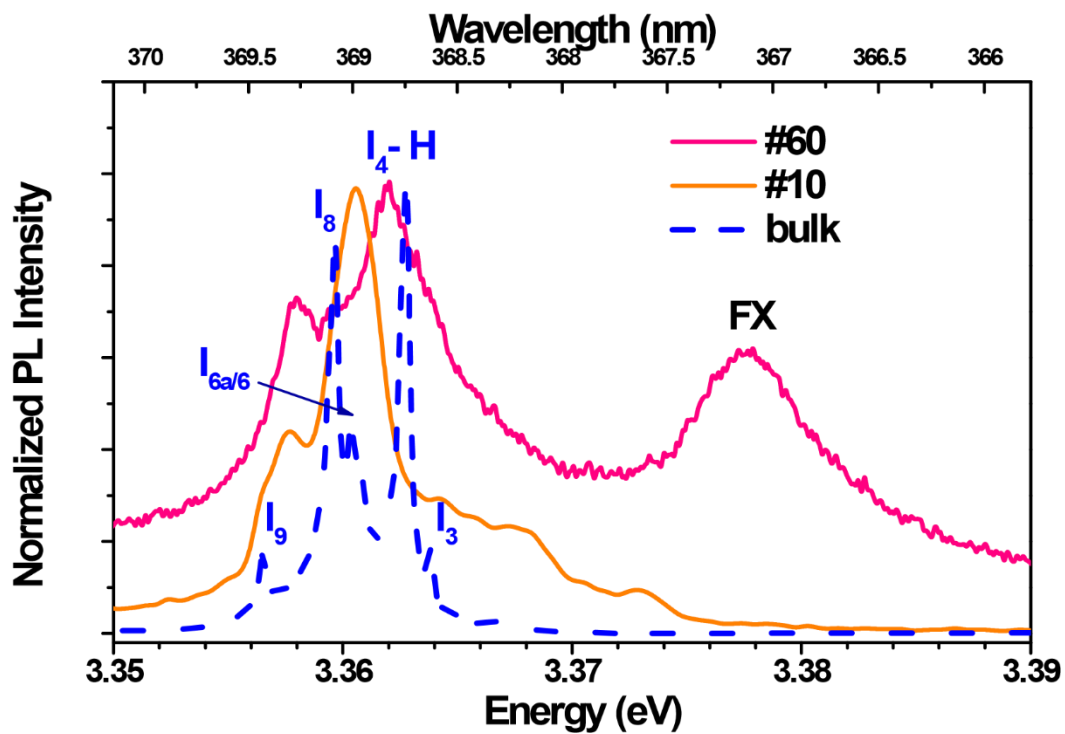


Figure S6: 14 K near band edge recombination (NBE) of the ZnO-T-C60 composites: FX and bound excitons spectral regions. The spectra were obtained with above ZnO bandgap excitation.

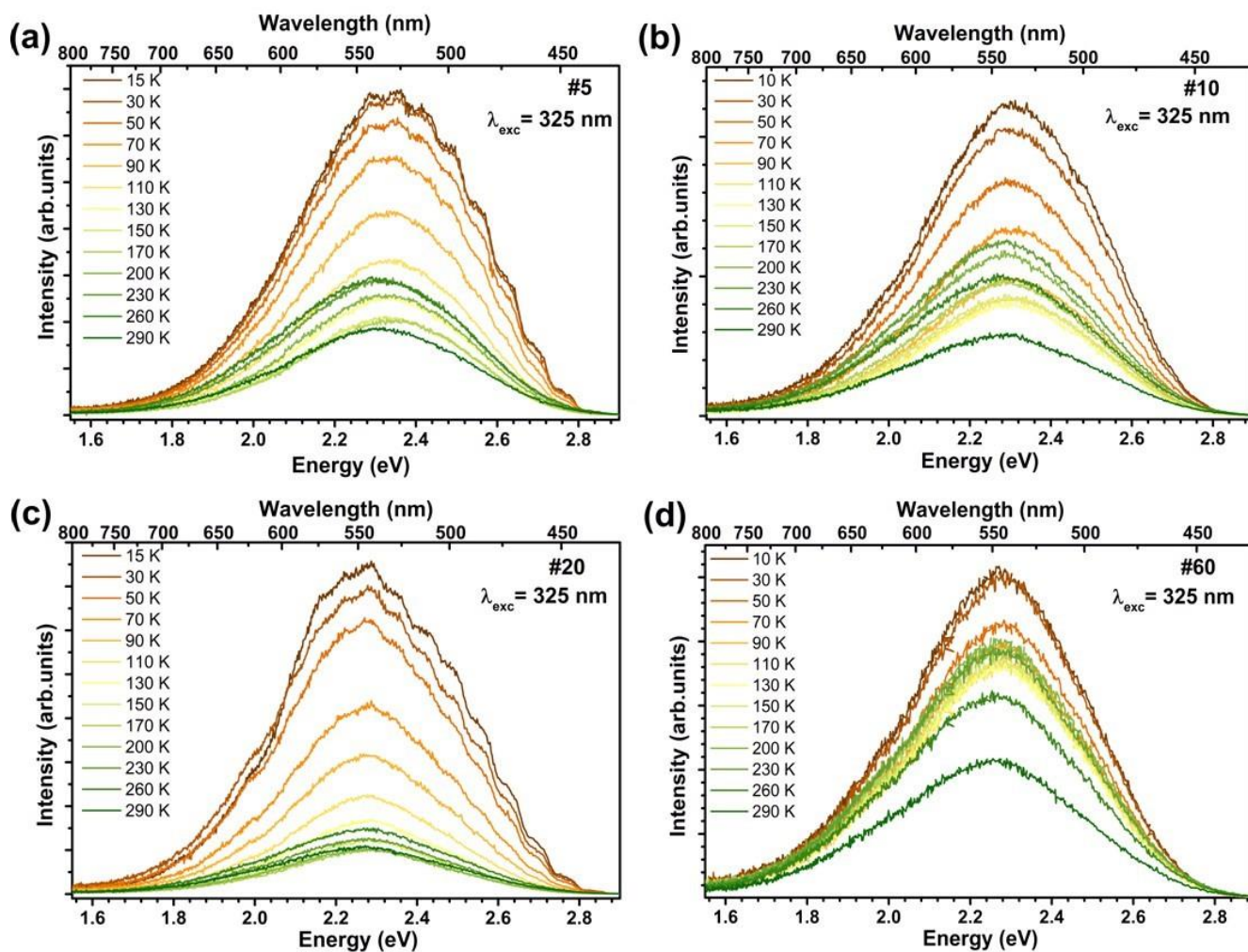


Figure S7: Temperature dependent PL spectra of the ZnO-T-C60 composites. The spectra were obtained with above ZnO bandgap excitation in the interval range 10 K - RT.

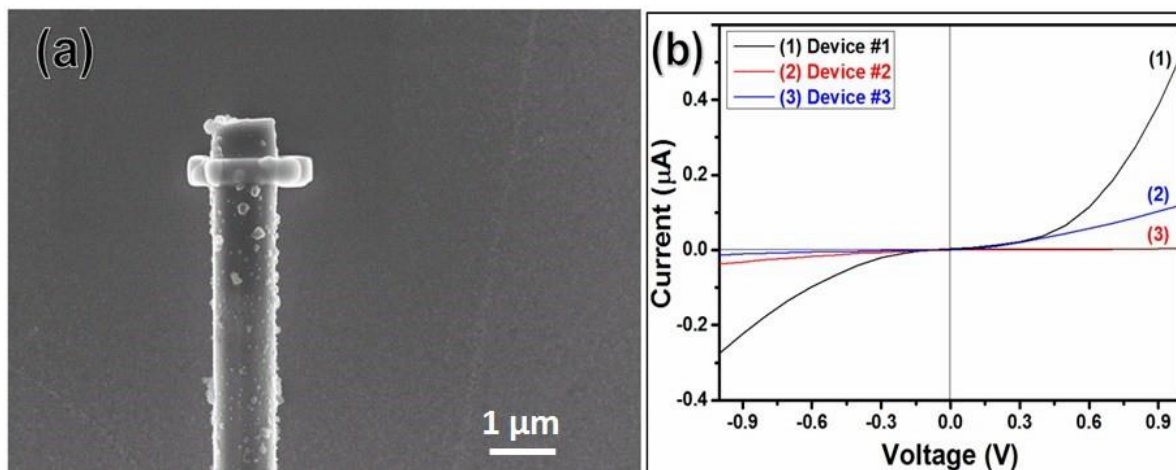


Figure S8: (a) The high magnification SEM image of Pt contacts on a nano-device 1 of a ZnO microtetrapod covered with 10 floodings of C60 aqueous solution. (b) Current – voltage characteristics of devices fabricated based on individual ZnO-T-C60 arms in the dark at room temperature.

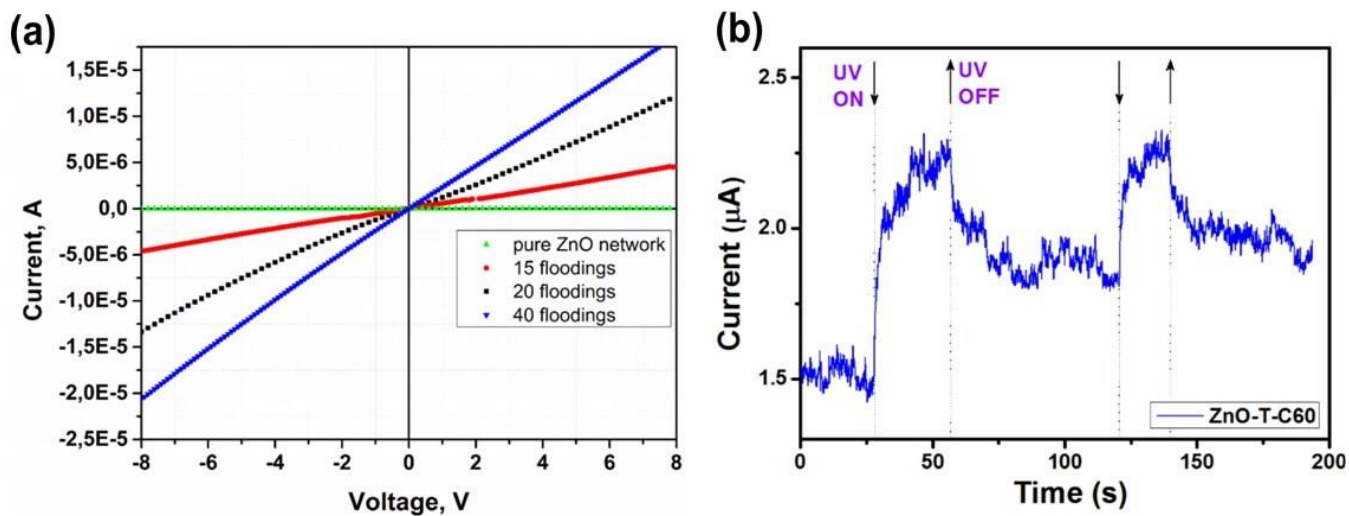


Figure S9: (a) Electrical characterization of a macroscopic template of a ZnO network and of ZnO-T-C60 networks with different number of floodings. Starting with a reference network (pure ZnO), followed by networks with coatings of 15, 20 and 40 floodings of C60. (b) Dynamic response of ZnO-T-C60 networks to illumination with UV light at room temperature.

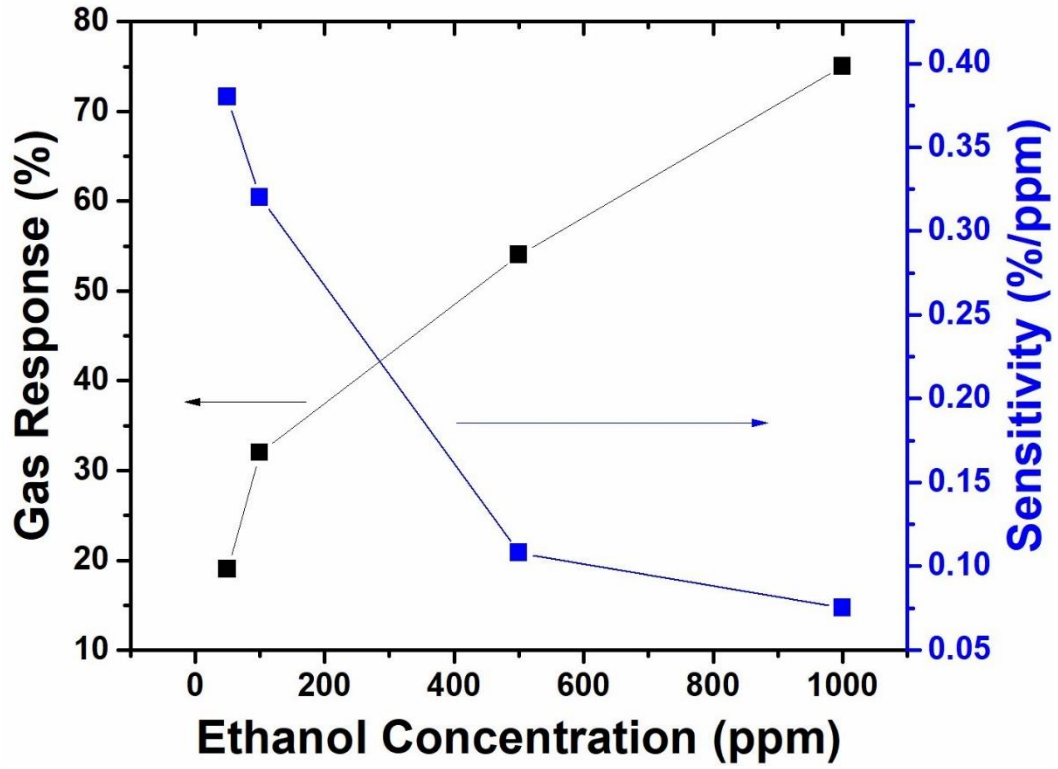


Figure S10: Dependence of room temperature gas response (%) and sensitivity (%/ppm) of Device #3 versus concentration of ethanol vapors (ppm).

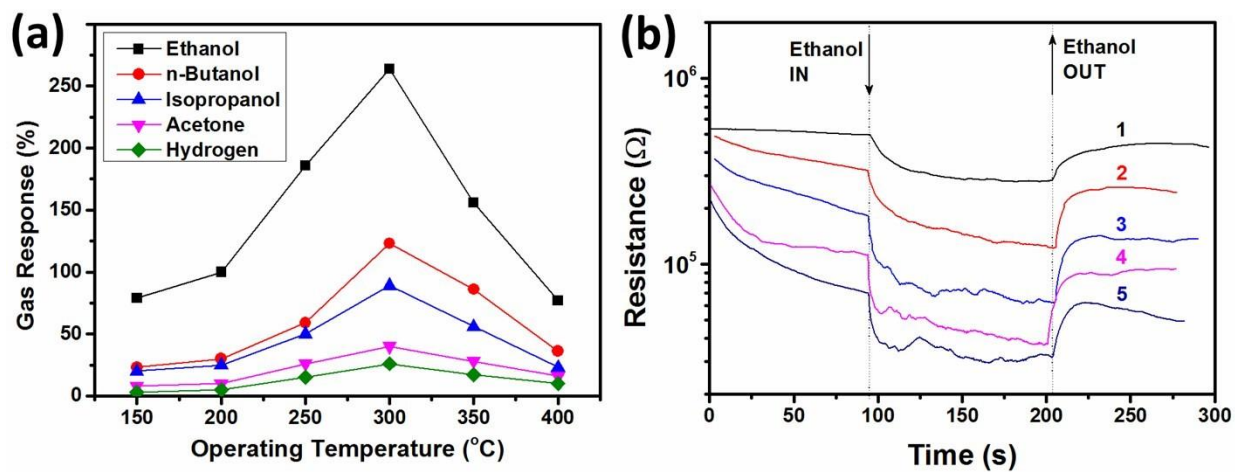


Figure S11: (a) The gas response versus operating temperature of ZnO-T-C60 networks. (b) The dynamic gas response to five time exposures under ethanol vapors at 300 °C operating temperature of ZnO-T-C60 networks.

4. Influence of Activated Carbon on the catalysis of Tetrapodal ZnO

An eco-friendly method of producing activated carbon from sugarcane bagasse is introduced in this chapter. A significant improvement in catalyzing the reduction of the Cr(VI), a contaminant found in the industrial waste water was realized by the micro-nano composite made of T-ZnO and activated carbon.

Personal contributions in the following article:

- Fabrication of the T-ZnO utilized in this study
- SEM investigation of the composite
- Partial manuscript preparation

The following content is reproduced with formal permission from “M. Sharma, M. Joshi, S. Nigam, S. Shree, D. K. Avasthi, R. Adelung, S. K. Srivastava, Y. K. Mishra, *Chemical Engineering Journal*, **2019**, 358, 540”, (© 2018 Elsevier B.V. All rights reserved).



Contents lists available at ScienceDirect

Chemical Engineering Journal

 journal homepage: www.elsevier.com/locate


ZnO tetrapods and activated carbon based hybrid composite: Adsorbents for enhanced decontamination of hexavalent chromium from aqueous solution

Mahima Sharma^a, Monika Joshi^{a,*}, Subhasha Nigam^b, Sindu Shree^c, Devesh Kumar Avasthi^a, Rainer Adelung^c, Sanjeev Kumar Srivastava^d, Yogendra Kumar Mishra^{c,*}

^aAmity Institute of Nanotechnology, Amity University, Noida, Uttar Pradesh, India

^bAmity Institute of Biotechnology, Amity University, Noida, Uttar Pradesh, India

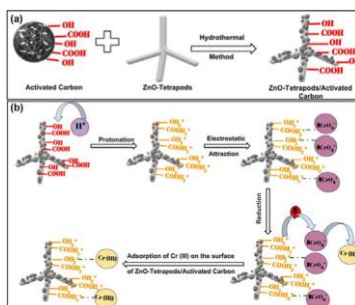
^cFunctional Nanomaterials, Institute for Materials Science, Kiel University, Kaiserstr. 2, D-24143 Kiel, Germany

^dDepartment of Physics, Indian Institute of Technology Kharagpur, India

HIGHLIGHTS

- Large scale synthesis of ZnO tetrapods by flame transport synthesis.
- Eco-friendly extraction of activated carbon from sugarcane.
- ZnO tetrapods-activated carbon based advance composite fabrication.
- ZnO tetrapods-activated carbon composites as efficient Cr(VI) adsorbents.

GRAPHICAL ABSTRACT



ARTICLE INFO

Keywords:

Cr(VI)
ZnO tetrapods
Activated carbon
Nanocomposites
Adsorption and decontamination

ABSTRACT

Owing to its acute toxicity and mobility, the hexavalent chromium [Cr(VI)] in water and wastewater is an immense risk to the environment. Herein, ZnO-tetrapods/activated carbon (ZnO-T/AC) nanocomposite was synthesized as an adsorbent for an efficient decontamination of Cr(VI) from an aqueous medium. The tetrapodal ZnO was synthesized by flame transport synthesis (FTS) approach. The utilized activated carbon (AC) was successfully prepared from sugarcane bagasse with sodium hydroxide (NaOH) impregnation, followed by carbonization. Finally the ZnO-T/AC nanocomposite was synthesized by the hydrothermal method. The structural and chemical properties of the obtained nanocomposite (NC) were systematically characterized using X-ray diffraction (XRD) technique, scanning electron microscopy (SEM), X-ray photoelectron spectroscopy (XPS), Fourier transform infrared (FTIR) spectroscopy and Brunauer–Emmett–Teller (BET) analysis. Batch experiments were performed with the AC, ZnO-T and ZnO-T/AC to study their maximum adsorption efficiency for the Cr(VI). The effect of operational parameters such as contact time, pH and adsorbent dosage on the removal of Cr(VI) were also investigated. Different kinetic models were employed to comprehend the adsorption mechanism. The removal efficiency (97%) of Cr(VI) using ZnO-T/AC adsorbent was achieved at pH 2. The synthesized nanocomposite showed significant potential for the decontamination of Cr(VI) and can be further explored at a large scale for the efficient removal of hazardous heavy metal ions from the industrial contaminates.

* Corresponding authors.

E-mail addresses: mjoshi@amity.edu (M. Joshi), ykm@tf.uni-kiel.de (Y. Kumar Mishra).

<https://doi.org/10.1016/j.cej.2018.10.031>

Received 29 August 2018; Received in revised form 3 October 2018; Accepted 5 October 2018

Available online 06 October 2018 1385-8947/© 2018 Elsevier B.V. All rights reserved.

1. Introduction

The prevalence of the polluted water is becoming a pandemic day by day [1–3]. Among different types of aquatic pollutants, heavy metals are the most fatal ones because of their high toxicity even at a very low concentration [4–6]. Therefore, the development of cost-effective and eco-friendly water purification strategies are in urgent demand. Due to their unique capabilities, the nanostructured based materials could really help in this context [3,7–10]. Semiconducting metal oxide nanostructures are widely being used for water purification due to their large surface area, biofriendly nature, lower agglomeration, effective pollutant removal efficiency and low cost, etc. [11–15]. A large variety of nanostructures from different metals, metal oxides, etc., have been used for water purification purpose however this field is still seeking for reliable approaches as nanomaterials themselves exhibit a lot of challenges when it comes to large scale applications, few major issues include appropriate size and shape, biocompatibility, large scale production, reusability, cost-effectiveness, user friendliness, etc. [11–13]. Nanoscopic materials with a selective size and shape could play a major role towards water purification and in this context ZnO-tetrapods (ZnO-T) with prominent nano-arms exhibit a significant research potentials because of their multifunctionalities [9,16,17]. The interlocking nature of the tetrapod structure is helpful in creating a porous macroscopic three dimensional (3D) flexible network which exhibits unique properties such as high porosity, sufficiently high mechanical strength, greater surface area and durability even under harsh conditions. These properties make ZnO-T, a possible material candidate for water purification and related applications [16,17] and this motivated us about exploring its capability towards removal of heavy metal ions from waste water.

The hexavalent chromium [Cr(VI)] is among one of the most dangerous pollutants which has been considered as an environmental and a biological hazard [18]. Cr(VI), is generally discharged into the water bodies from the waste created by the paper

industry, leather tanning, chromium mining, electroplating, petroleum refining, metallurgy, battery, textile and dyeing industry, wood preservation and glass industry, etc. [19–21]. The wastewater effluent from these industries contains a high concentration of Cr(VI) varying from 5.0 to 280,000 mg/L in water as soluble ions like chromate (CrO_4^{2-}), dichromate ($\text{Cr}_2\text{O}_7^{2-}$) and hydrogen chromate (HCrO_4^-) [22]. Exposure to high level of Cr(VI) might lead to serious damage to kidneys, liver and nerve tissues and its short-term exposure causes skin and eye irritation or ulceration [23–25]. Due to its high toxicity, World Health Organization (WHO) has set the permissible limit of the Cr(VI) in potable water at 0.05 mg/L (WHO/SDE/WSH/03.04/04) [26,27]. So, it is very essential to reduce concentration of the Cr(VI) to an acceptable level before discharging it into water bodies.

Water and wastewater has been treated with the following traditional methods such as adsorption [28], reduction [29–31], filtration [32], reverse osmosis [33], ion-exchange [34], foam flotation [35] and electrolysis [36]. Among all the mentioned methods, the adsorption approach has been observed to be the most suitable methodology for the expulsion of different contaminations including metals, due to low treatment cost, simple operation, high removal efficiency and availability of a large number of adsorbents [37].

Utilization of industrial and agricultural wastes and biological materials such as activated carbon (AC), carbon nanotubes [38,39], zeolites [40], chitosan [41], activated alumina [42] and bentonite [43] etc., as effective adsorbents have been extensively researched. In particular, AC, is preferred for its availability, a large surface area with abundant functional groups [44], high chemical and thermal stability and hydrophobicity. However, the commercial AC is expensive due to high resource costs, its synthesis and activation procedure. Several studies have reported about the extraction of AC from coconut shells [45], olives [46], sugarcane bagasse

[47], sawdust [48], rice husk [49], coffee [50], etc. The large pore sizes of AC enable easy diffusion of Cr (VI) and the high pore volumes facilitate space to retain more ions [51]. However, it is difficult to separate and recover the AC from the contaminated water and the filtration method causes loss of carbon or even damaging the filter.

The previously reported works demonstrated the use of common adsorbents such as carbon nanotubes (CNT), mesoporous silica, aluminum oxides (Al_2O_3) and composites of iron [52–55] for water treatment. Unfortunately, their high cost, complicated and time consuming synthesis process and weak separation property limit their practical applications. Here, we present a simple strategy for removal of Cr(VI) ions in waste water by using the unique composite material based on ZnO tetrapods and activated carbon. The proposed adsorbent provides high efficiency, low cost and ecofriendly material with facile synthesis methodology with high production rate. The proposed composite with ZnO-T and AC could integrate their individual properties of high porosity, high mechanical strength, large surface area with abundant functional groups, durability towards harsh conditions and non-toxicity, make it a unique adsorbent with great potential for heavy metal removal with enhanced efficiency.

The activated carbon was synthesized using sugarcane bagasse by chemical impregnation with sodium hydroxide and carbonization, which leads to the enhancement of its adsorption efficiency. Then, ZnO tetrapods/activated carbon (ZnO-T/AC) nanocomposite was synthesized by hydrothermal method. The kinetics about the adsorption of Cr (VI) on the synthesized nanomaterials has been examined in detail. The effects of several performance parameters, such as pH, contact time and adsorbate dosage on the adsorption efficiency, etc. were investigated in detail which suggest the potential application scope of the composite towards purification.

2. Materials and methods

2.1. Materials

Sugarcane bagasse used as a raw material to synthesize AC in this work was obtained from a local cane juice shop at Noida (India). Analytical grade Sodium hydroxide (NaOH), Hydrochloric acid (HCl), Potassium dichromate ($\text{K}_2\text{Cr}_2\text{O}_7$) and Zn powder (particle size $\sim 10\ \mu\text{m}$) were procured from Sigma-Aldrich India. Polyvinyl Butyral (PVB) and Zn powder (particle size $\sim 1\text{--}5\ \mu\text{m}$) was procured from Kuraray Europe GmbH and GoodFellow GmbH respectively. All the chemicals were utilized as received without further treatment. Deionized (DI) water was used for the preparation of all the chemicals unless otherwise mentioned.

2.2. Synthesis of activated carbon

Firstly, the bagasse was washed manually with DI water exhaustively and dried in an oven at $100\ ^\circ\text{C}$ for 24 h. Then bagasse was grinded with a roller mill and sieved through $100\ \mu\text{m}$ mesh. For carbonization, the above material was kept in a furnace at $700\ ^\circ\text{C}$ for 60 min. The carbonized material was soaked in 1M NaOH solution in weight ratio of 1:1 for 48 h. The produced char was washed with DI water to achieve pH 7 and was dried out in an oven overnight at $100\ ^\circ\text{C}$.

2.3. Synthesis of ZnO-tetrapods (ZnO-T)

The FTS method [7,16,56] was employed for the preparation of tetrapodal ZnO structures. In this method, Zn particles and PVB powder (mixed in a ratio of 1:2) was filled in a crucible and heated in a furnace (preheated to $450\ ^\circ\text{C}$) for 30 min at $900\ ^\circ\text{C}$. Before placing crucible in the furnace, the furnace was pre-heated to $450\ ^\circ\text{C}$. Due to the high temperature of the furnace, the sacrificial polymer PVB burns and the generated flame carries the Zn microparticles upwards which are then converted into ZnO nano- and microscale tetrapod structures.

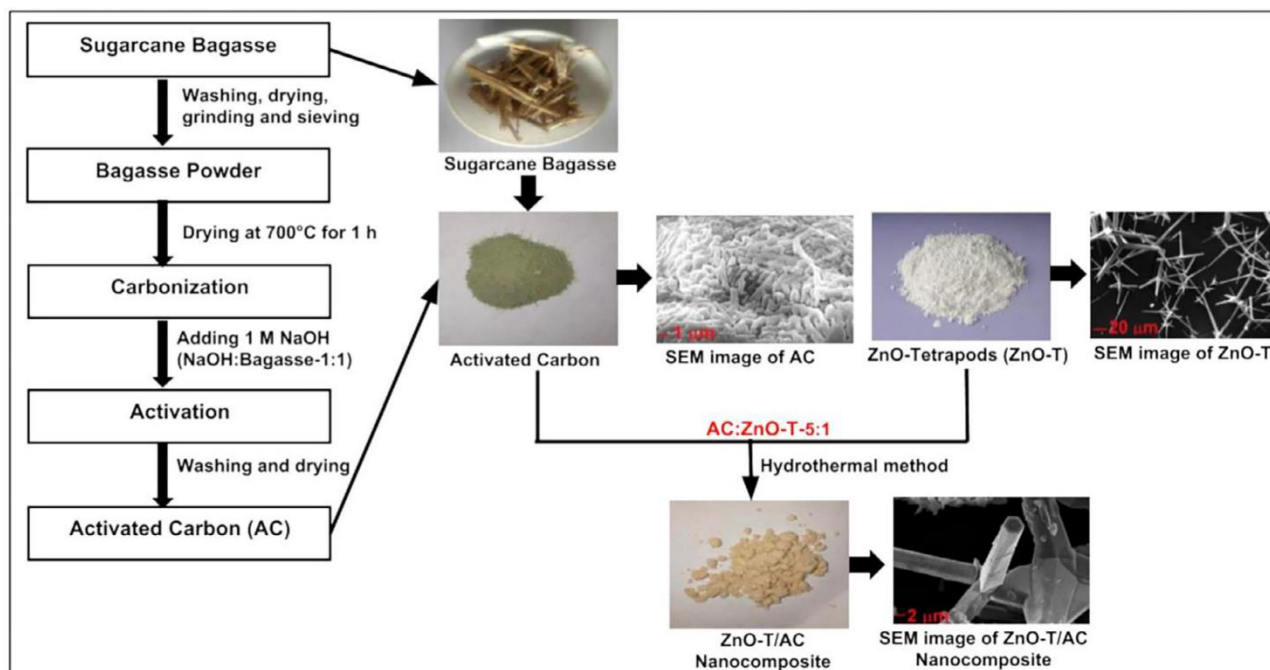


Fig. 1. Synthesis steps for activated carbon from sugarcane bagasse and ZnO-T/AC (ZAC) nanocomposite.

Depending on the synthesis parameters, the subsequent ZnO structures change in their size, shape, morphology and angle proportion contingent [16].

2.4. Synthesis of ZnO-tetrapods/activated carbon (ZAC) nanocomposite

ZnO-T/AC nanocomposite (ZAC) was synthesized by conventional hydrothermal method. 5 g AC and 1 g ZnO-T was mixed in 50 mL DI and stirred for 2 h. Then the suspension was placed in a 50 mL Teflon-sealed autoclave and maintained at 120 °C for 2 h. Finally, the sample was centrifuged and dried in an oven for 18 h at 80 °C. The ZnO-T/AC nanocomposite was obtained by annealing at 650 °C for 2 h. Synthesis steps for activated carbon from sugarcane bagasse and ZnO-T/AC (ZAC) are shown in Fig. 1.

2.5. Point of zero charge (PZC)

The point of zero charge (PZC) is the pH at which the net electrical charge density on the surface of any material becomes zero. The PZC of the ZnO-T/AC nanocomposite was determined by salt addition method using 10 mM KCl solution. In this method, a series of 50 mL test tubes containing 20 mL of 10 mM KCl solution was taken [57]. The

pH of solution was adjusted in the range of 2–10 using 0.1 N HCl and 0.1 N NaOH. 0.02 g of ZnO-T/AC nanocomposite was added to each test tube separately and solutions were kept on shaker at 170 rpm for 48 h. Then, solutions were centrifuged, and final pH of filtrates was measured. A graph between change in pH and initial pH was plotted and value of initial pH at which change in pH is zero is noted, which represented the PZC of sample.

2.6. Adsorption studies

The adsorption of Cr(VI) from aqueous medium onto samples was performed using batch equilibrium experiment. For an adsorption experiment, 20 mg of the adsorbent was introduced into a flask containing 100 mL of Cr(VI) solution (10 mg/L). For pH adjustment throughout the experiment, HCl and/or NaOH were utilized as necessary. This flask was agitated on an orbital shaker (Tarsonspinix) and shaken at 240 rpm for 24 h in order to achieve adsorption equilibrium. Upon reaching the equilibrium, the solid particles were removed by centrifugation and the equilibrium concentration of Cr(VI) in supernatant was examined by spectrophotometer

using 1,5-diphenylcarbazide method at measured at a wavelength of 530 nm. The removal efficiency (%) was calculated according to the equation:

$$\text{Removal efficiency (\%)} = \frac{(C_0 - C_e) \times 100}{C_0} \% \quad (1)$$

where C_0 and C_e are the initial and equilibrium concentrations of Cr(VI) solution respectively. The adsorption coefficient (q_e in $\text{mg}\cdot\text{g}^{-1}$) was obtained from:

$$q_e = \frac{(C_0 - C_e) \times V}{m} \% \quad (2)$$

where, V (in l) is the volume of the medium, and m (in g) is the mass of adsorbent used.

2.7. Characterizations

The phase and crystallinity of adsorbents were studied by X-ray diffraction [Bruker D2 Phaser and $\text{CuK}\alpha$ ($\lambda = 1.5406 \text{ \AA}$) radiation]. The XRD spectra were recorded from 10 to 80° . The specific area and micropore size distribution of activated

carbon, ZnO-T and ZnO tetrapodsactivated carbon were analysed by Brunauer–Emmett–Teller (BET) method. The size and shape of AC, ZnO tetrapods and ZnO tetrapodsactivated carbon nanocomposite, elemental analysis were confirmed using scanning electron microscope (ZeissSupra 55VP). The chemical state of the surface was characterized by X-ray photoelectron spectroscopy (XPS) on a PHI 5000 Veraprobe II spectrometer with Al $\text{K}\alpha$ X-ray source. Cr (VI) concentration was evaluated by UV–Visible spectroscopy (Shimadzu, UV 800). The Fourier transform infrared (FTIR) spectra of ZnO-T/AC nanocomposite were recorded using a PerkinElmer 1430 infrared spectrophotometer within the range of $400\text{--}4000 \text{ cm}^{-1}$.

3. Results and discussion

3.1. Morphological and structural studies

Surface morphologies of the activated carbon, ZnO-T and ZnO-T/AC nanocomposite were

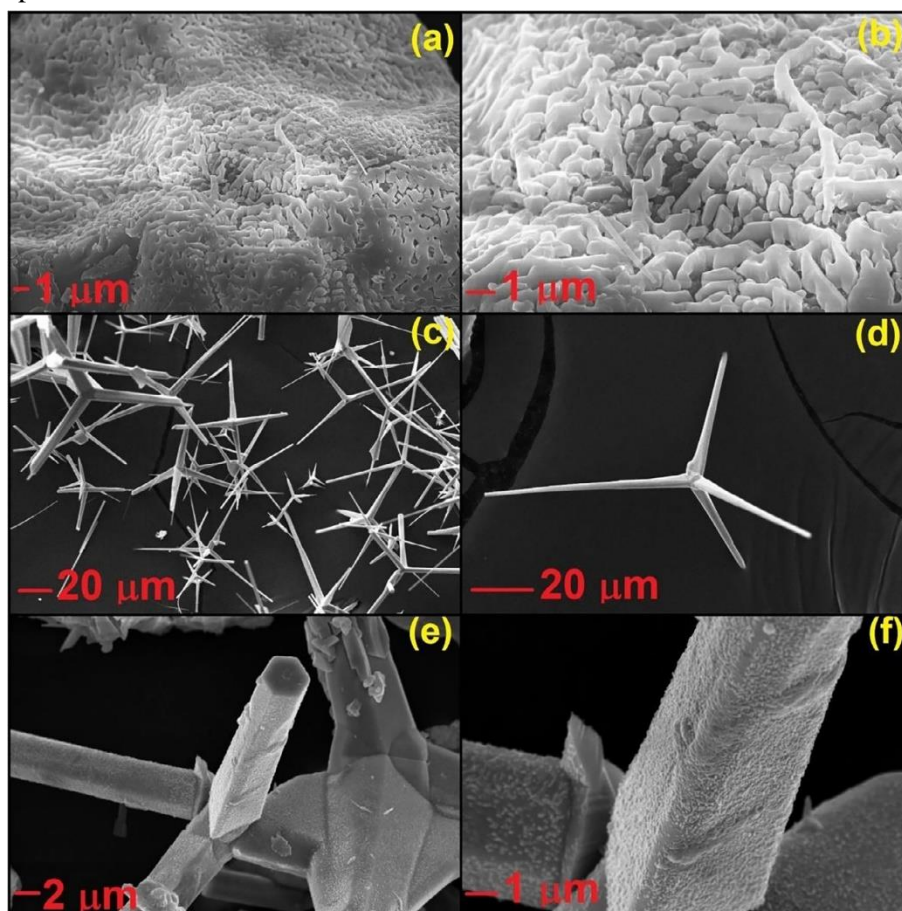


Fig. 2. (a, b) SEM images (increasing order of magnifications) of AC, (c, d) SEM images (increasing order of magnifications) ZnO-T, and (e, f) SEM images (increasing order of magnifications) ZnO-T/AC nanocomposite.

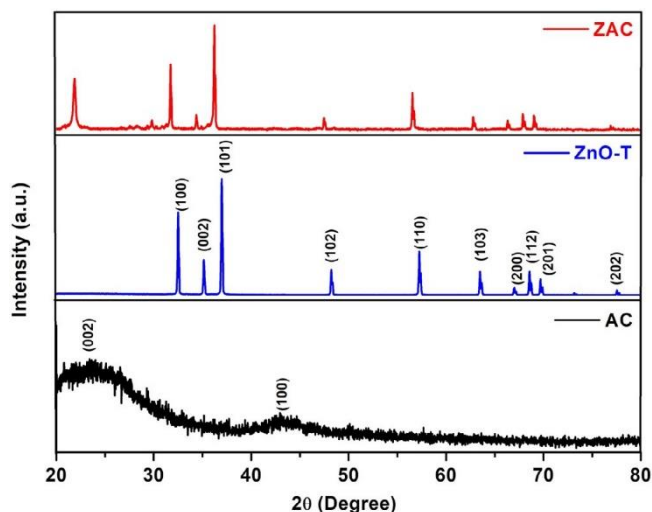


Fig. 3. XRD patterns of AC, ZnO-T and ZnO-T/AC (ZAC) nanocomposite.

observed under SEM. SEM images of the bagasse-derived activated carbon at increasing order of magnification are shown in Fig. 2(a and b). SEM images revealed that the outer surface of activated carbon is rough and has micropores of various size and shapes. The NaOH impregnated external surface (made up from lignocellulose) of activated carbon developed pores after carbonization at 700 °C. Fig. 2(c and d) demonstrates the interconnected 3D tetrapods of ZnO at increasing order of magnifications. Fig. 2(e and f) display SEM images of ZnO-T/AC composite at an increasing order of magnification, these images depict the dispersion of activated carbon on the surface of ZnO-T. AC with abundant functional groups are deposited on large surface area of ZnO-T/AC providing higher Cr (VI) adsorption efficiency [44,58]. The information on the crystal structure of the prepared composite adsorbent was obtained from X-ray diffraction patterns. XRD pattern for bagasse synthesized AC after carbonization at 700 °C for 1 h, ZnO-T and ZnO-T/AC nanocomposite are depicted in Fig. 3. XRD peak of AC showed amorphous nature. The conclusion is based on the presence of a well-known hump back characteristic at $2\theta = 23.70^\circ$ peculiar to amorphous material [47]. Diffraction peaks for ZnO at $2\theta = 31.69^\circ, 34.54^\circ, 36.21^\circ,$

$47.57^\circ, 56.74^\circ, 62.95^\circ, 66.43^\circ, 67.88^\circ, 69.14^\circ$ and 77.03° corresponding to (1 0 0), (0 0 2), (1 0 1), (1 0 2), (1 1 0), (1 0 3), (2 0 0), (1 1 2), (2 0 1) and (2 0 2) orientation planes respectively, confirmed wurtzite structure of ZnO (JCPDS-36-1451) [59]. In the diffraction pattern of ZnO-T/AC, the peak appearing at 21.70° is ascribed to the hexagonal phased carbon (JCPDS file No. 50-0926). The crystalline nature of AC may be attributed to hydrothermal process and annealing of nanocomposite at 650 °C. In addition to the diffraction peak of hexagonal carbon, the XRD pattern of ZnO-T/AC nanocomposite also showed characteristic diffraction peak of ZnO. This indicated the dispersion of AC on the surface of ZnO tetrapods.

3.2. FTIR investigations

FTIR spectrum of ZnO-T/AC nanocomposite (before and after Cr adsorption) is shown in Fig. 4. The characteristic peak at 3375 cm^{-1} corresponds to presence of -OH groups associated with water. The peak at 2651 cm^{-1} was mainly assigned to the stretching vibration of

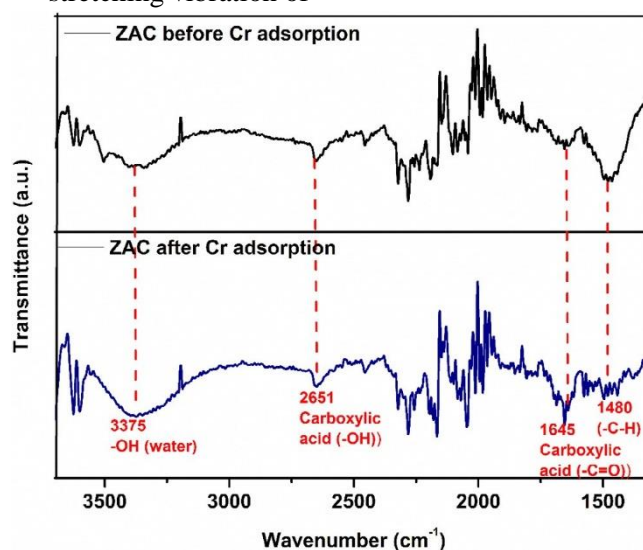


Fig. 4. FTIR spectra of ZnO-T/AC (ZAC) nanocomposite before and after Cr adsorption.

-OH and -OH of carboxylic acid [60]. The peak at 1645 cm^{-1} was related to the stretching vibration of -C=O of carboxylic acid [61]. The absorbance band near 1480 cm^{-1} was the bending vibration of

–C–H. The stretching vibration of –OH and –C=O shifted marginally after Cr adsorption. These changes indicated that –OH and –COOH groups could be the main functional groups for Cr (VI) adsorption [61].

3.3. XPS analysis

To study the mechanism of interaction between ZnO-T/AC and Cr (VI), X-ray Photoelectron spectroscopy (XPS) was done before and after its exposure to 10 mg/L Cr(VI) at pH 2. High-resolution XPS spectra and their fits in Zn 2p_{3/2}, Cr 2p, O 1s and C 1s regions before and after Cr (VI) exposure are shown in Fig. 5. The Zn 2p_{3/2} peaks for both the ZnO-T/AC adsorbent before (untreated sample) and after Cr(VI) adsorption (treated sample) consist of two subpeaks – one at 1020.8 eV and the other at 1022.4 eV (Fig. 5a). These peaks can be assigned to ZnO and Zn (OH)₂,

respectively, both components being expected in ZnO [62]. The two broad peaks in the Cr 2p region at 576.3 and 585.3 eV in untreated sample are not actually XPS peaks of Cr, as it is absent in the sample; they, instead, correspond to L₃M₂₃M₄₅ (¹P) and L₃M₂₃M₄₅ (³P) Auger electrons from Zn (Fig. 5b) [63]. In the presence of these Auger peaks, any appearance of a Cr peak after treatment would come with a narrower and less intense contribution, and therefore will be masked by the Auger peaks. The only way by which a subtle Cr contribution can be identified is that if a Cr peak is in the neighborhood of an Auger peak, the peak would have a tendency to shift toward the Cr position. Cr(III) 2p_{3/2} peaks corresponding to Cr₂O₃, Cr(OH)₃ occur at 577.0 and 577.8 eV, while Cr(VI) 2p_{3/2} peak occurs at 579.96 eV [64], all of them occurring at a binding energy higher than the first Auger peak at 576.3 eV. The slight high-energy (+0.6 eV) shift of the first Auger peak (occurring now at 576.9 eV) after Cr(VI) treatment may, thus, be considered as an evidence of the

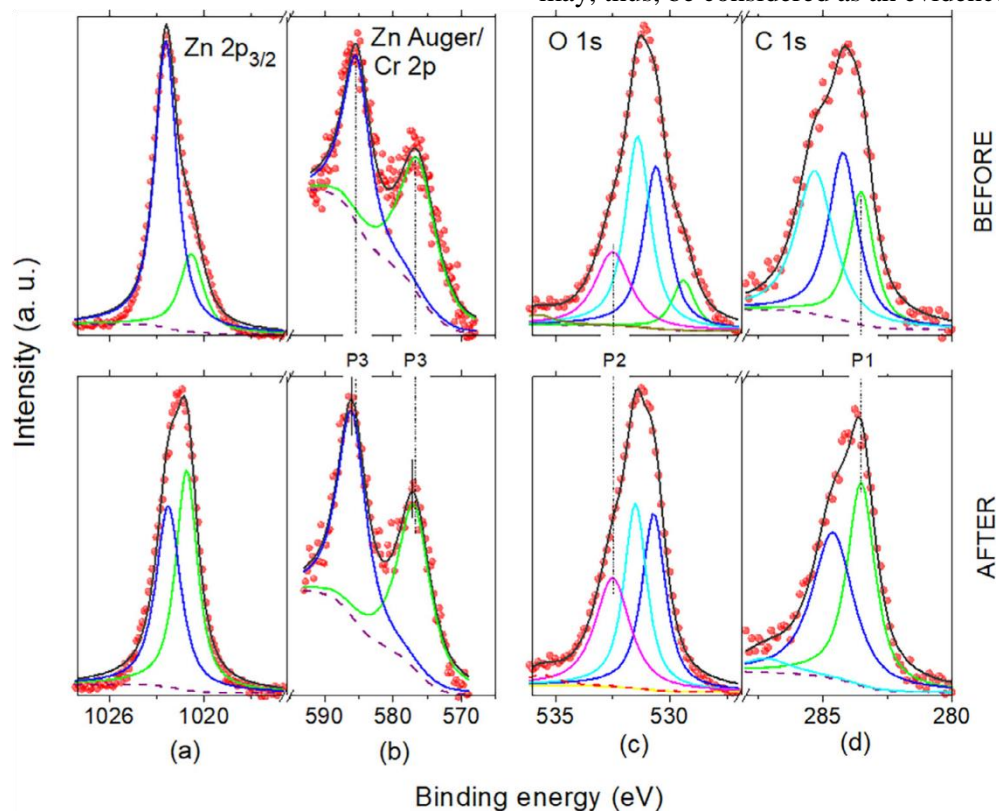


Fig. 5. High resolution XPS spectra of ZnO-T/AC nanocomposite and their fits in (a) Zn 2p_{3/2}, (b) Zn Auger/Cr 2p, (c) O 1s and (d) C 1s regions before and after Cr(VI) exposure. The peak position P1 corresponds to C=C or Cr₃C₂ or Cr(CO)₆, P2 to ZnO or Cr (OH)₃, and P3 corresponds to CrO₃ or Cr(OH)₃ or Cr₂O₃.

Table 1 BET analysis of AC and ZnO-T/AC nanocomposite.

Adsorbent	BET Specific Surface Area (m ² g ⁻¹)	Total Pore Volume (cm ³ g ⁻¹)	Average Pore Diameter (nm)
Activated carbon	551.00	0.01	3.73
ZnO-Tetrapods	754.00	0.01	1.68
ZnO-Tetrapods/ activated carbon NC	642.70	0.01	3.62

presence of Cr(III) or Cr(VI) in the treated sample. The peak at 586.1 eV for the Cr(VI) treated sample is the corresponding 2p_{1/2} Cr peak, with 9.2 eV spin-orbit splitting [63], its presence strengthening the conjecture of the incorporation of Cr in the treated sample. The O 1s region for the untreated sample consists of four peaks at 529.4, 530.6, 531.4 and 532.5 eV, all of which are assignable to different forms of O in ZnO (Fig. 5c) [62]. The treated sample also exhibits peaks at almost the same positions. However, the intensity of the 532.5 eV peak, which also may correspond to Cr(OH)₃ [65], increases by one and a half times. This can be considered as a complementary evidence of presence of Cr, in the form of Cr(III) in the treated sample. In the high resolution C 1s spectrum (Fig. 5d) of ZnO-T/ AC (Fig. 5d), peaks at 283.5, 284.2 and 285.3 eV can be assigned to C]C, CeC and CeO bond respectively, which are due to oxygen-containing functional groups in ZnO-T/AC [66]. The only two peaks (283.5 and 284.6 eV) for the Cr(VI) treated sample are tentatively the first two peaks of the untreated one. Incidentally, the first of these peaks occurs close to the C 1s peak of Cr(CO)₆ (283.3 eV) or of Cr₃C₂ (283.4 eV) [67], both being zero-valent Cr compounds. A 1.7 – fold increase in the intensity of this peak after Cr(VI) treatment further substantiates the incorporation of Cr in the treated sample. The high-resolution XPS spectra, thus, confirm the presence of Cr (in 0, +3 or +6 oxidation states) in the sample after Cr(VI) treatment. Apparently, at pH 2, the surface of the protonated ZnO-T/AC got attracted towards Cr(VI) anions through electrostatic attraction [68–70].

3.4. Surface area adsorption analysis

The specific surface area (m²g⁻¹), average pore diameter (nm) and total pore volume (cm³g⁻¹) of by applying the Brunauer–Emmett–Teller (BET)

Table 2 Optimum conditions for Cr(VI) removal using ZnO-T/AC nanocomposite.

S. No.	Variables	Optimum Value
1	pH	2
2	Adsorbent dosage	2 g/L
3	Contact time	6 h
4	PZC	5.4
5	Average pore diameter	3.62 nm
6	% Removal efficiency	96%

AC, ZnO-T and ZnO-T/AC nanocomposites were evaluated nitrogen gas (N₂) adsorption method, as shown in Table 1. Surface area of the all adsorbents was determined by BET equation (relative pressure = 0.10–1.0). It can be noticed from Table 1 that the specific surface area of ZnO-T, ZnO-T/AC nanocomposite and AC follows a descending order: ZnO-T > ZnO-T/AC > AC. But the value of pore diameter is highest for AC and lowest for the ZnO-T/AC nanocomposite. All of three types of adsorbents contained micropores as well as mesopores but the volume of mesopore was greater than the micropore. The smaller particle sizes of a porous carbon leads to the adsorption at higher rate [71]. The adsorption-desorption isotherms of adsorbents as shown in Fig. 6, display isotherms of type IV with a H3 hysteresis loop because of the capillary condensation steps at a relative pressure of 0.1 < P/Po < 0.9. Fig. 6 (inset graph) displays, pore size distribution (Barrett-Joyner-Halenda, BJH) for all of three types of adsorbents. The optimum conditions for the adsorption of chromium (VI) were investigated and shown in Table 2. According to the table the maximum percentage of chromium removal was 97% with 2 g/L of adsorbent at pH2 with a contact time of 3 h.

3.4.1. Effect of pH on Cr(VI) removal

The pH is an important parameter affecting the adsorption process. It determines the formation and stability of different Cr(VI) species in the aqueous solution. The effect of pH on adsorption of Cr(VI) ions is shown in Fig. 7(a). The Cr(VI) exists in various ionic forms as hydrogen chromate (HCrO₄⁻), dichromate (Cr₂O₇⁻), and chromate (CrO₄⁻²) and stability of these ions is dependent on

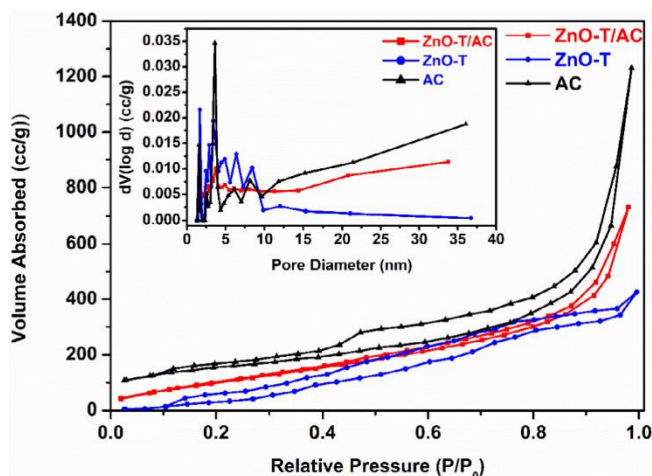
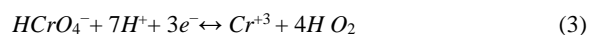


Fig. 6. The adsorption-desorption isotherms and corresponding pore size distribution of AC, ZnO-T and ZnO-T/AC nanocomposite (inset graph).

the total chromate concentration and pH of the solution [28]. It is clear from Fig. 7(a) that the removal efficiency of Cr(VI) for ZnO-T/AC adsorbent was reasonably high in the acidic pH, and it could reach upto 97% at pH 2. Subsequently, it decreased gradually with increasing pH. The PZC of ZnO-T/AC was obtained to be 5.4 (Fig. 8). Thus, it is practical to elucidate that anionic species of Cr (VI), such as HCrO_4^- , Cr_2O_7^- , and CrO_4^{2-} can be easily adsorbed on the positively charged surface of nanocomposite below PZC. The reduction of Cr (VI) to Cr(III) ions is shown by following equations (Eqs. (3)–(5)):

Under acidic conditions:



Under neutral conditions:



Under basic conditions:



At acidic pH, HCrO_4^- and Cr_2O_7^- ions are the predominant oxyanionic forms and at basic pH, the CrO_4^{2-} is the only stable form of Cr (VI) [72]. The CrO_4^{2-} ion possesses two negative charges, therefore, it needs two active sites for effective adsorption, moreover HCrO_4^- or Cr_2O_7^- ions requires one active site [73]. Hence, the adsorption capacity in the HCrO_4^- or Cr_2O_7^- is double to that of CrO_4^{2-} . Moreover, at low pH, electrostatic

attraction existed between protonated functional group of adsorbent and the anionic Cr(VI) ions, which favor the adsorption of Cr(VI) [37]. Whereas, at high pH, Cr(VI) adsorption is negatively affected by the deprotonation of the chromium. Decline in the removal efficiency may be described by the competitive adsorption between CrO_4^{2-} and OH^- ions [18].

3.4.2. Effect of contact time on Cr(VI) removal

For the designing of a cost-effective and efficient wastewater treatment systems, it is essential to calculate the equilibrium time for maximum adsorption of Cr(VI) ions. The effect of contact time on the Cr (VI) removal by AC, ZnO-T and ZnO-T/AC adsorbents (dose of 2.0 g/L at pH 2) at 10 mg/L initial Cr(VI) concentration was determined. It is apparent from Fig. 7(b) that the removal of Cr(VI) is proportional to the contact time [74]. In AC and ZnO-T, the increase in percent removal was observed till 30 min with contact time, while in ZnO-T/AC, it was till 60 min. The equilibrium was achieved after about 240 min, 360 min and 360 min for AC, ZnO-T and ZnO-T/AC respectively. Among adsorbent studied, ZnO-T/AC showed highest percent removal as compared to AC and ZnO-T at every interval. Protonated ZnO-T induces an enhancement in density of active site for uptake of Cr(VI), which further causes increased electrostatic attraction between ZnO-T/AC and Cr(VI) at pH 2 [51]. So the synergistic effect of ZnO-T and AC improves the Cr(VI) removal from aqueous solution.

3.4.3. Effect of adsorbent dosage on Cr(VI) removal

To examine the effect of adsorbent dosage (Fig. 7c), batch adsorption experiments were performed with varying amount of adsorbent ranging from 0.5 to 5.0 g/L. While keeping

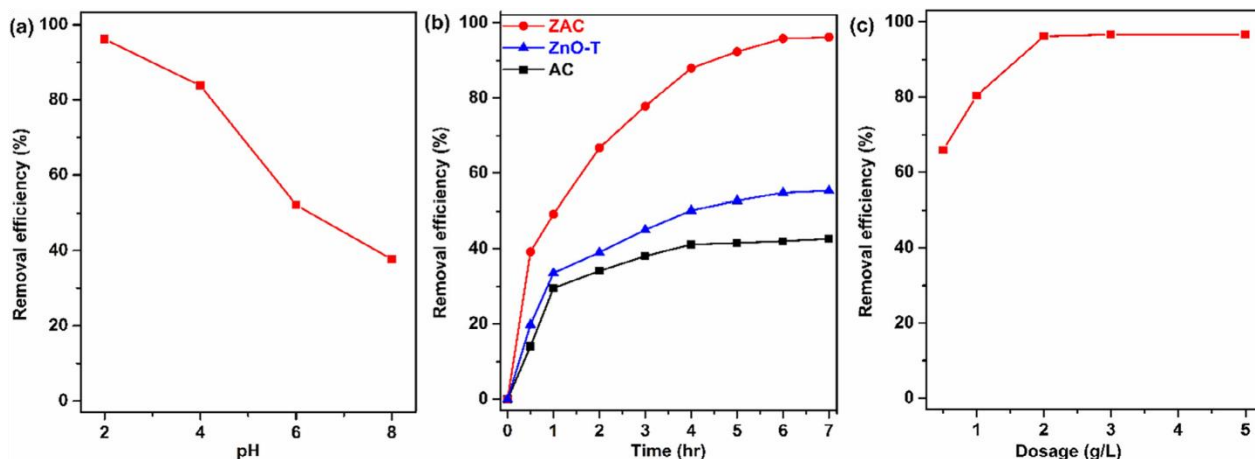


Fig. 7. Effect of (a) pH on Cr (VI) removal by ZnO-T/AC adsorbent, (b) contact time on Cr (VI) removal by AC, ZnO-T and ZnO-T/AC adsorbents and (c) adsorbent dosage on Cr (VI) removal by ZnO-T/AC adsorbent.

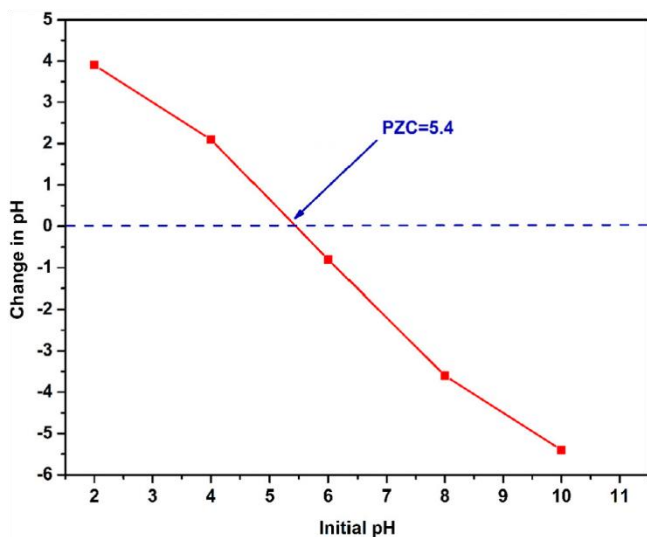


Fig. 8. Point of zero charge (PZC) of ZnO-T/AC composite dosage on Cr(VI) removal by ZnO-T/AC adsorbent.

concentration, contact time and pH as 10 mg/L, 6 h and 2 respectively. It is observed from the Fig. 6(c) that by increasing adsorbent dosage from 0.05 to 5 g/L, the Cr(VI) removal increases from 65.95% to 96.68%. The results suggest that the number of active adsorption sites for Cr(VI) adsorption are directly proportional to the dose applied, leading to higher removal efficiency [74]. At higher dosages (> 2.0 g/L), percentage removal remains constant due to attainment of adsorption equilibrium between the adsorbent and Cr(VI) in the solution [72]. Therefore, the

optimum adsorbent dosage was taken as 2.0 g/L for further adsorption assays.

3.5. Adsorption kinetics

The adsorption kinetics for Cr(VI) removal by AC, ZnO-T and ZnO-T/AC adsorbents were analyzed using pseudo-first-order model [75], pseudo-second-order model [76], intra-particle diffusion model [77] and Elovich model [78].

3.5.1. Pseudo-first-order and pseudo-second-order models

The pseudo-first-order kinetics provide the knowledge about the reaction dynamics and the type of reactions that are independent of initial concentration and conditions, while pseudo-second-order kinetics provides the best correlation of the experimental data and the adsorption mechanism. The pseudo-first-order (Eq. (6)) and pseudo-second-order (Eq. (7)) equations are usually expressed as:

$$\ln(q_e - q_t) = \ln q_e - k_1 t \quad (6)$$

$$\frac{1}{q_1} = \frac{1}{k_2 q_e^2} + \frac{1}{q_e} \quad (7)$$

where q_t (mg g^{-1}) and q_e (mg g^{-1}) are the adsorption capacity at time t (h) and at equilibrium respectively. k_1 (h^{-1}) and k_2 ($\text{g mg}^{-1} \text{h}^{-1}$) is the pseudo-first-order and pseudo-second-order constant respectively. q_e

can be determined from the intercept, while the rate constants of pseudo-first-order and pseudo-second-order can be determined from the slopes of the linear plots of $\ln(q_e - q_t)$ vs. t and t/q_t vs. t respectively. The kinetic fitting of experimental data by pseudo-first-order and pseudo-second-order models are shown in Fig. 9(a and b). The fitting parameters obtained from above kinetics are listed in Table 1. Depending on correlation coefficient (R^2) values the best fitting model was selected. As per Table 3, the R^2 value of pseudo-second-order model was higher than that of pseudo-first-order model. Moreover, the calculated values of the adsorption capacities ($q_{e, cal}$) by pseudo-second-order model were in good agreement with the experimental adsorption capacities ($q_{e, exp}$). Therefore, it can be suggested that adsorption of Cr(VI) on AC, ZnO-T and ZnO-T/AC is best fitted to the pseudo-second-order kinetic model. According to the literature the rate limiting step might be chemisorption process [79]. It can also be observed that among the studied adsorbents, value of the adsorption capacities (q_e) of the adsorbents follow a descending order: ZnO-T/AC > ZnO-T > AC and the value of rate constant of pseudo-second-order kinetic model is lowest for ZnO-T/AC and highest for the AC.

3.5.2. Intra-particle diffusion and Elovich model

For further evaluation of transport process and chemisorption on heterogeneous adsorbents, intra-particle diffusion and Elovich models were used. The intra-particle diffusion process explains the movement of species from the bulk of the solution to the solid phase [77] and Elovich model describes the kinetics of chemisorption on heterogeneous adsorbents [80]. Intra-particle diffusion (Eq. (8)) and Elovich (Eq. (9)) equations are expressed as:

$$q_1 = k_{id}t^{0.5} + C \quad (8)$$

$$q_1 = (1/\beta) \ln(\alpha\beta) + 1/\beta \ln(t) \quad (9)$$

where k_{id} ($\text{mg g}^{-1} \text{h}^{-0.5}$) is intra-particle diffusion rate constant. C (mg g^{-1}) is the intercept and they provide information about the thickness between adsorbent and adsorbate α ($\text{mg g}^{-1} \text{h}^{-1}$) is the initial adsorption coefficient and β (g mg^{-1}) is desorption coefficient. The rate constant of intra-particle diffusion model (k_{id}) can be determined from the slopes of the linear plots of q_t vs. $t^{0.5}$. The kinetic fitting of experimental data by intra-particle diffusion and Elovich kinetic models are shown in Fig. 9(c and d). The fitting parameters of the intra-particle diffusion and Elovich models are also presented in Table 4. The correlation coefficient (R^2) for intra-particle diffusion model was larger than 0.90, indicating that intra-particle diffusion model can also be fit for the adsorption process. Similarly, the correlation coefficient (R^2) for Elovich model with the value of 0.95, describing that Elovich model can also fit the adsorption process. From the Fig. 9(c), it is observed that the plot is multi-linear and not passing through the origin, revealing the involvement of multiple processes. The exhibition of three straight lines in plot q_t versus $t^{1/2}$ illustrates the participation of three governing mechanisms. In the first stage, HCrO_4^- metal ions migrated to the positively charged surface of ZnO-AC adsorbent under electrostatic attraction. In the second stage, HCrO_4^- ions moved to the pores and adsorbed on the inner sites of adsorbent, process called as intra-particle diffusion. In the third stage comprise of diffusion of ions through smaller pores, process called as inter-particle

3.5.3. Proposed mechanism

The possible adsorption process was shown in Fig. 10, which may be the diffusion through porous and surface interactions of Cr(VI) ions by ZnO-T/AC adsorbent. pH is the important factor, which controls the adsorption mechanism. Present adsorption studies suggested that maximum adsorption occurs at

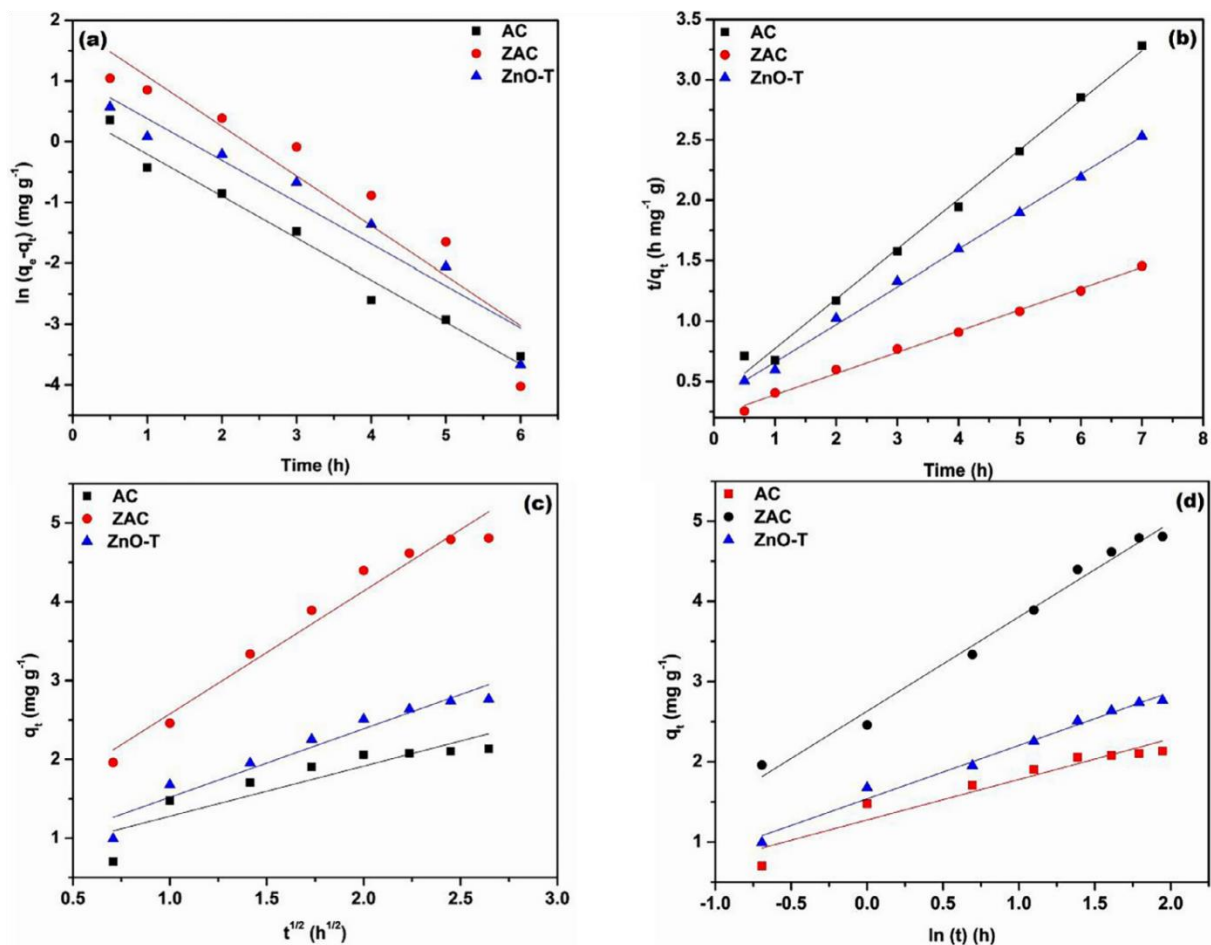


Fig. 9. Plots for (a) pseudo-first-order kinetics, (b) pseudo-second-order kinetics, (c) intra-particle diffusion model and (d) Elovich model ($C_0=10$ mg/L; dose = 2 g/ L; pH =2).

Table 3
Kinetic parameters for pseudo-first-order and pseudo-second-order models.

Adsorbent	pseudo-first-order			pseudo-second-order		
	k_1 (h^{-1})	q_e ($mg\ g^{-1}$)	R_2	k_2 ($g\ mg^{-1}\ h^{-1}$)	q_e ($mg\ g^{-1}$)	R_2
Activated carbon	0.690	1.621	0.977	0.465	2.433	0.993
ZnO-Tetrapods	0.688	2.912	0.925	0.276	3.215	0.997
ZnO-Tetrapods/AC NC	0.819	6.646	0.871	0.145	5.682	0.995

Table 4
Kinetic parameters for intra-particle diffusion and Elovich models.

Adsorbent	Intra-particle diffusion model			Elovich model		
	k_{id} ($mg\ g^{-1}\ h^{-0.5}$)	C ($mg\ g^{-1}$)	R_2	α ($mg\ g^{-1}\ h^{-1}$)	β ($g\ mg^{-1}$)	R_2
Activated carbon	0.636	0.643	0.781	6.309	1.980	0.908
ZnO-Tetrapods	0.869	0.650	0.928	6.725	1.504	0.984
ZnO-Tetrapods/ AC NC	1.560	1.016	0.962	10.995	0.850	0.985

pH 2. At this pH, $Cr_2O_7^{2-}$ is converted to $HCrO_4^-$ species [72] according to Eq. (10):
diffusion [49,75,81]



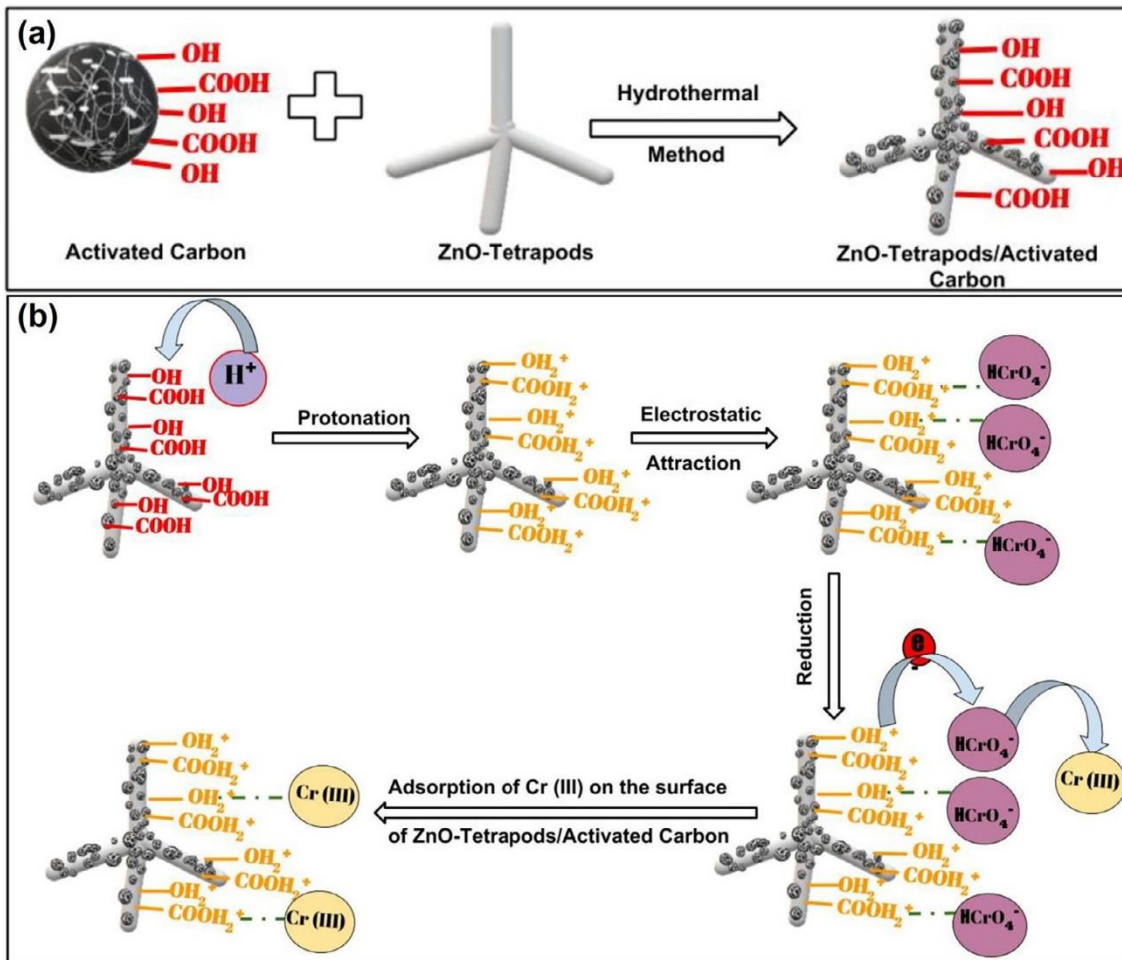


Fig. 10. (a) Synthesis step for ZnO-T/AC nanocomposite and (b) Proposed mechanism of Cr(VI) removal by ZnO-T/AC nanocomposite.

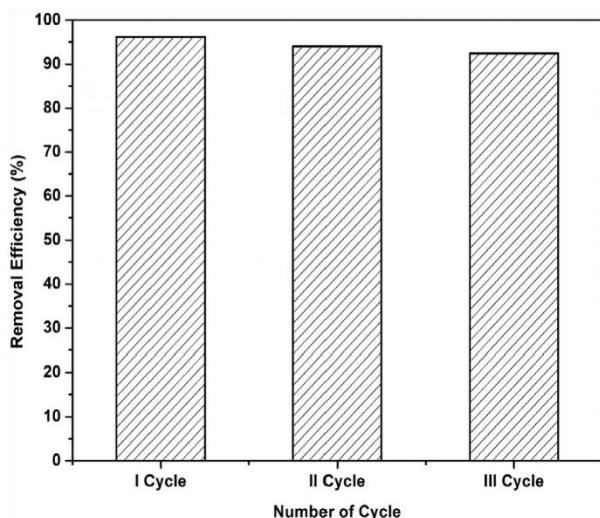


Fig. 11. Stability and reusability of ZnO-T/AC nanocomposite up-to 3 cycles.

At this condition, toxic Cr(VI) in aqueous solution adsorbed onto the surface of the ZnO-T/AC adsorbent by the electrostatic attraction and then reduced to Cr(III) by a heterogeneous redox process [75,79] (as shown in Fig. 10). pH 2 caused the surface of ZnO-T/AC adsorbent to be protonated to a great extent, resulting in a strong electrostatic attraction between HCrO₄⁻ and positively charged adsorbent, which can be easily reduced to Cr(III) due to high redox potential (range: 1.33–1.38 V) [18,74] (as shown by Eqs. (11) and (12)):

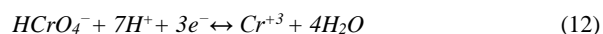
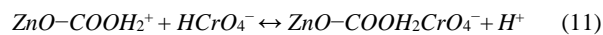


Table 5

Comparison of Cr (VI) Concentration, nanomaterials dosage, pH, and % removal efficiency of ZnO-T/AC nanocomposite with other available nanomaterials and various methods.

Nanomaterial	Cr (VI) Concentration (mg/L)	Nanomaterial dosage (g/L)	pH	Removal Efficiency (%)	Ref
Magnetic iron oxide NP-MWCNT composites	5	1	2	95	[28]
Longan seed activated carbon	100	2	3	63	[73]
Acid modified activated carbon	1	50	3	96	[22]
Combustion synthesized TiO ₂	10	0.5	7	70	[29]
Bentonite-supported nanoscale zerovalent Iron	100	2.5	5	90	[43]
Tamarind wood activated carbon activated with zinc chloride	10	2	6.5	88	[71]
Tea waste/Fe ₃ O ₄ NP composite	10	2	2	90	[75]
ZnO-T/AC	10	2	2	97	Present Work

3.5.4. Stability and reusability

In addition, the investigation of stability and reusability of ZnO-T/ AC nanocomposite was performed by the removal of Cr(VI) for three cycles at optimum condition (Fig. 11). Before reuse, the sample was washed with 0.1 M NaOH, kept at 120 rotations per minute (rpm) for 8 h and dried in vacuum at 60 °C. No significant decrease in percentage removal efficiency was observed till three cycles. Additionally, the removal efficiency was also evaluated after six months of adsorbent synthesis. This indicates that obtained nanocomposite has good stability and reusability. Performance of the ZnO-T/AC adsorbent for adsorption of Cr(VI) was compared with other reported adsorbents (Table 5). Higher adsorption efficiency (97%) was achieved using ZnO-T/AC adsorbent. This can be attributed to the larger surface area with abundant functional groups available on the ZnO-T/AC surface and high porosity.

4. Conclusions

In summary, activated carbon was successfully synthesized from sugarcane bagasse by chemical activation with sodium hydroxide. The synthesized AC was introduced into the 3-dimensional ZnO-T network using hydrothermal method and was used as an adsorbent for the removal of Cr(VI) (at 10 mg/L). The reduction of Cr(VI) using ZnO-T/AC adsorbent was affected by the pH,

contact time and dose of the adsorbent. The maximum removal efficiency of Cr(VI) to Cr(III) by AC, ZnO-T and ZnO-T/AC adsorbents occurred at pH 2.0. At the optimum pH 2, AC, ZnO-T and ZnO-T/AC showed 43%, 55% and 97% Cr (VI) removal respectively. Pseudo-second-order model, Intra-particle diffusion model and Elovich models, determined by adsorption capacity, kinetic rate constant, fitted well for all the adsorbents. The mechanism of Cr(VI) removal by ZnO-T/AC was further investigated. Therefore, this study offers new opportunities in investigating the feasible and economic method for Cr(VI) and other contaminants remediation from wastewater.

Acknowledgements

This work was financially supported by a project Grant from Department of Science and Technology, Govt. of India, New Delhi {Project no. 352 (DST/TM/WTI/2K16/265, G)}. Kiel authors acknowledge the financial support from Deutsche Forschungsgemeinschaft (DFG) under schemes SFB 677 (C14) and GRK 2154 (Project P3).

References

- [1] A. Bhatnagar, M. Sillanpää, Utilization of agro-industrial and municipal waste materials as potential adsorbents for water treatment-a review, *Chem. Eng. J.* 157 (2010) 277–296, <https://doi.org/10.1016/j.cej.2010.01.007>.
- [2] A. Bhatnagar, E. Kumar, M. Sillanpää, Fluoride removal from water by adsorption-a review, *Chem. Eng. J.* 171 (2011) 811–840, <https://doi.org/10.1016/j.cej.2011.05.028>.
- [3] C. Santhosh, V. Velmurugan, G. Jacob, S.K. Jeong, A.N. Grace, A. Bhatnagar, Role of nanomaterials in water treatment applications: a review, *Chem. Eng. J.* 306 (2016) 1116–1137, <https://doi.org/10.1016/j.cej.2016.08.053>.
- [4] C. Santhosh, R. Nivetha, P. Kollu, V. Srivastava, M. Sillanpää, A.N. Grace,

- A. Bhatnagar, Removal of cationic and anionic heavy metals from water by 1D and 2D-carbon structures decorated with magnetic nanoparticles, *Sci. Rep.* 7 (2017) 1–11, <https://doi.org/10.1038/s41598-017-14461-2>.
- [5] A. Singh, P. Khare, S. Verma, A. Bhati, A.K. Sonker, K.M. Tripathi, S.K. Sonkar, Pollutant soot for pollutant dye degradation: soluble graphene nanosheets for visible light induced photodegradation of methylene blue, *ACS Sustain. Chem. Eng.* 5 (2017) 8860–8869, <https://doi.org/10.1021/acssuschemeng.7b01645>.
- [6] K.M. Tripathi, T.S. Tran, Y.J. Kim, T. Kim, Green fluorescent onion-Like carbon nanoparticles from flaxseed oil for visible light induced photocatalytic applications and label-free detection of Al(III) ions, *ACS Sustain. Chem. Eng.* 5 (2017) 3982–3992, <https://doi.org/10.1021/acssuschemeng.6b03182>.
- [7] J. Gröttrup, F. Schütt, D. Smazna, O. Lupan, R. Adelung, Y.K. Mishra, Porous ceramics based on hybrid inorganic tetrapodal networks for efficient photocatalysis and water purification, *Ceram. Int.* (2017), <https://doi.org/10.1016/j.ceramint.2017.08.008>.
- [8] X. Qu, P.J.J. Alvarez, Q. Li, Applications of nanotechnology in water and wastewater treatment, *Water Res.* 47 (2013) 3931–3946, <https://doi.org/10.1016/j.watres.2012.09.058>.
- [9] K.M. Lee, C.W. Lai, K.S. Ngai, J.C. Juan, Recent developments of zinc oxide based photocatalyst in water treatment technology: a review, *Water Res.* 88 (2016) 428–448, <https://doi.org/10.1016/j.watres.2015.09.045>.
- [10] S. Mosleh, M.R. Rahimi, M. Ghaedi, K. Dashtian, S. Hajati, Sonochemical-assisted synthesis of CuO/Cu₂O nanoparticles as efficient photocatalyst for simultaneous degradation of pollutant dyes in rotating packed bed reactor: LED illumination and central composite design optimization, *Ultrason. Sonochem.* 40 (2018) 601–610, <https://doi.org/10.1016/j.ultrsonch.2017.08.007>.
- [11] M. Hua, S. Zhang, B. Pan, W. Zhang, L. Lv, Q. Zhang, Heavy metal removal from water/wastewater by nanosized metal oxides: a review, *J. Hazard. Mater.* 211–212 (2012) 317–331, <https://doi.org/10.1016/j.jhazmat.2011.10.016>.
- [12] N. Savage, M.S. Diallo, Nanomaterials and water purification: opportunities and challenges, *J. Nanoparticle Res.* (2005) 331–342, <https://doi.org/10.1007/s11051005-7523-5>.
- [13] T. Pradeep, Anshup, Noble metal nanoparticles for water purification: a critical review, *Thin Solid Films* 517 (2009) 6441–6478, <https://doi.org/10.1016/j.tsf.2009.03.195>.
- [14] L.K. Adams, D.Y. Lyon, P.J.J. Alvarez, Comparative eco-toxicity of nanoscale TiO₂, SiO₂, and ZnO water suspensions, *Water Res.* 40 (2006) 3527–3532, <https://doi.org/10.1016/j.watres.2006.08.004>.
- [15] M. Ghaedi, F.N. Azad, K. Dashtian, S. Hajati, A. Goudarzi, M. Soyak, Central composite design and genetic algorithm applied for the optimization of ultrasonicassisted removal of malachite green by ZnO nanorod-loaded activated carbon, *Spectrochim. Acta, Part A* 167 (2016) 157–164, <https://doi.org/10.1016/j.saa.2016.05.025>.
- [16] Y.K. Mishra, G. Modi, V. Cretu, V. Postica, O. Lupan, T. Reimer, I. Paulowicz, V. Hrkac, W. Bencke, L. Kienle, R. Adelung, Direct growth of freestanding ZnO tetrapod networks for multifunctional applications in photocatalysis, UV photodetection, and gas sensing, *ACS Appl. Mater. Interfaces* 7 (2015) 14303–14316, <https://doi.org/10.1021/acsami.5b02816>.
- [17] Y.K. Mishra, R. Adelung, ZnO tetrapod materials for functional applications, *Mater. Today* 21 (2018) 631–651, <https://doi.org/10.1016/j.mattod.2017.11.003>.
- [18] L. Tang, G. De Yang, G.M. Zeng, Y. Cai, S.S. Li, Y.Y. Zhou, Y. Pang, Y.Y. Liu, Y. Zhang, B. Luna, Synergistic effect of iron doped ordered mesoporous carbon on adsorption-coupled reduction of hexavalent chromium and the relative mechanism study, *Chem. Eng. J.* 239 (2014) 114–122, <https://doi.org/10.1016/j.cej.2013.10.104>.
- [19] H. Lahmar, M. Benamira, F.Z. Akika, M. Trari, Reduction of chromium (VI) on the hetero-system CuBi₂O₇/TiO₂ under solar light, *J. Phys. Chem. Solids* 110 (2017) 254–259, <https://doi.org/10.1016/j.jpcs.2017.06.021>.
- [20] L. Vimercati, M.F. Gatti, T. Gagliardi, F. Cuccaro, L. De Maria, A. Caputi, M. Quarato, A. Baldassarre, Environmental exposure to arsenic and chromium in an industrial area, *Environ. Sci. Pollut. Res.* 24 (2017) 11528–11535, <https://doi.org/10.1007/s11356-017-8827-6>.
- [21] Q. Cheng, C. Wang, K. Doudrick, C.K. Chan, Hexavalent chromium removal using metal oxide photocatalysts, *Appl. Catal., B* 176–177 (2015) 740–748, <https://doi.org/10.1016/j.apcatb.2015.04.047>.
- [22] F.A. Insanullah, B. Al-Khaldi, A.M. Abu-Sharkh, M.I. Abulkibash, T. Qureshi, M.A. Laoui, Atieh, Effect of acid modification on adsorption of hexavalent chromium (Cr(VI)) from aqueous solution by activated carbon and carbon nanotubes, *Desalin. Water Treat.* 57 (2016) 7232–7244, <https://doi.org/10.1080/19443994.2015.1021847>.
- [23] V.N. Bhusari, R. Dahake, S. Rayalu, A. Bansiwal, Comparative study of removal of hexavalent chromium from water using metal oxide nanoparticles, *Adv. Nanopart.* 05 (2016) 67–74, <https://doi.org/10.4236/anp.2016.51008>.
- [24] R.R. Ray, Adverse hematological effects of hexavalent chromium: an overview, *J. Phys. Chem.* 9 (2016) 55–65, doi:10.1515/jntox-2016-0007.
- [25] P.B. Tchounwou, C.G. Yedjou, A.K. Patolla, D.J. Sutton, Heavy Metals Toxicity and the Environment, (2014) 1–30, doi:10.1007/978-3-7643-8340-4.
- [26] K.G. Pavithra, P.S. Kumar, F.C. Christopher, A. Saravanan, Removal of toxic Cr(VI) ions from tannery industrial wastewater using a newly designed three-phase three-dimensional electrode reactor, *J. Phys. Chem. Solids* 110 (2017) 379–385, <https://doi.org/10.1016/j.jpcs.2017.07.002>.
- [27] D. Huang, G. Wang, Z. Shi, Z. Li, F. Kang, F. Liu, Removal of hexavalent chromium in natural groundwater using activated carbon and cast iron combined system, *J. Cleaner Prod.* 165 (2017) 667–676, <https://doi.org/10.1016/j.jclepro.2017.07.152>.
- [28] W. Lu, J. Li, Y. Sheng, X. Zhang, J. You, One-pot synthesis of magnetic iron oxide nanoparticle-multiwalled carbon nanotube composites for enhanced removal of Cr (VI) from aqueous solution, *J. Colloid Interface Sci.* (2017), <https://doi.org/10.1016/j.jcis.2017.07.013>.
- [29] P. Sane, S. Chaudhari, P. Nemade, S. Sontakke, Photocatalytic reduction of chromium (VI) using combustion synthesized TiO₂, *J. Environ. Chem. Eng.* 6 (2018) 68–73, <https://doi.org/10.1016/j.jece.2017.11.060>.
- [30] B.A. Marinho, R.O. Cristóvão, R. Djellabi, J.M. Loureiro, R.A.R. Boaventura, V.J.P. Vilar, Photocatalytic reduction of Cr(VI) over TiO₂-coated cellulose acetate monolithic structures using solar light, *Appl. Catal., B* 203 (2017) 18–30, <https://doi.org/10.1016/j.apcatb.2016.09.061>.
- [31] A. Asfaram, M. Ghaedi, K. Dashtian, G.R. Ghezalbash, Preparation and characterization of Mn_{0.4}Zn_{0.6}Fe₂O₄ nanoparticles supported on dead cells of *Yarrowia lipolytica* as a novel and efficient adsorbent/biosorbent composite for the removal of azo food dyes: central composite design optimization study, *ACS Sustain. Chem. Eng.* 6 (2018) 4549–4563, <https://doi.org/10.1021/acssuschemeng.7b03205>.
- [32] X. Fang, J. Li, X. Li, S. Pan, X. Zhang, X. Sun, J. Shen, W. Han, L. Wang, Internal pore decoration with polydopamine nanoparticle on polymeric ultrafiltration membrane for enhanced heavy metal removal, *Chem. Eng. J.* 314 (2017) 38–49, <https://doi.org/10.1016/j.cej.2016.12.125>.
- [33] Y. Li, Z. Xu, S. Liu, J. Zhang, X. Yang, Molecular simulation of reverse osmosis for heavy metal ions using functionalized nanoporous graphenes, *Comput. Mater. Sci.* 139 (2017) 65–74, <https://doi.org/10.1016/j.commatsci.2017.07.032>.
- [34] O. Tavakoli, V. Goodarzi, M.R. Saeb, N.M. Mahmoodi, R. Borja, Competitive removal of heavy metal ions from squid oil under isothermal condition by CR11 chelate ion exchanger, *Elsevier B.V.*, 2017, doi:10.1016/j.jhazmat.2017.04.023.
- [35] M. Taseidifar, F. Makavipour, R.M. Pashley, A.F.M.M. Rahman, Removal of heavy metal ions from water using ion flotation, *Environ. Technol. Innov.* 8 (2017) 182–190, <https://doi.org/10.1016/j.eti.2017.07.002>.
- [36] L. Cui, G. Li, Y. Li, B. Yang, L. Zhang, Y. Dong, C. Ma, Electrolysis-electrodialysis process for removing chloride ion in wet flue gas desulfurization wastewater (DW): influencing factors and energy consumption analysis, *Chem. Eng. Res. Des.* 123 (2016) 240–247, <https://doi.org/10.1016/j.cherd.2017.05.016>.
- [37] R. Ali, M. Naushad, Hexavalent chromium removal from aqueous medium by activated carbon prepared from peanut shell: adsorption kinetics, equilibrium and thermodynamic studies, *Chem. Eng. J.* 184 (2012) 238–247, <https://doi.org/10.1016/j.cej.2012.01.048>.
- [38] A.A.F.H.A. Abdel, T.S.A. Abdel, M. Rehab, Functionalization of acidified multiwalled carbon nanotubes for removal of heavy metals in aqueous solutions, *J. Nanostruct. Chem.* 7 (2017) 101–111, <https://doi.org/10.1007/s40097-0170227-4>.
- [39] A. Muhulet, F. Miculescu, S.I. Voicu, F. Schütt, V.K. Thakur, Y.K. Mishra, Fundamentals and scopes of doped carbon nanotubes towards energy and biosensing applications, *Mater. Today Energy* 9 (2018) 154–186, <https://doi.org/10.1016/j.mtener.2018.05.002>.
- [40] D.O. Jacir, D. Magro, Adsorption of heavy metals from wastewater graphic industry using clinoptilolite zeolite as adsorbent, *Process Saf. Environ. Prot.* (2016), <https://doi.org/10.1016/j.psep.2016.11.008>.
- [41] S. Pu, H. Ma, A. Zinchenko, W. Chu, Novel highly porous magnetic hydrogel beads composed of chitosan and sodium citrate: an effective adsorbent for the removal of heavy metals from aqueous solutions, (2017), doi:10.1007/s11356-017-9213-0.
- [42] H. Lee, S. Prabha, A. Dhar, M. Sillanp, Y. Kwon, C. Lee, Chemosphere Adsorption of As(V) by boehmite and alumina of different morphologies prepared under hydrothermal conditions, 169 (2017) 99–106, doi:10.1016/j.chemosphere.2016.11.052.
- [43] A. Saliemanzadeh, M. Fekri, The application of green tea extract to prepare bentonite-supported nanoscale zero-valent iron and its performance on removal of Cr (VI): effect of relative parameters and soil experiments, *Microporous Mesoporous Mater.* 239 (2017) 60–69, <https://doi.org/10.1016/j.micromeso.2016.09.050>.
- [44] T. Yang, L. Meng, S. Han, J. Hou, S. Wang, X. Wang, Simultaneous reductive and sorptive removal of Cr(VI) by activated carbon supported β -FeOOH, *RSC Adv.* 7 (2017) 34687–34693, <https://doi.org/10.1039/c7ra06440c>.
- [45] A. Islam, M.J. Ahmed, W.A. Khanday, M. Asif, B.H. Hameed, Mesoporous activated coconut shell-derived hydrochar prepared via hydrothermal carbonization-NaOH activation for methylene blue adsorption, *J. Environ. Manage.* 203 (2017) 237–244, <https://doi.org/10.1016/j.jenvman.2017.07.029>.
- [46] L. Limousy, I. Ghouma, A. Ouederni, M. Jeguirim, Amoxicillin removal from aqueous solution using activated carbon prepared by chemical activation of

- olive stone, *Environ. Sci. Pollut. Res.* 24 (2017) 9993–10004, <https://doi.org/10.1007/s11356016-7404-8>.
- [47] M. Alhassan, I. Andrew, M. Auta, M. Umaru, M.U. Garba, A.G. Isah, B. Alhassan, M. Alhassan, I. Andrew, M. Auta, M. Umaru, Comparative studies of CO₂ capture using acid and base modified activated carbon from sugarcane bagasse, *Biofuels* (2017) 1–10, <https://doi.org/10.1080/17597269.2017.1306680>.
- [48] P.S. Thue, G.S. Reis, Activated carbon obtained from sapelli wood sawdust by microwave heating for o-cresol adsorption, *Res. Chem. Intermed.* (2016), <https://doi.org/10.1007/s11164-016-2683-8>.
- [49] S. Roy, P. Das, S. Sengupta, Treatability study using novel activated carbon prepared from rice husk: column study, optimization using response surface methodology and mathematical modeling, *Process Saf. Environ. Prot.* (2016), <https://doi.org/10.1016/j.psep.2016.11.007>.
- [50] H. Laksaci, A. Khelifi, M. Trari, A. Addoun, Synthesis and characterization of microporous activated carbon from coffee grounds using potassium hydroxides, *J. Cleaner Prod.* (2017), <https://doi.org/10.1016/j.jclepro.2017.01.102>.
- [51] S. Li, L. Liu, Y. Yu, G. Wang, H. Zhang, A. Chen, Fe₃O₄ modified mesoporous carbon nanospheres: magnetically separable adsorbent for hexavalent chromium, *J. Alloys Compd.* (2017), <https://doi.org/10.1016/j.jallcom.2016.12.163>.
- [52] X. Li, X. Gao, L. Ai, J. Jiang, Mechanistic insight into the interaction and adsorption of Cr(VI) with zeolitic imidazolate framework-67 microcrystals from aqueous solution, *Chem. Eng. J.* 274 (2015) 238–246, <https://doi.org/10.1016/j.cej.2015.03.127>.
- [53] X. Li, L. Ai, J. Jiang, Nanoscale zerovalent iron decorated on graphene nanosheets for Cr(VI) removal from aqueous solution: surface corrosion retard induced the enhanced performance, *Chem. Eng. J.* 288 (2016) 789–797, <https://doi.org/10.1016/j.cej.2015.12.022>.
- [54] M.R. Awwal, T. Yaita, S.A. El-Safy, H. Shiwaku, S. Suzuki, Y. Okamoto, Copper(II) ions capturing from water using ligand modified a new type mesoporous adsorbent, *Chem. Eng. J.* 221 (2013) 322–330, <https://doi.org/10.1016/j.cej.2013.02.016>.
- [55] M.R. Awwal, M.M. Hasan, Colorimetric detection and removal of copper(II) ions from wastewater samples using tailor-made composite adsorbent, *Sens. Actuators, B* 206 (2015) 692–700, <https://doi.org/10.1016/j.snb.2014.09.086>.
- [56] Y.K. Mishra, S. Kaps, A. Schuchardt, I. Paulowicz, X. Jin, D. Gedamu, S. Freitag, M. Claus, S. Wille, A. Kovalev, S.N. Gorb, R. Adelung, Fabrication of macroscopically flexible and highly porous 3D semiconductor networks from interpenetrating nanostructures by a simple flame transport approach, *Part. Part. Syst. Charact.* 30 (2013) 775–783, <https://doi.org/10.1002/ppsc.201300197>.
- [57] M. Keshvardoustchokami, P. Bigverdi, A. Zamani, A. Parizanganeh, F. Piri, Silver@ graphene oxide nanocomposite: synthesis and application in removal of imidacloprid from contaminated waters, *Environ. Sci. Pollut. Res.* 25 (2018) 6751–6761, <https://doi.org/10.1007/s11356-017-1006-y>.
- [58] B. Xing, C. Shi, C. Zhang, G. Yi, L. Chen, H. Guo, G. Huang, J. Cao, Preparation of TiO₂/activated carbon composites for photocatalytic degradation of RhB under UV light irradiation, *J. Nanomater.* 2016 (2016) 1–10, <https://doi.org/10.1155/2016/8393648>.
- [59] C. Lei, M. Pi, C. Jiang, B. Cheng, J. Yu, Synthesis of hierarchical porous zinc oxide (ZnO) microspheres with highly efficient adsorption of Congo red, 2017, doi:10.1016/j.jcis.2016.11.049.
- [60] N.N.N.A. Rahman, M. Shahadat, C.A. Won, F.M. Omar, FTIR study and bioadsorption kinetics of bioadsorbent for the analysis of metal pollutants, *RSC Adv.* 4 (2014) 58156–58163, <https://doi.org/10.1039/c4ra05931j>.
- [61] C. Gan, Y. Liu, X. Tan, S. Wang, G. Zeng, B. Zheng, T. Li, Z. Jiang, W. Liu, Effect of porous zinc-biochar nanocomposites on Cr(VI) adsorption from aqueous solution, *RSC Adv.* 5 (2015) 35107–35115, <https://doi.org/10.1039/c5ra04416b>.
- [62] L.S. Dake, D.R. Baer, J.M. Zachara, Auger parameter measurements of zinc compounds relevant to zinc transport in the environment, *Surf. Interface Anal.* 14 (1989) 71–75, <https://doi.org/10.1002/sia.740140115>.
- [63] D. Briggs, *Handbook of X-ray Photoelectron Spectroscopy* C. D. Wanger, W. M. Riggs, L. E. Davis, J. F. Moulder and G. E. Muilenberg Perkin-Elmer Corp., Physical Electronics Division, Eden Prairie, Minnesota, USA, 1979. 190 pp. \$195, Surf. Interface Anal. 3 (1981), <https://doi.org/10.1002/sia.740030412>.
- [64] R. Chapaneri, G. Critchlow, I. Sutherland, An X-ray photoelectron spectroscopy investigation of chromium conversion coatings and chromium compounds, (2008). Available from: <http://creativecommons.org/licenses/by-nc-nd/2.5/> <https://dspace.lboro.ac.uk/dspace-jspui/handle/2134/9632>.
- [65] M.C. Biesinger, C. Brown, J.R. Mycroft, R.D. Davidson, N.S. McIntyre, X-ray photoelectron spectroscopy studies of chromium compounds, *Surf. Interface Anal.* 36 (2004) 1550–1563, <https://doi.org/10.1002/sia.1983>.
- [66] V.-D. Dao, N.T.Q. Hoa, L.L. Larina, J.-K. Lee, H.-S. Choi, Graphene–platinum nanohybrid as a robust and low-cost counter electrode for dye-sensitized solar cells, *Nanoscale* 5 (2013) 12237, <https://doi.org/10.1039/c3nr03219a>.
- [67] R. Nowak, P. Hess, H. Oetzmann, C. Schmidt, XPS characterisation of chromium films deposited from Cr(CO)₆ at 248 nm, *Appl. Surf. Sci.* 43 (1989) 11–16, [https://doi.org/10.1016/0169-4332\(89\)90183-9](https://doi.org/10.1016/0169-4332(89)90183-9).
- [68] R. Li, Q. Da An, B.Q. Mao, Z.Y. Xiao, S.R. Zhai, Z. Shi, PDA-mediated green synthesis of amino-modified, multifunctional magnetic hollow composites for Cr (VI) efficient removal, *J. Taiwan Inst. Chem. Eng.* 80 (2017) 596–606, <https://doi.org/10.1016/j.jtice.2017.08.036>.
- [69] X. Li, R. Zhao, B. Sun, X. Lu, C. Zhang, Z. Wang, C. Wang, Fabrication of α -Fe₂O₃- γ -Al₂O₃ core-shell nanofibers and their Cr(VI) adsorptive properties, *RSC Adv.* 4 (2014) 42376–42382, <https://doi.org/10.1039/C4RA03692A>.
- [70] K. Zhu, C. Chen, H. Xu, Y. Gao, X. Tan, A. Alsaedi, T. Hayat, Cr(VI) reduction and immobilization by core-double-shell structured magnetic polydopamine@zeolitic imidazolate frameworks-8 microspheres, *ACS Sustain. Chem. Eng.* 5 (2017) 6795–6802, <https://doi.org/10.1021/acsschemeng.7b01036>.
- [71] J. Acharya, J.N. Sahu, B.K. Sahoo, C.R. Mohanty, B.C. Meikap, Removal of chromium (VI) from wastewater by activated carbon developed from Tamarind wood activated with zinc chloride, 150 (2009) 25–39, doi:10.1016/j.cej.2008.11.035.
- [72] M. Fazlzadeh, R. Khosravi, A. Zarei, Green synthesis of zinc oxide nanoparticles using Peganum harmala seed extract, and loaded on Peganum harmala seed powdered activated carbon as new adsorbent for removal of Cr (VI) from aqueous solution, *Ecol. Eng.* 103 (2017) 180–190, <https://doi.org/10.1016/j.ecoleng.2017.02.052>.
- [73] J. Yang, M. Yu, W. Chen, Adsorption of hexavalent chromium from aqueous solution by activated carbon prepared from longan seed: kinetics, equilibrium and thermodynamics, *J. Ind. Eng. Chem.* (2014), <https://doi.org/10.1016/j.jiec.2014.02.054>.
- [74] C. Jung, J. Heo, J. Han, N. Her, S. Lee, J. Oh, J. Ryu, Y. Yoon, Hexavalent chromium removal by various adsorbents: powdered activated carbon, chitosan, and single/multi-walled carbon nanotubes, *Sep. Purif. Technol.* 106 (2013) 63–71, <https://doi.org/10.1016/j.seppur.2012.12.028>.
- [75] S. Fan, Y. Wang, Y. Li, J. Tang, Z. Wang, J. Tang, X. Li, K. Hu, Facile synthesis of tea waste/Fe₃O₄ nanoparticle composite for hexavalent chromium removal from aqueous solution, *RSC Adv.* 7 (2017) 7576–7590, <https://doi.org/10.1039/C6RA27781K>.
- [76] Y.S. Ho, G. McKay, Pseudo-second order model for sorption processes, *Process Biochem.* 34 (1999) 451–465, [https://doi.org/10.1016/S0032-9592\(98\)00112-5](https://doi.org/10.1016/S0032-9592(98)00112-5).
- [77] M. Barkat, D. Nibou, S. Chegrouche, A. Mellah, Kinetics and thermodynamics studies of chromium(VI) ions adsorption onto activated carbon from aqueous solutions, *Chem. Eng. Process. Process Intensif.* 48 (2009) 38–47, <https://doi.org/10.1016/j.cep.2007.10.004>.
- [78] G. Ho, Y.S. McKay, A comparison of chemisorption kinetic models applied to pollutant removal on various sorbents, *Trans IchemE* 76 (1998) 332–340.
- [79] Z. Xiao, H. Zhang, Y. Xu, M. Yuan, X. Jing, J. Huang, Q. Li, D. Sun, Ultra-efficient removal of chromium from aqueous medium by biogenic iron based nanoparticles, *Sep. Purif. Technol.* 174 (2017) 466–473, <https://doi.org/10.1016/j.seppur.2016.10.047>.
- [80] R. Juang, M. Chen, Application of the Elovich equation to the kinetics of metal sorption with solvent-impregnated resins, *Ind. Eng. Chem. Res.* 36 (1997) 813–820.
- [81] J. Zhao, J. Liu, N. Li, W. Wang, J. Nan, Z. Zhao, F. Cui, Highly efficient removals of bivalent heavy metals from aqueous systems by magnetic porous Fe₃O₄-MnO₂: adsorption behavior and process study, *Chem. Eng. J.* 304 (2016) 737–746, <https://doi.org/10.1016/j.cej.2016.07.003>.

5. Tetrapodal ZnO Decorated by Entangled MWCNTs

Current chapter focuses on investigating the electrical and thermal conductivity of the T-ZnO and MWCNTs composite in comparison to free standing hollow tubes made of MWCNTs without T-ZnO. High electrical conductivity of the CNTs and high thermal conductivity of the ceramic T-ZnO at low temperatures were combined to obtain a versatile hybrid material with prominent features from both the constituents.

Personal contributions in the following article:

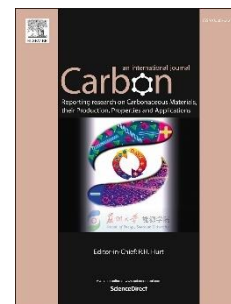
- Fabrication of the T-ZnO utilized in this study
- Compositional investigation under Raman spectrometer
- Partial manuscript preparation

The following content is reproduced with formal permission from “J-H. Pöhls, F. Schütt, C. O'Neill, S. Shree, M. B. Johnson, Y. K. Mishra, R. Adelung, M. A. White, *Carbon*, **2019**, *144*, 423”, (© 2018 Elsevier Ltd. All rights reserved).

Accepted Manuscript

Thermal and electrical transport properties in multi-walled carbon nanotube-coated ZnO tetrapods and self-entangled multi-walled carbon nanotube tubes

Jan-Hendrik Pöhls, Fabian Schütt, Catherine O'Neill, Sindu Shree, Michel B. Johnson, Yogendra Kumar Mishra, Rainer Adelung, Mary Anne White



PII: S0008-6223(18)31181-3

DOI: <https://doi.org/10.1016/j.carbon.2018.12.047>

Reference: CARBON 13750

To appear in: *Carbon*

Received Date: 19 September 2018

Revised Date: 4 December 2018

Accepted Date: 14 December 2018

Please cite this article as: J.-H. Pöhls, F. Schütt, C. O'Neill, S. Shree, M.B. Johnson, Y.K. Mishra, R. Adelung, M.A. White, Thermal and electrical transport properties in multi-walled carbon nanotube-coated ZnO tetrapods and self-entangled multi-walled carbon nanotube tubes, *Carbon* (2019), doi: <https://doi.org/10.1016/j.carbon.2018.12.047>.

This is a PDF file of an unedited manuscript that has been accepted for publication. As a service to our customers we are providing this early version of the manuscript. The manuscript will undergo copyediting, typesetting, and review of the resulting proof before it is published in its final form. Please note that during the production process errors may be discovered which could affect the content, and all legal disclaimers that apply to the journal pertain.

Thermal and Electrical Transport Properties in Multi-Walled Carbon Nanotube-coated ZnO Tetrapods and Self-Entangled Multi-Walled Carbon Nanotube Tubes

Jan-Hendrik Pöhls,^{a,b} Fabian Schütt,^c Catherine O'Neill,^a Sindu Shree,^c Michel B. Johnson,^d Yogendra Kumar Mishra,^c Rainer Adelung,^c Mary Anne White^{a,b,d,*}

^a Department of Chemistry, Dalhousie University, Halifax, Nova Scotia, Canada B3H 4R2

^b Department of Physics and Atmospheric Science, Dalhousie University, Halifax, NS, Canada B3H 4R2

^c Institute for Materials Science, Kiel University, Kaiserstr. 2, D-24143 Kiel, Germany

^d Clean Technologies Research Institute, Dalhousie University, Halifax, NS, Canada B3H 4R2

*Corresponding author. Email: Mary.Anne.White@Dal.ca (Mary Anne White)

Abstract

We present the electrical and thermal properties of highly porous (~ 94% porous) three-dimensional (3D) ZnO network structures coated with a thin layer of self-entangled multi-walled carbon nanotubes (MWCNTs), resulting in the formation of MWCNT microtubes (MWCNTTs) around the ceramic backbone. Additionally, we compare the properties of the composite (MWCNT/ZnO) structures to free-standing MWCNTTs, a hierarchical network consisting solely of randomly interconnected MWCNTs. The random 3D architecture of the ZnO network results in isotropic properties, in contrast to the typical one-dimensional (1D) properties of other CNT assemblies. The electrical conductivity of the MWCNT/ZnO composite increases with MWCNT content suggesting that MWCNTs are dominant over the entire temperature range. On the other hand, the thermal conductivity is mainly determined by the ceramic ZnO backbone at low temperature while the thermal conductivity of the MWCNTs is mainly dominant above 300 K. The electrical conductivity of the MWCNT/ZnO composites could reach values of up to $49 \pm 2 \text{ S m}^{-1}$ at room temperature whereas the room-temperature thermal conductivity of the MWCNTTs is $0.08 \pm 0.02 \text{ W m}^{-1} \text{ K}^{-1}$. Direct comparison between both the composite and the pure MWCNTTs allows for a better understanding concerning which material in the composite dominates the transport properties.

1. Introduction

Since their discovery in 1991, carbon nanotubes (CNTs) are among the most studied materials due to their unique properties, such as high electrical and thermal conductivities, and extremely high tensile strengths.^[1,2,3] These properties have been utilized in several applications, *e.g.* field emission^[4] and hydrogen storage,^[5] creating new markets for microscopic applications.^[6] Two different approaches have been applied to create high-performance, macroscopic functional CNT materials: hybrid materials (CNTs dispersed in a matrix) and pure CNT bulk materials. However, overall enhancement of desired properties by incorporation of individual of CNTs into macroscopic materials is still a challenging task.

CNT-reinforced metals, polymers and ceramics are anticipated to exhibit enhanced mechanical strength, and high electrical and thermal conductivity.^[7,8,9,10] For example, VelascoSantos *et al.* reported that the mechanical toughness can increase significantly by addition of as little as 1 mass% functionalized CNTs to a polymer matrix.^[11] Functionalization of the CNTs can be important to enhance interactions between the matrix and CNTs; without functionalization, addition of CNTs can reduce the toughness relative to the pure polymer.^[11] Similar behavior was reported in ceramic matrices in which no change in toughness was observed with addition of unfunctionalized CNTs.^[12] While improvement of the mechanical properties is limited by the weak interactions between the matrix and the CNTs, enhanced electrical conductivities have been reported for various ceramic^[13,14] and polymer matrices.^[15,16] For instance, Zhan *et al.* measured an electrical conductivity of $33.5 \Omega^{-1} \text{ cm}^{-1}$ in an alumina/single wall CNT (SWCNT) nanocomposite using 15 vol% SWCNT,^[13] an increase of more than 15 orders of magnitude compared to pure alumina. Furthermore, Sandler *et al.* reported an ultra-low electrical conductivity percolation threshold of 0.0025 mass% in a CNT-epoxy composite where the CNTs were aligned in the epoxy matrix.^[15] Due to these exceptionally low percolation thresholds, CNTreinforced hybrid materials are attractive for large-scale applications. For example, small amounts of CNTs incorporated in materials for energy storage and generation resulted in an improvement of the cyclability and capacity of anode materials in Li-ion batteries^[17,18] and in the performance of thermoelectric materials.^[19,20]

In addition to improved mechanical and electronic properties, enhancement of the thermal conductivity in polymers is desirable for various applications such as thermal management.^[21] However, whereas the electrical conductivity can be modified by many orders of magnitude, the improvement of the thermal conductivity is much smaller, generally below one order of magnitude.^[22] Although individual CNTs have a high aspect ratio and high thermal conductivity, which would suggest a low thermal conductivity percolation threshold, it is challenging to determine the CNT thermal threshold in hybrid materials due to the low values of the thermal conductivity. Furthermore, the thermal conductivity of the CNTs in the matrix depends on several factors, including interfacial/contact resistance (CNT-CNT and CNT-matrix), CNT dispersion and CNT alignment.^[23] In particular, the dispersion of CNTs in hybrid materials is challenging due to the strong intrinsic van der Waals interactions between the CNTs, often leading to an

agglomeration of the CNTs in the hybrid material. Song *et al.* observed an increase in thermal conductivity if CNTs were well dispersed in a polymer matrix.^[24] However, the differences in thermal conductivity between poorly and well-dispersed CNTs decreased with increasing CNT content. Huang *et al.* reported, in this context, that the thermal conductivity of aligned CNTs in silicone can be twice that of composites with the same proportion of dispersed CNTs.^[25] While the thermal conductivities in polymer matrices are in general quite low, the thermal conductivity in ceramics can vary, leading to different effects with the incorporation of CNTs. For example, the thermal conductivity for silica/CNT nanocomposites increases with increasing CNT content, whereas due to the dominance of phonon scattering from the CNTs^[26] the opposite effect was observed in high thermal conductivity alumina.^[27] For a better understanding of the influence of CNTs on the physical properties in hybrid materials, a deeper knowledge of the physical properties of pure CNT materials is essential.

The mechanical and transport properties of various macroscopic pure CNT materials have been previously reported, such as for CNT fibres,^[28] CNT yarns,^[29,30,31] CNT arrays,^[32] and CNT sheets.^[28,33] Sears *et al.* reported the tensile strength of CNT yarns in relation to the twist.^[31] Whereas small twists led to high tensile strength (480-580 MPa), the tensile strength dropped to 180 MPa for large twists. Even lower tensile strength was found for CNT sheets (~7.5 MPa) due to an increase in defect concentration.^[33] As for the mechanical properties, the electrical conductivity of CNT bulk materials varies widely between samples, from $7 \Omega^{-1} \text{ cm}^{-1}$ for CNT arrays^[32] to about $800 \Omega^{-1} \text{ cm}^{-1}$ for CNT yarns.^[30] Jakubinek *et al.* observed a reduction in electrical conductivity with increasing yarn diameter, most likely due to a decrease in migration length and alignment.^[30] Gspann *et al.* showed that the density and quality of CNT bundle alignment is the predominant factor in controlling electrical conductivity of CNT films.^[28] An increase in electrical conductivity was observed for more aligned and defect-free CNT sheets. The thermal conductivity of bulk CNT shows behavior similar to the electrical conductivity with the lowest thermal conductivity reported for CNT arrays ($0.5\text{-}1.2 \text{ W m}^{-1} \text{ K}^{-1}$),^[32] followed by CNT sheets ($2.5\text{-}110 \text{ W m}^{-1} \text{ K}^{-1}$)^[28,33] and CNT yarns ($20\text{-}80 \text{ W m}^{-1} \text{ K}^{-1}$).^[29,30] Niven *et al.* showed that the thermal conductivity can increase from 20 to $80 \text{ W m}^{-1} \text{ K}^{-1}$ by decreasing the defect concentration.^[29] The highest room-temperature thermal conductivity to date for CNT bulk materials was observed for CNT fibres ($770 \text{ W m}^{-1} \text{ K}^{-1}$)^[28] which is only a factor of about 5 smaller than the highest value for individual CNTs.^[2] However, the large discrepancies between measured physical properties of CNT bulk samples makes it challenging to delineate the influence of CNTs on the properties of the hybrid materials. A potential approach to investigate the impact of CNTs in a matrix is by removing the matrix and measuring solely the physical properties of free-standing CNT structures.

In a recent study, a simple wet chemical infiltration strategy was introduced to fabricate open porous, cm^3 -sized three-dimensional (3D) nanomaterial assemblies (*e.g.*, MWCNT), based on a super-hydrophilic and highly porous (~94 porous%) 3D ceramic template.^[34,35] The ceramic template consists of interconnected and micrometer-sized ZnO tetrapods (*i.e.*, four arms radiate from a ZnO core with angle of 109° to each other), resulting in micrometer-sized voids between

the individual arms. Infiltrating the template with an appropriate aqueous MWCNT dispersion results in the formation of self-entangled MWCNT carpets around the individual arms of the tetrapods during drying, similar to so-called CNT buckypapers. The amount of MWCNTs covering the ceramic backbone can be adjusted by the concentration of the dispersion as well as by the number of infiltration steps. At high CNT loadings, interconnected and micrometer-sized tubes consisting of self-entangled CNTs are formed around the entire template structure. By employing this method, advanced 3D MWCNT/ceramic (MWCNT/ZnO) composite structures, MWCNT/polymer composites, and free-standing MWCNT assemblies (so-called MWCNT tubes [MWCNTT]), can be fabricated by either infiltrating the composite structure with a polymer or by etching out the ceramic backbone.^[34,36] The formation of self-entangled CNT layers around the ceramic backbone results in mechanically strong, conductive and open porous 3D composites and MWCNTT foams, even though no additional crosslinking exists between the individual MWCNTs. The highly porous ceramic is significantly reinforced by the deposited self-entangled MWCNTs. Compressing the composite structure (MWCNT/ZnO) deploys the strong tensile properties of the MWCNTs: the compressive stress applied on the porous 3D composite structure is redirected into a tensile stress. Additionally, the deposition of MWCNTTs on the porous ceramic enhances electrical conductivity due to the formation of percolation pathways. This situation leads to high conductivities even at low CNT concentrations. Therefore, such structures can be used as an effective filler material for the fabrication of mechanically reinforced, conductive polymers. In addition, removal of the ZnO template results in a 3D double hierarchical MWCNTT structure with enhanced mechanical and electrical properties compared to other 3D assemblies prepared by wet chemistry.^[34] The 3D architecture and the fact that the pure MWCNTT structure should possess similar alignment and defect concentration to the MWCNTTs attached to the ZnO tetrapods, the system allows for a better understanding of the change in electrical and thermal properties between hybrid (MWCNT/ZnO) and pure CNT materials, which is rather very difficult to achieve by conventional fabrication strategies. Furthermore, in contrast to other bulk CNT materials which have enhanced properties only in a single direction, the properties in MWCNT-coated ZnO tetrapods and MWCNTTs are nearly isotropic and the MWCNT content can be simply changed by increasing the number of infiltration steps or the concentration of the used dispersion.^[34] Additionally, the approach is versatile as CNTs can be replaced by other nanomaterial dispersions, allowing investigations of other composite systems. In the present study, the electrical and thermal properties of MWCNT/ZnO composites and MWCNTTs were investigated as a function of temperature to compare the transport properties of hybrid (MWCNT/ZnO) and free-standing MWCNTT materials.

2. Synthesis and Characterization

For the MWCNT-coated ZnO tetrapods (MWCNT/ZnO) and MWCNTTs, first ZnO tetrapods^[37] were synthesized using a flame transport approach developed at Kiel University.^[35] In this method, a mixture of zinc powder (Sigma Aldrich, dust < 10 μm , purity: $\geq 98\%$) and polyvinyl butyral (PVB) (Kuraray) in a ratio of 1:2 (total mass between 10 to 20 g) was placed in

a ceramic crucible and heated to 900 °C for 30 min under ambient atmosphere. The resulting loose powder of ZnO tetrapods was consolidated to a pellet (with a mass density of 0.3 g cm⁻³, 6 mm in diameter, and 2.2-3.5 mm in height) and sintered at 1150 °C for 5 hours, to form an interconnected ZnO template. After sintering, a dispersion of ~1 mass% MWCNT (CARBOBYK-9810 purchased from Byk Additives & Instruments) was infiltrated in the ZnO tetrapod-based template and afterwards dried on a hotplate (40 °C) for at least three hours in air. The infiltration step was repeated one to six times to investigate the thermal and electrical properties in relation to the MWCNT coverage. The amount of infiltrated MWCNT dispersion was adjusted in such a way that the free volume (~94%) of the template is completely filled with dispersion. Samples were investigated in the present study with 2, 5, and 7 infiltration steps, corresponding to MWCNT concentrations in the overall final sample of ~17-65 kg m⁻³, respectively. In addition to MWCNT/ZnO, MWCNTTs were prepared by placing an as fabricated cylindrical MWCNT/ZnO pellet having a CNT concentration of ~62 kg m⁻³ in 1 M HCl aqueous solution for at least two days, to dissolve the ZnO template. Afterwards, these samples were washed several times with deionized water and pure ethanol. In the final step, the samples were dried using critical-point-drying (EMS 3000), resulting in stable, cylindrical shaped MWCNTT samples. No shrinkage was observed during the etching and drying process.

The MWCNTT-coated ZnO tetrapods and MWCNTTs were characterized using a Zeiss Supra 55VP scanning electron microscope (SEM). Raman spectra were recorded from 50 to 3200 cm⁻¹ with a scanning micro-Raman spectrometer (WiTec Instruments Alpha300 RA) equipped with a 532 nm laser. The spectral resolution and laser power were set to 1 cm⁻¹ and 50 μW, respectively. Thermograms were acquired using a TA Instruments SDT Q600 in the temperature range from 25 °C to 950 °C with a heating rate of 5 K min⁻¹ and an air flow of 100 mL min⁻¹. For thermogravimetric studies, an SDT Q600 thermogravimetric analyzer (TGA) from TA Instruments™ was used with a scanning rate of 10 K min⁻¹ in air.

The electrical and thermal transport properties were measured under steady-state conditions using a Quantum Design physical properties measurement system (PPMS) in the temperature range from 2 K to 390 K under high vacuum (<10⁻⁷ bar). The pellets were sandwiched between two gold-plated copper plates using silver-loaded epoxy (Tria-Bond 2902) adhesive and affixed to the thermal transport option station. Blackbody radiation was corrected by setting the emissivity to one. Further information about the transport properties measurements is given elsewhere.^[38,39]

3. Results and Discussion

3.1. Materials Fabrication and Morphologies

Figure 1 (a) shows the schematic process for the fabrication of the hybrid MWCNT/ZnO and MWCNTT structures. First, the highly porous 3D ZnO template was infiltrated (one or more infiltrations steps) with an aqueous MWCNT dispersion, resulting in even coating of MWCNT on the template. Using a simple wet chemical etching process (dilute HCl) the ZnO backbone was

removed, resulting in a hierarchical 3D MWCNT assembly consisting of microtubes of self-entangled MWCNT networks. SEM images were acquired to provide information of the microstructure of the hybrid MWCNT/ZnO networks from various numbers of CNT dispersion infiltrations, as well as of the free-standing MWCNTs. Figure 1 (a) shows the microstructure of the ZnO template structure, consisting of interconnected tetrapods in which four arms radiate from a ZnO core at angles of 109° to each other. The arms are cone-shaped and between 5 and 25 μm long. The MWCNTs were deposited on the tetrapods and an increased number of infiltration steps led to increased MWCNT content on the individual arms. While the ZnO tetrapods are only slightly coated using two infiltration steps, the seven-step infiltration ZnO tetrapods are nearly completely coated (Figure 1 (e),(g)). The increase in MWCNT content enhances the interconnection between individual MWCNTs. The MWCNTs are randomly oriented on the tetrapods, forming self-entangled networks at higher CNT amounts, as a result of the self-organized drying process. Therefore, the MWCNTs can overlap creating a continuous path for electrical and thermal transport, even at very low coverage (twice-infiltrated samples). Note that the MWCNT content can vary slightly between samples with the same number of infiltration steps. The free-standing MWCNTs investigated in detail here were synthesized from the MWCNT/ZnO hybrid materials having a high CNT concentration (seven infiltrations [$\sim 14\%$ mass MWCNT]), followed by removing the ZnO template using HCl. The SEM images reveal the interconnected MWCNT structure of hollow microrods consisting solely of MWCNTs (Figure 1 (h-j)). The high mechanical stability of these structures is directly attributed to the self-entangled CNT layers formed by the infiltration process. The arrangement of the MWCNTs is the same for the hybrid structure, with overlapping tubes forming pathways for electrical and thermal transport. However, in contrast to the seven-times infiltrated MWCNT/ZnO samples, some MWCNTs are perpendicular to the microtubes and therefore do not contribute to the transport (Figure 1 (j)). Thus, a slight reduction of the electrical and thermal conductivity would be anticipated in comparison to the seven-times infiltrated MWCNT/ZnO sample.

Because the MWCNT dispersion contains a surfactant to enhance the dispersion of the MWCNTs, thermogravimetric analysis (TGA) was performed on a seven-times infiltrated and a MWCNT sample to determine the mass ratio of the surfactant and the MWCNTs (Figure S1 in Supplementary Information). For the MWCNT/ZnO sample a mass loss of 18.2% was recorded at around 300 $^\circ\text{C}$ most likely due to the removal of the surfactant (Figure S1 (a)). At higher temperature (~ 550 $^\circ\text{C}$), another mass loss of 14.1% was observed which can be assigned to the decomposition of the MWCNTs. The temperatures of these two peaks are consistent with the MWCNT sample which has a lower surfactant (21.6%) to MWCNT (71.6%) ratio (Figure S1 (b)). To determine the density of MWCNTs in the sample, the mass ratio was considered as constant and the resulting densities can be found in Table 1.

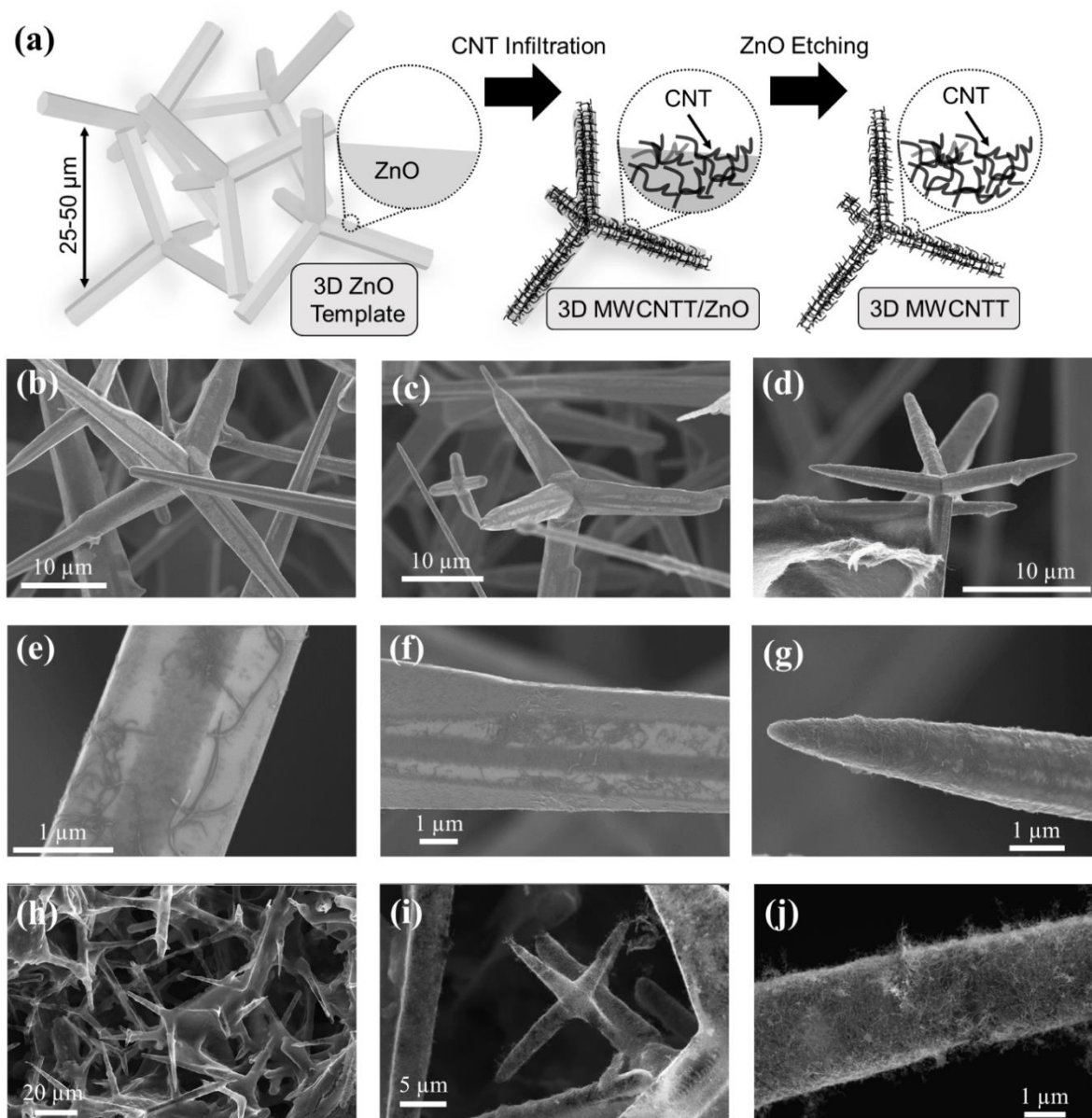


Figure 1: (a) Scheme for the fabrication of MWCNT/ZnO composites and free-standing MWCNTT. The ZnO tetrapod template is coated by MWCNTs using an infiltration procedure and the template is removed by aqueous HCl. SEM images of ZnO tetrapods coated with MWCNTs with (b,e) two infiltrations, (c,f) five infiltrations, and (d,g) seven infiltration steps. (h-j) SEM images of the hollow MWCNTTs, indicating a continuous transport pathway through the sample.

To gain information concerning the interaction between MWCNTs and ZnO, the Raman spectra of MWCNT/ZnO composites were recorded and compared to the Raman spectra of pure ZnO tetrapods and MWCNTTs (Figure 2). The ZnO tetrapods have a Raman spectrum similar to single-crystalline ZnO.^[40] The optical modes can be represented by $\Gamma_{\text{opt}} = 2B_1 + A_1 + E_1 + 2E_2$ where B_1 is Raman and IR silent, A_1 and E_1 are Raman- and infrared-active modes, and E_2 is only Raman

3.2. Electrical Properties

Transport properties as a function of temperature were measured for different MWCNT/ZnO samples with various MWCNT infiltrations and thicknesses. (Room-temperature transport properties (after first heating cycle) are given in Table 1.) All physical properties were measured on heating from 300 K to 390 K, followed by measurements on cooling from 390 K to 2 K and re-heating from 2 K to 300 K.

The electrical conductivities, σ_{el} , of the MWCNT/ZnO samples and MWCNTTs are shown as a function of temperature in Figure 3. A similar temperature trend was observed for all samples, *i.e.*, σ_{el} increases with temperature, indicating semiconducting behavior. The electrical conductivities are all similar in magnitude, suggesting that the MWCNTs dominate the electron transport over the entire temperature range. This finding is consistent with the zero-band gap of MWCNTs^[33] and the wide band gap of undoped ZnO ($E_g = 3.37$ eV).^[44] Although thermal energy is required for electrons to transfer between individual MWCNTs, Ebbesen *et al.* reported a positive temperature coefficient for the electrical conductivity of individual metallic CNTs.^[45] They linked the positive temperature trend to an interplay of changes in the mobility and carrier concentration with temperature. Furthermore, the Raman spectra indicate an increase in electron phonon coupling from ZnO tetrapods to ZnO/MWCNT samples. Stronger electron-phonon couplings are generally linked to lower electrical conductivities. However, due to the low electrical conductivity of the ZnO tetrapods compared to MWCNTs, it is not feasible to observe any change in electrical conductivity at the ZnO-ZnO interfaces with the inclusion of MWCNTs.

In addition to the temperature behavior, we found that the electrical conductivity increases with MWCNT content, likely due to an increased probability of electrical connections, again consistent with MWCNTs as the dominant transport of electrons. However, no electrical conductivity percolation threshold (*i.e.*, a large change in electrical conductivity with increasing CNT content) was observed, indicating that this low MWCNT concentration (<20 kg m⁻³) is sufficient for efficient charge transport in the network structure. The increase in electrical conductivity with MWCNT concentration is non-linear with the infiltration steps (*i.e.*, density). Higher MWCNT concentration are more likely to generate a larger number of electrical paths through the sample. Figure 2 (e) indicates that several MWCNTs in the composite with two infiltration steps are not connected to each other reducing the number of electron paths and also the electrical conductivity. The electrical conductivity of MWCNTTs was slightly less than the seven-infiltrated MWCNT/ZnO sample, most likely due to the dangling MWCNTs in the former (Figure 1 (j)) or due to some damage induced by the critical point drying process or sample mounting. (The densities of the MWCNTs in MWCNTTs and MWCNT/ZnO sample are similar; see Table 1.) For a more qualitative analysis of the interfaces between MWCNT-MWCNT and MWCNT-ZnO, higher MWCNT concentrations are required to reduce the number of dangling MWCNT compared to the conductive MWCNTs and dramatically enhance the mechanical stability of the samples.

The temperature-dependence of the electrical conductivity can be separated into two regions. In the temperature range from 50 K to 390 K the electrical conductivity of all samples increased with $T^{0.2}$ behavior. Below 50 K a dramatic decrease in electrical conductivity was observed, with electrical conductivity of all samples nearly converging at low temperature, likely because the probability of electron transfer between individual MWCNTs decreased with temperature. Similar temperature trends were also observed for MWCNT sheets^[33] and MWCNT yarns.^[29] However, whereas the electrical conductivity in the present samples increased as $T^{0.2}$, a linear increase in electrical conductivity with temperature was reported for MWCNT sheets (above 75 K) and MWCNT yarns (above 30 K).

In a recent study it was reported that the electrical conductivity in MWCNT yarns can be changed by heating the sample above 373 K due to outgassing of absorbed oxygen and water.^[29] While no hysteresis was observed here in the range from 2 K to 300 K, the electrical conductivity of the MWCNT-coated ZnO tetrapods and MWCNTTs did increase after heating the sample to 390 K (Figure 4 (a)). The change in electrical conductivity might be due to desorption of water or due to oxygen in the porous structure of the ZnO tetrapod samples. Lekawa *et al.* discussed the influence of water vapor on the electrical conductivity in CNTs.^[46] They reported an increase in electrical conductivity with absorbing water which is in contrast to the present study where an increase in electrical conductivity was measured with outgassing (Figure 4 (a)).

MWCNTs generally exhibit *p*-type behavior as also confirmed here by the positive Seebeck coefficient measured at room temperature (Figure 4 (b)). The Seebeck coefficient is relatively low ($<20 \mu\text{V K}^{-1}$) as observed for MWCNT arrays.^[32] A lower Seebeck coefficient was observed for the MWCNT/ZnO composites compared to MWCNTTs. The reduction of the Seebeck coefficient in the composites is most likely due to the interaction between MWCNTs and ZnO tetrapods. While electrons are dominant in ZnO leading to a negative Seebeck coefficient, MWCNTs have a positive Seebeck coefficient. Although the total Seebeck coefficient of two compounds in a composite is weighted by the electrical conductivity and hence, the contribution of ZnO to the total Seebeck coefficient should be negligible, the reduction in the Seebeck coefficient of the composites indicates that the ZnO tetrapods play a role in the electrical transport properties.

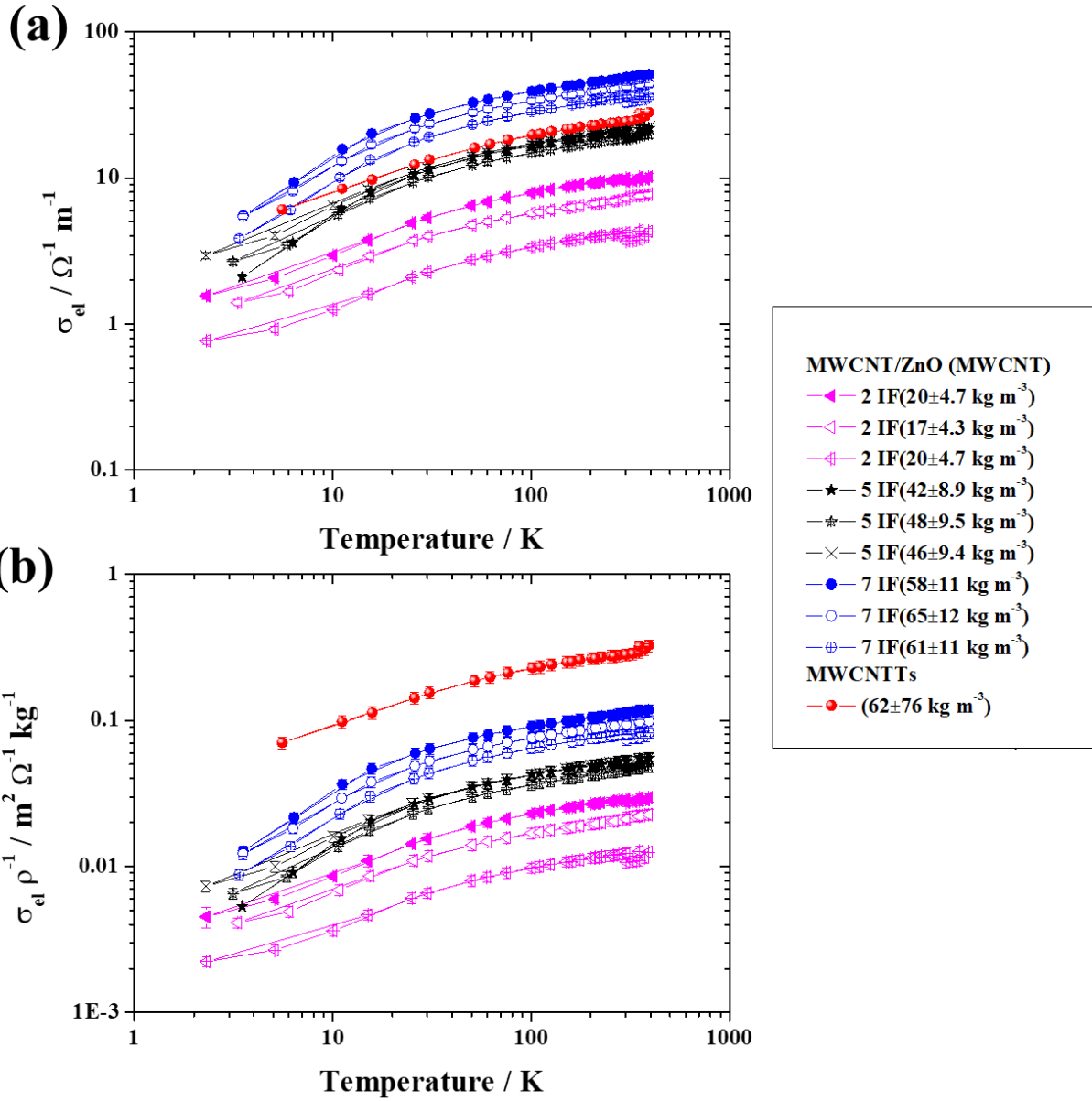


Figure 3: Electrical conductivity of MWCNT/ZnO samples with various infiltrations steps (IF) and MWCNTTs, where the density for each sample is indicated in the legend. (a) Electrical conductivity increases with increasing temperature and MWCNT content. (b) Specific electrical conductivity (i.e., electrical conductivity per unit density determined from the dimensions and mass of the MWCNT/ZnO and MWCNTTs pellets [Table 1]) exhibits a similar trend except for MWCNTTs which have a higher specific electrical conductivity due to lower density.

Similar to the electrical conductivity, the Seebeck coefficient exhibited hysteresis when the sample was cycled between room temperature and 390 K. The Seebeck coefficient increased with temperature to 350 K to 375 K, following by a decrease in Seebeck coefficient to 390 K. On cooling, the Seebeck coefficient decreased almost linearly with temperature resulting in a lower

Seebeck coefficient than the initial value. The Seebeck coefficient is proportional to the effective mass and inversely proportional to the carrier concentration while the electrical conductivity increases with carrier concentration and decreasing effective mass. Zahab *et al.* reported that the *p*-type electrical conductance decreases with water vapor on a single-walled CNT mat to the compensation point, followed by an increase in *n*-type conductance.^[47] This behavior is consistent with the present electrical measurement in which an increase in hole carrier concentration would enhance the electrical conductivity and simultaneously reduce the Seebeck coefficient. For stable electrical measurements, MWCNT samples have to be heated to 390 K in vacuum prior the measurements to remove adsorbed species, as was done here. The roomtemperature electrical and thermal conductivities reported in Table 1 (also in Figure 3 and Figure 5) were determined after annealing at 390 K. It is important to note that a higher electrical conductivity was reported for MWCNTs in a previous study.^[34] However, a different type of MWCNT (Baytubes) was used and the electrical conductivity was measured under ambient conditions and hence may have a contribution from adsorbed species, as observed for CNT films.^[28]

In addition to dependence on the number of infiltration steps, the electrical conductivity of the MWCNT/ZnO samples was found to depend on the overall density of the sample and the thickness of the measured pellet. The electrical conductivity is in general higher for denser samples, which is understandable. Rather surprisingly, the pellets exhibited higher electrical conductivity with reduced thickness (< 3 mm). For the 2-probe configuration required for the electrical conductivity measurements (4-probe not possible due to a reduced mechanical stability for larger samples), the contact resistance between sample and probes should contribute less to thicker samples, leading to higher electrical conductivity for thicker samples, whereas the opposite was observed here. However, the MWCNT solution was infiltrated from the top of the pellet, most likely leading to a concentration gradient of MWCNTs across the sample. Despite sonication to reduce agglomeration that could hinder the penetration of MWCNTs deep in the network, some agglomeration could still take place, resulting in a concentration gradient. Thus, thinner samples have most likely a more uniform MWCNT-concentration gradient through the entire pellet resulting in an increase in electrical conductivity. For a better comparison, the specific electrical conductivity (*i.e.*, the electrical conductivity per unit density) of the samples was calculated and compared to literature values of MWCNT bulk materials. Because it is assumed that electrons flow only through the MWCNTs, the contribution of the ZnO can be neglected due to its low electrical conductivity ($0.3 \Omega^{-1} \text{ m}^{-1}$ for fully dense ZnO sample at 300 K).^[48] The electrical conductivity in ZnO, however, can change with the impurity concentration, *i.e.*, doping level, leading to a wide range of electrical conductivities. A 40% lower specific electrical conductivity was measured for the MWCNT/ZnO composites than for MWCNTs because the ZnO tetrapods contribute solely to the density. (Note that the surfactant contribution to the electrical and thermal properties is not known). The specific electrical conductivity of MWCNTs is about two orders of magnitude lower than reported for bulk MWCNT samples (Table 2).^[33,28] While the MWCNTs are aligned and oriented in one direction in MWCNT arrays, yarns and sheets, the MWCNTs are randomly oriented in MWCNT-coated tetrapods and MWCNTs (Figure 1). Gspann *et al.* reported an increase in

electrical conductivity with the degree of alignment in CNTs films.^[28] Furthermore, Niven *et al.* showed that the electrical conductivity of MWCNT yarns is highly dependent on the defect concentration and increase with heating.^[29] Similar heating procedures enhanced the electrical conductivity of SWCNT/double-walled CNT (DWCNT) aerogels leading to relative high specific electrical conductivities (Table 2).^[49] Therefore, reducing the defect concentration in MWCNTs and improving the fabrication procedure can lead to more enhanced transport properties in the present samples.

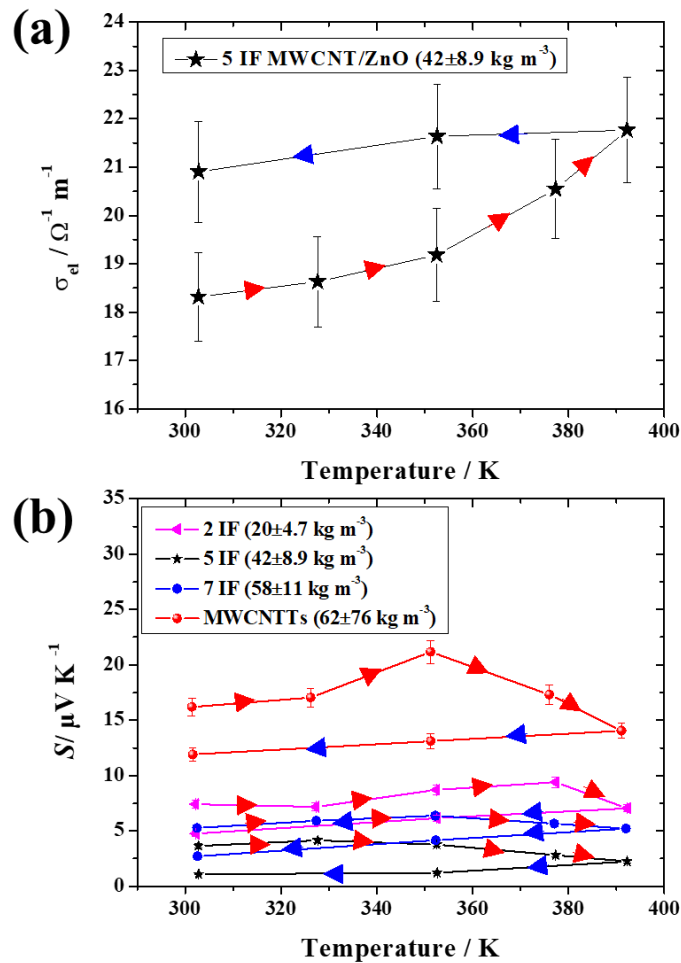


Figure 4: (a) Hysteresis of the electrical conductivity of a MWCNT/ ZnO pellet prepared using five infiltration steps. Conductivity increased due to degassing above 390 K. (b) Seebeck coefficient, S , for various MWCNT/ZnO samples and MWCNTTs. The Seebeck coefficient decreased at elevated temperature most likely due to an increase in carrier concentration.

Table 1: Thickness, L , density, ρ , MWCNT concentration, room-temperature electrical conductivity, σ_{el} , after annealing at 390 K and room-temperature thermal conductivity, κ , of ZnO tetrapods with various MWCNT infiltration steps (IF) and MWCNTTs.

Sample	L / mm	ρ / kg m ⁻³	MWCNT conc. / kg m ⁻³	σ_{el} / Ω^{-1} m ⁻¹	κ / W m ⁻¹ K ⁻¹
2 IF 2 mm	2.40 ± 0.04	345 ± 83	20 ± 5	9.93 ± 0.50	0.24 ± 0.02
2 IF 3 mm	3.34 ± 0.04	340 ± 83	17 ± 4	7.20 ± 0.36	0.28 ± 0.03
2 IF 3 mm (2)	3.38 ± 0.04	345 ± 83	20 ± 5	4.23 ± 0.21	0.28 ± 0.03
5 IF 2 mm	2.20 ± 0.04	396 ± 84	42 ± 9	20.90 ± 1.05	0.34 ± 0.02
5 IF 3 mm	3.44 ± 0.04	409 ± 82	48 ± 10	18.78 ± 0.94	0.31 ± 0.03
5 IF 3 mm (2)	3.34 ± 0.04	405 ± 83	46 ± 9	21.47 ± 1.07	0.36 ± 0.03
7 IF 2 mm	2.20 ± 0.04	432 ± 84	58 ± 11	49.00 ± 2.45	0.43 ± 0.02
7 IF 3 mm	3.50 ± 0.04	448 ± 82	65 ± 12	42.34 ± 2.12	0.45 ± 0.04
7 IF 3 mm (2)	3.50 ± 0.04	439 ± 82	61 ± 11	35.44 ± 1.63	0.46 ± 0.04
MWCNTTs	3.42 ± 0.04	86 ± 93	62 ± 76	24.39 ± 1.22	0.08 ± 0.02

Information concerning the quality of the MWCNTs can be provided by Raman spectroscopy using the ratio of the intensities of the G , I_G , and D , I_D , peaks (Figure 2). All studied samples have a low I_G/I_D ratio (0.7, 0.8, and 1.0 for MWCNTTs and MWCNT-coated ZnO tetrapods with two and seven infiltrations, respectively) compared to MWCNT sheets ($I_G/I_D \sim 1.3$ -2.5 depending on E_{las})^[33] and MWCNT yarns ($I_G/I_D \sim 1.8$ -7.5 depending on annealing temperature).^[29] It is important to note that the I_G/I_D ratio is strongly related to E_{las} and for a more quantitative analysis, the crystallite size, L_c , can be calculated using^[50]

$$L_c = \frac{560 \text{ nm eV}^{-1}}{E_{las}^4} \left(\frac{I_G}{I_D} \right). \quad (1)$$

For the MWCNT-coated ZnO tetrapods a crystallite size of 15-20 nm was calculated which is lower than for MWCNT sheets ($L_c \sim 25$ -50 nm)^[33] and MWCNT yarns ($L_c \sim 30$ -115 nm).^[29] The MWCNTTs have even a lower crystallite size ($L_c \sim 12$ nm) indicating a high defect concentration that could significantly reduce the electrical and thermal transport properties. The high defect concentration of the MWCNTs in the present MWCNT/ZnO samples and MWCNTTs can occur due to low-quality MWCNT solution (as commercially available) and sample preparation. An improved MWCNT solution would most likely reduce the defect concentration in the MWCNTTs and hence, improve the electrical conductivity.

Despite the electrical conductivity being lower than reported for MWCNT fibres, yarns, and sheets, the MWCNT/ZnO and MWCNTT samples are interesting for macroscopic applications due to their isotropic mechanical and transport properties. MWCNT fibres, yarns, and sheets exhibit high electrical conductivity only in the direction of alignment and extremely low electrical conductivities in the other two directions. However, in many macroscopic applications enhanced properties are required in all directions, which could be a niche for MWCNTT compounds. Furthermore, MWCNTT pellets can be easily infiltrated with various polymers creating tough MWCNTT/polymer composites as previously reported.^[34,35] Although SWCNT/DWCNT aerogels also exhibit isotropic properties, the MWCNT content in the MWCNTT/polymer composites can be easily tuned by the number of infiltration steps or by adjusting the MWCNT concentration, and the dispersion can be fixed with the size of ZnO tetrapods and the density of ZnO template. In addition to the isotropic and tuneable properties, these ZnO/MWCNT samples were prepared using a wet chemistry approach which is cheaper, faster, more energy-efficient and simpler than the common CVD method.

Table 2: Specific electrical conductivity, σ_{el}/ρ , and specific thermal conductivity, κ/ρ , of ZnO tetrapods with various MWCNT content, MWCNTTs, ZnO, and diverse CNT bulk materials, all at room temperature.

Sample	$\sigma_{el}/\rho / (\text{m}^2 \Omega^{-1} \text{kg}^{-1})$	$\kappa/\rho / (\text{W cm}^2 \text{kg}^{-1} \text{K}^{-1})$	Reference
ZnO	$1.78 \cdot 10^{-5}$	2.8-95.1	[48,51,52]
CNT arrays	23	200	[32]
CNT sheets	51		[33]
CNT fibers	N/A	12,200	[28]
SWCNT/DWCNT aerogel	1.8-22	N/A	[49]
ZnO tetrapods + MWCNTs (2 FL)	0.01-0.03	6.6-8.2	Present
ZnO tetrapods + MWCNTs (5 FL)	0.05-0.06	7.6-9.4	Present
ZnO tetrapods + MWCNTs (7 FL)	0.07-0.09	9.9-10.2	Present
MWCNTTs	0.28 ± 0.03	8.8 ± 2.6	Present

3.3. Thermal Conductivity

In addition to the electrical conductivity, the temperature-dependent thermal conductivity was investigated for MWCNT/ZnO samples and MWCNTTs (Figure 5). In contrast to the electrical conductivity, above 300 K the thermal conductivity is only proportional to the MWCNT content and no hysteresis was observed at high temperature. At very low temperature, the thermal conductivity was nearly independent of the number of infiltrations, indicating that ZnO is the dominant thermal conductor. Furthermore, the temperature trend of the thermal conductivity at low temperature can provide information concerning the crystallinity. According to Fourier's law, the thermal conductivity is proportional to the heat capacity per unit volume, the phonon group velocity, and the phonon mean free path. While the heat capacity slightly increases with temperature and the phonon group speed is nearly temperature-independent, the phonon mean free path increases at low temperature as the Normal process is dominant. However, with increasing temperature, phonons that are longer than the first Brillouin zone can be created, leading to phonons with wave vector directions opposite to the initial phonons and hence, dramatically reduced phonon mean free path due to Umklapp scattering. If the sample is highly crystalline, a distinct peak in the thermal conductivity could be observed between the Normal process-dominant (low-temperature) region and the Umklapp process-dominant (hightemperature) region. A more crystalline sample exhibits a more distinct peak, with its maximum at lower temperature. The highest crystallinity was found among the present materials for the 2 IF sample with a MWCNTTs density of $20 \pm 5 \text{ kg m}^{-3}$, with a thermal conductivity peak at $\sim 80 \text{ K}$. The peak temperature is higher than for single-crystalline ZnO ($\sim 10 \text{ K}$)^[53] indicating that the phonon mean free path is limited by the small dimensions of the ZnO tetrapods. Larger tetrapods or enhanced interconnections of the ZnO tetrapods might increase the crystallinity and thus increase the low-temperature thermal conductivity.

The temperature-dependent thermal conductivity of MWCNTTs increases approximately linearly with temperature to about 300 K. Above 300 K, the increase in thermal conductivity is more rapid, which is most likely an artefact resulting from underestimation of blackbody radiation. Although the thermal conductivity of MWCNTTs is lower than for MWCNT/ZnO samples, the specific thermal conductivity (*i.e.*, thermal conductivity per unit density: Figure 5(b)) indicates that MWCNTTs contribute significantly at high temperature. This is consistent with the temperature trends of the ZnO tetrapods. While the thermal conductivity of the tetrapods with two infiltration steps decreased above 100 K, the samples with five and seven infiltration exhibited nearly temperature-independent thermal conductivity from 100 K to 390 K. Note that the thermal conductivity is not a simple sum of the thermal conductivities of ZnO tetrapods and MWCNTs. At 390 K, the difference between the thermal conductivities of the samples with two and seven infiltration steps was twice as large as the thermal conductivity of MWCNTTs. This can have two reasons: The thermal conductivity of MWCNTTs is lower due to dangling MWCNTs or defects from sample mounting and the fabrication process, or the thermal conductivity of the seven-infiltrated sample is higher due to enhanced ZnO-ZnO interface heat transport through the connections of the MWCNTs. The former is consistent with the decrease in compressive strength

from ZnO/MWCNT samples to MWCNTTs and therefore, a lower mechanical stability, while the latter agrees with the increase in compressive strength from individual ZnO tetrapods to ZnO/MWCNT composites enhancing the thermal connections between the individual ZnO tetrapods.^[34] Furthermore, the interactions of the ZnO-MWCNT interface can also increase the heat transport through the composite sample. An unknown factor is the contribution of the thermal conductivity of the surfactant which can play a role in the total thermal conductivity.

To understand the influence of the surfactant to the transport properties, one ZnO/MWCNT sample with seven infiltration steps was heated to 450 °C (*i.e.*, above the decomposition temperature of the surfactant as shown in Figure S1). The electrical and thermal conductivities of the heat-treated sample were measured between 150 K and 390 K and compared to the untreated samples (see Figure S2). While the electrical conductivity of the sample without the surfactant only slightly decreased comparable to MWCNTTs (Figure S2 (a)), the thermal conductivity decreased by about a factor of two relative to the untreated samples (Figure S2 (b)). The electrical conductivity result indicates that the surfactant does not contribute significantly to the electronic transport. However, removing the surfactant likely reduced the entanglement of the MWCNTs and thus impaired the electron pathway. The reduction of the MWCNT entanglements can also worsen the heat transport through the material. The larger reduction in thermal conductivity of the heat-treated sample indicates that the surfactant also contributes to the heat transfer (Figure S2 (b)). In several applications, such as thermoelectric materials, the goal is to enhance the ratio of electron to heat transfer. Figure S2 (c) shows that of the materials studied, MWCNTTs have the highest such ratio, which decreased with temperature. The ZnO/MWCNT samples (7 IF) have much lower ratios with similar temperature trends. However, the ratio for the heat-treated sample *increased* with temperature above 250 K, approaching the ratio for MWCNTTs. This trend is encouraging for further studies of the transport properties of ZnO/MWCNT and MWCNTTs without surfactants.

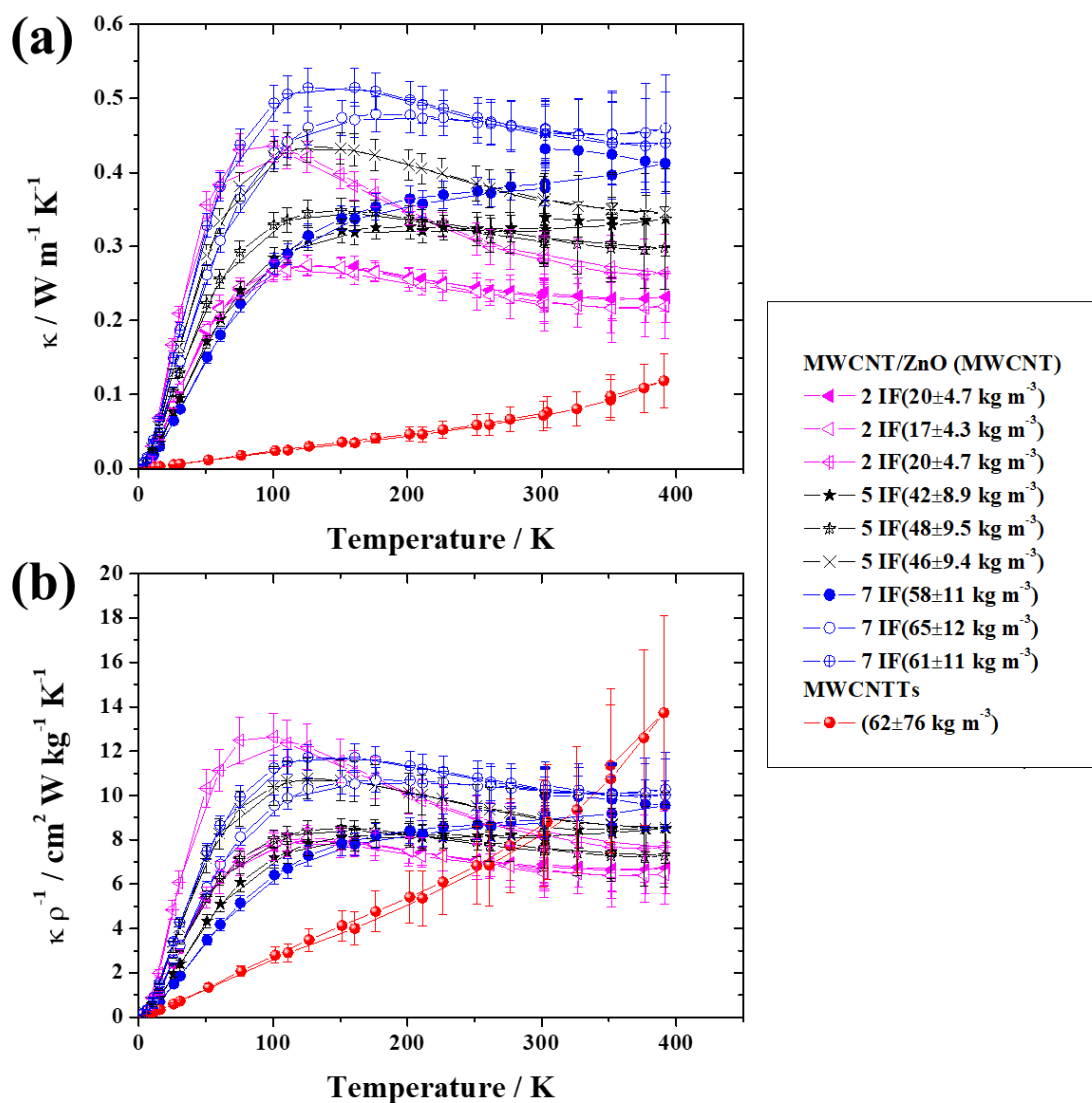


Figure 5: Thermal conductivity of MWCNT/ZnO tetrapods with various infiltrations steps (IF) and MWCNTs, where the densities are presented in the legend. (a) The low-temperature thermal conductivity is nearly independent of the infiltration steps whereas the high-temperature thermal conductivity increases with MWCNT content. (b) The specific thermal conductivity (*i.e.*, thermal conductivity per unit density) indicates that the thermal conductivity of ZnO is dominant at low temperature.

Similar to the electrical conductivity, the specific thermal conductivity (Figure 5(b)) can provide a better insight concerning the influence of the infiltration steps to the thermal conductivity. Although the thermal conductivity is dominated by MWCNTs at high temperature, the specific thermal conductivity difference between the samples with the lowest and highest infiltration steps decreased in comparison to the thermal conductivity (Figure 5 (a)). At lower temperature, the ZnO tetrapods contribute more significantly to the specific thermal conductivity

than MWCNTTs. MWCNT/ZnO samples and MWCNTTs have several orders of magnitude lower specific thermal conductivity than CNT bulk materials, such as CNT arrays ($200 \text{ W cm}^2 \text{ kg}^{-1} \text{ K}^{-1}$),^[32] CNT sheets ($650 \text{ W cm}^2 \text{ kg}^{-1} \text{ K}^{-1}$)^[33] and CNT fibres ($12,200 \text{ W cm}^2 \text{ kg}^{-1} \text{ K}^{-1}$)^[28] (Table 2). The small discrepancy between the specific thermal conductivities of samples with different infiltration steps suggests that MWCNTs do not contribute significantly to the total thermal conductivity and most heat is transported through the ensembles of ZnO tetrapods. This is consistent with the specific thermal conductivity of bulk ZnO which ranges between 2.8 to 95.1 $\text{W cm}^2 \text{ kg}^{-1} \text{ K}^{-1}$,^[Error! Bookmark not defined.] encompassing the present results. The difference between the MWCNT bulk materials and MWCNTTs is most likely a result of the high defect concentration in the MWCNTs and the randomly oriented MWCNTs in the MWCNTTs materials. Thus, the electrical and thermal properties can most likely be further improved using higher-quality MWCNT solutions and removal of the surfactant.

4. Conclusions

The electrical and thermal conductivities of MWCNT-coated ZnO tetrapods with a range of MWCNT content, and also MWCNTTs were compared, indicating that MWCNTs are the dominant contributor for the electronic transport over the entire temperature range and thermal transport at elevated temperatures ($> 300 \text{ K}$). At low temperature, the ZnO tetrapods dominate the thermal transport because of their highly crystalline nature. The electrical conductivity showed hysteresis at high temperature, likely reflecting desorption of adsorbed species. The hysteresis in electrical conductivity was consistent with the measured Seebeck coefficient suggesting an increase in hole carrier concentration. In contrast with CNT bulk materials, the specific thermal and electrical conductivities in MWCNT/ZnO samples and MWCNTTs are lower than many bulk CNT materials, due to their high defect concentration as observed from Raman spectroscopy and poor alignment of the MWCNTs. However, the MWCNTs in the present samples were highly dispersed, creating continuous electrical and thermal path. Furthermore, the amounts of MWCNTs in the samples could be finely tuned by the number of infiltration steps and the concentration of the MWCNT solution. In particular, due to the three-dimensional structure of the tetrapods, these materials can be incorporated in various macroscopic applications where isotropic properties are required, giving a significant advantage over the one-dimensional properties in MWCNT fibres, yarns, and sheets. Furthermore, the MWCNTTs could be infiltrated by appropriate polymers to fabricate new CNT/polymer composites. Because the thermal and electrical properties of MWCNTTs can be determined with and without a matrix material, the present system provides information concerning the interface between diverse matrices and MWCNTs. Furthermore, the simple fabrication process allows also for the study of other systems such as graphene or MoS_2 by simply changing the used nanoparticle dispersion used for infiltration.

Acknowledgments

J-H. P. acknowledges support from Dalhousie Research in Energy, Advanced Materials and Sustainability (DREAMS), an NSERC CREATE program, and a Nova Scotia scholarship. M. A. W. acknowledges support from NSERC and the Clean Technologies Research Institute at Dalhousie University. R.A. gratefully acknowledge project funding by the Deutsche Forschungsgemeinschaft under contracts Ad183-17/1 and FOR1616. We thank Prof. Norbert Stock for helping with the critical-point-dryer.

References

- [1] M. Terrones, *Annu. Rev. Mater. Res.* 2003, 33, 419–501.
- [2] E. Pop, D. Mann, Q. Wang, K. Goodson, H. Dai, *Nano Letters* 2006, 6, 96–100.
- [3] L. Hu, D. S. Hecht, G. Grüner, *Chem. Rev.* 2010, 110, 5790–844.
- [4] Z. Xu, X. D. Bai, E. G. Wang, Z. L. Wang, *Appl. Phys. Lett.* 2005, 87, 163106.
- [5] Y. Ye, C. C. Ahn, C. Witham, B. Fultz, J. Liu, A. G. Rinzler, D. Colbert, K. A. Smith, R. E. Smalley, *Appl. Phys. Lett.* 1999, 74, 2307–2309.
- [6] W. A. Curtin, B. W. Sheldon, *Mater. Today* 2004, 7, 44-49.
- [7] Z. Spitalsky, D. Tasis, K. Papagelis, C. Galiotis, *Prog. Polym. Sci.* 2010, 35, 357-401.
- [8] Q. Zhang , J.-Q. Huang , W.-Z. Qian , Y.-Y. Zhang , F. Wei, *small* 2013, 9, 1237-1265.
- [9] G. Mittal, V. Dhand, K. Yop Rhee, S.-J. Park, W. Ro Lee, *J. Ind. Eng. Chem.* 2015, 21, 11-25.
- [10] C. Velasco-Santos, A. L. Martínez-Hernández, F. T. Fisher, R. Ruoff, V. M. Castaño, *Chem. Mater.* 2003, 15, 4470-4475.
- [11] X. Wang, N. P. Padture, H. Tanaka, *Nat. Mater.* 2004, 3, 539-544.
- [12] G.-D. Zhan, J. D. Kuntz, J. E. Garay, A. K. Mukherjee, *Appl. Phys. Lett.* 2003, 83, 1228-1230.
- [13] A. Kasperski, A. Weibel, D. Alkattan, C. Estournès, Ch. Laurent, A. Peigney, *Ceram. Int.* 2015, 41, 13731-13738.
- [14] J. K.W. Sandler, J.E. Kirk, I.A. Kinloch, M.S.P. Shaffer, A.H. Windle, *Polymer* 2003, 44, 5893-5899.
- [15] X. J. He, J. H. Du, Z. Ying, H. M. Cheng, X. J. He, *Appl. Phys. Lett.* 2005, 86, 062112.
- [16] A. Palmieri, R. Kashfi-Sadabad, S. Yazdani, M. Pettes, W. E. Mustain, *Electrochim. Acta* 2016, 213, 620-625.
- [17] J. H. Lee, C. S. Yoon, J.-Y. Hwang, S.-J. Kim, F. Maglia, P. Lamp, S.-T. Myung, Y.-K. Sun, *Energy Environ. Sci.* 2016, 9, 2152-2158.
- [18] N. Farahi, S. Prabhudev, M. Bugnet, G. A. Botton, J. Zhao, J. S. Tse, J. R. Salvador, H. Kleinke, *RSC Adv.* 2015, 5, 65328-65336.
- [19] N. Nandihalli, S. Gorse, H. Kleinke, *J. Solid State Chem.* 2015, 226, 164-169.
- [20] M. J. Biercuk, M. C. Llaguno, M. Radosavljevic, J. K. Hyun, A. T. Johnson, J. E. Fischer, *Appl. Phys. Lett.* 2002, 80, 2767-2769.
- [21] P. Bonnet, D. Sireude, B. Garnier, O. Chauvet, *Appl. Phys. Lett.* 2007, 91, 201910.
- [22] Z. Han, A. Fina, *Prog. Polym. Sci.* 2011, 36, 914-944.
- [23] Y. S. Song, J. R. Youn, *Carbon* 2005, 43, 1378-1385.
- [24] H. Huang, C. Liu, Y. Wu, S. Fan, *Adv. Mater.* 2005, 17, 1652-1656.
- [25] R. Sivakumar, S. Guo, T. Nishimura, Y. Kagawa, *Scr. Mater.* 2007, 56, 265-268.

- [26] K. Ahmad, P. Wie, C. Wan, *J. Mater. Sci.* 2014, 49, 6048-6055.
- [27] T. S. Gspann, S. M. Juckes, J. F. Niven, M. B. Johnson, J. A. Elliott, M. A. White, A. H. Windle, *Carbon* 2017, 114, 160–168.
- [28] J. F. Niven, M. B. Johnson, S. M. Juckes, M. A. White, N. T. Alvarezd, V. Shanov, *Carbon* 2016, 99, 485–490.
- [29] M. B. Jakubinek, M. B. Johnson, M. A. White, C. Jayasinghe, G. Li, W. Cho, M. J. Schulz, V. Shanov, *Carbon* 2012, 50, 244-248.
- [30] K. Sears, C. Skourtis, K. Atkinson, N. Finn, W. Humphries, *Carbon* 2010, 48, 4450-4456.
- [31] M. B. Jakubinek, M. A. White, G. Li, C. Jayasinghe, W. Cho, M. J. Schulz, V. Shanov, *Carbon* 2010, 48, 3947-3952.
- [32] J.-H. Pöhls, M. B. Johnson, M. A. White, R. Malik, B. Ruff, C. Jayasinghe, M. J. Schulz, V. Shanov, *Carbon* 2012, 50, 4175–4183.
- [33] F. Schütt, S. Signetti, H. Krüger, S. Röder, D. Smazna, S. Kaps, S. N. Gorb, Y. K. Mishra, N. M. Pugno, R. Adelung, *Nat. Commun.* 2017, 8, 1215.
- [34] Y. K. Mishra, S. Kaps, A. Schuchardt, I. Paulowicz, X. Jin, D. Gedamu, S. Freitag, M. Claus, S. Wille, A. Kovalev, S. N. Gorb, R. Adelung, *Part. Part. Syst. Charact.* 2013, 30, 775-783.
- [35] F. Schütt, V. Postica, R. Adelung, O. Lupan, *ACS Appl. Mater. Interfaces* 2017, 9, 2307-2318.
- [36] Y. K. Mishra, R. Adelung, *Materials Today* 2017, in Press (<https://doi.org/10.1016/j.mattod.2017.11.003>).
- [37] O. Maldonado, *Cryogenics* 1992, 32, 908.
- [38] C. A. Kennedy, M. A. White, *Solid State Commun.* 2005, 134, 271.
- [39] R. Cuscó, E. Alarcón-Lladó, L. Artús, J. Ibáñez, J. Jiménez, B. Wang, M. Callahan, *Phys. Rev.* 2007, 75, 165202.
- [40] E.F. Antunesa, A.O. Loba, E.J. Corata, V.J. Trava-Airoldia, A.A. Martinb, C. Veríssimo, *Carbon* 2006, 44, 2202-2211.
- [41] M. S. Dresselhaus, G. Dresselhaus, R. Saito, A. Jorio, *Phys. Rep.* 2005, 409, 47–99.
- [42] R. P. Wang, G. Xu, P. Jin, *Phys. Rev. B* 2004, 69, 113303.
- [43] T. Tsubota, M. Ohtaki, K. Eguchi, H. Arai, *J. Mater. Chem.* 1997, 7, 85–90.
- [44] T. W. Ebbesen, H. J. Lezec, H. Hiura, J. W. Bennett, H. F. Ghaemi, T. Thio, *Nature* 1996, 382, 54-56.
- [45] A. Lekawa-Raus, L. Kurzepa, G. Kozłowski, S. C. Hopkins, M. Wozniak, D. Lukawski, B. A. Glowacki, K. K. Koziol, *Carbon* 2015, 87, 18–28.
- [46] A. Zahab, L. Spina, P. Poncharal, C. Marlière, *Phys. Rev. B* 2000, 62, 10000-10003.
- [47] J. P. H. Miller, *Physical Review* 1941, 60, 890–895.
- [48] M. A. Pimenta, G. Dresselhaus, M. S. Dresselhaus, L. G. Cançado, A. Jorio, R. Saito, *Phys. Chem. Chem. Phys.* 2007, 9, 1276–1291.
- [49] T. Olorunyolemi, A. Birnboim, Y. Carmel, O. C. W. Jr., I. K. Lloyd, *J. Am. Ceram. Soc.* 2002, 85, 1249–1253.
- [50] O. Madelung, U. Rössler, M. Schulz, eds., *Zinc oxide (ZnO) thermal conductivity*, pp. 1–5. Berlin, Heidelberg: Springer Berlin Heidelberg, 1999.
- [51] M. W. Wolf, J. J. Martin, *physica status solidi (a)* 1973, 17, 215–220.

Supplementary Information

Carbon, 2019

Thermal and Electrical Transport Properties in Multi-Walled Carbon Nanotube-coated ZnO Tetrapods and Self-Entangled Multi-Walled Carbon Nanotube Tubes

Jan-Hendrik Pöhls,^{a,b} Fabian Schütt,^c Catherine O'Neill,^a Sindu Shree,^c Michel B. Johnson,^d

Yogendra Kumar Mishra,^c Rainer Adelung,^c Mary Anne White^{a,b,d}

^a Department of Chemistry, Dalhousie University, Halifax, Nova Scotia, Canada B3H 4R2

^b Department of Physics and Atmospheric Science, Dalhousie University, Halifax, NS, Canada B3H 4R2

^c Institute for Materials Science, Kiel University, Kaiserstr. 2, D-24143 Kiel, Germany

^d Clean Technologies Research Institute, Dalhousie University, Halifax, NS, Canada B3H 4R2

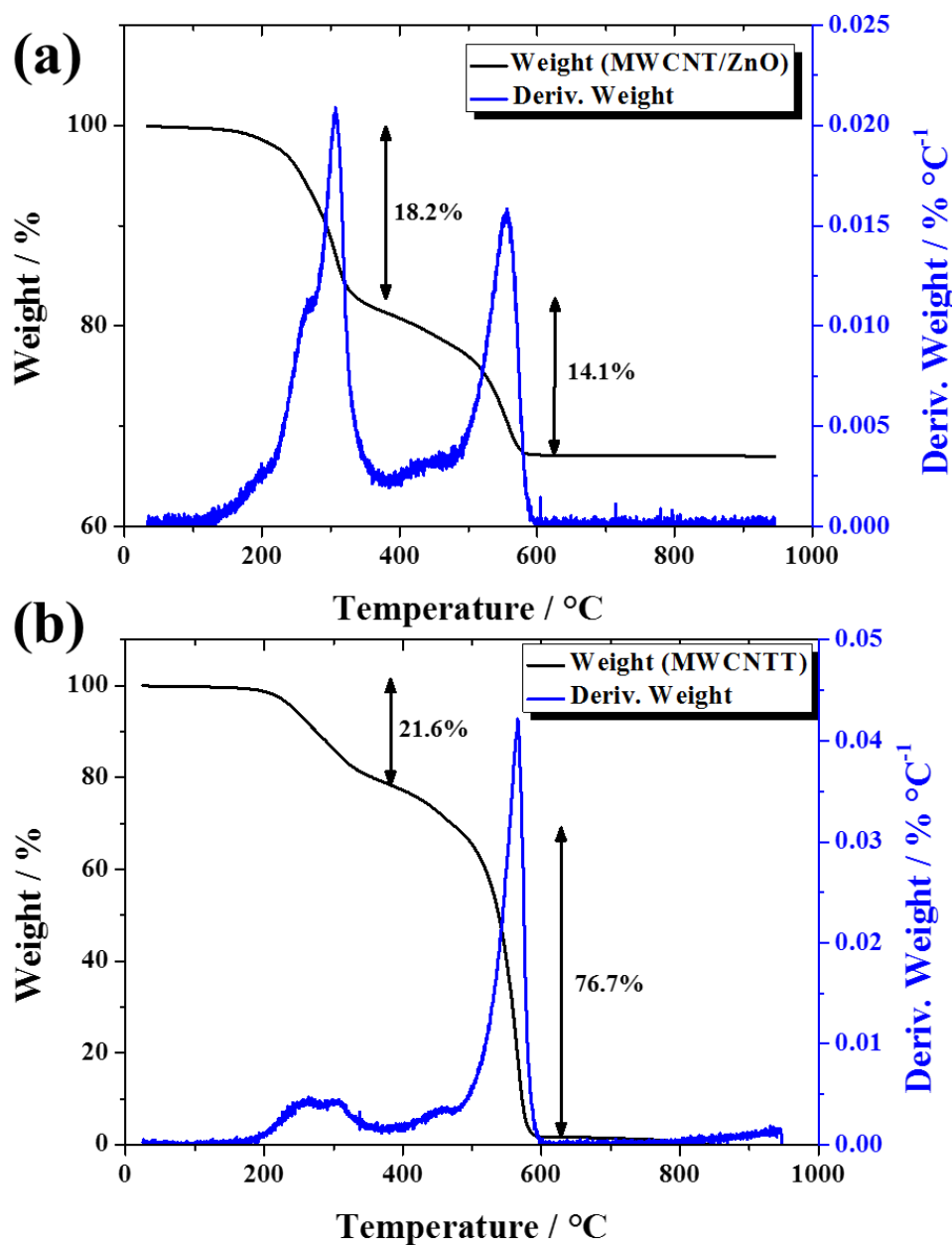


Figure S1: Thermogram of (a) MWCNT/ZnO with seven infiltrations and (b) MWCNTTs. Both thermograms display two weight losses peaks. While the first peak is most likely the removal of the surfactant, the latter can be assigned to the decomposition of the MWCNTs.

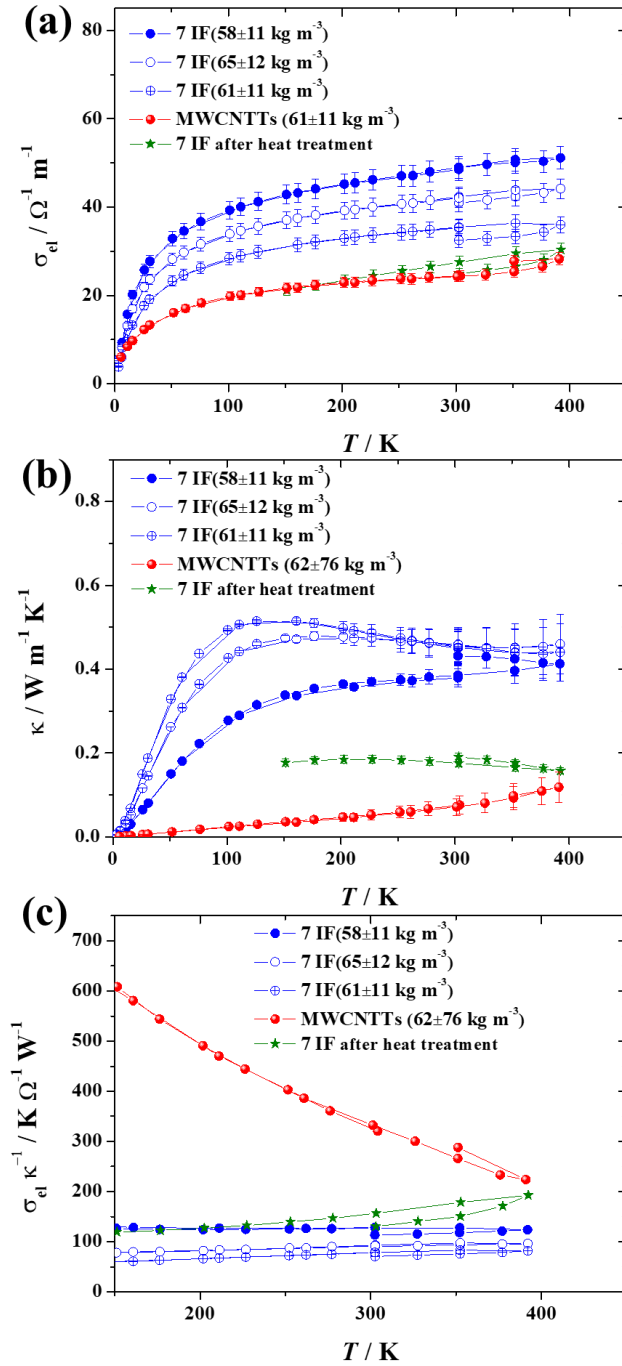


Figure S2: Comparison of the (a) electrical conductivity and (b) thermal conductivity of ZnO/MWCNT samples before and after heating to 400 °C (for comparison the transport properties of MWCNTs were included). Electrical and thermal conductivity of the ZnO/MWCNT decreased after the heat treatment. (c) Ratio of electrical to thermal conductivity indicates that the heat treatment reduced the heat transport more than the electron transport above 300 K and hence, increasing the ratio.

Table S1: Electrical conductivity, σ_{el} , of MWCNT/ZnO with two infiltration (IF) steps; in order of data collection. Note that the electrical conductivity from 300 K to 390 K on the first heating cycle is not reliable due to absorbed water or oxygen. Dimensions and densities of samples are given in Table 1.

T / K	$\sigma_{el} / \Omega^{-1} m^{-1}$ (2 IF 2 mm)	T / K	$\sigma_{el} / \Omega^{-1} m^{-1}$ (2 IF 3 mm)	T / K	$\sigma_{el} / \Omega^{-1} m^{-1}$ (2 IF 3 mm (2))
301.603	9.44±0.47	301.987	7.40±0.37	301.708	3.69±0.18
302.153	9.45±0.47	326.877	7.53±0.38	326.641	3.73±0.19
327.261	9.59±0.48	351.749	7.58±0.38	351.554	3.78±0.19
352.449	9.67±0.48	376.572	7.64±0.38	376.463	3.96±0.20
377.275	9.88±0.49	391.579	7.70±0.39	391.421	4.31±0.22
392.255	10.2±0.5	351.797	7.48±0.37	351.602	4.36±0.22
352.51	10.2±0.5	302.001	7.20±0.36	301.712	4.23±0.21
302.192	9.93±0.50	276.673	7.06±0.35	276.414	4.16±0.21
276.345	9.77±0.49	251.719	6.92±0.35	251.426	4.09±0.20
251.364	9.59±0.48	226.326	6.78±0.34	226.077	4.02±0.20
226.022	9.42±0.47	201.384	6.63±0.33	201.09	3.93±0.20
201.066	9.22±0.46	175.981	6.46±0.32	175.765	3.83±0.19
175.732	8.98±0.45	150.677	6.26±0.31	150.233	3.71±0.19
150.204	8.69±0.43	125.72	6.02±0.30	125.264	3.56±0.18
125.247	8.35±0.42	100.597	5.73±0.29	100.276	3.37±0.17
100.206	7.91±0.40	75.439	5.34±0.27	75.265	3.12±0.16
75.184	7.33±0.37	50.504	4.77±0.24	50.105	2.75±0.14
50.103	6.48±0.32	25.58	3.72±0.19	25.06	2.09±0.10
25.077	4.92±0.25	10.782	2.35±0.12	10.058	1.25±0.06
10.072	2.94±0.15	6.058	1.67±0.08	5.112	0.921±0.046
5.127	2.06±0.10	3.324	1.40±0.07	2.309	0.768±0.038
2.307	1.55±0.08	15.426	2.92±0.15	15.028	1.60±0.08
15.036	3.76±0.19	30.463	4.01±0.20	30.041	2.26±0.11
30.056	5.34±0.27	60.446	5.03±0.25	60.028	2.92±0.15
60.079	6.87±0.34	110.549	5.84±0.29	110.206	3.44±0.17
110.391	8.09±0.40	160.571	6.32±0.32	160.242	3.75±0.19
160.381	8.80±0.44	210.897	6.66±0.33	210.63	3.95±0.20
210.639	9.28±0.46	261.603	6.93±0.35	261.307	4.10±0.20
261.232	9.63±0.48	301.921	7.16±0.36	301.655	4.20±0.21
301.548	9.89±0.49				

Table S2: Electrical conductivity, σ_{el} of MWCNT/ZnO with five infiltration (IF) steps; in order of data collection. Note that the electrical conductivity from 300 K to 390 K on the first heating cycle is not reliable due to absorbed water or oxygen. Dimensions and densities of samples are given in Table 1.

T / K	$\sigma_{el} / \Omega^{-1} m^{-1}$ (5 IF 2 mm)	T / K	$\sigma_{el} / \Omega^{-1} m^{-1}$ (5 IF 3 mm)	T / K	$\sigma_{el} / \Omega^{-1} m^{-1}$ (5 IF 3 mm (2))
302.769	18.3±0.9	301.649	18.7±0.9	301.982	21.0±1.1
327.653	18.6±0.9	326.573	19.0±1.0	327.095	21.3±1.1
352.491	19.2±1.0	351.486	19.2±1.0	352.271	21.6±1.1
377.34	20.6±1.0	376.41	19.6±1.0	377.156	22.0±1.1
392.247	21.8±1.1	391.377	19.8±1.0	392.111	22.4±1.1
352.591	21.6±1.1	351.549	19.4±1.0	352.334	22.2±1.1
302.843	20.9±1.1	301.684	18.8±0.9	302.008	21.5±1.1
277.41	20.5±1.0	276.392	18.4±0.9	276.231	21.1±1.1
252.46	20.2±1.0	251.404	18.1±0.9	251.235	20.7±1.0
226.942	19.8±1.0	226.068	17.7±0.9	225.918	20.3±1.0
202.036	19.4±1.0	201.112	17.3±0.9	200.959	19.9±1.0
176.508	18.9±0.9	175.787	16.8±0.8	175.65	19.4±1.0
151.07	18.3±0.9	150.542	16.3±0.8	150.171	18.8±0.9
126.126	17.6±0.9	125.585	15.7±0.8	125.212	18.1±0.9
100.919	16.7±0.8	100.493	14.8±0.7	100.186	17.2±0.9
75.702	15.6±0.8	75.383	13.8±0.7	75.176	16.0±0.8
50.788	13.8±0.7	50.432	12.2±0.6	50.095	14.2±0.7
25.902	10.6±0.5	25.484	9.41±0.47	25.065	10.9±0.6
11.063	6.17±0.31	10.632	5.59±0.28	10.065	6.45±0.32
6.286	3.60±0.18	5.874	3.48±0.17	5.117	4.04±0.20
3.503	2.10±0.10	3.15	2.68±0.13	2.291	2.95±0.15
15.635	8.09±0.40	15.345	7.23±0.36	15.032	8.40±0.42
30.733	11.5±0.6	30.392	10.2±0.5	30.052	11.8±0.6
60.7	14.6±0.7	60.384	12.9±0.7	60.073	15.0±0.8
110.749	17.1±0.9	110.44	15.1±0.8	110.364	17.5±0.9
160.774	18.5±0.9	160.423	16.4±0.8	160.341	19.0±1.0
211.391	19.5±1.0	210.698	17.3±0.9	210.569	20.1±1.0
262.344	20.2±1.0	261.282	18.0±0.9	261.137	20.8±1.0
302.739	20.7±1.0	301.589	18.6±0.9	301.41	21.4±1.1

Table S3: Electrical conductivity, σ_{el} , of MWCNT/ZnO with seven infiltration (IF) steps; in order of data collection. Note that the electrical conductivity from 300 K to 390 K on the first heating cycle is not reliable due to absorbed water or oxygen. Dimensions and densities of samples are given in Table 1.

T / K	$\sigma_{el} / \Omega^{-1} m^{-1}$ (7 IF 2 mm)	T / K	$\sigma_{el} / \Omega^{-1} m^{-1}$ (7 IF 3 mm)	T / K	$\sigma_{el} / \Omega^{-1} m^{-1}$ (7 IF 3 mm (2))
302.497	49.0±2.5	302.787	40.9±2.1	302.66	32.5±1.6
327.365	49.7±2.5	327.617	41.6±2.1	327.549	32.9±1.7
352.229	50.1±2.5	352.47	42.4±2.1	352.436	33.4±1.7
377.074	50.3±2.5	377.248	43.2±2.2	377.256	34.3±1.7
392.017	51.2±2.6	392.219	44.2±2.2	392.212	36.0±1.8
352.331	50.7±2.5	352.538	43.8±2.2	352.47	36.4±1.8
302.594	49.0±2.5	302.781	42.3±2.1	302.649	35.4±1.8
277.195	48.0±2.4	277.358	41.5±2.1	277.209	34.9±1.7
252.269	47.1±2.4	252.415	40.8±2.0	252.25	34.3±1.7
226.807	46.2±2.3	226.904	40.0±2.0	226.753	33.7±1.7
201.921	45.2±2.3	202.013	39.2±2.0	201.841	33.0±1.7
176.447	44.1±2.2	176.508	38.2±1.9	176.329	32.1±1.6
151.036	42.8±2.1	151.079	37.1±1.9	125.906	29.9±1.5
126.131	41.3±2.1	126.145	35.7±1.8	100.74	28.4±1.4
100.954	39.3±2.0	100.945	33.9±1.7	75.553	26.3±1.3
75.738	36.7±1.8	75.705	31.6±1.6	50.622	23.2±1.2
50.905	32.9±1.6	50.8	28.2±1.4	25.7	17.6±0.9
26.08	25.8±1.3	25.918	21.9±1.1	10.87	10.1±0.50
11.202	15.8±0.8	11.079	13.1±0.7	6.12	6.03±0.30
6.376	9.32±0.47	6.309	8.12±0.41	3.385	3.85±0.19
3.546	5.53±0.28	3.535	5.45±0.27	15.497	13.3±0.7
15.744	20.2±1.0	15.647	16.9±0.9	30.567	19.2±1.0
30.879	27.7±1.4	30.744	23.6±1.2	60.566	24.6±1.2
60.799	34.6±1.7	60.694	29.8±1.5	110.695	29.0±1.5
110.893	40.0±2.0	110.799	34.6±1.7	160.79	31.5±1.6
160.946	43.2±2.2	160.89	37.5±1.9	211.232	33.2±1.7
211.338	45.5±2.3	211.366	39.5±2.0	262.146	34.4±1.7
262.178	47.1±2.4	262.283	40.9±2.0	302.5	

Table S4: Electrical conductivity, σ_{el} , of MWCNTTs; in order of data collection. Dimensions and densities of samples are given in Table 1.

T / K	$\sigma_{el} / \Omega^{-1} \text{m}^{-1}$ (MWCNTTs)
304.131	24.4±1.2
276.312	24.1±1.2
251.576	23.8±1.2
226.367	23.4±1.2
201.739	23.0±1.2
176.381	22.4±1.1
151.355	21.7±1.1
126.79	20.9±1.0
101.628	19.8±1.0
76.255	18.3±0.9
51.897	16.1±0.8
25.892	12.3±0.6
11.176	8.45±0.42
5.566	6.07±0.30
15.803	9.74±0.49
30.73	13.4±0.7
62.231	17.1±0.9
111.181	20.1±1.0
160.897	21.8±1.1
211.097	22.9±1.2
261.024	23.7±1.2
301.381	24.3±1.2
326.192	24.7±1.2
351.216	25.4±1.3
376.025	26.5±1.3
391.058	28.3±1.4
351.264	27.8±1.4

Table S5: Seebeck coefficient, S , of MWCNT/ZnO with various infiltration (IF) steps and MWCNTTs; in order of data collection. Dimensions and densities of samples are given in Table 1.

T / K	$S / \mu\text{V}$ (2 IF 2 mm)	T / K	$S / \mu\text{V}$ (5 IF 2 mm)
302.153	7.42±0.37	302.769	3.64±0.18
327.261	7.17±0.36	327.653	4.14±0.21
352.449	8.70±0.43	352.491	3.77±0.19
377.275	9.41±0.47	377.34	2.81±0.14
392.255	7.05±0.35	392.247	2.23±0.11
352.51	6.15±0.31	352.591	1.22±0.06
302.192	4.75±0.24	302.843	1.09±0.05

T / K	$S / \mu\text{V}$ (7 IF 2 mm)	T / K	$S / \mu\text{V}$ (MWCNTTs)
302.153	7.42±0.37	302.769	3.64±0.18
327.261	7.17±0.36	327.653	4.14±0.21
352.449	8.70±0.43	352.491	3.77±0.19
377.275	9.41±0.47	377.34	2.81±0.14
392.255	7.05±0.35	392.247	2.23±0.11
352.51	6.15±0.31	352.591	1.22±0.06
302.192	4.75±0.24	302.843	1.09±0.05

Table S6: Thermal conductivity, κ , of MWCNT/ZnO with two infiltration (IF) steps; in order of data collection. Dimensions and densities of samples are given in Table 1.

T / K	$\kappa / \text{mW m}^{-1} \text{K}^{-1}$ (2 IF 2 mm)	T / K	$\kappa / \text{mW m}^{-1} \text{K}^{-1}$ (2 IF 3 mm)	T / K	$\kappa / \text{mW m}^{-1} \text{K}^{-1}$ (2 IF 3 mm (2))
301.603	238±20	301.987	226±30	301.708	283±32
302.153	237±20	326.877	221±30	326.641	272±37
327.261	233±24	351.749	217±34	351.554	265±43
352.449	230±28	376.572	217±39	376.463	262±48
377.275	229±32	391.579	219±44	391.421	264±52
392.255	232±34	351.797	217±47	351.602	273±43
352.51	228±28	302.001	224±39	301.712	288±32
302.192	234±20	276.673	232±29	276.414	296±27
276.345	239±17	251.719	239±25	251.426	311±22
251.364	245±14	226.326	247±20	226.077	329±17
226.022	251±13	201.384	256±16	201.09	347±17
201.066	258±13	175.981	266±13	175.765	373±19
175.732	267±13	150.677	272±14	150.233	398±20
150.204	271±14	125.72	275±14	125.264	421±21
125.247	274±14	100.597	269±13	100.276	436±22
100.206	266±13	75.439	245±12	75.265	431±22
75.184	242±12	50.504	190±9	50.105	356±18
50.103	186±9	25.58	86.4±4.3	25.06	167±8
25.077	84.8±4.2	10.782	20.3±1.0	10.058	30.3±1.5
10.072	17.4±0.9	6.058	7.37±0.37	5.112	6.54±0.33
5.127	4.28±0.21	3.324	3.09±0.15	2.309	1.31±0.07
2.307	0.932±0.047	15.426	37.5±1.9	15.028	68.4±3.4
15.036	37.2±1.9	30.463	109±5	30.041	209±10
30.056	108±5	60.446	216±11	60.028	384±19
60.079	218±18	110.549	268±13	110.206	426±21
110.391	273±14	160.571	262±13	160.242	382±19
160.381	273±14	210.897	247±12	210.63	337±17
210.639	256±13	261.603	234±13	261.307	300±24
261.232	241±15	301.921	220±22	301.655	281±32
301.548	231±20				

Table S7: Thermal conductivity, κ , of MWCNT/ZnO with five infiltration (IF) steps; in order of data collection. Dimensions and densities of samples are given in Table 1.

T / K	$\kappa / \text{mW m}^{-1} \text{K}^{-1}$ (5 IF 2 mm)	T / K	$\kappa / \text{mW m}^{-1} \text{K}^{-1}$ (5 IF 3 mm)	T / K	$\kappa / \text{mW m}^{-1} \text{K}^{-1}$ (5 IF 3 mm (2))
302.769	339±22	301.649	311±34	301.982	364±35
327.653	334±26	326.573	303±40	327.095	354±42
352.491	336±30	351.486	298±46	352.271	352±48
377.34	335±35	376.41	296±52	377.156	344±55
392.247	337±38	391.377	298±56	392.111	346±59
352.591	329±30	351.549	303±46	352.334	350±48
302.843	324±21	301.684	312±34	302.008	363±35
277.41	325±18	276.392	318±28	276.231	375±29
252.46	324±16	251.404	324±22	251.235	385±23
226.942	326±16	226.068	331±18	225.918	399±20
202.036	326±16	201.112	338±17	200.959	410±20
176.508	326±16	175.787	346±17	175.65	424±21
151.07	321±16	150.542	348±17	150.171	433±22
126.126	310±15	125.585	345±17	125.212	435±22
100.919	285±14	100.493	329±16	100.186	422±21
75.702	241±12	75.383	293±15	75.176	380±19
50.788	172±9	50.432	223±11	50.095	289±14
25.902	75.9±3.8	25.484	103±5	25.065	128±6
11.063	20.4±1.0	10.632	25.3±1.3	10.065	26.7±1.3
6.286	8.41±0.42	5.874	9.05±0.45	5.117	6.61±0.33
3.503	3.85±0.19	3.15	3.66±0.18	2.291	1.40±0.07
15.635	34.3±1.7	15.345	46.6±2.3	15.032	56.5±2.8
30.733	95.1±4.8	30.392	130±6	30.052	164±8
60.7	202±10	60.384	256±13	60.073	334±17
110.749	294±15	110.44	336±17	110.364	432±22
160.774	319±16	160.423	345±17	160.341	431±22
211.391	321±16	210.698	333±17	210.569	405±20
262.344	322±16	261.282	317±25	261.137	378±25
302.739	320±21	301.589	307±34	301.41	360±35

Table S8: Thermal conductivity, κ , of MWCNT/ZnO with seven infiltration (IF) steps; in order of data collection. Dimensions and densities of samples are given in Table 1.

T / K	$\kappa / \text{mW m}^{-1} \text{K}^{-1}$ (7 IF 2 mm)	T / K	$\kappa / \text{mW m}^{-1} \text{K}^{-1}$ (7 IF 3 mm)	T / K	$\kappa / \text{mW m}^{-1} \text{K}^{-1}$ (7 IF 3 mm (2))
302.497	432±25	302.787	454±42	302.66	459±41
327.365	430±29	327.617	451±50	327.549	450±48
352.229	424±34	352.47	452±58	352.436	441±56
377.074	415±38	377.248	454±66	377.256	436±64
392.017	413±41	392.219	460±72	392.212	440±68
352.331	397±32	352.538	450±57	352.47	439±55
302.594	385±23	302.781	455±42	302.649	452±40
277.195	381±19	277.358	462±34	277.209	464±33
252.269	375±19	252.415	467±27	252.25	474±27
226.807	370±19	226.904	474±24	226.753	487±24
201.921	364±18	202.013	477±24	201.841	498±25
176.447	354±18	176.508	479±24	176.329	510±25
151.036	338±17	151.079	474±24	125.906	515±26
126.131	315±16	126.145	461±23	100.74	494±25
100.954	277±14	100.945	427±21	75.553	437±22
75.738	222±11	75.705	364±18	50.622	328±16
50.905	150±8	50.8	262±13	25.7	150±7
26.08	64.5±3.2	25.918	116±6	10.87	38.5±1.9
11.202	18.4±0.9	11.079	31.4±1.6	6.12	14.9±0.8
6.376	8.02±0.40	6.309	13.1±0.7	3.385	6.52±0.33
3.546	3.79±0.19	3.535	6.02±0.30	15.497	67.5±3.4
15.744	29.8±1.5	15.647	52.7±2.6	30.567	188±9
30.879	80.5±4.0	30.744	145±7	60.566	381±19
60.799	181±9	60.694	308±15	110.695	506±25
110.893	290±14	110.799	442±22	160.79	515±26
160.946	337±17	160.89	471±24	211.232	491±25
211.338	358±18	211.366	473±24	262.146	466±29
262.178	372±19	262.283	468±30	302.577	450±40
302.529	379±23	302.682	458±42		

Table S9: Thermal conductivity, κ , of MWCNTTs; in order of data collection. Dimensions and densities of samples are given in Table 1.

T / K	$\kappa / \text{mW m}^{-1} \text{K}^{-1}$ (MWCNTTs)
304.131	76.1±21.2
276.312	66.9±17.1
251.576	59.1±14.2
226.367	52.7±11.5
201.739	46.8±9.2
176.381	41.2±7.0
151.355	35.7±5.1
126.79	30.1±3.5
101.628	24.2±2.1
76.255	18.0±1.1
51.897	11.6±0.6
25.892	5.18±0.26
11.176	2.01±0.10
5.566	0.831±0.042
15.803	2.89±0.14
30.73	6.23±0.20
111.181	25.0±2.6
160.897	34.6±5.6
211.097	46.4±9.8
261.024	59.3±14.9
301.381	71.5±19.8
326.192	80.8±23.3
351.216	92.9±27.5
376.025	109±33
391.058	119±36
351.264	98.1±28.5

6. Antibacterial Scaffolds made of Fibrous Polymer Composite

In addition to high mechanical strength, the interconnected T-ZnO network offers significant resistance to bacterial activity. Reported in this chapter are the effects of shape and concentration of ZnO on the tensile strength of the polymer composite and its ability to be a scaffold for eukaryote cell growth.

Personal contributions in the following article:

- Fabrication of the T-ZnO utilized in this study
- Raman spectroscopic investigations of the membranes
- Morphological analysis under SEM
- Partial manuscript preparation

The following content is adapted with permission from “A. Nasajpour, S. Mandla, S. Shree, E. Mostafavi, R. Sharifi, A. Khalilpour, S. Saghazadeh, S. Hassan, M. J. Mitchell, J. Leijten, X. Hou, A. Moshaverinia, N. Annabi, R. Adelung, Y. K. Mishra, S. R. Shin, A. Tamayol, and A. Khademhosseini *Nano Letters* **2017** 17 (10), 6235-6240”. Copyright (2017) American Chemical Society.

Nanostructured Fibrous Membranes with Rose Spike-Like Architecture

Amir Nasajpour,^{†,‡} Serena Mandla,^{†,‡} Sindu Shree,[§] Ebrahim Mostafavi,^{||} Roholah Sharifi,^{†,‡} Akbar Khalilpour,^{†,‡} Saghi Saghadzadeh,^{†,‡} Shabir Hassan,^{†,‡} Michael J. Mitchell,^{‡,‡} Jeroen Leijten,^{†,‡,∇} Xu Hou,^{||} Alireza Moshaverinia,[□] Nasim Annabi,^{†,‡,||} Rainer Adelung,[§] Yogendra Kumar Mishra,[§] Su Ryon Shin,^{*•■} Ali Tamayol,^{*•■,○} and Ali Khademhosseini^{*•■,•,△}

[†]Biomaterials Innovation Research Center, Division of Biomedical Engineering, Department of Medicine, Brigham and Women's Hospital, Harvard Medical School, Cambridge, Massachusetts 02139, United States

[‡]Harvard-MIT Division of Health Sciences and Technology, Massachusetts Institute of Technology, Cambridge, Massachusetts 02139, United States

[§]Institute for Materials Science, Kiel University, Kaiserstraße 2, D-24143 Kiel, Germany

^{||}Department of Chemical Engineering, Northeastern University, Boston, Massachusetts 02115-5000, United States

[‡]Department of Bioengineering, University of Pennsylvania, Philadelphia, Pennsylvania 19104, United States

[∇]Department of Chemical Engineering, David H. Koch Institute for Integrative Cancer Research, Massachusetts Institute of Technology, Cambridge, Massachusetts 02139, United States

[∇]Department of Developmental BioEngineering, MIRA Institute for Biomedical Technology and Technical Medicine, University of Twente, Drienerlolaan 5, 7522 NB Enschede, The Netherlands

[□]State Key Laboratory of Physical Chemistry of Solid Surface, Collaborative Innovation Center of Chemistry for Energy Materials, College of Chemistry and Chemical Engineering, Xiamen University, Xiamen 361005, China

[□]Weintraub Center for Reconstructive Biotechnology Division of Advanced Prosthodontics, School of Dentistry, University of California, Los Angeles, California 90095, United States

[•]Wyss Institute for Biologically Inspired Engineering, Harvard University, Boston, Massachusetts 02115, United States

[○]Department of Mechanical and Materials Engineering, University of Nebraska, Lincoln, Nebraska 68588, United States

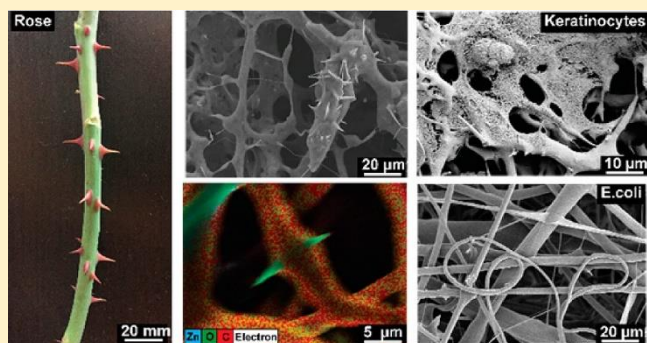
[•]Department of Bioindustrial Technologies, College of Animal Bioscience and Technology, Konkuk University, Seoul, 143-701, The Republic of Korea

[△]Center of Nanotechnology, King Abdulaziz University, Jeddah 21569, Saudi Arabia

* Supporting Information

ABSTRACT: Nanoparticles have been used for engineering composite materials to improve the intrinsic properties and/or add functionalities to pristine polymers. The majority of the studies have focused on the incorporation of spherical nanoparticles within the composite fibers. Herein, we incorporate anisotropic branched-shaped zinc oxide (ZnO) nanoparticles into fibrous scaffolds fabricated by electrospinning. The addition of the branched particles resulted in their protrusion from fibers, mimicking the architecture of a rose stem. We demonstrated that the encapsulation of different-shape particles significantly influences the physicochemical and biological activities of the resultant composite scaffolds. In particular, the branched nanoparticles induced heterogeneous crystallization of the polymeric matrix and enhance the ultimate mechanical strain and strength. Moreover, the three-dimensional (3D) nature of the branched ZnO nanoparticles enhanced adhesion properties of the composite scaffolds to the tissues. In addition, the rose stem-like constructs offered excellent antibacterial activity, while supporting the growth of eukaryote cells.

KEYWORDS: Branched tetrapod nanoparticles, zinc oxide, electrospinning, nanocomposites, antimicrobial, scaffolds



Polymeric nanocomposites are widely processed into fibrous materials for various disciplines such as tissue engineering,^{1,2} energy harvesting,³ flexible electronics,⁴ drug delivery,⁵ and methods of filtration.⁶ Generally, some nanoscale structures from inorganic materials, e.g., from metals, metal oxides, are dispersed into polymer structures to provide additional chemical and/or physical functionalities.^{7,8} Previous works of spherical zinc oxide (ZnO) nanoparticles dispersed within semicrystalline polycaprolactone (PCL) fibrous structures have demonstrated enhancements in antimicrobial activities,⁹ angiogenesis *in vivo*,¹⁰ and dermal regeneration.¹¹ However, the recent advances in nanomaterial synthesis allow the production of a new class of branched ZnO nanoparticles via the flame transport synthesis technique.¹² The unique branched geometry of this nanomaterial allows the creation of physical interlocking segments, which provides diverse functionalities in the field of self-reporting

materials,¹³ antifouling surfaces,¹⁴ electronic sensing devices,¹⁵ gene transfection agents,¹⁶ and antiviral materials,¹⁷ as well as bonding to nonadherent surfaces.¹⁸ In this work, flame-made branched ZnO nanostructures (spikes length in the 1–5 μm range and diameters in the 50–200 nm range, as confirmed by scanning electron microscopy images shown in Figures S1 and S2) were incorporated into the PCL scaffold via electrospinning. We studied the physical and chemical properties of engineered composites as compared to pristine PCL and electrospun PCL scaffold embedded with spherical particles. Due to the irregular shape of the branched ZnO particles, these nanostructures could not be fully confined into the fibers, resulting in protrusions from fibers' surfaces. Such protrusions mimic the natural structure of rose spikes. As reported by Zander et al., nanosized spikes increase the roughness and surface area of the material and affect the

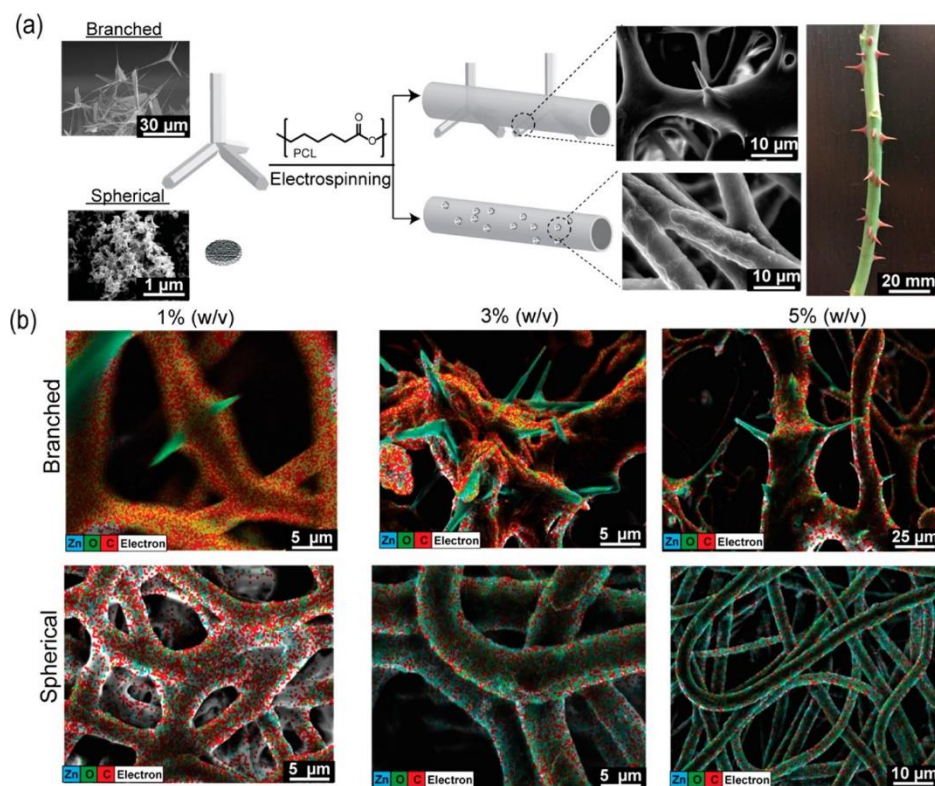


Figure 1. Fabrication of the rose stem-like composite constructs containing spherical and branched nanoparticles. (a) Schematic illustration of fibrous composite fabrication: ZnO particles are dispersed within a PCL solution and extruded under high voltage. SEM images show the inability to confine the branched particle with consequent protrusion formation (rose stem-like structure). (b) EDAX map of dibranched and spherical ZnO particles at different concentrations (1, 3, and 5% w/v) and their distribution into the fibers. Elemental map demonstrates the distribution of Zn (blue), O (green), and C (red) in the composites.

overall chemical and physical properties of the resultant hybrid structures.¹⁹ In

this study, we investigated the effects of particle geometry on the physical, chemical, and biological properties of the composite fibers by manipulating particle-fiber interphase.

Spherical and branched ZnO particles were dispersed in a 10% (w/v) solution of PCL in hexafluoroisopropanol (HFIP) and electrospun to obtain fibrous composite scaffolds. Pristine PCL fibrous scaffolds were also prepared. The strong particle-polymer interactions between ZnO and PCL inhibited

phase separation during the solvent evaporation.²⁰ The scanning electron microscopy (SEM) images of the branched composite scaffold illustrated that the nanostructures were not totally confined within the fibers, showing branching protrusions through the fibers' surfaces, mimicking the rose spikes architecture (Figure 1a and Figure S1). The surface of the spherical-particle encapsulated nanofibers on the other hand appeared to be just slightly rough at the fiber

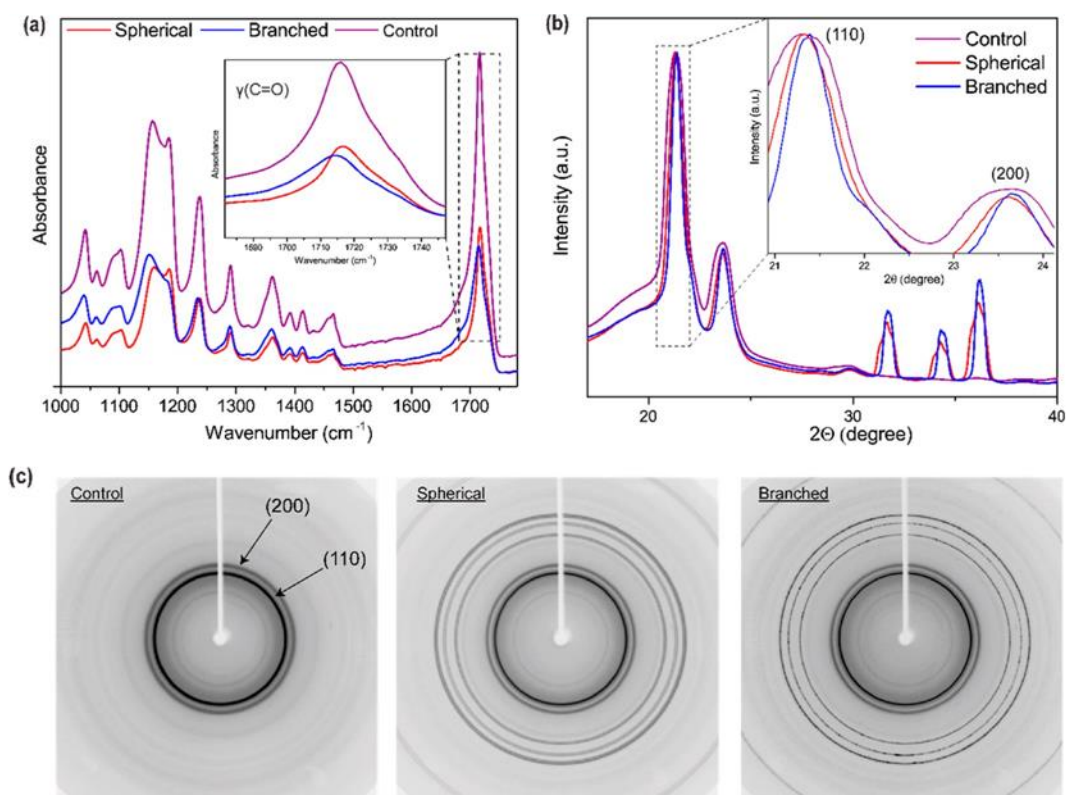


Figure 2. Chemical and physical characterization of fibrous composite scaffolds. (a) Fourier transformer infrared spectroscopy (FTIR) spectra of the tested fibers. The inset within the graph highlights the carbonyl stretching peaks. (b) Wide-angle X-ray diffraction (WAXD) showing the effect of the ZnO nanoparticles on the carrier polymer (PCL) (110) and (200) crystal planes. The inset demonstrates that the incorporation of ZnO induces narrowing of the crystal planes, correlating with an enhanced crystallization, compared to the control (purple). (c) Two-dimensional WAXD images show the effect of ZnO nanoparticles on the reflection banding arcs annotated within with arrows.

characteristic	control	spherical	branched
C–O and C–C stretching in the amorphous phase V_{am}	-1156 cm^{-1}	-1159 cm^{-1}	-1152 cm^{-1}
symmetric COC stretching V_s (COC)	-1185 cm^{-1}	-1185 cm^{-1}	
asymmetric COC stretching V_{as} (COC)	-1238 cm^{-1}	-1238 cm^{-1}	-1235 cm^{-1}
carbonyl stretching $\nu(\text{C}=\text{O})$	-1716 cm^{-1}	-1716 cm^{-1}	-1714 cm^{-1}

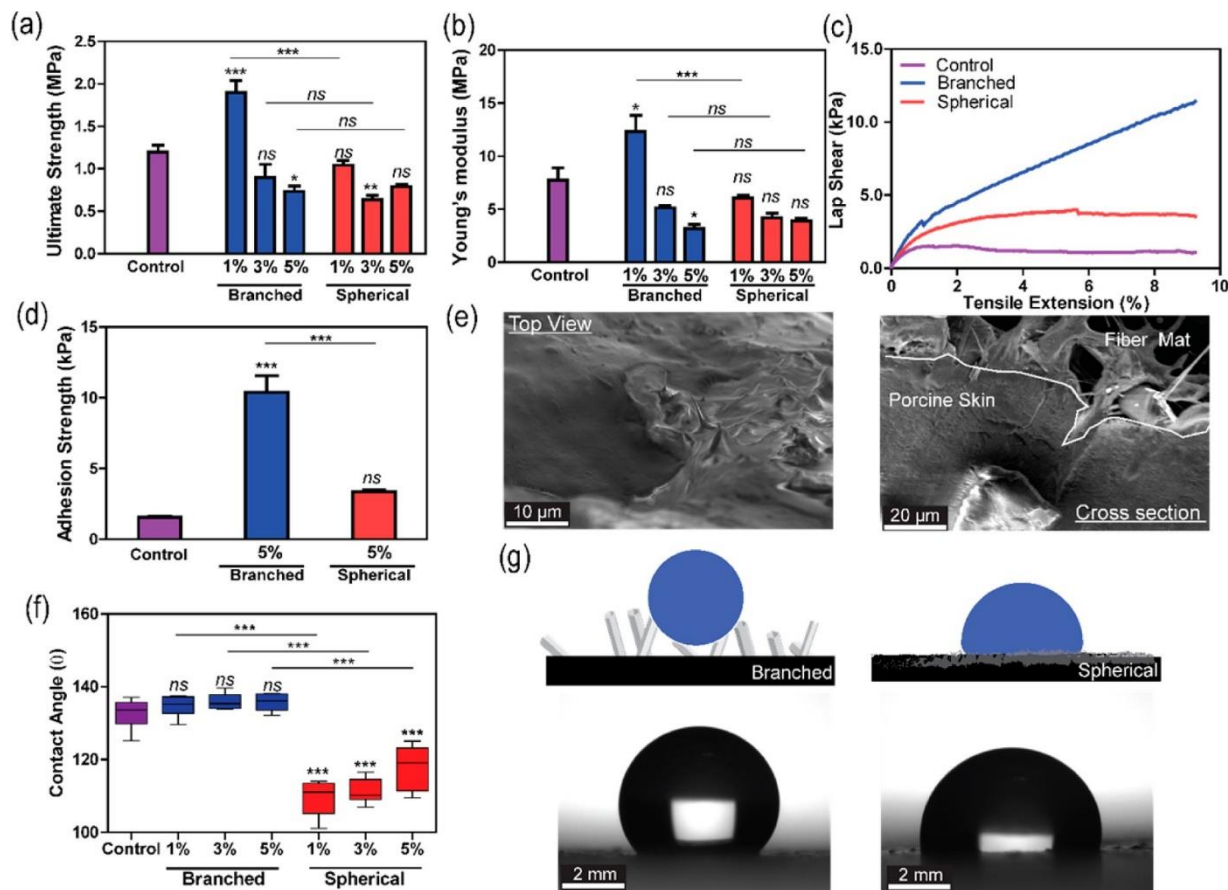


Figure 3. Mechanical and surface characterization of the nanocomposite structures. (a) Comparison of ultimate strength among the control sample (PCL), branched, and spherical composite scaffolds. The reports of statistical analysis placed directly on top of the bars refer to the comparison of the sample with the control (pristine PCL). The comparison between different samples is shown by lines. (b) Comparison of constructs' Young's modulus. (c) Representative lap shear curves of scaffolds sandwiched between porcine skins. (d) Comparison of the adhesion strength of different composite structures (data is derived from lap shear tests with porcine skin). (e) Representative SEM images from top and cross-sectional view of a branched composite scaffold after failure during lap shear test. (f) Measurements of contact angle between a deionized water drop and the material surfaces. (g) Schematic illustration of fibrous structures wetting behavior (top), coupled with optical imaging analysis (bottom) ($n = 4$ for ultimate strength and Young's modulus data, $n = 3$ for adhesion strength data, and $n = 6$ for contact angle data, *: $P < 0.33$, **: $P < 0.002$, ***: $P < 0.001$).

interphase while the pristine PCL fibrous surface was smooth (Supporting Information S1A). Higher branched particle fractions (3 and 5% w/v) led to an overlapping of the protrusions, forming macropores within the fibrous substrates (Figure S4). Energy dispersive X-ray microanalysis (EDX) was deployed and merged with the SEM analysis to map the elemental atoms and to identify the particle distribution within the fibrous networks. The highest distribution of zinc atoms on the fiber surface was visible on

constructs with spherical particles, which was proportional to the nanomaterial concentration. This evidence was related to the greater surface-area-to-volume ratio of the spherical nanoparticles as compared to the branched particles (considering equal weight per volume ratio) (Figure 1b).

Fourier transform infrared spectroscopy (FTIR) analysis was performed to identify the variations in the particle–polymer interphase interactions induced by the geometrical nature of the nanomaterials²¹ (Figure 2a, c).

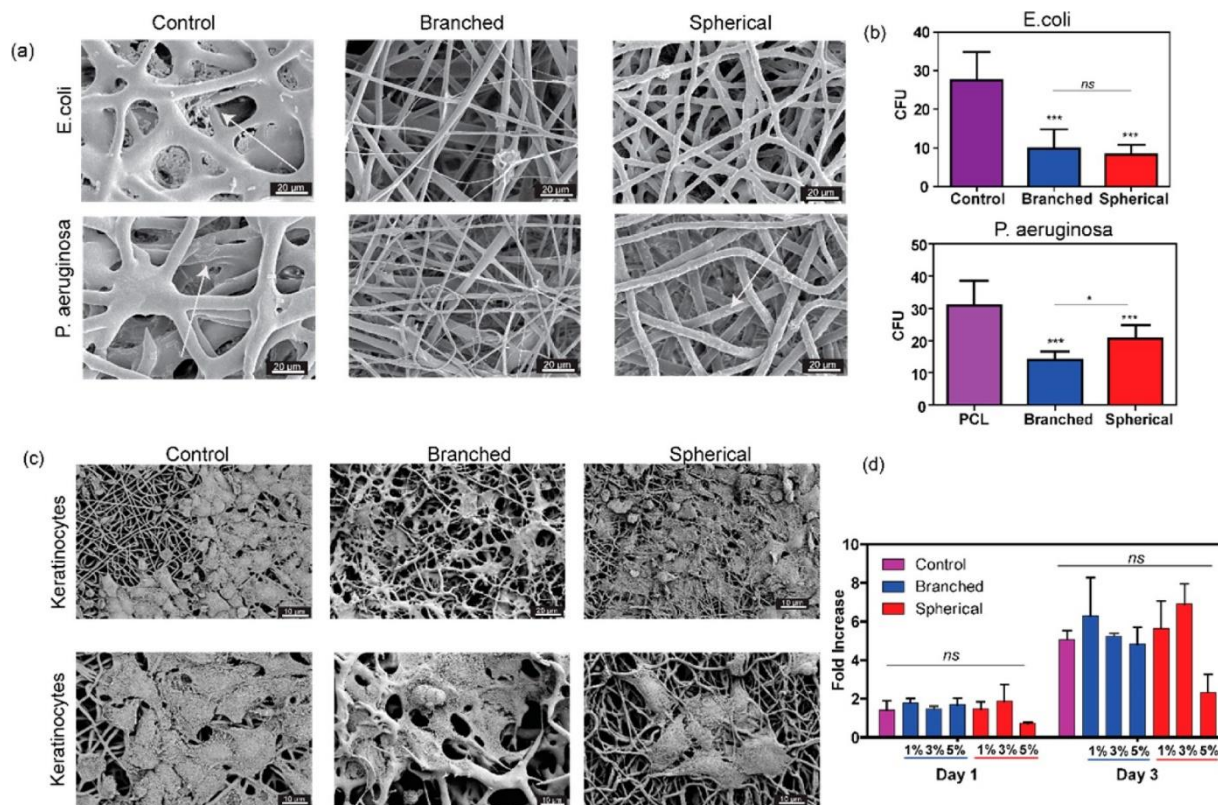


Figure 4. Characterization of the antimicrobial and biological properties of the composite scaffolds. (a) Representative SEM images of control (PCL), branched, and spherical samples after 24 h incubation with *E. coli* (top) and *P. aeruginosa* (bottom). (b) Number of colony forming units (CFU) over the samples after 24 h incubation with *E. coli* (top) and *P. aeruginosa* (bottom). The arrows are showing the presence of bacteria on the surface of the nanofibers. (c) Representative SEM images of keratinocytes attachment to control, branched, and spherical composite scaffolds. (d) Metabolic activity of HACATs assessed by PrestoBlue assay after 1 and 3 days of culture over pristine PCL compared with ZnO nanocomposites with different concentrations (1, 3, 5%) of branched and spherical ZnO nanoparticles. ($n = 7$ for antimicrobial tests, $n = 5$ for metabolic activity tests, *: $P < 0.33$, **: $P < 0.002$, ***: $P < 0.001$).

As shown in Figure 2a, the carbonyl peaks [$\nu(\text{C=O})$] of pristine PCL and spherical-particle incorporated fibrous materials appeared at 1716 cm^{-1} while for the branched system the peak shifted to a lower wavenumber (1714 cm^{-1}). Moreover, the asymmetrical ester peak of branched composite scaffold was also shifted to 1235 cm^{-1} compared to the other tested structures. We speculate that the branched morphology and the nanostaired surface of the spikes affected the two chemical functional groups of the semicrystalline polymer carrier (Figure 2a,c and Table 1). To further characterize the physical effect of the particle-polymer interphase interactions on PCL's crystalline

planes, wide-angle X-ray diffraction (WAXD) was carried out. As shown in the Figure 2b,c, addition of ZnO nanoparticles within the fibrous polymer matrix led to sharpening of the PCL reflection planes, suggesting the variation in crystalline polymer domain sizes compared to pristine PCL nanofibers (4.2 \AA).²² This reflection displacement was more intense in substrates containing branched particles [displacement to the plane (110) (3.75 \AA)], confirming the hypothesis that protrusions of the branched particles altered the PCL's overall crystallinity. These results are in good agreement with the previous observations, pointing out that the branched ZnO

nanoparticles induced crystallization in nylon-based composites.²³

The mechanical properties of the composite fibers were assessed through the uniaxial tensile test to investigate the effect of the particles on the ultimate strength and the Young's modulus of the fibers. Figure 3a demonstrates that the incorporation of 1% (w/v) branched particles into polymer network led to a significant enhancement of the ultimate strength of the pristine PCL from 1.2 MPa to 1.9 MPa in the branched composite. A similar observation was reported in computational and experimental studies that demonstrated an improvement of bulk polymer properties due to the introduction of branched nanomaterials.²⁴ The trend is further evident considering the Young's modulus of the structures which drastically increased from 7 MPa for pristine PCL to ~13 MPa for the composite containing 1% branched ZnO ($p < 0.33$, Figure 3b). However, the addition of 3 and 5% (w/v) ZnO particles did not further reinforce the PCL structure but introduced weak point in the polymer network.²⁵

The geometry of the branched particles and the rose-like constructs formed after their incorporation within the polymeric membranes could facilitate the physical interlocking and penetration to soft substrate (such as tissues) to improve the adhesive properties. Surface topography can indeed play an important role in the adhesion strength between substrates and skin. In addition to the penetration of the spike of the rose-like substrates into skin, their high surface area may also positively contribute to the adhesion strength.

To prove our hypothesis, the electrospun fibers were sandwiched between two pieces of porcine skin and a uniform force with a 150 g weight was applied for 1 min. The use of the 5% (w/v) composite substrates in the adhesion tests was to note the effect of particle shape, on adhesion strength. We

expected that the highest particle concentration would exhibit the most distinct difference. Samples were then subjected to lap shear test. Results showed that the rose stem-like composites containing 5% branched particles had significant higher adhesive properties (10.4 MPa) as compared to those containing 5% spherical particles (3.3 MPa) and pristine PCL (1.6 MPa) ($p < 0.001$ Figure 3c,d). SEM images from the interface of the porcine skin and the fiber mat with branched nanoparticles indicated the penetration of the spikes of branched particles into the porcine skin. Therefore, the increased adhesive strength might be due to the physical between topographically heterogenous electrospun fibers and the porcine skin (Figure 3e).

The variations in surface composition and architecture affect interfacial properties including the contact angle. The contact angle (CA) measurements on the scaffolds surface were performed to evaluate their wettability and hydrophilic/hydrophobic properties (Figure 3f). Pristine PCL was hydrophobic and showed a nonwetting regime (CA ~ 130°). The incorporation of spherical particles slightly reduced the CA, improving the wetting regime of the PCL structure. In contrast, the branched composites showed higher CA, increasing the overall hydrophobicity of the fibrous constructs. The similarity between the contact angle of pristine PCL and rose-like structures might be due to coating of PCL on the surface of the spikes. SEM images suggested the presence of a thin layer of PCL on the surface of the spikes (Figure S2).

The antibacterial properties of ZnO nanoparticles have been previously shown and used for various medical applications.²⁶ To assess the antibacterial potency of the fabricated hybrid scaffolds, we used the lowest ZnO concentration (1% w/v). Substrates containing 1% (w/v) branched particles were seeded with prokaryotic

microorganisms (*E. coli* and *P. aeruginosa*). Data reported in Figure 4a,b showed poor adhesion and proliferation of both tested microorganisms on ZnO composite fibrous scaffolds. Moreover, the reduction of the biofilm formation as compared to pristine PCL, confirmed that antibacterial properties were preserved following incorporation of the ZnO branched nanoparticles into the PCL electrospun fiber. The observed behavior might be due to the difference between the surface topography of substrates containing spherical and branched particles. In addition, the exposure of the ZnO nanopikes might have also contributed to the enhanced antibacterial activity.

Cells attachment on pristine PCL and ZnO containing fibrous substrates containing 5% (w/v) of particles was assessed by seeding human keratinocytes on the substrate. After 48 h, cells were fixed and imaged by SEM (Figure 4c). The images demonstrated a high cell attachment to fibrous scaffolds. The *in vitro* biocompatibility of fabricated scaffolds was further assessed by measuring the metabolic activity of the cells cultured on scaffolds using a PrestoBlue assay after 1 and 3 days (Figure 4d). Results showed that the branched ZnO particles do not induce any cytotoxic effects after incorporation within PCL mats. On the other hand, the scaffolds containing 5% (w/v) of spherical particles showed slight inhibitory effects on cellular growth. Considering the reduced bacteria growth and improved cellular growth, the engineered rose-like constructs may be an interesting candidate for regenerative applications susceptible to infection.

In conclusion, we have developed a PCL-based fibrous nanocomposite system embedded with spherical or branched ZnO nanoparticles. The focus of the work is to shed light on the difference in characteristics of composite substrates where the particles are exposed and not embedded within the

polymeric fibers. However, the difference in particle size could also contribute to some of the observed differences in the properties of the fabricated composite substrates. Incorporation of the branched particles resulted in the formation of rose stem-like thorns. These geometric features resulted in enhanced mechanical properties and adhesion strength to soft tissue. The lower surface area of the branched ZnO nanoparticles in the electrospun fibers also led to higher biocompatibility as well as reduced antimicrobial activity. Therefore, at low concentrations of branched ZnO particles, the rose stem-like engineered constructs can be appropriate candidates for regenerative applications susceptible to infection as they support cellular growth and reduce bacterial adhesions.

■ ASSOCIATED CONTENT

* Supporting Information

The Supporting Information is available free of charge on the ACS Publications website at DOI: [10.1021/acs.nanolett.7b02929](https://doi.org/10.1021/acs.nanolett.7b02929).

Materials and methods; scanning electron microscopy (supplementary Figures S1–S4); stress strain curves (supplementary Figure S5) supplementary references (PDF)

■ AUTHOR INFORMATION

Corresponding Authors

*E-mail: alikh@bwh.harvard.edu. Phone: (617)-768-8395. Fax: (617)-768-8477.

*E-mail: atamayol@bwh.harvard.edu.

*E-mail: sshin4@partners.org.

ORCID 

Michael J. Mitchell: 0000-0002-3628-2244

Yogendra Kumar Mishra: 0000-0002-8786-9379

Ali Khademhosseini: 0000-0002-2692-1524

Notes

The authors declare no competing financial interest.

■ ACKNOWLEDGMENTS

The authors gratefully acknowledge the financial support from the Presidential Early Career Award for Scientists and Engineers (PECASE), and Air Force Office of Sponsored Research under award # FA9550-15-1-0273 and the National Institutes of Health (AR066193, AR066193, EB022403, AR057837, HL137193, EB021857, EB024403). M.J.M. was supported by a Burroughs Wellcome Fund Career Award at the Scientific Interface, a NIH F32 fellowship (award number CA200351), and a grant from the Burroughs Wellcome Fund (no. 1015145).

Dr. Anas Chalah (Harvard SEAS). X.H. acknowledges the National Natural Science Foundation of China (grant 21673197) and Young Overseas High-level Talents Introduction Plan. S.H. acknowledges funding from SNSF, Switzerland. S.R.S. would like to recognize and thank Brigham and Women's Hospital President Betsy Nabel, MD, and the Reny family, for the Stepping Strong Innovator Award through their generous funding. S.S. acknowledges financial support from Henri Benedictus postdoctoral fellowship from Belgian American Educational Foundation (BAEF) and King Baudouin Foundation (KBF). J.L. acknowledges financial support from Innovative Research Incentives Scheme (Veni, #14328) from the Netherlands Organization for Scientific Research (NWO).

REFERENCES

- Leijten, J.; Rouwkema, J.; Zhang, Y. S.; Nasajpour, A.; Dokmeci, M. R.; Khademhosseini, A. *Small* 2016, 12, 2130–2145.
- Li, D.; Xia, Y. *Adv. Mater.* 2004, 16, 1151–1170.
- Persano, L.; Dagdeviren, C.; Su, Y.; Zhang, Y.; Girardo, S.; Pisignano, D.; Huang, Y.; Rogers, J. A. *Nat. Commun.* 2013, 4, 1633.
- Najafabadi, A. H.; Tamayol, A.; Annabi, N.; Ochoa, M.; Mostafalu, P.; Akbari, M.; Nikkhah, M.; Rahimi, R.; Dokmeci, M. R.; Sonkusale, S.; Ziaie, B.; Khademhosseini, A. *Adv. Mater.* 2014, 26, 5823–5830.
- Goldberg, M.; Langer, R.; Jia, X. *J. Biomater. Sci., Polym. Ed.* 2007, 18, 241–268.
- Gopal, R.; Kaur, S.; Ma, Z.; Chan, C.; Ramakrishna, S.; Matsuura, T. *J. Membr. Sci.* 2006, 281, 581–586.
- Huang, Z.-M.; Zhang, Y. Z.; Kotaki, M.; Ramakrishna, S. *Compos. Sci. Technol.* 2003, 63, 2223–2253.
- Keledi, G.; Hari, J.; Pukanszky, B. *Nanoscale* 2012, 4, 1919–1938.
- Augustine, R.; Malik, H. N.; Singhal, D. K.; Mukherjee, A.; Malakar, D.; Kalarikkal, N.; Thomas, S. *J. Polym. Res.* 2014, 21, 347.
- Augustine, R.; Dominic, E. A.; Reju, I.; Kaimal, B.; Kalarikkal, N.; Thomas, S. *RSC Adv.* 2014, 4, 51528–51536.
- Augustine, R.; Dominic, E. A.; Reju, I.; Kaimal, B.; Kalarikkal, N.; Thomas, S. *RSC Adv.* 2014, 4, 24777–24785.
- Mishra, Y. K.; Kaps, S.; Schuchardt, A.; Paulowicz, I.; Jin, X.; Gedamu, D.; Freitag, S.; Claus, M.; Wille, S.; Kovalev, A.; Gorb, S. N.; Adelung, R. *Part. Part. Syst. Charact.* 2013, 30, 775–783.
- Jin, X.; Götz, M.; Wille, S.; Mishra, Y. K.; Adelung, R.; Zollfrank, C. *Adv. Mater.* 2013, 25, 1342–1347.
- Holken, I.; Hoppe, M.; Mishra, Y. K.; Gorb, S. N.; Adelung, R.; Baum, M. *J. Phys. Chem. Chem. Phys.* 2016, 18, 7114–7123.
- Mishra, Y. K.; Modi, G.; Cretu, V.; Postica, V.; Lupan, O.; Reimer, T.; Paulowicz, I.; Hrkac, V.; Benecke, W.; Kienle, L.; Adelung, R. *ACS Appl. Mater. Interfaces* 2015, 7, 14303–14316.
- Nie, L.; Gao, L.; Feng, P.; Zhang, J.; Fu, X.; Liu, Y.; Yan, X.; Wang, T. *Small* 2006, 2, 621–625.
- Antoine, T. E.; Hadigal, S. R.; Yakoub, A. M.; Mishra, Y. K.; Bhattacharya, P.; Haddad, C.; Valyi-Nagy, T.; Adelung, R.; Prabhakar, B. S.; Shukla, D. *J. Immunol.* 2016, 196, 4566–4575.

- (18) Jin, X.; Strueben, J.; Heepe, L.; Kovalev, A.; Mishra, Y. K.; Adelong, R.; Gorb, S. N.; Staubitz, A. *Adv. Mater.* 2012, 24, 5676–5680.
- (19) Zander, N. *Polymers* 2013, 5, 19.
- (20) Han, T.; Yarin, A. L.; Reneker, D. H. *Polymer* 2008, 49, 1651–1658.
- (21) Elzein, T.; Nasser-Eddine, M.; Delaite, C.; Bistac, S.; Dumas, P. J. *Colloid Interface Sci.* 2004, 273, 381–387.
- (22) Wang, X.; Zhao, H.; Turng, L.-S.; Li, Q. *Ind. Eng. Chem. Res.* 2013, 52, 4939–4949.
- (23) Ma, Y.-l.; Hu, G.-s.; Ren, X.-l.; Wang, B.-b. *Mater. Sci. Eng., A* 2007, 460–461, 611–618.
- (24) Raja, S. N.; Olson, A. C. K.; Limaye, A.; Thorkelsson, K.; Luong, A.; Lin, L.; Ritchie, R. O.; Xu, T.; Alivisatos, A. P. *Proc. Natl. Acad. Sci. U. S. A.* 2015, 112, 6533–6538.
- (25) Raja, S. N.; Luong, A. J.; Zhang, W.; Lin, L.; Ritchie, R. O.; Alivisatos, A. P. *Chem. Mater.* 2016, 28, 2540–2549.
- (26) Amna, S.; Shahrom, M.; Azman, S.; Kaus, N. H. M.; Ling Chuo, A.; Siti Khadijah Mohd, B.; Habsah, H.; Dasmawati, M. *Nano-Micro Lett.* 2015, 7, 219–242.

Supplementary Information for:

Nanostructured fibrous membranes with rose spike-like architecture

Amir Nasajpour^{1,2}, Serena Mandla^{1,2}, Sindu Shree³, Ebrahim Mostafavi⁴, Roholah Sharifi^{1,2}, Akbar Khalilpour^{1,2}, Saghi Saghazadeh^{1,2}, Shabir Hassan^{1,2}, Michael J. Mitchell^{5,6}, Jeroen Leijten^{1,2,7}, Xu Hou⁸, Alireza Moshaverinia⁹, Nasim Annabi^{1,2,4}, Rainer Adelung³, Yogendra Kumar Mishra³, Su Ryon Shin^{1,2,10}, Ali Tamayol^{1,2,10,11*}, Ali Khademhosseini^{1,2, 10,12,13*}*

¹Biomaterials Innovation Research Center, Division of Biomedical Engineering, Department of Medicine, Brigham and Women's Hospital, Harvard Medical School, Cambridge, Massachusetts 02139, United States

²Harvard–MIT Division of Health Sciences and Technology, Massachusetts Institute of Technology, Cambridge, Massachusetts 02139, United States

³Institute for Materials Science, Kiel University, Kaiserstraße 2, D-24143 Kiel, Germany

⁴Department of Chemical Engineering, Northeastern University, Boston, Massachusetts 021155000, United States

⁵Department of Bioengineering, University of Pennsylvania, Philadelphia, Pennsylvania 19104, USA

⁶Department of Chemical Engineering, David H. Koch Institute for Integrative Cancer Research, Massachusetts Institute of Technology, Cambridge, Massachusetts 02139, United States

⁷Department of Developmental BioEngineering, MIRA Institute for Biomedical Technology and Technical Medicine, University of Twente, Enschede, 5, 7522NB Enschede, The Netherlands.

⁸State Key Laboratory of Physical Chemistry of Solid Surface, Collaborative Innovation Center of Chemistry for Energy Materials, College of Chemistry and Chemical Engineering, Xiamen University, Xiamen 361005, China

⁹Weintraub Center for Reconstructive Biotechnology Division of Advanced Prosthodontics, School of Dentistry University of California, Los Angeles, CA. 90095, United States

¹⁰Wyss Institute for Biologically Inspired Engineering, Harvard University, Boston, Massachusetts 02115, United States

¹¹Department of Mechanical and Materials Engineering, University of Nebraska, Lincoln, NE, 68588, USA

¹²Department of Bioindustrial Technologies, College of Animal Bioscience and Technology, Konkuk University, Seoul, 143-701, the Republic of Korea

¹³Center of Nanotechnology, King Abdulaziz University, Jeddah 21569, Saudi Arabia

Corresponding Authors:

*Email: alik@bwh.harvard.edu, atamayol@bwh.harvard.edu, sshin@bwh.harvard.edu
Phone Number: (617)-768-8395 Fax: (617)-768-8477

This file includes:

Materials and Methods
Supplementary Figures S1-S5
Supplementary References

Materials

Poly ϵ -caprolactone (PCL) with an average molecular weight of 80,000, and 1,1,1,3,3,3hexafluoroisopropanol (HFIP) was purchased from Sigma-Aldrich (St. Louis, MO, USA). Cell culture supplies including Dulbecco's modified Eagle medium (DMEM), 0.05% trypsin-EDTA (10X), fetal bovine serum (FBS), antibiotics, fibronectin, and PrestoBlue[®] Assay were purchased from Invitrogen (Carlsbad, CA, USA).

Branched ZnO Nanoparticle Synthesis

To produce branched ZnO nanoparticles, a flame transport synthesis technique was used. This method offered direct conversion from metallic Zn microparticles into complex shaped ZnO nano- and microstructures in a single step conversion within the flame in the presence of normal air environment. The mixture (2:1 weight ratio) of sacrificial polyvinylbutyral polymer and / or ethanol and Zn microparticles from Goodfellow, UK was burned in a simple muffle type oven where Zn particles were directly converted into branched ZnO nanostructures via solid-vapor/solid growth in a further modified flame transport synthesis process, as described in a previous work¹.

Electrospinning Zinc Oxide Composites

400 mg of PCL (Mn 80,000) was added to a scintillation and 4 mL of HFIP solvent to create a 10 % (w/v) solution, which was stirred overnight. To disperse the particles, ZnO was added to the polymer solution and bath sonicated for 30-50 min prior to electrospinning. The composite was then added to a 3 mL syringe, attached to a 23-gauge blunt-tip needle. The polymer was extruded at a flow rate of 2 mL/h, and the grounded electrode was placed 25 mm below the needle. A voltage in the range of 17.0 to 18.0 kV was applied to generate the fibrous substrates. During the electrospinning process, the relative humidity and temperature were set at 15% and 26° C respectively.

Optical and Elemental Analysis of Zinc Oxide Composites

The nanocomposite fiber morphology was investigated using a scanning electron microscope (SEM; Zeiss Ultra Plus, 7 kV) with an energy-dispersive X-ray (EDX) spectrometer. The nanocomposite fibers were sputtered with a thin gold layer to reduce the surface charge; subsequently compositional analysis was performed merging the SEM data.

Fourier Transformer Infrared Spectroscopy (FTIR)

Nanocomposite structure absorbance spectra were obtained by a Bruker Alpha FTIR (Bruker Optic GmbH, Ettlingen, Germany) using attenuated total reflection (ATR) configuration. The machine was tarred by running a blank sample to subtract the background absorbance. Electrospun samples were then loaded into the instrument, and absorbance spectra were detected.

X-ray Fiber Diffraction

The electrospun samples were sliced to obtain 2 mm x 10 mm ribbons, and then were carefully mounted and aligned, with their long ribbon axis vertical, onto the Cu monochromatic X-ray beam using an Oxford XCalibur PX Ultra diffractometer equipped with a low noise CCD Onyx area detector. All experimental conditions such as time of scanning θ , χ , theta, chi, phi Kappa diffractometer were kept constant for all the tested conditions. The detector distance was calibrated using the sharp 104 reflections at 3.035 Å of CaCO₃.

Tensile Experiment

The tensile properties were calculated using a uniaxial tensile machine (Instron, Norwood, MA) with cell load capacity of 10 N setting the extension rate at 15 mm/min. The specimens were cut from the mat sheets in order to obtain standard dimension: 3.5 mm width, 9.5 mm length, 400 μm thickness. The stress-strain curves were plotted (n=4) and the elastic modulus was derived from the initial 0-10% linear region of the stress-strain curves.

Lap Shear Adhesion Test

The adhesive properties of electrospun were analyzed using an ASTM standard lap shear test (F2255-05). Briefly, the fiber was sandwiched in between a piece of porcine skin (24.0 mm width, 15.0 mm length, and 3.0 mm height). A small 500-gram weight was placed on top of the sandwiched fibers for 1 min then immediately tested until failure in a lap shear setup using an Instron 5542 mechanical tester equipped with a 10 N load cell at a cross-head speed of 5 mm/min.

Contact Angle Measurements of Fiber Composites

Samples containing 1, 3, and 5% (w/v) ZnO were electrospun onto a glass slide to retain flat surfaces. The slide was deposited with a homogenize layer of fibers. The contact angle measurement (n=6) was performed by a contact measurement system (KSV CAM 101) at room temperature, and 20% relative humidity. The machine was calibrated before measurements to insure quality of measurements. A water droplet volume of 29 μL was placed on the fibrous surface and the droplet profile was captured with the camera, finally contact angles were measured.

Bacteria Culture and Antimicrobial Studies

Control (pristine PCL), spherical, and branched samples containing 1% (w/v) particles were placed in separate wells of a 24 well plate, and sterilized under UV light. *Pseudomonas aeruginosa* and *Escherichia coli* were used to evaluate the antimicrobial properties of the electrospun sheets. A single colony of each strain of bacteria was mixed in 5 mL of tryptic soy broth (TSB, Sigma-Aldrich), and incubated overnight in a shaker incubator (200 rpm at 37 °C). The optical density of the resulting bacterial suspension was adjusted to 562 nm, which corresponds to a density of 10^9 CFU/ml. This suspension was then serially diluted to a density of 10^6 CFU/mL. Subsequently, 1 ml of the bacterial suspension was added directly on top of each sample and incubated at 37 °C and 5% CO₂ for 24 h. After incubation, the scaffolds were carefully washed 3 times with PBS to

remove excess bacteria. For CFU assays, the scaffolds were placed in 1 mL DPBS in 1.5 mL microcentrifuge tubes. The tubes were vigorously vortexed (3000 rpm) for 15 min to release all bacteria from the scaffold into the solution. Each bacterial suspension was serially diluted in DPBS over 4 logarithmic dilutions. Then, three 10 μ L drops of each dilution were seeded on tryptic soy agar plates, which were then incubated for 24 hr. at 37 °C and 5% CO₂. Lastly, the number of bacterial colonies formed on each agar plate was counted, and the dilution factor was used to calculate CFU values.

Cell Culture and Cell Viability Methods

Human keratinocytes were grown to confluence in Dulbecco's modified eagle medium, supplemented with 10% (v/v) FBS and 1% (v/v) streptomycin-penicillin maintained at 37 °C in a 5% CO₂ environment. Cells with a passage number between 6-8 were used for the experiments. Fibrous structures with a diameter of 5 mm were sterilized with 70% ethanol and washed with antibiotic-antimycotic solution and DPBS. Prior to cell seeding, the fibers were coated with 10 μ g/mL of fibronectin for 2 h. Cells were seeded at a concentration of 1.875×10^6 cells/mL. In vitro metabolic activity of the cells was analyzed after 1 and 3 days of culture with PrestoBlue[®] assay as per manufacturer's instructions. Samples fluorescence was recorded at 560 nm (excitation) and 590 nm (emission) using a microplate reader (BioTek synergy[™] 2, USA).

Statistical Analysis

The results were reported as the mean \pm standard deviation. Graphpad Prism version 7 was used to perform one-way ANOVA with Tukey post hoc tests to determine the significance of the differences between groups (*: $P < 0.05$, **: $P < 0.002$, ***: $P < 0.001$).

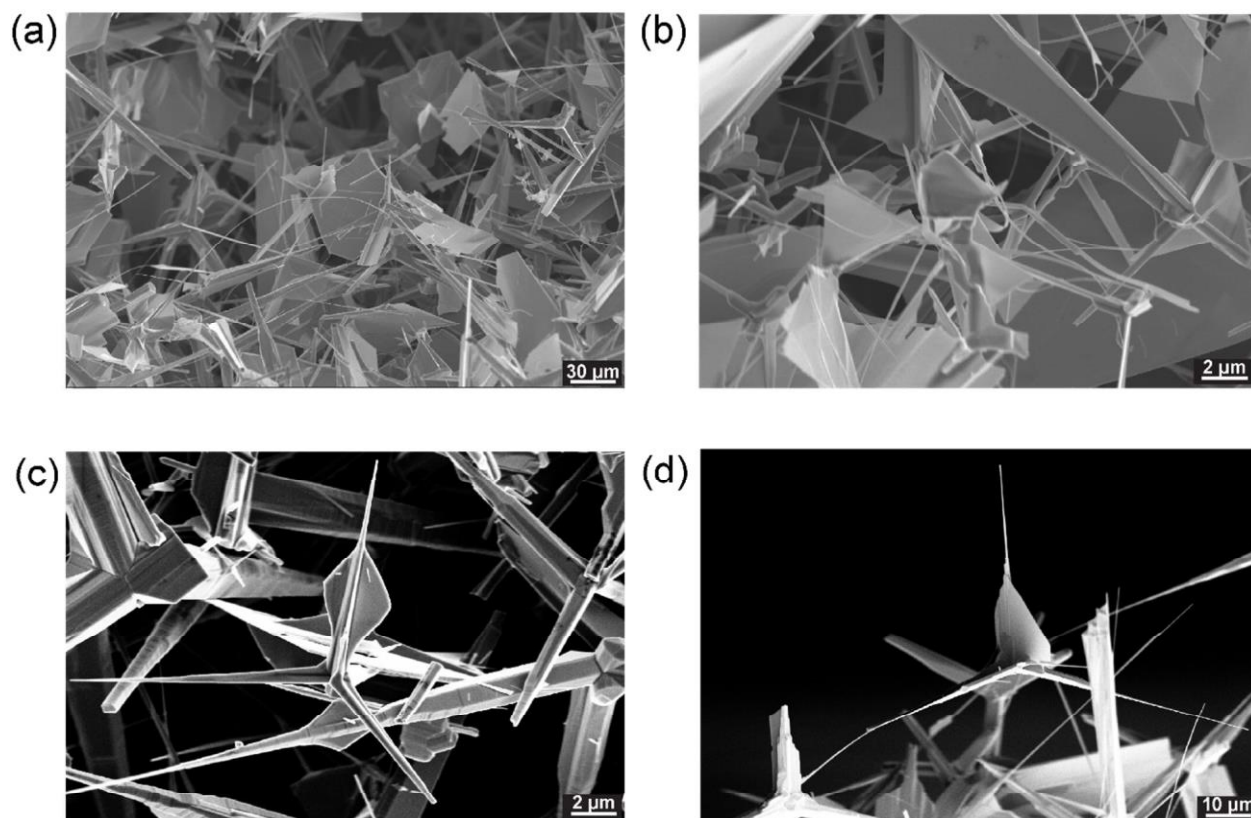


Figure S1. SEM imaging of pristine branched ZnO. (a-d) SEM images of branched ZnO nanoparticles produced *via* modified flame transport synthesis

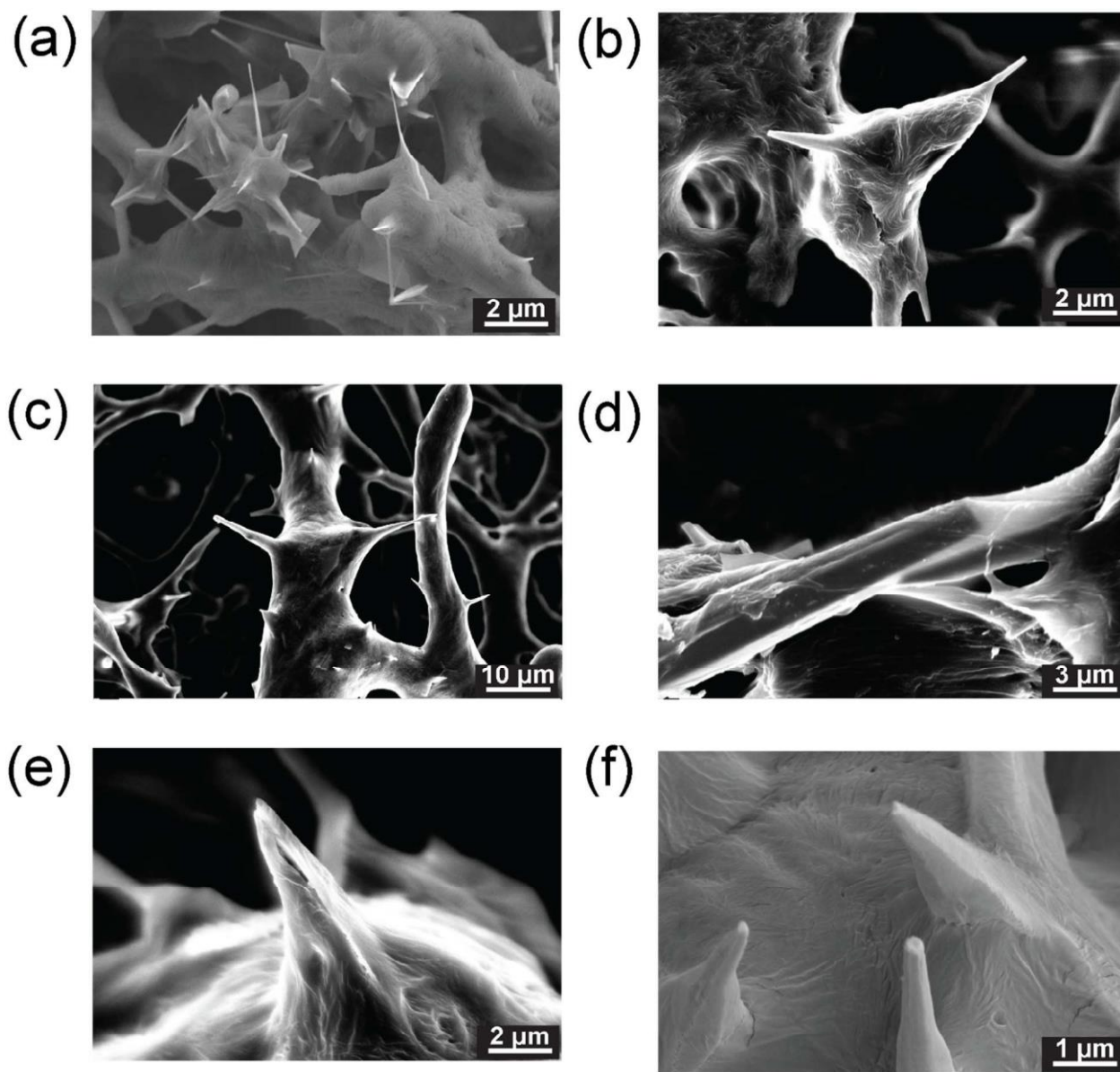


Figure S2. SEM imaging of composite branched ZnO fibers. (a-f) SEM analysis of branched ZnO nanoparticles composite fibers with varying magnification.

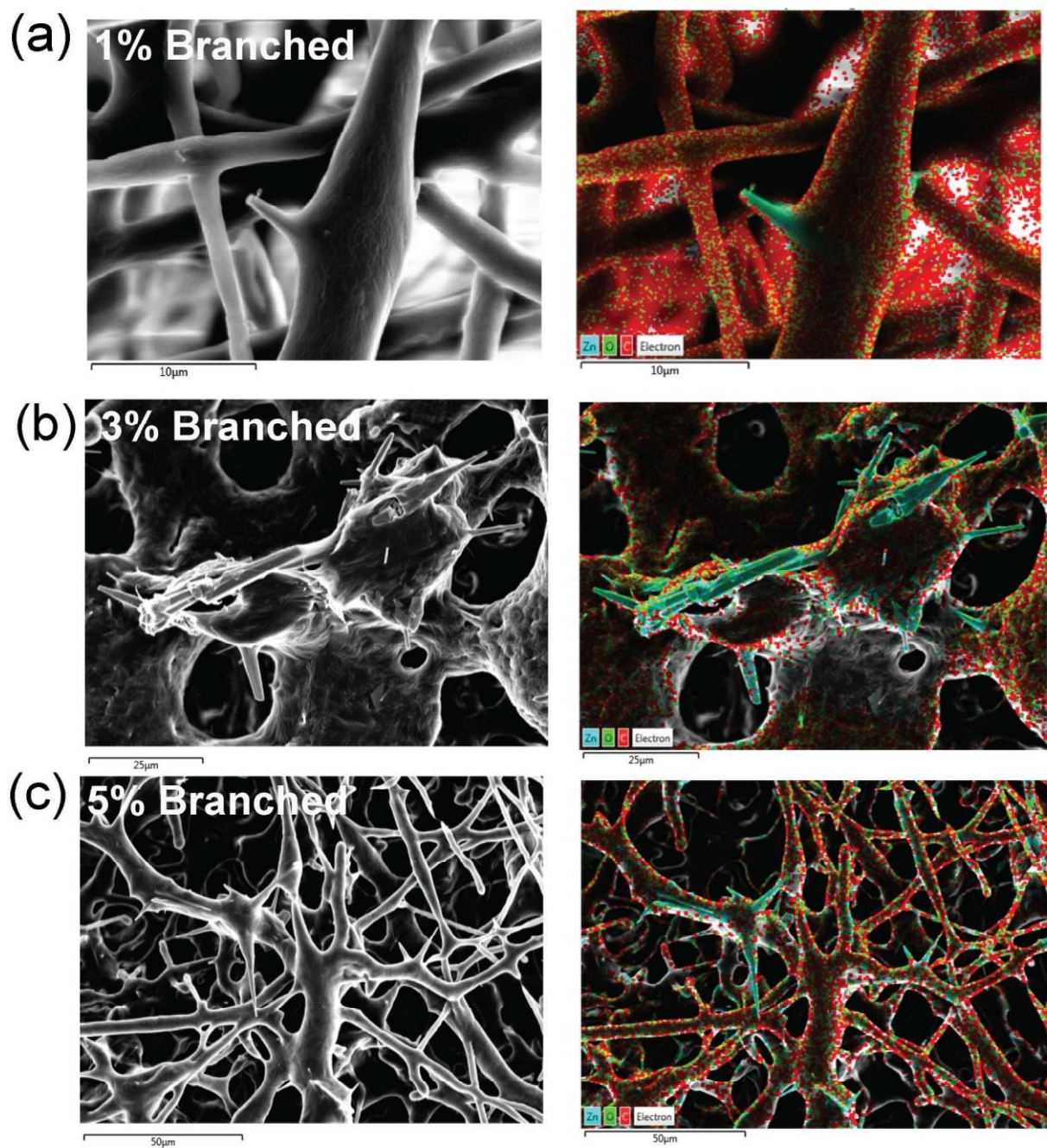


Figure S3. EDAX imaging of composite branched ZnO fibers. (a) 1% w/v Branched Composite (b) 3% w/v Branched Composite (c) 5% w/v Branched Composite

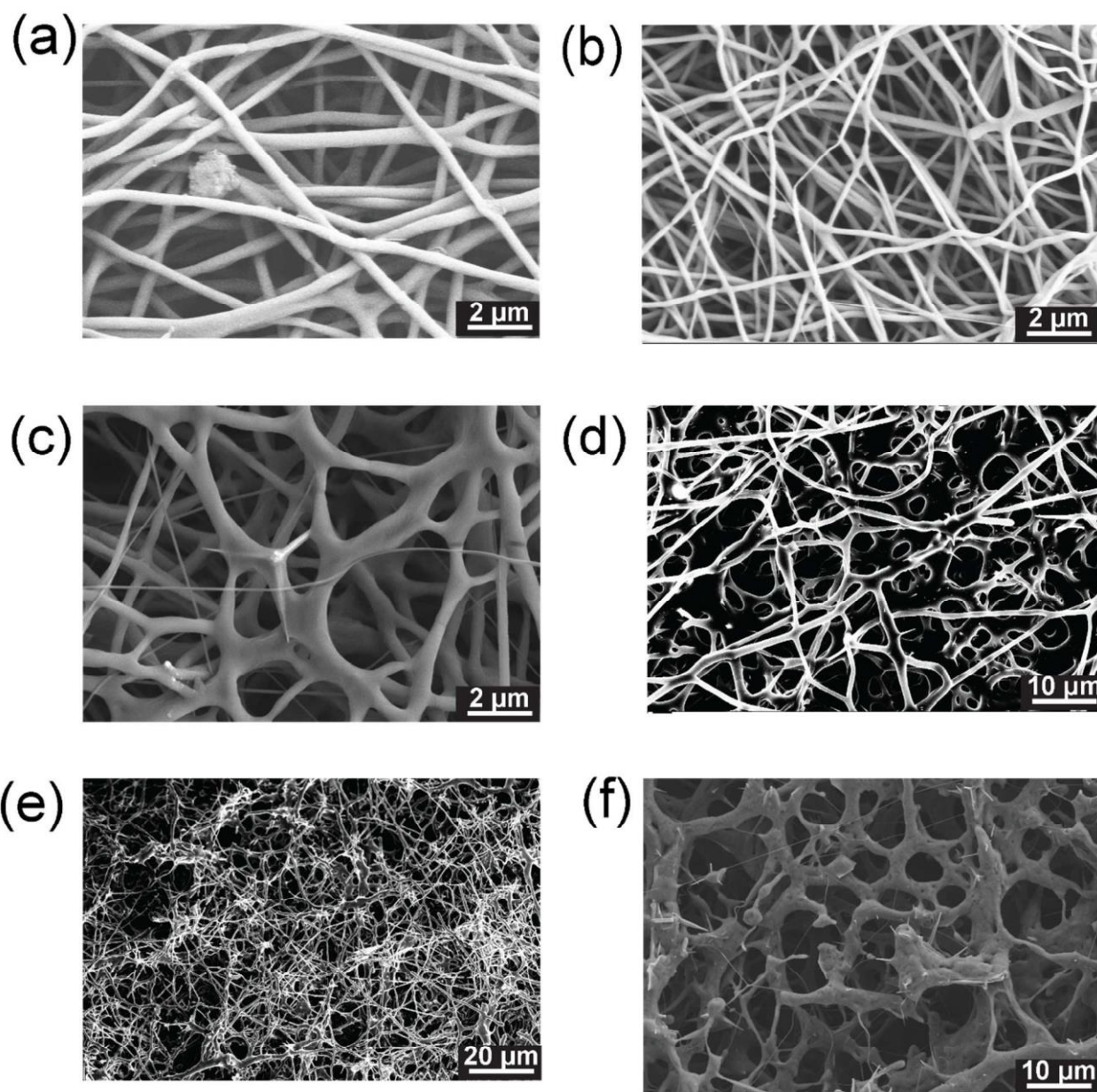


Figure S4: Low Magnification SEM image of engineered membranes. (a, b) PCL fiber morphology (c,d) 3% (w/v) branched particles (e,f) 5% (w/v) branched particles

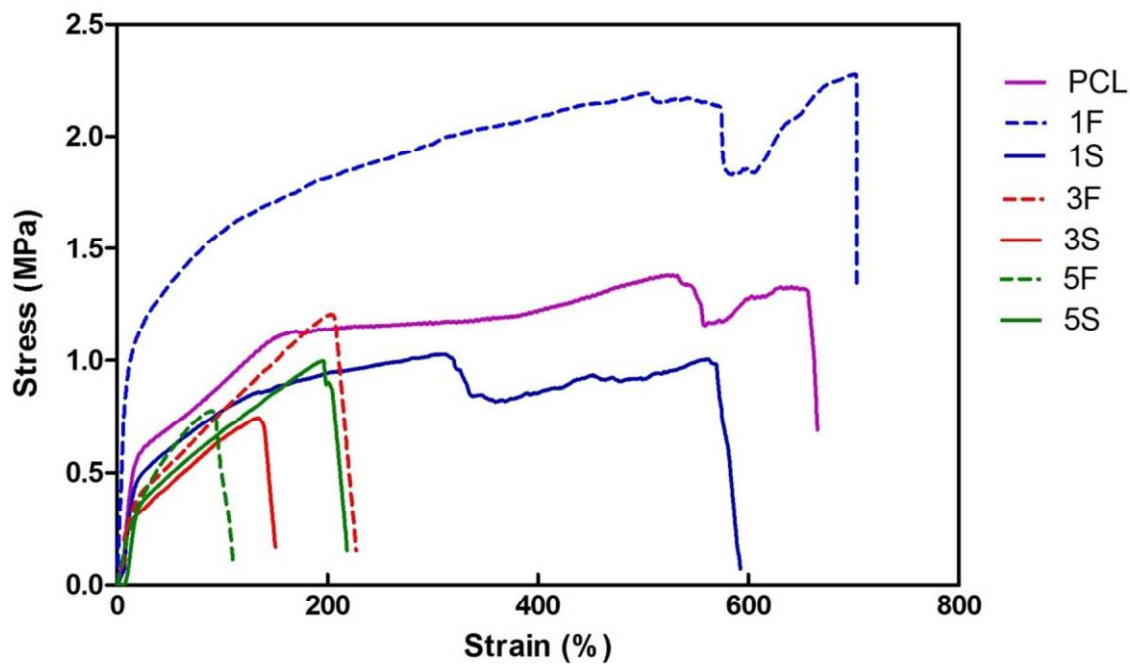


Figure S5: Stress-Strain curve. Tested scaffolds with varying particle concentrations and shape tested (branched versus spherical ZnO particles).

Supplementary References:

1. Mishra, Y. K.; Kaps, S.; Schuchardt, A.; Paulowicz, I.; Jin, X.; Gedamu, D.; Freitag, S.; Claus, M.; Wille, S.; Kovalev, A.; Gorb, S. N.; Adlung, R. *Part. Part. Syst. Charact.* 2013, 30, (9), 775-783.

7. Multi-functional Spiropyran based Polymer Composites

The subsequent reports are dedicated to studying spiropyran as a multi-functional component in different polymer matrices. An effortless method of producing self-reporting material was introduced and verified in the succeeding three articles.

Light, Force, and Heat: A Multi-Stimuli Composite that Reveals its Violent Past: In this first article, spiropyran as a particle filler in a PTU based polymer composite was tested for its response to various stimuli. For optical and mechanical reinforcement T-ZnO was employed. This helped in obtaining optimum working conditions for different applications. Contents of this article are adapted with permission from “S. Shree, M. Schulz-Senft, N. H. Alsleben, Y. K. Mishra, A. Staubitz, R. Adelung *ACS Applied Materials & Interfaces*, **2017** 9, 38000”. Copyright 2017 American Chemical Society

Mechanochromic Matrix Predicts Impact Induced Damage in a Reinforced Polymer Composite: The second article deals with self-reporting mechanochromic glassfiber reinforced polymer composite with two different matrices. During the compatibility tests polymer matrix was observed to influence the switching behavior of spiropyran. This article is under revision for a publication in *Materials Horizons*.

Spiropyran based Smart Composites: Memorizing Polymer with Enhanced Molecular Switches: The third article of this section verifies thermochromic properties of spiropyran as an additive in PTU in turn establishing a polymer composite that can be utilized as a temperature sensor. Contents of this article are adapted from S. Shree, M. Schulz-Senft, X. Jin, Y.K. Mishra, A. Staubitz, R. Adelung, *In: Sontea V., Tiginyanu I. (eds) 3rd International Conference on Nanotechnologies and Biomedical Engineering. IFMBE Proceedings*, **2016**, 55, Springer, Singapore

Personal contributions in the following articles:

- Designing the multi-stimuli experiments
- Fabrication all the polymer comosite samples
- Multi-stimuli investigations of the polymer composites
- Data analyses and manuscript preparation

Light, Force, and Heat: A Multi-Stimuli Composite that Reveals its Violent Past

Sindu Shree,^{*,†} Mathias Schulz-Senft,[‡] Nils H. Alsleben,[†] Yogendra Kumar Mishra,^{*,†} Anne Staubitz,^{*,‡,§,||} and Rainer Adelung^{*,†}

[†]Institute for Materials Science, Functional Nanomaterials, Kiel University, Kaiserstr. 2, D-24143 Kiel, Germany

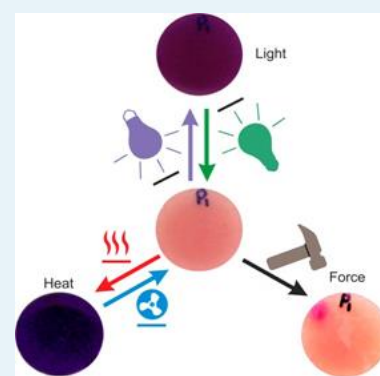
[‡]Otto-Diels-Institute for Organic Chemistry, Kiel University, Otto-Hahn-Platz 4, D-24118 Kiel, Germany

[§]Institute for Organic and Analytical Chemistry, University of Bremen, Leobener Str. 7, NW2 C, 28359 Bremen, Germany

^{||}MAPEX Center for Materials and Processes, University of Bremen, Bibliothekstraße 1, Bremen 28359, Germany

* Supporting Information

ABSTRACT: A self-reporting polythiourethane/tetrapodal-ZnO (PTU/T-ZnO) composite is produced using spiropyran as an additive at a concentration as low as 0.5 wt %. Exposure to heat, UV light and mechanical force caused the spiropyran to undergo reversible isomerization indicated by a reversible color change. The studies have been conducted with a constant spiropyran concentration at 0.5 wt %, meanwhile varying the T-ZnO concentration from 0 to 7.5 wt %. The tetrapodal ZnO served as a prism: the light scattering effect of T-ZnO created a visual impression of uniform color distribution. The interconnected network of the tetrapodal of ZnO embedded in the PTU matrix enhanced the mechanical stability of the polymer leading to high impact resistance up to ~232 kPa. PTU/spiropyran also emerged as a possible thermal sensing coating, due to its temperature sensitivity. Due to the broad green luminescence band (~535 nm) in T-ZnO, the colored merocyanine form which absorbs in this region of the spectrum switches back to spiropyran at this wavelength. High concentrations of T-ZnO were shown to reduce the effect one of the switching triggers i.e., ultraviolet light. Using this property of T-ZnO it was possible to achieve a switchable system with the possibility of separating the stimuli.



KEYWORDS: Self-reporting spiropyran switch, merocyanine (MC), polythiourethane (PTU), tetrapodal-zinc oxide (T-ZnO), photochromic, thermochromic and mechanochromic properties

1. INTRODUCTION

Self-reporting materials are capable of showing a measurable, often visible indication of the conditions they have been subjected to. Spiropyran is a molecular switch that undergoes a reversible molecular transformation to a merocyanine (MC) form in response to different stimuli such as mechanical stress,^{1–4} light,⁵ and heat⁶ and thereby showing a color change.^{7,8} As the intensity of the color is linked to the amount of active molecules present, spiropyran should be an ideal self-reporting material.^{9,10} Several self-assembly, self-reporting materials and optical sensors based on spiropyran have been successfully produced.^{11–15} In most of such systems, the spiropyran is either covalently linked to a polymer chain,^{16–18} or grafted on metallic surfaces.^{19–22} Most known systems of spiropyran as a mechanical stress indicator require its covalent

incorporation into the main chain or as cross-links of the polymer.^{23–27} This results in long synthesis routes from commercially available starting materials to the final product, thus complicating the scale-up process.^{1,5} There have been examples of studies on the mechanical sensitivity of spiropyran derivatives in crystal form, illustrating mechanochromic switching under high hydrostatic pressure.^{28–32} This implies that spiropyran can be used as an additive in the polymer composite system and would provide a more cost-effective solution.^{33–35}

Received: July 3, 2017

Accepted: October 2, 2017

Published: October 2, 2017

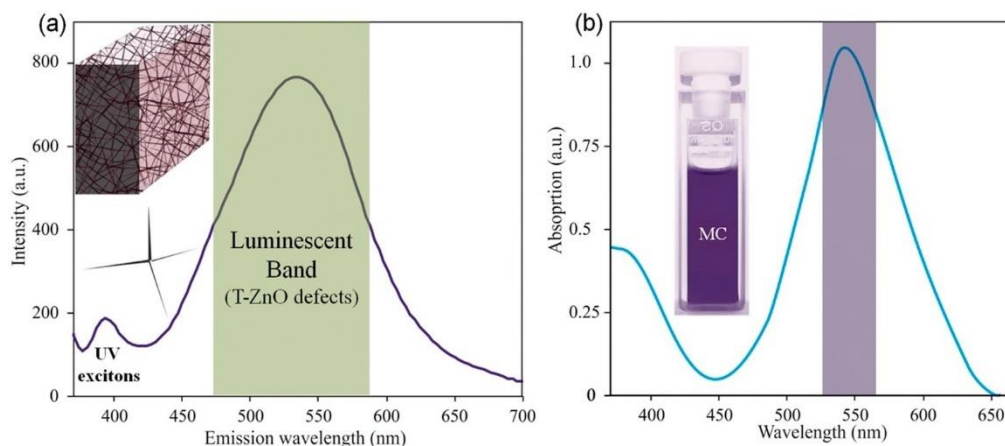


Figure 1. Sketch of (a) a PL spectrum of PDMS/T-ZnO composite and (b) an absorption spectrum of MC, which shows the ring opening reaction of spiropyran upon UV light irradiation (365 nm) to the open MC form.

Photoinduced mechanical switching of spiropyran in a composite system has been demonstrated in poly(ethyl methacrylate-co-methyl acrylate) (PEMMA) films.³⁶ These films were produced by blending 3 wt % of spiropyran, and the stiffness of the material was altered by the photoinduced switching. However, mechanoswitching has not yet been demonstrated.³⁶ In order to use spiropyran as sensor for mechanical stress, it is crucial to reduce the weight fraction of spiropyran to an absolute minimum such that the physical and chemical properties of the polymer matrix remain uninfluenced. Applications involving stress indicators used as coatings, must withstand exposure to sunlight.^{36,37} As several stimuli induce switching in spiropyran, for outdoor applications it is substantial to separate the stimuli. Such stress sensitive coatings should not switch due to UV irradiation. To create stimuli separation, the presented research uses tetrapodal zinc oxide (T-ZnO) as an additional filler. ZnO is an n-type inorganic semiconductor with a direct wide band gap of ~ 3.3 eV at 300 K and exhibits a blue-green luminescence at room temperature and can be efficiently used for engineering different properties of the polymer based composites, e.g., optical, mechanical, electrical, wettability, etc.³⁸⁻⁴⁵ For example, in the PDMS/T-ZnO composite system, where the polymer matrix is highly cross-linked, T-ZnO exhibits a strong defect mediated green emission (520–570 nm) under UV irradiation.^{40,46} The representative images for the T-ZnO based PDMS composite and corresponding

photoluminescence (PL) spectrum are schematically shown in Figure 1a.^{40,47} The PL emission around 380 nm corresponds to bandgap exciton emission from T-ZnO, however the broad green emission band is mainly the contribution from different types of defects such as zinc interstitials, oxygen vacancies, etc. present in the T-ZnO.⁴⁰ At high filling fractions of T-ZnO, the intensity of green PL emission with respect to exciton increases. Therefore, a defined amount of T-ZnO could be used for required luminescence features in a polymer composite. In the present work composites with merely 3.5–7.5 wt % T-ZnO have been fabricated for the accessibility of the broad green PL band. The open form that is merocyanine (Figure 1b) which has a strong absorption peak in the visible region (550–570 nm) closes to the spiropyran form under green light illumination.^{8,9,16} The defects present in ZnO induce green emissions under UV irradiation^{45,48,49} and this should accelerate the switching of the merocyanine form back to the spiropyran, thus shifting the photostationary equilibrium toward the spiropyran form. In addition, the tetrapodal structure of T-ZnO forms an interconnected 3D network thus increasing the overall mechanical stability of the polymer matrix.^{47,50-53} The composite samples presented here were prepared with a commercially bought polythiourethane (PTU) kit. This kit contains pentaerythritol tetrakis(3-mercaptopropionate) (PETMP) and hexamethylene diisocyanate (HDI) monomers.^{50,52} The monomers were mixed and polymerized in a solvent-free

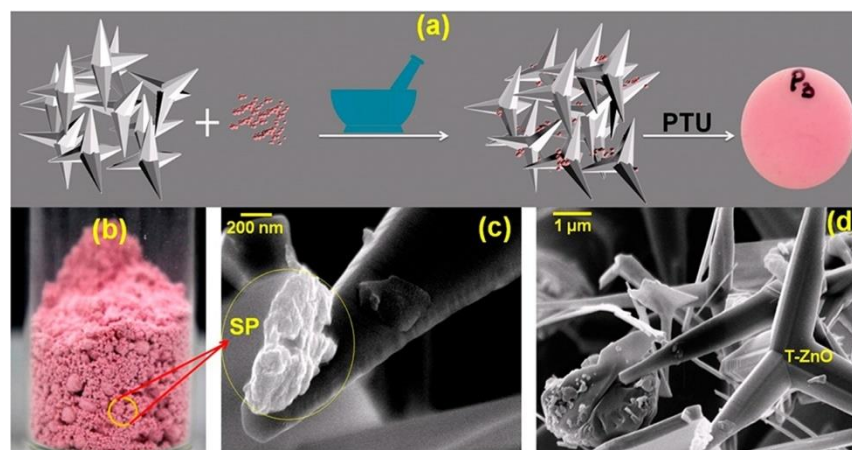


Figure 2. Schematic in (a) is a pictorial representation of the sample preparation method. Digital camera image (right panel in a) of a representative polymer composite after dispersion and polymerization. (b) Digital camera image of the mixture of T-ZnO and spiropyran before dispersing into the PTU matrix. (c) and (d) SEM micrographs at high and low magnifications corresponding to the powdered T-ZnO and spiropyran mixture.

polyaddition reaction with negligible shrinking.⁵² Because of the highly cross-linking PETMP component and the linear HDI component, the PTU uniquely possesses both, thermo-set and thermoplastic properties. PTU is an ideal matrix for coatings, because it is stable up to 250 °C and it is relatively chemically inert.⁵⁰ In a two component composite, T-ZnO was used to enhance the mechanical stability of the PTU matrix which led to a high impact resistance.^{50–52}

Table 1. Abbreviations and the Details on the Varying Concentration of T-ZnO and Spiropyran in PTU

sample name	total additives in PTU (wt %)	T-ZnO in PTU (wt %)	spiropyran in PTU (wt%)
SP	0.5	0	0.5
P1	1	0.5	0.5
P2	2	1.5	0.5
P3	4	3.5	0.5
P4	8	7.5	0.5

Here we present the first example of a polymer/ceramic composite, which acts as a sensor to impact pressure, temperature and UV irradiation by a visible color change. The photoinduced switching of spiropyran was altered successfully by the addition of T-ZnO, while the mechanically induced switching was maintained. In addition, this is the first report on the mechanically induced switching of spiropyran in a polymer composite. In

the chosen three-component system PTU/T-ZnO/spiropyran, the mechanochromic sensor is the most expensive component. Reducing the weight fraction of spiropyran to 0.5 wt % offers the production feasibility of these composites at a larger scale. In previous reports, spiropyran has been used as an initiation center from which polymerization in two directions has been performed. Well known examples include PMA,⁵⁴ PMMA⁵⁵ (which were polymerized using ATRP) or PLA¹⁴ (which has been performed with ring opening polymerization). In these examples, the spiropyran content by weight was ca. 0.2 wt %, ca. 0.1 wt %, or 0.04–0.43 wt %, respectively.¹⁴ However, it must not be overlooked that the covalent linking of the spiropyran in the main chain of the polymer adds reaction steps and thus involves additional costs. In context to industry level productions, the presented strategy will save the fabrication costs which is the main motivation of the study here.

2. EXPERIMENTAL SECTION

1,3,3-Trimethyl-2-methyleneindoline was purchased from SigmaAldrich Co. (Aldrich, 97%), 2-hydroxy-5-nitrobenzaldehyde was purchased from TCI Co. (>97%) and ethanol was purchased from Acros(anhydrous, ≥ 99.5%, stored over molecular sieves). All reagents were used without further purification. The spiropyran dye (SP) was synthesized as follows. 1,3,3-Trimethyl-2-methyleneindoline (5.20 g, 30.0 mmol) and 2-hydroxy-5-nitrobenzaldehyde (5.01 g, 30.0 mmol)

were dissolved in EtOH (350 mL) and heated to 78 °C for 6 h. Then the reaction mixture was cooled to -25 °C and the crystallized product was obtained after filtration as a green powder (7.69 g, 23.8 mmol, 79%). The highly cross-linked polythiourathane (PTU) was produced by combining two components, pentaerythritol tetrakis(3mercaptopropionate) (PETMP) and hexamethylene diisocyanate (HDI). These were procured from FPT Fluid- & Prozesstechnik GmbH. The NMR studies of the as purchased components revealed that the PETMP and HDI were >95% pure. The used abbreviations and analytical equipment have listed at text page in Supporting Information. The molecular structures of 1,3,3-Trimethyl-2-methyleneindoline compound and PTU polymer are given at the materials page in Supporting Information. The plotted NMR spectra corresponding to materials under different conditions are shown in Supporting Information (SI) Figures S1–S4. The tetrapodal zinc oxide (T-ZnO) powder was produced by the flame transport synthesis method (FTS).^{18,20} T-ZnO and the spiropyran were ground together with a mortar and pestle (Figure 2a). This powdered mixture was then dispersed by hand into the first component of PTU, the PETMP (4.17 g, 8.50 mmol). The prepared mixture was degassed in a desiccator to remove all the remaining air bubbles for 10 min. To this PETMP blend, the second component, HDI (5.83 g, 34.6 mmol) was added, mixed well and degassed. The Spiropyran did not dissolve in the mixture, behaving like a typical additive in the polymer composite system. Finally, this mixture of components was poured into silicone molds to fabricate pellet shaped samples with a diameter of 15 mm (the panel on the far right in Figure 2a). The molds were placed in an oven at 80 °C for 3 h. The PTU formed due to the polyaddition reaction between PETMP and HDI.

In all the samples, the concentration of spiropyran was kept constant at 0.5 wt % with respect to weight of PTU and the concentration of T-ZnO in PTU was varied from 0 wt % to 7.5 wt %. The details of all the fabricated samples are given in Table 1. All samples were prepared in a chemical fume hood with a UV shielding door under identical experimental conditions. Photochromic, thermochromic and mechanophoric tests were performed in a dark room to avoid accidental switching.

The “Hammer test” test (schematic is given in Supporting Information, SI Figure S5) involved a hammer weighing 2.141 kg with a hinge at its base falling freely on the samples. The test was repeated until a color change was observed. The force required to damage the system was determined by the number of hits needed to cause a color change from orange to purple. The impact force was calculated using the following equation $F = m \cdot g \cdot \sin \theta \cdot h = m \cdot g \cdot h / l$ where F is Force, m is weight of the hammer head, g is acceleration due to gravity, h is height of fall, and l is length of the hammer. The force per impact was calculated to be 3.63 N. Pressure per impact was calculated using $P = F/a$ where a is the area of impact or point of contact. The measured area of impact was $1.53 \times 10^{-4} \text{ m}^2$, hence pressure per impact was 24 kPa.

3. RESULTS AND DISCUSSION

The ZnO (including the tetrapods used) is known to be very stable and is a nonreactive semiconductor in solid state under atmospheric conditions. The spiropyran that was used in the experiments presented here is also chemically stable. Therefore, no chemical interaction is expected between the additives. However, to further reduce the interaction possibility, solvent free grinding procedure was followed for sample preparation. Since these tetrapods are solid in nature, the spiropyran is mainly coated on their surface as it is almost impossible for spiropyran to penetrate inside bulk T-ZnO. The photograph in Figure 2b shows the powdered mixture of spiropyran and T-ZnO before adding it to the PTU matrix. To understand the morphology of the hand ground additive mixture, it was studied using scanning electron microscopy (SEM). The SEM micrographs in Figure 2(c-d) corresponding to mixed powder (Figure 2b) reveal intact T-ZnO crystals with clusters of spiropyran molecules and amorphous particles around the arms of the tetrapods. In the final state of the sample (digital camera image on the right panel, Figure 2a), the color appears to be quite uniform. Due to the light scattering effect caused by the hexagonal wurtzite-type ZnO crystals, the spiropyran visually appeared to be homogeneously distributed throughout the powdered mixture.³⁹

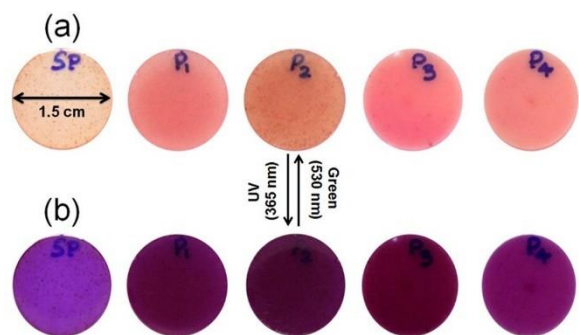


Figure 3. (a) The polymer composites, SP, P1, P2, P3, and P4 before UV irradiation, the composites appear yellow-orange in color. (b) The photochromic response of polymer composites was analyzed by irradiating the samples with UV light (365 nm) for 30 s. The reversibility of the isomerization was verified by switching the samples back to their original form with a green light (520–530 nm) irradiation for 30 s. All the images were taken using a white standard for white balancing the camera.

The photochromic activity of spiropyran in the polymer composite was studied in a sample sequence, i.e., SP, P1, P2, P3, and P4 were subjected to UV irradiation for 30 s (central wavelength = 360–370 nm), (Figure 3a), and were switched back with green light (central wavelength = 520–530 nm) irradiation for 30 s, (Figure 3b). The sample series with T-ZnO, P1, P2, P3, and P4 showed negligible agglomeration of the ZnO or spiropyran in the PTU matrix. Within the sample series, the addition of increased amounts of T-ZnO seemed to deepen the coloring before and after illumination. The variation in the color of the polymer composites suggested that in this case it might not be a straightforward isomerization from spiropyran to merocyanine. Referring to the works of Uchida et al., such color

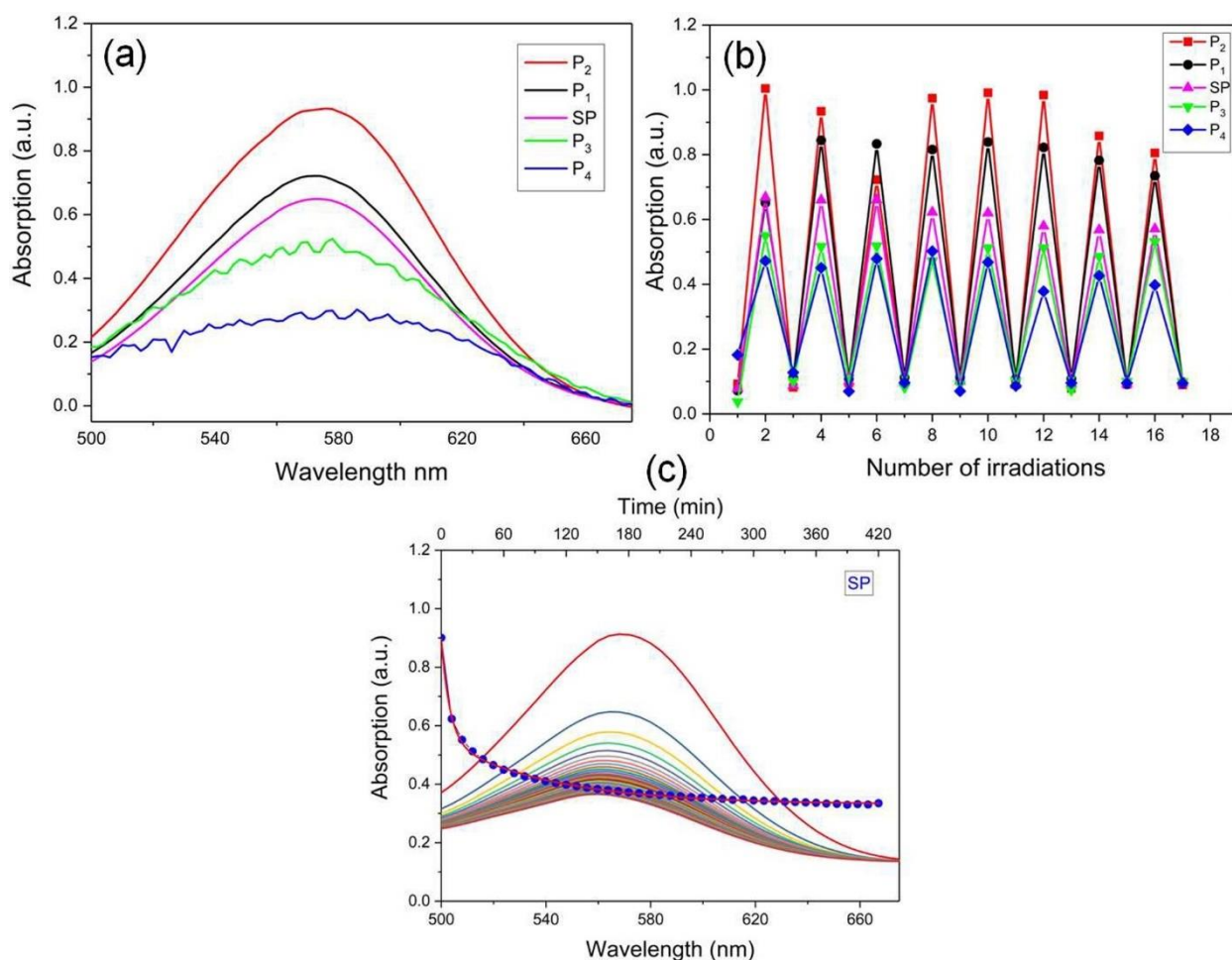


Figure 4. (a) Absorption spectra of the polymer composites SP, P1, P2, P3 and P4 after UV irradiation for 30 s. (b) Cyclic absorbance measurements of SP, P1, P2, P3 and P4 at 560–570 nm before and after UV illumination followed by green illumination for 17 irradiation series. (c) Back switching or thermal relaxation of merocyanine to spiropyran in the sample SP.

variation is observed when there is molecular stacking of the merocyanine form.⁵⁶ The observed switching in some of the samples might be between merocyanine in the form of H stacking to merocyanine in the form of J stacking.⁵⁶ Further reports underline this hypothesis, which requires more detailed analyses in this particular case.^{57,58}

Compared to the SP sample (Figure 3a, b, first on the left), the samples P1 with 0.5 wt % and P2 with 1.5 wt % of T-ZnO (2nd and third samples from left) showed a darker color. A further increase of the fraction of T-ZnO appeared to reduce the color intensity (P3 and P4, 3.5 and 7.5 wt % T-ZnO) UV/Visible spectroscopy supports this observation. Absorption spectra in the range 700–500 nm were recorded for the switched samples (Figure 4a). The samples P1 and P2 showed higher absorptions than the SP sample. The sample P4 with the highest fraction of T-ZnO exhibited the smallest absorption. The observed higher absorption in samples P1 and P2 is most likely due to the multiple reflections caused by the prism like tetrapodal ZnO structures as compared to the pure sample SP. As there is no green emission in the pure sample SP, the absorption is higher than that of samples P3 and P4. These findings validated the theory that the T-ZnO may function as a light guide for UV irradiation and that it thereby can serve to improve the photochromic switching of spiropyran. The photochromicity of spiropyran was restrained in the samples P3 and P4, this was probably due to a combination of the UV absorption of T-ZnO and its green emission. These combined effects appeared to reduce the effective photoswitching of spiropyran under UV irradiation. Despite their different photoswitching efficiencies, all samples showed a clear reversible switching with no signs of photo bleaching up to 17 irradiations (Figure 4b). The ripples observed in the spectra of the samples P3 and P4 might be an effect caused by the whispering gallery mode resonances from the hexagonal arms of ZnO tetrapods.^{59,60} For a qualitative study on the “Turn Off” mechanism of merocyanine to spiropyran, the sample SP was irradiated with UV light for 30 s and was allowed to

thermally relax to a photostationary equilibrium. Meanwhile, an absorption spectrum was recorded every 10 min, cf. Figure 4c. To follow the decay of merocyanine, the absorbance between the range 562–568 nm has been recorded and is plotted in Figure 4c. The thermal decay of merocyanine at this range follows a biexponential curve with the individual half lifetimes of $\tau_1 = 7 \text{ min } 15 \text{ s}$ and $\tau_2 = 83 \text{ min } 23 \text{ s}$. This system with the second order kinetics is similar to the solid suspension of spiropyran nanocrystals studied by Breslin et al.^{61,62} However, the total relaxation of merocyanine was not observed even after 6 h of thermal decay time, the broad peak of merocyanine can still be observed in the absorption spectra shown in Figure 4c. This is an ideal system for an indication of damage by a color change which is easily detectable even for the naked eye hours after the damage has occurred. The response of the composites with respect to mechanical force was analyzed by exposing the samples to a “Hammer test” (for more details see SI Figure S5). In this test, a hammer with a spherical shaft (tip) was allowed to fall from a defined height onto the sample (each hit generating pressure up to 24 kPa), while observing the color and other changes occurring in the sample during repeated hammering. Over several hits, a color change from yellow-orange to purple occurred, while at the same time cracks appeared. To help visualization the hammering test, a schematic representation of the color changing effect and the crack appearance in the polymer composites is shown in Figure 5a. The average impact force required to change the color of the polymer composites SP, P1, P2, P3, and P4 governed by the conservation of momentum was calculated (Supporting Information, SI Table S1) and plotted (with error bars) as shown in Figure 5b. From the plot (Figure 5b) it is clear that the force needed to cause switching of spiropyran in the sample P4 was much higher in comparison to the other samples with lower weight fraction of T- ZnO. This might be the effect of the interconnected nature of T-ZnO, higher concentration of the network of tetrapodal

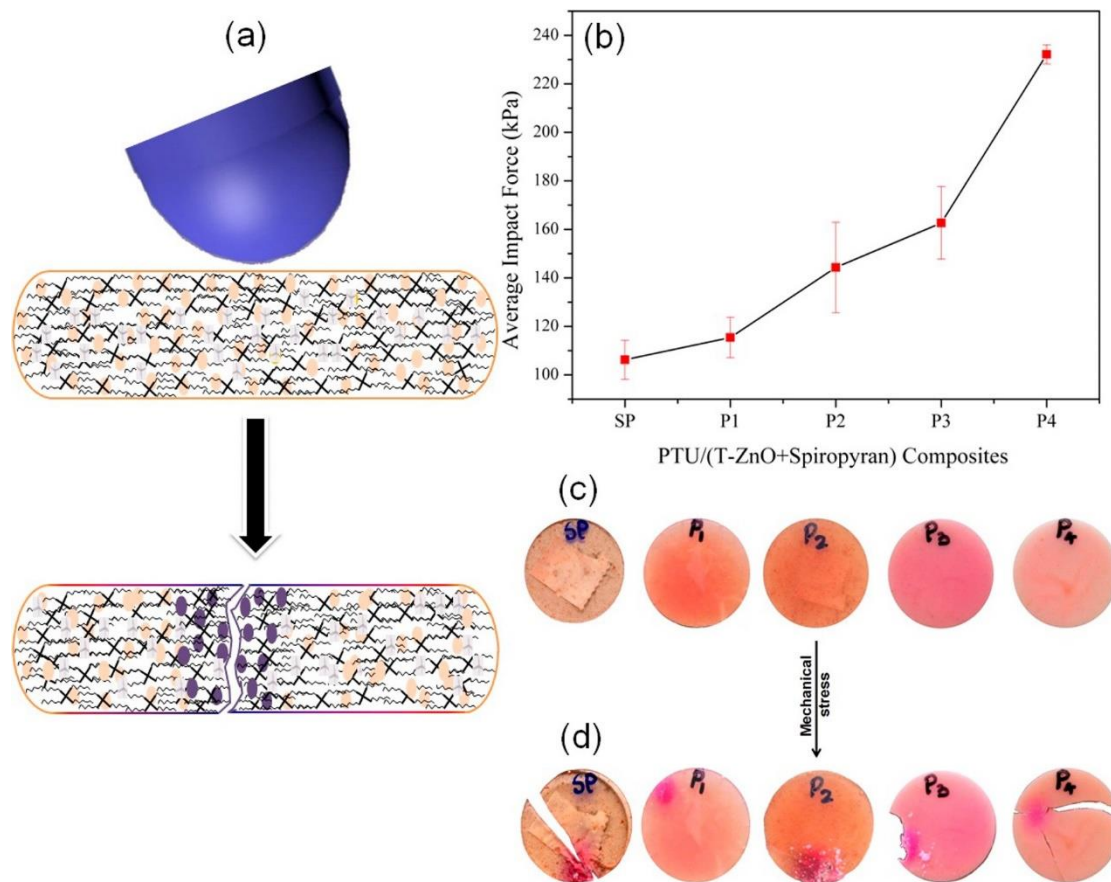


Figure 5. (a) Pictorial representation of the crack formation and the color switching in the polymer composites subjected to the “Hammer test”. (b) Plot showing the average impact force required to damage the polymer matrix causing a color change (c) Polymer composites before being subjected to the mechanical stress. (d) Polymer composites after being subjected to the “Hammer test”. The bruises caused by the high impact force of the hammer in the samples are visible as the polymer composites at the point of impact, which turned purple.

structure embedded in the polymer matrix enhanced the mechanical stability allowing the system to endure higher impact force.^{38,40,47} The digital camera pictures in Figure 5c and d demonstrate the samples before and after they were subjected to the “Hammer test”. In Figure 5d, the color change after the mechanical stress is clearly visible. In all the samples, the color change only appeared at the point of impact (POI) evidently indicating the area which underwent the high mechanical stress. The sample P1 showed a color change at the POI before the cracks appeared. The force required to cause a switch in P1 is slightly (~115 kPa) higher than for the sample SP (~106 kPa). With merely 0.5 wt % of T-ZnO in the polymer composite, P1 showed higher impact resistance and effective fatigue indication. Monitoring the samples after hammering is a challenging task. It is difficult to measure the

absorption spectra of these samples after the “Hammer Test” as the samples either have cracks or they fall apart.

In addition to the composite’s response to light and force, heat was also investigated. The effect of T-ZnO on the thermochromic activity of spiropyran was examined in detail. The samples SP, P1, P2, P3, and P4 were positioned as represented in the enclosed black frame of Figure 6 and heated on a heating plate. The red frame encloses all the samples, which were heated together and held for a period of 30 s at 60, 80, 100, and 150 °C. With the exception of sample SP, which turned opaque, no polymer composites with T-ZnO showed any changes. All the samples seemed to attain a similarly colored state at each temperature.

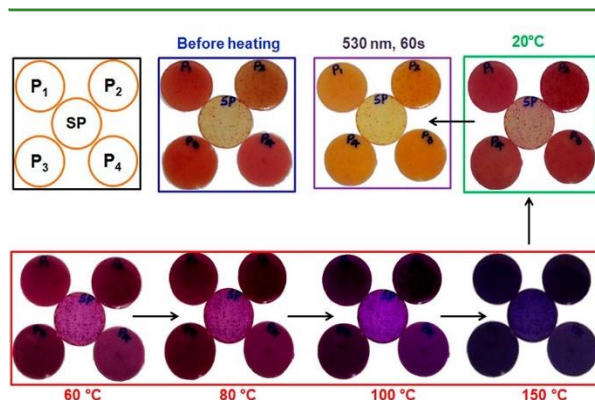


Figure 6. Schematic representation of the sample positions during the thermochromic tests for clarity. The polymer composites shown in the blue frame are the SP, P1, P2, P3 and P4 before heat treatment. The red frame shows the samples heated up to 60, 80, 100, and 150 °C and held for 30 s. The green frame presents the composites cooled to room temperature, 20 °C. The purple frame shows the cooled composites after green light irradiation (560 nm) 60 s.

The polymer composites at 150 °C displayed an intense color change. At such high temperature, the unordered polymer chains in PTU gain higher mobility increasing the free volume in the polymer matrix. With higher free volume, there is lower spatial hindrance to form merocyanine. Hence, in the red frame of Figure 6, the image captured at 150 °C illustrates that every sample reached similar dark purple colored state independent of the concentration of T-ZnO. In some cases reported in the literature, heat is used to switch the mechanically opened merocyanine back to spiropyran²⁵ and examples of inverse thermal switching of the spiropyran derivative that was used here in aqueous media have also been published before.⁶³ However, the thermodynamic equilibrium between spiropyran and the merocyanine depends mainly on two effects, the first effect comes from the functional groups of the spiropyran dye which changes the electron density in the molecule and second effect comes from the polarity of the surrounding (typically the solvent). Mostly studied mechanochromic systems consist of spiropyran in the polymer backbones whereas the system presented here can be visualized as a “frozen colloidal solution”.²⁴ The PTU matrix can be seen as solvent and due to its high polarity, merocyanine is

stabilized. The effect of inverse thermal switching of the same spiropyran dye dissolved in an aqueous media has been reported. However, the addition of T-ZnO seemed to have no particular effect on the thermochromic activity of spiropyran. To avoid decomposition of PTU, the samples were cooled together from 150 °C to room temperature (20 °C). As seen in the image enclosed by the green frame in Figure 6, all the polymer composites switched back to almost their preheated state. Whereas heating caused no damage to the switches, the samples did not completely recover their original state after cooling. The cooled samples were irradiated with green light (530 nm) for 60 s to prove that the remaining merocyanine present can be switched back to spiropyran.

4. CONCLUSIONS

In summary, our research findings demonstrate a simple dispersion based method to produce multistimuli composite materials with potential real life applications such as stress reporting sensor, photochromic and thermochromic coating etc. It consists of a polymer matrix, polythiourethane (PTU), in which tetrapodal ZnO particles are dispersed as a solid support. The most important component of the system studied here, responsible for the multistimuli activity, is spiropyran. Spiropyran was successfully utilized as a thermo-, photo-, and mechanochromic switch as a composite at a low concentration of 0.5 wt % with respect to the polymer matrix. This is the first example of mechanochromism of spiropyran in a polymer composite system, without covalently binding to the polymer matrix. Additionally, it was possible to tune the response of spiropyran to UV light with the assistance of T-ZnO. Both enhancing and suppressing the photochromism was achieved by merely varying the concentration of T-ZnO, while keeping the thermo- and mechanical switching behavior of spiropyran unaffected. At low concentrations, T-ZnO works as a light guide for the UV light, because of its crystalline facets. High concentrations of T-ZnO lead to a decrease in the photoswitching of spiropyran, which is a result of the combination of its UV absorption and the broad green emission. Additionally, the T-ZnO increased

the impact resistivity of the PTU/SP composites. The switching under stress and heat of spiropyran were proven independent from the fraction of T-ZnO. This successful stimuli separation by a nonstandard integration of self-reporting ability in polymer composites opens the door for numerous outdoor applications.

■ ASSOCIATED CONTENT

* Supporting Information

The Supporting Information is available free of charge on the ACS Publications website at DOI: 10.1021/acsami.7b09598.

Used abbreviations and analytical equipment (Text); Material structural formula and details (Materials); Plotted NMR spectra of different materials analytical plotted NMR spectra under different conditions (Figures S1–S4); Hammer test setup (Figure S5); Average impact forces required to damage the samples (Table S1) (PDF)

■ AUTHOR INFORMATION

Corresponding Authors

*(S.S.) E-mail: sisi@tf.uni-kiel.de.

*(Y.K.M.) E-mail: ykm@tf.uni-kiel.de.

*(A.S.) E-mail: staubitz@uni-bremen.de.

*(R.A.) E-mail: ra@uni-kiel.de.

ORCID 

Yogendra Kumar Mishra: 0000-0002-8786-9379

Author Contributions

The manuscript was written through contributions of all authors. All authors have given approval to the final version of the manuscript.

Notes

The authors declare no competing financial interest.

■ ACKNOWLEDGMENTS

This project was supported by the Special Research Area 677 “Function by Switching” project C14 of the Deutsche Forschungsgemeinschaft (DFG). The Institutional Strategy of the University of Bremen, funded by the German Excellence Initiative, has supported this research. The authors thank Dr. Viktor Hrkac for the fruitful feedback and discussions.

■ REFERENCES

- (1) Caruso, M. M.; Davis, D. A.; Shen, Q.; Odom, S. A.; Sottos, N. R.; White, S. R.; Moore, J. S. Mechanically-Induced Chemical Changes in Polymeric Materials. *Chem. Rev.* 2009, 109 (11), 5755–5798.
- (2) Schulz-Senft, M.; Lipfert, M.; Staubitz, A. Mechanopolymerchemie. *Chem. Unserer Zeit* 2014, 48 (3), 200–214.
- (3) Mo, S.; Meng, Q.; Wan, S.; Su, Z.; Yan, H.; Tang, B. Z.; Yin, M. Tunable Mechanoresponsive Self-Assembly of an Amide-Linked Dyad with Dual Sensitivity of Photochromism and Mechanochromism. *Adv. Funct. Mater.* 2017, 27 (28), 1701210.
- (4) Gossweiler, G. R.; Brown, C. L.; Hewage, G. B.; Sapiro-Gheiler, E.; Trautman, W. J.; Welshofer, G. W.; Craig, S. L. Mechanochemically Active Soft Robots. *ACS Appl. Mater. Interfaces* 2015, 7 (40), 22431–22435.
- (5) Zhang, J.; Zou, Q.; Tian, H. Photochromic Materials: More Than Meets The Eye. *Adv. Mater.* 2013, 25 (3), 378–399.
- (6) Funasako, Y.; Takaki, A.; Inokuchi, M. Photo-, Thermo-, and Piezochromic Nafion Film Incorporating Cationic Spiropyran. *Chem. Lett.* 2016, 45 (12), 1397–1399.
- (7) Seefeldt, B.; Kasper, R.; Beining, M.; Mattay, J.; Arden-Jacob, J.; Kemnitzer, N.; Drexhage, K. H.; Heilemann, M.; Sauer, M. Spiroprans as Molecular Optical Switches. *Photochem. Photobiol. Sci.* 2010, 9 (2), 213–220.
- (8) Schulz-Senft, M.; Gates, P. J.; Sönnichsen, F. D.; Staubitz, A. Diversely Halogenated Spiroprans - Useful Synthetic Building Blocks for a Versatile Class of Molecular Switches. *Dyes Pigm.* 2017, 136, 292–301.
- (9) Klajn, R. Spiropyran-Based Dynamic Materials. *Chem. Soc. Rev.* 2014, 43 (1), 148–184.
- (10) Radu, A.; Byrne, R.; Alhashimy, N.; Fusaro, M.; Scarmagnani, S.; Diamond, D. Spiropyran-Based Reversible, Light-Modulated Sensing with Reduced Photofatigue. *J. Photochem. Photobiol., A* 2009, 206 (2–3), 109–115.
- (11) Malic, E.; Weber, C.; Richter, M.; Atalla, V.; Klamroth, T.; Saalfrank, P.; Reich, S.; Knorr, A. Microscopic Model of the Optical Absorption of Carbon Nanotubes Functionalized with Molecular Spiropyran Photoswitches. *Phys. Rev. Lett.* 2011, 106 (9), 97401.

- (12) Kinashi, K.; Nakamura, S.; Imamura, M.; Ishida, K.; Ueda, Y. The Mechanism for Negative Photochromism of Spiropyran in Silica. *J. Phys. Org. Chem.* 2012, 25 (6), 462–466.
- (13) Araujo, J. V.; Rifaie-Graham, O.; Apebende, E. A.; Bruns, N. Chapter 11. Self-Reporting Polymeric Materials with Mechanochromic Properties. In *Bio-inspired Polymers*; Royal Society of Chemistry: Cambridge, 2016; pp 354–401.
- (14) Peterson, G. I.; Larsen, M. B.; Ganter, M. A.; Storti, D. W.; Boydston, A. J. 3D-Printed Mechanochromic Materials. *ACS Appl. Mater. Interfaces* 2015, 7 (1), 577–583.
- (15) Nam, Y.-S.; Yoo, I.; Yarimaga, O.; Park, I. S.; Park, D.-H.; Song, S.; Kim, J.-M.; Lee, C. W.; Sun, L.-D.; Zhang, Y.-W.; Yan, C.-H. Photochromic Spiropyran-Embedded PDMS for Highly Sensitive and Tunable Optochemical Gas Sensing. *Chem. Commun.* 2014, 50 (32), 4251–4254.
- (16) Bonafacio, J.; Tse, M.-L. V.; Pun, C.-F. J.; Cheng, X.; Chan, W. K. E.; Boersma, A.; Tam, H.-Y. Characterization of Spirooxazine and Spiropyran Hosted in Poly (Methyl Methacrylate) for Germicidal UV Source Indicator Application. *Opt. Photonics J.* 2013, 3 (7A), 11–16.
- (17) Lee, C. K.; Davis, D. A.; White, S. R.; Moore, J. S.; Sottos, N. R.; Braun, P. V. Force-Induced Redistribution of a Chemical Equilibrium. *J. Am. Chem. Soc.* 2010, 132 (45), 16107–16111.
- (18) Huang, C.-Q.; Wang, Y.; Hong, C.-Y.; Pan, C.-Y. SpiropyranBased Polymeric Vesicles: Preparation and Photochromic Properties. *Macromol. Rapid Commun.* 2011, 32 (15), 1174–1179.
- (19) Xie, X.; Mistlberger, G.; Bakker, E. Reversible Photodynamic Chloride-Selective Sensor Based on Photochromic Spiropyran. *J. Am. Chem. Soc.* 2012, 134 (41), 16929–16932.
- (20) Gelebart, A. H.; Jan, M. D.; Varga, M.; Konya, A.; Vantomme, G.; Meijer, E. W.; Selinger, R. L. B.; Broer, D. J. Making Waves in a Photoactive Polymer Film. *Nature* 2017, 546 (7660), 632–636.
- (21) Wan, S.; Zheng, Y.; Shen, J.; Yang, W.; Yin, M. On-off-on” Switchable Sensor: A Fluorescent Spiropyran Responds to Extreme pH Conditions and Its Bioimaging Applications. *ACS Appl. Mater. Interfaces* 2014, 6 (22), 19515–19519.
- (22) Binil, I. I.; Mahima, S.; Thomas, K. G. Light-Induced Modulation of Self-Assembly on Spiropyran-Capped Gold Nanoparticles: A Potential System for the Controlled Release of Amino Acid Derivatives. *J. Am. Chem. Soc.* 2003, 125 (24), 7174–7175.
- (23) Belhboub, A.; Boucher, F.; Jacquemin, D. Grafting Spiropyran Molecular Switches on TiO₂: A First-Principles Study. *J. Phys. Chem. C* 2016, 120 (32), 18281–18288.
- (24) Davis, D. A.; Hamilton, A.; Yang, J.; Cremar, L. D.; Van Gough, D.; Potisek, S. L.; Ong, M. T.; Braun, P. V.; Martínez, T. J.; White, S. R. Force-Induced Activation of Covalent Bonds in Mechanoresponsive Polymeric Materials. *Nature* 2009, 459 (7243), 68–72.
- (25) Wan, S.; Ma, Z.; Chen, C.; Li, F.; Wang, F.; Jia, X.; Yang, W.; Yin, M. A Supramolecule-Triggered Mechanochromic Switch of Cyclodextrin-Jacketed Rhodamine and Spiropyran Derivatives. *Adv. Funct. Mater.* 2016, 26 (3), 353–364.
- (26) Florea, L.; Diamond, D.; Benito-Lopez, F. Photo-Responsive Polymeric Structures Based on Spiropyran. *Macromol. Mater. Eng.* 2012, 297 (12), 1148–1159.
- (27) Li, M.; Liu, W.; Zhang, Q.; Zhu, S. Mechanical Force Sensitive Acrylic Latex Coating. *ACS Appl. Mater. Interfaces* 2017, 9 (17), 15156–15163.
- (28) Wang, Y.; Tan, X.; Zhang, Y.-M.; Zhu, S.; Zhang, L.; Yu, B.; Wang, K.; Yang, B.; Li, M.; Zou, B. Dynamic Behavior of Molecular Switches in Crystal Under Pressure and Its Reflection on Tactile Sensing. *J. Am. Chem. Soc.* 2015, 137 (2), 931–939.
- (29) Rosario, R.; Gust, D.; Hayes, M.; Jahnke, F.; Springer, J.; Garcia, A. A. Photon-Modulated Wettability Changes on Spiropyran-Coated Surfaces. *Langmuir* 2002, 18 (21), 8062–8069.
- (30) Choi, C. L.; Koski, K. J.; Olson, A. C. K.; Alivisatos, A. P. Luminescent Nanocrystal Stress Gauge. *Proc. Natl. Acad. Sci. U. S. A.* 2010, 107 (50), 21306–21310.
- (31) Choi, C. L.; Li, H.; Olson, A. C. K.; Jain, P. K.; Sivasankar, S.; Alivisatos, A. P. Spatially Indirect Emission in a Luminescent Nanocrystal Molecule. *Nano Lett.* 2011, 11 (6), 2358–2362.
- (32) Choi, C. L.; Koski, K. J.; Sivasankar, S.; Alivisatos, A. P. StrainDependent Photoluminescence Behavior of CdSe/CdS Nanocrystals with Spherical, Linear, and Branched Topologies. *Nano Lett.* 2009, 9 (10), 3544–3549.

- (33) Larkowska, M.; Wuebbenhorst, M.; Kucharski, S. Spirooxazine Photoisomerization and Relaxation in Polymer Matrices. *Int. J. Polym. Sci.* 2011, 2011, 627195.
- (34) Hemmer, J. R.; Smith, P. D.; Horn, M.; Alnemrat, S.; Mason, B. P.; Alaniz, J. R.; Osswald, S.; Hooper, J. P. High Strain-rate Response of Spiropyran Mechanophores in PMMA. *J. Polym. Sci., Part B: Polym. Phys.* 2014, 52 (20), 1347–1356.
- (35) Wu, Z.; Pan, K.; Lü, B.; Ma, L.; Yang, W.; Yin, M. Tunable Morphology of Spiropyran Assemblies: From Nanospheres to Nanorods. *Chem. - Asian J.* 2016, 11 (21), 3102–3106.
- (36) Samoylova, E.; Ceseracciu, L.; Allione, M.; Diaspro, A.; Barone, A. C.; Athanassiou, A. Photoinduced Variable Stiffness of SpiropyranBased Composites. *Appl. Phys. Lett.* 2011, 99 (20), 201905.
- (37) Pardo, R.; Zayat, M.; Levy, D. Reaching Bistability in a Photochromic Spirooxazine Embedded Sol-gel Hybrid Coatings. *J. Mater. Chem.* 2009, 19 (37), 6756–6760.
- (38) Mishra, Y. K.; Kaps, S.; Schuchardt, A.; Paulowicz, I.; Jin, X.; Gedamu, D.; Freitag, S.; Claus, M.; Wille, S.; Kovalev, A.; Gorb, S. N.; Adelung, R. Fabrication of Macroscopically Flexible and Highly Porous 3D Semiconductor Networks from Interpenetrating Nanostructures by a Simple Flame Transport Approach. *Part. Part. Syst. Charact.* 2013, 30 (9), 775–783.
- (39) Rodnyi, P. A.; Khodyuk, I. V. Optical and Luminescence Properties of Zinc Oxide (Review). *Opt. Spectrosc.* 2011, 111 (5), 776–785.
- (40) Jin, X.; Götz, M.; Wille, S.; Mishra, Y. K.; Adelung, R.; Zollfrank, C. A Novel Concept for Self-Reporting Materials: Stress Sensitive Photoluminescence in ZnO Tetrapod Filled Elastomers. *Adv. Mater.* 2013, 25 (9), 1342–1347.
- (41) Wang, C. H.; Liao, W. S.; Lin, Z. H.; Ku, N. J.; Li, Y. C.; Chen, Y. C.; Wang, Z. L.; Liu, C. P. Optimization of the Output Efficiency of GaN Nanowire Piezoelectric Nanogenerators by Tuning the Free Carrier Concentration. *Adv. Energy Mater.* 2014, 4 (16), 1400392.
- (42) Chang, M.; Cao, X.; Zeng, H. Electrodeposition Growth of Vertical ZnO Nanorod/Polyaniline Heterostructured Films and Their Optical Properties. *J. Phys. Chem. C* 2009, 113 (35), 15544–15547.
- (43) Song, J.; Li, J.; Li, X.; Xu, L.; Dong, Y.; Zeng, H. Quantum Dot Light-Emitting Diodes Based on Inorganic Perovskite Cesium Lead Halides (CsPbX₃). *Adv. Mater.* 2015, 27 (44), 7162–7167.
- (44) Faraji, N.; Ulrich, C.; Wolff, N.; Kienle, L.; Adelung, R.; Mishra, Y. K.; Seidel, J. Visible-Light Driven Nanoscale Photoconductivity of Grain Boundaries in Self-Supported ZnO Nano- and Microstructured Platelets. *Adv. Electron. Mater.* 2016, 2 (9), 1600138.
- (45) Janotti, A.; Van de Walle, C. G. Fundamentals of Zinc Oxide as a Semiconductor. *Rep. Prog. Phys.* 2009, 72 (12), 126501.
- (46) Diep, V. M.; Armani, A. M. Flexible Light-Emitting Nanocomposite Based on ZnO Nanotetrapods. *Nano Lett.* 2016, 16 (12), 7389–7393.
- (47) Jin, X.; Deng, M.; Kaps, S.; Zhu, X.; Holken, I.; Mess, K.; Adelung, R.; Mishra, Y. K. Study of Tetrapodal ZnO-PDMS Composites: A Comparison of Fillers Shapes in Stiffness and Hydrophobicity Improvements. *PLoS One* 2014, 9 (9), e106991.
- (48) Zeng, H.; Duan, G.; Li, Y.; Yang, S.; Xu, X.; Cai, W. Blue Luminescence of ZnO Nanoparticles Based on Non-equilibrium Processes: Defect Origins and Emission Controls. *Adv. Funct. Mater.* 2010, 20 (4), 561–572.
- (49) Kaps, S.; Bhowmick, S.; Gröttrup, J.; Hrkac, V.; Stauffer, D.; Guo, H.; Warren, O. L.; Adam, J.; Kienle, L.; Minor, A. M.; Adelung, R.; Mishra, Y. K. Piezoresistive Response of Quasi-One-Dimensional ZnO Nanowires Using an in Situ Electromechanical Device. *ACS Omega* 2017, 2 (6), 2985–2993.
- (50) Strzelec, K.; Bączek, N.; Ostrowska, S.; Wąsikowska, K.; Szyrkowska, M. I.; Grams, J. Synthesis and Characterization of Novel Polythiourethane Hardeners for Epoxy Resins. *C. R. Chim.* 2012, 15 (11), 1065–1071.
- (51) Raja, S. N.; Olson, A. C. K.; Thorkelsson, K.; Luong, A. J.; Hsueh, L.; Chang, G.; Gludovatz, B.; Lin, L.; Xu, T.; Ritchie, R. O.; Alivisatos, A. P. Tetrapod Nanocrystals as Fluorescent Stress Probes of Electrospun Nanocomposites. *Nano Lett.* 2013, 13 (8), 3915–3922.
- (52) Hölken, I.; Hoppe, M.; Mishra, Y. K.; Gorb, S. N.; Adelung, R.; Baum, M. Complex Shaped ZnO Nano- and Microstructure Based Polymer Composites: Mechanically Stable and Environmentally Friendly Coatings for Potential

- Antifouling Applications. *Phys. Chem. Chem. Phys.* 2016, 18 (10), 7114–7123.
- (53) Nasajpour, A.; Mandla, S.; Shree, S.; Mostafavi, E.; Sharifi, S.; Khalilpour, A.; Saghazadeh, S.; Hassan, S.; Mitchell, M. J.; Leijten, J.; Hou, X.; Moshaverinia, A.; Annabi, N.; Adelung, R.; Mishra, Y. K.; Shin, S. R.; Tamayol, A.; Khademhosseini, A. Nanostructured Fibrous Membranes with Rose Spike-like Architecture. *Nano Lett.* 2017, 17, 6235–6240.
- (54) Potisek, S. L.; Davis, D. A.; Sottos, N. R.; White, S. R.; Moore, J. S. Mechanophore-Linked Addition Polymers. *J. Am. Chem. Soc.* 2007, 129 (45), 13808–13809.
- (55) Beiermann, B. A.; Davis, D. A.; Kramer, S. L. B.; Moore, J. S.; Sottos, N. R.; White, S. R. Environmental Effects on Mechanochemical Activation of Spiropyran in Linear PMMA. *J. Mater. Chem.* 2011, 21 (23), 8443–8447.
- (56) Emi, U.; Reiko, A.; Yasuo, N. Switching between Solid and Liquid Phases of Spiropyran by Photochromic Reaction. *Chem. Lett.* 2014, 43 (10), 1619–1621.
- (57) Kajikawa, K.; Anzai, T.; Takezoe, H.; Fukuda, A. Noncentrosymmetric and Centrosymmetric J-Aggregation in Photomerocyanine Monolayer Studied by Second-Harmonic Generation and Absorption Spectroscopy. *Thin Solid Films* 1994, 243 (1–2), 587–591.
- (58) Kajikawa, K.; Hara, M.; Sasabe, H.; Knoll, W. J. Aggregates in a Langmuir-Blodgett Monolayer Probed by Scanning Near-Field Optical Microscopy. *Colloids Surf., A* 1997, 126 (2–3), 97–101.
- (59) Zhang, Y.; Zhou, H.; Liu, S. W.; Tian, Z. R.; Xiao, M. Second Harmonic Whispering-Gallery Modes in ZnO Nanotetrapod. *Nano Lett.* 2009, 9 (5), 2109–2112.
- (60) Reimer, T.; Paulowicz, I.; Röder, R.; Kaps, S.; Lupan, O.; Chemnitz, S.; Benecke, W.; Ronning, C.; Adelung, R.; Mishra, Y. K. Single Step Integration of ZnO Nano- and Microneedles in Si Trenches by Novel Flame Transport Approach: Whispering Gallery Modes and Photocatalytic Properties. *ACS Appl. Mater. Interfaces* 2014, 6 (10), 7806–7815.
- (61) Godsi, O.; Peskin, U.; Kapon, M.; Natan, E.; Eichen, Y. Site Effects in Controlling the Chemical Reactivity in Crystals: Solid-State Photochromism of N-(N-Propyl)nitrospiropyran. *Chem. Commun.* 2001, 0 (20), 2132–2133.
- (62) Breslin, V. M.; Garcia-Garibay, M. A. Transmission Spectroscopy and Kinetics in Crystalline Solids Using Aqueous Nanocrystalline Suspensions: The Spiropyran-Merocyanine Photochromic System. *Cryst. Growth Des.* 2017, 17 (2), 637–642.
- (63) Shiraishi, Y.; Itoh, M.; Hirai, T. Thermal Isomerization of Spiropyran to Merocyanine in Aqueous Media and Its Application to Colorimetric Temperature Indication. *Phys. Chem. Chem. Phys.* 2010, 12 (41), 13737–13745.

Light, Force and Heat: A Multi-Stimuli Composite that Reveals its Violent Past

Sindu Shree,^{†} Mathias Schulz-Senft,[‡] Nils H. Alsleben,[†] Yogendra Kumar Mishra,^{†,*} Anne
Staubitz,^{‡,¥,§,*} Rainer Adelung^{†,*}*

[†]Institute for Materials Science, Functional Nanomaterials, University of Kiel, Kaiserstr. 2,
24143 Kiel, Germany

[‡]Otto-Diels-Institute for Organic Chemistry, University of Kiel, Otto-Hahn-Platz 4, 24118 Kiel,
Germany

[¥]Institute for Organic and Analytical Chemistry, University of Bremen, Leobener Str. NW2 C,
28359 Bremen, Germany

[§]MAPEX Center for Materials and Processes, University of Bremen Bibliothekstraße 1, 28359
Bremen, Germany

SS (sisi@tf.uni-kiel.de), YKM (ykm@tf.uni-kiel.de), AS (staubitz@uni-bremen.de)
RA (ra@uni-kiel.de)

Text

1. Abbreviations

The use of abbreviations follows the conventions from the ACS Style guide. In addition, the following abbreviations were used.

Abbreviation	Meaning
ATR	Attenuated total reflection (IR)
COSY	Correlation spectroscopy
dd (NMR)	Doublet of doublets
EI	Electron ionization
FT	Fourier transform
HMBC	Heteronuclear multiple bond correlation
HPLC	High performance liquid chromatography
HSQC	Heteronuclear single quantum coherence
NOESY	Nuclear Overhauser enhancement spectroscopy
TOF	Time-of-flight mass detector

2. Analytical Equipment

NMR spectra were either recorded on a Bruker DRX 500 (^1H NMR: 500 MHz) FT-NMR spectrometer. ^1H NMR and $^{13}\text{C}\{^1\text{H}\}$ NMR spectra were referenced against the solvent residual proton signals (^1H) or the solvent itself (^{13}C).

The exact assignment of the peaks was performed by two-dimensional NMR spectroscopy such as ^1H COSY, ^1H NOESY, $^1\text{H}/^{13}\text{C}$ HSQC or $^1\text{H}/^{13}\text{C}$ HMBC if possible.

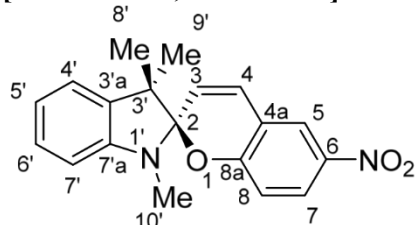
Mass spectrometric measurements were performed in the positive ion collection mode using a JEOL-Accu TOF 4GGCV EI mass spectrometer. Electron ionization was performed using an ionization potential of 70 eV.

UV spectra were recorded at 20 °C using a Perkin Elmer Lambda 900 UV spectrometer. Melting points were measured on an electrothermal IA6304 capillary melting point apparatus and are uncorrected.

The irradiation experiments were carried out using LED light sources with an optical power of 680 mW (360-370 nm) and 20 W (520-530 nm).

Materials

1',3',3'-Trimethyl-6-nitrospiro[chromene-2,2'-indoline]



Molecular structures of 1',3',3'-Trimethyl-6-nitrospiro[chromene-2,2'-indoline]

Melting point: $T = 160\text{ }^{\circ}\text{C}$, Lit:¹ 178 – 179 $^{\circ}\text{C}$

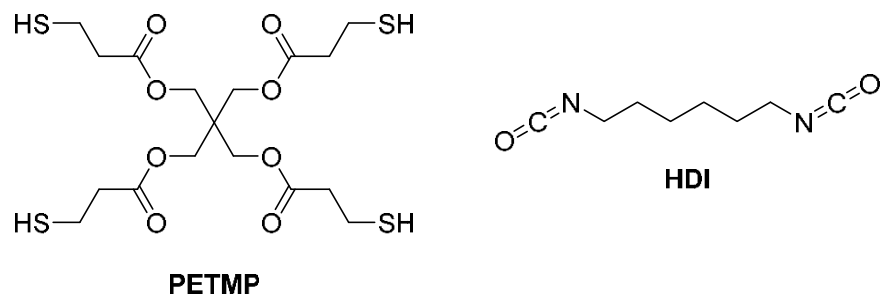
¹H NMR (500 MHz, CDCl₃, 300 K): $\delta = 8.03 - 7.99$ (m, 2H, H-5, H-7), 7.21 (ddd, ³ $J = 7.7$ Hz, ³ $J = 7.4$ Hz, ⁴ $J = 1.0$ Hz, 1H, H-6'), 7.09 (dd, ³ $J = 7.2$ Hz, ⁴ $J = 1.0$ Hz, 1H, H-4'), 6.93 (d, ³ $J = 10.3$ Hz, 1H, H-4), 6.89 (ddd, ³ $J = 7.4$ Hz, ³ $J = 7.2$ Hz, ⁴ $J = 1.0$ Hz, 1H, H-5'), 6.77 (d, ³ $J = 8.5$ Hz, 1H, H-8), 6.56 (d, ³ $J = 7.7$ Hz, 1H, H-7'), 5.86 (d, ³ $J = 10.3$ Hz, 1H, H-3), 2.75 (s, 3H, H10'), 1.30 (s, 3H, H8'), 1.19 (s, 3H, H-9')

¹³C NMR (126 MHz, CDCl₃, 300 K): $\delta = 160.0$ (C-6), 147.8 (C-7'a), 141.1 (C-4a), 136.3 (C3'a), 128.4 (C-4), 128.0 (C-6'), 126.0 (C-7), 122.8 (C-5), 121.8 (C-3), 121.7 (C-4'), 119.9 (C-5'), 118.8 (C-8a), 115.6 (C-8), 107.2 (C-7'), 106.5 (C-2), 52.4 (C-3'), 29.0 (C-10'), 26.0 (C-9'), 20.1 (C-8')

IR (ATR): $\tilde{\nu} = 3068$ (w), 2963 (m), 2866 (m), 1656 (w), 1609 (m), 1575 (m), 1509 (m), 1488 (s), 1441 (m), 1382 (w), 1364 (m), 1330 (s), 1301 (m), 1269 (s), 1184 (m), 1122 (m), 1089 (s), 1022 (m), 1016 (m), 949 (s), 916 (s), 838 (m), 807 (s), 782 (m), 750 (vs), 681 (s), 627 (m), 573 (m), 550 (m) cm^{-1}

HRMS (EI-TOF): m/z (%): $[\text{M}]^+$ calcd for $[\text{C}_{19}\text{H}_{18}\text{N}_2\text{O}_3]^+$ 322.13174; found 322.13148 (56), 159.10 (100) $[\text{M}-\text{Ph}-\text{O}-\text{NO}_2-\text{C}_2\text{H}_2]^+$.

Monomers for the Synthesis of Polythiourethane (PTU)



Molecular structures of the two components pentaerythritol tetrakis(3-mercaptopropionate) (PETMP) and hexamethylenediisocyanate (HDI) of polythiourethane (PTU).

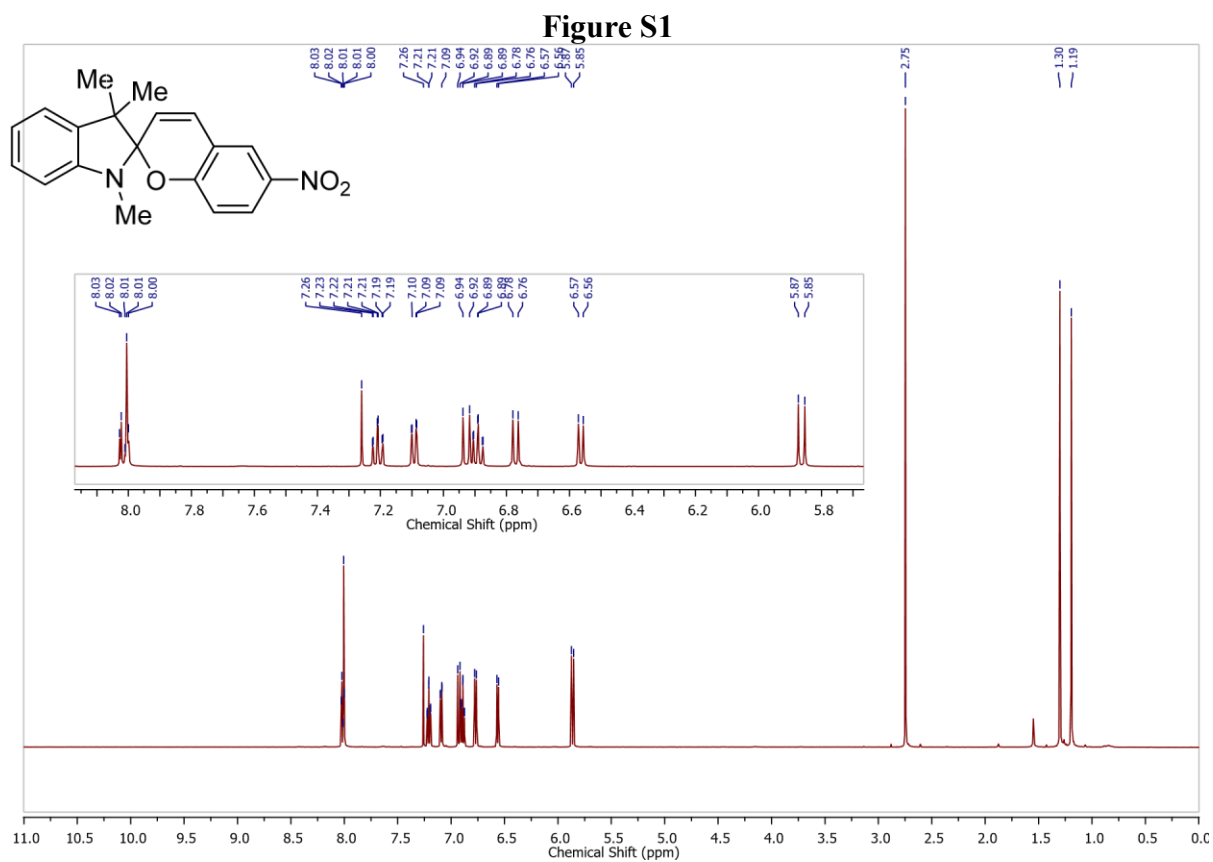


Figure S1: ¹H NMR spectrum of 1',3',3'-trimethyl-6-nitrospiro[chromene-2,2'-indoline] in CDCl₃.

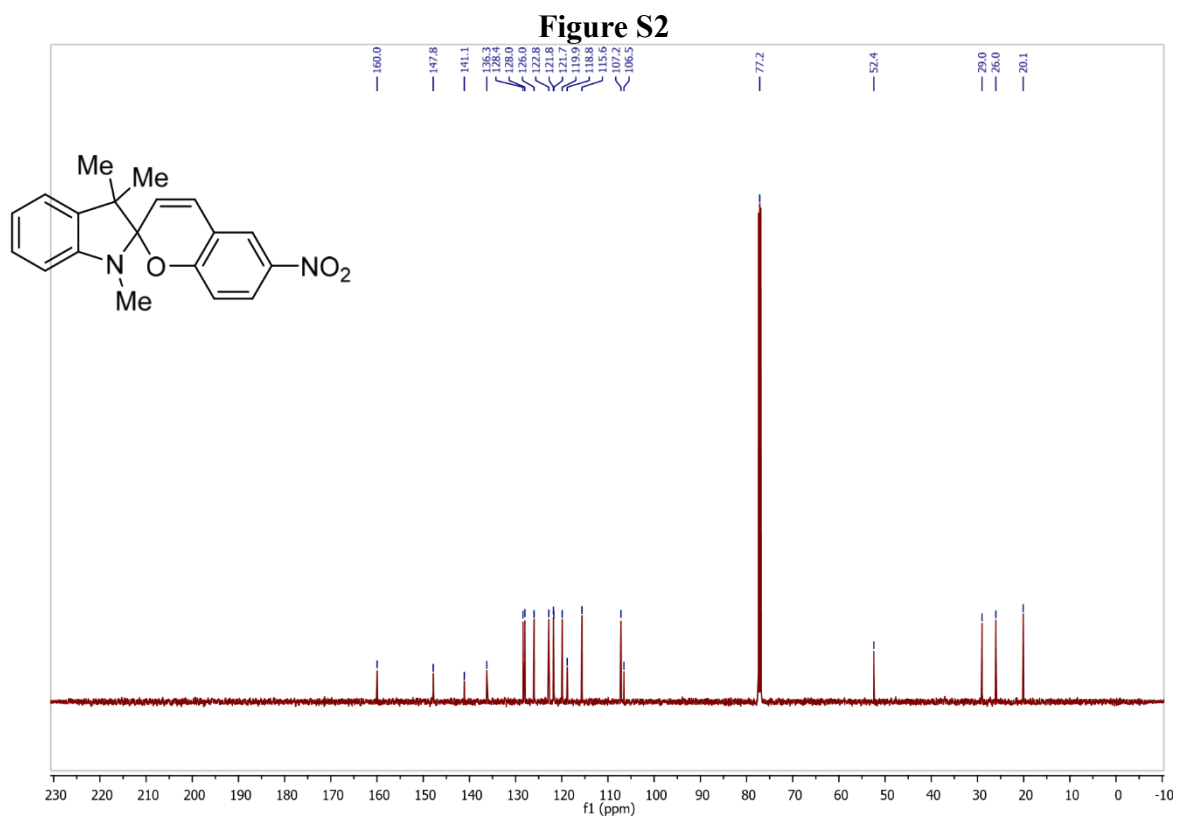


Figure S2: $^{13}\text{C}\{^1\text{H}\}$ NMR spectrum of 1',3',3'-trimethyl-6-nitrospiro[chromene-2,2'-indoline] in CDCl_3 .

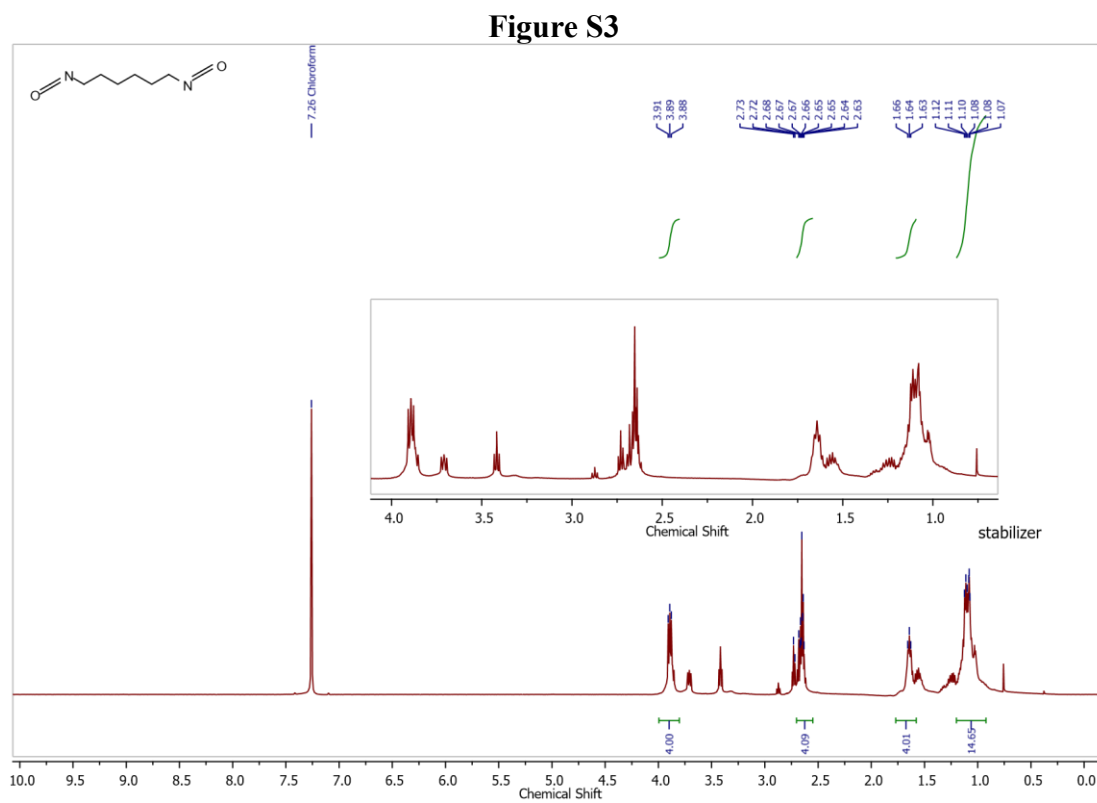


Figure S3: ^1H NMR spectrum of hexamethylenediisocyanate (HDI) in CDCl_3 (PTU-Monomer).

Figure S4

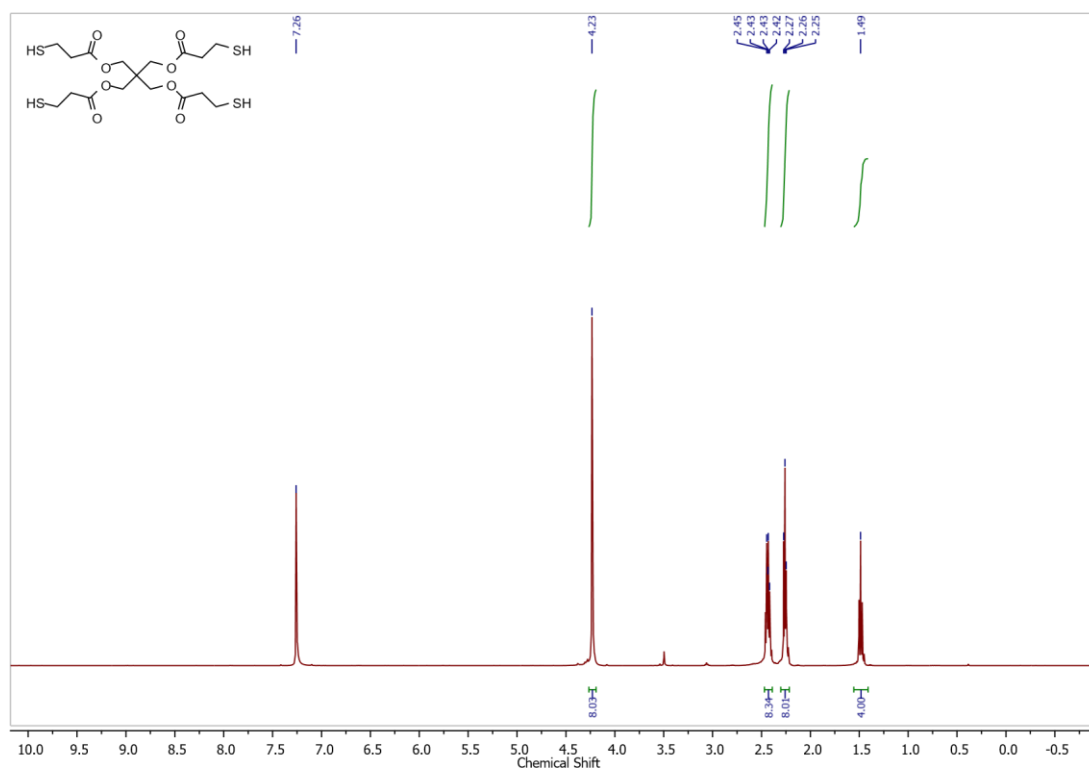


Figure S4: ^1H NMR spectrum of pentaerythritol tetrakis(3-mercaptopropionate) (PETMP) in CDCl_3 (PTU-Monomer).

Figure S5

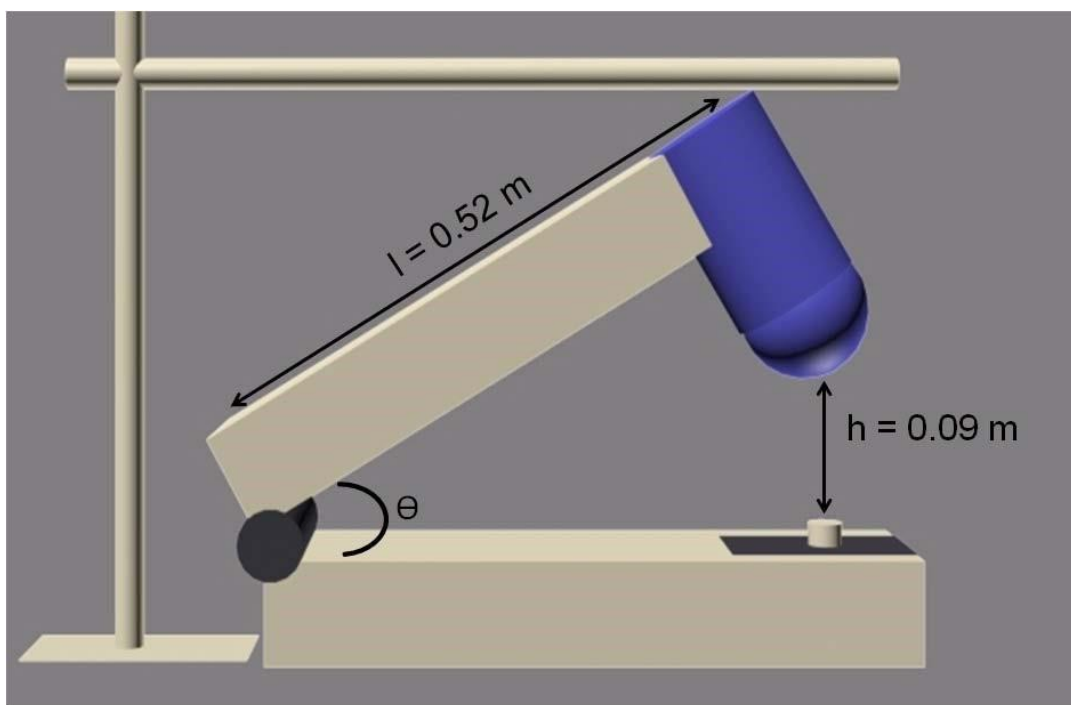


Figure S5: Schematic drawing of the “Hammer test”. The hammer is pulled up to a pre set height and released to fall on the sample freely.

Table S1: The average impact force measured required to damage the polymer matrix causing a color change

Sample name	Average impact pressure to cause switching (kPa)	Standard error (yEr±)
SP	106.252	8.064
P ₁	115.434	8.296
P ₂	144.293	18.643
P ₃	162.657	14.956
P ₄	232.18	3.935

References

- (1) Roxburgh, C. J.; Sammes, P. G.; Abdullah, A. Steric and Substituent Effects on the Photoreversibility of Novel Indolospirobenzopyrans: Acid Deuterolysis, UV and ¹H NMR Spectroscopy. *Dyes Pigments* **2009**, *82* (2), 226–237.

Mechanochromic Matrix Predicts Impact Induced Damage in a Reinforced Polymer Composite

Sindu Shree^{*a}, Mathias Schulz-Senft^b, Alina Kuntze^a, Yogendra Kumar Mishra^a, Anne Staubitz^{b,c,d}, and Rainer Adelung^a

^aFunctional Nanomaterials, Institute for Materials Science, Kiel University, Kaiserstr. 2, D-24143, Kiel, Germany.

^bOtto-Diels-Institute for Organic Chemistry, Kiel University, Otto-Hahn-Platz 4, 24118 Kiel, Germany.

^cInstitute for Organic and Analytical Chemistry, University of Bremen, Leobener Str. 7, 28359 Bremen, Germany.

^dMAPEX Center for Materials and Processes, University of Bremen Bibliothekstraße 1, 28359 Bremen, Germany

Abstract

A major conflict faced in the largescale machineries is real-time damage identification. High mechanical stability offered by the glassfiber reinforced polymer composites (GFRPCs) also poses issues with unpredictable material failure. This creates a requirement for cost-effective stress sensors to indicate material damage before a malfunction occurs and to precisely identify the initial site and the extent of a damage. The challenge in GFRPCs is that the failure may originate at arbitrary positions, minute differences in the fiber/matrix coupling eventually develops into the primary point of a failure. This work presents a molecular stress-sensitive sensor embedded in polymer matrices such as polythiourethane (PTU) and Epoxy, reinforced by glassfibers. Spiropyran (SP) is used as a self-reporting particle filler. Polymer matrix covering the woven glassfibers contains as little as 0.5 wt% SP. In the given study, the PTU/SP composite with and without glassfiber reinforcement are studied for their self-reporting property. However, only the samples with reinforcement behave like ideal self-reporter by exposing a damage via color change well before any visible cracks appeared. Comparison tests of SP with different matrices show that the amine-based hardener used to cross-link epoxy resin reacts with the SP molecules. Underlying mechanisms involved in the mechanochromic responses of the PTU/SP composites are investigated and discussed.

Introduction

Prognostic of an internal damage in a polymer composite well before it leads to material failure has been an objective of several studies.^[1-3] In addition to damage indication, a reliable material requires high mechanical strength and flexibility.^[4-6] The lightweight glass and carbon fiber reinforced polymer composites (GFRPC or CFRPC) are high-performance materials due to its superior mechanical stability. They have been commercialized in numerous fields such as the automotive, aviation industry, wind energy power generators and construction engineering.^[4,7] Environmental conditions such as exposure to UV

irradiation, temperature changes, high winds, humidity etc. lead to accumulative and irreparable damages over time affecting such polymer composites.^[8,9] To uncover the sources of damages, industries employ non-destructive methods namely acoustic emission, shearography, pulsed thermography, X-ray/gamma-ray analysis etc.^[10] Despite the effectivity of these methods, they are mostly applicable for post damage analysis and are time consuming as the entire length and width of the material needs to be scanned to discover and evaluate the depth of a damage. To reduce the inspection time and to receive live information on the state of a material, more recently self-reporting coatings were developed. For example, fluorescent proteins functionalized glass fibers embedded in epoxy resin were used as delamination indicators.^[11] Another example is photoluminescent tetrapodal zinc oxide (ZnO-T) filled polydimethylsiloxane (PDMS) composites demonstrated stress induced damages.^[12-14] However, such components must be dismantled and they require additional equipment for assessment, making this an ex-situ technique as well. The key disadvantage of an ex-situ analysis is that the damaged parts need to be removed and transported for testing, furthermore these processes can be inconclusive in finding the point of impact. With a built-in sensor, this intricate step of handling damaged parts can be avoided. The current study therefore focuses on fabricating a polymer composite with an in-situ stress sensor with pre-failure indication.

Spiropyran (SP) is a widely employed stimuli responsive molecular switch that has been used in composite systems as a particle filler.^[15-18] It is an organic molecule that isomerizes in response to heat, light and most importantly, to mechanical stress.^[17,19-22] By undergoing a transformation from the closed (spiropyran) to the open (merocyanine) form the dye changes its color in response to the afore mentioned stimuli from almost colorless to an intense purple.^[16,18] Making SP a molecular sensor, which is sensitive to the changes in its surroundings. Such molecular force sensors can be embedded in a polymer composite, which can indicate damages at an early stage. To study the compatibility of SP as a particle filler with different polymer matrices, highly cross-linked epoxy resin and polythiourethane (PTU) were used. The thermally and chemically inert PTU is highly transparent and stable to UV exposure, it has emerged as an ideal matrix for antifouling and anticorrosion coatings.^[23,24] Monomers involved in the fabrication of PTU^[25] are solvent free and are comparatively less toxic than a bisphenol-A containing epoxy resin.^[26-28]

Fabrication of components with an in-situ force indicator involves only an additional step to the standardised hand lay-up^[29] method of lamination, however, the overall cost is comparatively much lower than the cumulative cost of a post-damage analysis approach. The molecular switch based damage identifying strategy is minimal and efficient, merely ~0.5 wt% of SP in a composite is sufficient for direct damage detection as demonstrated in recent work on PTU/SP composite where interconnected network of ZnO-T was used as an additional filler to enhance the photochromic response and to provide mechanical reinforcement.^[15] However, this stress responsive composite only showed color change concurrent to material failure. Presented work demonstrates the straightforward production of a mechanochrome combined glassfibers reinforced PTU composite. Detailed investigations on the composite samples reveal the in-situ mechanochromic sensing capability of the polymer composite which provides pre-indication of a propagating material failure. Direct relevance of the gradual color change in the mechanochromic polymer composite to the accumulated impact force was established in the given study.

Periodic impact testing of the mechanochromic polymer composite

The PTU and spiropyran polymer composite without reinforcement is labelled as PTU/SP, the PTU and spiropyran sample with glassfiber reinforcement is called as GFPS and the epoxy and spiropyran composite with reinforcement is named as GFES. All the samples comprised 0.5 wt% of SP. These samples were subjected to a periodic impact force using a self-made „Hammer test” generating one strike per second (each strike yielding up to ~24 kPa impact pressure).^[15] For an ideal damage detection, it is essential that a color change appears before the material fails. The reinforced polymer composites were examined under SEM after sample preparation. The cross-sectional micrographs of the samples GFPS and GFES (**Figure 1.**) showed no sign of delamination between the glassfibers and the polymer matrix.

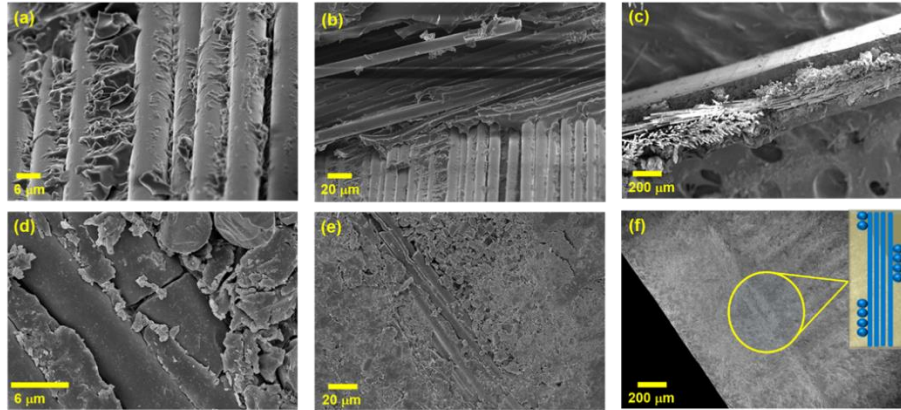


Figure 1. SEM micrographs of the cross-section of the GFPS and GFES samples at consecutively decreasing magnifications. (a)-(c) Are the micrographs with decreasing magnification of the woven glassfiber mat covered by PTU/spiropyran. (d)-(f) Are the micrographs with decreasing magnification of the woven glassfiber mat embedded in the epoxy/spiropyran matrix. The sketch in the image (f) represents the alignment of the fiber mat uniformly infiltrated by the SP containing matrix, yellow surrounding symbolizes the polymer matrix.

During the periodic impact test, two stages were verified: average number of hits required to induce color change and the average number of hits leading to material failure. To track these features, an image was taken after each impact and the photomontage of the tests on the polymer composite SP and GFPS are shown in **Figures 2. and 3.** (related image stacks of the impact tests are attached in the SI). The corresponding forces were calculated with the equation presented in the SI and the results are summarized in **Table 1.**^[15]

Table 3. The average number of hits under the “Hammer test” required to cause damage in the polymer composites with and without the woven glassfibers are calculated and recorded in the following table.

Sample	Force required to show visible color change (kPa)	Force required to cause material failure (kPa)
PTU/SP	408	432
GFPS	648	1248
GFES	No color change	720

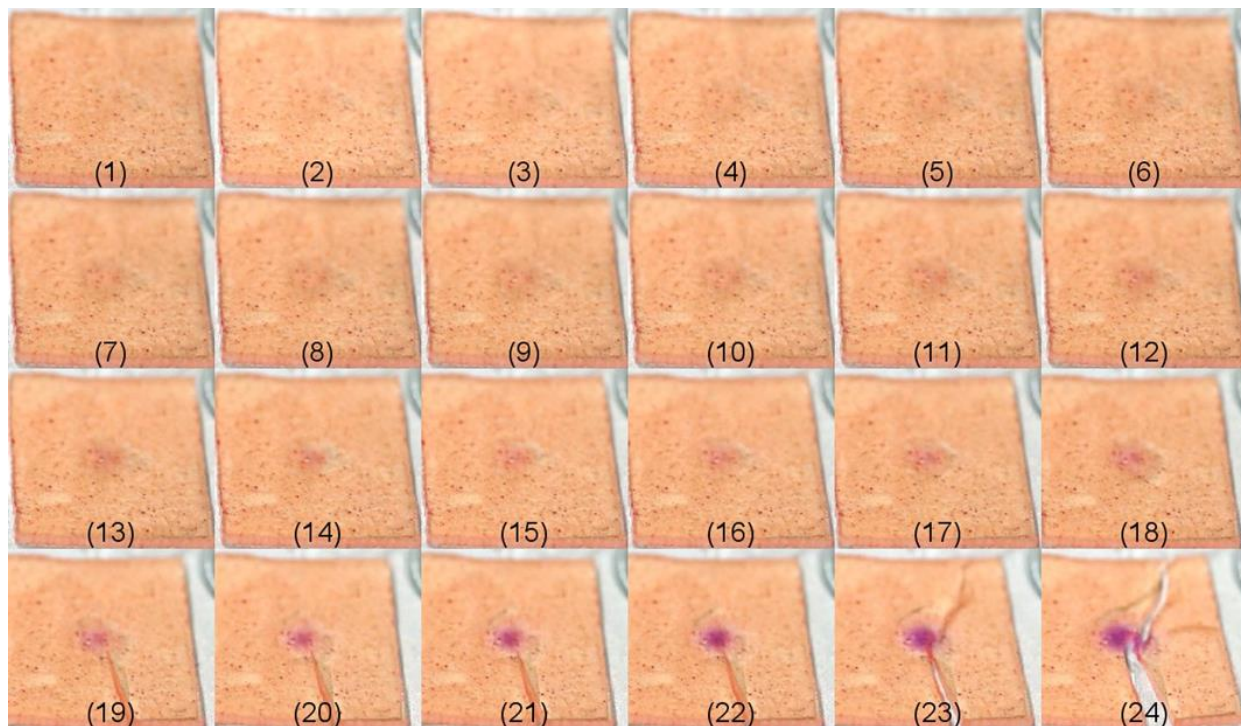


Figure 2. Periodic impact test of the polymer composites without glassfiber reinforcement. (1) First image of the series was of the sample before the test started. An image was taken after every strike to make a photo montage of the test until material failure occurred (at (19)). A discoloration appears already in the fourth image at the point of impact. Purple color of the open form of the mechanochrome (merocyanine) develops in the 12th image. A crack emerges at the 19th strike with further color change. Color change as a result of mechanical stress intensifies gradually until the sample cracks further.

In the sample PTU/SP, switching of SP to merocyanine and the material failure occurred almost simultaneously (see **Figure 2.** and **Table 1.**). At the impact pressure of ~ 432 kPa, the sample PTU/SP failed while a strong color developed only a strike earlier (408 kPa). Although a discoloration (in **Figure 2.**), could already be observed at 264 kPa (image 12, strike 11), it was not an evident enough indication of the upcoming damage. The SP additive in the sample GFPS (**Figure 3.**) self-reports damage with a strong color change at the point of impact at ~ 432 kPa (image 19), well before the cracks appear. Even in GFPS a slight color change emerged at 264 kPa (image 12 in **Figure 2.**), such changes could only be tracked by camera with a high resolution, whereas the color change arising at ~ 456 kPa was visible to the naked eye.

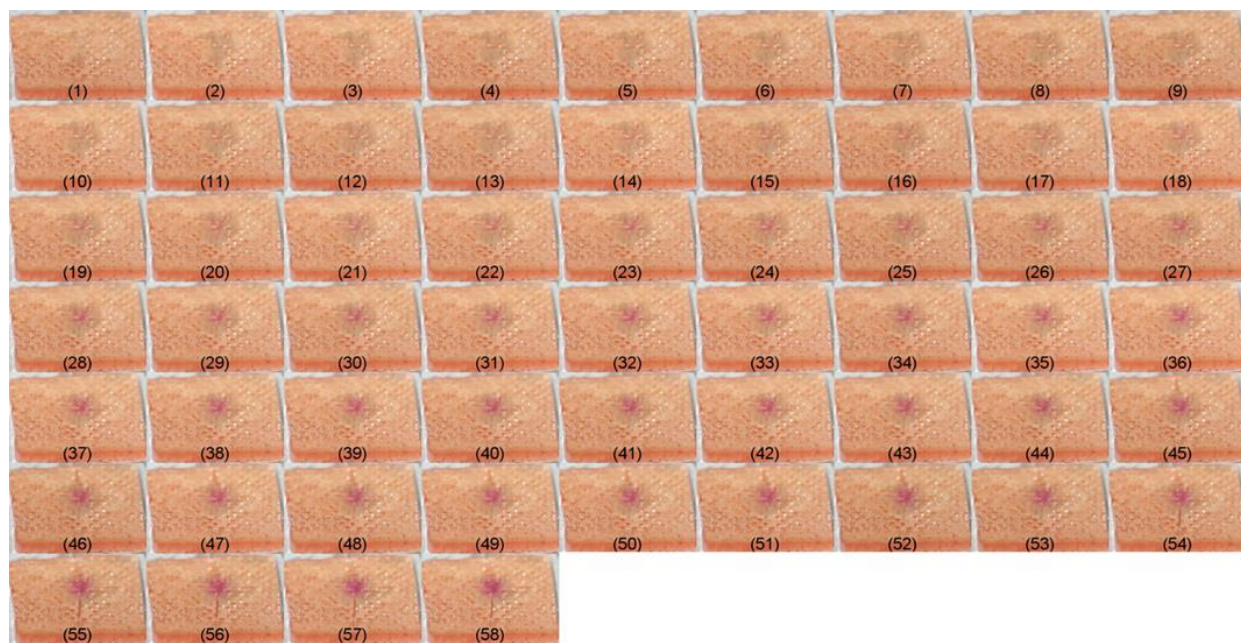


Figure 3. Periodic impact test of the polymer composites with glassfiber reinforcement (GFPS). (1) First image of the series was of the sample before the test started. An image was taken after every strike to track material damage with a mechanochrome. This photo montage contains images of every strike until material failure occurred. A discoloration appeared in the second image at the point of impact. Visibly perceivable color change due to mechanical stress (spiropyran to merocyanine) developed in the 19th image. After the 54 strikes, a crack emerged with further color change. The color change intensified gradually until the sample cracked further.

For more precise quantification in tracking the color change, average brightness of the green color channel contribution in these images was tracked at the point of impact using *ImageJ* (**Figure 4.**). As these samples were not colorless to begin with, rather yellow-orange, the red and blue channels were less sensitive than the green channel to the color change (separated RGB image stacks are given in the SI). Accumulated impact pressure corresponding to the number of strikes were plotted against the green color contribution (see **Figure 4.**), a standardised green color scalebar is provided for reference. The average green color intensity was observed to be in direct relevance to the development of merocyanine. The plot (**Figure 4.**) contains the response of PTU/SP and GFPS to mechanical stress. For the initial three strikes on the sample PTU/SP there was a very slight color development, and four to six strikes induced continuous and substantial color change finally showed a significant drop in green color intensity immediately after the material failed.

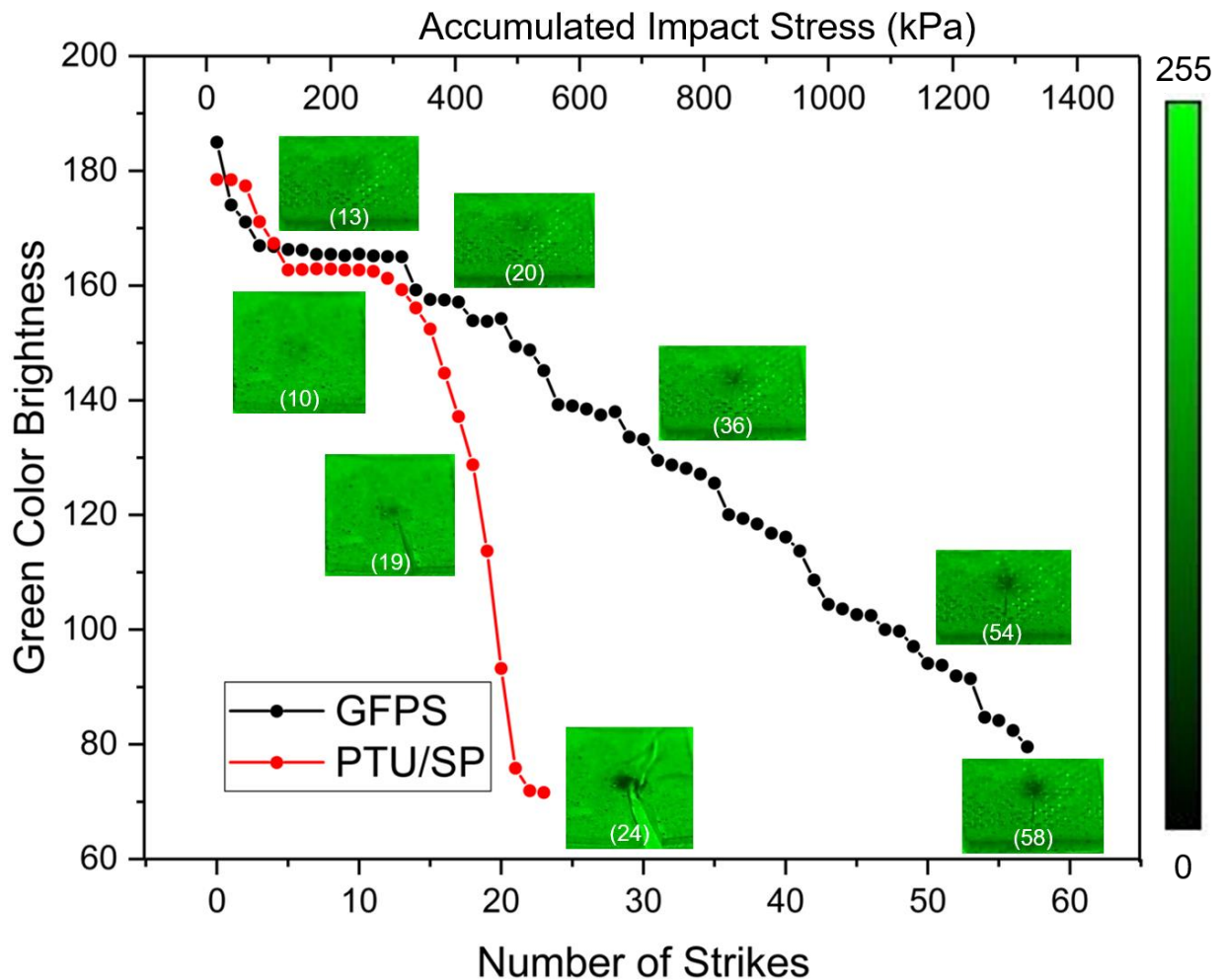


Figure 4. Quantitative analysis of the color development during the periodic impact test. This plot demonstrates changes in the brightness of the green color channel under impact. Images of the sample PTU/SP and GFPS showing color change corresponding to the subjected impact are presented. On the right side of the plot is the green color scale bar that was used as a reference for quantification.

The strikes six to twelve caused no further color development. After the 13th strike (288 kPa), a prompt decline in green channel could be observed until the 18th strike (408 kPa), strikes 19 to 22 induced cracks and drastic color change at the same time. A maximum color change was visible after the material failed at ~528-552 kPa. Contrary to this, the sample GFPS showed a notable color development before severe material damage. Similar to the sample PTU/SP, the color development paused after 288 kPa. As the periodic impact test continued, the color change progressed steadily, the green channel darkened around 35th strike. This visible indication grew stronger episodically until the material failed at the 52nd strike (**Figure 4.**). The glassfiber reinforced samples GFPS and GFES demonstrated much higher

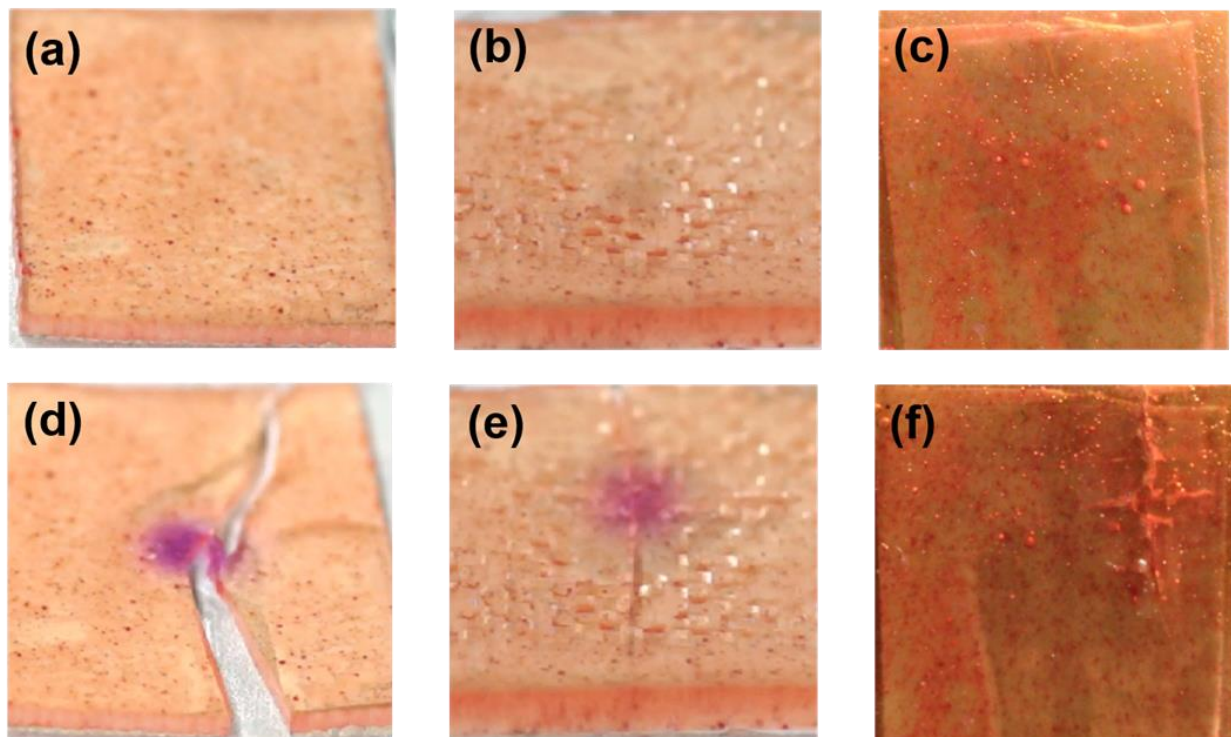


Figure 5. (a), (b) and (c) are the samples PTU/SP, GFPS and GFES before the “Hammer test”. (d), (e) and (f) are the respective images after impact test. (a) and (b) polymer composites PTU/SP and GFPS before the mechanochromic test showed a similar color as they had the same PTU matrix. (c) GFES showed a different and darker color before the mechanochromic test. (d) and (e) are the images of the completely damaged PTU/SP and slightly cracked GFPS after the mechanochromic test showing an evident color change. (f) is the fractured GFES that does not exhibit a color change.

impact resistance compared to the sample PTU/SP. The samples GFPS and GFES developed cracks only after 57 hits (corresponding to ~ 1.2 MPa) and 30 hits (~ 720 kPa) respectively (**Figure 5.**). Although the polymer composite with epoxy matrix (GFES) exhibited a good impact resistivity with only minor fractures after 30 hits (~ 720 kPa), no color change occurred at the point of impact.

Interaction of the mechanochrome with epoxy resin and amine-based hardener

The mechanochrome in GFES samples (**Figure 5.**) clearly did not respond to the applied force. As the curing mixture of the commercial epoxy resin is a complex system to study, to simplify the issue, reactivity of SP with each component of the polymer was investigated separately. The physical curing conditions were adapted in a way that the reactions could be analyzed by nuclear magnetic resonance (NMR) spectroscopy. For these experiments, SP was

dissolved in tetrahydrofuran (THF) with individual and representative components of both hardener and epoxy resin. During these tests, evidence of an amine induced cleavage of SP to form its precursor indoline and imines was observed. In an equimolar mixture with xylylenediamine, 90% of the SP molecules reacted to form indoline. This observation was unexpected, as the spiropyran was synthesized under basic conditions using secondary amines as catalysts.^[18] However, in the NMR experiments with the other components such as salicylic acid and two epoxy compounds, SP remained inert. The exact experimental procedure and evaluation of the obtained data are provided in the SI. Despite the differences compared to the normal curing procedure, it is likely that this or a similar reaction occurs in the mixture of epoxy resin, hardener and SP while curing. Excess amines present in the hardener while producing the polymer composites with only 0.5 wt% of SP facilitates such a reaction. The fragmentation product, 1,3,3-trimethyl-2-methyleneindoline is commercially available as dark red liquid, explaining the red coloration of the sample GFES.

Conclusions

Compatibility tests of the mechanochrome, SP, with PTU and commercial epoxy matrix (GFES) were performed. SP proved to be compatible and showed an excellent mechanochromic property in PTU, however it was incompatible with the curing conditions of an epoxy matrix. In the periodic impact test, reinforced PTU showed a 60% higher impact resistance than the reinforced commercial epoxy matrix. The curing conditions were simulated in solution with the representative compounds of the hardener and the epoxy prepolymers and the results were monitored by NMR spectroscopy. It was possible to observe a degradation of up to 90% of SP in presence of one equivalent of xylylenediamine. Consequently, there is a need to find other, less reactive mechanochromes which would be compatible with the epoxy curing process. The PTU/spiropyran polymer composite was reinforced with woven glassfiber mats, to improve its impact strength. The presented system displayed a color switch at the point of impact to approx. 25% of the impact force corresponding to material failure. In the range between the first notable color change and the point of failure, the sample's color change responded almost linearly to the applied impact force. This is an evident indication provided by the built-in stress sensor SP. The color change due to mechanical stress in the sample GFPS occurred at the initial stage of the

surface damage before the integrity of the composite's internal structure was compromised. Reinforced PTU composites, GFPS, were produced and tested for its mechanosensitivity and emerged as an ideal material for impact sensing. To observe the change of SP to merocyanine, (color change from yellow to purple) the histogram of the green color channel in the image series can be used as an efficient tool to track the stress applied to a coating to learn about the stage of a damage.

Materials and methods

Detailed synthetic procedure of the molecular switch, SP and its analytical data can be found in the supporting information. The "epoxy resin L" and the "hardener S" and the plain woven glassfibers with an areal density of 163 gm⁻² used for the reinforcement were purchased from R&G Faserverbundwerkstoffe GmbH. The PTU matrix, a two-component polymer, was bought from FPT Fluid- & Prozesstechnik GmbH. Both matrices were used and processed without further treatment, following the suppliers' instructions.

Different types of samples were prepared: polymer composites with and without glassfibers. SP was used in all the samples as a stress indicator to compare the mechanochromocity and the impact resistance of the composite system. In all the samples, SP was used at a concentration of 0.5 wt% and the glassfiber concentration was at ~8 wt%. The PTU composite containing solely spiropyran (PTU/SP) as an additive without the glassfibers was produced analogously to previous work.[15] This composite system was further reinforced with of woven glassfibers (GFPS). The PTU/spiropyran was coated onto the woven glassfibers as explained in the following procedure: A 20 vol% of the mixture made of monomers pentaerythritol tetrakis(3-mercaptopropionate) (PETMP) and hexamethylene diisocyanate (HDI) were mixed at a weight ratio of 1:1.4 respectively with SP (0.5 wt% of the whole polymer composite) casted into a mold so that a uniform layer was obtained. A rectangular woven glassfiber mat (70*70 mm²) was placed over the mixture and the remaining 80 % of the uncured monomer / SP mixture was poured over the glassfiber mat. Subsequently, the sample was placed for 20 h in a furnace at 80 °C. To compare the GFPS composite system to the commercially available epoxy polymer, epoxy/spiropyran coated glassfiber (GFES) samples were prepared similarly. SP was first well dispersed into the hardener and epoxy resin (45:100 parts by volume of hardener : resin) was later added to

the dispersion, the unpolymerized mixture was coated onto the glassfiber mat. The coated glassfiber mats (thickness, 5 mm) were later cut into smaller samples of the size 20*20 mm² for further investigations.

References

- 1 B. J. Blaiszik, S. L. B. Kramer, S. C. Olugebefola, J. S. Moore, N. R. Sottos, S. R. White, *Annu. Rev. Mater. Res.* **2010**, *40*, 179.
- 2 N. Bruns, D. S. Clark, *Chimia* **2011**, *65*, 245.
- 3 S. N. Raja, A. C. K. Olson, K. Thorkelsson, A. J. Luong, L. Hsueh, G. Chang, B. Gludovatz, L. Lin, T. Xu, R. O. Ritchie, A. P. Alivisatos, *Nano Lett.* **2013**, *13*, 3915.
- 4 K. J. Narayana, R. Gupta Burela, *Mater. Today Proc.* **2018**, *5*, 5580.
- 5 S. S. Yao, F. L. Jin, K. Y. Rhee, D. Hui, S. J. Park, *Compos. Part B Eng.* **2018**, *142*, 241.
- 6 S. Y. Fu, X. Q. Feng, B. Lauke, Y. W. Mai, *Compos. Part B Eng.* **2008**, *39*, 933.
- 7 T. Ozbakkaloglu, J. C. Lim, T. Vincent, *Eng. Struct.* **2013**, *49*, 1068.
- 8 K. K. Singh, R. K. Singh, P. Kumar, *J. Reinf. Plast. Compos.* **2009**, *28*, 601.
- 9 V. Tamužs, J. Andersons, K. Aniskevich, J. Jansons, J. Korsgaard, *Mech. Compos. Mater.* **1998**, *34*, 321.
- 10 R. Yang, Y. He, H. Zhang, *Renew. Sust. Energ. Rev.* **2016**, *60*, 1225.
- 11 O. Rifaie-Graham, E. A. Apebende, L. K. Bast, N. Bruns, *Adv. Mater.* **2018**, *30*, 1.
- 12 X. Jin, M. Götz, S. Wille, Y. K. Mishra, R. Adelung, C. Zollfrank, *Adv. Mater.* **2013**, *25*, 1342.
- 13 T. Reimer, I. Paulowicz, R. Röder, S. Kaps, O. Lupan, S. Chemnitz, W. Benecke, C. Ronning, R. Adelung, Y. K. Mishra, *ACS Appl. Mater. Interfaces* **2014**, *6*, 7806.
- 14 V. M. Diep, A. M. Armani, *Nano Lett.* **2016**, *16*, 7389.
- 15 S. Shree, M. Schulz-Senft, N. H. Alsleben, Y. K. Mishra, A. Staubitz, R. Adelung, *ACS Appl. Mater. Interfaces* **2017**, *9*, 38000.
- 16 S. Shree, M. Schulz-Senft, X. Jin, Y. K. Mishra, A. Staubitz, R. Adelung, *3rd Int. Conf. Nanotechnologies Biomed. Eng. IFMBE Proc., Springer, Singapore, 2016*, 146.
- 17 R. Klajn, *Chem. Soc. Rev.* **2014**, *43*, 148.
- 18 E. Samoylova, L. Ceseracciu, M. Allione, A. Diaspro, A. C. Barone, A. Athanassiou, *Appl. Phys. Lett.* **2011**, *99*, 1.
- 19 M. Schulz-Senft, P. J. Gates, F. D. Sönnichsen, A. Staubitz, *Dye. Pigm.* **2017**, *136*, 292.
- 20 M. Schulz-Senft, M. Lipfert, A. Staubitz, *Chem. Unserer Zeit* **2014**, *48*, 200.
- 21 B. Seefeldt, R. Kasper, M. Beining, J. Mattay, J. Arden-jacob, N. Kemnitzer, K. Heinz, M. Heilemann, M. Sauer, *Photochem. Photobiol. Sci.* **2016**, *9*, 213.
- 22 J. Zhang, J. Wang, H. Tian, *Mater. Horizons* **2014**, *1*, 169.
- 23 I. Hölken, M. Hoppe, Y. K. Mishra, S. N. Gorb, R. Adelung, M. J. Baum, *Phys. Chem. Chem. Phys.* **2016**, *18*, 7114.
- 24 K. Strzelec, N. Baczek, S. Ostrowska, K. Wąsikowska, M. I. Szyrkowska, J. Grams, *C. R. Chim.* **2012**, *15*, 1065.
- 25 M. D. Campiñez, C. Ferris, M. V. De Paz, A. Aguilar-De-Leyva, J. Galbis, I. Caraballo, *Int. J. Pharm.* **2015**, *480*, 63.

- 26 J. Michałowicz, *Environ. Toxicol. Phar.* **2014**, *37*, 738.
- 27 J. I. Eid, S. M. Eissa, A. A. El-Ghor, *J. Basic. Appl. Zool.* **2015**, *71*, 10.
- 28 L. B. Bourne, F. J. M. Milner, K. B. Alberman, *Br. J. Ind. Med.* **1959**, *16*, 81.
- 29 T.P Sathishkumar, S Satheeshkumar, J Naveen, *J. Reinf. Plast. Compos.* **2014**, *33*, 1258.

Supporting Information

Mechanochromic Matrix Predicts Impact Induced Damage in a Reinforced Polymer Composite

Sindu Shree*^a, Mathias Schulz-Senft^b, Alina Kuntze^a, Yogendra Kumar Mishra^a, Anne Staubitz^{b,c,d}, and Rainer Adelung^a

^a Functional Nanomaterials, Institute for Materials Science, Kiel University, Kaiserstr. 2, D-24143, Kiel, Germany.

^b Otto-Diels-Institute for Organic Chemistry, Kiel University, Otto-Hahn-Platz 4, 24118 Kiel, Germany.

^c Institute for Organic and Analytical Chemistry, University of Bremen, Leobener Str. 7, 28359 Bremen, Germany.

^d MAPEX Center for Materials and Processes, University of Bremen Bibliothekstraße 1, 28359 Bremen, Germany

Keywords: Glassfiber, polythiourethane, polymer composite, spiropyran, self-reporting, mechanochromic

Contents

1. Abbreviations	178
2. Analytical Equipment	178
3. Materials	179
1',3',3'-Trimethyl-6-nitrospiro[chromene-2,2'-indoline]	179
4. Sample preparation	180
5. Hammer Test.....	180
6. Image Analysis	182
7. Analysis of the Spiropyran Failure in the Epoxy Matrix	182
8. Plotted NMR Spectra	187
¹ H and ¹³ C{ ¹ H} NMR Spectra of 1',3',3'-Trimethyl-6-nitrospiro[chromene-2,2'-indoline] in CDCl ₃	187
¹ H NMR Spectra of SP, Isopropyl glucidyl ether (iPr-Epoxy) and the Reaction Mixture in THF- <i>d</i> ₈	188
¹ H NMR Spectra of SP, Phenyl Glucidyl Ether (Ph-Epoxy) and the Reaction Mixture in THF- <i>d</i> ₈	189
¹ H NMR Spectra of SP, 2-Hydroxybenzoic acid (HBA) and the Reaction Mixture in THF- <i>d</i> ₈ ..	189
¹ H and ¹³ C{ ¹ H} NMR Spectra of SP, Xylylenediamine (XDA), 1,3,3-Trimethyl-2-methyleneindoline (Ind) and the Reaction Mixture in THF- <i>d</i> ₈	190

Abbreviations

The use of abbreviations follows the conventions from the ACS Style guide.^[1] In addition, the following abbreviations were used.

Abbreviation	Meaning
ATR	Attenuated total reflection (IR)
COSY	Correlation spectroscopy
dd (NMR)	Doublet of doublets
EI	Electron ionization
FT	Fourier transform
HMBC	Heteronuclear multiple bond correlation
HSQC	Heteronuclear single quantum coherence

Analytical Equipment

NMR spectra were recorded on a Bruker Avance Neo 500 (^1H NMR: 500 MHz) FT-NMR spectrometer at 300 K. ^1H NMR and $^{13}\text{C}\{^1\text{H}\}$ NMR spectra were referenced against the solvent residual proton signals (^1H) or the solvent itself (^{13}C).

The exact assignment of the peaks was performed by two-dimensional NMR spectroscopy such as ^1H COSY, ^1H NOESY, $^1\text{H}/^{13}\text{C}$ HSQC and $^1\text{H}/^{13}\text{C}$ HMBC.

Mass spectrometric measurements were performed in the positive ion collection mode using a JEOL-Accu TOF 4GGCV EI mass spectrometer. For electron spray ionization (ESI), a Thermo Fisher Q Exactive Plus mass spectrometer with a quadrupole orbitrap was used in positive and negative ion collection mode with an ionization potential of 3.2 kV.

IR spectra were measured using a Perkin Elmer Paragon 1000 FT-IR spectrometer equipped with an A531-G Golden-Gate-ATR-unit.

The irradiation experiments were carried out using LED light sources with an optical power of 680 mW (360-370 nm) and 20 W (520-530 nm) at the LED.

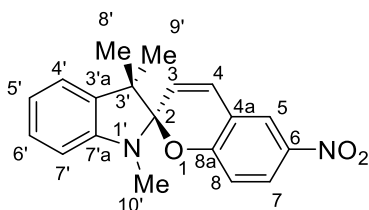
Scanning electron microscope (SEM) from Carl Zeiss (10 kV, 10 μA) was used to investigate the samples in the presented work.

Materials

1',3',3'-Trimethyl-6-nitrospiro[chromene-2,2'-indoline]

Materials: 1,3,3-Trimethyl-2-methyleneindoline was purchased from Sigma-Aldrich Co. (Aldrich, 97%), 2-hydroxy-5-nitrobenzaldehyde was purchased from TCI Co. (>97%) and ethanol was purchased from Acros (anhydrous, $\geq 99.5\%$, stored over molecular sieves). All reagents were used without further purification.

1,3,3-Trimethyl-2-methyleneindoline (7.80 g, 45.0 mmol) and 2-hydroxy-5-nitrobenzaldehyde (7.52 g, 45.0 mmol) were dissolved in EtOH (125 mL) and heated to 78 °C for 3 h. Then the reaction mixture was cooled to -25 °C and the crystallized product was obtained after filtration as a green powder (12.7 g, 39.4 mmol, 88 %, Lit.: 89 %)



Melting point: $T = 176$ °C, Lit: 178 – 179 °C^[2]

¹H NMR (500 MHz, CDCl₃, 300 K): $\delta = 8.03 - 7.99$ (m, 2H, H-5, H-7), 7.21 (ddd, $^3J = 7.7$ Hz, $^3J = 7.4$ Hz, $^4J = 1.0$ Hz, 1H, H-6'), 7.09 (dd, $^3J = 7.2$ Hz, $^4J = 1.0$ Hz, 1H, H-4'), 6.93 (d, $^3J = 10.3$ Hz, 1H, H-4), 6.89 (ddd, $^3J = 7.4$ Hz, $^3J = 7.2$ Hz, $^4J = 1.0$ Hz, 1H, H-5'), 6.77 (d, $^3J = 8.5$ Hz, 1H, H-8), 6.56 (d, $^3J = 7.7$ Hz, 1H, H-7'), 5.86 (d, $^3J = 10.3$ Hz, 1H, H-3), 2.75 (s, 3H, H-10'), 1.30 (s, 3H, H-8'), 1.19 (s, 3H, H-9') ppm.

¹³C{¹H} NMR (126 MHz, CDCl₃, 300 K): $\delta = 160.0$ (C-6), 147.8 (C-7'a), 141.1 (C-4a), 136.3 (C-3'a), 128.4 (C-4), 128.0 (C-6'), 126.0 (C-7), 122.8 (C-5), 121.8 (C-3), 121.7 (C-4'), 119.9 (C-5'), 118.8 (C-8a), 115.6 (C-8), 107.2 (C-7'), 106.5 (C-2), 52.4 (C-3'), 29.0 (C-10'), 26.0 (C-9'), 20.1 (C-8') ppm.

IR (ATR): $\tilde{\nu} = 3069$ (w), 2966 (w), 2866 (w), 1655 (w), 1610 (m), 1575 (m), 1509 (s), 1488 (s), 1443 (m), 1364 (m), 1333 (vs), 1303 (s), 1271 (vs), 1185 (m), 1123 (s), 1089 (vs), 1022 (s), 950 (vs), 930 (s), 913 (s), 807 (vs), 752 (vs), 681 (s), 628 (m), 575 (m), 550 (m), 518 (m) cm⁻¹.

HRMS (EI-TOF): m/z (%): [M]⁺ calcd. for [C₁₉H₁₈N₂O₃]⁺ 322.1317; found 322.1292 (67), 159.10 (100) [M-Ph-O-NO₂-C₂H₂]⁺.

Sample preparation

The “epoxy resin L”, the “hardener S” and the woven glassfibers with an areal density of 163 gm^{-2} used for the reinforcement were purchased from R&G Faserverbundwerkstoffe GmbH. The components for the PTU matrix, were bought from FPT Fluid- & Prozesstechnik GmbH. Both matrices were used and processed without further treatment, following the suppliers’ instructions.

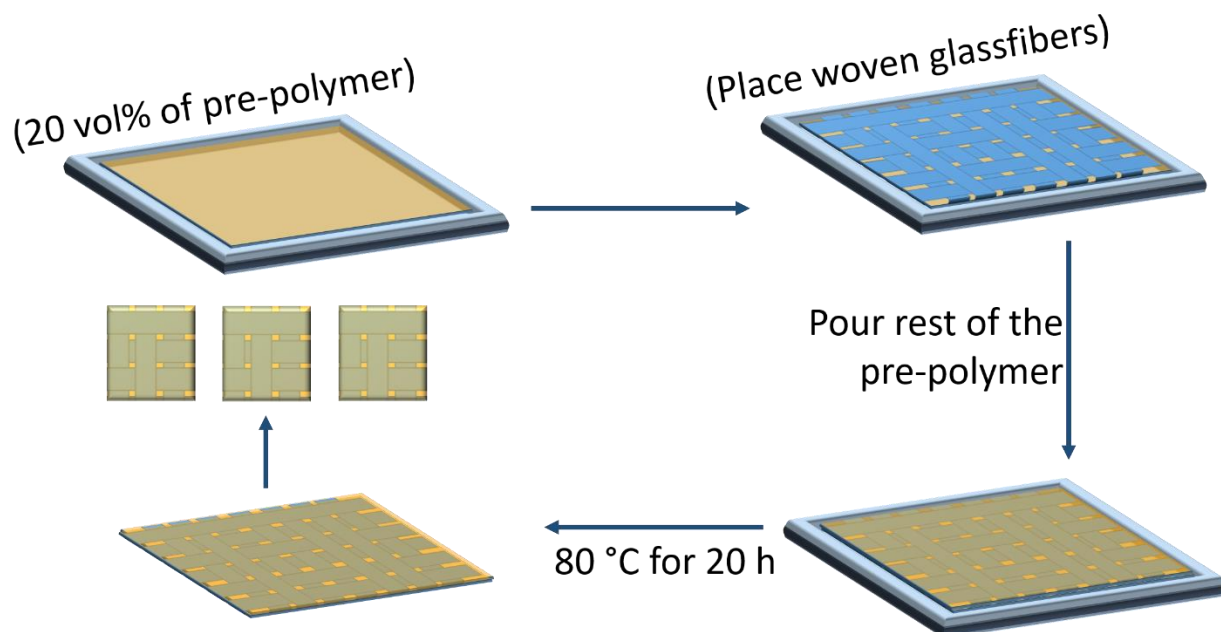


Figure SI-2. A sketch of the sample preparation method. Pre-polymer (20 vol%) was poured into a silicone mold as a first step. Woven glassfiber mat was sliced to exactly fit the mold and placed on the pre-polymer. Rest of the pre-polymer was poured on to the glassfiber mat. This arrangement was set in a furnace for 20 h at 80 °C for complete polymerization. The cured reinforced polymer composite was sliced into smaller pieces for “Hammer test”.

Polymer composites with and without glassfibers were produced as explained in this section. Spiropyran (SP) was used in all the samples as a stress indicator to compare the mechanochromicity and the impact resistance of the composite system. In all the samples, SP was used at a concentration of 0.5 wt% and the glassfiber concentration was at ~8 wt%. The PTU/spiropyran (PTU/SP) was coated onto the woven glassfibers as explained in the following procedure. The monomers pentaerythritol tetrakis(3-mercaptopropionate) (PETMP) and hexamethylene diisocyanate (HDI) were mixed at a weight ratio of 1:1.4 with SP. After 15 min of degassing, 20 vol% of this mixture was cast into a mold so that a uniform layer was obtained. A rectangular woven glassfiber mat ($70 \times 70 \text{ mm}^2$) was placed over the

unpolymerized layer and the remaining 80% of the mixture was poured over the glassfiber mat (see **Figure SI-1**). The sample was later placed for 20 h in a furnace at 80 °C. To compare the GFPS composite system to the commercially available epoxy polymer, epoxy/spiropyran coated glassfiber (GFES) samples were prepared similarly: PTU/SP was first hand-dispersed into the hardener and epoxy resin (45:100 parts by volume of hardener : epoxy) was later added to the dispersion, the unpolymerized mixture was coated onto the glassfiber mat as explained earlier. PTU/SP, GFPS and GFES i.e., sheets with and without glassfiber mats (thickness, 5 mm) were later cut into smaller samples of the size 20*20 mm² for further investigations.

Hammer Test

The “Hammer test” test (Figure SI-1) involved a hammer weighing 2.141 kg with a hinge at its base falling freely on the samples. The test was repeated periodically until a color change was observed. The force required to damage the system was determined by the number of hits needed to cause a color change from orange to purple.

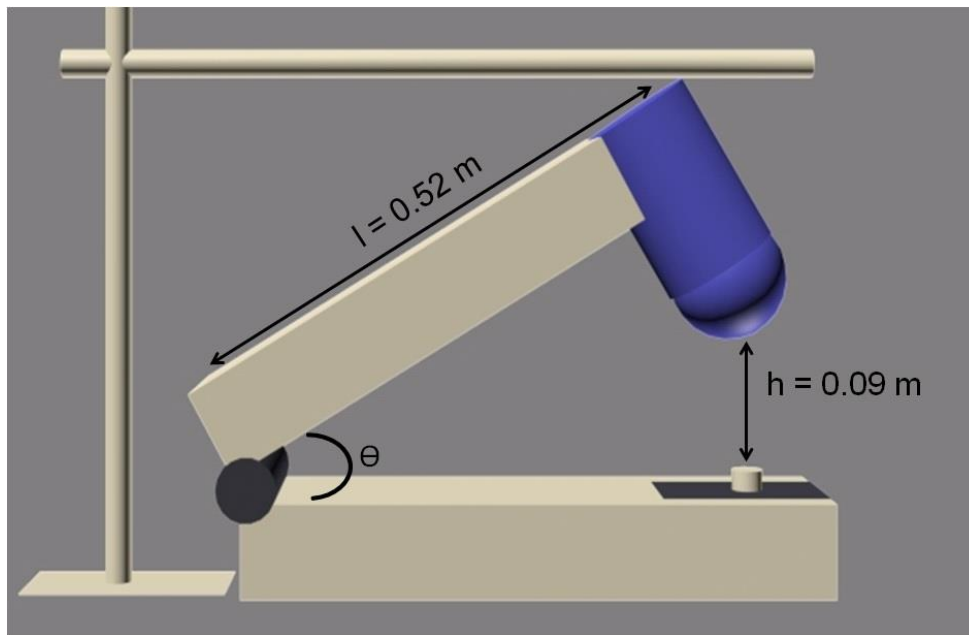


Figure SI-2. Sketch of the “Hammer test”. The hammer shaft is drawn to a defined height and released on to the sample freely.

The impact force was calculated using the following equation $F = m \cdot g \cdot \sin\theta = m \cdot g \cdot \frac{h}{l}$ where **F** is Force, **m** is weight of the hammer head, **g** is acceleration due to gravity, **h** is height

of fall, and **l** is length of the hammer. Pressure per impact was calculated using $P = F/a$ where **a** is the area of impact or point of contact. The measured area of impact was $1.53 \text{ e}^{-4} \text{ m}^2$.

Image Analysis

Corresponding videos were created with ImageJ by stitching the images taken after each hit under periodic impact test of the samples PTU/SP and GFPS. An RGB hyper stack was created using ImageJ for the purpose of quantitative analysis. Videos of the impact test of the sample PTU/SP with separated red, blue and green filter to observe which color shows the most transformation under impact. These videos are attached separately.

Analysis of the Spiropyran Failure in the Epoxy Matrix

SP in the epoxy matrix could not be used as a stress indicator. SP is a molecule with several functional groups and the components for the epoxy polymer also contains a high number of compounds with various functional groups. It is plausible that undesired reactions between these components and the SP making the molecule inactive. In order to shed some light on this, several experiments were performed:

The supplier of used epoxy system, R&G Faserverbundwerkstoffe GmbH, specifies the “Epoxy Resin L” as a three-component mixture, consisting of an epoxy resin as pre-polymer, phenylglycidyl ether formaldehyde resin as reactive pre-polymer and 1,6-hexanediol diglycidyl ether as reactive monomer (shown in **Figure SI-3**). The “Hardener S” is a mixture of six components. Two styrenated phenols, 2-hydroxy benzoic acid and three primary amines are combined to ensure complete curing within 24 hours above 5 °C. Since the supplier specifies only percentage ranges for each component, accurate investigation of the reaction of SP with the hardener and resin during the curing was not feasible. Instead, four model compounds representing the functional groups in both resin and hardener were chosen. Isopropyl glucidyl ether (**iPr-Epoxy**) and phenyl glucidyl ether (**Ph-Epoxy**) represent the reactive components in the “Epoxy Resin L”. The “Hardener S” contains phenol groups, benzoic acid groups and amines. Here 2-hydroxybenzoic acid (**HBA**) and *m*-xylylenediamine (**XDA**) was chosen as representative components.

The four reference compounds (**iPr-Epoxy**, 98%; **Ph-Epoxy**, 99%; **HBA**, $\geq 99\%$ and **XDA**, 99%) were purchased from TCI Co and used without further purification.

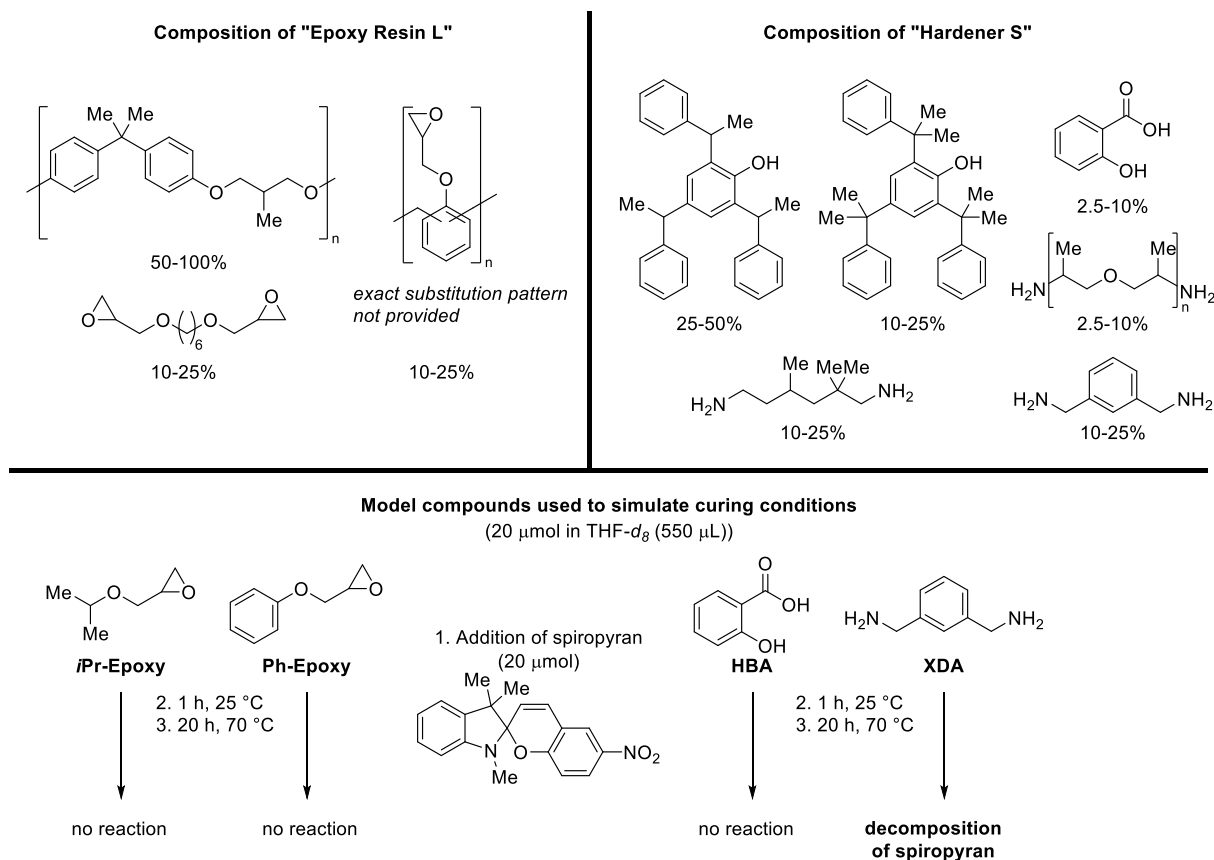


Figure SI-3: Composition of the commercial epoxy system. Top: Composition of the purchased Epoxy Resin L and Hardener S from R&G Faserverbundwerkstoffe GmbH. Bottom: Four model compounds were selected for the investigation of the possible reaction of SP during the curing process. The compounds were dissolved in THF- d_8 , before adding SP. Only the sample with **XDA** lead to decomposition of the SP as shown by NMR spectroscopy.

Each of the four compounds (20 μmol) were mixed with SP (20 μmol) in THF- d_8 and placed in sealable NMR tubes in a nitrogen filled glove box. To understand the interaction between SP and the components three ^1H NMR spectra were taken: immediately after mixing, after resting for 1 h at 25 °C and after resting for 20 h at 70 °C.

The ^1H spectra of the SP and the four equimolar mixtures after the complete heating cycle is displayed **Figure SI-3**. All spectra were recorded using the same settings and are not individually rescaled. The signals corresponding to the protons of the SP can be found in all spectra, however, are notably less intense in the top spectrum, corresponding to the mixture with **XDA**. The signals of the proton *H-3* and the methyl groups *H-8'* and *H-9'* (compare

section 4) are the most distinct ones to control the SP's stability and highlighted in **Figure SI-2**.

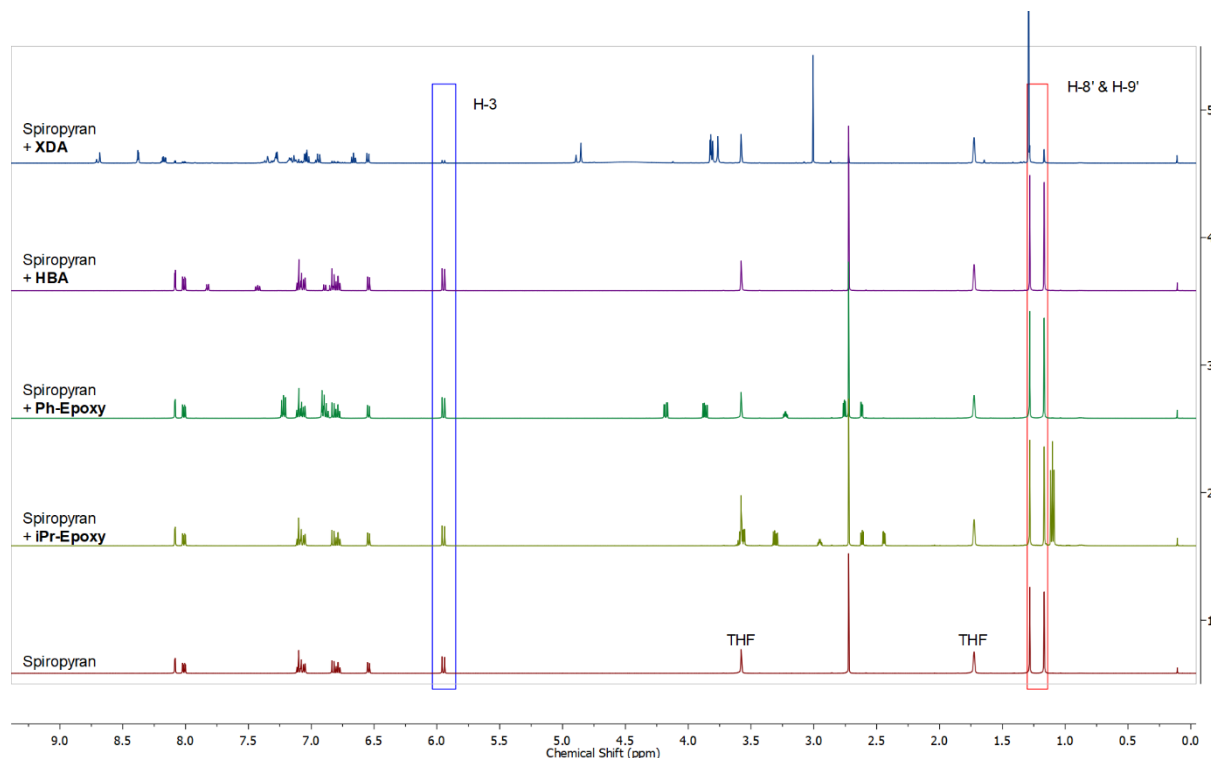
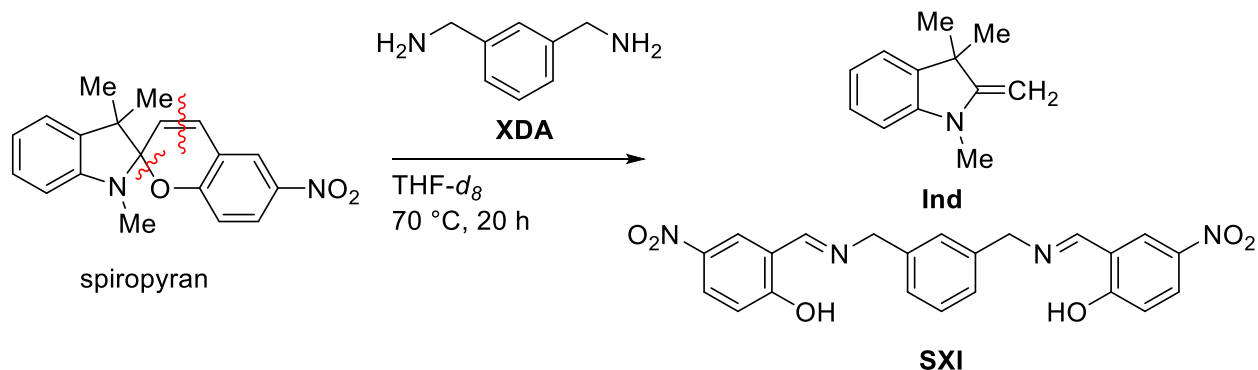


Figure SI-4: Overview of the stability test. The ^1H spectra of (bottom to top) SP, SP + *iPr*-Epoxy, SP + Ph-Epoxy, SP + HBA, SP + XDA after resting at 70 °C for 20 h are shown. All spectra were recorded with the same settings and were not rescaled. The blue box highlights the signal of the proton *H*-3 and the red box highlights the signal of the methyl protons *H*-8' and *H*-9' (compare section 4) of the SP. The intensity of these signals is drastically reduced in the top spectrum, corresponding to the mixture of SP and XDA. The signals corresponding to the solvent THF-d8 are labeled in the bottom spectrum.

In order to reveal the kind of reaction that could have occurred with XDA, the sample with SP and XDA was fully investigated using NMR methods. First, a switching to the open merocyanine form could be excluded as the characteristic signal of the ethylene bridge was absent. Whereas the coupling constant of the protons (*H*-3 and *H*-4, compare to **Chapter 0** in this SI) is approx. 10 Hz in the closed form, it increases to approx. 15 Hz in the open form.^[3] It was possible to identify 1,3,3-trimethyl-2-methyleneindoline (**Ind**) and 5-nitrosalicylaldehyde-1,3-xylylenediimine (**SXI**) as products, proving a cleavage of the ethylene bridge in the SP. ESI mass spectrometry of the reaction mixture proved the presence of the four mentioned compounds in high resolution. An additional set of signals was detected in ^1H and $^{13}\text{C}\{^1\text{H}\}$ NMR. As in **SXI**, it contains signals corresponding to imine bridges.

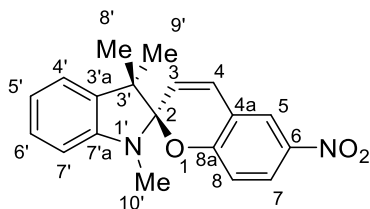
However, it might be structurally similar to **SXI** and could not be assigned this set of signals to a reasonable product.



Scheme SI-1: Confirmed ring opening reaction of SP in presence of xylylenediamine (**XDA**). 1,3,3-Trimethyl-2-methyleneindole (**Ind**) and 5-nitrosalicylaldehyde-1,3-xylylenediamine were identified as products. The broken SP bonds are indicated as red wavy lines.

The NMR shifts data were obtained by measuring the reaction mixture. Assignment of the peaks was done by using spectra of the pure compounds SP, **XDA** and **Ind** as reference. The ESI measurement was performed using an ionization potential of 3.2 kV. SP, **XDA** and **Ind** were detected in positive ion mode; **SXI** was detected in negative ion mode.

Signals assigned to SP:

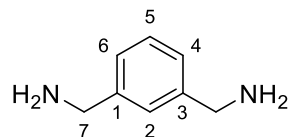


¹H NMR (500 MHz, THF-*d*₈, 300 K): δ = 8.08 (d, 4J = 2.8 Hz, 1H, H-5), 8.01 (dd, 3J = 9.0 Hz, 4J = 2.8 Hz, 1H, H-7), 7.12 – 7.08 (m, 2H, H-4, H-6'), 7.05 (dd, 3J = 7.4 Hz, 4J = 1.3 Hz, H-4'), 6.83 (d, 3J = 9.0 Hz, 1H, H-8), 6.79 (ddd, 3J = 7.4 Hz, 3J = 7.4 Hz, 3J = 1.0 Hz, 1H, H-5'), 6.54 (d, 3J = 7.7 Hz, 1H, H-7'), 5.95 (d, 3J = 10.3 Hz, 1H, H-3), 2.72 (s, 3H, H-10'), 1.28 (s, 3H, H-8'), 1.17 (s, 3H, H-9') ppm.

¹³C{¹H} NMR (126 MHz, THF-*d*₈, 300 K): δ = 160.6 (C-8a), 148.8 (C-7a'), 142.1 (C-6), 137.0 (C-3a'), 129.3 (C-4), 128.4 (C-6'), 126.3 (C-7), 123.3 (C-5), 122.3 (C-3), 122.1 (C-4'), 120.4 (C-5'), 120.0 (C-4a), 116.1 (C-8), 107.7 (C-7'), 107.3 (C-2), 52.9 (C-3'), 28.9 (C-10'), 26.2 (C-8'), 20.2 (C-9'). ppm.

HRMS (ESI-Sector): *m/z*: [M+H]⁺ calcd. for [C₁₉H₁₉N₂O₃]⁺ 323.1390; found 323.1385.

Signals assigned to xylylenediamine (XDA):

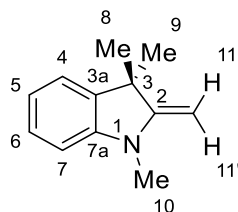


¹H NMR (500 MHz, THF-*d*₈, 300 K): δ = 7.30 – 7.27 (m, 1H, H-2), 7.19 – 7.11 (m, 3H, H-4, H-5, H-6), 3.76 (s, 4H, H-7), 1.39 (s, 4H, NH₂) ppm.

¹³C{¹H} NMR (126 MHz, THF-*d*₈, 300 K): δ = 145.3 (C-1, C-3), 128.6 (C-5), 126.4 (C-2), 125.6 (C-4, C-6), 47.4 (C-7) ppm.

HRMS (ESI-Sector): *m/z*: [M+H]⁺ calcd. for [C₈H₁₃N₂]⁺ 137.1073; found 137.1072.

Signals assigned to 1,3,3-trimethyl-2-methyleneindoline (Ind):

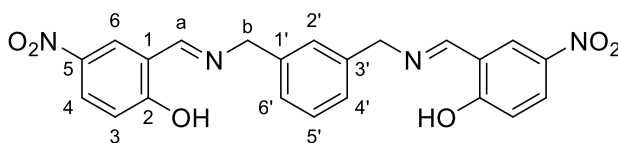


¹H NMR (500 MHz, THF-*d*₈, 300 K): δ = 7.06 – 7.01 (m, 2H, H-4, H-6), 6.67 (ddd, ³*J* = 7.4 Hz, ³*J* = 7.4 Hz, ³*J* = 1.0 Hz, 1H, H-5), 6.55 (d, ³*J* = 7.8 Hz, 1H, H-7), 3.82 (q, ⁵*J* = 1.9 Hz, 2H, H-11, H-11'), 3.01 (s, 3H, H-10), 1.29 (s, 6H, H-8, H-9) ppm.

¹³C{¹H} NMR (126 MHz, THF-*d*₈, 300 K): δ = 163.4 (C-2), 147.3 (C-7a), 138.2 (C-3a), 128.2 (C-6), 122.3 (C-4), 119.1 (C-5), 105.7 (C-7), 73.5 (C-11), 44.7 (C-3), 30.2 (C-8, C-9), 28.7 (C-10) ppm.

HRMS (ESI-Sector): *m/z*: [M+H]⁺ calcd. for [C₁₂H₁₆N]⁺ 174.1277; found 174.1275.

Signals assigned to 5-nitrosalicylaldehyde-1,3-xylylenediimine (SXI):



¹H NMR (500 MHz, THF-*d*₈, 300 K): ¹ δ = 8.68 (m, 2H, H-a), 8.38 (d, ⁴*J* = 2.9 Hz, 2H, H-6), 8.17 (dd, ³*J* = 9.2 Hz, ⁴*J* = 2.9 Hz, 2H, H-4), 7.35 (m, 1H, H-2'), 7.28 (m, H-5'), 7.18 (m, H-4', H-6'), 6.94 (d, ³*J* = 9.2 Hz, 2H, H-3), 4.85 (m, 4H, H-b) ppm.

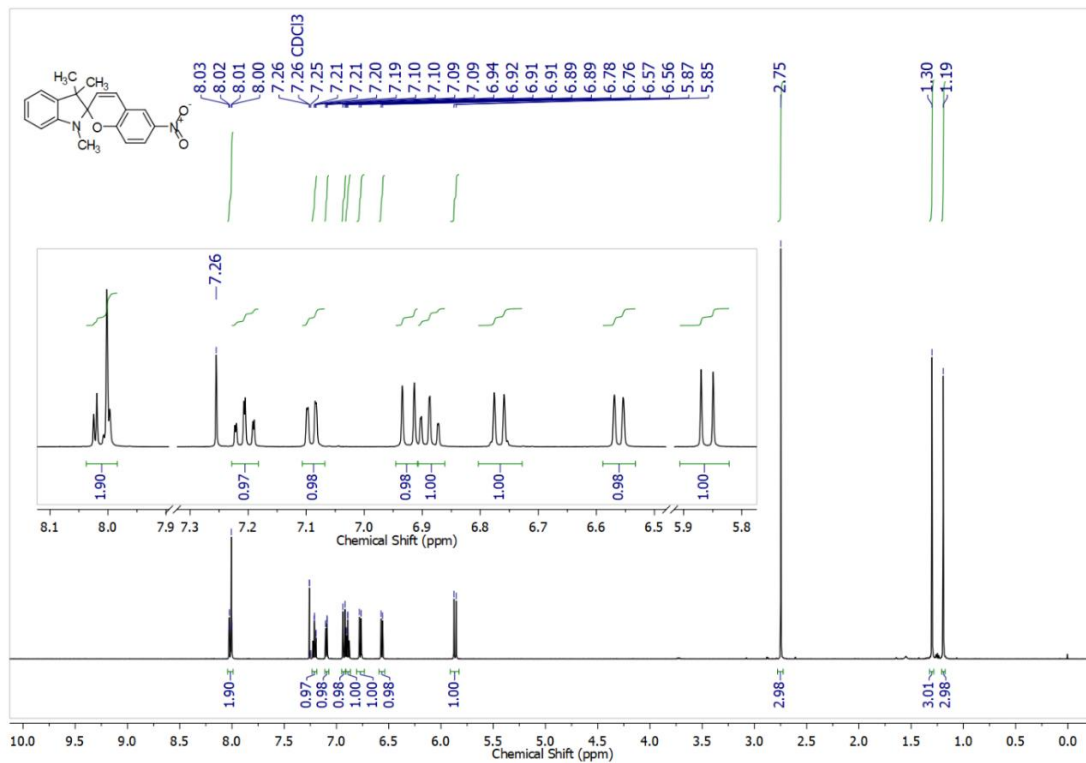
¹³C{¹H} NMR (126 MHz, THF-*d*₈, 300 K): δ = 169.5 (C-2), 166.4 (C-a), 139.9 (C-5), 138.2 (C-1', C-3'), 129.1 (C-6), 128.5 (C-4), 127.5 (C-2'), 127.1 (C-5'), 126.7 (C-4', C-6'), 119.2 (C-3), 118.4 (C-1), 62.45 (C-b) ppm.

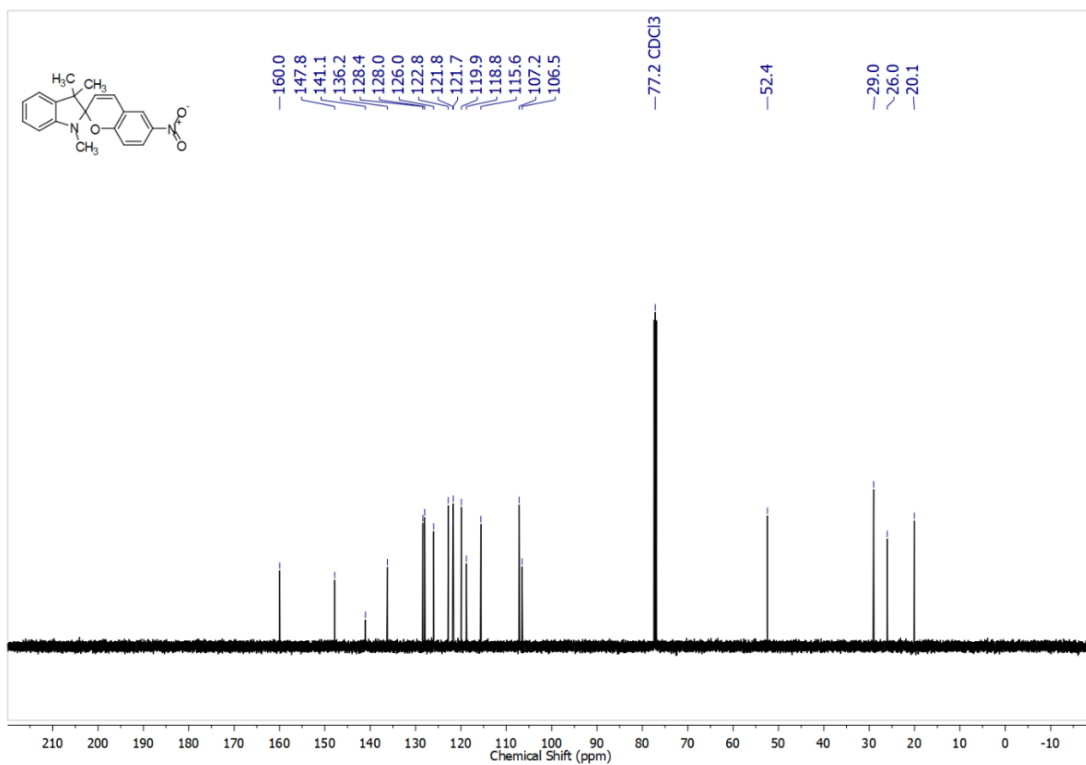
HRMS (ESI-Sector): *m/z*: [M-H]⁻ calcd. for [C₂₂H₁₇N₄O₆]⁻ 433.1154; found 433.1152.

¹ Due to the intensive overlap of signals with a chemical shift of 7.3 – 7.0 ppm in the ¹H NMR spectrum, it was not possible to integrate reliably.

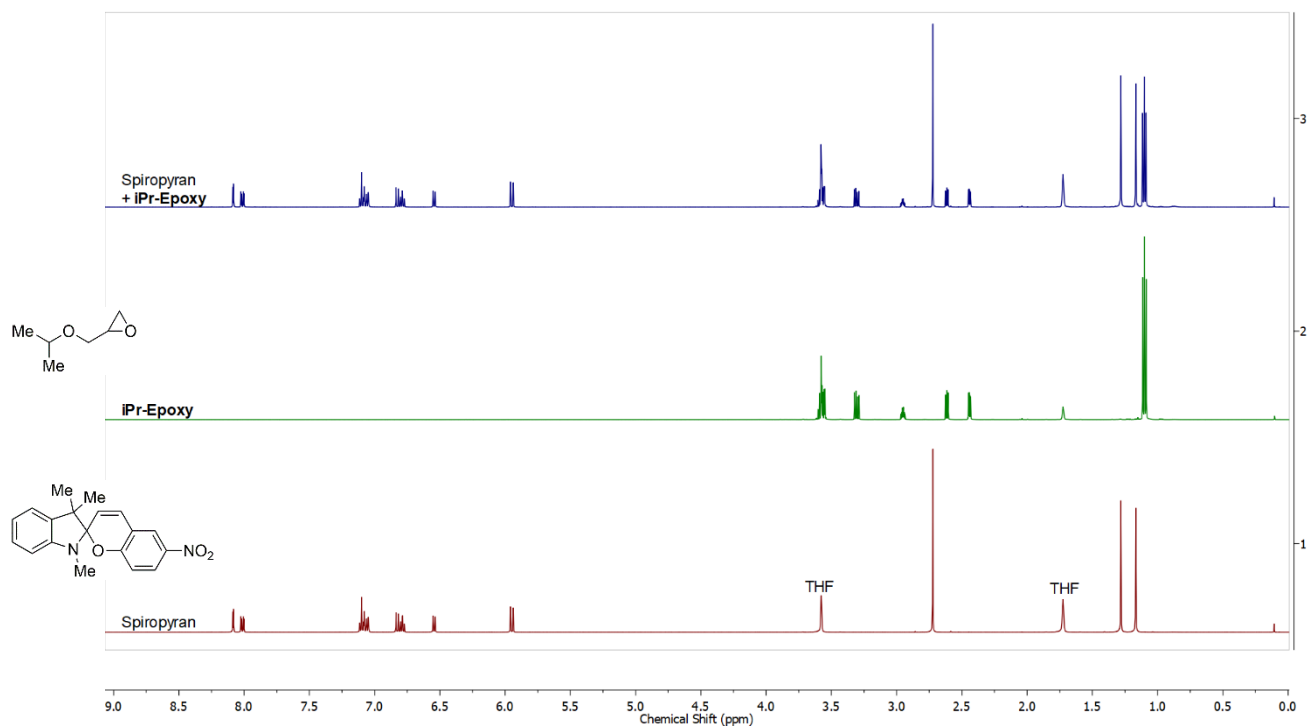
Plotted NMR Spectra

^1H and $^{13}\text{C}\{^1\text{H}\}$ NMR Spectra of 1',3',3'-Trimethyl-6-nitrospiro[chromene-2,2'-indoline] in CDCl_3

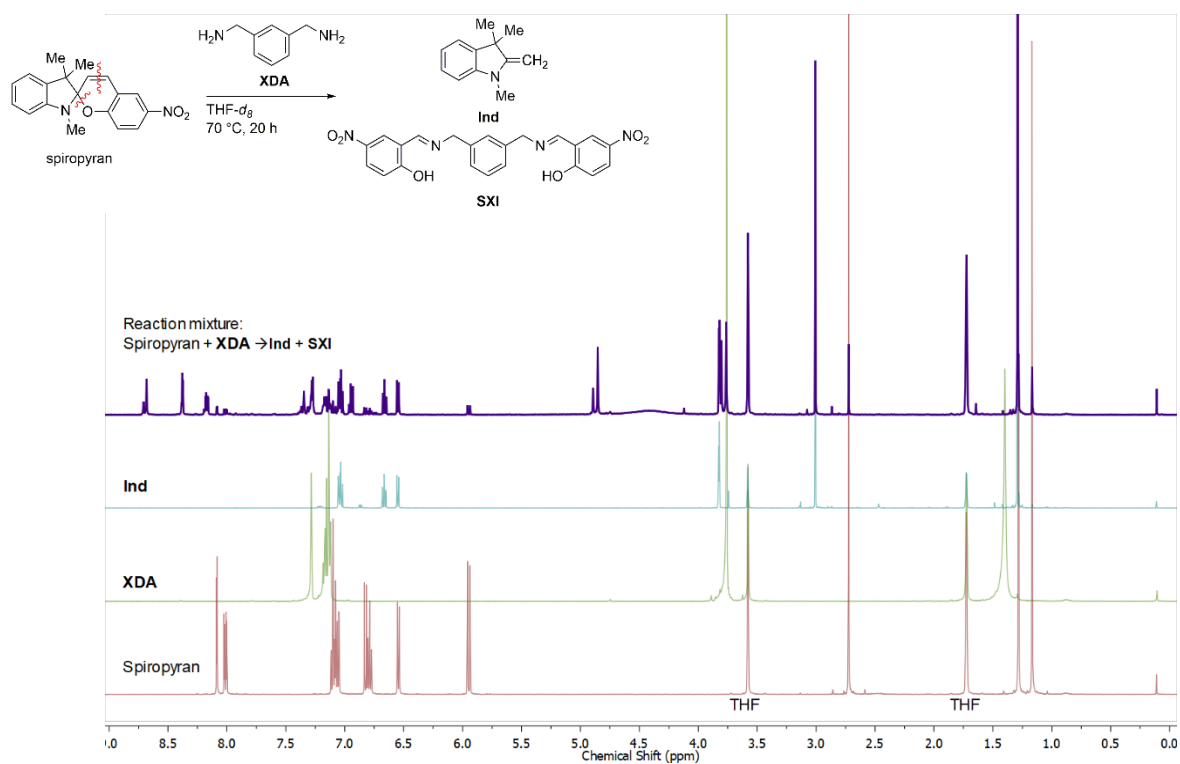


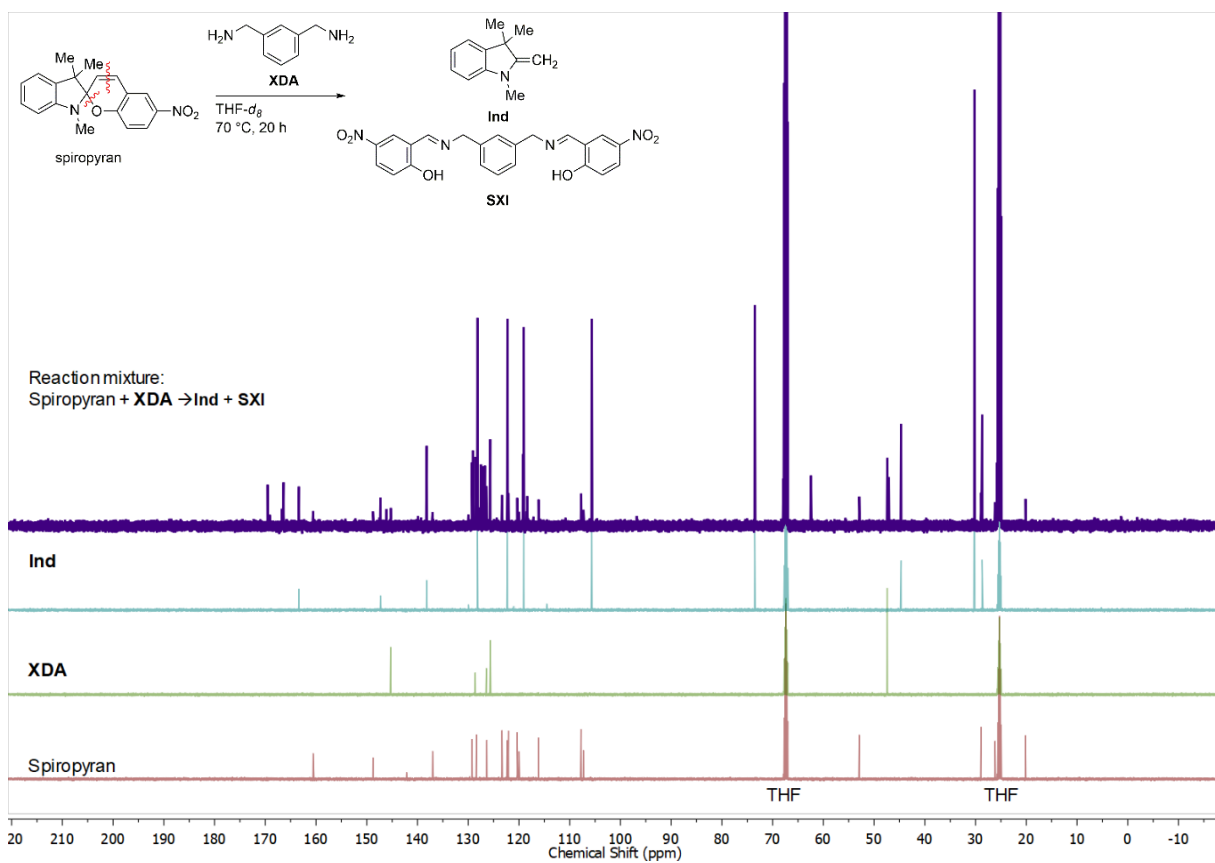
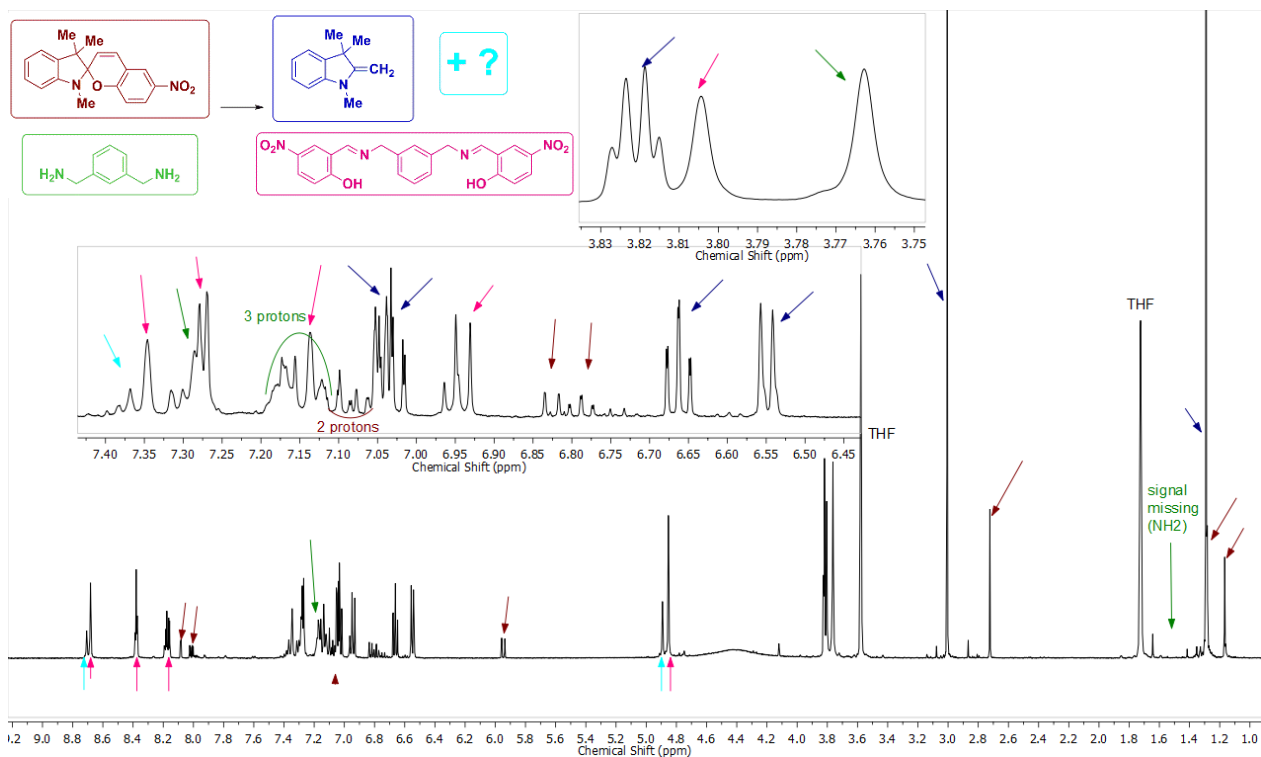


¹H NMR Spectra of SP, Isopropyl glucidyl ether (iPr-Epoxy) and the Reaction Mixture in THF-*d*₈



^1H and $^{13}\text{C}\{^1\text{H}\}$ NMR Spectra of SP, Xylylenediamine (XDA), 1,3,3-Trimethyl-2-methyleneindoline (Ind) and the Reaction Mixture in THF- d_8





References

1. A. M. Coghill, L. R. Garson, Eds., *The ACS Style Guide: Effective Communication of Scientific Information*, American Chemical Society, Washington, DC, **2006**.
2. C. J. Roxburgh, P. G. Sammes, A. Abdullah, *Dye. Pigment.* **2011**, *90*, 146.
3. M. Schulz-Senft, P. J. Gates, F. D. Sönnichsen, A. Staubitz, *Dye. Pigment.* **2017**, *136*, 292.

Spiropyran based smart composites: Memorizing Polymer with Enhanced Molecular Switches

Sindu Shree¹, Mattias Schulz-Senft², Xin Jin¹, Yogendra K. Mishra¹, Anne Staubitz², Rainer Adelung¹

¹ University of Kiel, Functional Nanomaterials, Institute for Materials Science, Kaiserstrasse 2, 24143 Kiel, Germany

² University of Kiel, Otto-Diels-Institute for Organic Chemistry, Otto-Hahn-Platz 3-4, 24118 Kiel, Germany

Abstract- We demonstrate the fabrication and response of a smart material combined with spiropyran molecules. Spiroyrans belong to a class of compound that constitute molecular switch. They change color in response to different stimuli such as heat, UV light or mechanical stress. These molecules have been incorporated in polythiourethane (PTU) which is a shape memory polymer. The observations revealed that the molecular switches do not alter the physical properties of the PTU in general; however, both, the spiropyran molecules and smart polymer show changes individually when exposed to heat. The microscopic mechanisms of switching process in response to external stimuli have been discussed in detail.

Keywords—Spiropyran, Merocyanine, Polythiourethane, Shape memory polymer.

I. Introduction

Polymer based functional composites, which exhibit the capability to respond to any external triggers, e.g., heat, UV light, stress, etc., are important material candidates for various applications. This kind of smart polymeric materials equipped with shape memory features, have found enormous applications in various fields ranging from aerospace to building industries [1]. Very recently, there has been significant progress in the direction of self-healing/reporting materials and these auto-responsive polymers are the most appropriate candidates in this context. The major drawbacks of the present heat/light sensitive smart polymer coatings are that they contain toxic metals and permanent deformations of the polymer decrease the life-time of the material.

The shape memorizing polymer matrix used in this paper is polythiourethane, a thermo-set polymer, which can be polymerized under solvent free conditions and is thermally stable. Hence it could have tremendous applications as a smart polymer. To make this shape memory polymer more efficient, spiropyran is added to the polymer matrix as a heat indicator.

Spiropyran has been used for its photo-responsive properties for several applications such as light modulated sensors [2] and for drug delivery [3].

These molecular switches have been used in our work and were incorporated into PTU. The usual ways of integrating spiropyran in a polymer matrix are either by polymerization of spiropyran based monomers or grafting of spiropyran on pre-formed polymer [4]. The downside of these methods of well defined covalent integration into a polymer is the accessible amount of material and its comparatively high cost, which might limit industrial usefulness. By adopting a simple strategy of dispersion of spiropyran molecules in the co-monomer, larger amounts can be obtained which is the main focus in present work.

II. EXPERIMENTS

A. Materials

Solvent free PTU, a two component system, was purchased from Fluid-& Prozesstechnik GmbH (Waltershausen, Germany). Preparation of the polymer was achieved by a poly-addition reaction between pentaerythritoltetrakis-(3 mercaptopropionate) (Tol) (2 mmol, 1 g) and 1,6-diisocyanatohexane (Iso) component (8.0 mmol, 1.4 g).

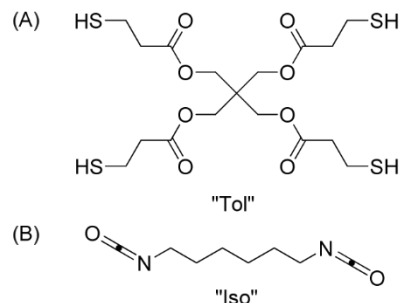


Fig. 1. Molecular structures of (A) the Tol component, and (B) the molecular structure of Iso the component.

B. Sample preparation

The samples were prepared by dispersing 0.01 wt% spiropyran in the co-monomer Tol for 20 min at 2000 rpm

in a dispersion machine to obtain homogeneous distribution of spiropyran. To this mixture, an appropriate amount of Iso was added. After degassing the mixture in a desiccator, the polymer blend was set into the moulds and placed in an oven for 2 h at 75 °C for polymerization process.

C. Response of PTU to heat

When heated, a pure PTU (without spiropyran) above its glass transition temperature (85 °C), softened. This allowed us to give the polymer any kind of shape which was maintained upon cooling. The deformed polymer returned to its original shape by an external stimulus such as heat.

D. Switching mechanism of spiropyran in response to an external stimulus

Spiropyran undergoes a reversible isomerization to the corresponding merocyanine form under the influence of an external stimulus such as heat. This causes changes in the molecular structure of thermochromic Spiropyran [5], resulting in the open ring structure called merocyanine as illustrated in Figure 2.

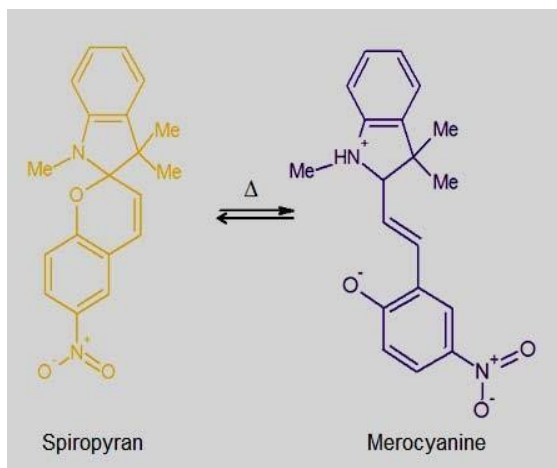


Fig. 2. Reversible isomerization between spiropyran and merocyanine in response to heat

III. RESULTS AND DISCUSSION

The PTU/spiropyran samples with a given flat shape (A) were heated to $T = 100\text{ °C}$ slightly above their glass transition temperature which softened the samples. While cooling down from 100 °C, different shapes have been given to the polymer, such as (B) and (C) [Figure 3 (B, C)].



Fig. 3 Different shapes of the PTU/spiropyran under temperature controlled conditions. (A) Corresponds to the original shape of PTU/spiropyran, (B) and (C) are folded and twisted shape of PTU/spiropyran respectively

A folded PTU/spiropyran sample (Figure 3B) was clamped on one side and solely its free end was heated up to 100 °C gradually with a heating gun (Figure 4). Under heat treatment, a complete shape recovery of the folded sample could be achieved as demonstrated clearly in by Figure 4 (a-h).

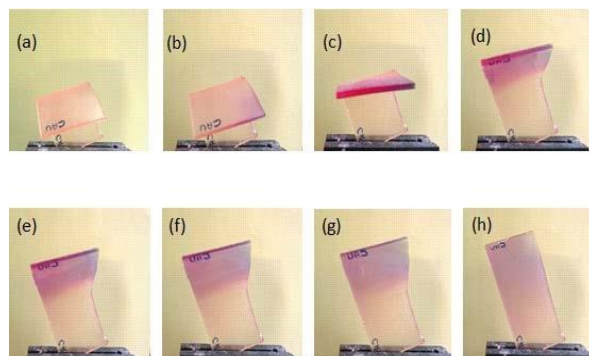


Fig. 4 PTU/spiropyran sample clamped on one end and only the folded end is heated with a heating gun. From (a) to (h) the sample was heated gradually up to 100 °C and the shape recovery behavior was clearly visible.

The PTU matrix consisted of a thermo-plastic and a thermo-set part. The thermo-plastic part of the polymer deforms upon heating. The thermo-set part of the polymer restrains deformation due to the crosslinking of SH-groups present in the Tol component with the NCO-groups in Iso component. When the temperature is above T_g , the polymer chains overcome inter-chain forces resulting in softening the polymer which is enough for deformation. Again when the polymer with temporary shape is heated, the chain relaxes which results in returning the polymer to its original shape.

This has been described by schematic representation in the Figure 5.

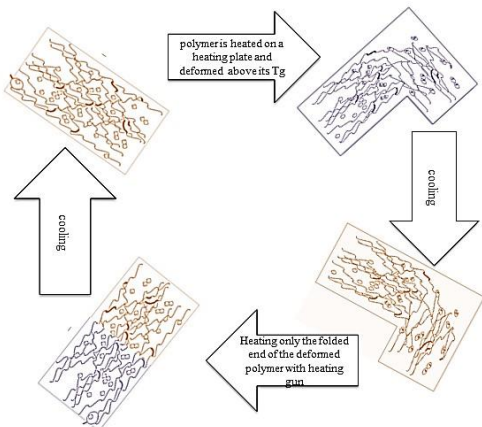


Fig. 5 Schematic representation of polymer chains incorporated with spiropyran undergoing structural changes independently

The added heat indicator gains enough energy for ring opening reaction at around 100 °C as presented in the Figure 2. When cooled merocyanine returns to the closed form independent of the changes taking place in the polymer chains.

IV. CONCLUSION

A shape memory polymer with an integrated heat Indicator has been successfully fabricated in a very simple approach. With mere PTU, it is difficult to recognize the reasons for the deformation process that the polymer undergoes when it returns to its original shape. However, with the spiropyran in the matrix, it enables one to recognize if the deformation of the polymer was due to the heat applied by the change of its color. This PTU/spiropyran matrix was synthesized in an intelligent way where the physical properties of both the materials involved, were maintained independent of each other.

V. ACKNOWLEDGEMENT

This project was funded by German Research Foundation (DFG) under the grant scheme of the SFB 677 "Function by Switching" Project C14.

REFERENCES

1. D. Ratna, J. Karger-Kocsis (2008) "Recent advances in shape memory polymers and composites: A review", *Journal of Materials Science*, 2008, pp 254-269
2. A. Radu, R. Byrne, N. Alhashimy, M. Fusaro, S. Scarmagnani, D. Diamond, "Spiropyran-based reversible, light-modulated sensing with reduced photofatigue", *Journal of Photochemistry and Photobiology A: Chemistry*, 2009, pp 109-115
3. S. Son, E. Shin, B. Kim, "Light-responsive micelles of spiropyran initiated hyperbranched polyglycerol for smart drug delivery", *Biomacromolecules*, 2014, pp 628-634
4. R. Klajn, "Spiropyran-based dynamic materials" *Chemical Society Reviews*, 2014, 148
5. C. F. Koelsch, "Steric Factors in Thermochromism of spiropyran and in reactivities of certain methylene groups" *Journal of Organic Chemistry*, 1951, pp 1362-1370
6. A. O. Bulanov¹, B. B. Safoklov², B. S. Luk'yanov¹, V. V. Tkachev², V. I. Minkin¹, S. M. Aldoshin², and Yu. S. Alekseenko¹, *Chemistry of Heterocyclic Compounds*, 2003, pp 350-357
7. R. Byrne, C. Ventura, F. Benito Lopez, A. Walther, Andreas Heise, D. Diamond, Characterisation and analytical potential of a photo-responsive polymeric material based on spiropyran, *Biosensors and Bioelectronics*, 2010, 4, pp 1392-1398
8. X. Jin, L. Heepe, J. Strueben, R. Adelung, S.N. Gorb and A. Staubitz "Challenges and Solutions in Joining Polymer Materials" *Macromolecular Rapid Communications*, 2014, pp 1551-1570
9. B. S. Lukyanov, M. B. Lukyanova, "Spiropyran: Synthesis, Properties, and Application. (Review)", *Chemistry of Heterocyclic Compounds*, 2005, pp 281-311
10. Y. Shiraishi, M. Itoh and T. Hirai, "Thermal Isomerization of Spiropyran to Merocyanine in Aqueous Media and its Application to Colorimetric Temperature Indication", *Physical Chemistry and Chemical Physics*, 2010, pp 13737-13745

8. Spiropyran Functionalized Microfibers

In this chapter, self-reporting spiropyran functionalised PMA fibers were centrifugally spun and examined. These mechanochromic micro fibers showed significant potential for materials that endure high strain. Enhancing the structural integrity of the PMA fibers by blending them with a fraction of PMMA is the focus of the following study.

Personal contributions in the following article:

- Mechanical tests of the fibers
- Morphological analysis of the fibers under SEM
- Co-writing the manuscript

This manuscript has been submitted to journal of American Chemical Society, *Applied Materials and Interfaces*

Self-Reporting Micro-Fibers from Polymer Blends: A Study on Photochromic and Mechanochromic Sensitivity

Ruchira A. Colaco,^{,§,‡,†} Sindu Shree,[†] Leonard Siebert,[†] Mathias Schulz-Senft,[‡] Sven Schultzke,[‡] Rainer Adelung,^{*,†} and Anne Staubitz^{*,‡,§,¥}*

[†] Institute for Materials Science, Functional Nanomaterials, Kiel University, Kaiserstr. 2, 24143 Kiel, Germany

[‡] Otto-Diels-Institute for Organic Chemistry, University of Kiel, Otto-Hahn-Platz 4, 24098 Kiel, Germany

[§] Institute for Organic and Analytical Chemistry, University of Bremen, Leobener Str. 7, 28359 Bremen, Germany

[¥] MAPEX Center for Materials and Process, University of Bremen, Bibliothekstr. 1, 28359 Bremen, Germany

ABSTRACT

Stimuli responsive polymers processed into micro-fibers bear the potential to be fabricated as systems detecting stress-induced failures. We report the high-throughput preparation of mechanochromic micro-fibers from a blend of poly(methyl acrylate) (PMA) functionalized with spiropyran (SP) and poly(methyl methacrylate) (PMMA) via centrifugal force spinning (CFS). To obtain mechanochromic fibers, the applied force must be sufficient to isomerize the colorless SP to the purple merocyanine (MC) form. For an effective translation of the force from the polymer chains to activate the mechanophore, bead free, non-fused, and uniformly aligned fibers were desired. PMMA was added (1 to 5 wt %) to improve structural stability, i.e. the shape of the micro-fibers. It emerged that a blend solution constituting 3 wt % PMMA with an overall concentration of 28%, gave high-throughput fibers with an average diameter of $8.0 \mu\text{m} \pm 2.3 \mu\text{m}$. The micro-fibers showed reversible photochromism on irradiation with ultraviolet (UV) light (360-370 nm) and green light (520-530 nm). Furthermore, during mechanical testing, the polymer chains aligned in the direction of the applied force switching SP into MC, indicated by a visible color change. These fibers detected high strain deformations in real-time, before material failure and retained the mechanochromic response after unloading. The outstanding benefit of processing high quantities of fibers from polymer blends is the development of stress detectors tuned to respond within the desired strain range. Such tunable mechanochromic micro-fibers may have exceptional applications as components in composite materials for active stress monitoring.

KEYWORDS: centrifugal spinning, mechanochromic, micro-fibers, poly(methyl acrylate), poly(methyl methacrylate), polymer blends, photochromic, self-reporting fibers (SRF), spiropyran (SP).

INTRODUCTION

Mechanochromic polymers have garnered a growing interest in the last decade due to their ability to signal material failures.¹⁻⁵ Chemical species known as *mechromes*, impart a stress sensing ability by altering their optical properties in response to the induced force.⁶⁻⁸ The best researched mechanochromic compound is the yellow to colorless spiropyran (SP), that reversibly switches to the highly colored purple merocyanine (MC) form.⁹⁻¹² At present, it is the primary choice to obtain mechanochromic polymers, as it can retain its switching properties both, when covalently or non-covalently incorporated into a variety of polymers.^{1,3,8,13,14} Furthermore, SP has been reported to respond to multiple stimuli in a polymer-ceramic material when added in an amount as low as 0.5 wt %.¹⁵ Ideally, the macroscopic force should align the polymer chains and SP in the direction of the applied force, isomerizing it to MC in order to observe mechano-activation in polymers.^{14,17} Additionally, for a detectable color change in response to the force *before* material failure, a high sensitivity is crucial. All of these properties can be fulfilled by micro- and nano-fibers which enhance stress indication due to an aligned microscopic matrix in contrast to bulk polymers.¹⁷ Due to the large surface to volume ratio, SP functionalized fibers make a promising stimuli-responsive material.¹⁸ The focus of the research presented here was placed on high-throughput processing of fibers from SP functionalized poly(methyl acrylate) (PMA-SP-PMA), using a self-designed centrifugal force spinning (CFS) machine. To account for maintaining uniformity and reproducibility, the fibers were desired to be bead free. Additionally, to overcome the structural deformations such as fiber-fiber fusion in PMA-SP-PMA due to its low glass transition temperature (T_g), blends of the former polymer with poly(methyl methacrylate) (PMMA) were prepared. The advantages of fabricating fibers made from a polymer blend of a functionalized and a non-functionalized polymer, is that the stimuli-responsive properties of the PMA-SP-PMA were imparted in the resulting blend.

This added stress-indicating property along with the high processing rate of the CFS method is expected to enhance the applications of existing polymeric fibers already that are used in textile,¹⁹ membranes,²⁰ as scaffolds to tissue engineering in the biomedical field,²¹⁻²³ for controlled drug release in cancer treatment²⁴ and as reinforcements in composite materials.²⁵

Micro-fibers can be prepared by a number of processes such as melt blowing,²² phase separation²⁶, pressurized gyration,²⁷ solution blowing,²⁸ electrospinning²⁹ and centrifugal force spinning.³⁰ Out of these techniques, electrospinning is widely used, however has drawbacks due to its low production rate and hence is non-economical at industrial scale.³¹ As for the other techniques like phase separation and melt blowing, material choices are limited to a narrow range of polymers.³¹ Therefore, there is a high demand to develop a technique which overcomes these limitations. Centrifugal force spinning, also called rotary jet spinning, gained attention due to its capability to produce nano- and micro-fibers at a reasonable cost from a wide range of materials.^{26,31,32}

In CFS (**Figure 3**), a concentrated polymer solution is rapidly ejected through a rotating nozzle and the fibers are collected on the radially placed rods. During the spinning process, both the centrifugal force and the air frictional force act on the solution.²⁵ However, only when the rotating speed exceeds a critical value, the centrifugal force overcomes the surface tension of the solution and the liquid jet is ejected from the nozzle tip. The solvent evaporates in-flight and the polymer fiber is finally caught on the collector rods.³¹ The fiber characteristics such as fiber diameter and morphology depend on the fluid properties such as viscosity and solution concentration as well on the operating parameters, namely nozzle-collector distance, nozzle diameter and rotating speed.³³

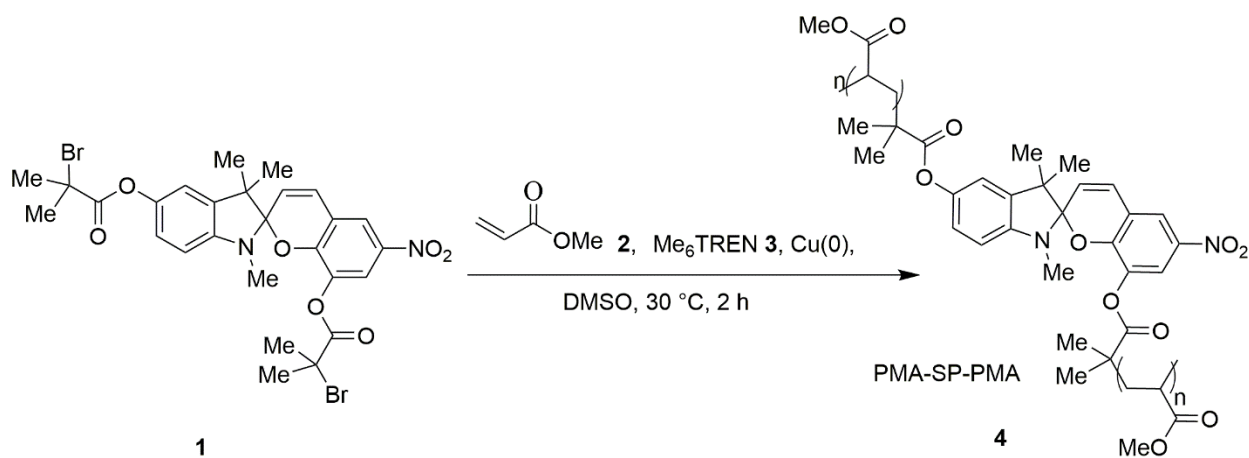
The main advantages of centrifugal spinning are the high production rate and the easy fiber fabrication of polymer blends. In this work, polymer blends solution were optimized by varying the weight ratio of PMA-SP-PMA and PMMA to achieve bead-free fibers. Finally, the response of the fibers to UV irradiation and mechanical force was studied to demonstrate their use as self-reporting fibers (SRF).

MATERIALS AND METHODS

If not stated otherwise, all chemicals were commercially available, of analytical grade and used without further purification. The monomer methyl acrylate (MA, 99%, inhibitor MEHQ (100 ppm)) was purchased from Sigma-Aldrich Ltd. and the poly(methyl methacrylate) PMMA (Mn : 100 kDa, a colorless coarse powder), was purchased from Kunststoff- und Farbengesellschaft mbH. The list of chemicals with purity and supplier (**Table S1** and **Table S2**) in section 2 of the Supporting Information (SI).

The covalent incorporation of SP into the polymer backbone of PMA was carried out with the spiropyran functionalized α -bromoester **1**, as an initiator (**Scheme 1**). Using methyl acrylate (MA) as the monomer (**2**), elemental copper as transition metal catalyst Cu(0), and the ligand tris[2-(dimethylamino)ethyl]amine (Me₆TREN) (**3**), the atom transfer radical polymerization (ATRP) was carried out in dimethyl sulfoxide (DMSO) as the solvent at 30 °C.² The synthetic route^{1,3} of the precursors molecules to **1** is shown in (**Scheme S1**, see SI section 4). All experimental procedures with the corresponding chemical characterizations (¹H NMR, ¹³CNMR, IR, HRMS (EI-TOF)) and the melting points from DSC measurements are given in the section 4 of the SI. The corresponding DSC plots, GPC plots and ¹H NMR, ¹³CNMR plots of the synthesized products are given in sections 9-11 of the SI.

Scheme 1. Synthesis of the mechanophore linked polymer PMA-SP-PMA via the ATRP method.³



To determine the ideal concentration for centrifugal spinning of the fibers, six different solutions of the synthesized PMA-SP-PMA (**A1** = 11 wt %, **A2** = 15 wt %, **A3** = 18 wt %, **A4** = 22 wt %, **A5** = 25 wt %, **A6** = 33 wt %) were prepared by dissolving the polymer in tetrahydrofuran ($\rho = 0.889 \text{ g/cm}^3$, b.p = 66 °C) (**Table S3**, see SI section 5). Furthermore, five polymer blends (**B1 to B5**) of PMA-SP-PMA and the PMMA polymer were prepared with increasing amount of PMMA (1 to 5 wt % respectively) and correspondingly decreasing amounts of PMA-SP-PMA (27 to 23 wt %), whilst maintaining the overall concentration to 28 wt % (**Table 4**). All the solutions were stirred at 30 °C for 24 h followed by stirring for 15 min at 50 °C prior to spinning, in order to induce faster in-flight solvent evaporation. Additional operating parameters are explained in the section 5 of the SI.

Table 4. Overview of the mixing ratios of solid PMA-SP-PMA and PMMA polymers for blend preparation of **B1 to B5** with a constant overall blend conc. of 28 wt %.

Entry	Label	PMA:PMMA weight ratio in blend	PMMA in blend (wt %)
1	B1	27 : 1	1.0
2	B2	13 : 1	2.0
3	B3	8.3 : 1	3.0
4	B4	6 : 1	4.0
5	B5	4.6 : 1	5.0

The polymer solutions **A1 to A6** and **B1 to B5** were processed into fibers using a self-designed centrifugal spinning machine at 5000 rpm equipped with a 0.15 mm or a 0.20 mm diameter nozzle respectively (**Figure 3**).

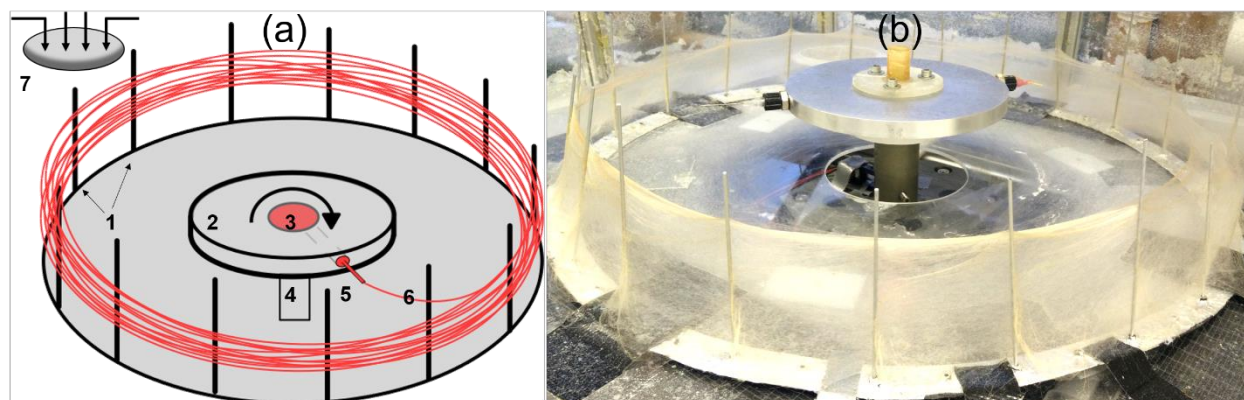


Figure 3. (a) Schematic and (b) the self-designed centrifugal spinning machine where 1) radially placed collector rods; 2) spinneret; 3) solution injection inlet and reservoir; 4) DC motor; 5) junction for nozzle attachment; 6) fibers; 7) exhaust to remove the solvent vapors produced during spinning.

Nuclear magnetic resonance spectroscopy (NMR) spectra (^1H NMR, $^{13}\text{C}\{^1\text{H}\}$ NMR) were either recorded on a Bruker Avance NEO 500 (500 MHz, 126 MHz) or on a Bruker Avance II HD 600 (600 MHz and 155 MHz) spectrometer. The NMR spectra were referenced against the solvent residual proton signals (^1H) or the solvent itself ($^{13}\text{C}\{^1\text{H}\}$).

Mass spectrometric (MS) measurements were performed in the positive ion mode using a JEOL-Accu TOF 4GGCV EI mass spectrometer or on the double focusing mass spectrometer MAT 95+ or Mat 8200 from Finnigan Mat. Electron ionization (EI) was performed using an ionization potential of 70 eV. Atmospheric pressure chemical ionization (APCI) experiments were performed on a Bruker Impact II from Bruker Daltonics.

Infrared spectroscopy (IR) spectra were recorded on a NICOLET iS10 IR spectrometer with a diamond-attenuated total reflectance (ATR) unit. Relative intensities of the IR bands were described by vs = very strong, s = strong, m = middle or w = weak, b = broad.

The gel permeation chromatography (GPC) was performed on a PSS (polymer standard service) SECurity GPC system after a conventional calibration using polystyrene standards (PS). The polymer PMA-SP-PMA was dissolved in THF (1.5 mg/mL) and GPC spectra was recorded and analysed ($M_n = 89.5$ kDa, $M_w = 161$ kDa, $PDI = M_w/M_n = 1.8$).

Thermogravimetric analysis (TGA) was performed on a Mettler Toledo TGA/DSC3+ instrument in aluminum crucibles (100 μ L), under nitrogen (N_2) at a flow rate of 20 mL/min.

Dynamic scanning calorimetry measurements (DSC) were performed on a Mettler Toledo DSC3+ instrument in aluminum crucibles (40 μ L, 100 μ L), under nitrogen (N_2) at a flow rate of 20 mL/min and heating rates of 10 K/min or 5 K/min.

The fiber samples for scanning electron microscopy (SEM) analyses were collected immediately after spinning. The samples were sputtered with gold to avoid sample charging and were examined under a Ultra 55 Zeiss SEM (8-10 kV) at varying magnifications to determine the fiber characteristics.

The UV-vis absorption measurements of the fibers (collected on the rods) were recorded at 20 °C in a Perkin Elmer UV/VIS NIR Spectrometer Lambda 900. The irradiation experiments were carried out using UV light (central wavelength = 360-370 nm; optical power = 680 mW; intensity = 2.2 mW/cm²) and green light (central wavelength = 520-530 nm; optical power = 20 W; intensity = 64 mW/cm²). Absorption of each sample was measured after 10 min of UV and 6 min of green light irradiation.

The tensile tests to characterize the mechanochromic behavior as well as the stress-strain relationship were recorded on the tensile test machine Zwick 1445 with a 10 kN capacity load cell.

RESULTS AND DISCUSSION

The outcome of the spinning process has been observed to produce either beads-only, beaded-fibers or the desired bead-free fibers.^{31,34} Fluid properties such as solution viscosity, concentration, surface tension along with the rotational speed and the centrifugal force acting on the solution jet, predominantly influence the resulting fiber morphologies.³¹ The type of morphology obtained can be correlated to the polymer solution concentration spun at a constant rotational speed.³⁴ Therefore, the concentrations (wt %) of the polymer solutions were controlled and optimized to yield uniform and bead-free micro-fibers at a rotational speed of 5000 rpm through the smallest nozzle diameter (0.15 mm) available. For the PMA-SP-PMA solutions, it was observed that the low-concentrated solutions **A1**, **A2** and **A3** (11 wt %, 15 wt % and 18 wt % respectively) spun into a beads-only network (**Figure S2**, see SI). It has been shown in the literature that a low polymer concentration and hence low viscosity is insufficient to achieve the critical chain entanglement, essential for spinning bead-free fibers.³⁴ In order to reduce the bead formation as seen in **A1** to **A3**, the viscosity and thereby the polymer chain entanglement was increased by using higher solution concentration. The increase in concentration to **A4** (22 wt %), changed the fiber morphology from beads-only to beaded-fibers (**Figure 4**). Further increase in the concentration to **A5** (25 wt %) and **A6** (33 wt %) reduced the bead formation, however, multiple fibers fused together on contact with other fibers (**Figure 4**).

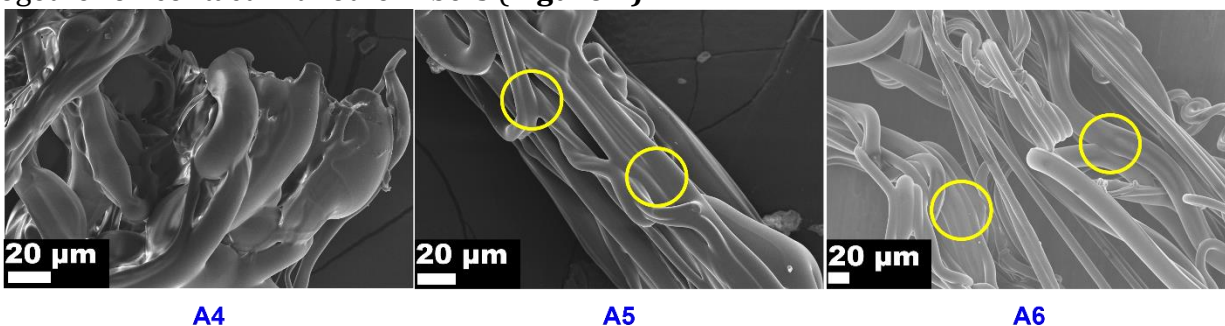


Figure 4. SEM images of the **A4**, **A5** and **A6** fibers of the functionalized PMA-SP-PMA spun at 5000 rpm from a 0.15 mm diameter nozzle. The marked regions (yellow) in **A5** and **A6** show fused fibers.

Additional increase in concentration above 33 wt % limited the laminar volumetric flow at the given nozzle diameter (0.15 mm) due to the Hagen-Poiseuille law.³⁵ As a result, the throughput of the fibers reduced, considering which the nozzle diameter was changed to

0.20 mm. The increased nozzle size yielded fibers with uneven diameter distribution, some very large PMA-SP-PMA fibers (71 μm), along with some sites of inter-fiber fusion (**Figure S3**, see SI). Therefore, the optimization of the solution concentration and nozzle diameter shows reduced bead formation but increased fiber fusing.

Such deformations in fibers may be due to an incomplete solvent evaporation, which is crucial for high quality fibers and takes place in two stages. First, the mass transfer of the solvent takes place at the surface of the jet in-flight, before reaching the collectors. Secondly, the remaining solvent diffuses into the polymer matrix and evaporates post fiber formation.³² However, the thermogravimetric analyses (TGA) of the **A6** fibers (**Figure S4**, see SI), show no sign of residual solvent in the fibers. Henceforth, we suspect that the low glass transition temperature (T_g) of the elastomeric PMA (14 °C-17 °C)³⁵ might be a reason for the structural deterioration in the fibers. From the differential scanning calorimetry (DSC) measurements, the T_g of the synthesized PMA-SP-PMA was found to be 14 °C (**Figure S5**, see SI). Therefore, even at a higher polymer concentration (33 wt%), fiber-fiber fusion (**Figure 4**) could not be avoided due to the intrinsic property (low T_g) of PMA-SP-PMA. Consequently, in order to impart structural stability and retain the fibers' structural integrity, PMMA was added (1 wt% to 5 wt %) to the PMA-SP-PMA polymer and blends (**B1 to B5**) in THF (**Table 4.**) were prepared.

Atactic PMMA has a T_g of 106 °C to 114 °C,³⁵ which should stabilize the structural integrity of the fibers at ambient temperatures. The T_g of the commercially purchased PMMA was measured to be 110 °C. The blend solutions were spun at 5000 rpm from a 0.20 mm diameter nozzle as the fiber throughput through the 0.15 mm nozzle was insufficient for further analyses. The fibers were collected for the SEM analyses and the images revealed that the solutions of the blends **B1 to B3** with PMMA (1 wt % to 3 wt % respectively), spun as bead-free fibers (**Figure 3**). They were structurally stable and showed no fiber-fiber deformation in comparison to the PMA-SP-PMA (**A5** and **A6**) fibers (**Figure 4**). This implies that, the addition of PMMA in merely 1 wt %, drastically reduces the deformities compared to fibers from pure PMA-SP-PMA solutions. The fibers obtained from the polymer blend **B1** were stable even when spun in a strongly twisted orientation (**Figure 3**), indicating a significant effect of PMMA for imparting mechanical stabilities in the fibers. Two more sets of bead-free

fibers **B2** (2 wt %) and **B3** (3 wt %) of PMMA were obtained. Further increase of the amount of PMMA, the solutions of the blends **B4** (4 wt %) and **B5** (5 wt %) formed fibers with large beads (**Figure S7**, see SI section 7), indicating that PMMA in 1 wt % to 3 wt % was the ideal blending range for efficiently obtaining bead-free micro-fibers.

Due to the bead formation in **B4** and **B5**, the average diameters of 15 fibers could only be calculated for **B1**, **B2** and **B3** fibers, as $8.0 \mu\text{m} \pm 1.5 \mu\text{m}$, $9.8 \mu\text{m} \pm 4.0 \mu\text{m}$ and $8.1 \mu\text{m} \pm 2.3 \mu\text{m}$ respectively. Among the bead-free micro-fibers (**B1** to **B3**), a high amount of fibers could be collected for **B3**, which is required for further photochemical and mechanochemical investigations. Additionally, the **B3** fibers were unidirectional compared to the **B1** and **B2** sample, which either spun in a twisted fashion or branched networks of fibers (**Figure 3**). For efficient mechano-switching, the alignment of both, the fibers and the mechano-phore (SP) are crucial. On account of which, **B3** fibers were further analyzed.

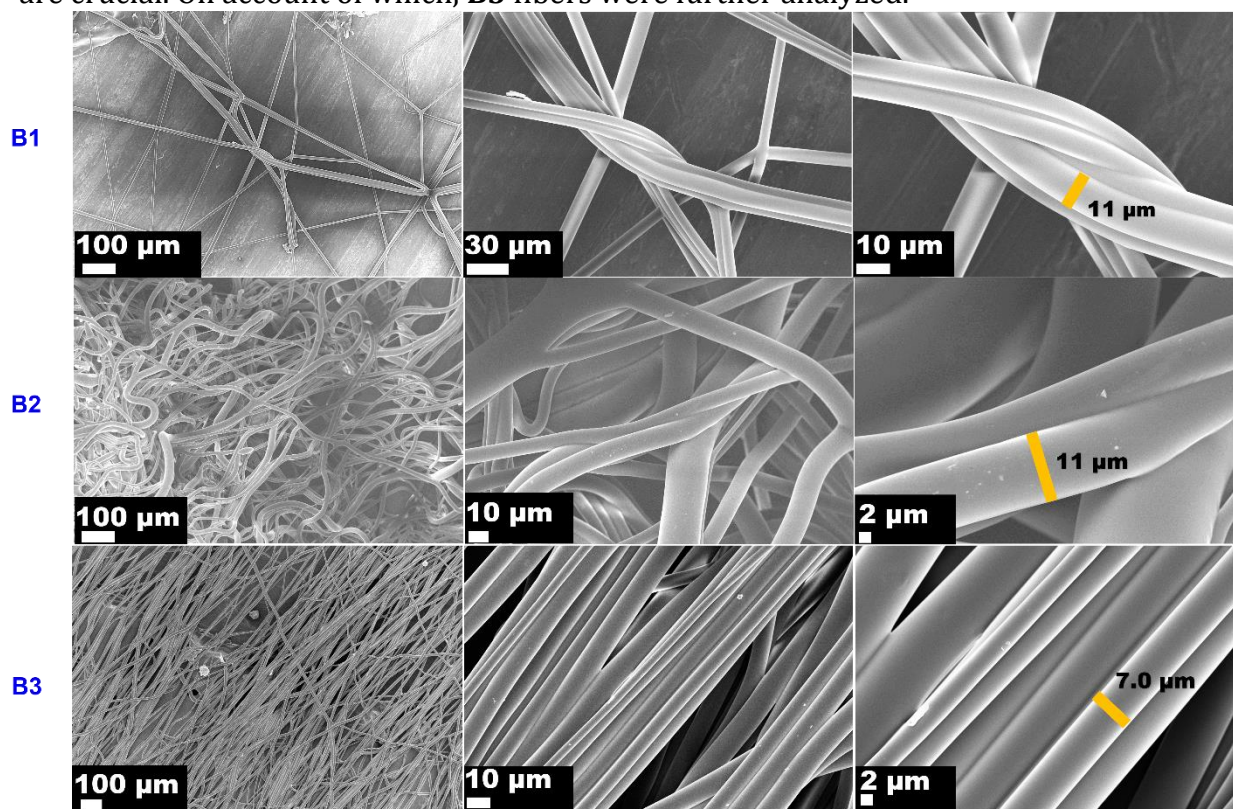


Figure 5. Bead free SEM images **B1**, **B2** and **B3** blends having 1, 2 and 3 wt % PMMA respectively spun at 5000 rpm from a 0.20 mm diameter nozzle. The marked regions (yellow) indicate a single fiber diameter.

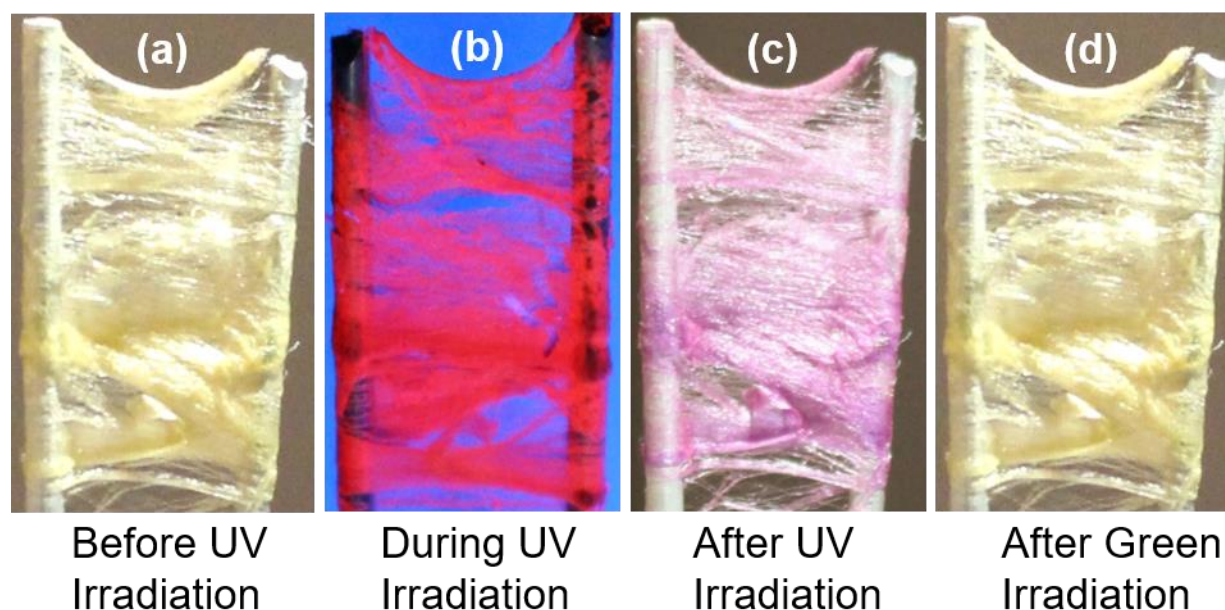


Figure 6. SP to MC reversible switching of **B3** fibers when irradiated with UV for 5 min on each side followed by green light for 3 min on each side. The photographs show a fiber-mat between two collector rods, folded several times to provide sufficient material.

The photochemical studies of the **B3** fiber-mat were carried out by UV illumination to isomerize the closed SP moieties and convert them to their open MC isomer.¹ The transformation of SP to MC is due to the cleavage of the heterolytic C-O bond,¹⁰ giving rise to an intense color change from light yellow to purple in the fibers (**Figure 6a**). The isomerization is also plausible from the fluorescence of the MC form observed during UV irradiation (**Figure 6b**).¹⁰ The highly colored MC form (**Figure 6c**) switches back to light yellow coloration upon irradiation with green light (**Figure 6d**). The formation of the highly colored, open-ring MC form is a result of the extended conjugation of the π -system, shifting the characteristic absorption into the visible region ($\lambda = 550$ to 570 nm) (**Figure 7a**). On illumination with green light, the MC signal ($\lambda_{\text{max}} = 564$ nm) disappeared, which confirmed MC to SP back switching behavior in the fibers (**Figure 7a**). Spiroyrans undergo photodegradation when subjected to multiple back and forth UV and green light irradiations.^{10,36} In order to examine the cyclic photochemical activity of SP in fibers, the **B3** fibers were illuminated with alternating UV and green light for six cycles and the corresponding spectra were measured after each irradiation. Absorption intensities at 564 nm were recorded and the ratio between the SP and MC values were plotted (**Figure 7b**). A non-significant linear decrease can be observed throughout the irradiation events.

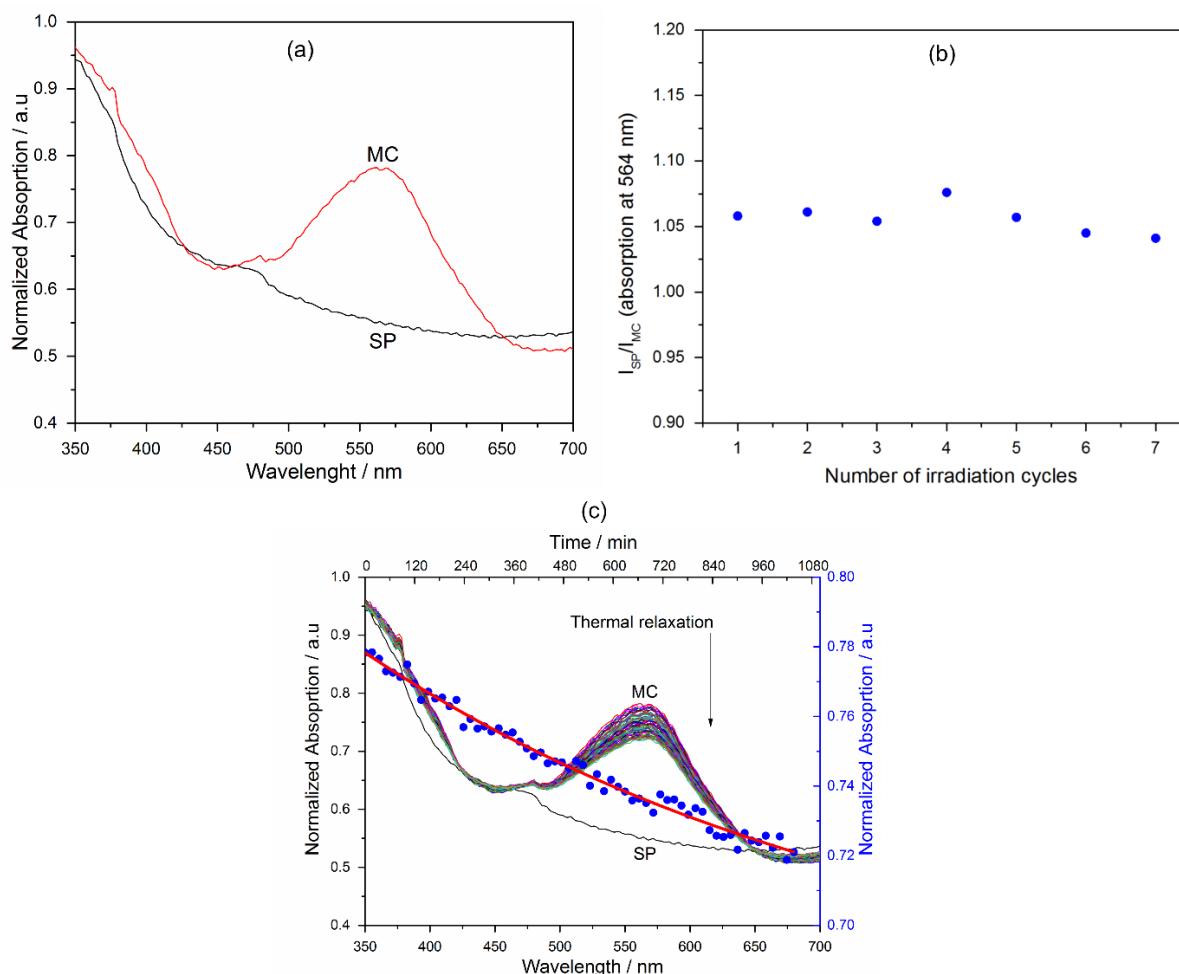


Figure 7. (a) UV-vis absorption spectra of the **B3** fibers for the open MC form (red line) and the closed SP form (black line) on irradiating with UV light and green light on each side for 5 min and 3 min respectively. (b) Absorption intensity (at $\lambda_{max} = 564$ nm) ratios of SP and MC of **B3** fibers on illumination with UV and green light. (c) Thermal relaxation of MC-SP was monitored for 17 h after irradiating the sample with UV light for 5 min on each side. The absorption values ($\lambda_{max} = 564$ nm) are fitted exponentially (red line with blue spots) to procure the half-life time of the fibers.

The deviation at the fourth cycle might be a result of an experimental error. There was no substantial photodegradation detected in the fibers for 12 irradiations. The reversible ring-closing reaction from MC to SP can also occur via spontaneous thermal relaxation over time (**Figure 7c**).³⁶ The thermal back conversion of MC to SP was monitored for 17 h after irradiating the fibers with UV light for 5 min on each side. At an interval of every 17 minutes, absorption spectra were recorded at 20 °C (**Figure 7c**). The study revealed a very gradual decrease in the absorption intensity with time. After 17 h of thermal relaxation, the intensity

of absorption was reduced by 20 % from that measured at 0 h, indicating slow transformation of the specimen towards the photostationary equilibrium. The exponential decay revealed a half-life time of $\tau = 15 \text{ h } 12 \text{ min } \pm 3 \text{ h}$. As a result, this system is well-suited to retain the color change and communicate the damage of UV light treatment in fibers for a substantial amount of time.

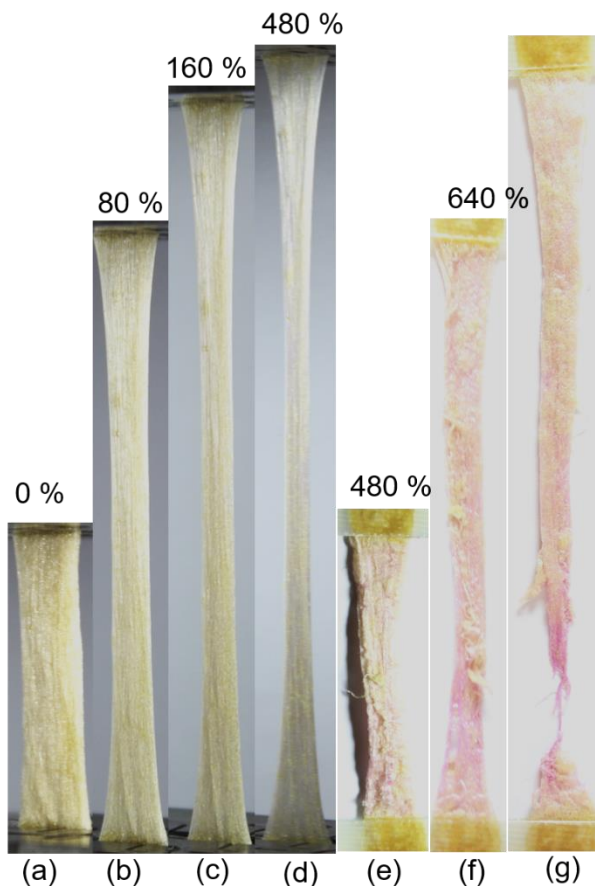


Figure 8. **B3** fiber sample pictures at specific elongation values: (a) 0%; (b) 80% (c) 240% and (d) 480%; **B3** fibers (e) unloaded fibers after 480% strain (145 mm elongation), in which the first sign of switching was observed; (f) unloaded after 640% strain (18.5 cm elongation), cycled five times; (g) sample after failure.

Furthermore, to investigate the mechano-activation in polymers, the orientation of mechanophores in the direction of the applied force is crucial.¹⁴ In order to qualitatively prove the hypothesis, that mechanical force can induce SP to MC isomerization in the fibers matrices, uniaxial tensile force was applied parallel to the **B3** fiber matrix. The fibers ($l_0 = 25 \text{ mm}$) were stretched in the tensile machine using a 10 kN load cell at the rate of 1 mm/s (**Figure 8**). For every cycle, the elongation was increased by 20 mm and the sample was

cycled between the extended position and the reference position. With increasing elongation length, necking was observed in the fibers (**Figure 8a-d**). After an elongation of 145 mm, i.e., 480% strain, a color change from yellow to light pink was observed throughout the sample (**Figure 8e**). Such a delay before any detectable mechano-activation may have several reasons. Firstly, the mechanical force may have been utilized to align the polymer chains of the fibers in the direction of the applied stress. This may be attributed to the role of chain entanglement, which is a dominant pre-requisite for fibers.³⁴ Secondly, to orient the mechanophores in the direction of the applied force. Therefore, a color change in fibers at 480% elongation demonstrates that sufficient mechanical force was applied to orient and induce ring opening of SP into MC. The elongation cycles were continued until 180 mm and then cycled five times, which enhanced the color change throughout the gauge length (**Figure 8f**), before failure. This is in agreement that increase in the strain, increases the force felt by the mechanophore which orients and isomerizes higher percentage of SP into MC.¹⁴ The fibers were further stretched until break point, where even the fragments had switched and retained the color visible to the bare eye, post-rupture (**Figure 8g**). This makes the fibers an ideal stress indicator, over a wide range of stresses/elongations. Such a system has the potential to be applied as a self-reporting material for desired strain values.

CONCLUSIONS

In conclusion, using the high production-rate technique of CFS, bead-free and aligned fiber mats from polymer blends were fabricated. The blend constituted of a mechanophore-linked polymer PMA imparting the switching functionality and PMMA to improve structural stability of the fibers. The method of polymer blending reduced the physical deformations in fibers of functional polymer PMA-SP-PMA, by merely adding PMMA (1 wt % to 3 wt %). Most importantly, the micro-fibers from the blend were structurally stable and active response of photochemical and mechanochemical isomerization of SP to MC could be observed. Therefore, stimuli-responsive properties of SP were successfully imparted in the resulting blend by mixing a SP functionalized PMA-SP-PMA and a non-functionalized polymer PMMA. The fibers reversibly respond to UV and green light for at least six cycles with negligible photodegradation, making it suitable for sensing history of light exposure. The micro-fibers withstand high pre-elongations of approx. 480%, after which uniform switching was

observed with a color change visible to the bare eye. Using the method of polymer blending, it may be possible to tune the pre-elongation of the resultant fibers, consequently tailoring the mechano-activation in the desired stress/strain range for sensing material damage before failure.

AUTHOR INFORMATION

Corresponding Authors

*Rainer Adelung: ra@tf.uni-kiel.de

*Anne Staubitz: staubitz@uni-bremen.de

Notes

The authors declare no competing financial interest.

ACKNOWLEDGMENT

This work was funded by the German Research Foundation (DFG) in the context of the Collaborative Research Center 677 “Function by Switching”, Project C14.

REFERENCES

- (1) Lee, C. K.; Davis, D. A.; White, S. R.; Moore, J. S.; Sottos, N. R.; Braun, P. V. Force-Induced Redistribution of a Chemical Equilibrium. *J. Am. Chem. Soc.* **2010**, *132* (45), 16107–16111. <https://doi.org/10.1021/ja106332g>.
- (2) Davis, D. A.; Hamilton, A.; Yang, J.; Cremar, L. D.; Van Gough, D.; Potisek, S. L.; Ong, M. T.; Braun, P. V.; Martínez, T. J.; White, S. R.; et al. Force-Induced Activation of Covalent Bonds in Mechanoresponsive Polymeric Materials. *Nature* **2009**, *459* (7243), 68–72. <https://doi.org/10.1038/nature07970>.
- (3) Potisek, S. L.; Davis, D. A.; Sottos, N. R.; White, S. R.; Moore, J. S. Mechanophore-Linked Addition Polymers. *J. Am. Chem. Soc.* **2007**, *129* (45), 13808–13809. <https://doi.org/10.1021/ja076189x>.
- (4) Degen, C. M.; May, P. A.; Moore, J. S.; White, S. R.; Sottos, N. R. Time-Dependent Mechanochemical Response of SP-Cross-Linked PMMA. *Macromolecules* **2013**, *46* (22), 8917–8921. <https://doi.org/10.1021/ma4018845>.
- (5) Caruso, M. M.; Davis, D. A.; Shen, Q.; Odom, S. A.; Sottos, N. R.; White, S. R.; Moore, J. S. Mechanically-Induced Chemical Changes in Polymeric Materials. *Chem. Rev.* **2009**, *109* (11), 5755–5798. <https://doi.org/10.1021/cr9001353>.
- (6) O’Bryan, G.; Wong, B. M.; McElhanon, J. R. Stress Sensing in Polycaprolactone Films via an Embedded Photochromic Compound. *ACS Appl. Mater. Interfaces* **2010**, *2* (6), 1594–1600. <https://doi.org/10.1021/am100050v>.

- (7) Li, M.; Zhang, Q.; Zhou, Y. N.; Zhu, S. Let Spiropyran Help Polymers Feel Force! *Prog. Polym. Sci.* **2018**, *79*, 26–39. <https://doi.org/10.1016/j.progpolymsci.2017.11.001>.
- (8) Sommer, M.; Komber, H. Spiropyran Main-Chain Conjugated Polymers. *Macromol. Rapid Commun.* **2013**, *34* (1), 57–62. <https://doi.org/10.1002/marc.201200688>.
- (9) Schulz-Senft, M.; Gates, P. J.; Sönnichsen, F. D.; Staubitz, A. Diversely Halogenated Spiropyran - Useful Synthetic Building Blocks for a Versatile Class of Molecular Switches. *Dye. Pigment.* **2017**, *136*, 292–301. <https://doi.org/10.1016/j.dyepig.2016.08.039>.
- (10) Klajn, R. Spiropyran-Based Dynamic Materials. *Chem. Soc. Rev.* **2014**, *43* (1), 148–184. <https://doi.org/10.1039/c3cs60181a>.
- (11) Minkin, V. I. Photo-, Thermo-, Solvato-, and Electrochromic Spiroheterocyclic Compounds. *Chem. Rev.* **2004**, *104* (5), 2751–2776. <https://doi.org/10.1021/cr020088u>.
- (12) Berkovic, G.; Krongauz, V.; Weiss, V. Spiropyran and Spirooxazines for Memories and Switches. *Chem. Rev.* **2000**, *100* (5), 1741–1754. <https://doi.org/10.1021/cr9800715>.
- (13) Schmidt, S. B.; Kempe, F.; Brügger, O.; Walter, M.; Sommer, M. Alkyl-Substituted Spiropyran: Electronic Effects, Model Compounds and Synthesis of Aliphatic Main-Chain Copolymers. *Polym. Chem.* **2017**, *8* (35), 5407–5414. <https://doi.org/10.1039/C7PY00987A>.
- (14) Beiermann, B. A.; Kramer, S. L. B.; Moore, J. S.; White, S. R.; Sottos, N. R. Role of Mechanophore Orientation in Mechanochemical Reactions. *ACS Macro Lett.* **2012**, *1* (1), 163–166. <https://doi.org/10.1021/mz2000847>.
- (15) Shree, S.; Schulz-Senft, M.; Alsleben, N. H.; Mishra, Y. K.; Staubitz, A.; Adelung, R. Light, Force, and Heat: A Multi-Stimuli Composite That Reveals Its Violent Past. *ACS Appl. Mater. Interfaces* **2017**, *9* (43), 38000–38007. <https://doi.org/10.1021/acsami.7b09598>.
- (16) Black, A. L.; Lenhardt, J. M.; Craig, S. L. From Molecular Mechanochemistry to Stress-Responsive Materials. *J. Mater. Chem.* **2011**, *21* (6), 1655–1663. <https://doi.org/10.1039/c0jm02636k>.
- (17) Raisch, M.; Genovese, D.; Zaccheroni, N.; Schmidt, S. B.; Focarete, M. L.; Sommer, M.; Gualandi, C. Highly Sensitive, Anisotropic, and Reversible Stress/Strain-Sensors from Mechanochromic Nanofiber Composites. *Adv. Mater.* **2018**, *30* (39), 1–6. <https://doi.org/10.1002/adma.201802813>.
- (18) Doan, H. N.; Tsuchida, H.; Iwata, T.; Kinashi, K.; Sakai, W.; Tsutsumi, N.; Huynh, D. P. Fabrication and Photochromic Properties of Forcespinning® Fibers Based on Spiropyran-Doped Poly(Methyl Methacrylate). *RSC Adv.* **2017**, *7* (53), 33061–33067. <https://doi.org/10.1039/c7ra03794e>.
- (19) Deitzel, J. M.; Kleinmeyer, J.; Harris, D.; Beck Tan, N. C. The Effect of Processing Variables on the Morphology of Electrospun Nanofibers and Textiles. *Polymer* **2001**,

- 42 (1), 261–272. [https://doi.org/10.1016/S0032-3861\(00\)00250-0](https://doi.org/10.1016/S0032-3861(00)00250-0).
- (20) Yanilmaz, M.; Zhang, X. Polymethylmethacrylate/Polyacrylonitrile Membranes via Centrifugal Spinning as Separator in Li-Ion Batteries. *Polymers* **2015**, *7* (4), 629–643. <https://doi.org/10.3390/polym7040629>.
- (21) Barnes, C. P.; Sell, S. A.; Boland, E. D.; Simpson, D. G.; Bowlin, G. L. Nanofiber Technology: Designing the next Generation of Tissue Engineering Scaffolds. *Adv. Drug Deliv. Rev.* **2007**, *59* (14), 1413–1433. <https://doi.org/10.1016/j.addr.2007.04.022>.
- (22) Ellison, C. J.; Phatak, A.; Giles, D. W.; Macosko, C. W.; Bates, F. S. Melt Blown Nanofibers: Fiber Diameter Distributions and Onset of Fiber Breakup. *Polymer* **2007**, *48* (11), 3306–3316. <https://doi.org/10.1016/j.polymer.2007.04.005>.
- (23) Li, W. J.; Laurencin, C. T.; Cateson, E. J.; Tuan, R. S.; Ko, F. K. Electrospun Nanofibrous Structure: A Novel Scaffold for Tissue Engineering. *J. Biomed. Mater. Res.* **2002**, *60* (4), 613–621. <https://doi.org/10.1002/jbm.10167>.
- (24) Chen, S.; Boda, S. K.; Batra, S. K.; Li, X.; Xie, J. Emerging Roles of Electrospun Nanofibers in Cancer Research. *Adv. Healthc. Mater.* **2018**, *7* (6), 1–20. <https://doi.org/10.1002/adhm.201701024>.
- (25) Huang, Z.-M.; Zhang, Y.-Z.; Kotaki, M.; Ramakrishna, S. A Review on Polymer Nanofibers by Electrospinning and Their Applications in Nanocomposites. *Compos. Sci. Technol.* **2003**, *63* (15), 2223–2253. [https://doi.org/10.1016/S0266-3538\(03\)00178-7](https://doi.org/10.1016/S0266-3538(03)00178-7).
- (26) Ma, P. X.; Zhang, R. Synthetic Nano-Scale Fibrous Extracellular Matrix. *J. Biomed. Mater. Res.* **1999**, *46* (1), 60–72. [https://doi.org/10.1002/\(SICI\)1097-4636\(199907\)46:1<60::AID-JBM7>3.0.CO;2-H](https://doi.org/10.1002/(SICI)1097-4636(199907)46:1<60::AID-JBM7>3.0.CO;2-H).
- (27) Mahalingam, S.; Edirisinghe, M. Forming of Polymer Nanofibers by a Pressurised Gyration Process. *Macromol. Rapid Commun.* **2013**, *34* (14), 1134–1139. <https://doi.org/10.1002/marc.201300339>.
- (28) Polat, Y.; Pampal, E. S.; Stojanovska, E.; Simsek, R.; Hassanin, A.; Kilic, A.; Demir, A.; Yilmaz, S. Solution Blowing of Thermoplastic Polyurethane Nanofibers: A Facile Method to Produce Flexible Porous Materials. *J. Appl. Polym. Sci.* **2016**, *133* (9), n/a-n/a. <https://doi.org/10.1002/app.43025>.
- (29) Krifa, M.; Yuan, W. Morphology and Pore Size Distribution of Electrospun and Centrifugal Forcespun Nylon 6 Nanofiber Membranes. *Text. Res. J.* **2016**, *86* (12), 1294–1306. <https://doi.org/10.1177/0040517515609258>.
- (30) Upson, S. J.; O’Haire, T.; Russell, S. J.; Dalgarno, K.; Ferreira, A. M. Centrifugally Spun PHBV Micro and Nanofibres. *Mater. Sci. Eng. C* **2017**, *76* (Supplement C), 190–195. <https://doi.org/10.1016/j.msec.2017.03.101>.
- (31) Zhang, X.; Lu, Y. Centrifugal Spinning: An Alternative Approach to Fabricate Nanofibers at High Speed and Low Cost. *Polym. Rev.* **2014**, *54* (4), 677–701. <https://doi.org/10.1080/15583724.2014.935858>.
- (32) Golecki, H. M. I.; Yuan, H.; Glavin, C.; Potter, B.; Badrossamay, M. R.; Goss, J. A.; Phillips,

- M. D.; Parker, K. K. Effect of Solvent Evaporation on Fiber Morphology in Rotary Jet Spinning. *Langmuir* **2014**, 13369–13374. <https://doi.org/10.1021/la5023104>.
- (33) Ren, L.; Ozisik, R.; Kotha, S. P.; Underhill, P. T. Highly Efficient Fabrication of Polymer Nanofiber Assembly by Centrifugal Jet Spinning: Process and Characterization. *Macromolecules* **2015**, 48 (8), 2593–2602. <https://doi.org/10.1021/acs.macromol.5b00292>.
- (34) Ren, L.; Pandit, V.; Elkin, J.; Denman, T.; Cooper, J. A.; Kotha, S. P. Large-Scale and Highly Efficient Synthesis of Micro- and Nano-Fibers with Controlled Fiber Morphology by Centrifugal Jet Spinning for Tissue Regeneration. *Nanoscale* **2013**, 5 (6), 2337–2345. <https://doi.org/10.1039/c3nr33423f>.
- (35) WEN, J. Poly(Methyl Acrylate). In *POLYMER DATA HANDBOOK*; 1999; 641–644. <https://doi.org/10.1021/ja907879q>.
- (36) Paine, M. F.; Hart, H. L.; Ludington, S. S.; Haining, R. L.; Rettie, A. E.; Zeldin, D. C. NIH Public Access. **2008**, 34 (5), 880–886. <https://doi.org/10.1038/jid.2014.371>.

Supporting Information

Self-Reporting Micro-Fibers from Polymer Blends: A Study on Photochromic and Mechanochromic Sensitivity

Ruchira A. Colaco,^{*,§,‡,†} Sindu Shree,[†] Leonard Siebert,[†] Mathias Schulz-Senft,[‡] Sven Schultze,[‡] Rainer Adelung^{*,†} and Anne Staubitz^{*,‡,§,¥}

[†] Institute for Materials Science, Functional Nanomaterials, Kiel University, Kaiserstr. 2, 24143 Kiel, Germany

[‡] Otto-Diels-Institute for Organic Chemistry, University of Kiel, Otto-Hahn-Platz 4, 24098 Kiel, Germany

[§] Institute for Organic and Analytical Chemistry, University of Bremen, Leobener Str. 7, 28359 Bremen, Germany

[¥] MAPEX Center for Materials and Process, University of Bremen, Bibliothekstraße 1, 28359 Bremen, Germany

Correspondence: ra@tf@uni-kiel.de; staubitz@uni-bremen.de

Table of Content

1. Abbreviations.....	215
2. Chemicals and Solvents.....	216
3. Analytical Equipment.....	218
4. Experimental Procedure.....	219
5. Polymer Solution Optimization for Centrifugal Spinning and Processing.	231
6. Fiber Morphology by SEM of non-blended PMA-SP-PMA Fiber.....	233
7. Fiber morphology by SEM of PMA-SP-PMA blended with PMMA.....	236
8. Mechanical Testing.....	237
9. Differential Scanning Calorimetry (DSC).....	239
10. Gel Permeation Chromatogram of the Synthesized PMA-SP-PMA.....	243
11. Corresponding ¹ H NMR and ¹³ C{ ¹ H} NMR Spectra.....	244
References.....	253

1. Abbreviations

ATRP	atom transfer radical polymerization
ATR	attenuated total reflection
calcd	calculated
DCM	dichloromethane
DMAP	4- <i>N,N</i> -dimethylaminopyridine
DMSO	dimethylsulfoxide
DSC	differential scanning calorimetry
EI	electron ionization
ESI	electron spray ionisation
GPC	gel permeation chromatography
HRMS	high resolution mass spectrometry
IR	infrared
I_{MC}	absorption intensity of MC
I_{SP}	absorption intensity of SP
MA	methacrylate
MC	merocyanine
Me ₆ TREN	tris[2-(dimethylamino)ethyl]amine
MEHQ	hydroquinone monomethyl ether
M_n	number average molecular weight
M_w	weight average molecular weight
PDI	polydispersity index
PMA	poly(methyl acrylate)
PMMA	poly(methyl methacrylate)
PTFE	poly(tetrafluoroethylene)
Py	pyridine
R_f	retention factor
RI	refractive index
SEM	scanning electron microscopy
SP	spiropyran
SPS	solvent purification system
SRF	self-reporting fibers
T_g	glass-transition temperature
TGA	thermogravimetric analyses
THF	tetrahydrofuran
TLC	thin layer chromatography
TOF	time-of-flight
TREN	tris(2-aminoethyl)amine
UV	ultraviolet
UV-vis	ultraviolet-visible
wt %	weight percent

2. Chemicals and Solvents

All chemicals and solvents were commercially available and were used as received unless noted otherwise. The dry solvents were either purchased or dried with a solvent purification system (SPS), from Inert Innovative Technology, Inc. Company. Inert reactions were carried out using Schlenk techniques under a dry, inert nitrogen atmosphere. The copper catalyst was stored in the glove box from the Inert, Innovative Technology, Inc. Company (0.1 ppm O₂ and 0.1 ppm H₂O).

Table S5. List of supplies and purities of the solvents used.

Solvent	Supplier	Purity
Acetic acid	Grüssing	99.5%
Chloroform-d	Euriso-top	99.8% D
Dichloromethane	VWR	HPLC grade, dry from SPS
Dimethyl sulfoxide	VWR	HPLC grade, dry from SPS
Dimethyl sulfoxide-d ₆	Euriso-top	99.8%
Ethanol	Sigma-Aldrich	>99.8%
Ethanol (dry)	Acros Organics	99.5%, extra dry
Ethyl acetate	VWR	99.9%
<i>n</i> -Heptane	AlfaAesar	>99%
<i>n</i> -Hexane	Sigma-Aldrich	>99.9%, HPLC grade
Tetrahydrofuran	VWR	HPLC grade

If not noted otherwise, all reagents were used as received.

Table S6. List of supplies and purities of the chemicals used.

Reagent	Supplier	Purity	Comments
2-Bromo-2-methylpropionyl bromide	Sigma-Aldrich	98%	stored in the glove box
3-Methyl-2-butanone	TCI	99%	
4-Dimethylaminopyridine	Acros Organics	99%	
4-Methoxy-phenyl hydrazine hydrochloride	TCI	>98%	
Ammonium chloride	Carl Roth	>99.7%	
Copper (Cu (0))	Sigma-Aldrich	>99.8%	stored in the glove box
Formaldehyde	Sigma-Aldrich	aq. 37% ACS, Reag. Ph. Eur	10-15% Methanol as stabilizer
Formic acid	Sigma-Aldrich	97%	
Hydrobromic acid (aq.)	Sigma-Aldrich	48%	
Hydrochloric acid in 2-propanol	Acros Organics	5-6 M	
Iodomethane	Sigma-Aldrich	97%	
Nitric acid	Sigma-Adrich	100% (fuming)	
Magnesium sulfate	Grüssing	99%	
Methylacrylate	Sigma-Aldrich	99%	inhibitor MEHQ (100 ppm)
Methyleneindolene	Sigma-Aldrich	97%	
Methylisopropylketone	Alfa Aesar	98%	
<i>o</i> -Vanillin	Sigma-Adrich	99%	
Poly(methyl methacrylate)	Kunststoff und Farbengesellschaft mbH		M _n : 100 kDa
Potassium hydroxide	Sigma-Aldrich	>85%	
Pyridine	Acros Organics	99.5%	

Piperidine	Acros Organics	99%	dried with CaH ₂ and stored in a J. Young's tube under nitrogen atmosphere
Sodium hydroxide	VWR	98.5%	
Sodium hydrogen carbonate	VWR	ACS, Reag. Ph. Eur	
Sodium sulphate	Sigma-Aldrich	>99%	
Silica gel 60	Merck		
Tris(2-aminoethyl)amine	Alfa Aesar	97%	

3. Analytical Equipment

Nuclear magnetic resonance spectroscopy (NMR) spectra (¹H NMR, ¹³C{¹H} NMR) were either recorded on a Bruker Avance NEO 500 (500 MHz, 126 MHz) or on a Bruker Avance II HD 600 (600 MHz and 155 MHz) spectrometer. The NMR spectra were referenced against the solvent residual proton signals (¹H) or the solvent itself (¹³C{¹H}).

Mass spectrometric (MS) measurements were performed in the positive ion mode using a JEOL-Accu TOF 4GGCV EI mass spectrometer or on the double focusing mass spectrometer MAT 95+ or Mat 8200 from Finnigan Mat. Electron ionization (EI) was performed using an ionization potential of 70 eV. Atmospheric pressure chemical ionization (APCI) experiments were performed on a Bruker Impact II from Bruker Daltonics.

Infrared spectroscopy (IR) spectra were recorded on a NICOLET iS10 IR spectrometer with a diamond-attenuated total reflectance (ATR) unit. Relative intensities of the IR bands were described by vs = very strong, s = strong, m = middle or w = weak, b = broad.

The gel permeation chromatography (GPC) was performed on a PSS (polymer standard service) SECurity GPC system after a conventional calibration using polystyrene standards (PS). The polymer PMA-SP-PMA was dissolved in THF (1.5 mg/mL) and GPC spectra was recorded. The number average molecular weight (M_n) of PMA-SP-PMA was found to be 89.5 kDa.

Thermogravimetric analysis (TGA) was performed on a Mettler Toledo TGA/DSC3+ instrument in aluminum crucibles (100 μL), under nitrogen (N₂) at a flow rate of 20 mL/min.

Dynamic scanning calorimetry measurements (DSC) were performed on a Mettler Toledo DSC3+ instrument in aluminum crucibles (40 μ L, 100 μ L), under nitrogen (N_2) at a flow rate of 20 mL/min and heating rates of 10 K/min or 5 K/min.

The fiber samples for scanning electron microscopy (SEM) analyses were collected immediately after spinning. The samples were sputtered with gold to avoid sample charging and were examined under a Ultra 55 Zeiss SEM (8-10 kV) at varying magnifications to determine the fiber characteristics.

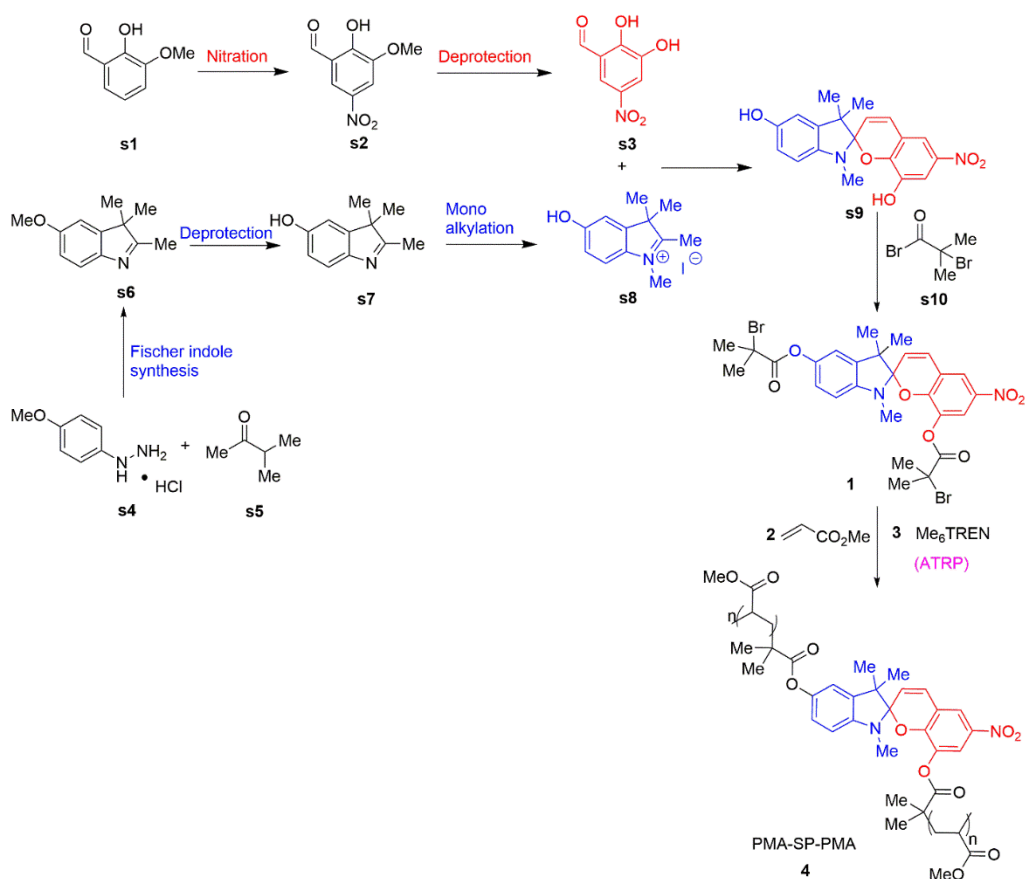
The UV-vis absorption measurements of the fibers (collected on the rods) were recorded at 20 $^{\circ}$ C in a Perkin Elmer UV/VIS NIR Spectrometer Lambda 900. The irradiation experiments were carried out using UV light (central wavelength = 360-370 nm; optical power = 680 mW; intensity = 2.2 mW/cm²) and green light (central wavelength = 520-530 nm; optical power = 20 W; intensity = 64 mW/cm²). Absorption of each sample was measured after 10 min of UV and 6 min of green light irradiation.

The tensile tests to characterize the mechanochromic behavior as well as the stress-strain relationship were recorded on the tensile test machine Zwick 1445 with a 10 kN capacity load cell.

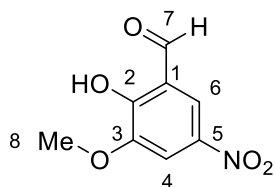
4. Experimental Procedure

The synthetic route (**Scheme S2**) was designed by Potisek et al.¹ and Davis et. al.² to incorporate spiropyran (SP) covalently into the polymer backbone of poly(methyl acrylate) (PMA). The precursors of SP have been previously synthesized,¹⁻³ followed by the functionalization of SP at position 5' and 8 using 2-bromo-2-methylpropionyl bromide.^{1,2} The reported polymerization reaction was optimized to synthesis SP linked polymer (PMA-SP-PMA) by a copper-catalyzed atom transfer radical polymerization (ATRP) method.¹

Scheme S2. Synthetic route to obtain SP covalently incorporation in the polymer backbone.¹



2-Hydroxy-3-methoxy-5-nitrobenzaldehyde (s2)³



To glacial acetic acid (138 mL) and water (7 mL), *o*-vanillin (30.0 g, 197 mmol) was added and the reaction mixture was cooled to 15 °C. A mixture of glacial acetic acid and fuming nitric acid (v/v), (2/1, 30 mL) was added over the course of 45 min and the reaction mixture stirred at 15 °C for another 90 min. Thereafter, the solution was diluted with water (300 mL). The formed yellow precipitate was filtered and washed with water (20 mL). The precipitate was then washed with diethyl ether (30 mL) and the obtained powder was dried

in vacuum (~ 1 mbar) to obtain the product 2-hydroxy-3-methoxy-5-nitrobenzaldehyde (**s2**) as a beige solid (20.1 g, 102 mmol, 52%, Lit.:³ 56%).²

¹H NMR (500 MHz, DMSO,): δ = 10.32 (s, 1 H, H-7), 8.09 (d, ⁴*J* = 2.7 Hz, 1 H, H-6), 7.92 (d, ⁴*J* = 2.7 Hz, 1 H, H-4), 3.99 (s, 3 H, H-8) ppm.

¹³C NMR (126 MHz, DMSO,): δ = 189.3 (C-7), 156.4 (C-5), 149.1 (C-3), 139.4 (C-2), 121.6 (C-1), 115.7 (C-6), 110.3 (C-4), 56.8 (C-8) ppm.

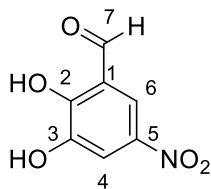
IR (ATR): $\tilde{\nu}$ = 3093 (m), 2880 (w), 1667 (s), 1518 (s), 1480 (s), 1446 (s), 1393 (s), 1340 (vs), 1267 (vs), 1198 (s), 1092 (vs), 953 (vs), 884 (s), 765 (s), 721 (vs) cm⁻¹.

HRMS (EI-TOF): *m/z* (%): [M]⁺ calcd. for [C₈H₇NO₅]⁺ 197.0324; found 197.03120 (100); 151.0276 (38) [M-NO₂]⁺.

Melting point: T = 138 °C.

² The ¹H NMR, ¹³C{¹H} NMR, IR, HRMS and mp data are in agreement with the reported.³

2,3-Dihydroxy-5-nitrobenzaldehyde (**s3**)³



A solution of 2-hydroxy-3-methoxy-5-nitrobenzaldehyde (**s2**) (21.5 g, 109 mmol) in aq. hydrobromic acid (48%, 363 mL, 6.70 mol) was heated to 140 °C for 5 h. Then, the solution was allowed to cool to 20 °C, diluted with water (500 mL), and then cooled to 0 °C and the precipitate that had formed was collected by filtration. It was washed with water (100 mL) and was dried at 5×10^{-2} mbar to yield 2,3-dihydroxy-5-nitrobenzaldehyde (**s3**) as a brown powder (18.2 g, 99.4 mmol, 92%, Lit.:³ 95%).³

¹H NMR (126 MHz, DMSO-*d*₆, 300 K): δ = 11.10 (s, -OH), 10.31 (s, 1 H, H-7), 7.99 (d, ⁴*J* = 2.8 Hz, 1 H, H-6), 7.79 (d, ⁴*J* = 2.8 Hz, 1 H, H-4) ppm.

¹³C NMR (126 MHz, DMSO): δ = 189.8 (C-7), 155.9 (C-2), 147.2 (C-3), 139.2 (C-5), 121.8 (C-1), 114.6 (C-6), 113.2 (C-4) ppm.

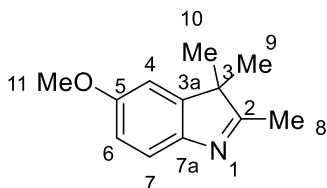
IR (ATR): $\tilde{\nu}$ = 3252 (b), 3088 (w), 1665 (s), 1624 (w), 1522 (s), 1461 (s), 1346 (vs), 1273 (vs), 1185 (s), 1094 (m), 951 (s), 903 (s), 756 (s), 743 (vs), 722 (s), 678 (s) cm⁻¹.

HRMS (EI-TOF): *m/z* (%): [M]⁺ calcd. for [C₇H₅NO₅]⁺ 183.0167; found 183.0158 (100).

Melting point: T = 231 °C.

³ The ¹H NMR, ¹³C{¹H} NMR, IR, HRMS and mp data are in agreement with the reported.³

5-Methoxy-2,3,3-trimethyl-3*H*-indole (**s6**)³



In dry ethanol (260 mL), (4-methoxy)-phenyl hydrazine hydrochloride (**s4**) (10.0 g, 57.3 mmol) and 3-methyl-2-butanone (**s5**) (4.93 g, 57.3 mmol) were dissolved and heated to 80 °C under a nitrogen atmosphere. After 5 h, the solution was cooled to 20 °C, and filtered through silica gel (eluent: EtOAc). Purification by column chromatography gave the product 5-methoxy-2,3,3-trimethyl-3*H*-indole (**s6**) as dark brown solid (8.30 g, 43.9 mmol, 77%, Lit.:³ 78%).⁴

TLC (UV): R_f = 0.5 (DCM/EtOAc = 0.5).

¹H NMR (500 MHz, CDCl₃,): δ = 7.46 (d, 3J = 8.3 Hz, 1 H, H-7), 6.84 - 6.81 (m, 2 H, H-4, H-6), 3.82 (s, 3 H, H-11), 2.28 (s, 3 H, H-8), 1.29 (s, 6 H, H-9, H-10) ppm.

¹³C NMR (126 MHz, CDCl₃,): δ = 186.4 (C-2), 158.3 (C-5), 147.1 (C-7a), 146.2 (C-3a), 120.0 (C-7), 112.3 (C-4), 108.3 (C-6), 55.8 (C-11), 53.9 (C-3), 23.3 (C-9, C-10), 15.3 (C-8) ppm.

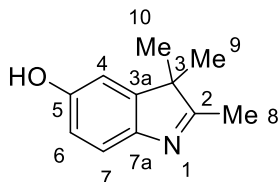
IR (ATR): $\tilde{\nu}$ = 2963 (m), 2930 (m), 2865 (m), 2835 (m), 1614 (m), 1579 (m), 1462 (vs), 1432 (s), 1379 (m), 1289 (s), 1212 (vs), 1179 (s), 1145 (m), 1068 (vs), 1030 (vs), 943 (m), 900 (m), 866 (m), 820 (vs), 747 (m), 698 (m), 616 (m), 587 (m) cm⁻¹.

HRMS (EI-TOF): m/z (%): [M⁺] calcd. For [C₁₂H₁₅NO]⁺ 189.1148, found 189.1147 (100), 174.1 (80) [M-CH₃]⁺.

Melting point: T = 46 °C.

⁴ The ¹H NMR, ¹³C{¹H} NMR, IR, HRMS and mp data are in agreement with the reported.³

5-Hydroxy-2,3,3-Trimethyl-3*H*-indole (**s7**)³



To aq. hydrobromic acid (48 %, 146 mL, 1.29 mol), 5-methoxy-2,3,3-trimethyl-3*H*-indole (**s6**) (8.30 g, 43.9 mmol) was added and the solution was heated to 140 °C for 2 h. The solution was cooled to 20 °C, diluted with water (200 mL) and neutralized with solid NaHCO₃ until the solution was basic (pH = 10). The aqueous solution layer was extracted with dichloromethane (4 x 100 mL). The combined organic layers were washed with brine (300 mL), dried over Na₂SO₄, filtered, and concentrated in vacuum to yield 5-hydroxy-2,3,3-trimethyl-3*H*-indole (**s7**) as a brown solid (7.52 g, 43.0 mmol, 98%, Lit.³: 79%).⁵

¹H NMR (500 MHz, CDCl₃,): δ = 7.32 (d, ³*J* = 8.3 Hz, 1 H, H-7), 6.85 (d, ⁴*J* = 2.3 Hz, 1 H, H-4), 6.78 (dd, ³*J* = 8.3 Hz, ⁴*J* = 2.3 Hz, 1 H, H-6), 2.27 (s, 3 H, H-8), 1.29 (s, 6 H, H-9, H-10) ppm.

¹³C NMR (126 MHz, CDCl₃,): δ = 186.2 (C-2), 155.7 (C-5), 147.3 (C-7a), 145.0 (C-3a), 120.0 (C-7), 114.3 (C-6), 109.9 (C-4), 53.8 (C-3), 23.3 (C-9, C-10), 15.1 (C-8) ppm.

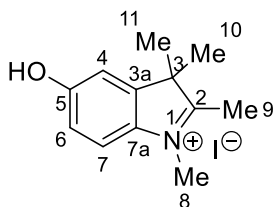
IR (ATR): $\tilde{\nu}$ = 2967 (m), 2928 (m), 1713 (w), 1613 (m), 1592 (m), 1582 (s), 1462 (vs), 1423 (m), 1387 (m), 1360 (s), 1293 (s), 1270 (m), 1200 (s), 1191 (s), 1061 (m), 846 (m), 816 (vs), 764 (m), 622 (m), 460 (m) cm⁻¹.

HRMS (EI-TOF): *m/z* (%): [M]⁺ calcd. for [C₁₁H₁₃NO]⁺ 175.0997; found 175.0995 (100); 160.0 (95) [M-CH₃]⁺.

Melting point: T = 178 °C.

⁵ The ¹H NMR, ¹³C{¹H} NMR, IR, HRMS and mp data are in agreement with the reported.³

5-Hydroxy-1,2,3,3-tetramethyl-3*H*-indolium iodide (**s8**)³



To iodomethane (75.0 mL, 1.20 mol), 5-hydroxy-2,3,3-trimethyl-3*H*-indole (**s7**) (7.52 g, 43.0 mmol) was dissolved under nitrogen atmosphere and the solution was heated to 40 °C for 15 h. The solution was cooled to 20 °C and was diluted with Et₂O (15 mL) and filtered. The crude product was purified by recrystallization from ethanol (20 mL) to yield 5-hydroxy-1,2,3,3-tetramethyl-3*H*-indolium iodide (**s8**) as a light brown solid (13.2 g, 41.6 mmol, 96%, Lit.:³ 94%).⁶

¹H NMR (500 MHz, DMSO): δ = 10.24 (s, 1 H, -OH), 7.68 (d, ³*J* = 8.7 Hz, 1 H, H-7), 7.12 (d, ⁴*J* = 2.3 Hz, 1 H, H-4), 6.94 (dd, ³*J* = 8.7 Hz, ⁴*J* = 2.3 Hz, 1 H, H-6), 3.90 (s, 3 H, H-8), 2.67 (s, 3 H, H-9), 1.47 (s, 6 H, H-10, H-11) ppm.

¹³C NMR (126 MHz, DMSO): δ = 191.9 (C-2), 159.0 (C-5), 143.7 (C-3a), 134.1 (C-7a), 116.0 (C-7), 115.0 (C-6), 110.3 (C-4), 53.4 (C-3), 34.5 (C-8), 21.8 (C-10, C-11), 13.6 (C-9) ppm.

IR (ATR): $\tilde{\nu}$ = 3127 (s), 2970 (s), 1610 (m), 1478 (m), 1447 (m), 1283 (m), 1218 (vs), 1128 (w), 1058 (w), 892 (m), 869 (m), 822 (vs), 648 (s), 553 (m) cm⁻¹.

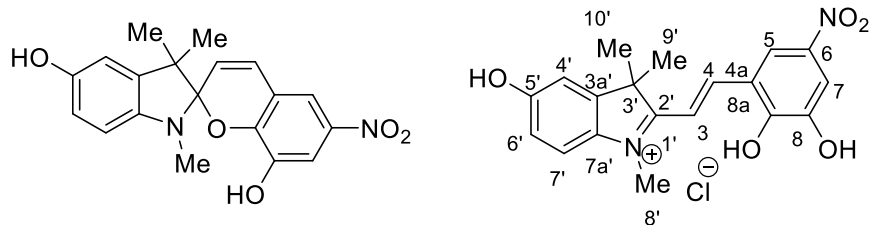
HRMS (ESI-TOF): *m/z* (%): [M-HI]⁺ calcd. for [C₁₂H₁₅NO]⁺ 190.1226; found 190.1227 (35); 174.0 (100) [M-HI-CH₃]⁺.

Melting point: T = 250 °C.

⁶ The ¹H NMR, ¹³C{¹H} NMR, IR, and HRMS data are in agreement with the reported.³

1',3',3'-Trimethyl-6-nitrospiro[chromene-2,2'-indoline]-5',8-diol (**s9**)³

To dry ethanol (180 mL), 5-hydroxy-1,2,3,3-tetramethyl-3*H*-indolium iodide (**s8**) (2.86 g, 9.02 mmol) and 2,3-



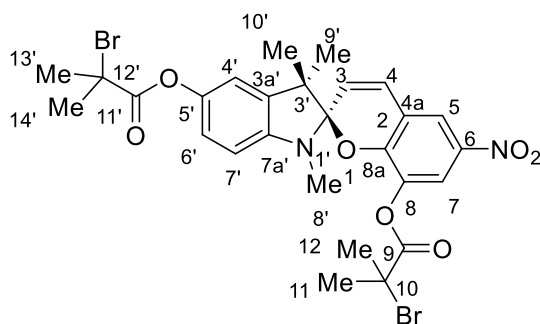
dihydroxy-5-nitrobenzaldehyde (**s3**) (1.67 g, 9.02 mmol) were added. Under a nitrogen atmosphere, dry piperidine (1.8 mL, 18.0 mol) was added. The reaction was heated to 80 °C for 3 h. After cooling down to -30 °C, the product **s9** was filtered. A dark green solid was obtained (2.94 g, 8.3 mmol, 92%, Lit.:³ 98%).⁷

IR (ATR): $\tilde{\nu}$ = 3206 (w, b), 2981 (w), 1627 (w), 1596 (m), 1512 (m), 1454 (m), 1412(s), 1273 (s), 1246 (s), 1214 (vs), 1180(vs), 1065 (s), 962(s), 864 (m), 814 (m), 801 (m), 765 (m), 740 (m), 545 (m) cm^{-1} .

HRMS (EI-TOF): m/z (%): $[\text{M}]^+$ calcd. $[\text{C}_{19}\text{H}_{18}\text{N}_2\text{O}_5]^+$ 354.36, found 354.120 (50), 175(100).

⁷ The ¹H NMR, ¹³C{¹H} NMR, IR, and HRMS data agree with the reported data.³ The compound started to decompose at 260 °C without a melting peak (see section 9).

1',3',3'-Trimethyl-6-nitrospiro[chromene-2,2'-indoline]-5',8-diylbis(2-bromo-2-methylpropanoate) (1)¹



In a 2-necked flask, 1',3',3'-trimethyl-6-nitrospiro[chromene-2,2'-indoline]-5',8-diol (**s9**) (1.50 g, 4.20 mmol) and DMAP (259 mg, 2.12 mmol) were combined. Under a nitrogen atmosphere, dry DCM (30.0 mL) was added. After 10 min, pyridine (1.40 mL, 17.0 mmol) was added, and the solution was cooled to 0 °C. 2-Bromo-2-methylpropionyl bromide (2.10 mL, 17.0 mmol) was added dropwise within the course of (0.05 mL/min) via a syringe pump into the cooled solution. The solution was stirred at 0 °C for 90 min. The cooling bath was removed and the reaction mixture stirred at 28 °C for 1 h before heating it to 50 °C for 2 h. The reaction was quenched with water (50 mL) and the organic layer was separated. The combined aqueous layers were extracted with EtOAc (3 x 60 mL) to collect remaining organic product. The combined organic layers were washed with aq. NH₄Cl (2 x 70 mL), with aq. NaHCO₃ (3 x 50 mL) and then with brine (2 x 70 mL). The organic layer was dried over MgSO₄, filtered and concentrated. The remaining solution of EtOAc (~ 10 mL) was overlaid with *n*-pentane (100 mL) to induce crystallization of the product overnight. After addition of another portion of *n*-pentane (200 mL), the solution was filtered to obtain the product **1** as brown powder (1.60 g, 4.51 mmol, 58%, Lit.:¹ 50%).⁸ ¹H, H-5⁴J = 2.6 Hz, 1 H, H-7),³J 1 H, H-4³J = 8.3 Hz, ⁴J = 2.3 Hz, 1 H, H-6⁴J = 2.3 Hz, 1 H, H-4' ³J = 8.3 Hz, 1 H, H-7' 3 H, H-8' 6 H, H-13', H-14' 2 H, H-12 or H-11, two overlapping singlets 3 H, H-9' 3 H, H-10') ¹³C NMR(126 MHz, CDCl₃): δ = 170.8 (C-11'), 169.3 (C-9), 150.9 (C-8a), 145.7 (C-7a'), 144.7 (C-

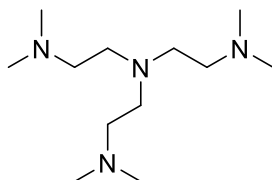
⁸ The product **1** was prepared by modification of synthesis previously reported.¹ The ¹H NMR, ¹³C{¹H} NMR, HRMS and mp data are in agreement with the reported.¹ IR data was not reported.

5'), 140.3 (C-8), 137.5 (C-3a'), 137.3 (C-6), 128.7 (C-4), 121.1 (C-3), 120.5 (C-5), 120.0 (C-6'), 119.6 (C-4a), 119.2 (C-7), 115.1 (C-4'), 107.9 (C-2), 107.5 (C-7'), 55.8 (C-12'), 54.1 (C-10), 52.1 (C-3'), 30.9 (C-13', C-14'), 30.4 (C-11), 30.3 (C-12), 29.0 (C-8'), 25.9 (C-10'), 19.5 (C-9') ppm. **IR** (ATR): $\tilde{\nu}$ = 2971 (w), 1752 (s), 1522 (m), 1485 (w), 1453 (m), 1390 (w), 1333 (s), 1258 (s), 1179 (m), 1132 (s), 1101 (vs), 1079 (s), 902.7 (s), 785 (m), 770 (m), 743 (s).

HRMS (EI-TOF): m/z (%): $[M^+]$ calcd. for $C_{27}H_{28}^{81}Br_2 N_2O_7$ 652.0065, found 652.0091 (100), 650 (50) $[M-^{79}Br_2]^+$.

Melting point: T = 171 °C.

Tris[2-(dimethylamino)ethyl]amine (3)⁴



Tris(2-aminoethyl)amine (TREN) was dissolved in dry methanol (150 mL). Then, hydrochloric acid in 2-propanol (21.0 mL, 5-6 M) was added over the course of 20-30 min using a syringe pump. The reaction mixture was stirred for 1 h at 24 °C, before the precipitate was filtered and washed with methanol (3 x 100 mL). The solvent was removed under vacuum and the slightly beige TREN-hydrochloride salt was dried (yield: 6.84 g). This intermediate (6.84 g) was added to a mixture of water (12.0 mL), formic acid (56.0 mL, 1.40 mol) and formaldehyde solution (56.0 mL) and were heated to 120 °C for 6 h. The residue was obtained by removing the volatile component via rotary evaporation and aqueous solution of NaOH (5 M, 100 mL) was added until complete dissolution was achieved. Solid KOH (50.0 g, 0.90 mol) was slowly added until the solution had a pH value of 14. The aqueous phase was extracted with EtOAc (5 x 75 mL). The combined organic phases were dried over solid KOH and the solvent was removed under vacuum, followed by fractioning vacuum distillation (52 °C, 5.7×10^{-2} mbar) under a nitrogen atmosphere. The

product Tris[2-(dimethylamino)ethyl]amine (**3**) was obtained as a liquid (6.96 g, 30.2 mmol, 83%, Lit.:⁴ 91%).⁹

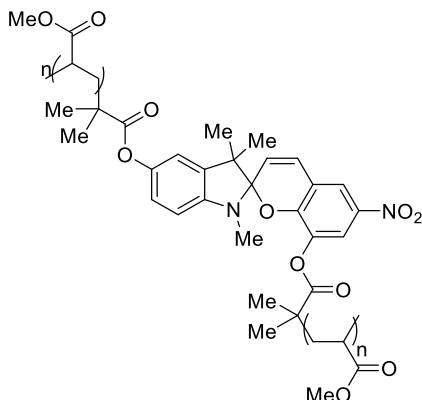
¹H NMR (500 MHz, CDCl₃): δ = 2.50-2.18 (m, 12 H, -CH₂), 2.08 (m, 18 H, -CH₃).

¹³C NMR (126 MHz, CDCl₃) δ = 57.3(-CH₂), 52.9 (-CH₂), 45.8 (-CH₃).

IR (ATR): $\tilde{\nu}$ = 2940 (m), 2850 (w), 2814 (m), 2762 (s), 1455 (s), 1263 (w), 1153 (s), 1122 (m), 1030 (s) cm⁻¹.

⁹ The product **3** was prepared by a modification of synthesis previously reported.^{4,5} The shift of ¹H NMR and ¹³C{¹H} NMR data are in agreement with the reported. As the molecule fragments during the mass measurement, the [M⁺] could not be measured. The fragments were in agreement with the structure.

PMA-SP-PMA 4¹



To the spiropyran initiator **1** (131 mg, 200 μmol), dimethyl sulfoxide (30 mL) was added and the reaction mixture was stirred until the compound had dissolved. The chelating ligand, Me_6TREN , (184 mg, 800 μmol , 4 eq.) was added. The catalyst, $\text{Cu}(0)$, (50.8 mg, 800 μmol , 4 eq.) was added and the flask was sealed inside the glovebox. The monomer, methyl acrylate (MA), (18.1 mL, 200 mmol, 1000 eq.) was added at the rate of 2 mL/min. The reaction was stirred at 30 $^\circ\text{C}$ for 2 h under nitrogen atmosphere. The reaction flask was opened to air and THF (100 mL) was quickly added to the viscous polymer solution. The reaction mixture was filtered through a PTFE (0.45 μm) syringe filter to remove the catalyst particles. It was purified by precipitation into diethyl ether (1 L) stirring vigorously, in five batches of 20 mL polymer solution per 200 mL of Et_2O . The viscous polymer was re-dissolved in THF and the precipitation step was carried out three times. The polymer was collected and was dried at 5×10^{-2} mbar for 24 h. The polymer **12** slight yellow in color (13.9 g, 77%).

$^1\text{H NMR}$ (500 MHz, CDCl_3): δ = 3.66 (s, 3 H, - OCH_3), 2.30 (s, -CH-), 1.94 – 1.39 (m, - CH_2 -) ppm.

$^{13}\text{C NMR}$ (126 MHz, CDCl_3) δ = 175.1 (-carboxyl C), 51.9 (- OCH_3), 41.2 (- CH_2) ppm. **IR** (ATR): $\tilde{\nu}$ = 2954 (m), 2918 (w), 1727 (vs), 1436 (m), 1195 (m), 1157 (vs).

GPC (THF, 1 mL/min): M_n = 89.5 kDa, M_w = 161 kDa, PDI = M_w/M_n = 1.8.

DSC: T_g = 14 $^\circ\text{C}$.

5. Polymer Solution Optimization for Centrifugal Spinning and Processing

The preparations of the PMA-SP-PMA solution are given in **Table S7**.

Table S7. Overview of solution optimization of fiber spinning from PMA-SP-PMA solutions in THF.

Entry.	Label	Polymer solution: PMA-SP-PMA/THF (wt %)
1	A1	11
2	A2	15
3	A3	18
4	A4	22
5	A5	25
6	A6	33

These solutions were processed into fibers using a self-designed centrifugal spinning machine (**Figure S9**). The machine was operated on a DC motor (430 W, 33 V), equipped with a spinneret, having a shaft length of 75 mm and rotational speeds that were adjustable between 2000-6500 rpm. With a centrally located sample reservoir, the spinneret was also harnessed with a junction for attaching dispensing needles of different sizes. The opening diameters for these needles ranged from 0.15 -1.0 mm. The collectors were positioned concentrically to the spinneret. The collectors were at a fixed distance of 10 cm from the periphery of the spinneret, which was kept constant for all the spinning processes. The entire setup was encased in a rectangular acrylic glass chamber. The fibers were processed by spinning a batch of 2 mL solution per spin cycle and rotation speeds of 3000, 4000 and 5000 rpm respectively. The solvent vapors were simultaneously vented out at the rate of 170 m³/h through an exhaust during the spinning process.

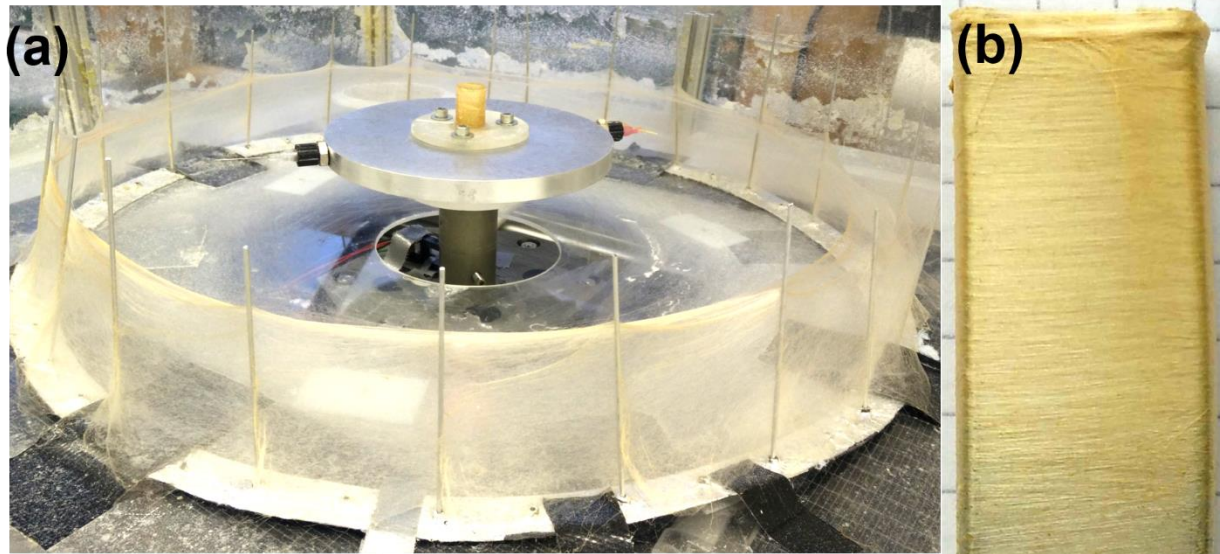


Figure S9. (a) Centrifugal force spinning machine with a spun fiber-mat of **A5** solution at 5000 r.p.m and 0.15 mm nozzle diameter. (b) Fibers of **A5** collected on a pair of tweezers.

6. Fiber Morphology by SEM of non-blended PMA-SP-PMA Fiber

Scanning electron microscopy was used to characterize the physical nature of the fibers at microscopic scale. Surface features such as texture and pore formation, outcome of spinning parameters such as fiber branching, variation of fiber diameter and bead formation were observed under SEM. This technique played the most significant role in optimizing the solutions to achieve bead free fibers. The effect of low solution concentrations on fiber morphology and bead formation can be seen in **A1** to **A3** in PMA-SP-PMA (**Figure S10**).

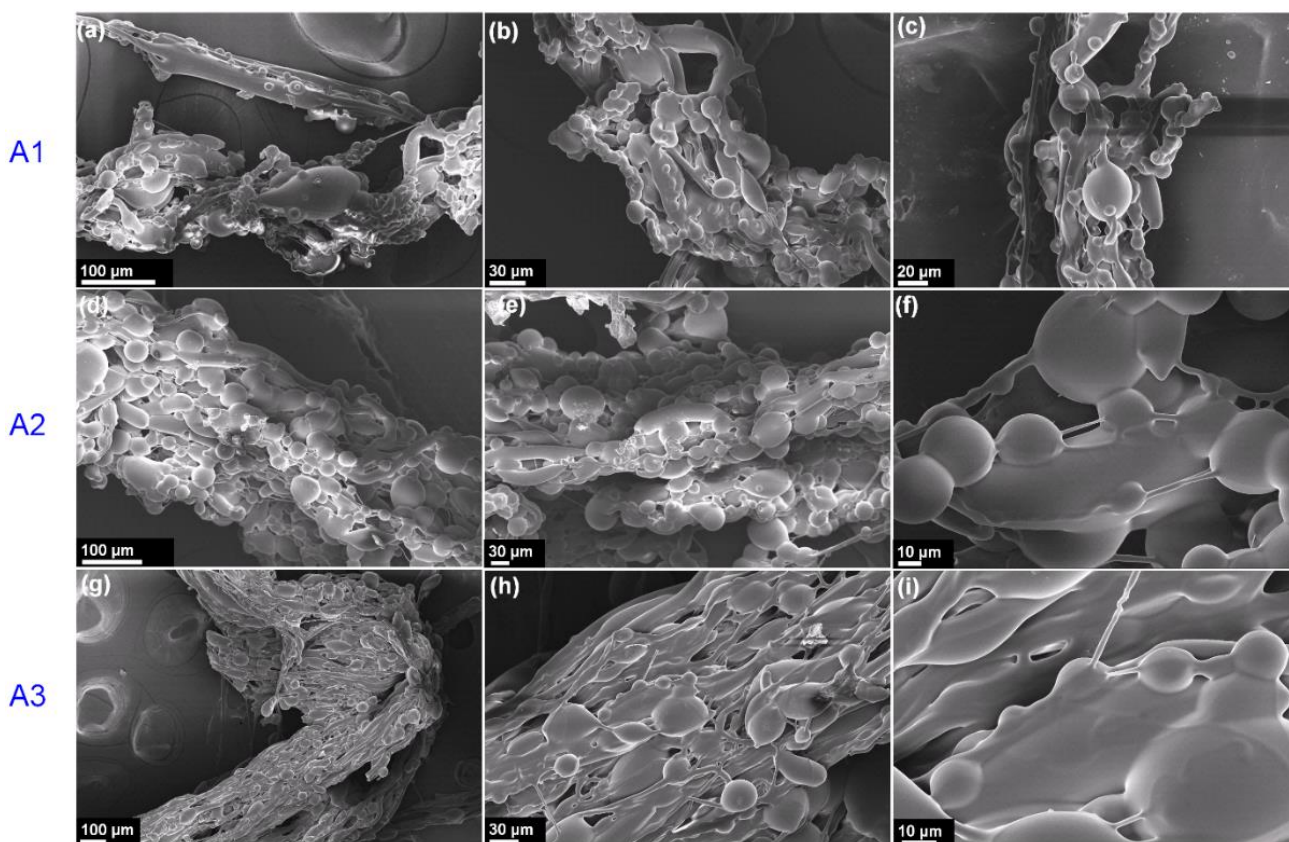


Figure S10. SEM images of fibers spun from solution **A1**, **A2** and **A3** at 5000 rpm with a nozzle of 0.15 mm diameter were: (a)-(c) **A1** = 11 wt %, (d)-(f) **A2** = 15 wt % and (g)-(i) **A3** = 18 wt % in three magnifications respectively.

The increase in the fiber diameter of **A6** solution due to large nozzle diameter (0.20 mm) is shown in **Figure S11**.

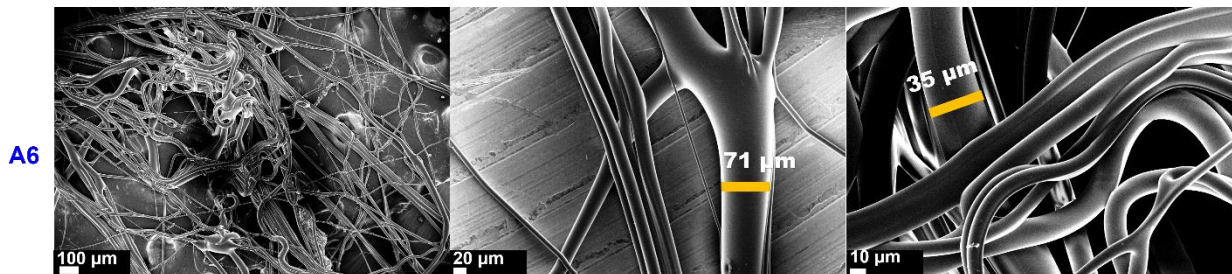


Figure S11. SEM images of fibers spun from **A6** at 5000 rpm, 0.20 mm nozzle diameter in three magnifications respectively. The marked region (yellow) indicate single fiber diameter.

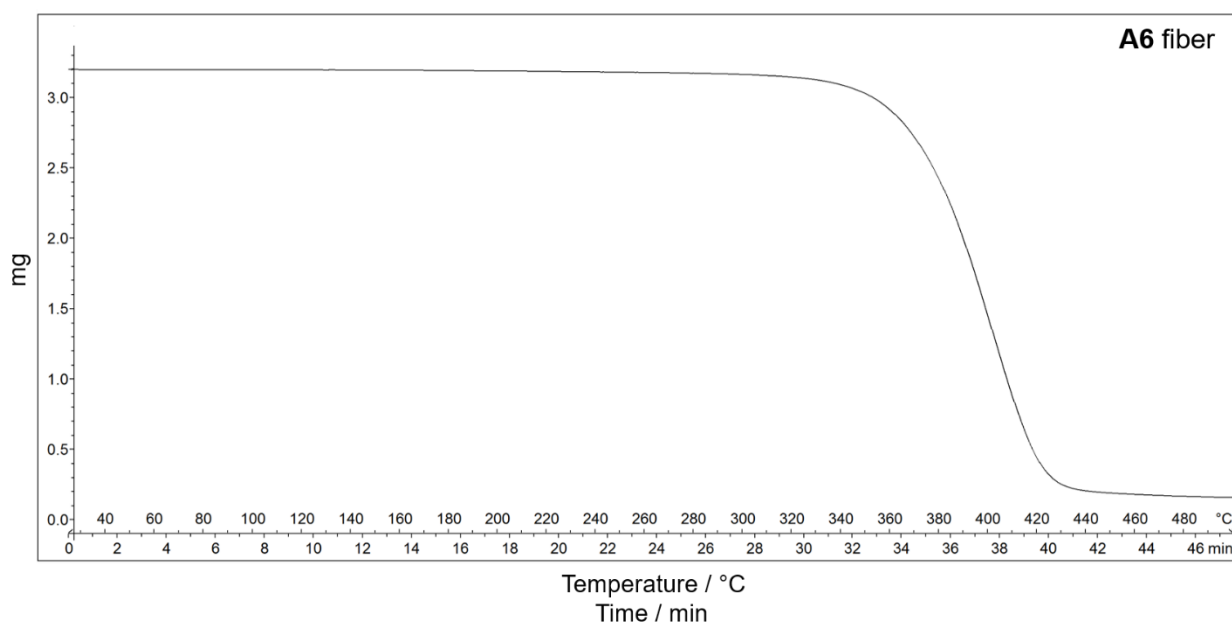


Figure S12. TGA plot of **A6** fibers indicating no traces of residual solvent.

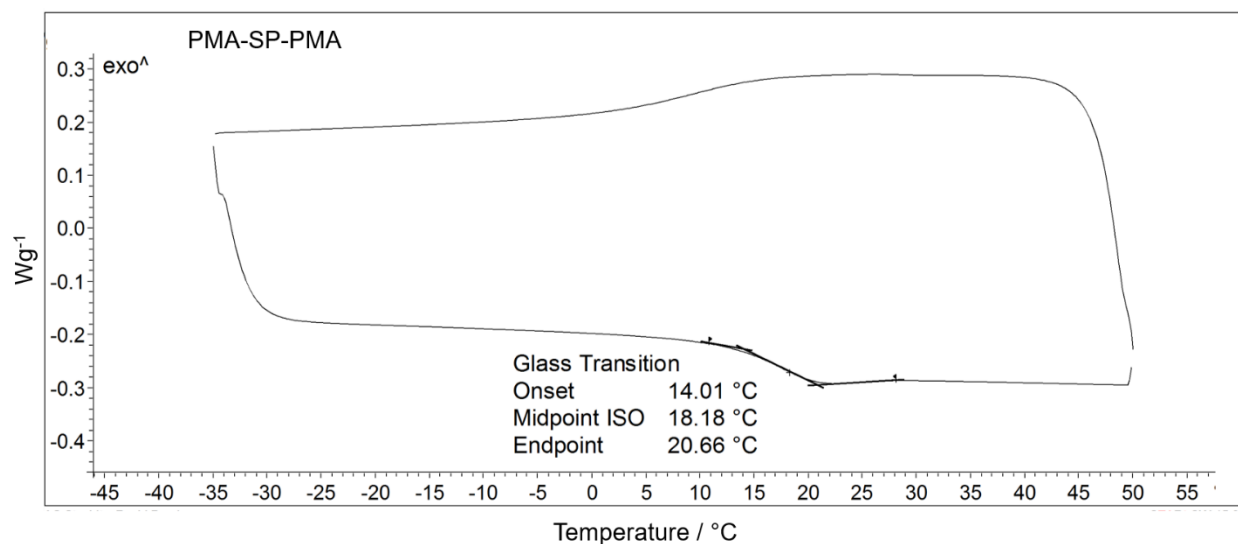


Figure S13. DSC plot of the elastomeric PMA-SP-PMA polymer indicating the glass transition temperature (T_g). The measurement was cycled between -35 to 50 °C at the heating rate of 10 K/min under N₂ with a flow rate of 20 mL/min and sample weight of 11.35 mg

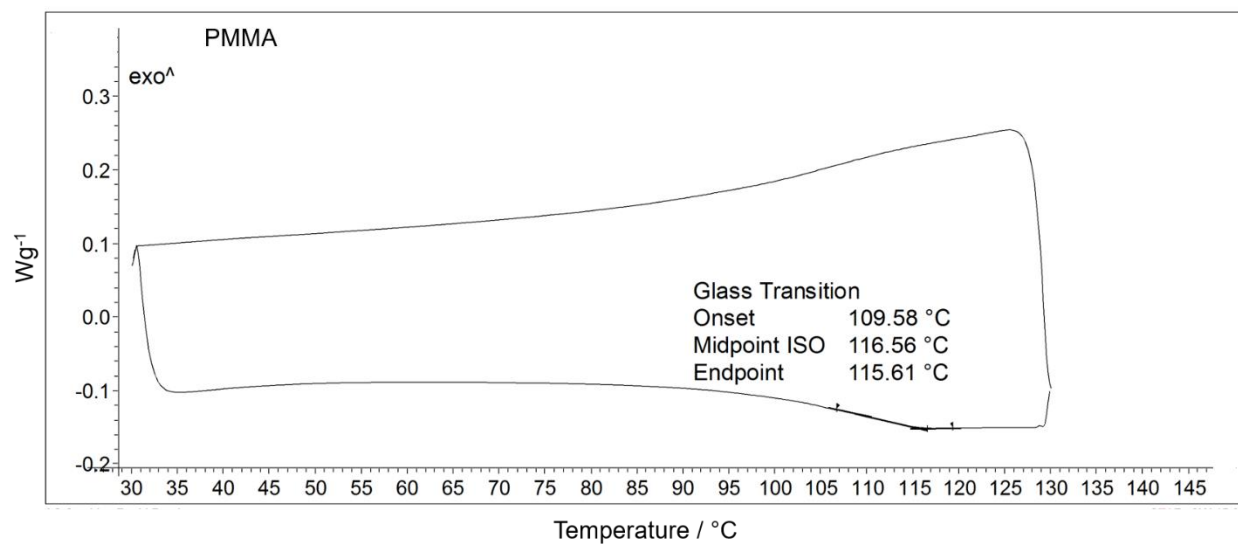


Figure S14. DSC plot of the commercial PMMA polymer indicating the glass transition temperature (T_g). The measurement was cycled between -35 to 130 °C at the heating rate of 10 K/min under N₂ with a flow rate of 20 mL/min and sample weight of 8.344 mg.

7. Fiber morphology by SEM of PMA-SP-PMA blended with PMMA

Polymer blends **B1** to **B5** were prepared by adding increasing amount of PMMA (1 wt % to 5 wt %) respectively to the PMA polymer. The solutions with an overall constant blend concentration of (28 wt %) were prepared by dissolving the polymer mixtures in THF. The solutions were stirred at 30 °C for 24 h followed by stirring for 15 min at 50 °C prior to spinning. The increase in the amount of PMMA in the blends **B4** (4 wt %) and **B5** (wt %), lead to bead formation (**Figure S15**).

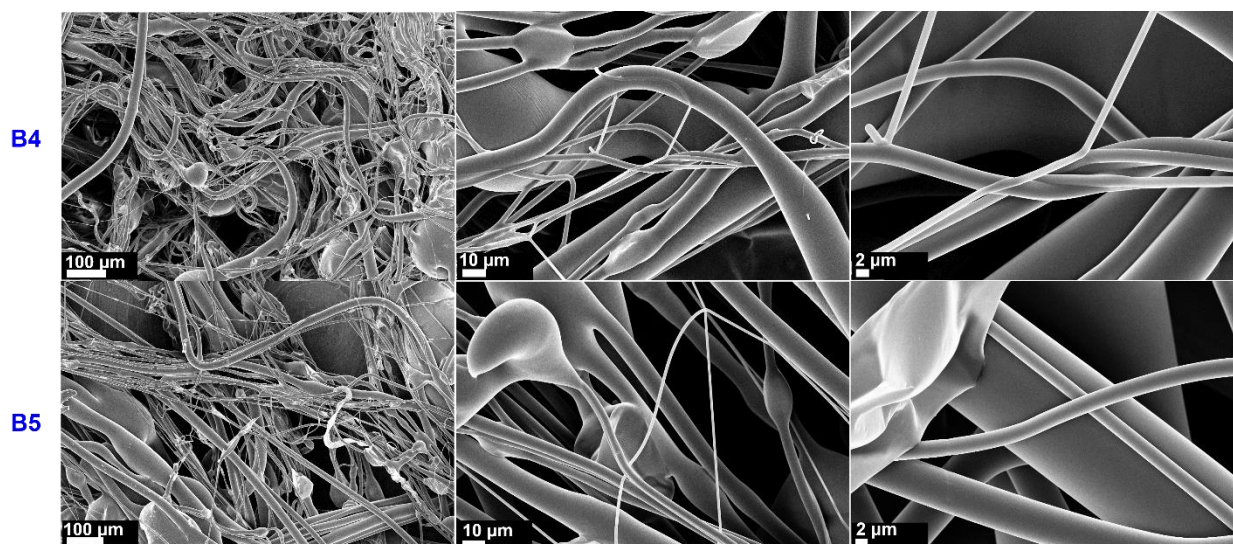


Figure S15. Fibers of **B4** and **B5** (4 and 5 wt % of PMMA respectively) spun at 5000 rpm from a 0.20 mm nozzle diameter.

8. Mechanical Testing

To observe the mechanochromic behavior in micro-fibers, uniaxial tensile measurements were carried out. All samples were collected from the same spinning batch to maintain the density of fibers per area / cm^2 . The fiber-mat formed between the collector sticks were cut in a dimension of approximately $\sim 10 \text{ cm}^2$. The fiber-mat were then folded into a bar shape and clamped to carry out tensile measurements (method 1). As the fiber were stretched to high strain, slippage of the fibers from the grips or sample breakage at the clamping site was a common problem. To overcome this, the fibers were taped at the sample ends (method 2) (**Figure S16**). The samples did not break anymore, but the problem of sample slippage continued. To avoid the slippage, the fibers were then glued with two component adhesive glue between two pieces of glass fiber laminates (**Figure S17**). The tests were performed at a speed of 1 mm/sec on samples with a gauge length of 20 mm.

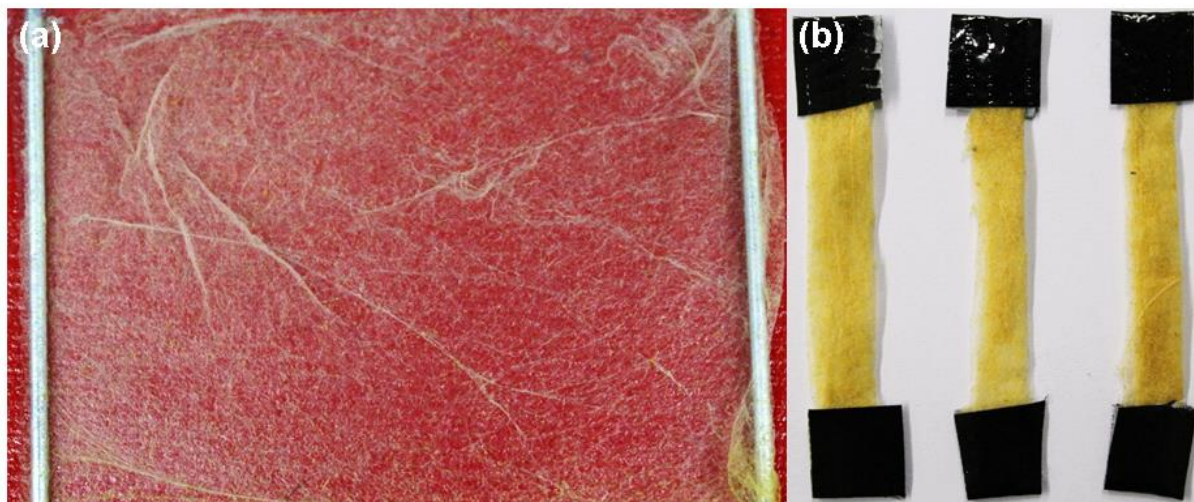


Figure S16. Method 2 of tensile sample preparation by clamping the ends of the fibers in adhesive tapes. Image (a) was taken on a red background and shows the fiber mat between two collector rods. Image (b) shows three folded fiber specimen.

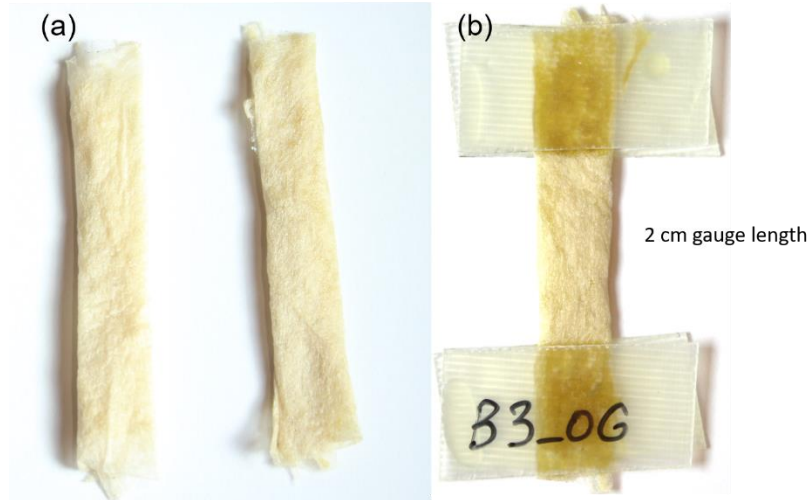


Figure S17. Method 3 of tensile sample preparation by fixing the fibers in between glass fiber laminates with a two component adhesive glue.

The stress-strain relationship of the B3 fibers is shown in **Figure S18**.

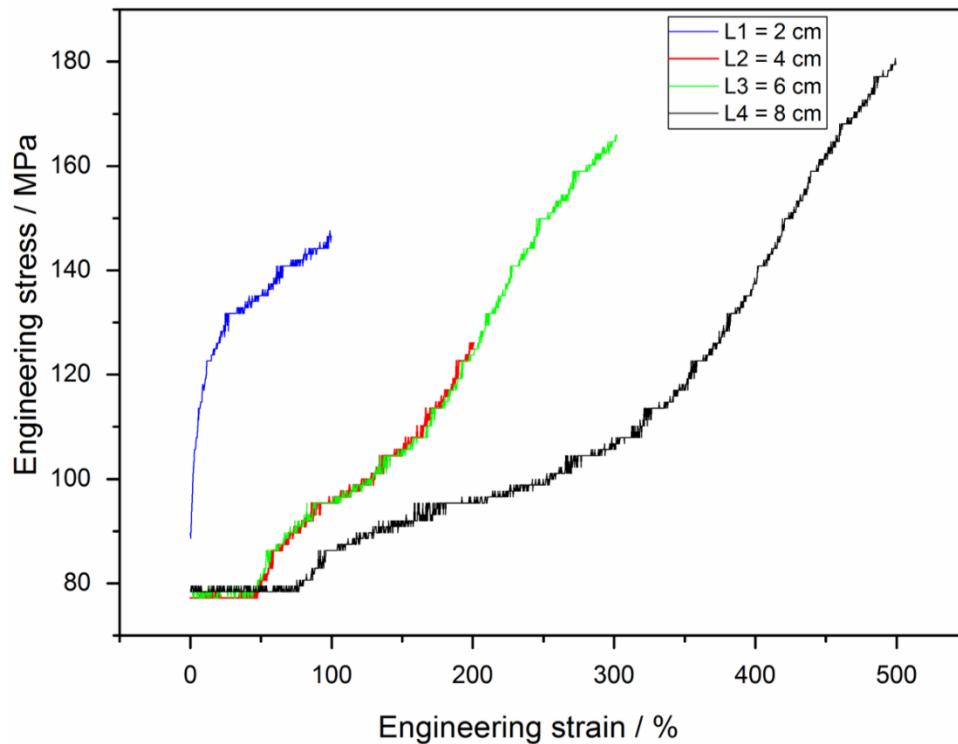


Figure S18. Stress-strain behavior of B3 fiber when stretched under tensile force at a rate of 1 mm/sec.

9. Differential Scanning Calorimetry (DSC)

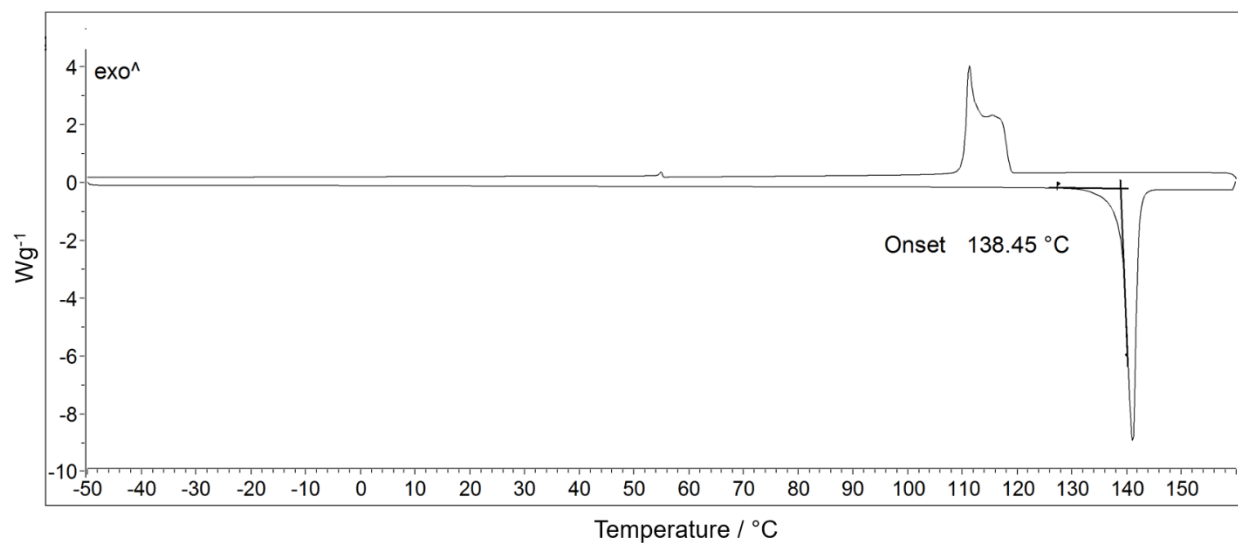


Figure S19. DSC plot of 2-hydroxy-3-methoxy-5-nitrobenzaldehyde (**s2**).

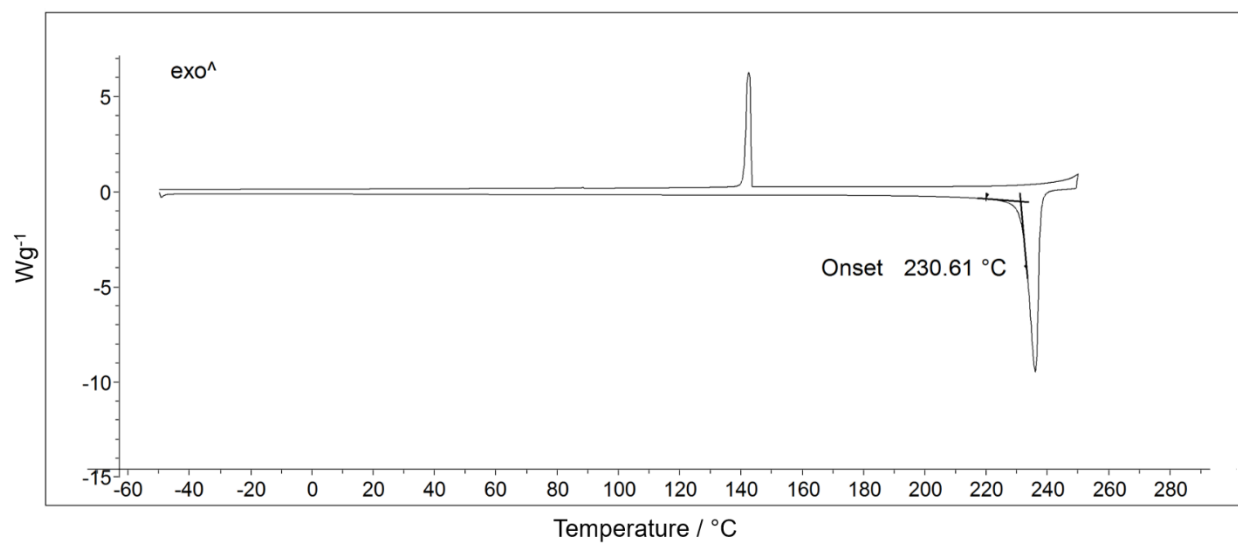


Figure S20. DSC plot of 2,3-dihydroxy-5-nitrobenzaldehyde (**s3**).

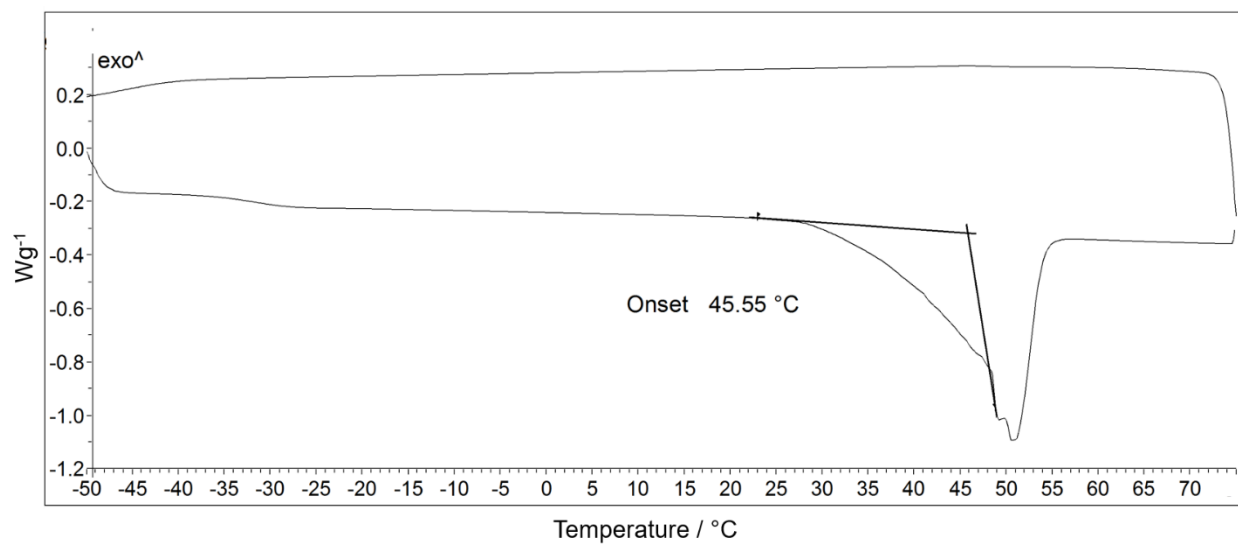


Figure S21. DSC plot of 5-methoxy-2,3,3-trimethyl-3H-indole (s6).

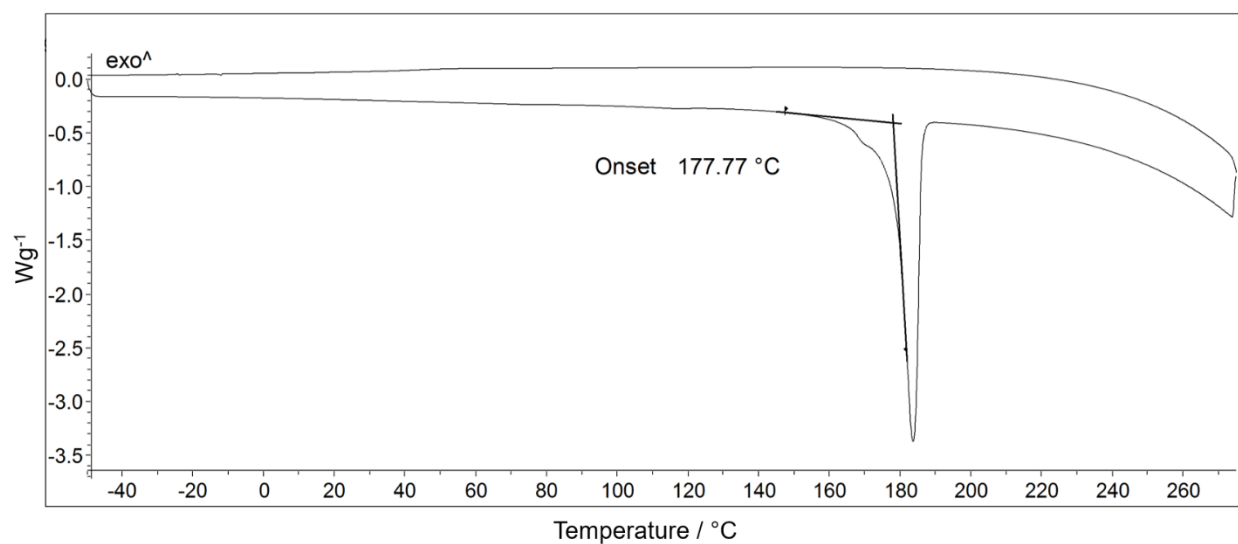


Figure S22. DSC plot of 2,3,3-trimethyl-3H-indol-5-ol (s7).

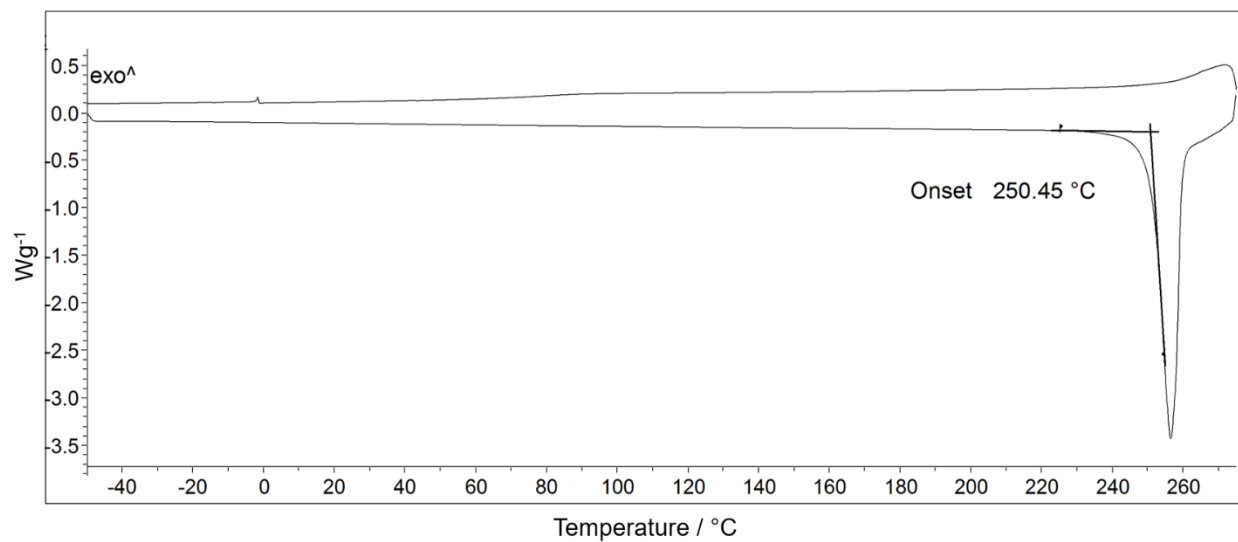


Figure S23. DSC plot of 5-Hydroxy-1,2,3,3-tetramethyl-3H-indolium iodide (s8).

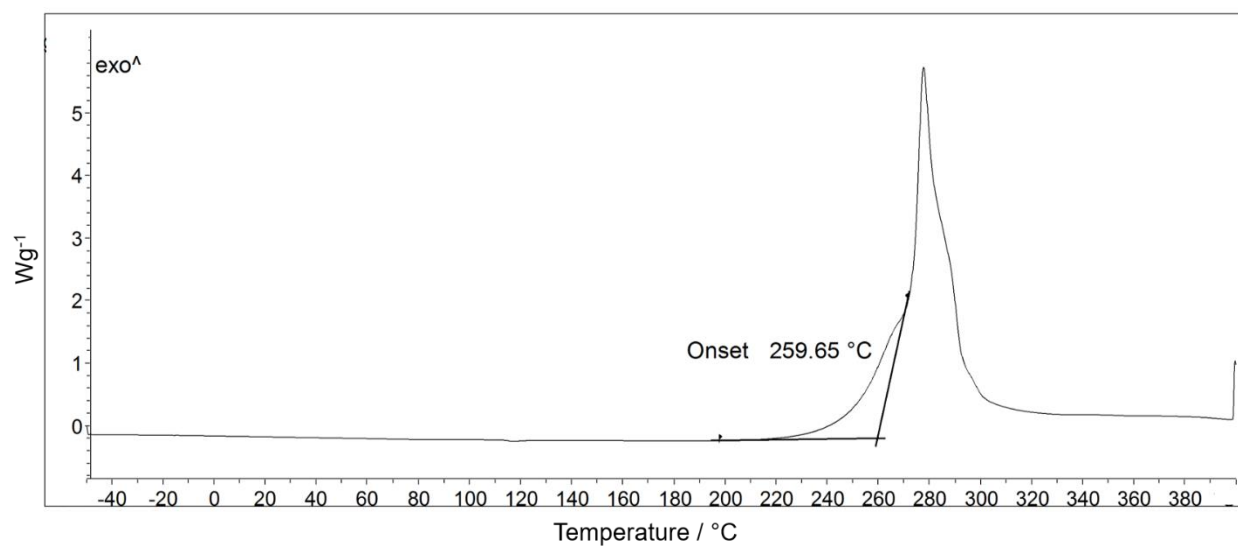


Figure S24. DSC plot of 1',3',3'-trimethyl-6-nitrospiro[chromene-2,2'-indoline]-5',8-diol (s9).

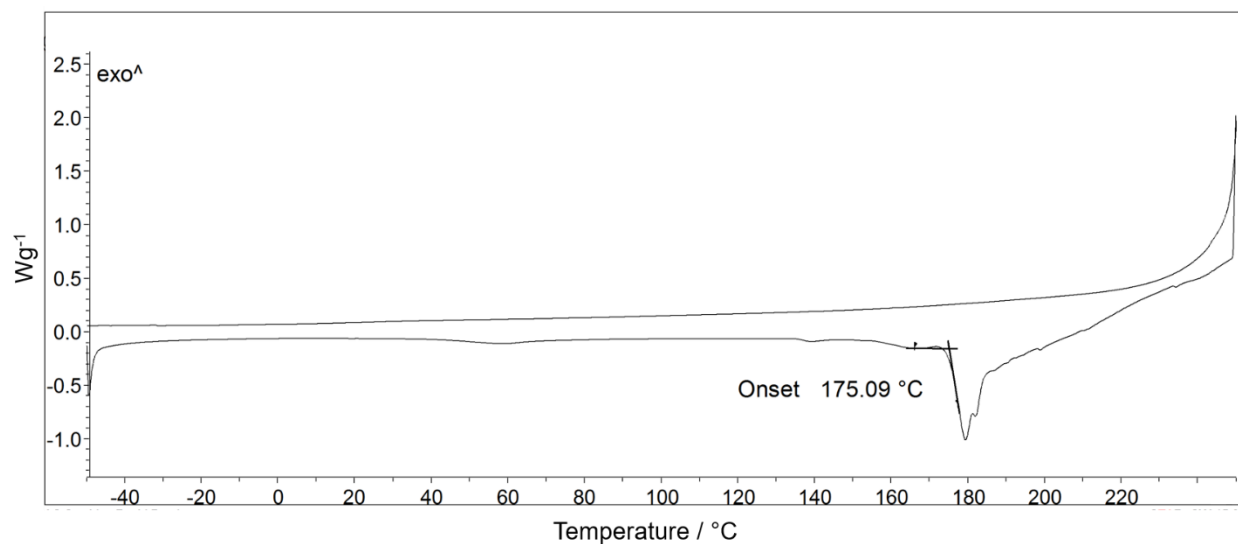


Figure S25. DSC plot of 1',3',3'-trimethyl-6-nitrospiro[chromene-2,2'-indoline]-5',8'-diylbis(2-bromomethyl propanoate) (**1**).

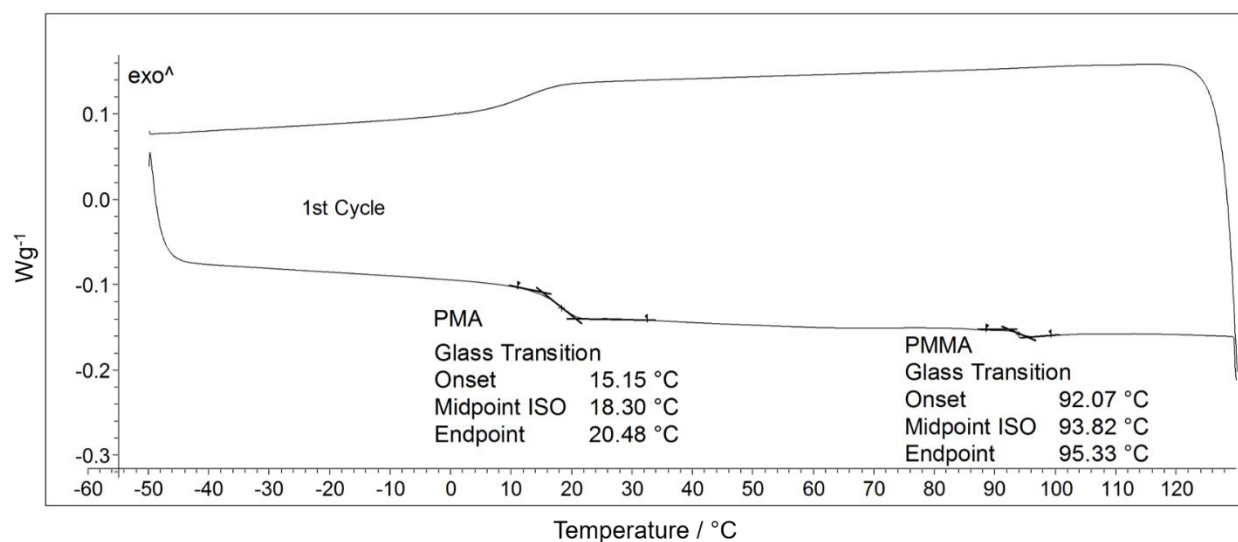


Figure S26. DSC plot of B3 fibers indicating the glass transition temperatures (T_g) for PMA-SP-PMA and PMMA. The measurement was cycled between -50 to 130 °C at the heating rate of 5 K/min under N_2 with flow rate of 20 mL/min and sample weight of 43.09 mg.

10. Gel Permeation Chromatogram of the Synthesized PMA-SP-PMA

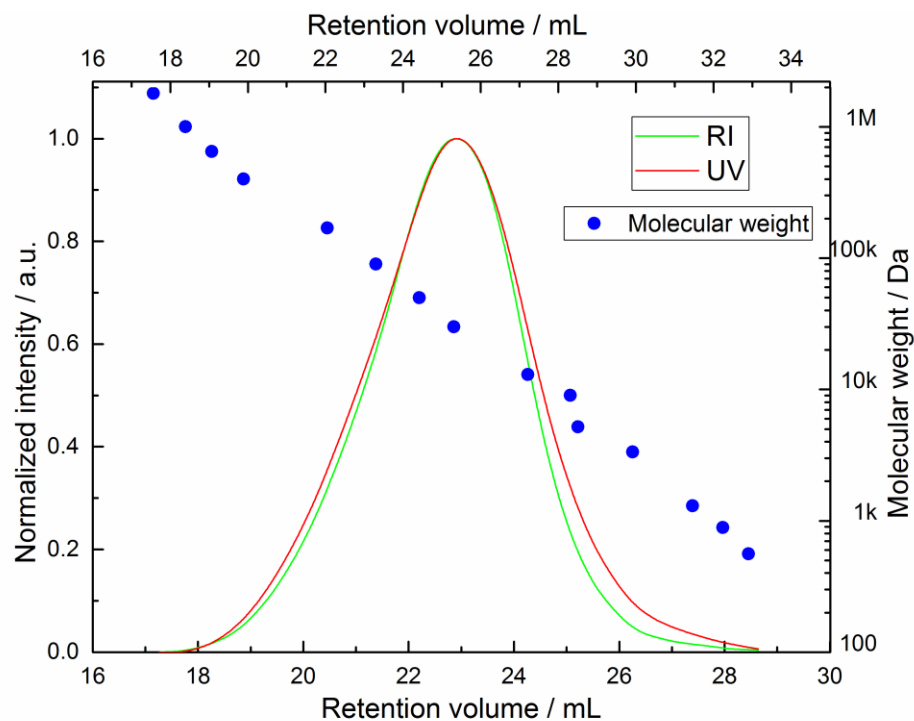
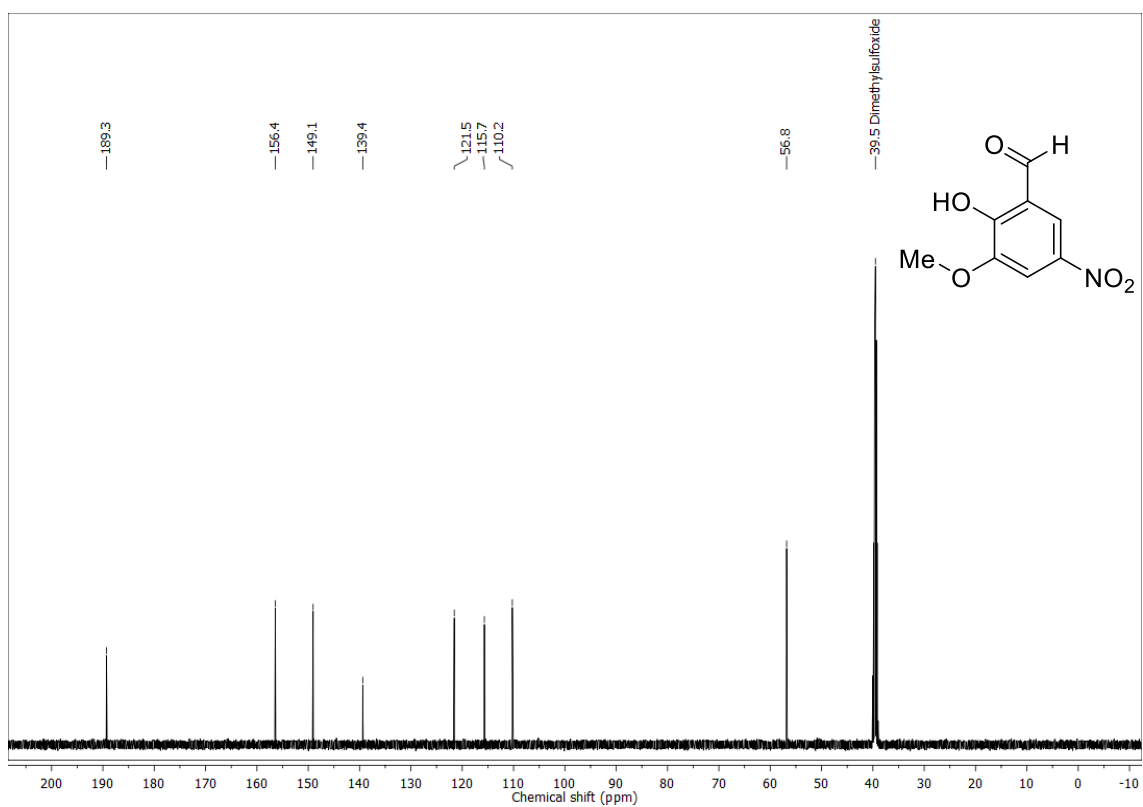
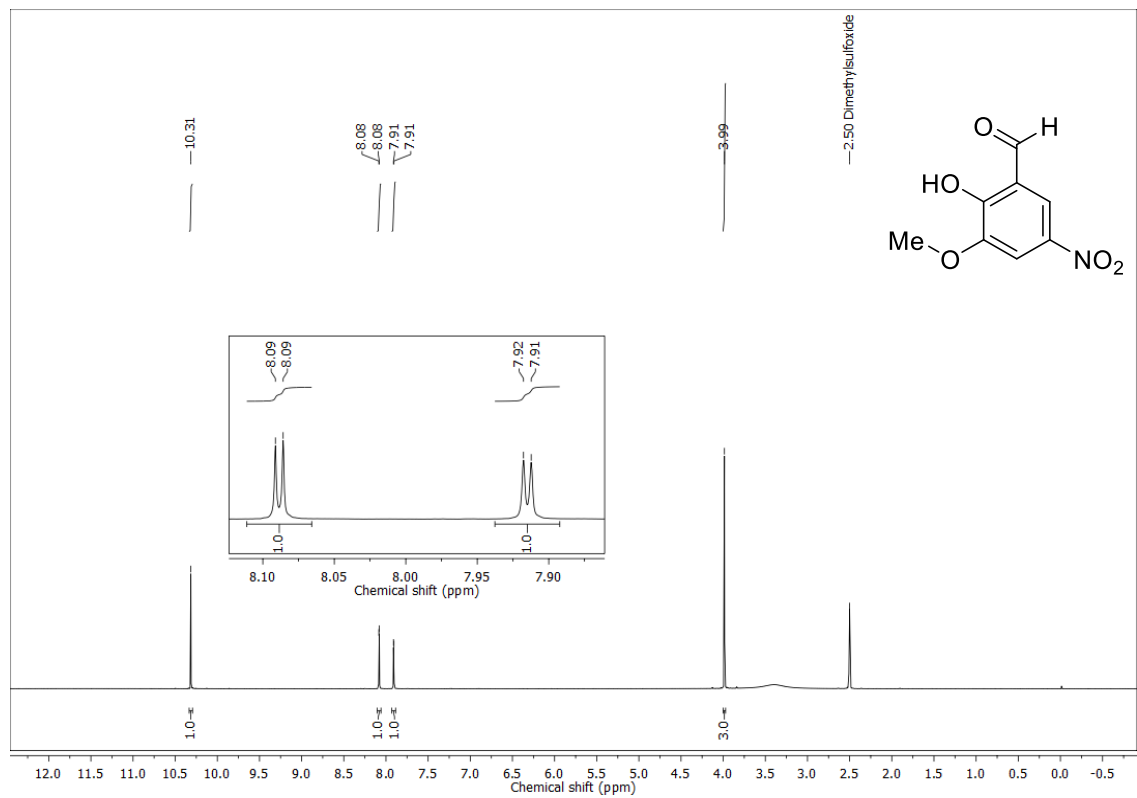


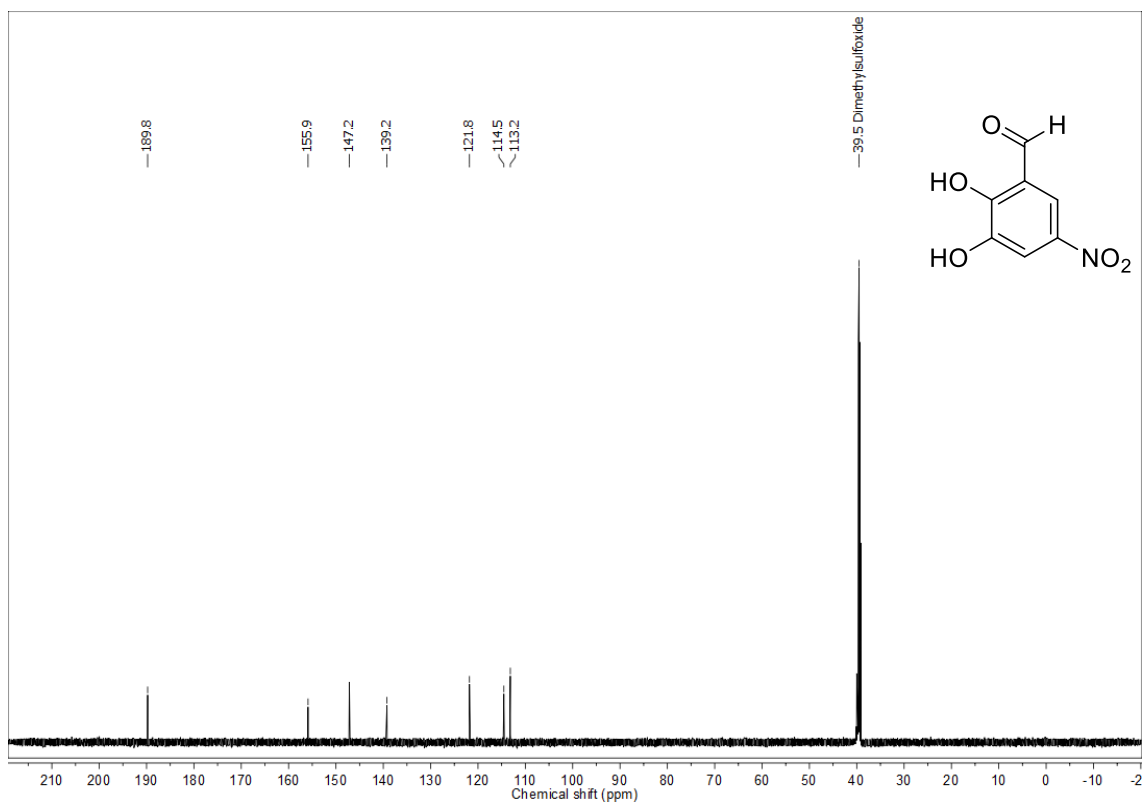
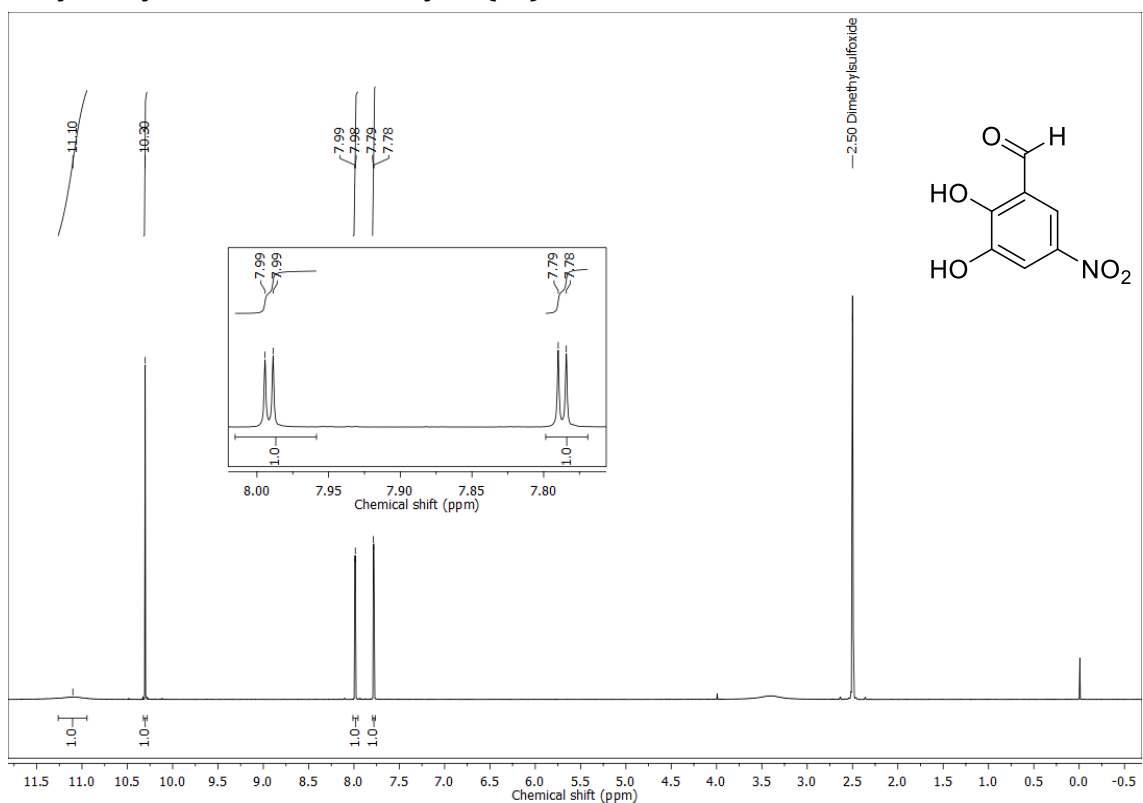
Figure S27. GPC plots of PMA-SP-PMA with the normalized intensity of RI (green) and UV (red) detector signal vs the retention volume/mL. Conventional calibration of the GPC with polystyrene standards and their molecular weight (blue).

11. Corresponding ^1H NMR and $^{13}\text{C}\{^1\text{H}\}$ NMR Spectra

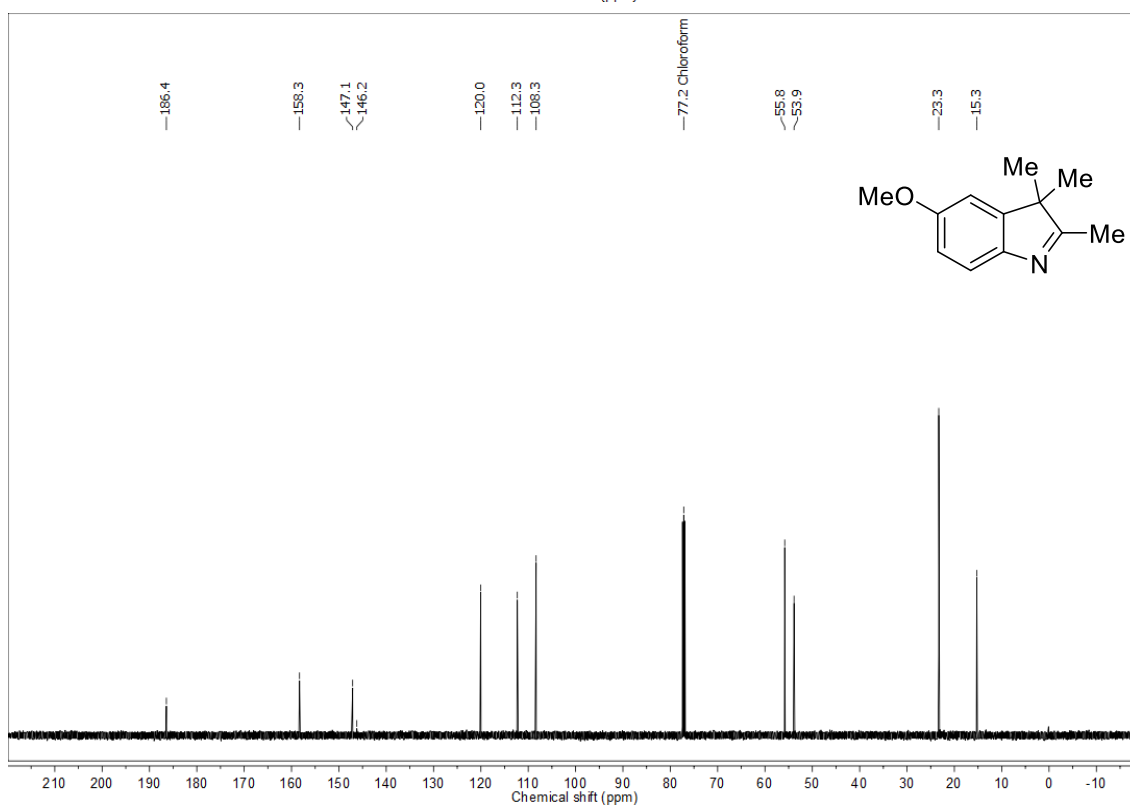
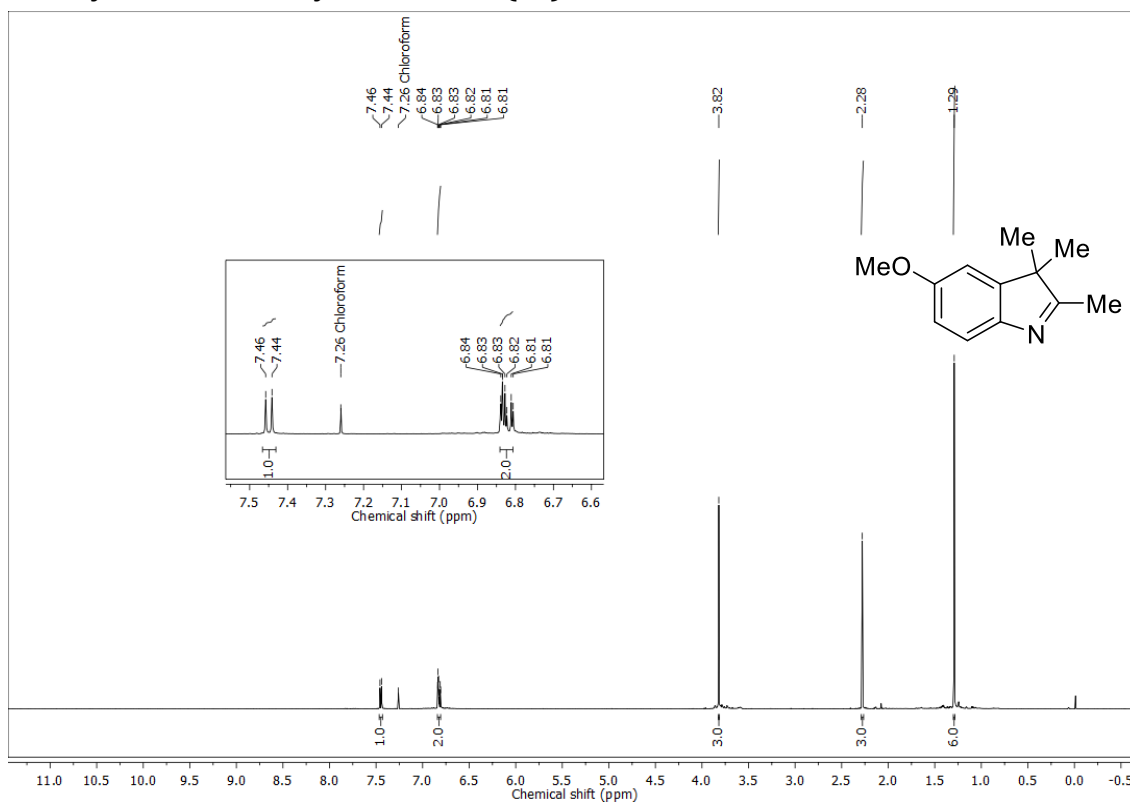
2-Hydroxy-3-methoxy-5-nitrobenzaldehyde (s2) in DMSO



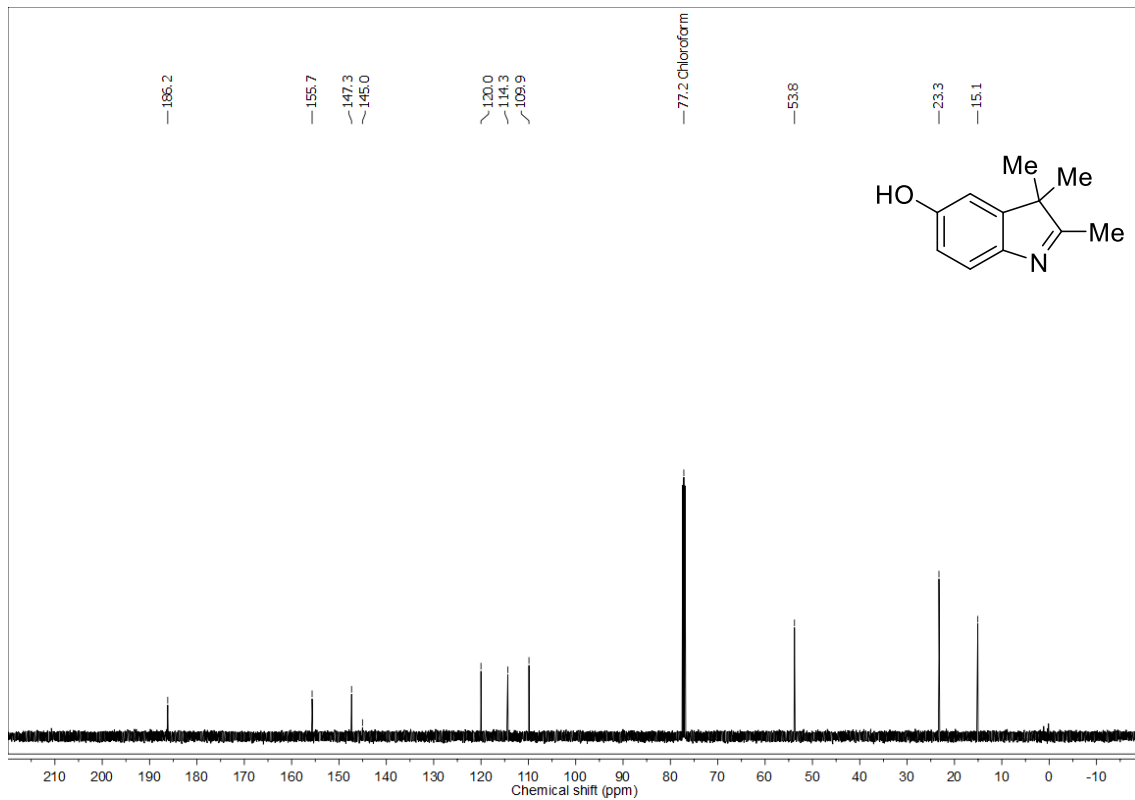
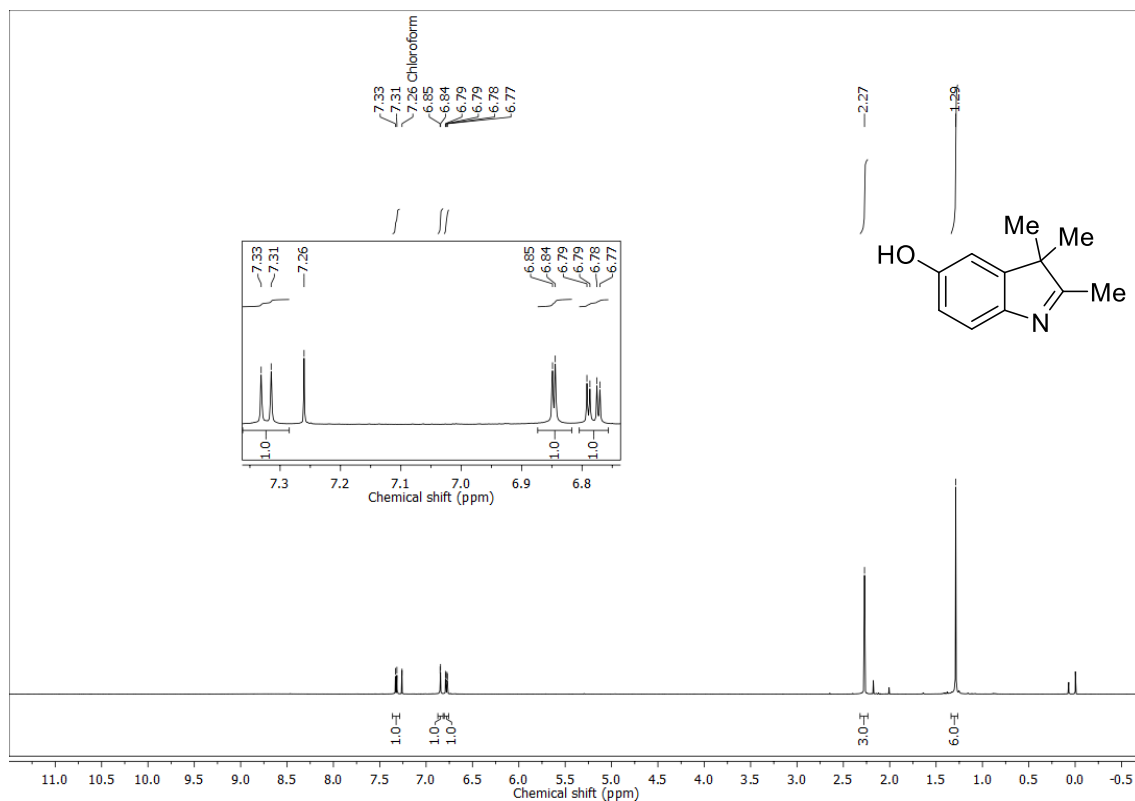
2,3-Dihydroxy-5-nitrobenzaldehyde (s3) in DMSO



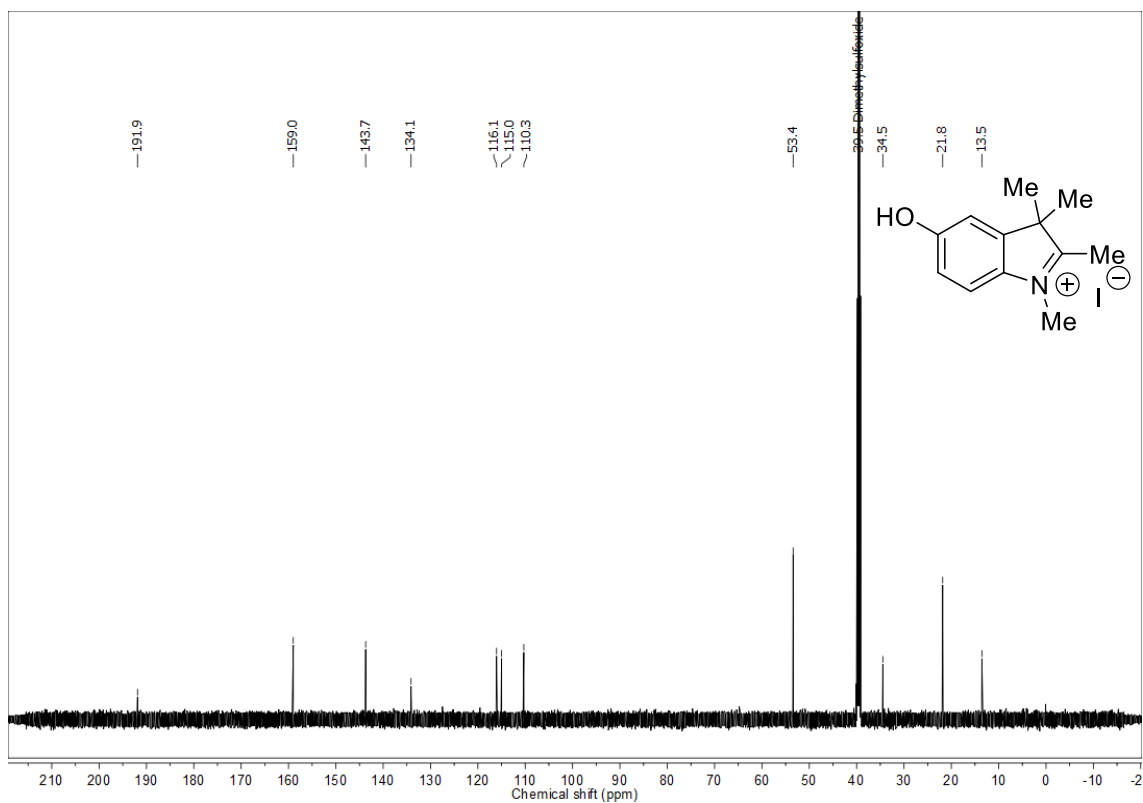
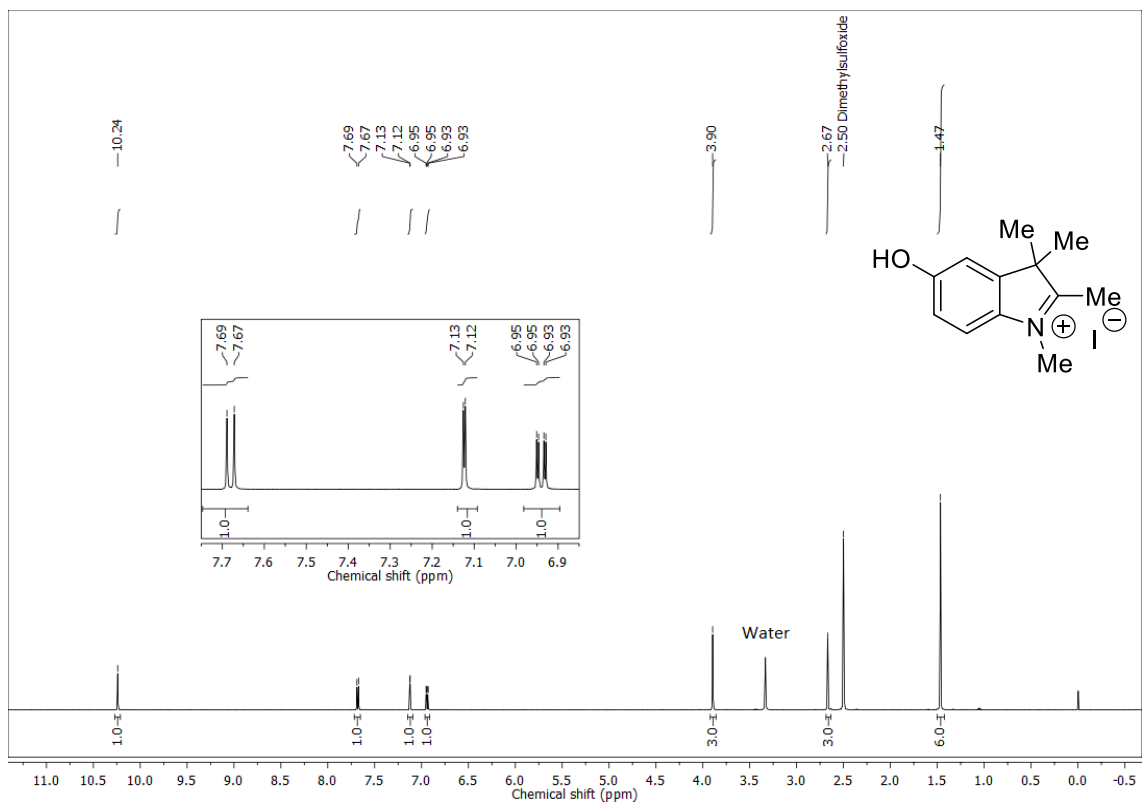
5-Methoxy-2,3,3-trimethyl-3H-indole (s6) in CDCl₃



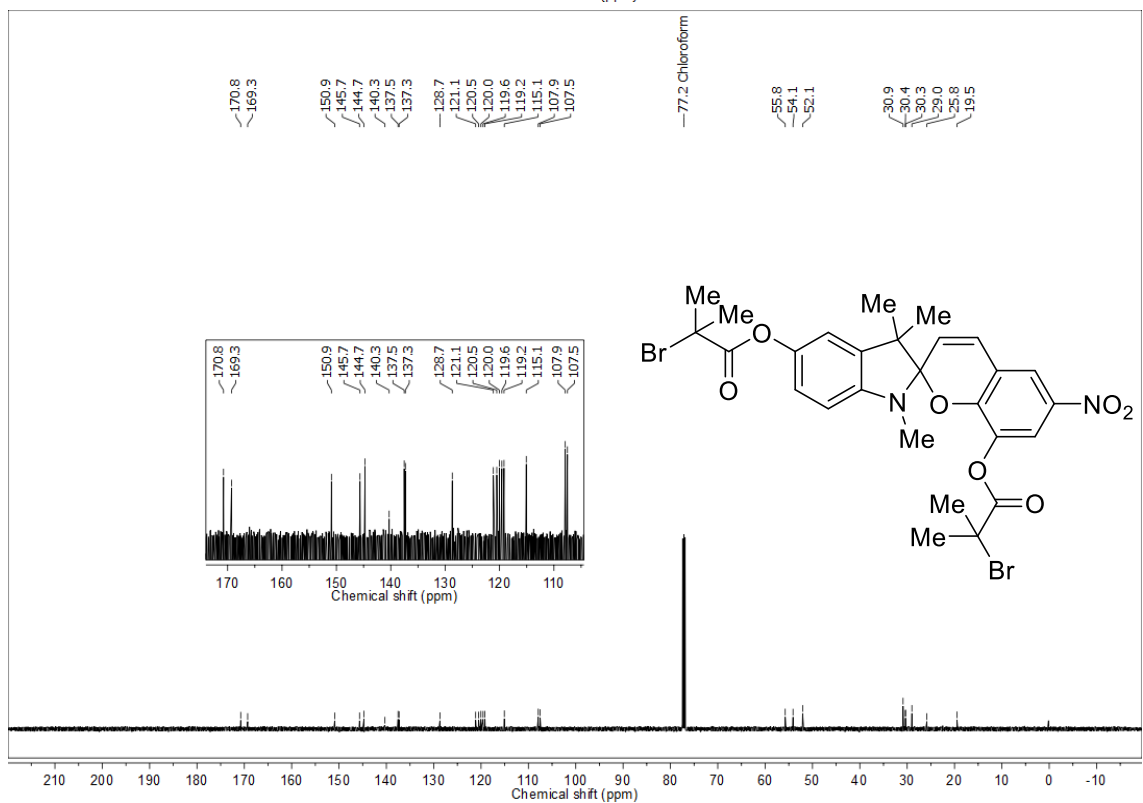
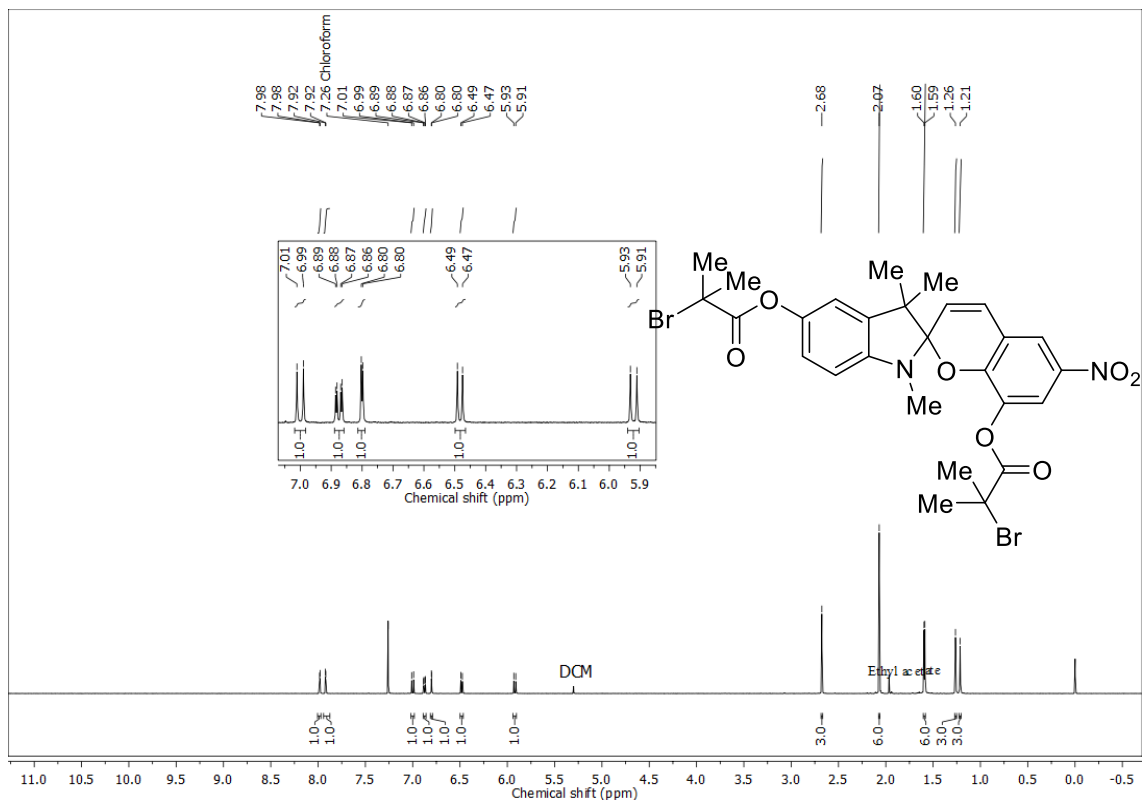
5-Hydroxy-2,3,3-trimethyl-3H-indol-5-ol (s7) in CDCl₃



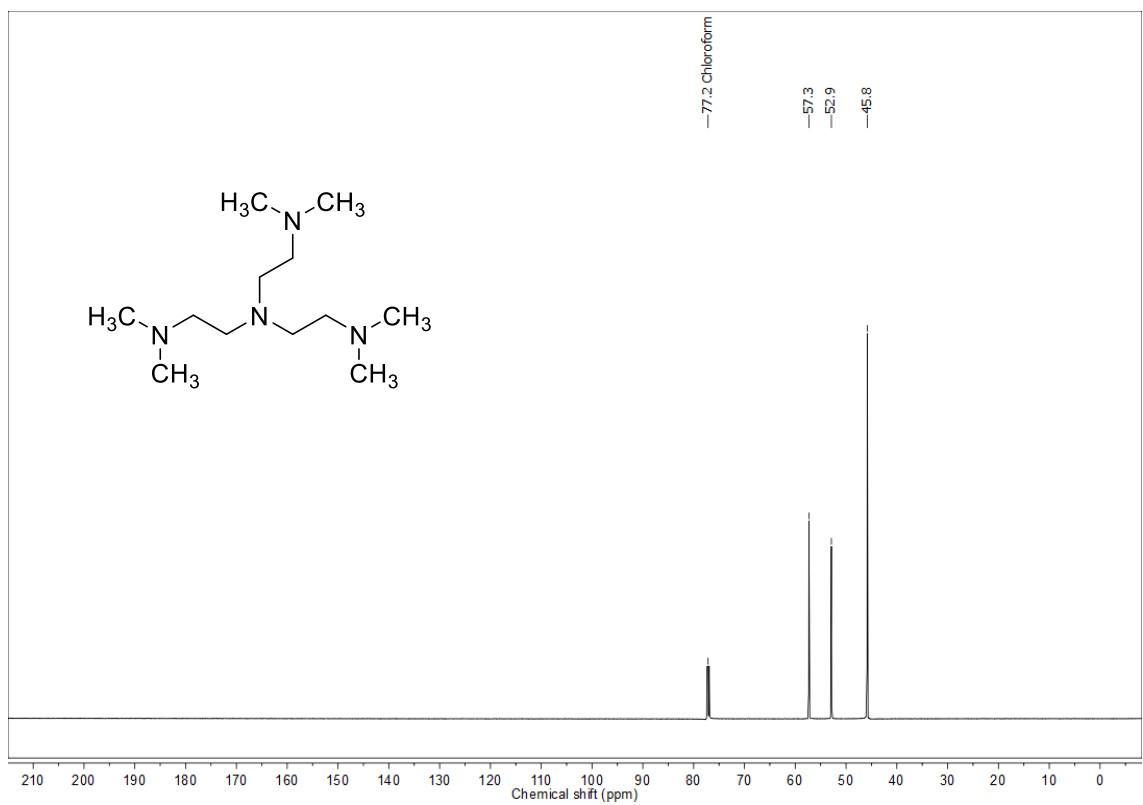
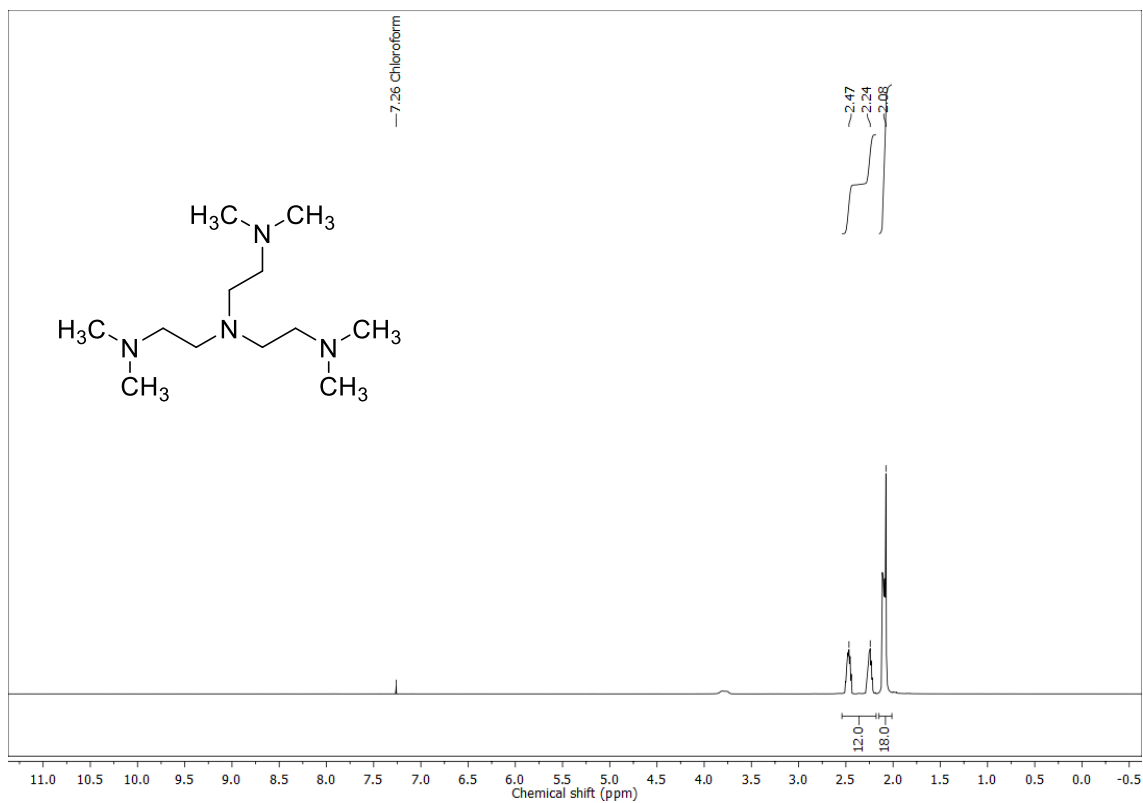
5-Hydroxy-1,2,3,3-tetramethyl-3*H*-indolium iodide (s8) in DMSO



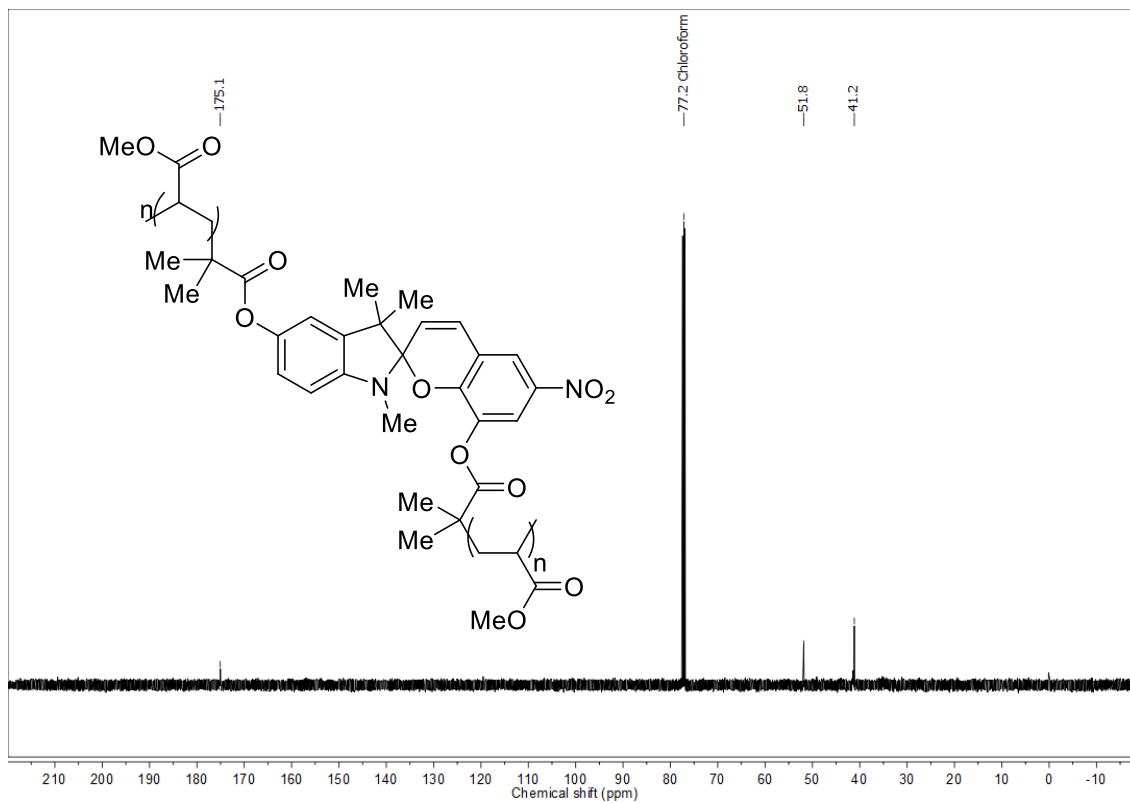
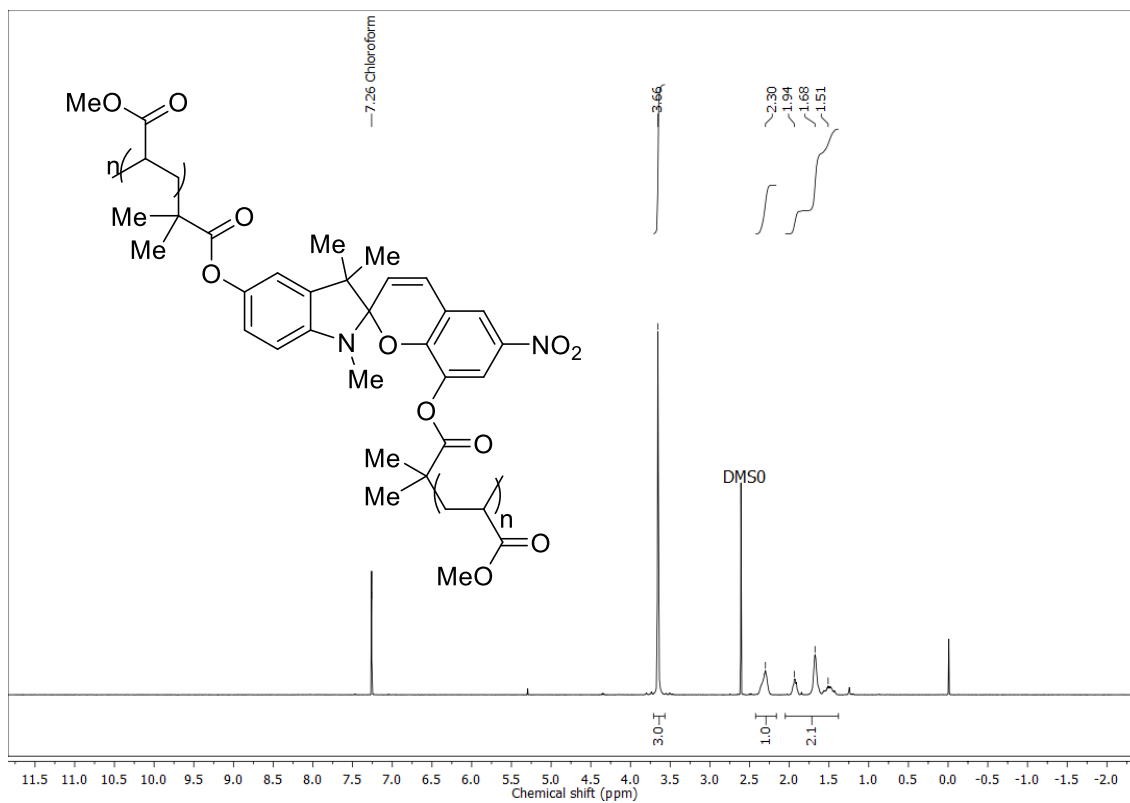
1',3',3'-trimethyl-6-nitrospiro[chromene-2,2'-indoline]-5',8-diylbis(2-bromomethylpropanoate) (1) in CDCl₃



Tris[2-(dimethylamino)ethyl]amine (3) in CDCl₃



PMA-SP-PMA 4



12. References

- (1) Potisek, S. L.; Davis, D. A.; Sottos, N. R.; White, S. R.; Moore, J. S. Mechanophore-Linked Addition Polymers. *J. Am. Chem. Soc.* **2007**, *129* (45), 13808–13809.
<https://doi.org/10.1021/ja076189x>.
- (2) Davis, D. A.; Hamilton, A.; Yang, J.; Cremar, L. D.; Van Gough, D.; Potisek, S. L.; Ong, M. T.; Braun, P. V.; Martínez, T. J.; White, S. R.; et al. Force-Induced Activation of Covalent Bonds in Mechanoresponsive Polymeric Materials. *Nature* **2009**, *459* (7243), 68–72.
<https://doi.org/10.1038/nature07970>.
- (3) Schulz-Senft, M.; Gates, P. J.; Sönnichsen, F. D.; Staubitz, A. Diversely Halogenated Spiropyrans - Useful Synthetic Building Blocks for a Versatile Class of Molecular Switches. *Dye. Pigm.* **2017**, *136*, 292–301.
<https://doi.org/10.1016/j.dyepig.2016.08.039>.
- (4) Ciampolini, M.; Nardi, N. Five-Coordinated High-Spin Complexes of Bivalent Cobalt, Nickel, and Copper with Tris(2-Dimethylaminoethyl)Amine. *Inorg. Chem.* **1966**, *5* (1), 41–44. <https://doi.org/10.1021/ic50035a010>.
- (5) Fu, Q.; McKenzie, T. G.; Tan, S.; Nam, E.; Qiao, G. G. Tertiary Amine Catalyzed Photo-Induced Controlled Radical Polymerization of Methacrylates. *Polym. Chem.* **2015**, *6* (30), 5362–5368. <https://doi.org/10.1039/c5py00840a>.

9. Photoexpansion of Poly(silazobenzyl-siloxane) Thin Film

Current section presents light induced reversible film expansion of amorphous azobenzene-based polysiloxane with a possibility of cross-linking. Atomic force microscopy was utilized to verify the reversible photoexpansion effects in the poly(silazobenzyl-siloxane) thin film. During the submission of this thesis the following manuscript was under preparation.

Personal contributions in the following article:

- Thin film preparation for solid state studies
- Examining photoisomerisation in solid state with UV-vis spectroscopy
- Photomechanical studies with AFM
- Co-writing the manuscript

Reversible Volume Switching of Poly(silazobenzyl-siloxane)

Mathias Schulz-Senft,^{‡1,2,3} Sindu Shree,^{‡4} Jan Strueben,¹ Xin Jin,⁴ David Presa Soto,¹ Rainer Adelung,^{*4} Anne Staubitz^{*1,2,3}

¹Otto-Diels-Institute for Organic Chemistry, University of Kiel, Otto-Hahn-Platz 4, 24098 Kiel (Germany),

²Institute for Organic and Analytical Chemistry, University of Bremen, Leobener Str. 7, 28359 Bremen (Germany),

³MAPEX Center for Materials and Processes, University of Bremen, Bibliothekstraße 1, 28359 Bremen (Germany),

⁴Institute for Materials Science, University of Kiel, Kaiserstr. 2, 24143 Kiel (Germany).

ABSTRACT: Poly(silazobenzyl-siloxane) is a class of novel polymers that contain azobenzene groups in the main chain, alternating with siloxane units. While the latter impart a low stiffness, high flexibility, and high endurance on the polymer, azobenzene units can reversibly photoisomerize from *E* to *Z*. There are examples in which this movement on a molecular level has been translated into a macroscopically observable change. This work provides the first example of a photoswitchable, linear polysiloxane with azobenzene in the main chain as a repeating unit as opposed to the side chain that can still switch in the solid state. Most known examples of photomechanical azobenzene-based polymers require a liquid crystalline arrangement of the switching moieties. Poly(silazobenzyl-siloxane) is amorphous and we show a reversible expansion of a polymer film of ~4% without any alignment of the azobenzenes. This photoexpansion was monitored by atom force microscopy (AFM) for four irradiation series.

Introduction

Azobenzene chromophores can undergo reversible light induced *E/Z* isomerization. The thermodynamically stable *E* form isomerizes to the *Z* form upon irradiation with UV light, the reverse reaction can be induced by irradiation with visible light, typically with a peak wavelength of ca. 440 nm.¹ This photoisomerization of the double bond in the azo group occurs at a high quantum yield with high fatigue resistance.² The isomerization is accompanied by changes in, spatial orientation (the *E* isomer is planar,³ the *Z* isomer shows a dihedral angle of 173.5° of the central C-N=N-C moiety⁴), length (the distance between the 4 and 4' position reduces from 0.99 nm⁵ to 0.55 nm⁴), and a reduction of the occupied volume of the *Z*-isomer (switching azobenzenes in polymer matrices reduces the free volume^{6,7}). Especially the spatial and volumetric changes require a sufficiently flexible environment for effective switching. Depending on which switching mechanism one assumes, the isomerization of azobenzenes is estimated to require volumes between 0.12 nm³ and 0.38 nm³.⁸

The facile synthetic access⁹ to azobenzenes was used to incorporate these photoswitches into various polymeric environments.⁸ Polymers containing azobenzenes show macroscopic responses to UV light illumination.⁸ Photomechanical effects have a broad range of applications namely, light activated self-healing polymers^{10,11} and photo-actuators^{12,13}. Azobenzenes in solution have served as crown ether based ions traps,^{14,15} and they have been discussed for drug delivery.¹⁶ Photo-controlled movement requires liquid crystalline arrangements of azobenzenes, which are immobilized during polymerization.¹⁷ If not located in mesogenic phases, switching of polymeric azobenzenes results in glass transition temperature

T_g changes.^{10,18} As T_g is a controlling parameter of several physical properties of the polymer such as stiffness, elasticity, hardness etc., a change in T_g is accompanied by changing film volumes¹⁹ and/or softening of surfaces.²⁰ Even without crossing above T_g , photoinduced switching of azobenzenes polymers affects the polymers' volumes. Generally, in amorphous polymers, polymer chain length is a determining factor of the extent of chain entanglement and this in turn determines how a polymer behaves at or above its T_g . Short polymer chains show low entanglements and the polymer flows at T_g . Long polymer chains show high entanglements which makes the agglomerated polymer to expand at T_g . This has been observed in amorphous azobenzene polymers as well, in which switching ($E \rightarrow Z$) of azobenzene moieties caused an expansion of 1-5%.²¹ Switching azobenzene in liquid crystalline polymers induces a compression. The combination of both, photoinduced expansion and compression can be utilized in the development of photoactuators or artificial muscles. E.g. the flight muscles of insects show only a change in length by 1-2%.²²

Poly(siloxanes) are amongst the most industrially important elastomers. They possess an advantageous combination of low glass transition temperatures (as low as $-120\text{ }^\circ\text{C}$),²³ thermal stability, and low surface tension.²⁴ This is required in applications such as medical implants, electric insulators, sealants, etc.²⁵⁻²⁷ The free volume of the polymers drastically increases at temperatures above their T_g .²⁸ The Si-O bond shows low energy barriers for rotation (approx. 2.5 kJ/mol) and for linearization of the Si-O-Si angle (1.3 kJ/mol), leading to the very flexible polysiloxane chains.²⁴ This flexibility makes polysiloxanes suitable scaffolds to tailor switchable azobenzenes into the side chains of these polymers.²⁹⁻⁴¹ However, we reasoned that siloxane linkers should provide sufficient flexibility to maintain the photoswitchability of the azobenzenes even in the backbone of polymers.

Above $200\text{ }^\circ\text{C}$, polysiloxanes degrade into shorter cyclic siloxanes, which can be suppressed by introducing aryl groups into the so-called poly(silarylene-siloxanes) (PSAS) main chain.⁴²⁻⁴⁴ In comparison to the linear polysiloxanes, PSAS possess more rigid chain elements and thus show higher glass transition temperatures.⁴⁵ Substitution of every third dimethylsilane unit in poly(dimethylsiloxane) (PDMS) by a phenyl ring increased the T_g from $-120\text{ }^\circ\text{C}$ to $-25\text{ }^\circ\text{C}$.⁴⁶ Elongating the resulting disiloxane bridge between the phenyl groups by one siloxane unit decreased the T_g to $-63\text{ }^\circ\text{C}$, further elongation of the bridge reduced the effect of additional siloxane units.⁴⁶ Therefore, short siloxanes are promising linkers to provide a sufficiently low glass transition to allow the switching of azobenzenes in the polymer backbone at room temperature in the condensed state.

In this study, the advancement of linear alternating poly(silazobenzyl-siloxanes) is presented. It was possible to incorporate vinyl side chains for further cross-linking and to investigate the light induced switching of volume. Photo induced expansion of films of polyacrylate with azobenzene units in the side chains was measured before by ellipsometry, giving a reversible expansion effect of 3% upon laser

irradiation.¹⁹ However, to the best of our knowledge, this work is the first example of investigating the cyclic switching of such azobenzene-based polysiloxane films by AFM.

Experimental Section

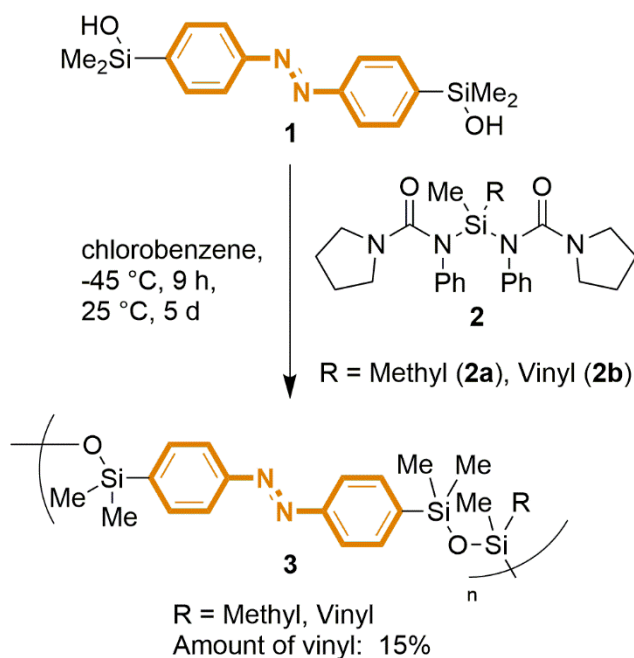
Materials

All used chemicals were purchased from Acros, Alfa Aesar, Grüssing, Merck and Sigma-Aldrich. Except for the dichlorosilanes, the chemicals were used without further purification. Dichlorodimethylsilane and dichloromethylvinylsilane were distilled from calcium hydride and were degassed before further use. Solvents and chemicals that were used in inert synthesis were dried (if not purchased anhydrous) and degassed prior to synthesis and stored under nitrogen either in J-Young glassware or a nitrogen filled glovebox from MBraun. Further details on the supplier of each chemical and solvent and the individual drying procedures are provided in the supporting information (SI).

Synthesis of the Polymer and its Precursors

Inert syntheses were carried out in nitrogen atmosphere using Schlenk techniques or inside a nitrogen filled glovebox. The cooling of inert syntheses was achieved by using a cooling block connected to a Julabo FP88 cryostate inside the glove box. Microwave assisted syntheses were performed on a Biotage Initiator+ SP Wave peptide synthesizer in the organic synthesis mode. A fixed hold time was turned off.

Scheme 1. Synthesis of the poly(silazobenzyl-siloxane) **3** containing 15% vinyl functional groups by polycondensation.



All synthesized air-stable precursors were characterized by melting points, IR and NMR (^1H , $^{13}\text{C}\{^1\text{H}\}$, ^{129}Sn , $^{29}\text{Si}\{^1\text{H}\}$) spectroscopy and high resolution mass spectrometry. The silane co-monomers **2a** and **2b** were too sensitive towards moisture to record more than NMR spectra. NMR experiments were performed

either on a Bruker Avance Neo 500 (^1H NMR: 500 MHz) or on a Bruker Avance II HD 600 (^1H NMR: 600 MHz) FT-NMR spectrometer at 300 K. and the assignment of peaks was performed with the help of two-dimensional NMR spectroscopy such as ^1H COSY, $^1\text{H}/^{13}\text{C}\{^1\text{H}\}$ HSQC, $^1\text{H}/^{13}\text{C}\{^1\text{H}\}$ HMBC or $^1\text{H}/^{29}\text{Si}\{^1\text{H}\}$ HMBC if possible. The spectra were referenced solvent residual proton signals (^1H) or the solvent itself (^{13}C) ^{129}Sn and ^{29}Si spectra were internally referenced against tetramethylsilane (TMS). Further details on the equipment used for analysis are provided in the supporting information.

The polymer **3** was synthesized inside the glove box and analyzed by IR, NMR, UV-Visible spectroscopy and gel permeation chromatography (GPC) in solution. A film of **3** was investigated by AFM, profilometry and UV-Visible measurements.

Preparation of the Polymer Film

A film of the polymer **3** was prepared by spin coating onto a quartz substrate: A solution of **3** with a concentration of 214 μM in 10 mL THF was applied to a cleaned and dried quartz substrate in a spin coater at a rotational frequency of 2000 rpm. The polymer film was dried and stored in a desiccator at reduced pressure to remove residual solvent. Average surface roughness was determined to be 5.7 nm ± 0.5 using AFM and the thickness was measured to be 110 nm ± 5 by profilometry.

Irradiation Equipment

The irradiation experiments of solutions of **3** were carried out using LED light sources by Sahlmann Photochemical Solutions with an optical power of 1000 mW (365 nm) and 900 mW (450 nm). The distance between the light source and sample was 10 mm with horizontal alignment of the light source. Irradiation of the film for AFM and UV-Visible measurements was achieved using the fiber-coupled LEDs M365FP1 (365 nm, 15.5 mW) and M455F3 (455 nm, 24.5 mW) from Thorlabs with an angle of 30° .

In this work, we use the terms “UV light” and “blue light” to refer to the nominal peak wavelengths of the irradiation equipment, 365 nm and 450 nm, respectively. The term “visible light” also refers to 450 nm.

UV-Visible Measurements

UV-Visible spectra of the film of polymer **3** were recorded in absorption mode in a Perkin Elmer Lambda 900 spectrometer. Spectra were recorded before and after irradiation with UV and blue light for five switching cycles. After the final UV irradiation, the thermal relaxation was followed by recording spectra every five minutes over the course of 19 hours. The according half-life time was determined using an exponential fit of the increase of the absorption at 330 nm over time.

In solution, the UV-Visible were recorded at 25 °C using a Perkin Elmer Lambda 14 UV-Visible spectrometer. Quartz cuvettes with a light path length of 10 mm from Hellma Analytics were used. The polymer was measured before and after irradiation with UV and visible light. To investigate the thermal relaxation after irradiation with UV light, repetitive measurements were performed every 15 minutes over the course of 40 hours. The half-life time of the relaxation was determined by an exponential fit of the increase of the absorption at 330 nm over time. Spectra of these measurements are provided in the supporting information.

AFM Measurements

Topographical AFM imaging were conducted resonance under the WITec RA 300 microscope with an Asylum cantilever with 2 Nm⁻¹, 70 kHz. To avoid damaging the thin film, the scans were performed in tapping mode, scanning an area of 100 μm². For this purpose, films of the polymer on quartz glass were irradiated with UV light (365 nm) without retracting the AFM probe (**Figure 1 (e and f)**). Thus, it was possible to track the same area throughout the irradiation cycles. The obtained surface maps (**Figure 1 (a-d)**) still reveal a slight drift between the irradiation cycles. After four irradiations, the drift was too large for a comparative analysis. Within this area, the height profile of three distinctive spots was monitored.

The series of AFM surface scans started after irradiation with UV light, followed by alternating irradiation with blue light and UV light.

GPC Measurements

Gel permeation chromatography was performed on a Viscotek GPC max VE2001 equipped with a Viscotek VE3580 RI detector and a column set of LT5000 and LT4000 in THF (VWR, HPLC-grade) with a flow rate of 1 mL/min. Conventional calibration and analysis was done with OmniSEC 4.6.2 software using polystyrene standards. The number average molecular weight (M_n) and the weight average molecular weight (M_w) were determined and used to derive the poly dispersity index (PDI).

For analyzing the switching of **3**, the solution was irradiated with UV light for one hour. Again, M_n , M_w and the PDI were determined.

Results & Discussion

Synthesis of the Poly(silazobenzyl-siloxane) **3**

The polymer **3** was obtained via a polycondensation reaction using the azobenzyl hydroxysilane **1** and two urea derivatives **2a,b** as monomers (**Scheme 1.**). The synthesis of the azobenzene derivative **1** was reported previously by us.⁴⁷ In order to investigate the influence of modifications of the backbone on the materials' behaviour., two urea functionalized silanes **2** that were to serve as co-monomers were also synthesized.⁴⁸ While the compound **2a** connects two azobenzene monomers via a SiMe₂ unit, compound

2b introduces a vinyl group into the backbone of polymer **3**. The bis(ureido)silanes **2** were added simultaneously to a solution of the azobenzene **1** at $-45\text{ }^{\circ}\text{C}$, thus statistically distributing the vinyl moieties throughout the polymer. The polymerization was monitored via GPC. To compensate small deviations in the ratio of the monomers **1** and **2**, when the growth of the polymer ceased, small portions of each monomer were added alternatively. After 8 d, the polymer was obtained with a M_n of 14.4 kDa, M_w of 23.3 kDa (corresponding to a polydispersity index (PDI) = 1.62). The number of repeating units bearing vinyl groups was determined by NMR spectroscopy to be 15%. Synthetic details of the polymerization, as well as of the synthetic routes to the monomers **1** and **2** are included in the supporting information, accompanied by their respective NMR spectra.

Analysis of the Switching in Film and Solution by UV-vis Spectroscopy

To investigate whether the azobenzene moieties were able to switch in the polymer film of **3**, a thin film (thickness = $110\pm 5\text{ nm}$) was analyzed by UV-vis spectroscopy in transmission mode. Upon irradiation with UV light (365 nm), the absorption of the $\pi\pi^*$ band at 330 nm decreased by 10%, whereas the change of the $n\pi^*$ band at 450 nm was barely notable (**Figure 1**). This development of *Z* azobenzene could be reversed by irradiation with blue light (450 nm). After five cycles, the polymer film showed no signs of photodegradation (**Figure 1(c)**). The thermal relaxation after irradiation with UV light was monitored at intervals of five minutes over the course of 19 hours. For determination of the half-life time, the absorption at the $\pi\pi^*$ band at 330 nm was plotted and an exponential fit was applied. The half-life time was $7:37\text{ h} \pm 9\text{ min}$ (**Figure 1 (b)**).

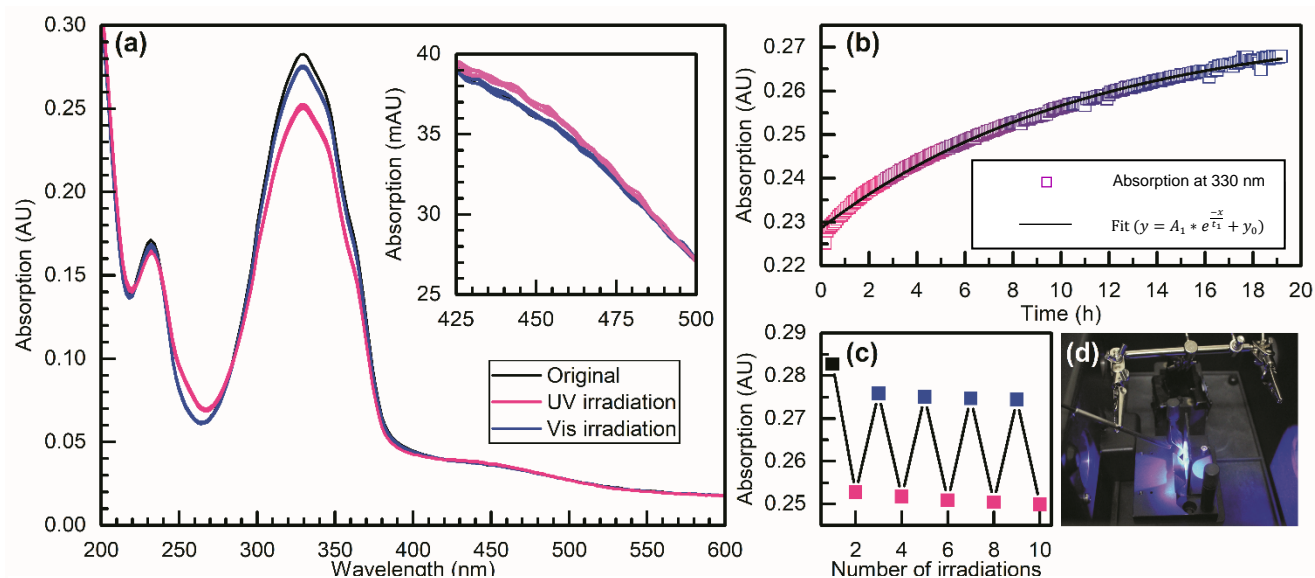


Figure 1. (a) Cyclic UV-visible spectra of polymer **3**. The thin film of **3** was irradiated with UV (365 nm) and blue (450 nm) back and forth for 5 cycles. Inset contains the zoomed-in spectra at the range of 420 – 500 nm. (b) Thermal relaxation after UV irradiation. The absorption at 330 nm was monitored in intervals of 5 minutes. Exponential fitting gave a half-life time of $7:37\text{ h} \pm 9\text{ min}$. (c) Shows stable cyclic behavior of **3** measured at 330 nm after every irradiation. (d) The measurement set-up for conducting UV-blue light irradiation before the UV-Visible spectrum was taken.

The UV-vis results of the film were complemented by UV-vis spectroscopy in solution. A solution of the polymer in THF was subjected to UV (365 nm) and visible light (450 nm). The measurements revealed under UV light irradiation a reduction of the $\pi\pi^*$ band at 330 nm by approx. two thirds, which was fully reversible upon irradiation with blue light (450 nm). The half-life time of the thermal relaxation reaction was determined to be $21 \text{ h} \pm 18 \text{ min}$ (see Supporting Information, **Figure SI-4**).

Measuring the Volume Switching of the Film by AFM

The photo-elastic behavior of the polymer **3** was tested by atomic force microscopy (AFM) in tapping mode, scanning an area of $100 \mu\text{m}^2$. For this purpose, films of the polymer on quartz glass were irradiated with UV light (365 nm) without retracting the AFM probe. Thus, it was possible to track the same area throughout the irradiation cycles. The obtained surface maps (**Figure 2**) still revealed a slight drift between the irradiation cycles, however, four irradiation sequences could be measured and compared. Within this area, the height profile of three distinctive spots was monitored. From the height profiles and calculated relative height differences of spot 1 (**Figure 3 (a) and (b)**) maximum height variations of 4 nm were observed. The series of AFM areal surface scans started after irradiation with UV light, followed by alternating irradiation with blue light and UV light. The film's height measured after UV light irradiation is significantly higher than after blue light irradiation. Compared to the initial UV irradiated state, the film

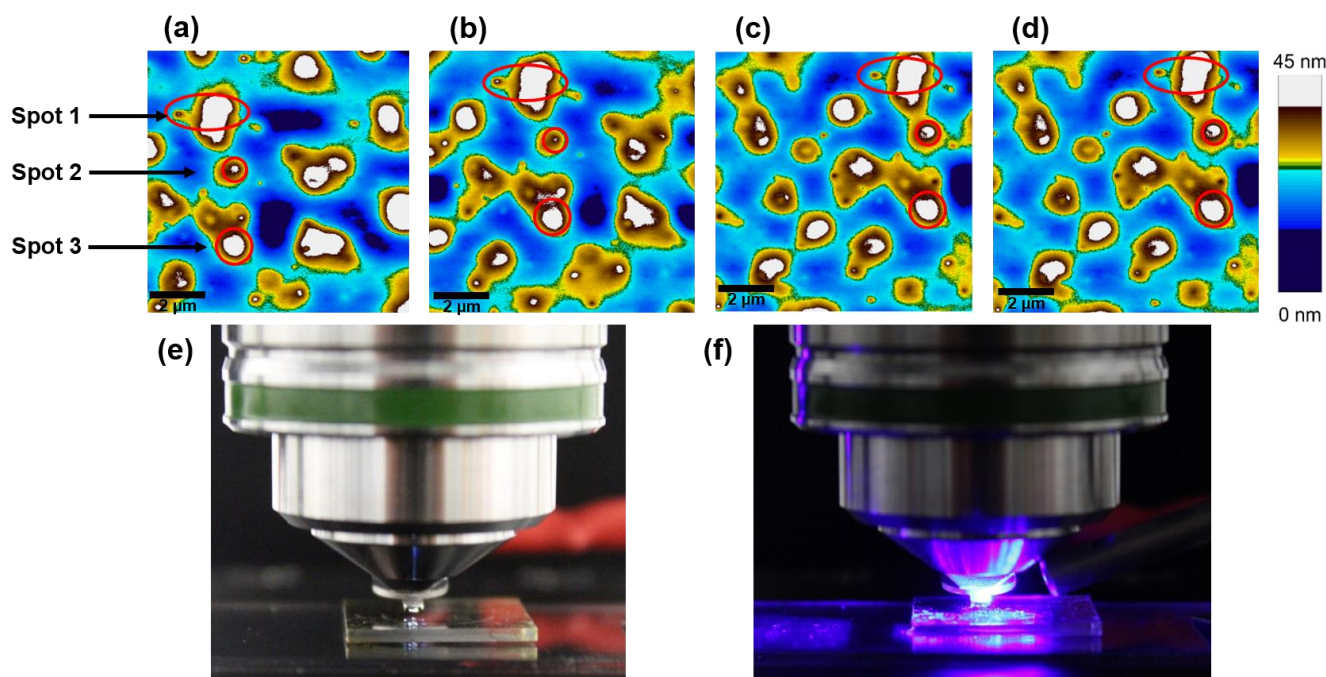


Figure 2. AFM topographical scans of the thin films of **3** coated on a quartz substrate. Each scan was acquired after 20 min of irradiation. (a) Surface scan after 1st UV light irradiation, (b) Surface scan after 1st blue light irradiation, (c) Surface scan after 2nd UV light irradiation and (d) Surface scan after 2nd UV light irradiation. Marked spots in the images are the common areas used for height measurement. On the far right is the scale bar representing the color profile of all scans. (d) Setup of the environmental AFM, with the probe head and tip on top of the quartz substrate with the polymer film. (e) Direct irradiation of the polymer film on the quartz substrate without removing the probe head.

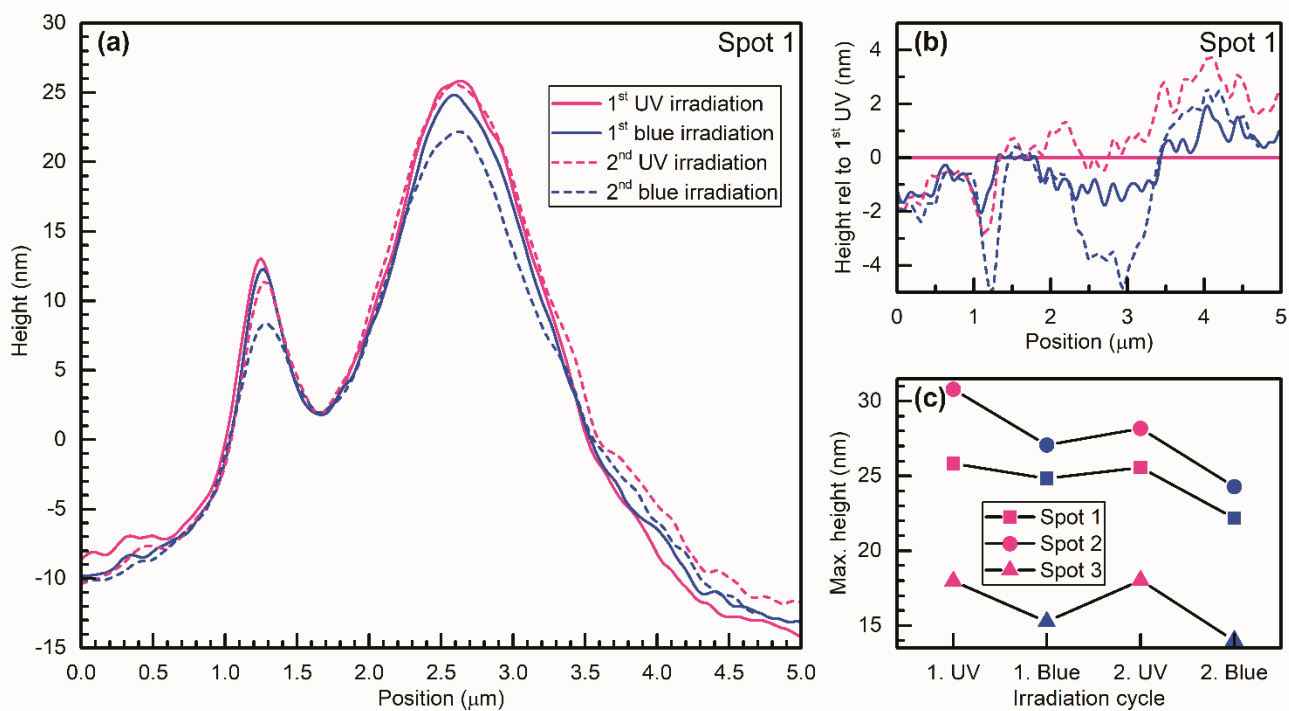


Figure 3. (a) Height profile of Spot 1 after the four irradiation stages. (b) Height differences relative to the 1st UV irradiation. (c) Maximum height values of all three spots after the four irradiation stages.

height decreased throughout the common areas measured. The second irradiation sequence confirms the reversibility of the switching, partially leading to larger effects. In all three spots (**Figure 3**), the maximum height changed by 1 – 4 nm per cycle. These findings are consistent with other studies that prove a higher spatial demand for *Z*-azobenzene moieties in polymer films.^{7,49,50} The height profiles of spots 2 and 3 are provided in the Supporting Information, **Figure SI-2** and **SI-3**.

Measuring the Volume Switching of the Solution by GPC

The switching could also be monitored by GPC. A solution of **3** in THF was measured before and after UV irradiation and the apparent molecular weights were determined after calibration against polystyrene. Upon irradiation with UV light, the apparent molecular weight decreased from 14.4 to 11.8 kDa (M_n) and 23.3 to 19.9 kDa (M_w), corresponding to a reduction by 18% (M_n) and 15% (M_w), respectively. This observed decrease in the apparent molecular weight might appear contradictory to the increase in volume of the film that was determined by AFM measurements. However, the intrinsic helicity of *Z* azobenzenes facilitates the formation of dense coils, as we have recently investigated in depth.⁴⁷ The GPC elugram and the weight distribution are shown in the Supporting Information, **Figure SI-1**.

Conclusion

In solution, a decrease in apparent molecular weight of 15 (M_w) to 18% (M_n) was determined by GPC analysis. UV-vis measurements in THF confirmed successful switching and the thermal half-life time of the back switching to be 21 h was observed.

A method of investigating a spin-coated film of the polymer throughout two irradiation cycles was successfully established under AFM. These measurements revealed a reversible relative height variation of the film by 10% and a 4% reversible film expansion. UV-visible spectroscopy of the film showed the switching of a minority of the azobenzene units in the polymer backbone, while thermal relaxation occurs with a half-life time of approx. 7.5 hours. The film's photostability was proven by cyclic irradiations with UV and blue light, giving no evidence of degradation.

The presented study proves the potential of the photoswitchable polymer system. Though the azobenzene units are located in the backbone of the polymer, linked by only trisiloxane bridges, it was possible to reversibly induce a photoexpansion without any signs of degradation. In the further development of these systems, the effect of cross-linking will be investigated.

ASSOCIATED CONTENT

Supporting Information. This material is available free of charge via the Internet at <http://pubs.acs.org>. Detailed list of used chemicals, solvents and equipment; synthetic details of **1**, **2a**, **2b**, **3** and their precursors; GPC and UV-vis (solution) spectra of **3**; ^1H , $^{13}\text{C}\{^1\text{H}\}$, ^{129}Sn and $^{29}\text{Si}\{^1\text{H}\}$ NMR spectra of all synthesized compounds; AFM height profiles of Spot 2 and Spot 3.

AUTHOR INFORMATION

Corresponding Author

* Rainer Adelung, ra@tf.uni-kiel.de

* Anne Staubitz, staubitz@uni-bremen.de

Author Contributions

A. S. and R. A. conceived and supervised the project. J. S. and D. P. S. established the synthesis of monomers. M. S.-S. optimized the synthesis of monomers and polymers and conducted NMR, GPC, UV-vis (solution) and MS analyses of all compounds. S.S. carried out AFM and UV-Visible (thin film) measurements. M.S.-S., S.S. and A.S. wrote the manuscript and all authors have given approval to the final version of the manuscript. / ‡These authors contributed equally.

Notes

The authors declare no competing financial interests.

ACKNOWLEDGMENT

This work was funded by the German Research Foundation (DFG) in the context of the Collaborative Research Center 677 "Function by Switching", Project C14. This research has been supported by the Institutional Strategy of the University of Bremen, funded by the German Excellence Initiative. D.P.S. thanks the EU COST Action CM 1302: Smart Inorganic Polymers.

REFERENCES

- (1) Bandara, H. M. D.; Burdette, S. C. Photoisomerization in Different Classes of Azobenzene. *Chem. Soc. Rev.* **2012**, *41* (5), 1809–1825. <https://doi.org/10.1039/C1CS15179G>.
- (2) Venkataramani, S.; Jana, U.; Dommaschk, M.; Sönnichsen, F. D.; Tuzcek, F.; Herges, R. Magnetic Bistability of Molecules in Homogeneous Solution at Room Temperature. *Science* **2011**, *331* (6016), 445–448. <https://doi.org/10.1126/science.1201180>.
- (3) Harada, J.; Ogawa, K.; Tomoda, S. Molecular Motion and Conformational Interconversion of Azobenzenes in Crystals as Studied by X-Ray Diffraction. *Acta Crystallogr. B* **1997**, *53* (4), 662–672. <https://doi.org/10.1107/S0108768197002772>.
- (4) Mostad, A.; Rømming, C. A Refinement of the Crystal Structure of Cis-Azobenzene. *Acta Chem. Scand.* **1971**, *25*, 3561–3568.
- (5) Brown, C. J. A Refinement of the Crystal Structure of Azobenzene. *Acta Crystallogr.* **1966**, *21* (1), 146–152. <https://doi.org/10.1107/S0365110X66002445>.
- (6) Naito, T.; Horie, K.; Mita, I. Photochemistry in Polymer Solids: 12. Effects of Main-Chain Structures and Formation of Hydrogen Bonds on Photoisomerization of Azobenzene in Various Polymer Films. *Polymer* **1993**, *34* (19), 4140–4145. [https://doi.org/10.1016/0032-3861\(93\)90680-9](https://doi.org/10.1016/0032-3861(93)90680-9).
- (7) Harms, S.; Rätzke, K.; Pakula, C.; Zaporojtchenko, V.; Strunskus, T.; Egger, W.; Sperr, P.; Faupel, F. Free Volume Changes on Optical Switching in Azobenzene-Polyethylmethacrylate Blends Studied by a Pulsed Low-Energy Positron Beam. *J. Polym. Sci. Part B Polym. Phys.* **2011**, *49* (6), 404–408. <https://doi.org/10.1002/polb.22201>.
- (8) Bushuyev, O. S.; Aizawa, M.; Shishido, A.; Barrett, C. J. Shape-Shifting Azo Dye Polymers: Towards Sunlight-Driven Molecular Devices. *Macromol. Rapid Commun.* **2018**, *39* (1), 1700253. <https://doi.org/10.1002/marc.201700253>.
- (9) García-Iriepa, C.; Marazzi, M.; Frutos, L. M.; Sampedro, D. E/Z Photochemical Switches: Syntheses, Properties and Applications. *RSC Adv.* **2013**, *3* (18), 6241. <https://doi.org/10.1039/c2ra22363e>.
- (10) Weis, P.; Tian, W.; Wu, S. Photoinduced Liquefaction of Azobenzene-Containing Polymers. *Chem. – Eur. J.* **2018**, *24* (25), 6494–6505. <https://doi.org/10.1002/chem.201704162>.
- (11) Wang, C.; Fadeev, M.; Zhang, J.; Vázquez-González, M.; Davidson-Rozenfeld, G.; Tian, H.; Willner, I. Shape-Memory and Self-Healing Functions of DNA-Based Carboxymethyl Cellulose Hydrogels Driven by Chemical or Light Triggers. *Chem. Sci.* **2018**, *9* (35), 7145–7152. <https://doi.org/10.1039/C8SC02411A>.
- (12) Nie, J.; Liu, X.; Yan, Y.; Zhang, H. Supramolecular Hydrogen-Bonded Photodriven Actuators Based on an Azobenzene-Containing Main-Chain Liquid Crystalline Poly(Ester-Amide). *J. Mater. Chem. C* **2017**, *5* (39), 10391–10398. <https://doi.org/10.1039/C7TC02943H>.
- (13) Xiong, Y.; Zhang, L.; Weis, P.; Naumov, P.; Wu, S. A Solar Actuator Based on Hydrogen-Bonded Azopolymers for Electricity Generation. *J. Mater. Chem. A* **2018**, *6* (8), 3361–3366. <https://doi.org/10.1039/C7TA1139H>.
- (14) Shinkai, S.; Nakaji, T.; Nishida, Y.; Ogawa, T.; Manabe, O. Photoresponsive Crown Ethers. 1. Cis-Trans Isomerism of Azobenzene as a Tool to Enforce Conformational Changes of Crown Ethers and Polymers. *J. Am. Chem. Soc.* **1980**, *102* (18), 5860–5865. <https://doi.org/10.1021/ja00538a026>.
- (15) Janus, K.; Sworakowski, J. Photochromism of Crown Ethers with Incorporated Azobenzene Moiety. *J. Phys. Chem. B* **2005**, *109* (1), 93–101. <https://doi.org/10.1021/jp0483268>.
- (16) Eom, T.; Yoo, W.; Kim, S.; Khan, A. Biologically Activatable Azobenzene Polymers Targeted at Drug Delivery and Imaging Applications. *Biomaterials* **2018**, *185*, 333–347. <https://doi.org/10.1016/j.biomaterials.2018.09.020>.
- (17) Ikeda, T.; Nakano, M.; Yu, Y.; Tsutsumi, O.; Kanazawa, A. Anisotropic Bending and Unbending Behavior of Azobenzene Liquid-Crystalline Gels by Light Exposure. *Adv. Mater.* **2003**, *15* (3), 201–205. <https://doi.org/10.1002/adma.200390045>.
- (18) Zhou, H.; Xue, C.; Weis, P.; Suzuki, Y.; Huang, S.; Koynov, K.; Auernhammer, G. K.; Berger, R.; Butt, H.-J.; Wu, S. Photoswitching of Glass Transition Temperatures of Azobenzene-Containing Polymers Induces Reversible Solid-to-Liquid Transitions. *Nat. Chem.* **2017**, *9* (2), 145–151. <https://doi.org/10.1038/nchem.2625>.
- (19) Tanchak, O. M.; Barrett, C. J. Light-Induced Reversible Volume Changes in Thin Films of Azo Polymers: The Photomechanical Effect. *Macromolecules* **2005**, *38* (25), 10566–10570. <https://doi.org/10.1021/ma051564w>.
- (20) Karageorgiev, P.; Neher, D.; Schulz, B.; Stiller, B.; Pietsch, U.; Giersig, M.; Brehmer, L. From Anisotropic Photo-Fluidity towards Nanomanipulation in the Optical near-Field. *Nat. Mater.* **2005**, *4* (9), 699–703. <https://doi.org/10.1038/nmat1459>.
- (21) Barrett, C. J.; Mamiya, J.; Yager, K. G.; Ikeda, T. Photo-Mechanical Effects in Azobenzene-Containing Soft Materials. *Soft Matter* **2007**, *3*, 1249–1261.
- (22) Josephson, R. K. Comparative Physiology of Insect Flight Muscle. In *Nature's Versatile Engine: Insect Flight Muscle Inside and Out*; Vigoreaux, J. O., Ed.; Molecular Biology Intelligence Unit; Springer US: Boston, MA, 2006; pp 34–43. https://doi.org/10.1007/0-387-31213-7_3.
- (23) Mark, J. E. *Polymer Data Handbook*; Oxford University Press: Oxford, 1999.
- (24) Jones, R. G. *Silicon-Containing Polymers: The Science and Technology of Their Synthesis and Applications*; Kluwer Academic Publishers: Dordrecht; Boston; London, 2000.
- (25) Moretto, H.-H.; Schulze, M.; Wagner, G. Silicones. In *Ullmann's Encyclopedia of Industrial Chemistry*; Wiley-VCH Verlag GmbH & Co. KGaA, Ed.; Wiley-VCH Verlag GmbH & Co. KGaA: Weinheim, Germany, 2000. https://doi.org/10.1002/14356007.a24_057.
- (26) Chandrasekar, V. *Inorganic and Organometallic Polymers*; Springer Verlag: Berlin Heidelberg, 2005.
- (27) Mark, J. E.; Allcock, H. R.; West, R. *Inorganic Polymers*, Second Edition.; Oxford University Press: Oxford, New York, 2005.
- (28) White, R. P.; Lipson, J. E. G. Polymer Free Volume and Its Connection to the Glass Transition. *Macromolecules* **2016**, *49* (11), 3987–4007. <https://doi.org/10.1021/acs.macromol.6b00215>.
- (29) Ohm, C.; Brehmer, M.; Zentel, R. Liquid Crystalline Elastomers as Actuators and Sensors. *Adv. Mater.* **2010**, *22* (31), 3366–3387. <https://doi.org/10.1002/adma.200904059>.
- (30) Miller, L. S.; Walton, D. J.; Stone, P. J. W.; McRoberts, A. M.; Sethi, R. S. Langmuir-Blodgett Films for Nonlinear Optical Applications. *J. Mater. Sci. Mater. Electron.* **1994**, *5* (2), 75–82. <https://doi.org/10.1007/BF00187116>.

- (31) Miller, L. S.; McRoberts, A. M.; Walton, D. J.; Parry, D. A.; Newton, A. L. Optical Gas Sensing Using Langmuir-Blodgett Films. *Mater. Sci. Eng. C* **1995**, *3* (3), 257–262. [https://doi.org/10.1016/0928-4931\(95\)00084-4](https://doi.org/10.1016/0928-4931(95)00084-4).
- (32) Öge, T.; Zentel, R. Manipulation of the Ferroelectricity in LC Polymers via Photomechanical Isomerization of Azobenzene Moieties. *Macromol. Chem. Phys.* **1996**, *197* (6), 1805–1813. <https://doi.org/10.1002/macp.1996.021970602>.
- (33) Cviklinski, J.; Tajbakhsh, A. R.; Terentjev, E. M. UV Isomerisation in Nematic Elastomers as a Route to Photo-Mechanical Transducer. *Eur. Phys. J. E* **2002**, *9* (1), 427–434. <https://doi.org/10.1140/epje/i2002-10095-y>.
- (34) Liu, X.; Cai, M.; Liang, Y.; Zhou, F.; Liu, W. Photo-Regulated Stick-Slip Switch of Water Droplet Mobility. *Soft Matter* **2011**, *7* (7), 3331–3336. <https://doi.org/10.1039/C0SM01144D>.
- (35) Guo, S.; Sugawara-Narutaki, A.; Okubo, T.; Shimojima, A. Synthesis of Ordered Photoresponsive Azobenzene–Siloxane Hybrids by Self-Assembly. *J. Mater. Chem. C* **2013**, *1* (42), 6989–6995. <https://doi.org/10.1039/C3TC30587B>.
- (36) Wen, H.; Zhang, W.; Weng, Y.; Hu, Z. Photomechanical Bending of Linear Azobenzene Polymer. *RSC Adv.* **2014**, *4* (23), 11776–11781. <https://doi.org/10.1039/C3RA48035F>.
- (37) Garcia-Amorós, J.; Martínez, M.; Finkelmann, H.; Velasco, D. Photoactuation and Thermal Isomerisation Mechanism of Cyanoazobenzene-Based Liquid Crystal Elastomers. *Phys. Chem. Chem. Phys.* **2014**, *16* (18), 8448–8454. <https://doi.org/10.1039/C4CP00446A>.
- (38) Guo, S.; Chaikittisilp, W.; Okubo, T.; Shimojima, A. Azobenzene–Siloxane Hybrids with Lamellar Structures from Bridge-Type Alkoxy-silyl Precursors. *RSC Adv.* **2014**, *4* (48), 25319–25325. <https://doi.org/10.1039/C4RA01709A>.
- (39) Finkelmann, H.; Nishikawa, E.; Pereira, G. G.; Warner, M. A New Opto-Mechanical Effect in Solids. *Phys. Rev. Lett.* **2001**, *87* (1), 015501. <https://doi.org/10.1103/PhysRevLett.87.015501>.
- (40) Garcia-Amorós, J.; Finkelmann, H.; Velasco, D. Influence of the Photo-Active Azo Cross-Linker Spacer on the Opto-Mechanics of Polysiloxane Elastomer Actuators. *J. Mater. Chem.* **2011**, *21* (4), 1094–1101. <https://doi.org/10.1039/C0JM02502J>.
- (41) Camacho-Lopez, M.; Finkelmann, H.; Palffy-Muhoray, P.; Shelley, M. Fast Liquid-Crystal Elastomer Swims into the Dark. *Nat. Mater.* **2004**, *3* (5), 307–310. <https://doi.org/10.1038/nmat1118>.
- (42) Dvornic, P. R.; Lenz, R. W. Exactly Alternating Silarylene–Siloxane Polymers: 6. Thermal Stability and Degradation Behaviour. *Polymer* **1983**, *24* (6), 763–768. [https://doi.org/10.1016/0032-3861\(83\)90016-2](https://doi.org/10.1016/0032-3861(83)90016-2).
- (43) Dvornic, P. R.; Perpall, H. J.; Uden, P. C.; Lenz, R. W. Exactly Alternating Silarylene–Siloxane Polymers. VII. Thermal Stability and Degradation Behavior of p-Silphenylene–Siloxane Polymers with Methyl, Vinyl, Hydrido, and/or Fluoroalkyl Side Groups. *J. Polym. Sci. Part Polym. Chem.* **1989**, *27* (10), 3503–3514. <https://doi.org/10.1002/pola.1989.080271027>.
- (44) Chen, X.; Cui, Y.; Yin, G.; Liao, L. Thermooxidative Degradation Behavior of Poly(Silphenylene-Siloxane)s. *J. Appl. Polym. Sci.* **2010**, *117* (2), 926–933. <https://doi.org/10.1002/app.31429>.
- (45) *Inorganic Polymeric Nanocomposites and Membranes*; Becker, O., Ed.; Advances in polymer science; Springer: Berlin ; New York, 2005.
- (46) Dvornic, P. R.; Lenz, R. W. Exactly Alternating Silarylene-Siloxane Polymers. 9. Relationships between Polymer Structure and Glass Transition Temperature. *Macromolecules* **1992**, *25* (14), 3769–3778. <https://doi.org/10.1021/ma00040a024>.
- (47) Schulz-Senft, M.; Bank, D.; Strueben, J.; Presa-Soto, D.; Sönnichsen, F. D.; Renth, F.; Temps, F.; Staubitz, A. Efficient Photoisomerisation and Size Switching in a Strictly Alternating Main-Chain Azobenzene-Trisiloxane Polymer with 45wt% Chromophore Load Rationalised by Ultrafast Dynamics. *Be Submitt. Chem Sci* **2019**.
- (48) Dvornic, P. R.; Lenz, R. W. Exactly Alternating Silarylene–Siloxane Polymers. II. The Condensation Polymerization of Arylenedisilanol and Bisureidosilanes. *J. Polym. Sci. Polym. Chem. Ed.* **1982**, *20* (4), 951–966. <https://doi.org/10.1002/pol.1982.170200405>.
- (49) Yager, K. G.; Tanchak, O. M.; Godbout, C.; Fritzsche, H.; Barrett, C. J. Photomechanical Effects in Azo-Polymers Studied by Neutron Reflectometry. *Macromolecules* **2006**, *39* (26), 9311–9319. <https://doi.org/10.1021/ma0617320>.
- (50) Yager, K. G.; Barrett, C. J. Photomechanical Surface Patterning in Azo-Polymer Materials. *Macromolecules* **2006**, *39* (26), 9320–9326. <https://doi.org/10.1021/ma061733s>.

Supporting Information

for

Reversible Volume Switching of a Cross-Linkable Poly(silazobenzyl-siloxane).

Mathias Schulz-Senft,^{†1,2,3} Sindu Shree,^{†4} Jan Strueben,¹ Xin Jin,⁴ David Presa Soto,¹ Rainer Adelung,^{*4} Anne Staubitz^{*1,2,3}

¹*Otto-Diels-Institute for Organic Chemistry, University of Kiel, Otto-Hahn-Platz 4, 24098 Kiel (Germany),*

²*Institute for Organic and Analytical Chemistry, University of Bremen, Leobener Str. 7 NW2 C, 28359*

Bremen (Germany), ³*MAPEX Center for Materials and Processes, University of Bremen Bibliothekstraße*

1, 28359 Bremen (Germany), ⁴*Institute for Materials Science, University of Kiel, Kaiserstr. 2, 24143 Kiel*

(Germany).

staubitz@uni-bremen.de

ra@tf.uni-kiel.de

Abbreviations

The use of abbreviations follows the conventions from the ACS Style guide.¹ In addition, the following abbreviations are used.

Abbreviation	Long form
at (NMR)	Apparent triplet
ATR	Attenuated total reflection (IR)
CI	Chemical ionization
COSY	Correlation spectroscopy
DCM	Dichloromethane
dd (NMR)	Doublet of doublets
DMSO	Dimethyl sulfoxide
EI	Electron ionization
ESI	Electrospray ionization
FT	Fourier transform
HMBC	Heteronuclear multiple bond correlation
HPLC	High performance liquid chromatography
HSQC	Heteronuclear single quantum coherence
NOESY	Nuclear Overhauser enhancement spectroscopy
PSS	Photostationary state
THF	Tetrahydrofuran
TOF	Time-of-flight mass detector
v/v	Volume concentration (volume/volume)

Analytical Equipment and Equipment for Syntheses

NMR spectra were either recorded on a Bruker Avance Neo 500 (^1H NMR: 500 MHz) or on a Bruker Avance II HD 600 (^1H NMR: 600 MHz) FT-NMR spectrometer at 300 K. ^1H NMR and $^{13}\text{C}\{^1\text{H}\}$ NMR spectra were referenced against the solvent residual proton signals (^1H) or the solvent itself (^{13}C).

The exact assignment of the peaks was performed by two-dimensional NMR spectroscopy such as ^1H COSY, ^1H NOESY, $^1\text{H}/^{13}\text{C}$ HSQC or $^1\text{H}/^{13}\text{C}$ HMBC if possible.

Mass spectrometric measurements were performed in the positive ion collection mode using a JEOL-Accu TOF 4GGCV EI mass spectrometer, a Bruker Daltonics Apex IV FT Ion Cyclotron Resonance ESI mass spectrometer or a VG Analytical Autospec apparatus for CI. Electron ionization (EI) was performed using an ionization potential of 70 eV.

IR spectra were measured using a Perkin Elmer Paragon 1000 FT-IR spectrometer equipped with an A531-G Golden-Gate-ATR-unit.

UV-vis spectra were recorded at 25 °C using a Perkin Elmer Lambda 900 spectrometer for the film that was spin-coated on quartz glass and a Perkin Elmer Lambda 14 UV spectrometer in solution. Quartz cuvettes with a light path length of 10 mm from Hellma Analytics were used. Melting points were measured on an electrothermal IA6304 capillary melting point apparatus and are uncorrected.

Gel permeation chromatography was performed on a Viscotek GPC max VE2001 equipped with a Viscotek VE3580 RI detector and a column set of LT5000 and LT4000 in THF (VWR, HPLC-grade) with a flow rate of 1 mL/min. Conventional calibration and analysis was done with OmniSEC 4.6.2 software using polystyrene standards.

Topographical AFM imaging were conducted under the WITec RA 300 microscope with an Asylum cantilever with 2 Nm^{-1} , 70 kHz. The same setup was also used for the determination of average surface roughness.

The polymer film was prepared by spin coating from a solution in THF at 2000 rpm. Quartz glass was used as substrate. The film thickness was measured under Ambios Xp2 profilometer. The irradiation experiments were carried out using LED light sources assembled by Sahlmann Photochemical Solutions with an optical power of 1000 mW (365 nm) and 900 mW (450 nm) in solution. Irradiation of the film for AFM and UV-visible measurements was achieved using

the fiber-coupled (400 μm in diameter) LEDs M365FP1 (365 nm, min. output: 9.8 mW, typical output: 15.5 mW) and M455F1 (455 nm, min. output: 9.5 mW, typical output: 11.0 mW) from Thorlabs with an angle of 30°.

Reactions that required inert workup were conducted in a labmaster 130 glove box by MBraun, flushed with nitrogen.

Microwave assisted syntheses were performed on a Biotage Initiator+ SP Wave peptide synthesizer in the organic synthesis mode. A fixed hold time was turned off.

The cooling of inert syntheses was achieved by using a cooling block connected to a Julabo FP88 cryostate inside the glove box.

Reagents

If not noted otherwise, all reagents were used as received. Hydrochloric acid solutions were prepared by diluting the concentrated acid.

Reagent	Supplier	Purity or concentration	Notes
[Pd(PPh₃)₄]	Aldrich	99%	
4-Iodoaniline	Acros	98%	
Copper (I) bromide	Sigma-Aldrich	98%	
Dichlorodimethylsilane	Acros	99%	Distilled from CaH ₂ and degassed before use
Dichloromethylvinylsilane	Aldrich	97%	Distilled from CaH ₂ and degassed before use
Hexamethyldistannane	Acros	99%	
Hydrochloric acid	Grüssing	37.5%	
Magnesium sulfate	Grüssing		
Methyl lithium	Acros	3% in MeTHF / Cumol	Exact concentration was determined by titration against menthol.
Monopotassium phosphate	Merck	Extra pure	
Phenyl isocyanate	Alfa Aesar	>98%	Degassed before use
Pyridine	Grüssing	99.5%	
Pyrrolidine	Alfa Aesar	99%	Degassed before use
Sodium hydroxide	Grüssing	99%	

Solvents

All solvents that were purchased in technical grade were purified by distillation prior to use. Solvents of purities higher than 99% were not purified further. Some solvents were degassed by three freeze-pump-thaw cycles, then the flask was again filled with nitrogen and the solvent stored over molecular sieves with the pore size 3 Å.

The following solvents were dried in a solvent purification system PS-MD-5 by Innovative Technology: dichloromethane, tetrahydrofuran.

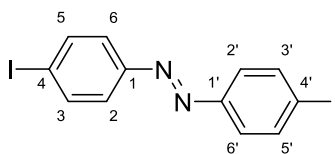
Solvent	Supplier	Purity	Drying procedure	Degassed
Acetonitrile	Sigma-Aldrich	>99.9%, HPLC grade	none	No
Benzene- <i>d</i> ₆	Deutero	99.5% D	Distilled from CaH ₂ , stored over molecular sieves 3 Å	yes
Chlorobenzene	Acros	99.9%, HPLC grade	Distilled from CaH ₂ , stored over molecular sieves 3 Å	yes
Chloroform	VWR	Techn. grade	none	No
Chloroform- <i>d</i>	Euriso-top	99.8% D	none	No
Dichloromethane	VWR	HPLC grade	PS-MD-5	Yes
Dichloromethane	BCD	Techn. grade	none	No
Dichloromethane- <i>d</i> ₂	Deutero	99.6% D	none	No
Diethyl ether	Alfa-Aesar	Spectrophotometric grade, >99%, inhibitor free	Molecular sieves 3 Å	Yes
Diethyl ether	BCD	Techn. grade	none	No
Ethanol	CMP Walther	Techn. grade, denaturated with benzine	none	No
<i>n</i> -Hexane	CMP Walther	Techn. grade	none	No
<i>n</i> -Hexane	CMP Walther	Techn. grade	Distilled from CaH ₂ , stored over molecular sieve 3 Å	Yes
Methanol	Acros	99.8%, anhydrous, stored over molecular sieves 3 Å		No
<i>n</i> -Pentane	CMP Walther	Techn. grade	none	No
Tetrahydrofuran	VWR	HPLC grade	PS-MD-5	Yes
Toluene	Acros	99.85%, Extra dry, stored over molecular sieves	none	Yes

References

- (1) *The ACS Style Guide: Effective Communication of Scientific Information*, 3rd ed.; Coghill, A. M., Garson, L. R., Eds.; American Chemical Society: Washington, DC, 2006.
- (2) Strueben, J.; Gates, P. J.; Staubitz, A. Tin-Functionalized Azobenzenes as Nucleophiles in Stille Cross-Coupling Reactions. *J. Org. Chem.* **2014**, *79* (4), 1719–1728. <https://doi.org/10.1021/jo402598u>.
- (3) Hughes, G. M. K.; Saunders, B. C. Studies in Peroxidase Action. Part IX. Reactions Involving the Rupture of the C–F, C–Br, and C–I Links in Aromatic Amines. *J. Chem. Soc. Resumed* **1954**, *0* (0), 4630–4634. <https://doi.org/10.1039/JR9540004630>.
- (4) Strüben, J.; Hoffmann, J.; Presa-Soto, D.; Näther, C.; Staubitz, A. Crystal Structures of 3,3'-Bis-(Hy-droxy-dimethylsilyl)Azo-benzene and 4,4'-Bis-(Hy-droxy-dimethyl-silane)Azo-benzene. *Acta Crystallogr. Sect. E Crystallogr. Commun.* **2016**, *72* (11), 1590–1594. <https://doi.org/10.1107/S2056989016016297>.
- (5) Passarelli, V.; Benetollo, F.; Zanella, P.; Carta, G.; Rossetto, G. Synthesis and Characterisation of Novel Zirconium(IV) Derivatives Containing the Bis-Amido Ligand SiMe₂(NRR')₂. *Dalton Trans.* **2003**, No. 7, 1411–1418. <https://doi.org/10.1039/B212705A>.
- (6) Dvornic, P. R.; Lenz, R. W. Exactly Alternating Silarylene–Siloxane Polymers. I. The Synthesis and Stability of Bis(1,1-tetramethylene-3-phenylureido)Dimethylsilane. *J. Appl. Polym. Sci.* **1980**, *25* (4), 641–652. <https://doi.org/10.1002/app.1980.070250411>.
- (7) Hedaya, E.; Kawakami, J. H.; Kopf, P. W.; Kwiatkowski, G. T.; McNeil, D. W.; Owen, D. A.; Peters, E. N.; Tulis, R. W. D₂-meta-carborane-siloxanes. IV. Synthesis of Linear, High Molecular Weight Polymers. *J. Polym. Sci. Polym. Chem. Ed.* **1977**, *15* (9), 2229–2238. <https://doi.org/10.1002/pol.1977.170150914>.

Synthetic Procedures

4,4'-Bis(iodo)azobenzene



CuBr (7.24 g, 45.7 mmol) was dissolved in pyridine (90 mL), and stirred for 30 min, before the precipitate was removed by filtration. The filtrate was diluted with pyridine (20 mL). 4-Iodoaniline (14.3 g, 65.3 mmol) was added in one portion and the mixture was stirred for 20 h at 24 °C while bubbling air through the solution via a syringe (0.2 bar, 250 L/h, diameter: 1 mm). Hydrochloric acid (2 N, 200 mL) was added to the solution and the aqueous phase was extracted with diethyl ether (1 x 300 mL) and dichloromethane (2 x 200 mL). The combined organic phases were washed with hydrochloric acid (2 N, 2 x 200 mL) and the solvents were removed in vacuo. The crude solid product was purified by washing it with boiling ethanol (300 mL). After drying the product in vacuo, an orange solid was obtained without further purification (9.24 g, 21.3 mmol, 65%, Lit.:² 61%).

Mp: 237 °C (Lit.:² 210°C, Lit.:³ 237-238 °C).

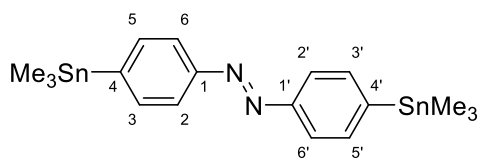
¹H NMR (500 MHz, CDCl₃): δ = 7.87 (d, ³J = 8.7 Hz, 4H, H-3,3',5,5'), 7.64 (d, ³J = 8.7 Hz, 4H, H-2,2',6,6') ppm.

¹³C{¹H} NMR (126 MHz, CDCl₃): δ = 151.9 (C-1,1'), 138.6 (C-3,3',5,5'), 124.7 (C-2,2',6,6'), 98.3 (C-4,4') ppm.

IR (ATR): $\tilde{\nu}$ = 3079 (w), 1575 (m), 1561 (m), 1470 (m), 1393 (s), 1297 (s), 1280 (s), 1156 (m), 1097 (s), 1051 (s), 1002 (s), 833 (vs), 811 (vs), 714 (vs), 539 (vs), 525 (vs) cm⁻¹.

HRMS (EI-TOF) *m/z* (%): [M]⁺ calcd. for [C₁₂H₈N₂I₂]⁺ 433.8777, found 433.8767 (60), 230.94 (100) [M-C₆H₄I]⁺, 202.93 (100) [M-C₆H₄IN₂]⁺.

4,4'-Bis(trimethylstannyl)azobenzene



This compound has been synthesized before,² the procedure was optimized as follows:

Under a nitrogen atmosphere, 4,4''-bis(iodo-)azobenzene (1.30 g, 3.00 mmol), hexamethyldistannane (2.29 g, 7.00 mmol) and [Pd(PPh₃)₄] (139 mg, 120 μmol, 4 mol%) were dissolved in toluene (18 mL) and THF (2 mL) in a microwave reaction vessel. The reaction mixture was heated for 30 min to 170 °C. Five such reaction batches were combined for the work-up. Then, the solvent was removed under reduced pressure followed by purification by column chromatography (eluent: *n*-pentane, R_f = 0.65). The product was obtained as orange solid (7.23 g, 14.3 mmol, 95%, Lit.:² 81%).

Mp: 54 °C (Lit.:² 54 °C).

¹H NMR (500 MHz, CDCl₃): δ = 7.87 (d, ³J = 8.2 Hz, 4 H, H-3, 3', 5, 5'), 7.65 (d, ³J = 8.2 Hz, 4 H, H-2, 2', 6, 6'), 0.34 (s, 18 H, Sn(CH₃)₃) ppm.

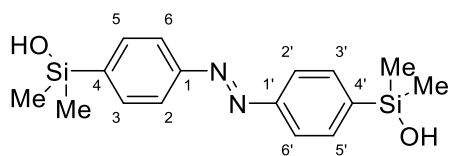
¹³C{¹H} NMR (126 MHz, CDCl₃): δ = 152.9 (C-4, 4'), 147.2 (C-1, 1'), 136.6 (C-2, 2', 6, 6'), 122.1 (C-3, 3', 5, 5'), -9.3 (Sn(CH₃)₃) ppm.

¹¹⁹Sn{¹H} NMR (187 MHz, CDCl₃): δ = -25.03 ppm.

IR (ATR): $\tilde{\nu}$ = 3067 (w), 3024 (w), 2987 (w), 2917 (w), 1925 (w), 1437 (m), 1383 (m), 1306 (m), 1067 (m), 1011 (m), 831 (s), 761 (s), 583 (s), 508 (s) cm⁻¹.

HRMS (ESI-FTMS) *m/z*: [M+H]⁺ calcd. for [C₁₈H₂₆N₂Sn₂+H]⁺ 511.0213, found 511.0227.

4,4'-Bis(hydroxydimethylsilane)azobenzene



This compound has been synthesized already,⁴ the procedure was optimized as follows: Under argon atmosphere, 4,4'-bis(trimethylstannyl-)azobenzene (3.00 g, 5.91 mmol) was dissolved in dry THF (70 mL). Methyl lithium (20 mL) was added at -78 °C. The orange solution turned dark and was stirred 15 min. Then, dichlorodimethylsilane (24 mL, 25.7 g, 199 mmol) was added. The reaction was allowed to warm to 25 °C by removing the cooling bath. The solvent and the excess of dichlorodi-methylsilane were removed *in vacuo*. The residual orange solid was dissolved in THF (40 mL) and added (rate: 1 mL/min) to a solution of sodium methoxide in methanol (13.5 mL of 4.5 N solution, diluted with 20 mL MeOH). Inert conditions were maintained until this point. The mixture was opened to air and a solution of sodium hydroxide in methanol and water (24 mL, 5 mol/L, MeOH:H₂O 10:1) was added. The resulting mixture was stirred 15 minutes, before a solution of sodium hydroxide in water (24 mL, 5 mol/L) was added. The reaction mixture was stirred 5 h, for all these steps, the temperature was held at 25 °C. This mixture was poured into a vigorously stirred solution of mono potassium phosphate in water (150 mL, 1 mol/L). The resulting solution was extracted with chloroform (4 x 50 mL). The combined organic phases were dried over MgSO₄ and the solvent was removed *in vacuo*. The crude product was purified by solvent diffusion crystallization: A saturated solution in chloroform was overlaid with *n*-hexane and cooled to -30 °C for 48 h. After three crystallization cycles, the product was obtained as orange solid (845 mg, 2.56 mmol, 43%, Lit.:⁴ 35%).

Mp.: T = 141 °C, Lit.:⁴ 141 °C.

¹H NMR (500 MHz, CDCl₃): δ = 7.91 (d, ³J = 8.3 Hz, 4 H, H-3,3',5,5'), 7.75 (d, ³J = 8.3 Hz, 4 H, H-2,2',6,6'), 1.99 (s, 1H, OH), 0.46 (s, 12 H, Si(CH₃)₂) ppm.

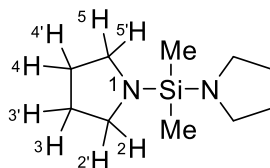
¹³C{¹H} NMR (126 MHz, CDCl₃): δ = 153.6 (C-1,1'), 143.0 (C-4,4'), 134.0 (C-3,3'), 122.3 (C-2,2'), 0.2 (Si(CH₃)₂) ppm.

²⁹Si{¹H} NMR (99 MHz, CDCl₃): δ = 7.77 ppm.

IR (ATR): $\tilde{\nu}$ = 3141 (m), 2956 (w), 1385 (m), 1251 (m), 1106 (w), 859 (s), 833 (s), 815 (s), 776 (s), 667 (s), 553 (s), 529 (m), 491 (m) cm⁻¹.

HRMS (EI-TOF) m/z (%): $[M]^+$ calcd for $[C_{16}H_{22}N_2O_2Si_2]^+$ 330.12198, found 330.12163 (35), 151.06 (100) $[M-HOSi(CH_3)_2C_6H_4N_2]^+$.

Bis(pyrrolidinyl)dimethylsilane



This reaction was performed entirely under nitrogen atmosphere. To a solution of dichlorodimethylsilane (80.0 mL, 85.6 g, 663 mmol) in *n*-hexane (150 mL), pyrrolidine (230 mL, 196 g, 2.76 mol) was added dropwise over the course of 1 h at 0 °C. After completion of the addition, the ice bath was removed and the reaction was stirred for 15 h. A precipitate of the amino hydrochloride, which had formed, was removed by filtration under inert conditions. The liquid was placed in a J. Young's flask and the remaining solvent was removed *in vacuo*. A colorless liquid (116 g, 585 mmol, 88%, Lit.:⁵ 95%) was obtained.

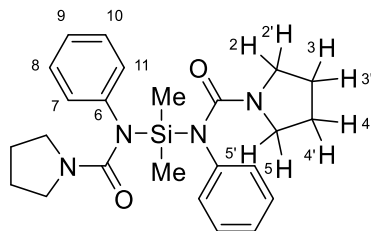
¹H NMR (500 MHz, CDCl₃): δ = 2.93 – 2.88 (m, 8 H, H-2,2',5,5'), 1.67 – 1.62 (m, 8 H, H-3,3',4,4'), 0.04 (s, 6 H, Si-CH₃) ppm.

¹³C{¹H} NMR (126 MHz, CDCl₃): δ = 46.8 (C-2,5), 26.9 (C-3,4), -3.3 (Si-CH₃) ppm

²⁹Si{¹H} NMR (187 MHz, CDCl₃): δ = -8.11 ppm.

HRMS (ESI-FTMS): m/z : $[M+H]^+$ calcd for $[C_{10}H_{23}N_2^{28}Si]^+$ 199.16250; found 199.16255.

Bis(N-phenyl-N-pyrrolidinecarbonylamino)dimethyl silane



The reaction was performed entirely under inert conditions. *Bis*(pyrrolidinyl)dimethyl silane (40.0 g, 201 mmol) was dissolved in dry diethyl ether (250 mL) and cooled in an ice bath to 0 °C. Then phenyl isocyanate (45.0 mL, 49.3 g, 410 mmol) was added dropwise at 0 °C over the course of 3 h and the reaction mixture was allowed to warm to 25 °C over the course of 15 h. The white precipitate of bis(*N*-phenyl-*N'*-pyrrolidinyl)dimethylsilane was collected by filtration under inert conditions. The product was washed with dry diethyl ether (20 mL) and dried at 0.05 mbar for 12 h to receive the product as colourless solid (79.6 g, 182 mmol, 91%, Lit.:⁶ 85%).^a

Mp.: T = 72 °C.

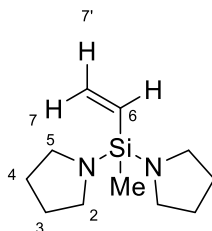
¹H NMR (500 MHz, CDCl₃): δ = 7.20 – 7.15 (m, H-8,10), 7.07 (t, ³J = 7.5 Hz, 2 H, H-9,9'), 6.95 – 6.91 (m, 4 H, H-7,11), 2.88 (m, 8 H, H-2,5), 1.58 (m, 8 H, H-3,4), 0.37 (s, 6 H, Si-CH₃) ppm.

¹³C{¹H} NMR (126 MHz, CDCl₃): δ = 159.7 (C=O), 143.0 (C-6), 128.9 (C-7,11), 128.5 (C-8,10), 125.1 (C-9), 47.7 (C-2,5), 25.4 (C-3,4), -1.5 (Si-CH₃) ppm.

²⁹Si{¹H} NMR (99 MHz, CDCl₃): δ = -3.57 ppm.

^a Due to the very high sensitivity of this compound, no IR or MS data could be obtained.

Bis(pyrrolidinyl)methylvinylsilane



This compound has been synthesized already,⁷ the procedure was altered as follows:

The reaction was performed entirely under inert conditions. A solution of pyrrolidine (11.3 mL, 9.60 g, 135 mmol) and *n*-hexane (60 mL) was cooled to -10 °C. To the cooled solution, dichloromethylvinylsilane (3.92 mL, 4.23 g, 30.0 mmol) was added with a rate of 0.1 mL/min. After complete addition, the mixture was heated to 25 °C and stirred for 3 h at 25 °C. The formed precipitate of pyrrolidine hydrochloride was removed by filtration and washed with *n*-hexane (100 mL). The solvent was removed under reduced pressure from the filtrate and after drying at 0.5 mbar for 10 h, the product was received as colorless liquid (4.24 g, 20.2 mmol, 67%, Lit.:⁷ 87%). The product is unstable under moisture.

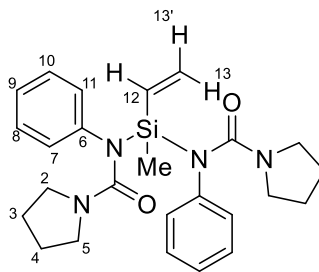
¹H NMR (500 MHz, C₆D₆): δ = 6.29 (dd, ³J_E = 20.4 Hz, ³J_Z = 14.7 Hz, 1H, H-6), 6.03 (dd, ³J_Z = 14.7 Hz, ²J = 4.3 Hz, 1H, H-7'), 5.85 (dd, ³J_E = 20.4 Hz, ²J = 4.3 Hz, 1H, H-7), 3.06 – 2.98 (m, 8H, H-2,5), 1.64 – 1.56 (m, 8H, H-3,4), 0.27 (s, 3H, Si-CH₃) ppm.

¹³C{¹H} NMR (126 MHz, C₆D₆): δ = 137.7(C-6), 132.2 (C-7), 47.1 (C-2,5), 27.2 (C-3,4), -4.1 (Si-CH₃)

²⁹Si{¹H} NMR (99 MHz, C₆D₆): δ = -19.1 ppm.

HRMS (EI-TOF) *m/z* (%): [M]⁺ calcd. for [C₁₁H₂₂N₂²⁸Si]⁺ 210.1534, found 210.15522 (40), 139.09 (100) [M-NH(CH₂)₄]⁺.

Bis(N-phenyl-N'-pyrrolidinecarbonylamino)methylvinyl silane



This compound has been synthesized previously,⁷ the procedure was optimized as follows:

The reaction was performed entirely under inert conditions. Bis(pyrrolidiny)methyl-vinylsilane (3.37 mL, 3.05 g, 14.5 mmol) was dissolved in diethyl ether (15 mL) and cooled to -10 °C, before phenyl isocyanate (3.59 mL, 3.93 g, 33.0 mmol) was added with a rate of 0.10 mL/min. After complete addition, the cooling bath was removed and the reaction stirred at 25 °C for 15 h. The crude product was recrystallized from diethyl ether (60 mL) at -30 °C, filtered and washed with diethyl ether (30 mL) to obtain the product as white solid (5.47 g, 12.2 mmol, 84%, Lit.: ⁷ 62%) after drying at 0.5 mbar for 20 h.^a

Mp.: T = 46 °C.

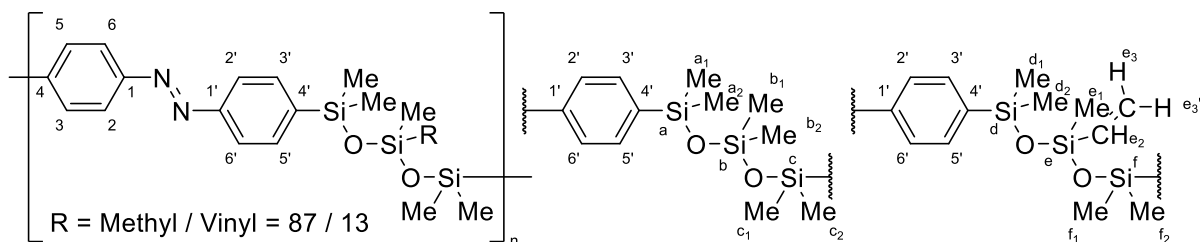
¹H NMR (500 MHz, CDCl₃): δ = 7.15 (t, ³J = 7.8, 4H, H-8,10), 7.06 (t, ³J = 7.8 Hz, 2H, H-9), 6.97 (t, ³J = 7.8 Hz, 4H, H-7,11), 6.35 (dd, ³J = 20.5 Hz, ³J = 14.8 Hz, 1H, H-12), 5.82 (dd, ³J = 14.8 Hz, ²J = 3.1 Hz, 1H, H-13'), 5.64 (dd, ³J = 20.5 Hz, ²J = 3.1 Hz, 1H, H-13), 2.87 (m, 8 H, H-2,5), 1.55 (m, 8 H, H-3,4), 0.37 (s, 3 H, Si-CH₃) ppm.

¹³C{¹H} NMR (126 MHz, CDCl₃): δ = 159.6 (C=O), 142.6 (C-6), 137.1 (C-12), 131.3 (C-13,13'), 129.0 (C-7,11), 128.4 (C-8,10), 125.1 (C-9), 47.6 (C-2,5), 25.1 (C-3,4), -2.0 (Si-CH₃) ppm.

²⁹Si{¹H} NMR (99 MHz, CDCl₃): δ = -18.31 ppm.

^a Due to the very high sensitivity of this compound, no IR or MS data could be obtained.

Poly(4,4'-azobenzene-alt-(hexamethyl-trisiloxane)-stat-(1,1,3,5,5-pentamethyl-3-vinyl-trisiloxane)) (3)



This reaction was performed in a nitrogen filled glove box. 4,4'-Bis(hydroxydimethylsilane)-azobenzene (317 mg, 960 μmol), was dissolved in chlorobenzene (2 mL). A solution of bis(*N*-phenyl-*N*-pyrrolidinecarbonylamino)dimethyl silane (**2a**) (398 mg, 912 μmol) and bis(*N*-phenyl-*N'*-pyrrolidinecarbonylamino)methylvinyl silane (**2b**) (21.5 mg, 48.0 μmol) in chlorobenzene (8 mL) was added with a rate of 15 $\mu\text{L}/\text{min}$ at $-45\text{ }^\circ\text{C}$. The solution was stirred for 8 d at $25\text{ }^\circ\text{C}$, while the reaction progress was monitored by GPC. After 3 d, another portion of **2b** (22.4 mg, 50.0 μmol) was added and a portion of **1** (8.3 mg, 25 μmol) was added after 6 d. Once the measured retention volume remained unchanged, the solvent was evaporated and the polymer was purified by dissolving in THF and precipitation into methanol (10 fold excess) for three times. After drying at 0.05 mbar and $70\text{ }^\circ\text{C}$ for 20 h, the product was obtained as orange solid (369 mg). The ratio of methyl and vinyl substitution at the marked R group was determined to be 87 / 13. The NMR integrals are normalized per repeating unit.

^1H NMR (600 MHz, CDCl_3):^a δ = 7.88 (d, 3J = 8.2 Hz, 4.00H, H-2,6,2',6'), 7.69 (d, 3J = 8.2 Hz, 3.98 H, H-3,5,3',5'), 6.05 – 5.93 (m, 0.28 H, H-e2, H-e3), 5.79 (dd, 3J = 19.3 Hz, 3J = 5.0 Hz, 0.14 H, H-e3'), 0.65 (s, 1.08 H, H-d1,2,f2), 0.39 (s, 9.44 H, H-a1,2,c1,2), 0.32 (s, 0.39 H,H-f1), 0.17 (s, 0.37 H-e1), 0.10 (s, 4.28 H, H-b1,2) ppm.

$^{13}\text{C}\{^1\text{H}\}$ NMR (151 MHz, CDCl_3):^a δ = 153.4 (C-1,1'), 144.5 (C-4,4' if R=vinyl), 143.6 (C-4,4' if R=Me), 141.9 (C-4,4' if R=Me),^b 141.7 (C-4,4' if R=Me),^a 137.0 (C-e2), 135.2,^c 135.1,^c 134.0,^c

^a Since the distribution of vinyl groups throughout the chain is random, partially very low intensities, overlapping signals in ^1H NMR and small chemical shift differences in all spectra made the full assignment of all signals to structural units impossible.

^b The repeating unit corresponding to these signals is probably neighboring one or more repeating units with a vinyl group.

^c The signals at 135.2, 135.1 and 134.0 could not be assigned by 2D experiments. However, they probably correspond to C-3,5,3',5' with a vinyl group in the same or adjacent repeating units.

133.9 (C-3,5,3',5' if R=Me), 133.5 (C-e3), 122.2 (C-2,6,2',6' if R=vinyl) 122.1 (C-2,6,2',6' if R=Me), 1.5 (C-b1,2), 1.4, 1.03, 0.95, 0.91, -0.15, -0.3 (C-e1), -1.0 (C-f1), -2.2 (C-d1,2,f2) ppm.

$^{29}\text{Si}\{^1\text{H}\}$ NMR (99 MHz, CDCl_3): δ = -2.4 (Si-a,c), -3.5 (Si-a,c)^a -7.2 (Si-d,f), -18.9 (Si-b), -33.0 (Si-e) ppm.

IR (ATR): $\tilde{\nu}$ = 3025 (w), 2958 (m), 2900 (w), 1670 (w), 1591 (w), 1407 (w), 1389 (m), 1309 (w), 1257 (s), 1109 (s), 1031 (vs), 1012 (vs), 835 (vs), 781 (vs), 687 (s), 665 (s), 622 (m), 555 (s), 529 (m) cm^{-1} .

GPC (THF, 1 mL/min, conv. calibration (PS), **ambient light**): M_n = 14.4 kDa; M_w = 23.3 kDa; PDI = 1.62.

GPC (THF, 1 mL/min, conv. calibration (PS), **365 nm, 60 min**): M_n = 11.8 kDa; M_w = 19.9 kDa; PDI = 1.69.

^a This repeating unit is probably adjacent to one with a vinyl group.

GPC Measurements

The polymer was dissolved in THF (ca. 1 mg/mL) and GPC spectra were recorded both without and after irradiation with UV light (365 nm, 60 min). Upon switching with UV light, the apparent molecular weight changes from 14.4 kDa to 11.8 kDa in case of M_n and from 23.3 kDa to 19.9 kDa in case of M_w (**Figure SI-1**). This corresponds to a decrease in apparent weight by 18% (M_n) and 15% (M_w), while the PDI remains almost constant, being 1.62 before and 1.69 after UV irradiation.

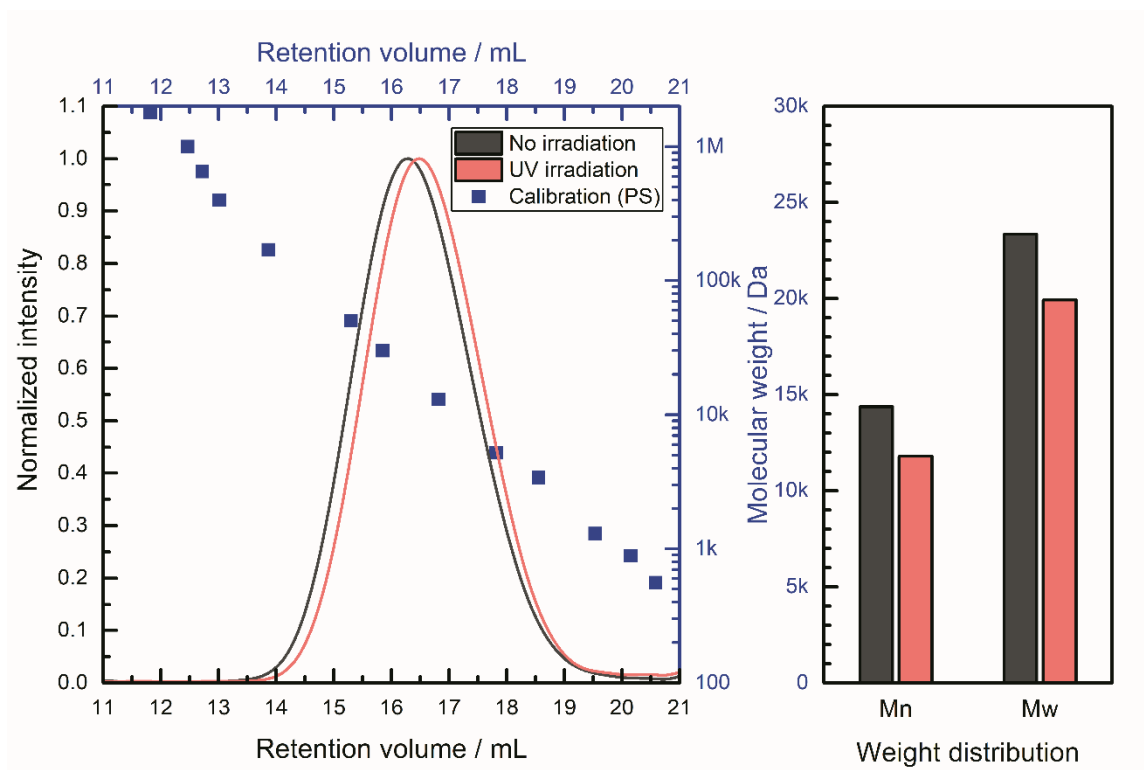


Figure SI-1. Analysis of the switching behavior of polymer **3** dissolved in THF (1 mg/mL). Left: the GPC chromatograms corresponding to the polymer without (grey) and after UV irradiation (red). The intensities were normalized for clarity. Blue squares indicate the retention volumes of the polystyrene standards used for calibration. Right: Comparison of the assigned apparent molecular weights. Shown are number average (M_n) and weight average (M_w) of the polymer without (grey) and after UV irradiation (red).

AFM Measurements

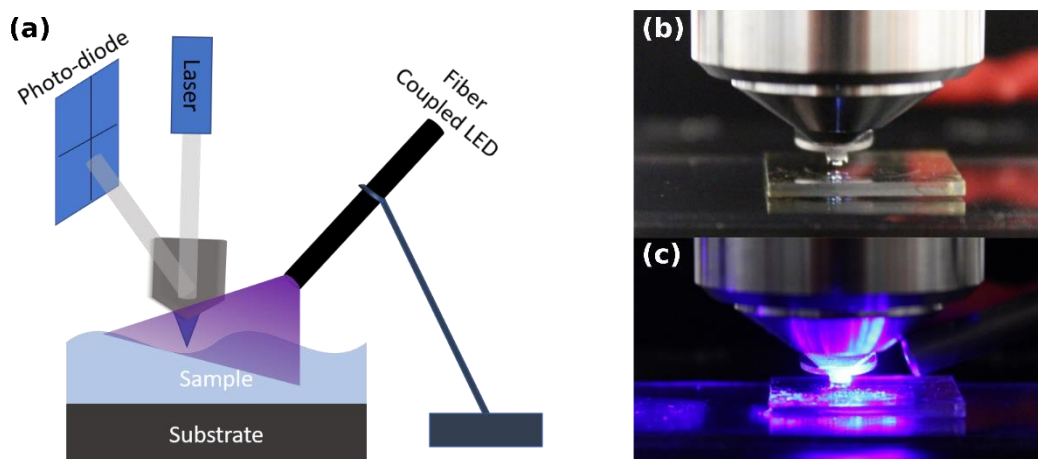


Figure SI-2. (a) Setup of the AFM experiments. The sample film was spin coated on a quartz glass slide. In addition to the conventional setup of the environmental AFM, the sample was illuminated through a fiber coupled LED in an angle of 30°. (b) Photograph of the setup without illumination in ambient light. (c) Photograph of the setup during illumination with UV light.

Height Profile of Spot 2

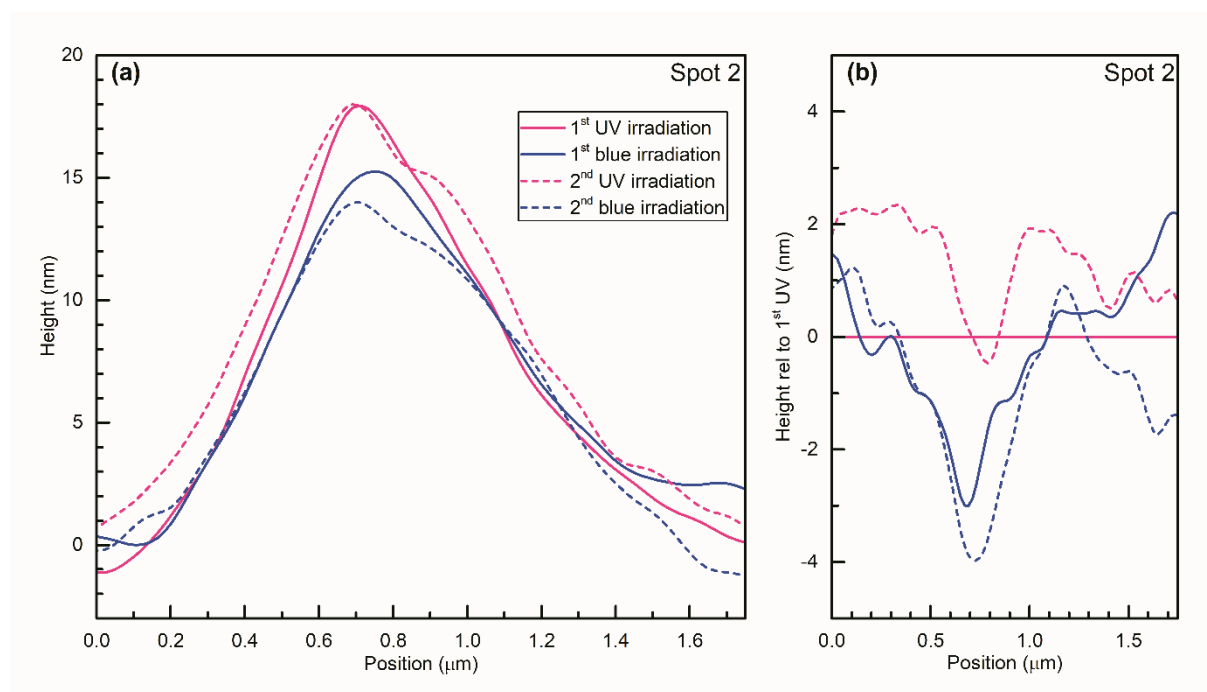


Figure SI-2. AFM analysis of Spot 2. (a) Height profile obtained from the AFM micrographs. (b) Height variations upon irradiation. Plotted are the differences in height relative to the 1st UV irradiation.

H

eight Profile of Spot 3

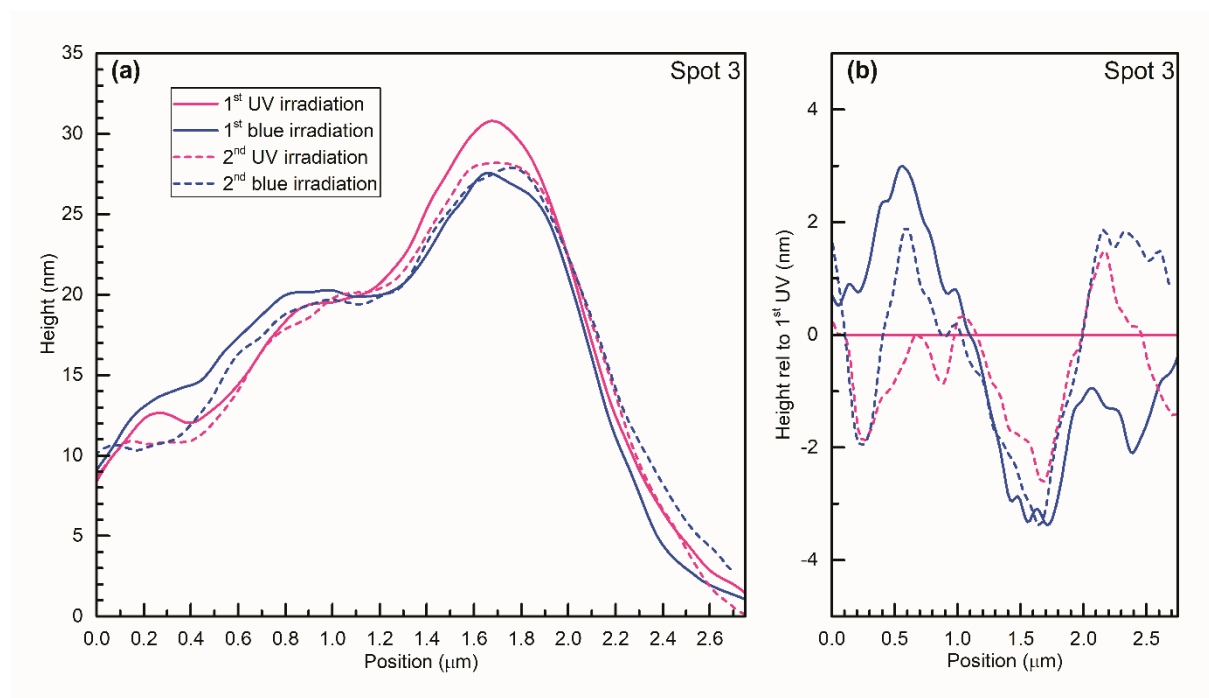


Figure SI-3. AFM analysis of Spot 3. (a) Height profile obtained from the AFM micrographs. (b) Height variations upon irradiation. Plotted are the differences in height relative to the 1st UV irradiation.

Plotted UV-Vis Spectra of the Polymer 3 in THF

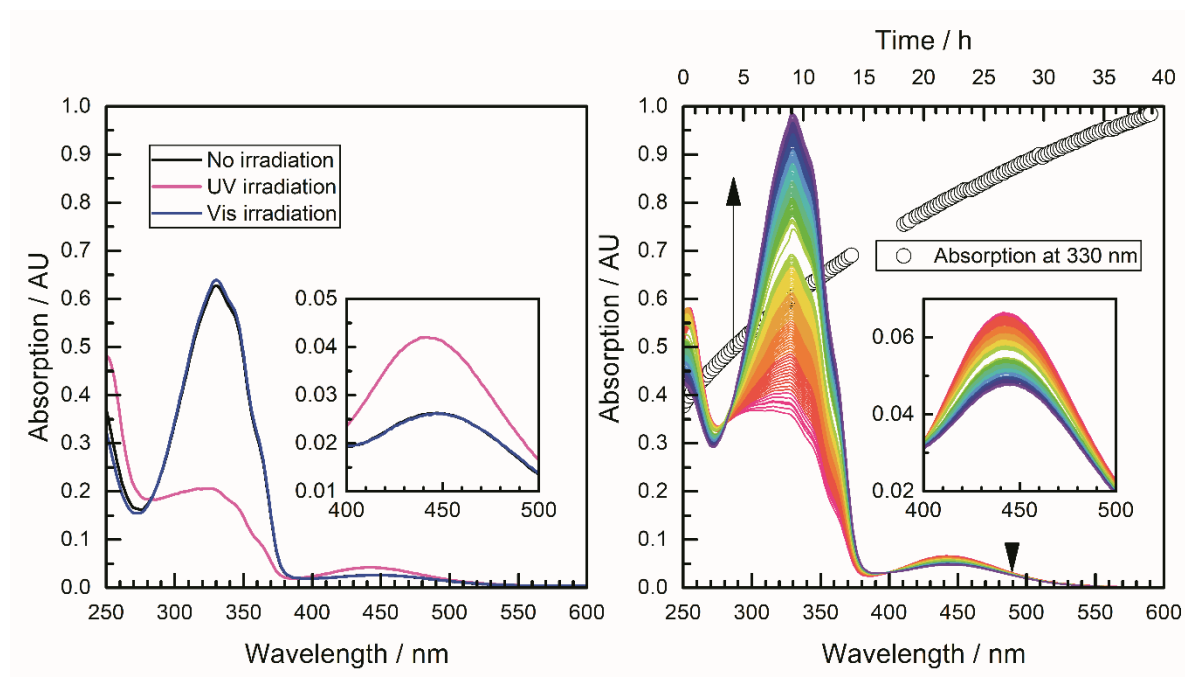
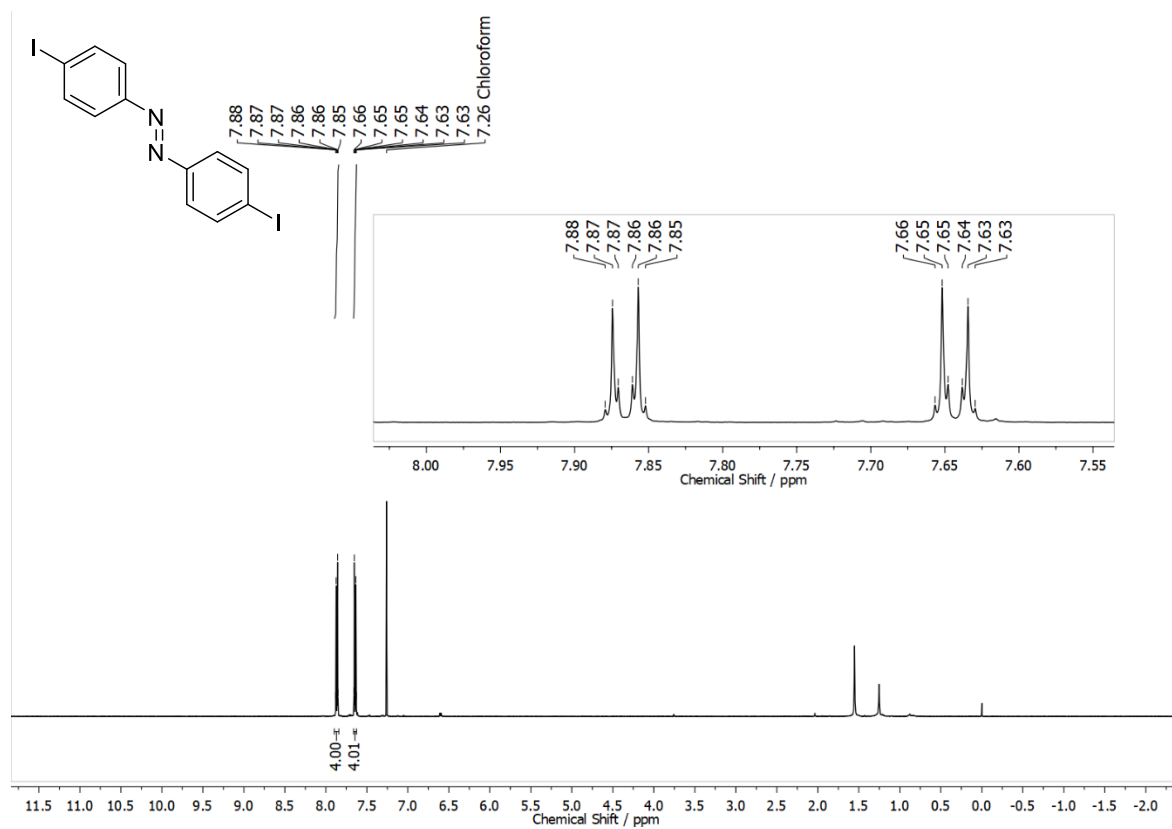
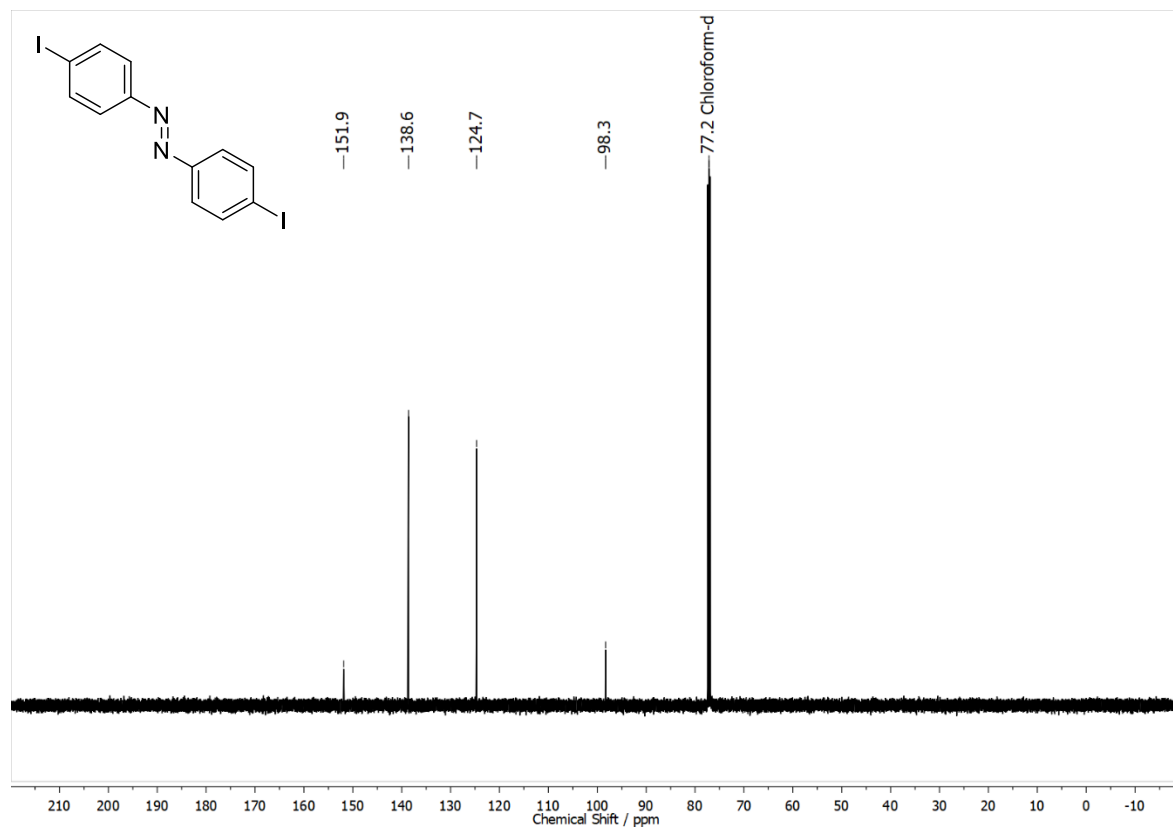


Figure SI-4. UV-vis spectra of the polymer **3** dissolved in THF. Left: comparison of without (black line), after UV- (pink line) and visible irradiation (blue line). The concentration of azobenzene moieties in the solution in acetonitrile was approx. 0.02 mmol/L. Right: Thermal relaxation after irradiation with UV light over the course of 40 h. The spectra were recorded with a delay of 15 min. The development of the absorption at 330 nm is shown as black circles. The concentration of azobenzene moieties in the solution was approx. 0.05 mmol/L. The half-life time was determined by an exponential fit to be 21 h \pm 18 min.

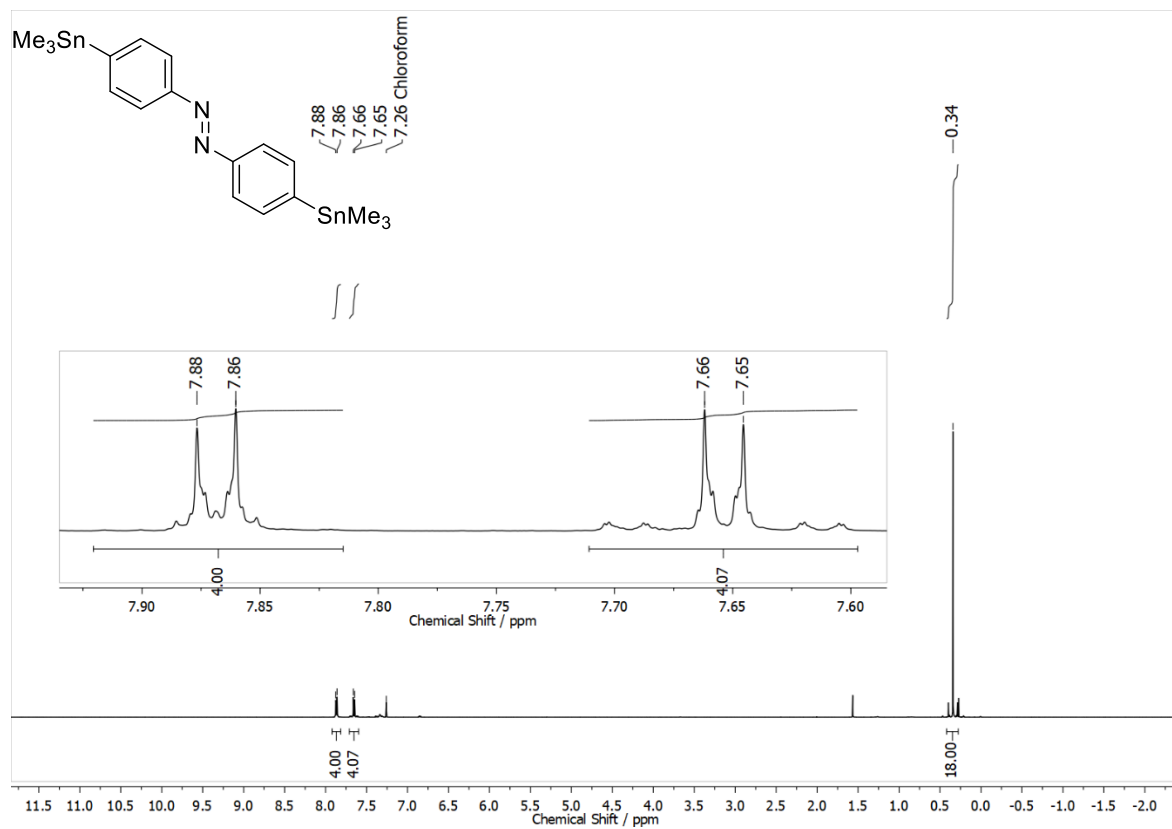
Plotted 1H, 13C{1H} and hetero NMR Spectra for All Compounds

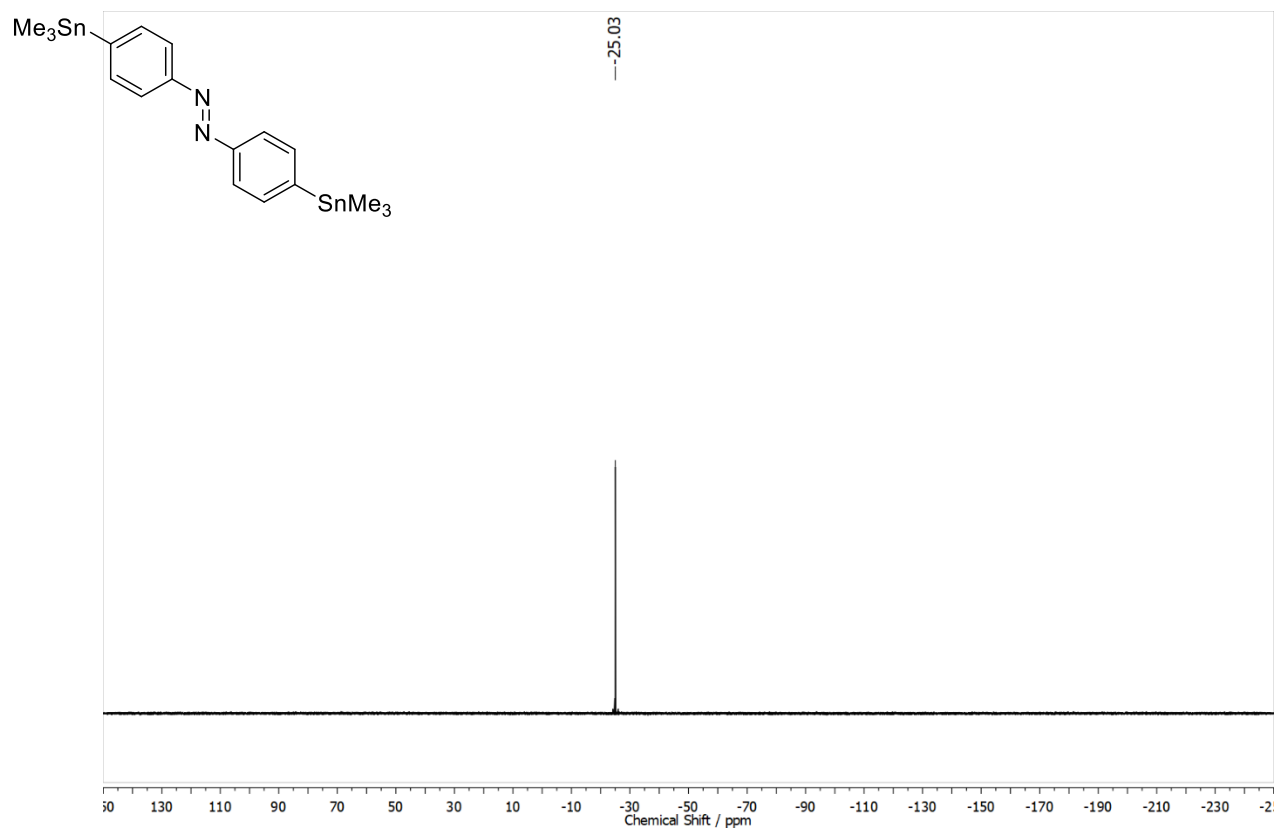
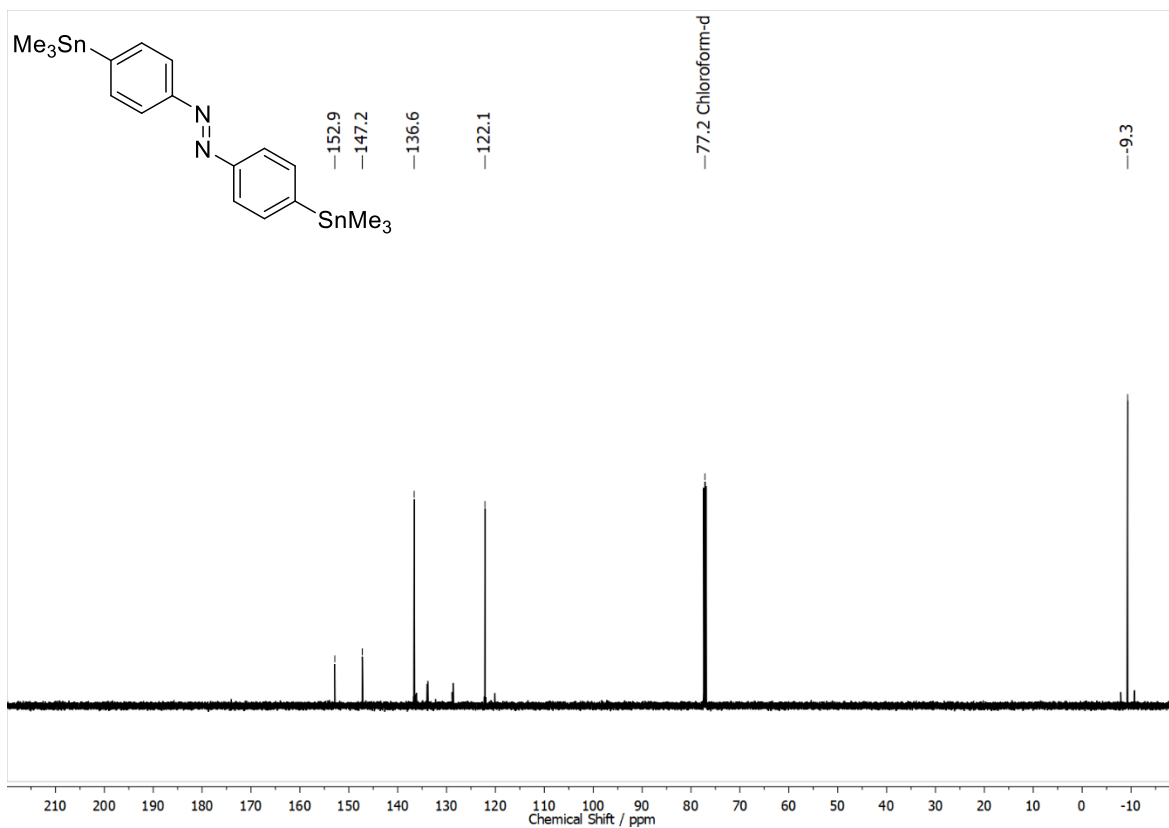
1H and 13C{1H} Spectra of 4,4'-Bis(iodo)azobenzene in Chloroform-d



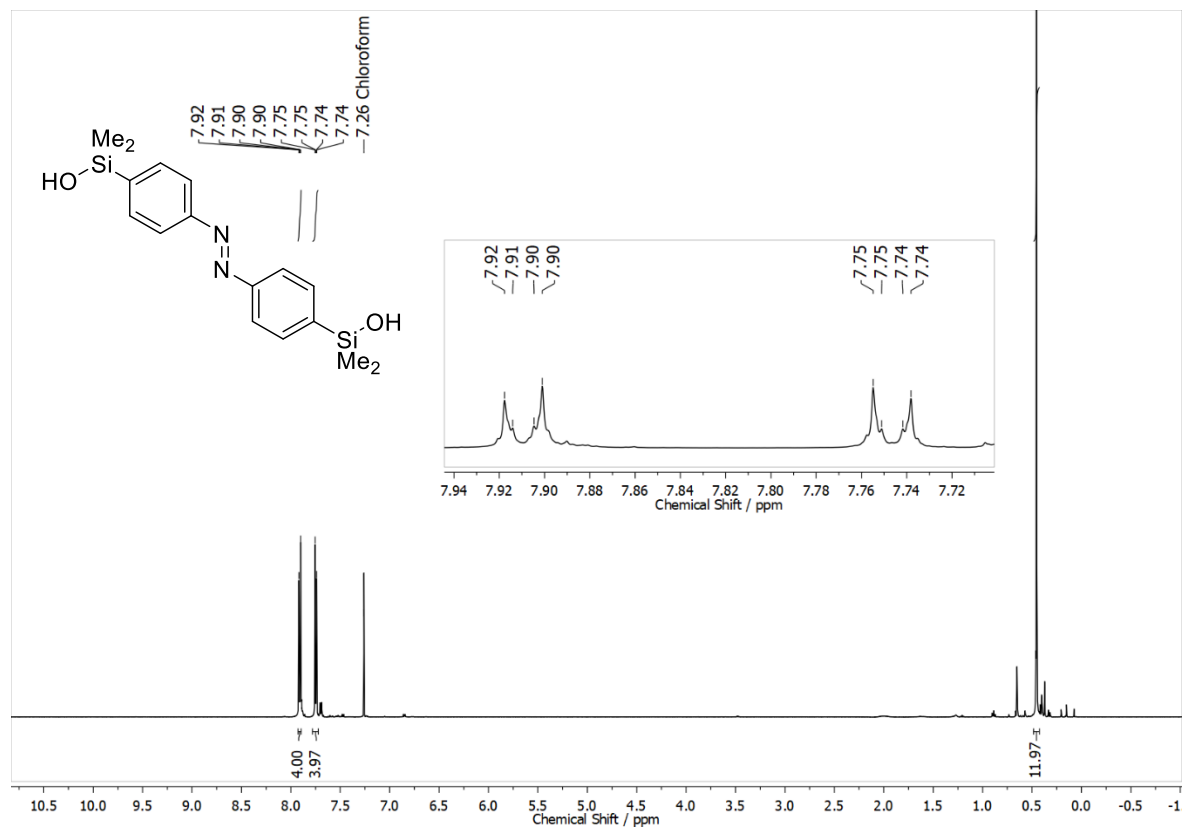


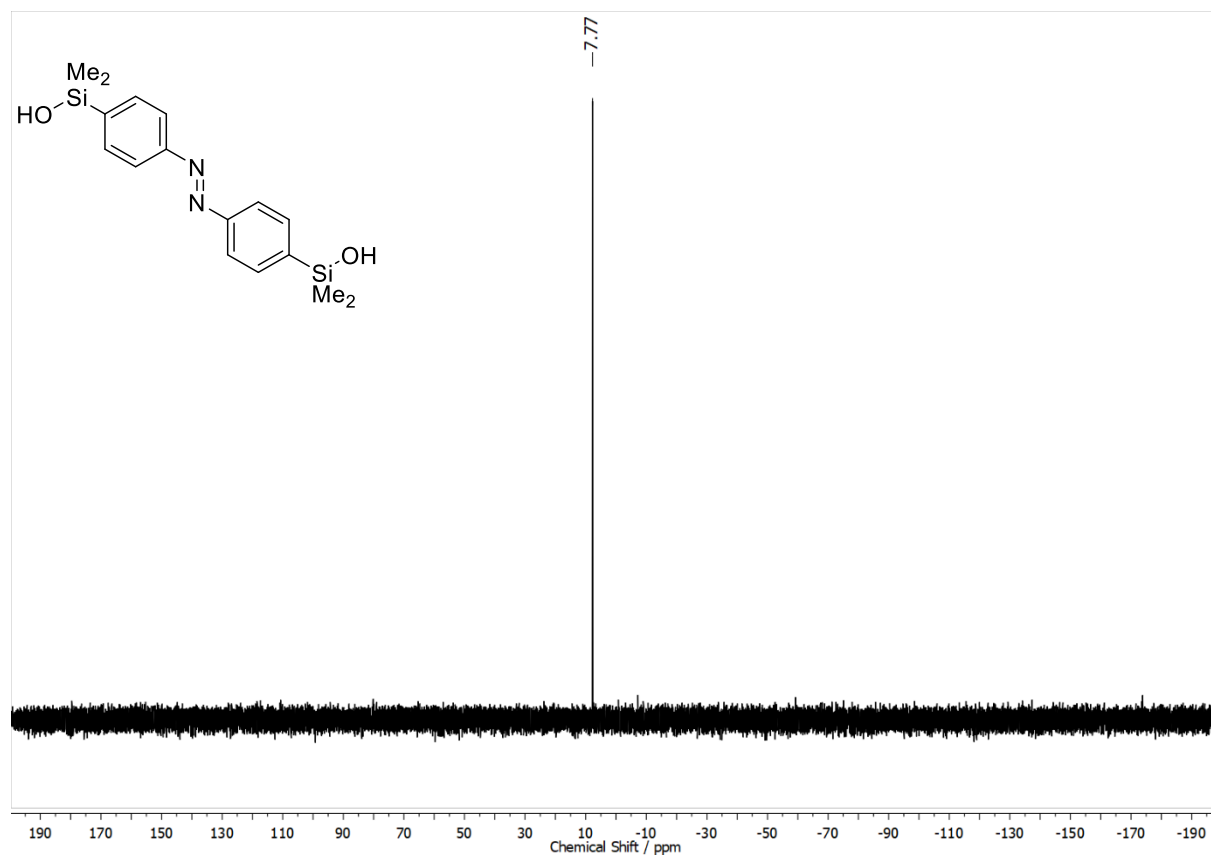
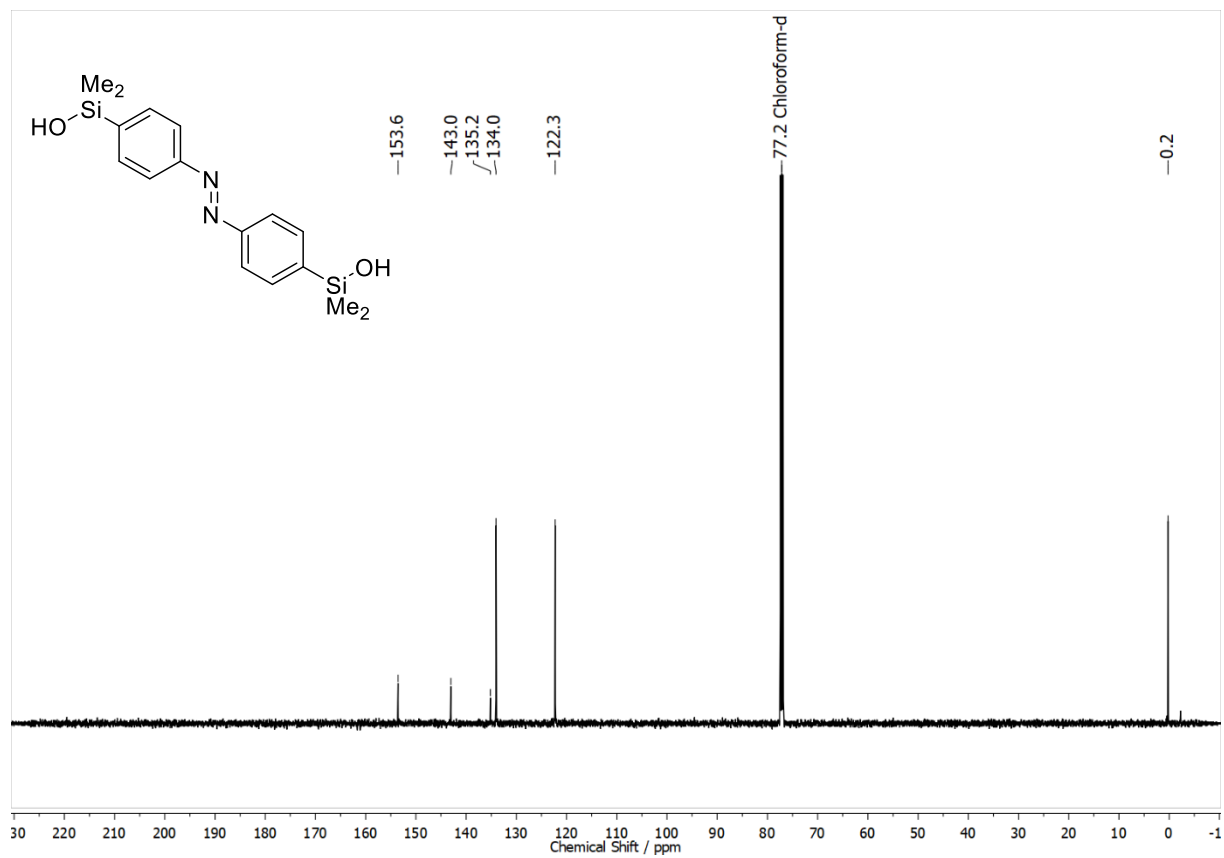
^1H , $^{13}\text{C}\{^1\text{H}\}$ and $^{129}\text{Sn}\{^1\text{H}\}$ Spectra of 4,4'-Bis(trimethylstannyl)azobenzene in Chloroform-d



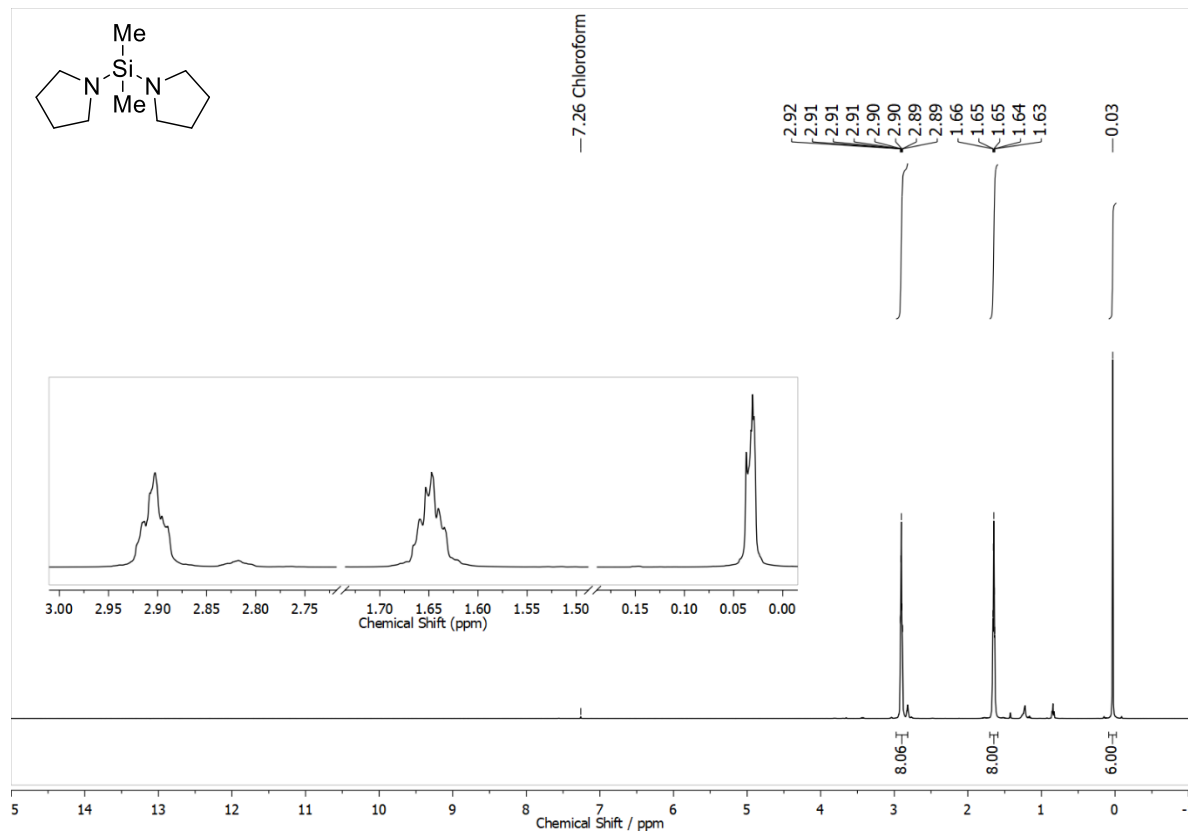


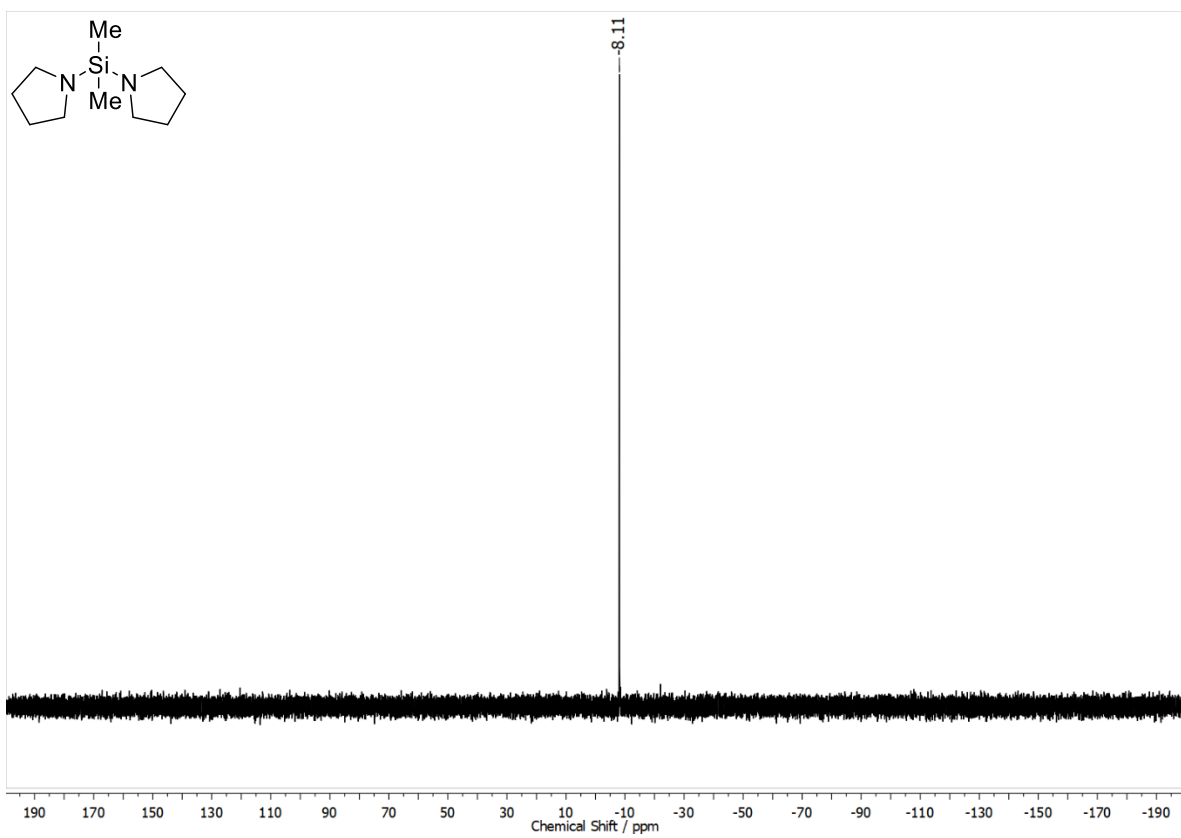
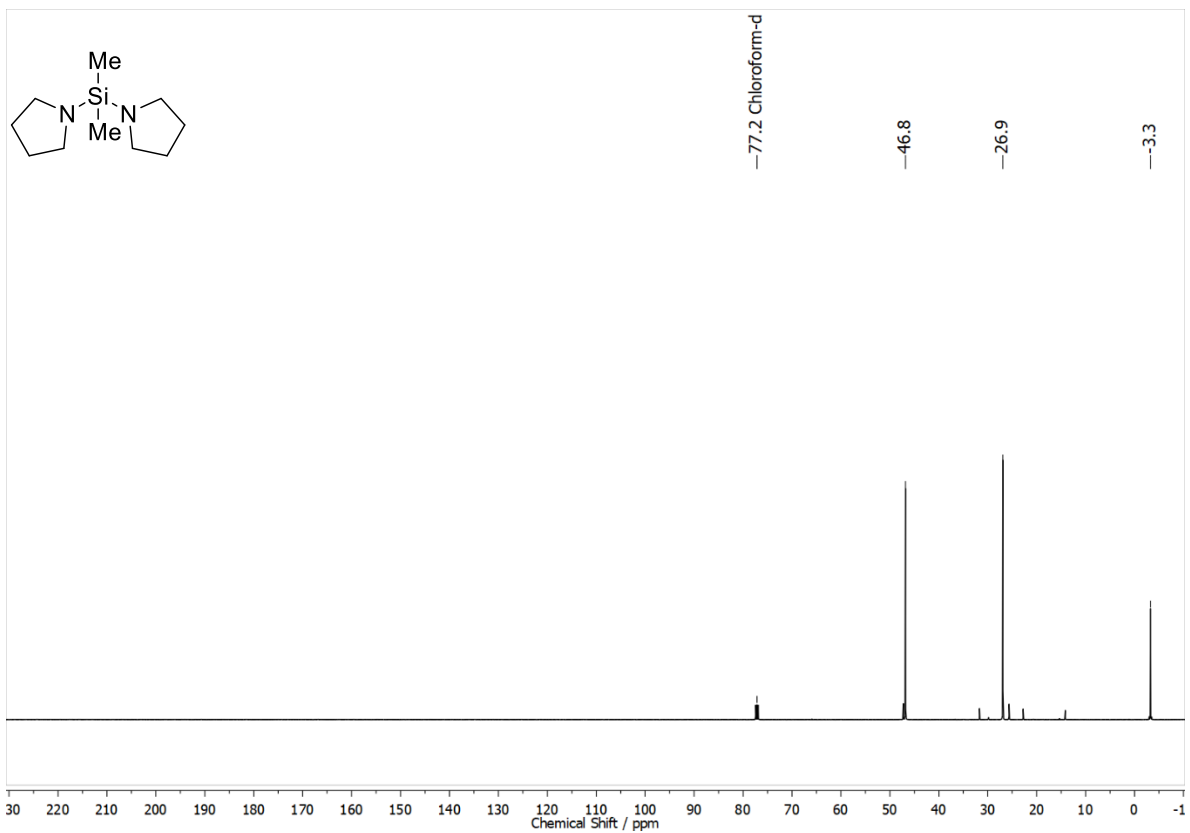
^1H , $^{13}\text{C}\{^1\text{H}\}$ and $^{29}\text{Si}\{^1\text{H}\}$ Spectra of 4,4'-Bis(hydroxydimethylsilane)azobenzene in Chloroform-d



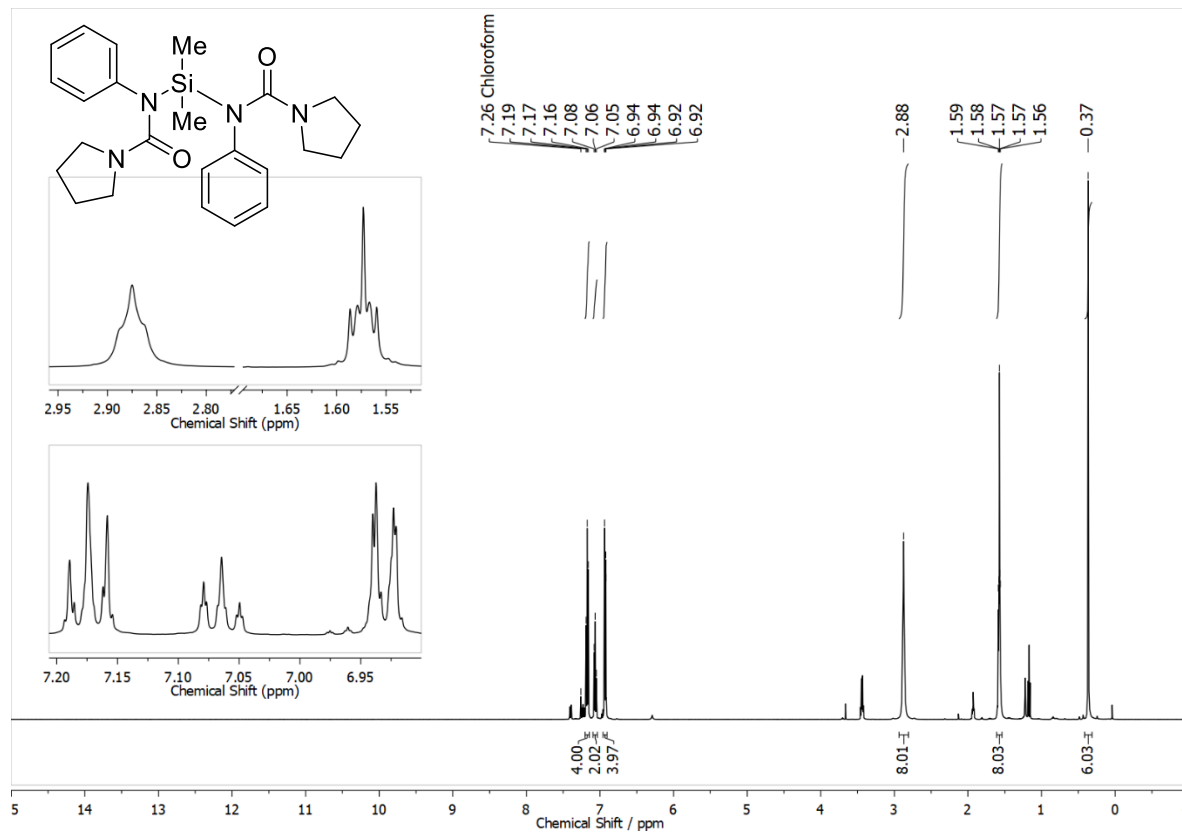


^1H , $^{13}\text{C}\{^1\text{H}\}$ and $^{29}\text{Si}\{^1\text{H}\}$ Spectra of Bis(Pyrrolidinyl)dimethylsilane in Chloroform-d

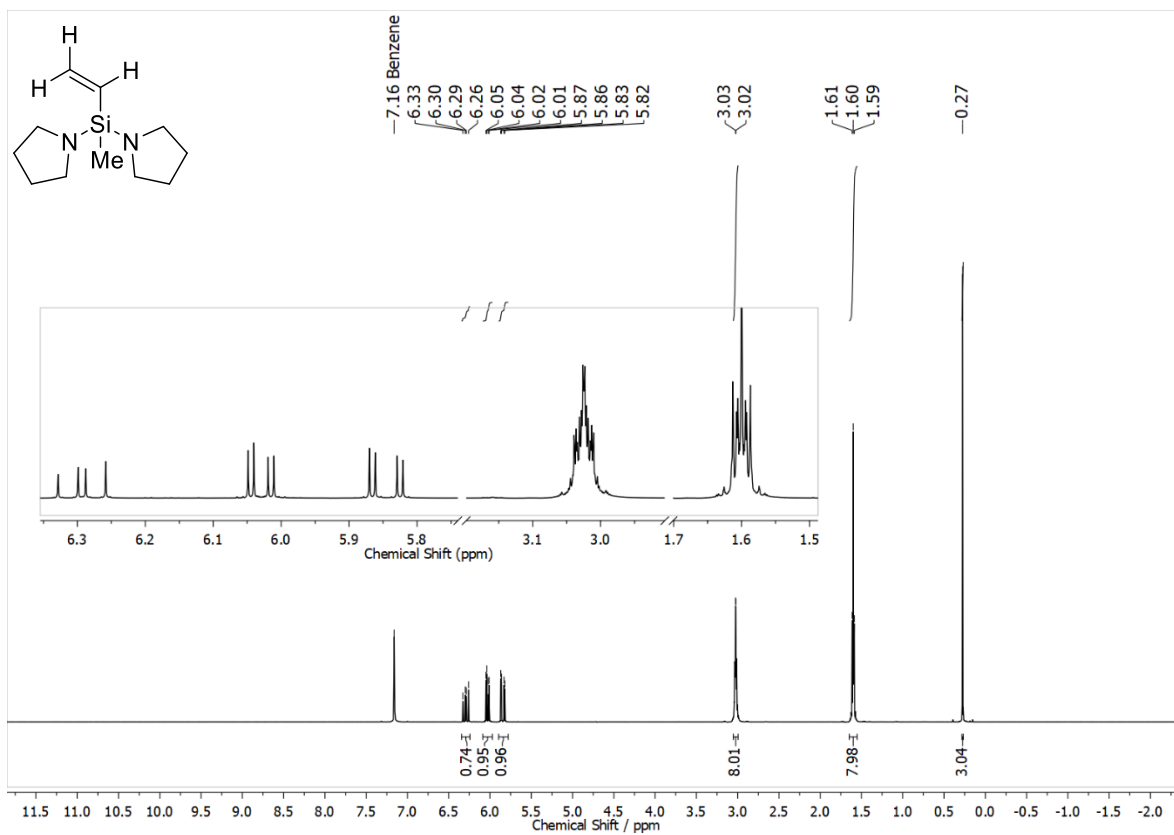


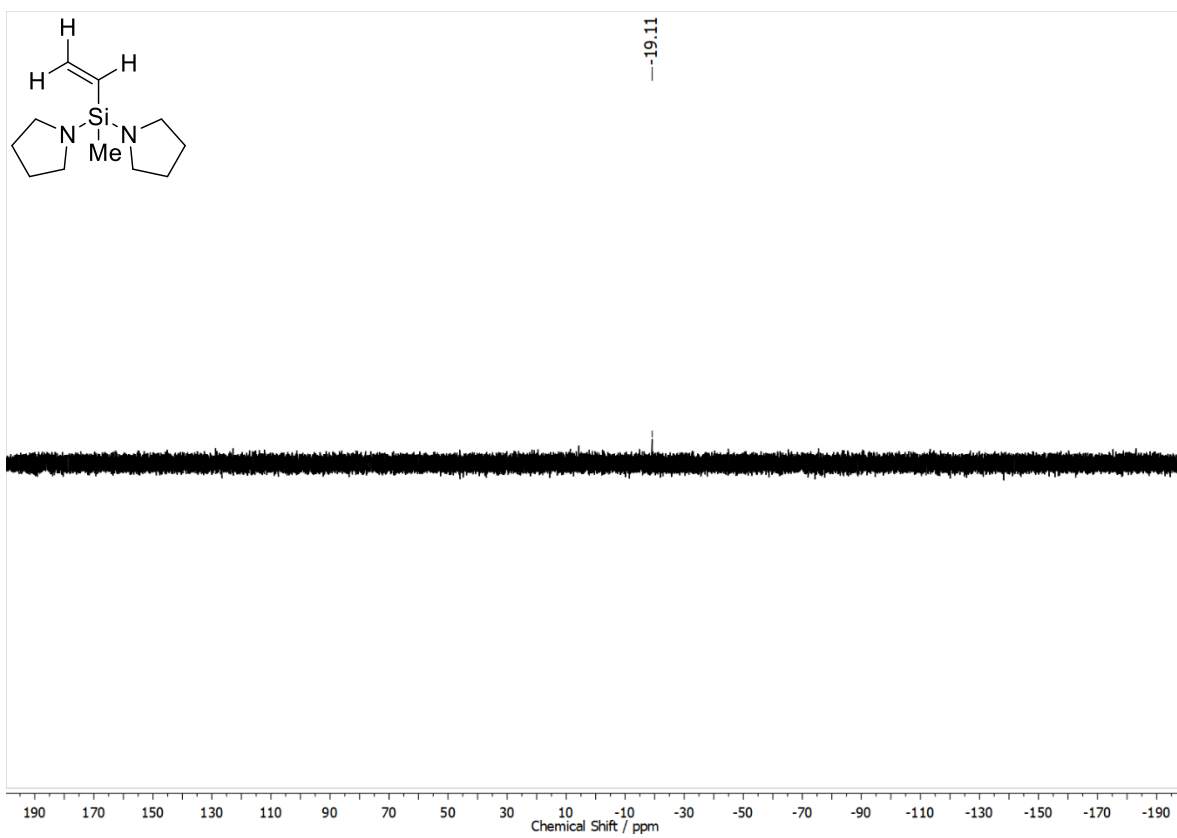
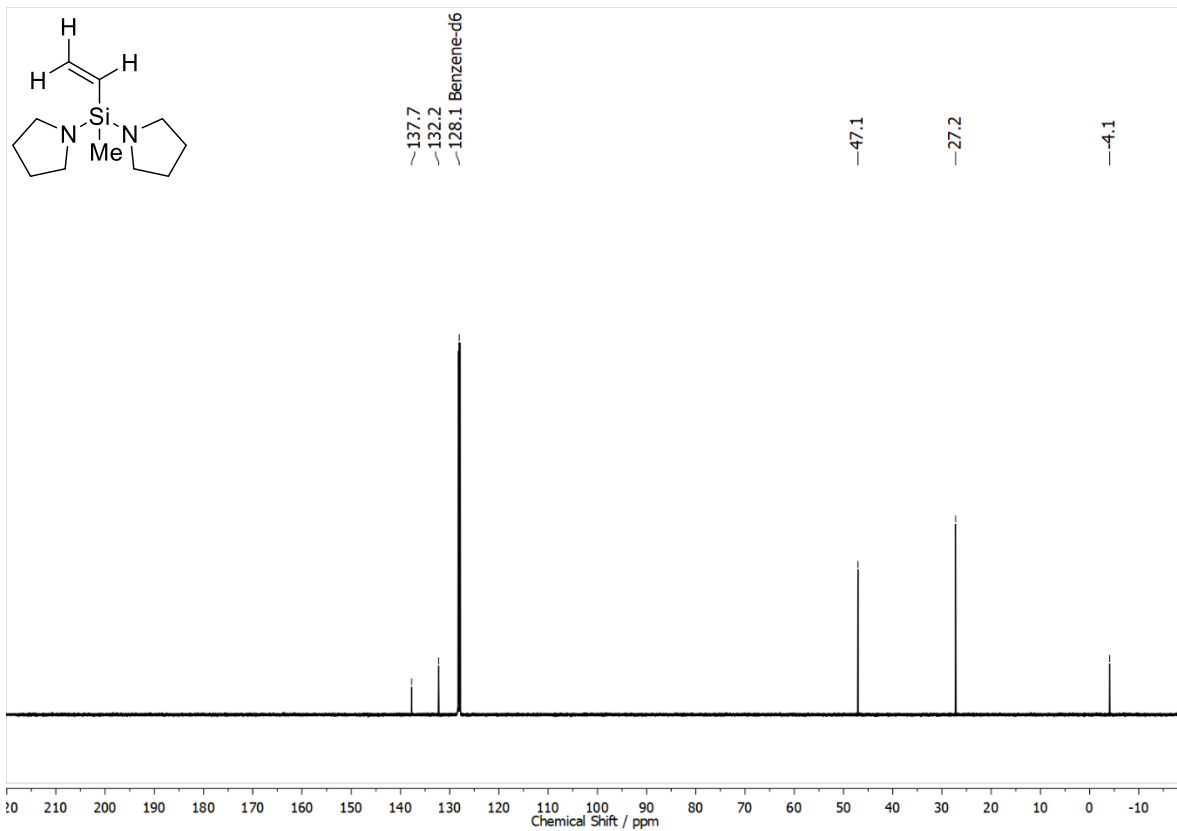


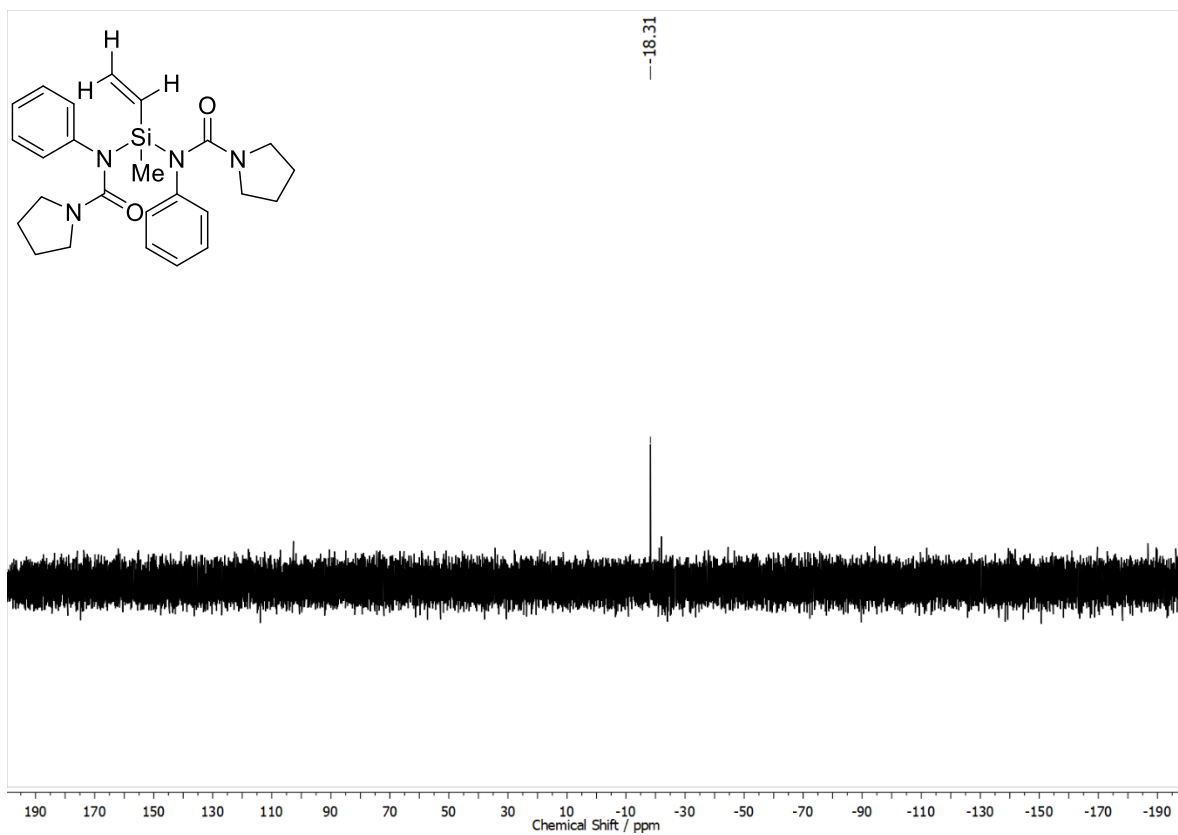
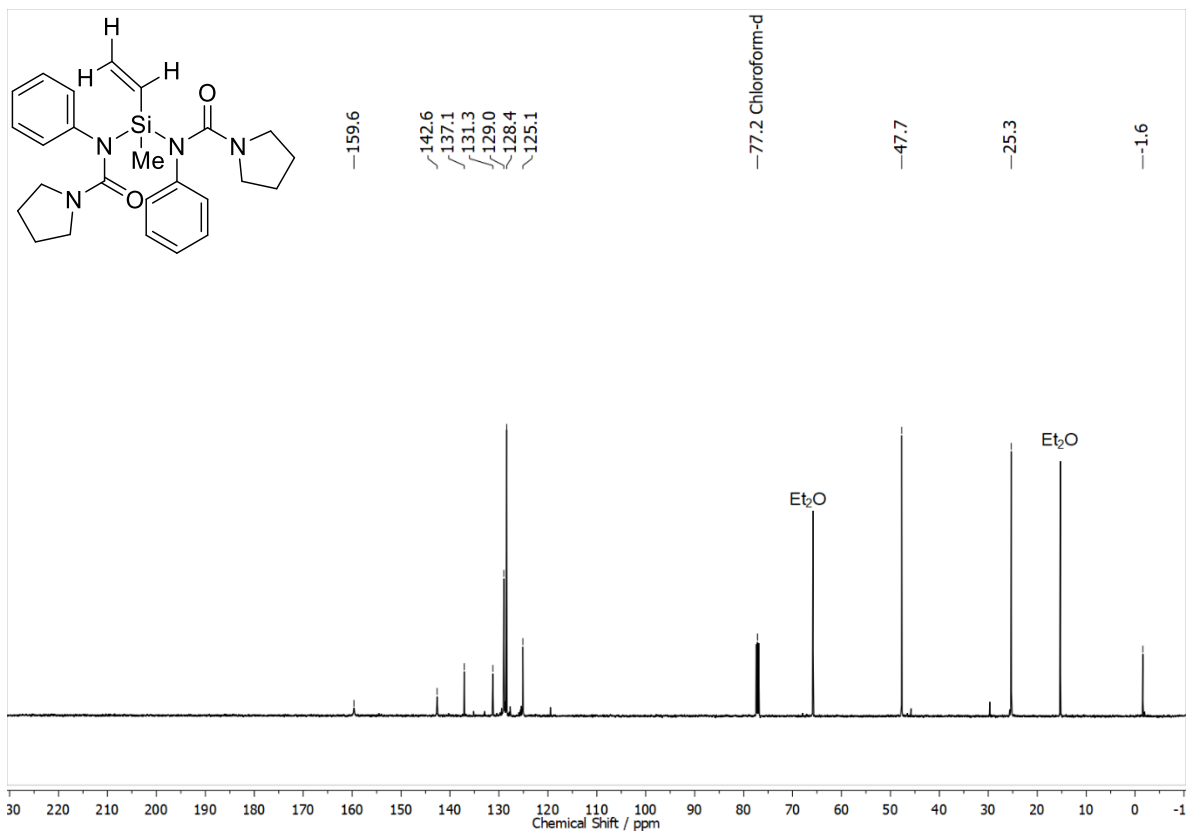
^1H , $^{13}\text{C}\{^1\text{H}\}$ and $^{29}\text{Si}\{^1\text{H}\}$ Spectra of Bis(N-phenyl-N-pyrrolidinecarbonylamino)dimethylsilane in Chloroform-d



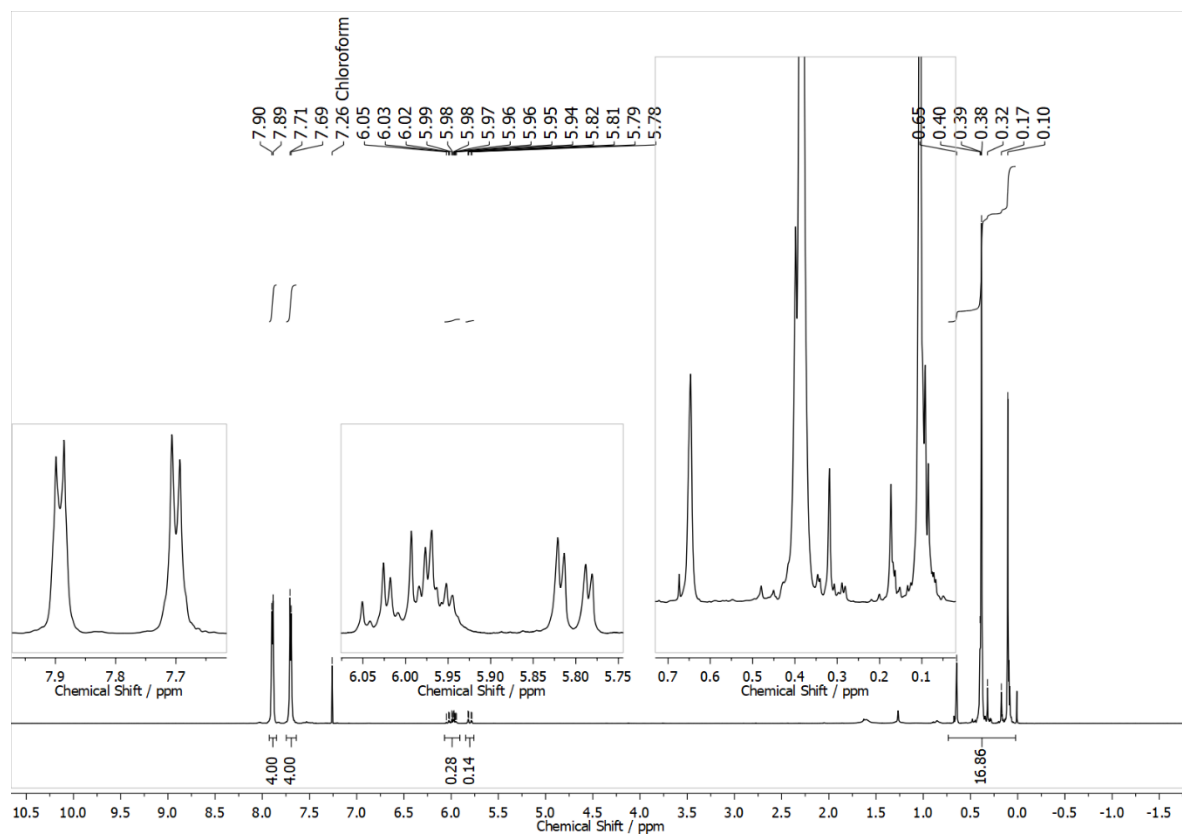
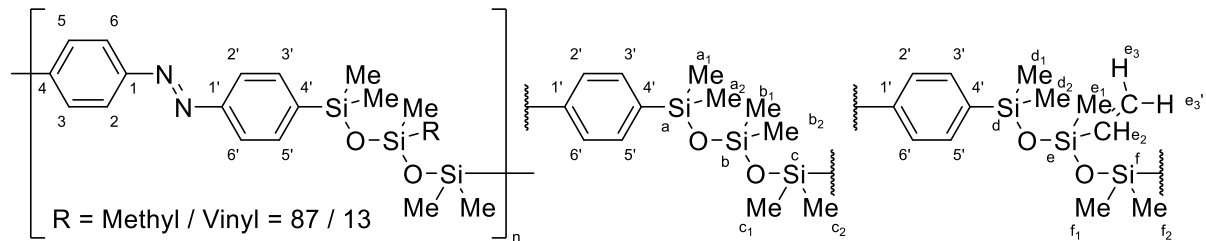
^1H , $^{13}\text{C}\{^1\text{H}\}$ and $^{29}\text{Si}\{^1\text{H}\}$ Spectra of Bis(pyrrolidinyl)methylvinylsilane in Benzene- d_6

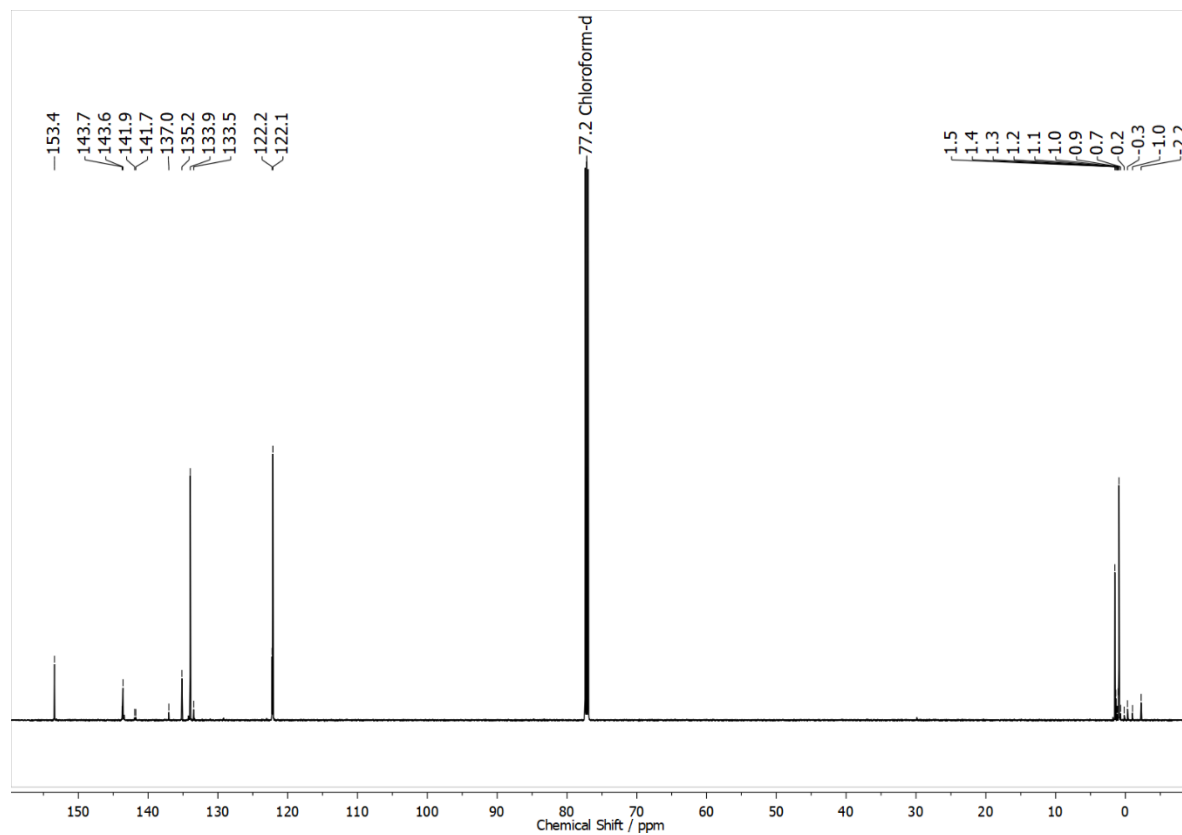
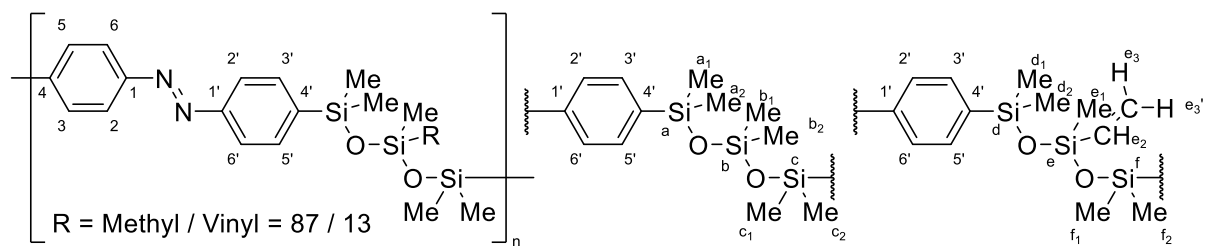


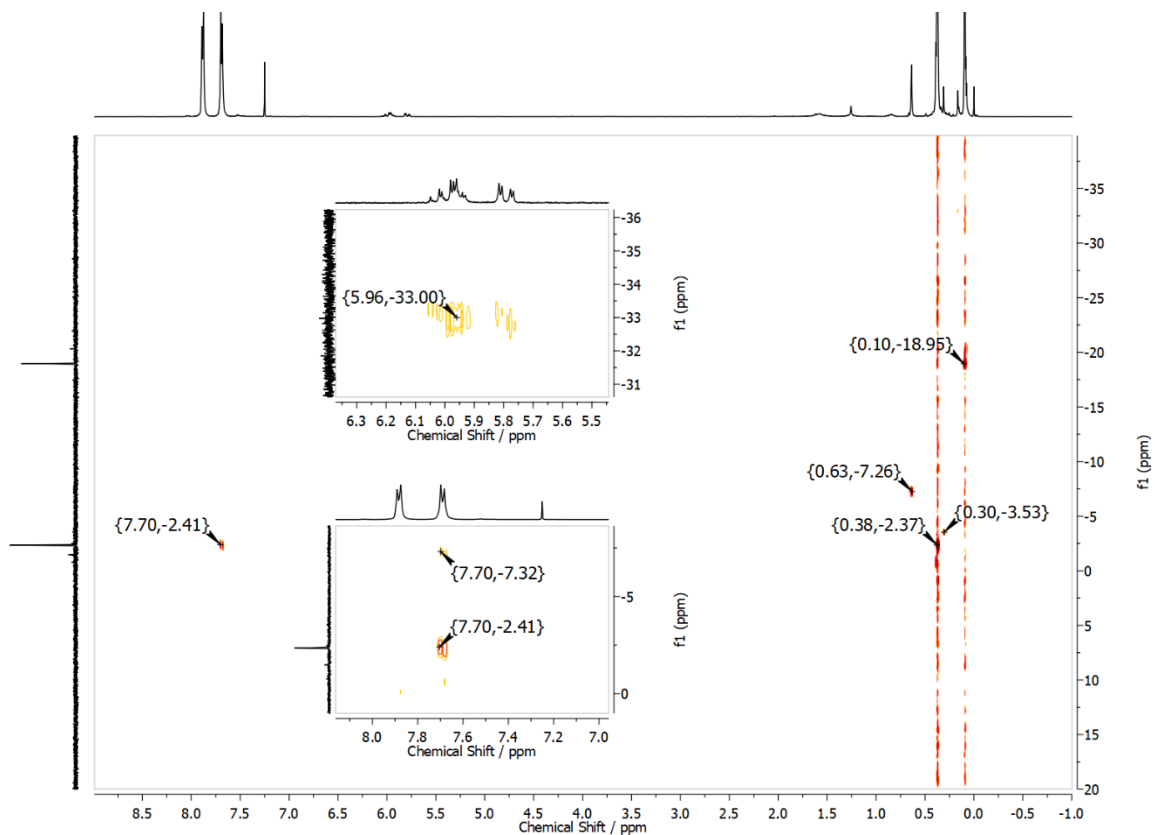
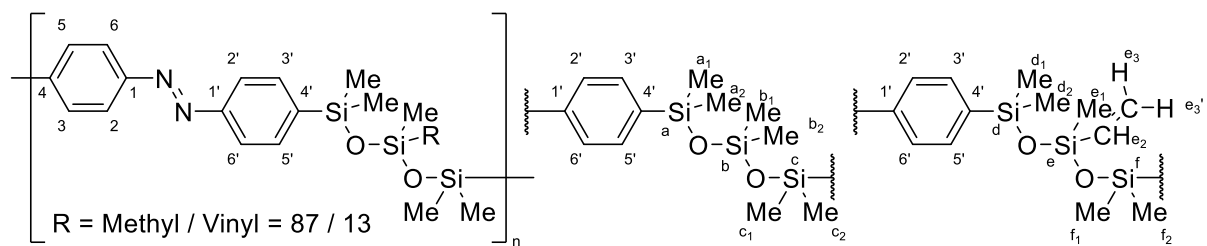




^1H , $^{13}\text{C}\{^1\text{H}\}$ and $^{29}\text{Si}\{^1\text{H}\}$ HMBC Spectra of Poly(4,4'-azobenzene-alt-(hexamethyl-trisiloxane)-stat-(1,1,3,5,5-pentamethyl-3-vinyl-trisiloxane)) (3) in Chloroform-d







10. Inference and Outlook

As intended, interconnected tetrapodal network of ZnO centered HNIs were successfully synthesized and assessed. The relative PL intensity of T-ZnO was detected to depend on the charge transfer mechanism occurring at the nano-interfaces of T-ZnO and fullerenes. Direct contact between the T-ZnO and C₆₀ structures enhanced the relative intensity of the 3.31 eV emission. Additionally, the composite displayed excellent gas sensing abilities, i.e., for ethanol vapors, ~35% gas response with a 90% recovery. Activated carbon coated T-ZnO network catalyzed the reduction of a highly toxic industrial contaminant, Cr(VI). This carbon-based nanocomposite demonstrated an excellent 97% removal efficiency of Cr(VI) at pH 2. The objective of combining the desirable attributes of both T-ZnO (thermal conductivity at low temperature) and MWCNTs (high electrical conductivity) was successfully optimized in the given report: The composite (T-ZnO/MWCNTs) exhibited significantly improved electronic conductivity at a wide temperature range and thermal conductivity at low temperatures in comparison to hollow tetrapodal MWCNTs. Morphological and Raman studies of these HNIs were performed and their compositional aspects were correlated to their macroscopic properties. The strain comparison tests performed on the PC fibers showed that the electrospun PCL with 1% (w/v) T-ZnO fibers have 58% higher ultimate strain than the pristine PCL fibers. Adhesive strength of the PCL fibers with 5% (w/v) T-ZnO was enhanced to 10.4 MPa as compared to the 5% (w/v) spherical particles (3.3 MPa) from 1.6 MPa of the pristine PCL fibers. The tetrapods as opposed to the spherical ZnO created rose stem-like structures which enhanced the bacterial resistance of the PCL membranes. After the shape and concentration optimization of ZnO concerning its antimicrobial activity, the PCL/T-ZnO composite was verified to be a highly suitable scaffold for cell growth.

During compositional analyses, key properties of all these HNIs displayed a high dependence on the surface defects of T-ZnO. As an outlook, in-depth analyses of defects and an improved real structure-to-property relation provide further information into creating a more regulated environment for various activities.

Damage control and preventive reporting being a pivotal goal of this study was achieved by producing spiropyran based self-reporting PTU composite. Spiropyran demonstrated mechanochromism, photochromism and thermochromism without a covalent integration

into the matrix. The experimental results in the *first article of section 7* highlights the interconnected T-ZnO network has high potential as optical and mechanical reinforcement. The optimization was based on balancing the composition ratio between T-ZnO and spiropyran in order to achieve the highest trio stimuli response of the material. Up to a certain concentration (1.5 wt%), multiple reflections caused by the prism-like ZnO enhanced the photochromic property of spiropyran. Above 2 wt% of the polymer matrix, ZnO acted as a UV light blocker, this was verified the declining photochromic activity of spiropyran in the UV-Visible spectrometer. The self-developed periodic impact test demonstrated an increase in mechanical impact stability with increasing concentration of ZnO. Compatibility tests performed in the presented work revealed higher stability of spiropyran in PTU than in Epoxy. Since Epoxy is a highly applicable polymer, other molecular switches that are less reactive towards epoxy resin and its amine-based hardeners has to be developed and tested. On the other hand, reinforced PTU with the mechanochromic additive, spiropyran behaved like an ideal accumulated force reporter, indicating damage before the material failed. This GFRPC with dispersed spiropyran changed its color at the point of impact under the accumulated stress test well before the visible cracks appeared. This proves the uniform distribution of the mechanochrome in the polymer matrix enables location of the impact before the damage deepens. Rather than an abrupt color conversion, the mechanochrome exhibited a gradual change, whose co-relation to impact force was quantified, foreshadowing a material failure. For advanced applications further studies on color-to-impact relations must be carried out to enable well-defined maintenance and interaction protocols. In all of these self-reporting PC studies the concentration of spiropyran was kept as low as possible (0.5 wt%) to reduce production costs.

The hybrid materials fabricated during the course of this study has a vast scope: To further improve the self-reporting properties of spiropyran as a composite, evolution of its mechanochromism in response to different types of mechanical force in a polymer matrix must be studied in detail. Effects of different types of damages on a self-reporting PC is another discipline which requires further theoretical and experimental assessment.

For efficient sensing in applications where the materials endure high strain requires alignment of the self-reporters in the direction of the applied force. This was achieved by centrifugally spinning spiropyran functionalized PMA. Due to the low structural integrity of

PMA, a fraction of PMMA was spun along as a structural stabilizer. Resulting fibers from the polymer blend revealed localized strain at 640% elongation through a clear change of color.

A prospect would be to spin fibers of spiropyran functionalized PMMA and to observe its response to force.

Lastly, the other molecular switch, azobenzene in a cross-linkable polysiloxane, displayed prominent photomechanical effects in response to UV and blue light irradiation. Height differences of the poly(silazobenzyl-siloxane) thin film was successfully tracked under AFM. Furthermore, poly(silazobenzyl-siloxane) must be crosslinked and the effects of cross-linking on the switching abilities of azobenzene must be investigated.

Based on the analytical understanding procured through the course of this work a solvent-free, an environmentally friendly and an efficient method of nanocomposite production could be pursued. Presented self-reporting material when developed further can be lifesaving. Large-scale appliances such as windmills, marinetime and airspace transportation, create excessive waste due to lower lifespan which is a result of inefficient maintenance. Incorporation of self-reporters into the most vulnerable parts of a machine helps indicate damages at a premature stage, with which preservation of heavy machinery comes to be feasible and aids in resolving these issues. The results obtained through the given study lays the prospect of fundamental understanding for monitoring the effects of external stimuli on structural components in operando.

List of abbreviations

AFM	Atomic Force Microscopy
Epoxy	Cross-Linked Epoxy Resin
FTS	Flame Transport Synthesis
GFRPC	Glassfiber Reinforced Polymer Composite
HDI	Hexamethylene Diisocyanate
HNI	Hybrid Nano Interfaces
MWCNT	Multi-Walled Carbon Nanotubes
NDT	Non-Destructive Technique
PC	Polymer Composite
PCL	Poly(Caprolactone)
PDMS	Polydimethylsiloxane
PETMP	Pentaerythritol Tetrakis(3-Mercaptopropionate)
PL	Photo-Luminescence
PMA	Polymethacrylate
PMMA	Polymethylmethacrylate
PTU	Polythiourethane
PU	Polyurethane
PVB	Polyvinyl Butane
SEM	Scanning Electron Microscopy
T-ZnO	Tetrapodal Zinc Oxide
UV	Ultraviolet
WBT	Wind Turbine Blade

List of Publications

1. S. Shree, M. Schulz-Senft, N.H. Alsleben, Y.K. Mishra, A. Staubitz, R. Adelung, Light, Force, and Heat: A Multi-Stimuli Composite that Reveals its Violent Past, *ACS Appl. Mater. & Interfaces*, **2017**, 9, 38000.
2. S. Shree, M. Schulz-Senft, N.H. Alsleben, Y.K. Mishra, A. Staubitz, R. Adelung, Mechanochromic Matrix Predicts Impact Induced Damage in a Reinforced Polymer Composite, **2019** (under revision).
3. S. Shree, M. Schulz-Senft, X. Jin, Y.K. Mishra, A. Staubitz, R. Adelung, Spiropyran Based Smart Composites: Memorizing Polymer with Enhanced Molecular Switches, *3rd Int. Conf. on Nanotechnologies and Biomedical*, **2016**, 55, 146
4. R.A. Colaco, S. Shree, L. Siebert, M. Schulz-Senft, S. Schultzke, R. Adelung, A. Staubitz, Self-Reporting Micro-Fibers from Polymer Blends: A Study on Photochromic and Mechanochromic Sensitivity, *ACS Appl. Mater. & Interfaces*, **2019** (submitted).
5. M. Schulz-Senft, S. Shree, J. Strueben, X. Jin, D.P. Soto, R. Adelung, A. Staubitz, Reversible Volume Switching of Poly(silazobenzyl-siloxane), **2019** (in preparation)
6. S. Hansen, S. Shree; G. Neubüser; J. Carstensen; L. Kienle; R. Adelung. Corset-like Solid Electrolyte Interface for Fast Charging of Silicon Wire Anodes, *J. Power Sources*, **2018**, 381, 8.
7. D. Smazna, S. Shree, M. Hoppe, L. Hansen, J. Marx, J. Dittman, Z. Kareh, B. Fiedler H. Kersten, R. Adelung, Surface Modification of Highly Porous 3D Networks via Atmospheric Plasma Treatment, *Contrib. to Plasma Phys.*, **2018**, 58, 384.
8. D. Smazna, S. Shree, O. Polonskyi, S.V. Lamaka, M. Baum, M. Zheludkevich, F. Faupel, R. Adelung, Y.K. Mishra, Mutual Interplay of ZnO Micro- and Nanowires and Methylene Blue During Cyclic Photocatalysis Process, *J. Environ. Chem. Eng.*, **2019**, 7, 103016
9. A. Nasajpour, S. Mandla, S. Shree, E. Mostafavi, R. Sharifi, A. Khalilpour, S. Saghazadeh, S. Hassan, M.J. Mitchell, J. Leijten, X. Hou, A. Moshaverinia, N. Annabi, R. Adelung, Y.K. Mishra, S.R. Shin, A. Tamayol, A. Khademhosseini, Nanostructured Fibrous Membranes with Rose Spike-Like Architecture, *Nano Lett.*, **2017**, 17, 6235
10. D. Smazna, J. Rodrigues, S. Shree, V. Postica, G. Neubuser, A.F. Martins, N.B. Sedrine, N.K. Jena, L. Siebert, F. Schutt, O. Lupan, R. Ahuja, M.R. Correia, T. Monteiro, L. Kienle, Y. Yang, R. Adelung, Y.K. Mishra, Buckminsterfullerene Hybridized Zinc Oxide Tetrapods: Defects and Charge Transfer Induced Optical and Electrical Response. *Nanoscale*, **2018**, 10, 10050

11. D. Smazna, N. Wolff, S. Shree, F. Schütt, Y.K. Mishra, L. Kienle, R. Adelung, Enhancing the Conductivity of ZnO Micro- and Nanowire Networks with Gallium Oxide, *IEEE 7th Int. Conf. Nanomater. Appl. Prop. N.*, **2017**.
12. J. Pöhls, F. Schütt, C. O'Neill, S. Shree, M. B. Johnson, Y.K. Mishra, R. Adelung, M.A. White, Thermal and Electrical Transport Properties in Multi-Walled Carbon Nanotube-Coated ZnO Tetrapods and Self-Entangled Multi-Walled Carbon Nanotube Tubes, *Carbon*, **2019**, *144*, 423
13. M. Sharma, M. Joshi, S. Nigam, S. Shree, D.K. Avasthi, R. Adelung, S.K. Srivastava, Y.K. Mishra, ZnO Tetrapods And Activated Carbon based Hybrid Composite: Adsorbents for Enhanced Decontamination of Hexavalent Chromium from Aqueous Solution, *Chem. Eng. J.*, **2019**, *358*, 54.
14. N. Ababii, M. Hoppe, S. Shree, A. Vahl, M. Ulfa, T. Pauporté, B. Viana, V. Cretu, N. Magariu, V. Postica, V. Sontea, M.-I. Terasa, O. Polonskyi, F. Faupel, R. Adelung, O. Lupan, Effect of Noble Metal Functionalization and Film Thickness on Sensing Properties of Sprayed TiO₂ Ultra-Thin Films, *Sensor Actuat A-Phys.*, **2019**, *293*, 242.
15. O. Lupan, V. Postica, N. Ababii, T. Reimer, S. Shree M. Hoppe, O. Polonskyi, V. Sontea, S. Chemnitz, F. Faupel, R. Adelung, Ultra-Thin TiO₂ Films by Atomic Layer Deposition and Surface Functionalization with Au Nanodots for Sensing Applications, *Mater. Sci. Semicond. Process.*, **2018**, *87*, 44.
16. I. Paulowicz, V. Postica, O. Lupan, N. Wolff, S. Shree, A. Cojocar, M. Deng, Y.K. Mishra, I. Tiginyanu, L. Kienle, R. Adelung, Zinc Oxide Nanotetrapods with Four Different Arm Morphologies for Versatile Nanosensors, *Sensor Actuat B-Chem.*, **2018**, *262*, 425.
17. A. Vahl, J. Dittmann, J. Jetter, S. Veziroglu, S. Shree, N. Ababii, O. Lupan, O. C. Aktas, T. Strunskus, E. Quandt, R. Adelung, S. K. Sharma, F. Faupel, The Impact of O₂/Ar Ratio on Morphology and Functional Properties in Reactive Sputtering of Metal Oxide Thin Films, *Nanotechnology*, **2019**, *30*, 235603.
18. L. Ghimpu, V.V. Ursaki, A. Pantazi, R. Mesterca, O. Brâncoveanu, S. Shree, R. Adelung, I.M. Tiginyanu, M. Enachescu, Characterization of Core/Shell Structures Based on CdTe and GaAs Nanocrystalline Layers Deposited on SnO₂ Microwires, **2018**, *116*, 6

Acknowledgements

Honored is what I feel to be amidst brilliant minds and it is humbling to be given a chance to acknowledge all the help I received during my research. I have immense gratitude for my doctor father, Prof. Rainer Adelung. His positive energy, motivating nature and his vast knowledge in multidisciplinary subjects taught me and several other scientists a new way of research. He always said there is something to learn from everything, no data is useless. I thank him for giving the opportunity to write my doctoral thesis under his supervision.

I have met my fair share of strong and confident women, Prof. Anne Staubitz is definitely one of them. I can say that I feel proud to have worked with her. Having an incredibly friendly personality she welcomes a collaboration from anyone and everyone irrespective of their scientific background. Combination of these two professors was tailor-made, creative, spontaneous and meticulous, I appreciate them both for keeping an open mind to all the odd ideas and experiments I came up with.

I could not have asked for better collaborators than Mathias Schulz-Senft and Shuo Li. They warm-heartedly welcomed me into their group and entertained every trivial and primitive questions or theories I had. Without Mathias Schulz-Senft providing me material and his expertise I would have not accomplished anything that is included in this thesis.

Dr. habil. Yogendra Kumar Mishra deserves my heartfelt admiration, because his guidance and perseverance was what helped me publish my scientific work. Also, under his supervision I received the opportunity to work with several esteemed material scientists.

Dr. Sören Kaps, Dr. Sandra Hansen, Dr. Fabian Schütt, Daria Smazna, Dr. Iris Hölken, Dr. Alajocaru, Dr. Martina Baum and Leonard Siebert are excellent co-workers who included me in their projects which helped me broaden my analytical knowledge. I thank them all for sharing their expertise and helping me through my doctoral study.

Katrin Brandenburg and Beate Minten deserve special mention for all their administrative support and I thoroughly enjoyed all our little friendly conversations.

Of course, none of my mechanochromic tests would have been possible without the help of our extraordinary lab engineer Jörg Bahr.

I want to thank Matthias Burmeister, Berndt Neumann and other co-workers at our workshop for being patient and building everything that was needed for my research. I thank them for welcoming me and my Hammer test after I was kicked out all the labs for being too loud.

I was not alone in obtaining all the experimental results, my research assistants (HIWIs), Alina Kuntze, Nils H. Alsleben, Laura Strodtmann Ruchira A Colaco and Ranjith S.C. helped me through it.

The project “C-14, Mechanochromic Polymer Composites” I worked for was funded by the SFB 677, Function by Switching. I enjoyed collaborating with Insa Stamer and Talina Rusch and I thank our coordinator Alexander Schlimm and all the members of the Integrated Research Training Group for organizing the very informative winter and summer schools.

The person who introduced me to this FUN will not go unforgotten, Ingo Paulowicz, was the one who brought me into this wonderful group as my supervisor. I thank him wholeheartedly for that.

It is undeniably a wonderful group; among highly supportive and open-minded individuals no one goes unnoticed and unappreciated. It was a pleasure working with each and every one of them.

I cannot express how much I will miss all the strange but scientific and worldly conversations I had with Mathias Hoppe. We encouraged and criticized each other equally whenever it was needed. I was lucky to have had the chance to share this misery with him. I think I owe him an apologize for all the delays caused by my hours long brainstorming breaks.

I am grateful to many colleagues who kindly helped me, with advices, helpful discussions and instrument introductions. Sincere thanks to: Prof. Dr. Franz Faupel, and his group members. I fully appreciate the corporation I received from Dr. Ulrich Schürmann, Christin Szillus, Prof. Oleg Lupan, Stefan Rehders and many other colleagues in the faculty of engineering in Christian-Albrechts-University of Kiel.

I could stay calm and still have a social life with my increasing forgetful nature during my writing period only due to the support of my crazy but lovely family and my amazing friends: Marleen Schweichel, Ruchira A Colaco, Heather Cavers, Prashanth Velvaluri, Mona Stölting, Jingxiang Su, Niklas Wolff, Xin Jin, Nawwar Salloum, Laila Salloum, Deepika Mishra, Khurram Saleem, Patricia Griem and my friends from home, I can't thank them enough for all the love and support. Their affection kept me afloat. I have to acknowledge my cousin Navya Shree for being my wall, she was one the who had to hear my continuous ranting.

If anyone deserves my unconditional gratitude is Dr. Viktor Hrkac, he is my rock, that I use to throw at others when I cannot handle them. He kept sane because he worried for me, his very important advice was to give him all my worries and just focus of writing, got me through this without much loss (just some grey hairs). I appreciate his patience and his support without which I probably would not have finished this thesis one time.

Dr. Veena Nagaraj, retired head of the chemistry department at Jain university is an inspiration. I cannot thank her enough for she is the reason that I am not lost, her empathic ways of teaching made me who I am. She was the only teacher I saw inspire and encourage every single student of hers. She is one who taught me not fear the chemicals but to respect them, fear leads to mistakes and respect leads to inventions.

I thank my lovely female dominated family for everything they have given me without obligations. I acknowledge all the privilege I received because of their hard work. My uncle Narayana Swamy has been like a father figure in my life, I am forever indebted to him.

Last but most definitely not the least, my mother, I did not have to look outside for a hero, I just observe her go through life she is my strength, my anchor that keeps my grounded. Her wise but peculiar words helped me grow through life. "Never pity yourself, by pitying you deny yourself from all the opportunities" she says every time I feel down.

Declaration

I hereby confirm that my thesis entitled "Interactive Interfaces of Smart Composites" is the result of my independent work. I did not receive any help or support from commercial consultants. All sources and/or materials applied here are listed and specified in the thesis. I also declare that the work was done in compliance with the rules of good scientific practice of the Deutsche Forschungsgemeinschaft

Furthermore, I confirm that this thesis has not yet been submitted as part of another examination process neither in identical nor in similar form.

Place, Date

Signature

Eidesstattliche Erklärung

Hiermit erkläre ich an Eides statt, die Dissertation "Interactive Interfaces of Smart Composites" eigenständig, d.h. insbesondere selbständig und ohne Hilfe eines kommerziellen Promotionsberaters, angefertigt und keine anderen als die von mir angegebenen Quellen und Hilfsmittel verwendet zu haben.

Ich erkläre außerdem, dass die Dissertation weder in gleicher noch in ähnlicher Form bereits in einem anderen Prüfungsverfahren vorgelegen hat.

Ich erkläre außerdem, dass die Arbeit unter Einhaltung der Regeln guter wissenschaftlicher Praxis der Deutschen Forschungsgemeinschaft entstanden ist.

Ort, Datum

Unterschrift

**Rightslink® by Copyright Clearance
Center**<https://s100.copyright.com/AppDispatchServlet>



RightsLink®

Home

Create
Account

Help



Title: ZnO tetrapods and activated carbon based hybrid composite: Adsorbents for enhanced decontamination of hexavalent chromium from aqueous solution

Author: Mahima Sharma, Monika Joshi, Subhasha Nigam, Sindu Shree, Devesh Kumar Avasthi, Rainer Adelung, Sanjeev Kumar Srivastava, Yogendra Kumar Mishra

Publication: Chemical Engineering Journal

Publisher: Elsevier

Date: 15 February 2019

© 2018 Elsevier B.V. All rights reserved.

Please note that, as the author of this Elsevier article, you retain the right to include it in a thesis or dissertation, provided it is not published commercially. Permission is not required, but please ensure that you reference the journal as the original source. For more information on this and on your other retained rights, please visit: <https://www.elsevier.com/about/our-business/policies/copyright#Authorrights>

Copyright © 2019 [Copyright Clearance Center, Inc.](#) All Rights Reserved. [Privacy statement](#). [Terms and Conditions](#). Comments? We would like to hear from you. E-mail us at customercare@copyright.com



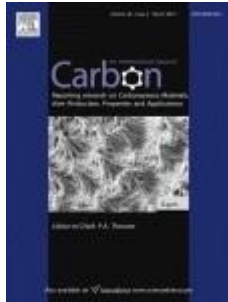
Rightslink® by Copyright Clearance Center
<https://s100.copyright.com/AppDispatchServlet>

RightsLink®

Home

Create Account

Help



Title: Thermal and electrical transport properties in multi-walled carbon nanotube-coated ZnO tetrapods and self-entangled multi-walled carbon nanotube tubes

Author: Jan-Hendrik Pöhls, Fabian Schütt, Catherine O'Neill, Sindu Shree, Michel B. Johnson, Yogendra Kumar Mishra, Rainer Adelung, Mary Anne White

Publication: Carbon

Publisher: Elsevier

Date: April 2019

© 2018 Elsevier Ltd. All rights reserved.

Please note that, as the author of this Elsevier article, you retain the right to include it in a thesis or dissertation, provided it is not published commercially. Permission is not required, but please ensure that you reference the journal as the original source. For more information on this and on your other retained rights, please visit: <https://www.elsevier.com/about/our-business/policies/copyright#Authorrights>

Copyright © 2019 [Copyright Clearance Center, Inc.](#) All Rights Reserved. [Privacy statement](#). [Terms and Conditions](#). Comments? We would like to hear from you. E-mail us at customercare@copyright.com



Home

Create
Account

Help



Title: Nanostructured Fibrous Membranes with Rose Spike-Like Architecture

Author: Amir Nasajpour, Serena Mandla, Sindu Shree, et al

Publication: Nano Letters

Publisher: American Chemical Society

Date: Oct 1, 2017

Copyright © 2017, American Chemical Society

PERMISSION/LICENSE IS GRANTED FOR YOUR ORDER AT NO CHARGE

This type of permission/license, instead of the standard Terms & Conditions, is sent to you because no fee is being charged for your order. Please note the following:

- Permission is granted for your request in both print and electronic formats, and translations.
- If figures and/or tables were requested, they may be adapted or used in part.
- Please print this page for your records and send a copy of it to your publisher/graduate school. Appropriate credit for the requested material should be given as follows: "Reprinted (adapted) with permission from (COMPLETE REFERENCE CITATION). Copyright (YEAR) American Chemical Society." Insert appropriate information in place of the capitalized words.
- One-time permission is granted only for the use specified in your request. No additional uses are granted (such as derivative works or other editions). For any other uses, please submit a new request.



Home

Create
Account

Help



Title: Light, Force, and Heat: A MultiStimuli Composite that Reveals its Violent Past

Author: Sindu Shree, Mathias Schulz- Senft, Nils H. Alsleben, et al

Publication: Applied Materials

Publisher: American Chemical Society

Date: Nov 1, 2017

Copyright © 2017, American Chemical Society

PERMISSION/LICENSE IS GRANTED FOR YOUR ORDER AT NO CHARGE

This type of permission/license, instead of the standard Terms & Conditions, is sent to you because no fee is being charged for your order. Please note the following:

- Permission is granted for your request in both print and electronic formats, and translations.
- If figures and/or tables were requested, they may be adapted or used in part.
- Please print this page for your records and send a copy of it to your publisher/graduate school. Appropriate credit for the requested material should be given as follows: "Reprinted (adapted) with permission from (COMPLETE REFERENCE CITATION). Copyright (YEAR) American Chemical Society." Insert appropriate information in place of the capitalized words.
- One-time permission is granted only for the use specified in your request. No additional uses are granted (such as derivative works or other editions). For any other uses, please submit a new request.



Rightslink® by Copyright Clearance Center
<https://s100.copyright.com/AppDispatchServlet>

RightsLink®

Home

Account
Info

Help

SPRINGER NATURE

Title: Spiropyran Based Smart Composites: Memorizing Polymer with Enhanced Molecular Switches

Author: S. Shree, M. Schulz-Senft, X. Jin et al

Publication: Springer eBook

Publisher: Springer Nature

Date: Jan 1, 2016

Copyright © 2016, Springer Science Business Media Singapore

Copyright © 2019 [Copyright Clearance Center, Inc.](#) All Rights Reserved. [Privacy statement](#). [Terms and Conditions](#). Comments? We would like to hear from you. E-mail us at customercare@copyright.com